Model of cosmic ray generation

V. P. Vlasov and B. A. Trubnikov

Kurchatov Institute, 123182 Moscow, Russia

S. K. Zhdanov

Moscow State Engineering Physics Institute, 115409 Moscow, Russia
(Submitted 2 June 1995; resubmitted 23 September 1996)
Zh. Éksp. Teor. Fiz. **111**, 385–403 (February 1997)

It is shown that the two bends observed in the cosmic ray energy spectrum can be well approximated by equations derived by assuming that cosmic rays can be generated and accelerated in plasma pinches. © *1997 American Institute of Physics.* [S1063-7761(97)00102-9]

1. THE PROBLEM OF BENDS IN THE COSMIC RAY SPECTRUM

The subject of the article is the origin of galactic cosmic rays and their spectrum, various parts of which are shown in Figs. 1–3.

The most widely accepted hypothesis is that cosmic ray particles are accelerated at shock fronts generated by supernova explosions (see Ref. 1 and the literature cited therein). We note that the explosion of a supernova generates a one-time, single expanding shock wave, but, for example, the Crab Nebula (a supernova remnant) continuously emits synchrotron radiation of ultrarelativistic electrons. For this reason a number of theoretical papers favor the hypothesis that cosmic ray particles are accelerated by plasma waves continuously generated by rotation of the central pulsar of a nebula together with its enormous magnetic field. It is therefore assumed here that the principal source of cosmic rays is not the supernova explosion *per se*, but its long-term activity following the explosion.

In the present article we discuss an alternative hypothesis (see Refs. 4–6 and the literature cited therein), specifically the possibility that the particles are accelerated in broken cosmic plasma pinches.

We postulate that closed toroidal magnetic field loops of the type shown in Fig. 4 can occur from time to time in a turbulent cosmic plasma, possibly in the vicinity of supernovae. The gradual constriction of the magnetic torus toward the axis can lead to the formation of a central current-carrying pinch, whose breakup can be accompanied by the acceleration of plasma particles.

More detailed information about the energy spectrum of galactic cosmic rays has appeared in recent years. Two prominent bends are observed in the spectrum: the first at energies of the order of $(3-5)\cdot 10^{15}$ eV and the second at $3\cdot 10^{18}$ eV. However, the cosmic ray spectrum at energies $E>10^{16}$ eV can only be determined by recording the secondary particles of extensive air showers generated in the earth's atmosphere by solitary primary particles. Here the transition from secondary to primary particles is not a trivial matter, and the presence of the first bend in the primary particle spectrum is challenged in Refs. 7 and 8. Conceivably it should be ascribed to a higher energy range (10^{16}–10^{17} eV), and for the energy range 10^{13}–10^{18} eV Nikol'skiĭ[7] proposes the purely approximate, ''bend-free'' expression

$$dN/dE=\text{const}\cdot E^{-\nu},\quad \nu=2.55+0.02\ \ln(2E) \tag{1}$$

(here the proton energy is measured in TeV). We propose to show that equations based on physical notions of the mechanisms of particle acceleration in pinches can be used with a certain choice of parameters to approximate the entire cosmic ray spectrum with all its subtle details.

2. APPROXIMATE EQUATIONS FOR THE COSMIC RAY SPECTRUM

It was first shown in Ref. 4 that the hydrodynamic squeezing of plasma from the waist of a pinch (as from a pipette) with a relativistic plasma gives rise to a spectrum of accelerated particles (commonly called ''pips'')

$$I_0(E)=\text{const}\cdot E^{-\nu},\quad \nu=1+\sqrt{3}, \tag{2}$$

with exponent $\nu=2.732$, which is very close to the actual ''observed'' value for cosmic ray particles (see Fig. 1) with energies $10^{10}\leqslant E\leqslant 3\cdot 10^{15}$ eV.

In addition to the pipette mechanism, however, there is also a second, induction mechanism in the pinch effect: the acceleration of peripheral plasma ions in the induced electric field (see Refs. 5 and 6), which in the ultrarelativistic case leads to a spectrum of the form

$$I_1(E)=C_1E^{-1}e^{(-E/E_1)},\quad E_1=eJ_1/c, \tag{3}$$

where J_1 is the pinch breaking current. If both spectra are summed for the many pinches ascribed to our Galaxy model, we obtain the equation for the total differential spectrum

$$\frac{dN}{dE}=\sum\ I_0+\sum\ I_1=\frac{c_{\text{pip}}}{E^{\nu}}+\frac{S(E)}{E},$$

$$S(E)=\sum_{i=1}^{?}\ C_i\ \exp\left(-\frac{E}{E_i}\right), \tag{4}$$

where c_{pip} and $E_i=eJ_i/c$ are constants. We do not have any information on the statistics of the breaking currents J_i in the Galaxy, but clearly the quantities ν, c_{pip} and the required number of parameters C_i, E_i can be chosen in such a way that an approximation equation can be formulated, reflecting all the nuances in the behavior of the spectrum. A single term in Eq. (4) can describe some kind of narrow peak in the

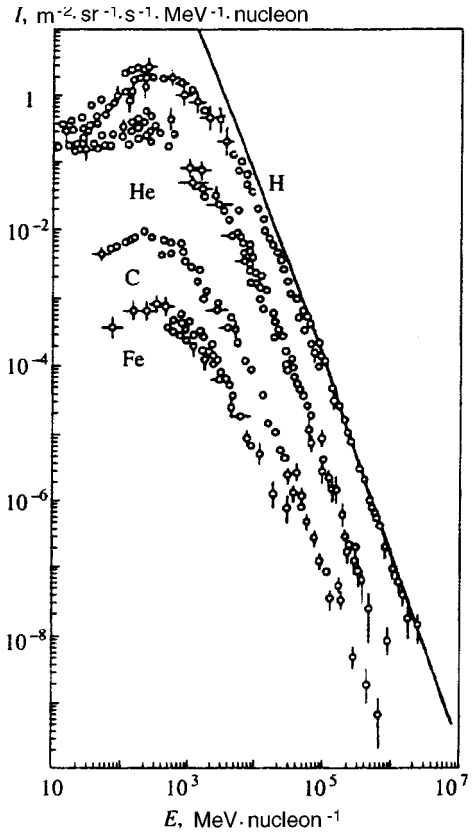

FIG. 1. Differential spectra of cosmic rays from Ref. 1. The straight line represents our approximation (2).

spectrum, while a broad, smooth bend can be attributed to the presence of a group of many continuously distributed currents, which are best analyzed separately.

We consider the following model as an example. We replace the sum $S(E)$ in Eq. (4) by an integral over the ''currents'' $J=eJ_i/c$, writing it in the form $S(E)=\int C(J)\exp(-E/J)dJ$. Assuming many small currents and few large ones, we assume that the function $C(J)$ decays according to a power law and, in addition, is cut off exponentially at high currents according to

$$C(J)=aJ^{-1-p}\ \exp(-J/4E_{\rm gal}), \tag{5}$$

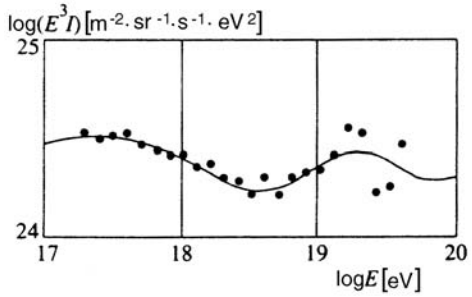

FIG. 2. Experimental cosmic ray spectrum from Refs. 1 and 2. The curve represents our approximation (7).

where a, p, and $E_{\rm gal}$ are fitting parameters. This choice adds the following continuous-current correction to the spectrum:

$$\frac{1}{E}\ S(E)=\frac{a}{E}\ \int_0^\infty J^{-1-p}\ \exp\left(-\frac{J}{4E_{\rm gal}}-\frac{E}{J}\right)dJ$$

$$=A\ \frac{K_p(x)}{x^{p+2}}, \tag{6}$$

where $A=4a(2E_{\rm gal})^{-p-1}$, $x=\sqrt{E/E_{\rm gal}}$, and $K_p(x)$ is a modified Bessel function, for which the following approximation is recommended for any value of x:

$$K_p(x)\approx\Gamma(p)2^{p-1}\ \frac{e^{-x}}{x^p}\ (1+\beta_p x)^{(2p-1)/2},$$

$$\beta_p=\frac{1}{2}\left[\frac{\sqrt{\pi}}{\Gamma(p)}\right]^{2/(2p-1)}. \tag{7}$$

For $p=3/2$ the approximation formula is exact and, for example, K_1 and K_2 are given by the expressions

$$K_1(x)\approx x^{-1}e^{-x}\sqrt{1+\frac{x\pi}{2}},$$

$$K_2(x)\approx 2x^{-2}e^{-x}\sqrt{\left(1+\frac{x\pi^{1/3}}{2}\right)^3}, \tag{8}$$

which differ at most by 3% from the tabulated values of $K_{1,2}$ for all values of x.

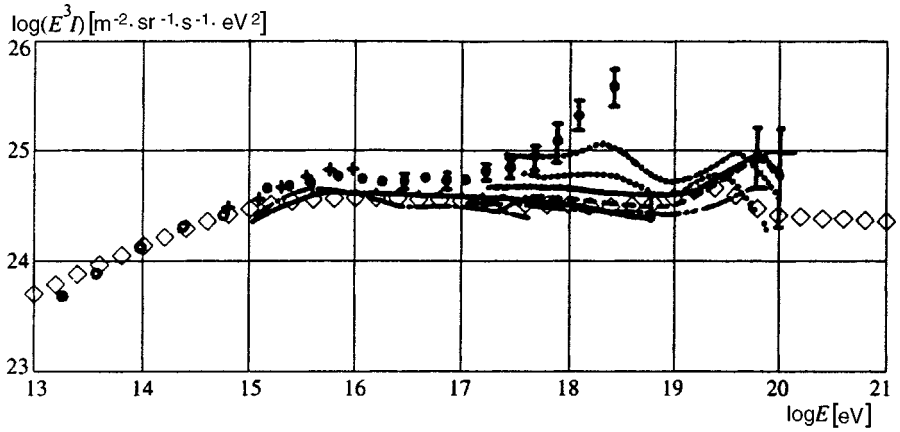

FIG. 3. Differential cosmic ray spectrum from Ref. 3. ◇) Our approximation (18).

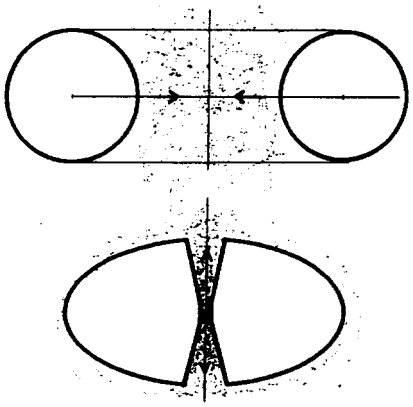

FIG. 4. Constriction of a magnetic torus with the formation of a centered pinch in the presence of external pressure.

If the rise of the spectrum after the second bend is identified with the cutoff of some sort of hypothetical metagalactic currents ($I_{\rm met}$), the spectrum can be augmented with at least one more term of the form (3), so that in the final analysis the pinch mechanism can be said to predict a spectrum of the form

$$dN/dE = I_{\rm pip} + I_{\rm gal} + I_{\rm met}, \quad I_{\rm pip} = C_1 E^{-\nu},$$
$$I_{\rm gal} = C_2 E^{-\mu} e^{-x} \xi_\mu(x), \quad I_{\rm met} = C_3 E^{-1} e^{-E/E_{\rm met}}, \qquad (9)$$

where $\xi_\mu(x) = (1 + x\beta_{\mu-1})^{\mu-3/2}$, $x = \sqrt{E/E_{\rm gal}}$, and $C_{1,2,3}$ are constants.

Let us compare our equations with the observed spectra. In Figs. 2 and 3 the factor E^3 is added to the spectrum for convenience and is taken into account by rewriting Eq. (9) in the form

$$\frac{dN}{dE} E^3 = c_{\rm pip} E^{3-\nu} + c_{\rm gal} E^{3-\mu} e^{-x} \xi_\mu(x) + c_{\rm met} E^2 \exp\left(-\frac{E}{E_{\rm met}}\right), \qquad (10)$$

where new notation has been introduced for the constants.

Here we have seven fitting parameters, and to plot the curve in Fig. 2, we have assigned them the values $c_{\rm pip} = 5 \cdot 10^{20}$, $\nu = 2.82$, $c_{\rm gal} = 8.2 \cdot 10^{19}$, $\mu = 2.73$, $E_{\rm gal} = 1.4 \cdot 10^{17}$ eV, $c_{\rm met} = 2.77 \cdot 10^{-14}$, and $E_{\rm met} = 9 \cdot 10^{18}$ eV. It is evident from Fig. 2 that these parameters lead to satisfactory approximation of the experimental points of Ref. 2 in the vicinity of the second bend. In the vicinity of the first bend, however, the situation is less satisfactory (the theoretical bend appears too smooth), and to improve the agreement, we introduce a new factor in the theory, the diffusion drift of cosmic ray particles out of the Galaxy.

3. ALLOWANCE FOR THE DIFFUSION DRIFT OF PARTICLES

We now show that the postulated pinch mechanism can be used to obtain a qualitatively correct description of particle drift from the Galaxy.

Roughly speaking, the spectrum of galactic cosmic rays takes the form of a power law $I \sim E^{-\nu}$ with exponent $\nu = 2.6$ in the interval up to the first bend at energy $E_1^* = 3 \cdot 10^{15}$ eV, and with exponent $\nu = 3.1$ after the bend (see Fig. 3). Here the difference in the experimental exponents is equal to $\delta\nu = 0.5$, and it is customarily assumed (see Refs. 9 and 10) that this can be attributed to the dependence of the diffusion coefficient on the energy associated with the faster drift of higher-energy particles in comparison with lower-energy particles, which are more thoroughly entangled in the random magnetic fields of the Galaxy.

Under steady-state conditions, the drift of particles with energy E is described by the diffusion equation

$$\mathrm{div}(D \nabla n) = Q_0(E),$$

where $n = n(\mathbf{r}, E) = I/c$ is the density of particles, and the right-hand side characterizes the primary particle sources. If we assume that the diffusion coefficient depends on the energy according to $D(E) = D_0 \Phi(E)$, the latter factor can be transferred to the right, and the observed spectrum should have the form $I \sim I_0(E)/\Phi(E)$. Consequently, the first bend can be correctly described by assuming that the diffusion coefficient is constant at low energies and is proportional to $\sqrt{E}$ in the high-energy range beyond the first bend.

We now show that the required form of the dependence $D(E)$ is obtained in a natural way in our theory when certain reasonable assumptions are made about the structure of the galactic magnetic field. Following convention (see Ref. 10), we assume that the field B is localized at inhomogeneities of scale r, and a particle that penetrates these is deflected by an angle $\varphi = r/\rho$, where $\rho = E/eB$ is the Larmor radius of an ultrarelativistic particle. We also assume that the field is not completely random, but is ''regular'' (see Ref. 10) in the sense that it has the same direction in neighboring inhomogeneities.

The collision cross section is now approximately $\sigma = \varphi r^2$ ($\approx \pi r^2$ for slow, back-scattered particles), and for the average diffusion coefficient we have the approximate expression

$$\langle D \rangle \approx \frac{1}{3} c\lambda = \frac{c}{3 n_r r^2} \left\langle \frac{1}{\varphi} \right\rangle, \quad \left\langle \frac{1}{\varphi} \right\rangle = \frac{E}{e} \left\langle \frac{1}{rB} \right\rangle, \qquad (11)$$

where n_r is the number density of inhomogeneities, and the angle brackets signify averaging over the field inhomogeneities, i.e., essentially over the distribution function of the currents producing the inhomogeneities. For the current distribution function, in the meantime, we have already in Eq. (5) adopted a model power law with a cutoff exponential, which is the one we shall use (since it yields the required result). Assuming closed currents, we assume that the field of the ring current J is approximately $B = \varphi_0 J/cr$, where φ_0 is a coefficient of the order of unity, and adopting the notation of Eq. (5), we have

$$\left\langle \frac{1}{\varphi} \right\rangle = \frac{E}{\varphi_0} \left\langle \frac{1}{J} \right\rangle = \frac{E}{\varphi_0} \frac{S_{p+1}(E)}{S_p(E)}, \qquad (12)$$

where (see (6))

$$S_p(E)=a\int_0^\infty J^{-p-1}\exp\left(-\frac{J}{4E_{\rm gal}}-\frac{E}{J}\right)dJ$$
$$=\frac{2a}{(2E_{\rm gal})^p}\frac{K_p(x)}{x^p}. \tag{13}$$

We therefore obtain

$$\left\langle\frac{1}{\varphi}\right\rangle=\frac{p\Phi(x)}{\varphi_0},\quad \Phi(x)=\frac{xK_{p+1}}{2pK_p}\begin{cases}\approx 1, & x\ll 1,\\ \approx x/2p, & x\gg 1.\end{cases} \tag{14}$$

Here the two asymptotes obviously satisfy

$$\Phi_{\rm app}(x)=\sqrt{1+(x/2p)^2}=\sqrt{1+E/4p^2E_{\rm gal}}, \tag{15}$$

which is also useful, so that the current-averaged diffusion coefficient (11) is equal to

$$\langle D\rangle=D_0\Phi(E),\quad D_0=\frac{c}{3n_r\pi r^2},\quad \Phi(E)\approx\sqrt{1+\varepsilon}, \tag{16}$$

where $\varepsilon=E/4p^2E_{\rm gal}$ is the normalized particle energy.

The diffusion coefficient determined from these casual estimates has the asymptotic forms that we want, and the first bend in the spectrum is located in the region $\varepsilon\approx 1$. We now examine the newly obtained spectra with allowance for diffusion.

4. SPECTRA WITH AND WITHOUT DIFFUSION

Here we discuss several alternative approximations of cosmic ray spectra. In the first case we discard the induction terms, taking only the pip term and diffusion into account, whereupon we obtain the following approximations:

$$1)\ \ I_1=I_{\rm pip+dif}=A_1\frac{E^{-\nu}}{\Phi(E)},\quad \Phi(E)=\sqrt{1+\frac{E}{E_1^*}}. \tag{17}$$

This spectrum can describe the first bend, but does not have a bump in the vicinity of the second bend; to include it, we add a ''metagalactic'' term, which yields

$$2)\ \ I_2=I_{\rm pip+dif}+I_{\rm met+dif}=A_1\frac{E^{-\nu}}{\Phi(E)}$$
$$\times\left[1+\left(\frac{E}{E_2^*}\right)^{\nu-1}\exp\left(-\frac{E}{E_{\rm met}}\right)\right]. \tag{18}$$

By trial and error we have found that the choice of parameters $A_1=7\cdot 10^{17}$, $\nu=2.55$, $E_1^*=1.2\cdot 10^{15}$ eV, $E_{\rm met}=10^{19}$ eV, and $E_2^*=7.4\cdot 10^{29}$ eV yields satisfactory agreement with Fig. 3, where the theoretical curve (18) is represented by diamonds.

However, the experimental data of Fig. 3 have too great a spread, and for definiteness we shall attempt to approximate the experimental points of Fig. 2, where the second bend is a dip with rounded left and right wings. On the other hand, in approximation 2 the left wing is straight, because it is formed by pips. Also, in this approximation the first bend is induced by the diffusion of ''galactic'' particles, even though such particles themselves are disregarded, and we now attempt to take them into account.

Once this has been accomplished, we can ignore pips altogether for simplicity, and then if we take diffusion into account, we have for the spectrum (cf. model 2)

$$3)\ \ I_3=I_{\rm gal+dif}+I_{\rm met+dif}=A_2\frac{E^{-\mu}}{\Phi(E)}\left[e^{-x}\xi_\mu(x)\right.$$
$$\left.+\left(\frac{E}{E_3^*}\right)^{\mu-1}\exp\left(-\frac{E}{E_{\rm met}}\right)\right]. \tag{19}$$

To preserve the initial part of the spectrum and the region of the first bend intact, we must proceed here as in model 2 and set $A_2=A_1=7\cdot 10^{17}$, $E_1^*=1.2\cdot 10^{15}$ eV, and $\mu=\nu=2.55$; we now find that $\xi_{2.55}=(1+x\beta_{1.55})^{1.05}\approx 1+x$. Subsequently, however, for $x=\sqrt{E/E_2^*}$ we need once again select three parameters: $E_2^*=1.3\cdot 10^{18}$ eV, $E_3^*=7.44\cdot 10^{29}$ eV, and $E_{\rm met}=10^{19}$ eV.

As another case we consider a model without pips and without diffusion:

$$4)\ \ I_4=I_{\rm gal}+I_{\rm met}=A_4E^{-\mu}\left[e^{-x}\xi_\mu(x)\right.$$
$$\left.+\left(\frac{E}{E_4^*}\right)^{\mu-1}\exp\left(-\frac{E}{E_{\rm met}}\right)\right], \tag{20}$$

with the new choice of parameters $A_4=2\cdot 10^{20}$, $\mu=2.75$, $x=\sqrt{E/E_2}$, $E_2=2.36\cdot 10^{17}$ eV, $\xi_{2.75}(x)=(1+0.845x)^{5/4}$, $E_4^*=1.6\cdot 10^{19}$ eV, and $E_{\rm met}=1.3\cdot 10^{19}$ eV.

Finally, we consider a special check model 5, which is similar to model 4 but has the half-integer exponent $\mu=5/2$ for low energies. This case is useful in that, first, Bessel functions with half-integer exponents can be expressed exactly in terms of polynomials and exponentials, so that here the asymptotic forms do not need to be matched in the diffusion coefficient as before. Second, the exponent $\mu=5/2$ is close to the value $\mu_N=2.55$ used by Nikol'skiĭ[4] at low energies. Thus, taking diffusion into account, we consider the equation (see (6))

$$5)\ \ I_5=I_{\rm gal+dif}^{\mu=5/2}+I_{\rm met+dif}=\frac{S(E)}{E\Phi(E)}=\frac{1}{\Phi(E)}\left[A\frac{K_{3/2}(x)}{x^{7/2}}\right.$$
$$\left.+\frac{B}{E}\exp\left(-\frac{E}{E_{\rm met}}\right)\right]=A_5\frac{E^{-5/2}}{\Phi(E)}\left[\frac{1+x}{e^x}\right.$$
$$\left.+\left(\frac{E}{E_5^*}\right)^{3/2}\exp\left(-\frac{E}{E_{\rm met}}\right)\right], \tag{21}$$

where $x=\sqrt{E/E_{\rm gal}}$. We reiterate that here we are using the exact expression for the Bessel function $K_{3/2}(x)=\sqrt{\pi/2}x^{-3/2}e^{-x}(1+x)$, and in the given situation it coincides perfectly with our approximation (7). For the diffusion we again obtain the elementary ''exact'' (see (14)) expression

$$D(E)=D_0\Phi(E),\quad \Phi(E)=\Phi(x_d),$$
$$\Phi(x)=\frac{xK_{5/2}}{3K_{3/2}}=1+\frac{x^2}{3+3x}, \tag{22}$$

where $x_d=\sqrt{E/E_{\rm dif}}$, and $E_{\rm dif}$ is the ''diffusion'' energy parameter, which must be properly chosen for the first bend to

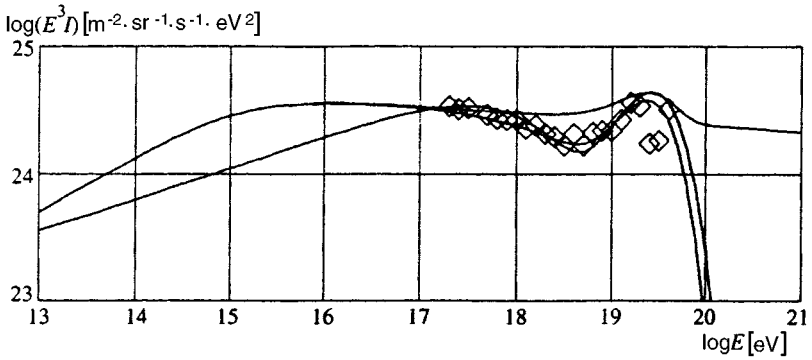

FIG. 5. Approximation of the cosmic ray spectrum according to Eqs. (18)–(20). ◇) Experimental data from Ref. 2.

be situated in the right place. With the appropriate choice of all the required parameters, the exactly solvable model 5 does not really differ from model 3, as is demonstrated for clarity in Fig. 5.

If diffusion is taken into account here in the same way as before, then by dividing expression (21) by $\sqrt{1+E/E_1^*}$ and making the necessary choice of the parameter E_1^* characterizing the position of the first bend, we find that model 5 does in fact coincide with model 3.

Figure 5 shows the experimental points from Ref. 2 (diamonds) and the three model approximations 2, 3, and 4.

The best approximation to the experimental data in Figs. 2 and 3 is No. 3, which can be regarded as a good practical approximation formula to be used in describing the full range of ultrarelativistic energies $10^{10} \leqslant E \leqslant 10^{20}$ eV. This distinguishes it from other approximation formulas (e.g., from the Nikol'skiĭ equation (1), which omits the second bend), which are generally aimed at describing limited intervals of the spectrum.

All the same, our equations are not simply chosen for the sake of approximation *per se*, but are based on definite model physical notions as to the mechanism of particle acceleration in electric fields; we therefore examine these physical models in greater detail (see below).

5. DISCUSSION OF PINCH MECHANISMS

Approximation 1 takes into account only pips and the diffusion responsible for the first bend. However, it disregards the second bend, which in our model can only be taken into account by adding a metagalactic term, as is done in approximation 2. In this approximation the (visually) straight parts of the profile in Fig. 5 between the first and second bend and after the metagalactic bump are formed by pips, which nonetheless appear to give excessively high intensities for the very high-energy range $10^{20} \leqslant E \leqslant 10^{21}$ eV. Pips are therefore totally disregarded in approximations 3 and 4.

Approximation 3, which takes ''galactic'' and ''metagalactic'' particles and diffusion into account, probably yields the best fit to the experimental data of Fig. 3. It is important to note, however, that in order to correctly position the first bend (assuming that it is diffusion-related), we have averaged the diffusion coefficient over the spectrum of currents of the form (5) using one value of the parameters $E_{\rm gal}=E_{\rm dif}=1.25\cdot 10^{14}$ eV, whereas to correctly position the second kind (assuming that its left wing is formed by galactic particles), we have used a spectrum of the same form (5) but with a different value of the parameter $E_{\rm gal}=1.3\cdot 10^{18}$ eV. This means that in approximation 3 we assume the presence of two sets of currents, the first being responsible for diffusion, and the second for the acceleration of a group of galactic particles.

We refine this explanation with a physical interpretation of the parameters. In Eq. (5) we have introduced the variable $J=eJ_i/c$; in application to diffusion the equation is more advantageously rewritten in the form

$$C(J)=aJ^{-1-p}\exp(-J/4E_{\rm gal}) = aJ^{-1-p}\exp(-J/J_{\rm max}^{\rm dif}). \tag{23}$$

Here we have introduced the notation $J_{\rm max}^{\rm dif}=4E_{\rm gal}c/e$ for the maximum current, so that $E_{\rm gal}=E_{\rm dif}=eJ_{\rm max}^{\rm dif}/4c$, while in application to diffusion the variable x has the form $x=\sqrt{E/E_{\rm dif}}$ and gives our postulated functional relation for the diffusion coefficient $D=D_0\sqrt{1+E/E_1^*}$. We thus obtain $E/E_1^*=(x/2p)^2$ and $E_1^*=4p^2E_{\rm dif}$. In approximations 2 and 3 the correct position of the first bend is achieved for the choice

$$E_1^*=1.2\cdot 10^{15}\ \text{eV}, \quad p=\mu-1=1.55,$$

so that here $E_{\rm dif}=1.25\cdot 10^{14}$ eV, which corresponds to the maximum current responsible for diffusion

$$J_{\rm max}^{\rm dif}=4cE_{\rm dif}/e=5\cdot 10^{22}\ \text{a.u.}=1.7\cdot 10^{13}\ \text{A}.$$

This numerical value can most likely be taken as an acceptable estimate for our Galaxy. In Raadu's survey,[11] for example, our Galaxy is in fact assigned a current of the order $J_G\sim 10^{13}$ A, and the same currents are ascribed to the interstellar medium in Peratt's book.[12]

On the other hand, galactic cosmic rays are known to have an energy density of 1 eV/cm^3, and the average energy density is the same for the magnetic field, which is therefore equal to $B=6\cdot 10^{-6}$ G. The above-determined maximum current $J_{\rm max}^{\rm dif}=1.7\cdot 10^{13}$ A could generate this field if the current channel had a radius $r_J=5.7\cdot 10^{17}$ cm$=0.6$ light years. It is well worth noting that this distance coincides with the Larmor radius of a particle in this field:

$$r_B=E/eB=E[\text{eV}]/300B[\text{G}]=5.7\cdot 10^{17}\ \text{cm}=0.6\ \text{ly},$$

if the critical energy of the particle is equal to $E_{\rm cr}=10^{15}$ eV. This value also corresponds to the first bend in the spectrum

(for us $E_1^* = 1.2 \cdot 10^{15}$ eV), which imparts a certain internal consistency to our conclusion that the diffusion coefficient $D = D_0 \sqrt{1 + E/E_1^*}$.

We now consider galactic particles in approximation 3 (with the diffusion-related first bend) and in approximation 4 (without diffusion). In both cases Eq. (21) is used for the current distribution, but with the parameter

$$E_{\text{gal}}^{(3)} = 1.3 \cdot 10^{18} \text{ eV} \quad \text{or} \quad E_{\text{gal}}^{(4)} = 2.36 \cdot 10^{17} \text{ eV}.$$

Converting to currents as above, we find

$$J_{\max} = 4 E_{\text{gal}} c/e, \quad J_{\max}^{(3)} = 1.7 \cdot 10^{15} \text{ A},$$

$$J_{\max}^{(4)} = 3.15 \cdot 10^{14} \text{ A}.$$

These currents are (respectively) 100 and 19 times greater than our ''diffusion'' current determined above, and they would produce a standard magnetic field $B = 6 \cdot 10^{-6}$ G for current channels having corresponding radii

$$r_J^{(3)} = 5.7 \cdot 10^{19} \text{ cm} = 60 \text{ ly} \quad \text{and} \quad r_J^{(4)} = 10^{19} \text{ cm} = 10 \text{ ly}.$$

The second result is approximately consistent with the average distance between stars in the Galaxy. If these radii of the current channels are set equal to the Larmor radii for the same magnetic field, we obtain the corresponding particle critical energies

$$E_{\text{cr}}^{(3)} = 10^{17} \text{ eV}, \quad E_{\text{cr}}^{(4)} = 2 \cdot 10^{16} \text{ eV}.$$

We now discuss the metagalactic term, which has been introduced in both approximations 3 and 4 with approximately the same cutoff parameter

$$E_{\text{met}} = 10^{19} \text{ eV} = e J_{\max}^{\text{met}}/c,$$

so that

$$J_{\max}^{\text{met}} = 3.3 \cdot 10^{17} \text{ A}.$$

These currents can be identified with the space between ordinary quiet galaxies (see Ref. 12), whereas based on numerical modeling of the active radio galaxy Cygnus A, according to numerical modeling results, it is ascribed a current of $2.5 \cdot 10^{19}$ A,[12] the periodic cutoff of which should lead to the generation of particles with maximum energy $E_{\text{met}}^{\max} = 7.5 \cdot 10^{20}$ eV. However, this radio galaxy is situated 75 Mpc from us, and it is not very likely that these particles could traverse such a distance after being slowed down by the cosmic background radiation (stopping length ~ 40 Mpc).

However, the well-known cluster of galaxies in the constellation Virgo is situated at a distance of 17 Mpc from us, and it has been hypothesized[9] that particles with a maximum observable energy (today) $E = 3 \cdot 10^{20}$ eV, which corresponds to a current of 10^{19} A, can reach us from this object. However, such particles do not move in a straight line, but instead in intergalactic fields $B_{\text{met}} \sim 5 \cdot 10^{-7}$ G wind around with the Larmor radius

$$r_B = E[\text{eV}]/300 B[\text{G}] = 2 \cdot 10^{24} \text{ cm} \approx 1 \text{ Mpc}.$$

This distance corresponds roughly to the distance between galaxies, so that no astronomical objects are visible there recorded observable directions of arrival of these very high-energy particles. We emphasize that approximations 3 and 4, in contrast with 1 and 2, theoretically suggest a sharp exponential cutoff of the spectrum at energies of the order of 10^{20} eV, which is consistent with observations.

One final point is that we have discussed approximation 4 without diffusion because, in particular, several authors[3,7] have questioned the existence of the sharp first bend, and the theory predicts a more rounded bend in the curve even without diffusion (or, more precisely, on the assumption that the diffusion coefficient does not depend on the energy). It is evident from Figs. 1 and 5 that the exponent of the power spectrum $\nu = 2.75$ ($\approx 1 + \sqrt{3}$) works quite well not only for the energy range $E \leqslant 10^{13}$ eV (Fig. 1), but also at higher energies up to $E \sim 10^{16} - 10^{17}$ eV.

The preceding estimates of the parameters of the pinch mechanism underlying the generation of galactic cosmic rays are reasonable. Clearly, cosmic rays are accelerated in certain electric fields and, according to the generally accepted shock wave hypothesis, these (relatively weak) fields exist in magnetohydrodynamic waves (or in MHD shock waves), with which the particles have resonantly interacted for a long time. The pinch mechanism proposed here is based on a different picture, namely acceleration in comparatively strong but short-lived electric fields produced by periodic current cutoffs in pinches of the cosmic plasma.

6. CONCLUSION

We summarize the investigation in five concluding remarks.

1) The observed cosmic ray spectra shown in Fig. 3 have appreciable differences but, roughly speaking, they exhibit eight characteristic parameters: a common normalization, the slope of the initial segment of the spectrum, the position of the first bend, the slope of the spectrum after it, the position of the second bend (see Fig. 2), the slope after it, and finally the position of the last maximum and the downslope following it. Clearly, an analytic approximation must contain the same number of fitting parameters, but in Eq. (19) (see also Fig. 5) we have succeeded in circumventing six parameters. Three of them (the characteristic energies E_1^*, E_2^*, and E_{met}) can be linked to three characteristic dimensions in a physically meaningful way, namely, the average distance between stars, the thickness of the galactic disk, and the dimensions of the halo (or average distance between galaxies).

2) Particles squeezed from the waist of a relativistic pinch must have a total spectrum with exponent $\sqrt{3}$ (see Appendix A), which is very close to the observed value. However, in Eq. (19) these particles are disregarded for simplicity, and the model essentially uses only Eq. (3) and the current distribution function.

3) The hypothesized form of the current distribution function gives the correct (close to the observed) jump ($\nu_2 - \nu_1 \approx 0.5$) of the exponents of the spectrum in the vicinity of the first bend, partially confirming the hypothesis. In the given model this jump is caused by the diffusive nature of the propagation of particles through the Galaxy after generation events, a process that imparts isotropy to the particle

flux as a whole, as is indeed observed. We note, however, that such an astrophysical explanation of the first bend is not unique, and in some papers (see Ref. 7) it is not attributed to the primary flux of cosmic rays, but to specific characteristics of the nuclear reactions in the secondary extensive air showers, which provide a basis only for the investigation of high-energy particles.

4) It is sometimes assumed that energetic particles themselves arrive from the nearest cluster of galaxies, 14 Mpc away in the constellation Virgo and possibly from more distant active galactic nuclei. In particular, to match the computer-generated radio emission of the galaxy Cygnus A with the observed pattern, it must be assumed (according to published data[12]) that circulating in the pinches of the galaxy is a colossal current of $2\cdot 10^{19}$ A, whose periodic cutoffs would be capable, according to our model, of producing particles with energy $E_{\max}=eJ/c=7\cdot 10^{20}$ eV, which appears to be consistent with the maximum possible cosmic ray energy (currently $E_{\max}=3\cdot 10^{20}$ eV).

5) Finally, there is one other hypothesis to consider, but it requires further study. We cannot rule out the possibility that gamma-ray bursts, the precise nature of which has yet to be established, are generated in the pinches (other possible hypotheses are discussed in a recent survey[13]).

The high forward directionality of bremsstrahlung from a narrow beam of ultrarelativistic electrons as they are slowed down by collisions with ions, but move almost rectilinearly, drastically shortens (by a factor of 10^{-4}; see Appendix B) the period of the instrument-recorded signal in comparison with the period of the emission of radiation itself. We note that a typical gamma-ray burst lasts 10 s on the average, but a rare instance with a duration of 1.5 h and a maximum photon energy of 18 GeV is described in Ref. 14. It is possible that here the short, roughly three-minute, high-intensity initial interval is attributable to the first pipette mechanism, while the subsequent long, low-intensity but high-energy ''tail'' is generated by a second, electrodynamic mechanism. Allowance for such highly directional propagation may prompt a reexamination of the existing estimates of the total power of gamma-ray bursts (it is conceivable that many rays simply miss our instruments).

Moreover, in gamma-ray bursts the generation of electron beams by the pinch mechanism must be accompanied by the generation of ion beams with $M/m\approx 2000$ times the energy (since electrons and ions have identical velocities in the pipette mechanism of a quasineutral plasma being squeezed from the waists of the pinches). In this light one cannot dismiss the possibility that the ''ionic'' power of gamma-ray bursts is high enough to sustain the continuous replenishment of cosmic rays whose particles, as the estimates show, are transported out of our Galaxy by diffusion to distances of approximately 100 million light years.

We note that several different mechanisms for the acceleration of charged particles might well be at work in space: shock waves associated with supernova outbursts, a ''reclosing relay'' mechanism in neutral current sheets along so-called X lines or ''tears'' (note, however, that these are defocusing lines, a property that would inhibit acceleration), two pinch mechanisms (along focusing O lines), and possibly other, as yet unknown mechanisms.

For example, some researchers believe that the so-called dark matter in galaxies, which is estimated to harbor ten times the total mass of their visible stars, could be composed of dust particles rather than a gas (see Ref. 15), endowing them with an observable transparency due to rarefaction. And would it not be possible for lightning to occur in them, similar to those observed in the turbulent ash clouds from volcano eruptions?

APPENDIX A: PIPETTE MODEL OF THE GENERATION OF GALACTIC COSMIC RAYS

In the main body of the text the equation for the spectrum of pips (1) is valid under the assumption that the plasma equation of state is nonrelativistic in proper coordinates. In this appendix we analyze a more general case.

We consider the cylindrical cavity of a stripped Z-pinch with a relativistic plasma inside it, of radius $a(t,z)$, with current $J=\text{const}$ and magnetic field $B=2J/ca$ at the boundary $r=a(t,z)$. The relativistic equation of continuity has the form

$$\frac{\partial}{\partial t}\ \gamma n=-\operatorname{div}(\gamma n\mathbf{v})=-\frac{\partial}{r\partial r}\ (r\gamma n v_r)-\frac{\partial}{\partial z}\ (\gamma n v_z),$$

$$\gamma=\frac{1}{\sqrt{1-\beta^2}},\quad \beta=\frac{\mathbf{v}}{c}, \tag{A1}$$

where $n=n_i=n_e$ is the density of ions and electrons in their proper coordinate system. At the boundary $r=a(t,z)$ we have

$$v_r|_{r=a}=\frac{da}{dt}=\frac{\partial a}{\partial t}+v_z\ \frac{\partial a}{\partial z},$$

and in the so-called narrow channel approximation we set $v_r=(r/a)da/dt$. Equation (A1) then assumes the form

$$\frac{\partial}{\partial t}\ (\gamma n a^2)+\frac{\partial}{\partial z}\ (\gamma n a^2 v)=0, \tag{A2}$$

where $v=v_z$. We denote $\tau=ct$, $\gamma=\cosh y$, $u=\gamma v/c=\sinh y$, $\rho_*=na^2/n_0a_0^2$ and introduce the two operators

$$\hat{P}=\gamma\ \frac{\partial}{\partial\tau}+u\ \frac{\partial}{\partial z},\quad \hat{Q}=u\ \frac{\partial}{\partial\tau}+\gamma\ \frac{\partial}{\partial z}. \tag{A3}$$

Equation (A2) then assumes the form $\hat{Q}y=-\hat{P}\ \ln\rho_*$, but at the boundary we have the pressure condition $p=2n\Theta=B_\varphi^2/8\pi=p_0(a_0/a)^2$, so that $\rho_*=\Theta_0/\Theta=\text{const}\cdot\mu$, where we have introduced the new and more convenient variable $\mu=M_ic^2/\Theta$ with the ion mass M_i and the temperature Θ in energy units. Now Eq. (A2) can be rewritten in the final form

$$\hat{Q}y=-\hat{P}\ \ln\mu. \tag{A4}$$

The second equation is the relativistic equation of motion $\nabla_i T_k^i = 0$, where $T_k^i = (e+p)u^i u_k - p\delta_k^i$ is the energy–momentum tensor. In the narrow channel approximation it assumes the form

$$(e+p)\hat{P}y = -\hat{Q}p, \quad \left(1+\frac{e}{p}\right)\hat{P}y = -\hat{Q}\ \ln p, \tag{A5}$$

where the scalar $e = e_i + e_e = n(M_i c^2 \langle\gamma\rangle T_i + m_e c^2 \langle\gamma\rangle T_e)$ denotes the energy density in proper coordinates. In addition, we have the adiabatic equation $dE = d(Ve) = -pdV$ and, since $nV = \text{const}$, this equation yields the function $n = n(\Theta)$:

$$\frac{dn}{n} = \frac{1}{2}\ \mu d\Gamma = \frac{1}{2}\ [d(\mu\Gamma) - \Gamma d\mu],$$

$$\Gamma = \langle\gamma\rangle_{T_i} + \frac{m_e}{M_i}\ \langle\gamma\rangle_{T_e}. \tag{A6}$$

Introducing the Bessel function

$$K_n(\mu) = \int_0^\infty \exp(-\mu\ \cosh\ x)\cosh(nx)dx,$$

we find

$$N(\mu) = \int_0^\infty e^{-\mu\sqrt{1+u^2}} u^2 du = \frac{K_2(\mu)}{\mu},$$

$$\langle\gamma\rangle = \frac{d}{d\mu}\ \ln\frac{1}{N}, \quad \Gamma = \frac{d}{d\mu}\ \ln\frac{1}{N_i N_e}, \tag{A7}$$

and integration of Eq. (6) yields the relativistic adiabatic law

$$p(\mu) = C\ \exp\left(\Lambda - \mu\ \frac{d}{d\mu}\ \Lambda\right), \quad \Lambda = \ln\ Z,$$

$$Z = \frac{1}{\mu^2}\ \sqrt{K_2(\mu)K_2\left(\frac{m_e}{M_i}\ \mu\right)}, \quad n(\mu) = \frac{\mu p(\mu)}{2M_i c^2}. \tag{A8}$$

Finally, the resulting equations (A4) and (A5) can be concisely rewritten as

$$\hat{P}\mu = -\mu\hat{Q}y, \quad \hat{P}y = -f\hat{Q}\mu, \quad f = \frac{\Lambda''_{\mu\mu}}{\Lambda'_\mu}$$

$$= \frac{d}{d\mu}\ \ln\left(\frac{d}{d\mu}\ \ln\ Z\right), \tag{A9}$$

and can lead to a linear system of equations.

To achieve the latter, we use a hodographic transformation, and as the first step introduce the inverse functions $\tau = \tau(\mu, y)$ and $z = z(\mu, y)$. The direct derivatives can then be expressed in terms of the inverse derivatives according to the equations

$$\frac{\partial}{\partial\tau}\ y(\tau,z) = \frac{z'_\mu}{J}, \quad \frac{\partial}{\partial\tau}\ \mu(\tau,z) = -\frac{z'_y}{J},$$

$$\frac{\partial}{\partial z}\ y(\tau,z) = -\frac{\tau'_\mu}{J}, \ \frac{\partial}{\partial z}\ \mu(\tau,z) = \frac{\tau'_y}{J}, \tag{A10}$$

where $J = \tau'_y z'_\mu - \tau'_\mu z'_y$ is the Jacobian of the transformation. Substituting Eqs. (A10) into (A9) and introducing the ''large'' functions $T = \gamma\tau - uz$ and $Z = \gamma z - u\tau$, we obtain the linear system of equations

$$Z'_y = -(\mu T)'_\mu, \quad Z'_\mu = -(Z + T'_y)f(\mu),$$

$$(\mu T)''_{\mu\mu} + [(\mu T)'_\mu - T''_{yy}]f(\mu) = 0, \tag{A11}$$

which can only be solved numerically. However, approximate solutions are worth considering as well.

For the nonrelativistic equation of state ($\mu \gg 1$) we have

$$K_2 \approx \sqrt{\frac{\pi}{2\mu}}\ e^{-\mu}, \quad Z \approx \text{const}\cdot\mu^{-5/2}e^{-\mu/2},$$

$$\Lambda' = (\ln\ Z)' \approx -\frac{1}{2} - \frac{5}{2\mu}, \quad f = \frac{\Lambda''}{\Lambda'} \approx -\frac{5}{\mu^2}, \tag{A12}$$

and if we introduce the new argument $x = 5/\mu$, the last equation in the set (A11) assumes the form

$$\hat{\mathscr{L}}T = x(T''_{xx} + T'_x) = T - T''_{yy}. \tag{A13}$$

Here $\hat{\mathscr{L}}$ is the Laguerre operator, which has the properties

$$\hat{\mathscr{L}}\psi_n = -(1+n)\psi_n, \quad n = 0, 1, 2, \ldots,$$

$$\psi_n = wL_n^{(1)}, \quad w = xe^{-x},$$

$$L_0^{(1)} = 1, \quad L_1^{(1)} = (2-x)/\sqrt{2},$$

$$\int_0^\infty L_m^{(1)} L_n^{(1)} w\ dx = \delta_{m,n}. \tag{A14}$$

Equation (A13) has a general solution of the form

$$T(x,y) = w(x)\sum_{n=0}^{\infty} C_n L_n^{(1)}(x) Y^{\sqrt{n+2}},$$

$$Y - e^{-|y|} = \gamma - \sqrt{\gamma^2 - 1}. \tag{A15}$$

Any function can be represented by a series in these polynomials and, in particular, for the delta function $\delta = \delta(x - x_0)$ and its derivative we have the expressions

$$\delta = \sum_0^\infty\ c_n L_n^{(1)}, \quad \frac{d}{dx}\ \delta = \sum_0^\infty\ c_n\ \frac{d}{dx}\ L_n^{(1)},$$

$$c_n = w(x_0)L_n^{(1)}(x_0). \tag{A16}$$

The assumption that a pinch does not have any perturbations at the ''initial'' time $t = -\infty$ implies that the condition $T(x,y) = -\infty$ holds at the point $x = x_0$, $y = 0$, total breakup at the waist corresponds to $x = \infty$, $T = 0$, and at this critical time all accelerated particles must be forced into the bulge, where $x = 0$. Consequently, at this time the distribution function is equal to

$$dN = n\gamma\pi a^2 dz = F du, \quad F = \frac{dN}{du} = \frac{A}{\gamma}\ T'_x\Big|_{x\to 0}, \tag{A17}$$

where $A = \pi a_0^2 n_0 x_0$. It has been shown[4,5] that the series (A15) must begin with $n = 0$ for the perturbation to be periodic along the pinch.

But typical perturbations are local, and for these, (A15) must begin with $n=1$. Then at ultrarelativistic velocities (for $Y\approx 1/2y$, but using the nonrelativistic equation of state), we obtain the particle energy distribution in the form of a power function

$$dN/dE = F/Mc^2 \propto E^{-\nu} \tag{A18}$$

with exponent $\nu = 1+\sqrt{3}$, which is very close to the value 2.74 ''observed'' for cosmic rays in the energy range $10^{10}-10^{16}$ eV.

We now consider the ultrarelativistic equation of state, for which instead of (A12) we find

$$K_2 \approx 2\mu^{-2}, \quad Z\sim \mu^{-4}, \quad \Lambda'_\mu = (\ln Z)'_\mu \approx -4/\mu,$$
$$f \approx -1/\mu. \tag{A19}$$

In this case the second equation (A11) assumes the quasi-Besselian form

$$T''_{\mu\mu} + \frac{1}{\mu}\, T'_\mu + \frac{1}{\mu^2}\,(T''_{yy} - T) = 0, \tag{A20}$$

and it can also be solved. However, the approximation model described below is more accurate.

The nonrelativistic case (A12) and the ultrarelativistic case (A18) can be combined by setting

$$f = -\frac{5}{\mu(\mu+5)} = \begin{cases} -5/\mu^2, & \mu \gg 1, \\ -1/\mu, & \mu \ll 1. \end{cases} \tag{A21}$$

This interpolation model simultaneously describes a nonrelativistic situation in the bulges of the pinch and an ultrarelativistic situation in the slender waists. For this kind of model it is convenient to introduce the argument $x = 5/\mu$, whereupon the last equation (A11) assumes the form

$$\hat{H}T - T + T''_{yy} = 0 = -4\pi\rho_{\text{eff}},$$
$$\hat{H}T = x(1+x)T''_{xx} + xT'_x. \tag{A22}$$

Here $\hat{H}$ is the hypergeometric operator, and the correct (real) solution of the equation $\hat{H}T = -k^2 T$ is the sum of two hypergeometric functions $F(a,b;c;z)$. Assuming that $T \sim zS_k(z)$, we find

$$S_k(z) = (1-z)^{ik} F(1+ik, 1+ik; 2; z) + (1-z)^{-ik} F(1-ik, 1-ik; 2; z), \tag{A23}$$

where $z = x/(1+x)$ is a new argument. It is the sum and not the difference that ensures the correct limit $S = 2 + (1-k^2)z + \ldots$, $T \sim z$ as $z \to 0$ in the bulges of the pinch. On the other hand (for $x \to +\infty$, $z \to 1$ in the waists), we have the asymptotic expression $S_k(z\to 1) = -k^{-1}\sin[k\ln(1-z)]$, which we use to express the delta function $\delta(k) = (\pi k)^{-1} \lim_{a\to\infty} \sin(ka)$. Then from the equations

$$\frac{d}{dz}\left[(1-z)\,\frac{d}{dz}\,T_1\right] = -\frac{k_1^2 T_1}{z(1-z)},$$
$$\frac{d}{dz}\left[(1-z)\,\frac{d}{dz}\,T_2\right] = -\frac{k_2^2 T_2}{z(1-z)} \tag{A24}$$

we obtain the orthogonality condition for the $S_k(z)$-functions:

$$\int_0^1 S_1 S_2\,\frac{z}{1-z}\,dz = \frac{\pi}{2k_1 k_2}\,\delta(k_1 - k_2). \tag{A25}$$

Using this condition, we obtain the following expressions for the delta function and its derivative:

$$\delta(z-z_0) = 2\pi \int_{-\infty}^{\infty} c_k S_k(z)\,dk,$$
$$\frac{d}{dz_0}\,\delta(z-z_0) = 2\pi \int_{-\infty}^{\infty} c_k^1 S_k(z)\,dk, \tag{A26}$$

where $c_k = k^2 z_0 S_k(z_0)/(1-z_0)$ and $c_k^1 = dc_k/dz_0$. Next, dropping the constant, we write the basic equation in the operator quasi-Laplacian form

$$\hat{\Delta}T = \hat{H}t - T + T''_{yy} = \delta(y)\,\frac{d}{dz_0}\,\delta(z-z_0),$$
$$T = \int_{-\infty}^{\infty} C_k z S_k(z) Y^q\,dk, \tag{A27}$$

where $Y = \exp(-|y|)$. Making use of the relations

$$\frac{d|y|}{dy} = \operatorname{sgn} y, \quad \frac{d}{dy}\operatorname{sgn} y = 2\delta(y),$$
$$\frac{d^2}{dy^2}\,Y^q = [q^2 - 2q\,\delta(y)]Y^q, \tag{A28}$$

for the left-hand side we have

$$\hat{\Delta}T = \int_{-\infty}^{\infty} C_k z S_k Y^q [q^2 - k^2 - 1 - 2q\,\delta(y)]\,dk. \tag{A29}$$

From this result we obtain $q = \sqrt{1+k^2}$ and, taking into account the limit $S_k(z_0 \ll 1) = 2$, we have

$$\int_{-\infty}^{\infty} C_k z S_k q\,dk = -\frac{d\,\delta(z-z_0)}{2dz_0},$$
$$C_k = -\frac{k^2}{\pi q z_0}\,\frac{d}{dz_0}\left[\frac{z_0 S_k(z_0)}{1-z_0}\right] = -\frac{2k^2}{\pi q z_0}. \tag{A30}$$

The ''time'' then turns out to be

$$T = -\frac{2z}{\pi z_0}\,J(z,y), \tag{A31}$$

where

$$J(z,y) = \int_{-\infty}^{\infty} S_k(z)\,\frac{k^2}{\sqrt{1+k^2}}\,\exp(-|y|\sqrt{1+k^2})\,dk,$$

and for $z = x/(1+x) = 0$ we obtain $J(z=0,y) = (4/|y|)K_1(|y|)$, where K_1 is a modified Bessel function with the asymptotic form $K_1 \approx \sqrt{\pi/2|y|}\,\exp(-|y|)$ for $|y| \gg 1$. Finally, since the spectrum equation (A17) is valid (as $x \to 0$) in both cases, (A15) and (A30), the spectrum for the interpolation model (A21) is now

$$dN/dp \sim K_1(|y|)/\gamma|y| \sim \gamma^{-2}(\ln\gamma)^{-3/2} \tag{A32}$$

and is sufficiently close to the spectrum (A18) $dN/dE \sim \gamma^{-\nu}$ with exponent $\nu = 1+\sqrt{3}$ obtained for the nonrelativistic plasma equation of state in proper coordinates.

APPENDIX B: DURATION OF BREMSSTRAHLUNG FROM ULTRARELATIVISTIC ELECTRONS

In this special Appendix we discuss the hypothesis of the possible generation of gamma-ray bursts in plasma pinches and, in particular, the problem of their having an observable duration of the order of several seconds.

If an ultrarelativistic electron with initial kinetic energy $E_0 = mc^2 k_0$ at time $t=0$ enters a plasma cloud at the point $x=0$, its kinetic energy is spent in bremsstrahlung and decays according to the exponential law $E(t) = E_0 \exp(-t/\tau_0)$, where for simplicity we assume that $\tau_0 = \text{const}$. The path traversed by the electron is then given by the equation

$$dx = c\sqrt{1-(1+k_0 e^{-t/\tau_0})^{-2}}\,dt, \quad x = c\tau_0 S(t), \tag{B1}$$

where

$$S(t) = 4\int_{s(0)}^{s(t)} \frac{x^2}{x^4-1}\,dx, \quad s(t) = \sqrt{1+2\mu(t)},$$

$$\mu(t) = \frac{mc^2}{E(t)},$$

and for ultrarelativistic energies ($\mu \ll 1$) we have approximately

$$x = x(t) = ct - \delta(t), \quad \text{where} \quad \delta(t) \approx c\tau_0 \left[\frac{\mu(0)}{2}\right]^2 (e^{2t/\tau_0}-1). \tag{B2}$$

Since an ultrarelativistic electron emits bremsstrahlung gamma rays in a narrow cone with vertex angle of the order of $1/\gamma$ in the forward direction, and $x_{\text{fr}} = ct$ is the position of the radiation front, the radiated energy is localized in a thin layer having a thickness of the order of δ between the front and the electron at a very slight distance from it. For $t \gg \tau_0$ we have $\delta(t) \approx c\tau_0 [mc^2/2E(t)]^2$, and if the radiation still enters the observing instrument, it produces a signal of short duration therein. If, for example, the initial electron energy is $E(0) = 1$ GeV and the electron loses $0.99E(0)$ in a time $t_* = 4.6\tau_0$, we obtain a signal of duration $\Delta t \approx 10^{-4} t_*$ in the observing instrument.

These considerations should be useful when cosmic gamma-ray bursts originate from bremsstrahlung produced by electron beams that have in some way been accelerated to ultrarelativistic energies. Moreover, their highly directional emitted radiation can miss the instruments, and only at the end of deceleration, after the energy has been reduced to values in the MeV range, does the radiation become almost isotropic and capable of entering the instrument. These considerations should help to improve estimates of the postulated primary power of gamma-ray burst sources, the nature of which remains a mystery at the present time.

This work was partially supported by Grant No. 94-3802 from INTAS.

[1] V. L. Ginzburg, Usp. Fiz. Nauk **166**, 169 (1996) [Phys. Usp. **39**, 155 (1996)].
[2] D. J. Bird, S. C. Corbató, H. Y. Dai *et al.*, Phys. Rev. Lett. **71**, 3401 (1993).
[3] L. I. Vil'danova, P. A. Dyatlov, N. M. Nesterova *et al.*, Izv. Ross. Akad. Nauk Ser. Fiz. **58**, 79 (1994).
[4] V. P. Vlasov, S. K. Zhdanov, and B. A. Trubnikov, JETP Lett. **49**, 667 (1989).
[5] B. A. Trubnikov, Usp. Fiz. Nauk **160**(12), 167 (1990) [Sov. Phys. Usp. **33**, 1061 (1990)]; V. A. Trubnikov, IEEE Trans. Plasma Sci. **PS-20**, 898 (1992).
[6] B. A. Trubnikov, S. K. Zhdanov, and V. P. Vlasov, JETP Lett. **64**, 245 (1996).
[7] S. I. Nikol'skiĭ, Izv. Ross. Akad. Nauk Ser. Fiz. **57**, 21 (1993).
[8] V. I. Yakovlev, Yu. M. Vasilyuk, V. V. Zhukov, and N. M. Nikol'skaya, Izv. Ross. Akad. Nauk Ser. Fiz. **58**, 7 (1994).
[9] J. Wdowczyk and A. W. Wolfendale, Nature **281**, 356 (1979).
[10] V. S. Berezinskiĭ, S. V. Bulanov, V. L. Ginzburg, V. A. Dogel', and V. S. Ptuskin, *Astrophysics of Cosmic Rays* [in Russian], Nauka, Moscow (1984), p. 173.
[11] M. A. Raadu, Phys. Rep. **178**, 1 (1989).
[12] A. L. Peratt, *Physics of the Plasma Universe*, Springer-Verlag, New York (1992), pp. 65–66.
[13] B. I. Luchkov, I. G. Mitrofanov, and I. L. Rozental', Usp. Fiz. Nauk **166**, 743 (1996) [Phys. Usp. **39**, 695 (1996)].
[14] K. Hurley, B. L. Dingus, R. Mukherjee *et al.*, Nature **372**, 652 (1994).
[15] O. B. Firsov, Yad. Fiz. **56**(3), 120 (1993) [Phys. At. Nucl. **56**, 354 (1993)].

Translated by James S. Wood

Nonlinear propagation of optical pulses of a few oscillations duration in dielectric media

S. A. Kozlov

St. Petersburg State Institute of Precision Mechanics and Optics, 197101 St. Petersburg, Russia

S. V. Sazonov

Astrakhan State Technical University, 414025 Astrakhan, Russia

(Submitted May 8, 1996)
Zh. Éksp. Teor. Fiz. **111**, 404–418 (February 1997)

Using a semi-phenomenological model of the polarization response of an isotropic solid dielectric that does not resort to the slowly-varying-envelope approximation, we have obtained a nonlinear wave equation for the electric field of a femtosecond light pulse propagating in the given dielectric. Evidence is presented that this equation possesses breatherlike solutions in the region of anomalous group dispersion and does not have any solutions in the form of steady-state traveling solitary video pulses. A universal relation is found linking the minimum possible duration of a breatherlike pulse with the medium parameters. It is shown that such a pulse contains roughly one and a half periods of the light-wave. © *1997 American Institute of Physics.* [S1063-7761(97)00202-3]

1. INTRODUCTION

The development of the laser technology of ultrashort light pulses has led to the creation of laser systems generating pulses only a few periods of the light field in duration.[1–5] It is natural to ask how such pulses propagate in optical media. Clearly, nonlinear propagation regimes—especially soliton regimes—are of the greatest interest since these pulses spread out rapidly in the case of low-intensity radiation due to dispersion, according to well-known laws.[6,7]

The nonlinear evolution of light pulses of duration τ_p down to the femtosecond range in dielectric media is usually treated theoretically by solving a wave equation of the form[8]

$$i\frac{\partial\varepsilon}{\partial z}+\alpha_1\frac{\partial^2\varepsilon}{\partial T^2}+i\alpha_2\frac{\partial^3\varepsilon}{\partial T^3}+\ldots+\beta_0|\varepsilon|^2\varepsilon + i\beta_1\frac{\partial}{\partial T}(|\varepsilon|^2\varepsilon)+\ldots=0, \tag{1}$$

where $\varepsilon(z,T)$ is the slowly varying envelope of the electric field E of the light pulse:

$$E=\frac{1}{2}\,\varepsilon\,\exp[i(\omega T-kz)]+\text{c.c.} \tag{2}$$

Here ω is the frequency, k is the wave number, $T=t-z/v_g$ is the time in the co-moving system of coordinates, and v_g is the group velocity. Dispersion of the linear and nonlinear refractive indices of the medium is taken into account in various approximations of dispersion theory with the help of phenomenological, generally complex coefficients $\alpha_1, \alpha_2, \ldots$ and $\beta_0, \beta_1, \ldots,$ respectively. However, analysis of the propagation of pulses consisting only of a few oscillations becomes qualitatively more complicated. For such ultrashort pulses it is difficult even to introduce the concept of an envelope. Therefore, we cannot use the slowing-varying-envelope approximation—so fruitful in traditional nonlinear optics—to describe their evolution; nor, consequently, can we use the wave equation (1) obtained in this approximation.

At present there is a large body of work (see, e.g., Refs. 9–23) dedicated to an analysis of the self-action of ultrashort pulses in optical media which do not use the slowly-varying-envelope approximation. The closed system of the wave equation and the material equations, written not for the envelope of the light pulse but directly for the wave field itself, is analyzed in these treatments, as a rule, in terms of the model of a two-level medium. Such a system of nonlinear equations, e.g., in the form of the Maxwell–Bloch equations, for the case of ultrashort pulses frequently simplifies significantly. Thus, for pulses that are very long,[11,13,16,17,22,24]

$$(\omega_0\tau_p)^2\gg 1, \tag{3}$$

in comparison with the characteristic time of intra-atomic processes ω_0^{-1} the given system reduces in the monodirectional wave approximation to the modified Korteweg–de Vries (MKdV) equation, and for very short pulses[10,11,13,14,16,18]

$$(\omega_0\tau_p)^2\ll 1, \tag{4}$$

to the sine-Gordon equation. However, in the analysis of the nonlinear propagation in a dielectric of ultrashort pulses whose spectrum belongs to the transparency region of the medium, the results of the above-mentioned works are, in our opinion, inapplicable. This has to do, primarily with two factors. First, modeling the electronic nonlinearity of the polarization response using the two-level medium approximation gives a uniformly negative value for the nonlinear refractive index coefficient n_2 in the transparency region of the dielectric.[25] At the same time, the experimentally measured values of n_2 for glasses and crystals are positive.[25] This difference in the results of theory and experiment is understandable since the two-level medium approximation in essence allows for only one nonlinearity mechanism—variation of

the level populations. This mechanism, as a rule, is not the main one in the nonresonant interaction of light with matter.[25] Second, the two-level model describes normal dispersion of the group velocity, but does not account for anomalous dispersion, whereas it is well known from the nonlinear optics of pico- and subpicosecond pulses that the nature of their self-action differs qualitatively depending on whether the pulse spectrum lies in the region of normal or anomalous dispersion of their group velocity.[8]

The present paper presents material equations which adequately describe the dispersion of both the linear and nonlinear refractive indices in their transparency region. A nonlinear wave equation is derived which characterizes the evolution of the field of ultrashort pulses in dielectric media for the case in which the pulse spectrum belongs to the transparency region of the medium. Both the derived equation and its solution are analyzed.

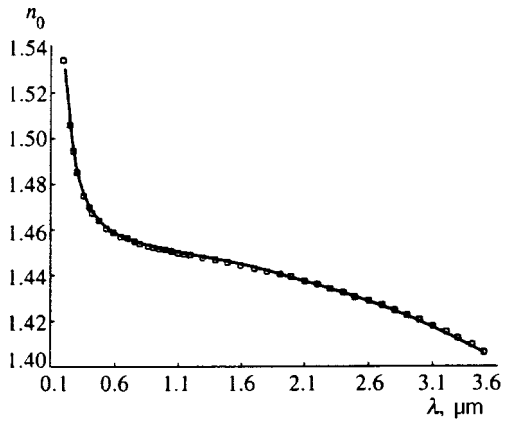

FIG. 1. Dispersion of the linear refractive index $n_0(\lambda)$ of quartz glass (λ is the wavelength, the points are experimental data, the solid curve is the dispersion calculated according to the theoretical model (5).

2. POLARIZATION RESPONSE OF A DIELECTRIC MEDIUM IN THE FIELD OF ULTRASHORT PULSES

The polarization response of a dielectric medium in an intense light field can be completely rigorously described in the semiclassical approximation in terms of the equations for the density matrix in which the electric field E is represented classically.[26] However, to write out such equations exactly is difficult even for the simplest atomic gas media. Therefore it is necessary to use reasonable physical approximations which, on the one hand, considerably simplify the system of material equations and, on the other, preserve the features of the optical medium that are most important for an analysis of the problem. In the study of the self-action of ultrashort pulses, i.e., pulses with a very wide spectrum, it is essential that the material equations adequately account for dispersion of both the linear and the nonlinear susceptibility of the dielectric medium over practically its entire transparency range.

In Refs. 25, 27–30, usng the density matrix formalism Azarenkov *et al.* derived material equations satisfying this requirement. Their treatment of the linear polarization response takes into account the contribution of both the electron and phonon subsystems of the dielectric. This made it possible to describe both normal and anomalous group dispersion. Their treatment of the nonlinearity of the medium response takes into account its most important mechanisms in an ultrashort pulse field—namely, electronic and electronic–vibrational. Each of these mechanisms was described in the approximation of a three-level medium. It has been proved[31] that such an approximation provides the minimum accuracy needed for an adequate description of the dispersion of the nonlinear refractive index of the medium in its transparency range. Reference 32 gives an intuitive interpretation of the resulting material equations in terms of the classical theory of dispersion of intense light fields. The essence of this interpretation is that in the classical theory of dispersion the dependence of the nonlinear refractive index of an optical medium on the frequency of the light wave has the same form as in quantum theory if the structural unit of the material in the Lorentz model is taken to be not one, but at least two parametrically coupled nonlinear oscillators. Thus, it has been shown that the polarization response of the dielectric medium $P=P_e+P_i$ is described by the system of material equations

$$\frac{\partial^2 P_e}{\partial t^2}+\frac{2}{T_e}\frac{\partial P_e}{\partial t}+\omega_e^2 P_e=\alpha_e E+\beta(R_e+R_v)E,$$

$$\frac{\partial^2 P_i}{\partial t^2}+\frac{2}{T_i}\frac{\partial P_i}{\partial t}+\omega_i^2 P_i=\alpha_i E,$$

$$\frac{\partial^2 R_e}{\partial t^2}+\frac{2}{T_{e1}}\frac{\partial R_e}{\partial t}+\omega_{e1}^2 R_e=\gamma_e(P_e+P_i)E,$$

$$\frac{\partial^2 R_v}{\partial t^2}+\frac{2}{T_v}\frac{\partial R_v}{\partial t}+\omega_v^2 R_v=\gamma_v(P_e+P_i)E, \qquad (5)$$

where P_e and P_i are the contributions to the polarization of the electronic and ionic components; the oscillators described by the dynamical variables R_e and R_v give rise to nonlinear parametric coupling between the pulse electric field and the medium [here the dynamical parameter R_e is responsible for the electronic nonlinearity, and the dynamical parameter R_v—for the electronic–vibrational (Raman) nonlinearity; the phenomenological parameters of the medium α_e, ω_e, T_e and α_i, ω_i, T_i characterize the dispersion of the electronic linear polarization response and ionic (vibrational) in Gaussian linear polarization response, respectively; and the coefficients β, γ_e, ω_{e1}, T_{e1} and γ_v, ω_v, T_v characterize the dispersion of the electronic and electronic–vibrational nonlinear polarization response, respectively]. System of equations (5) adequately describes the dispersion both of the linear and of the nonlinear refractive index of a dielectric medium over practically its entire transparency range. Thus, for example, for quartz glasses for $\omega_e=2.096\times10^{16}$ s^{-1}, $\alpha_e=3.862\times10^{31}$ s^{-2}, $\omega_i=2.154\times10^{14}$ s^{-1}, and $\alpha_i=2.534\times10^{27}$ s^{-2} the dispersion of the linear refractive index in the visible and near-infrared is described by equations (5) out to four significant figures (Fig. 1), and for $\omega_{e1}=3.0\times10^{16}$ s^{-1}, $\omega_v=8.3\times10^{13}$ s^{-1}, and $\beta=2.0\times10^{43}$, $\gamma_e=2.9\times10^{9}$, and $\gamma_v=8.0\times10^{3}$ in Gaussian units they also describe the dispersion of the low-inertia coefficient of the nonlinear refractive index n_2 (Fig. 2) in good

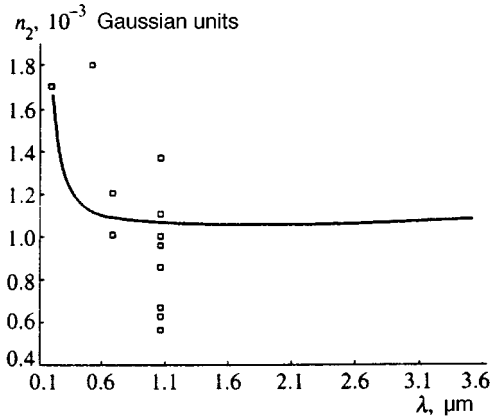

FIG. 2. Dispersion of the nonlinear refractive index coefficient $n_2(\lambda)$ of quartz glass (λ is the wavelength, the points are experimental data, the solid curve is the dispersion calculated according to the theoretical model (5).

agreement with known experimental results. Figure 2, of course, requires comment. Quartz glass is the dielectric material for which the largest number of measurements of the low-inertia coefficient n_2 have been carried out, and at different wavelengths (see the review in Ref. 25). However, as can be seen from the figure, the experimental results of different authors (denoted in Fig. 2 by squares) differ substantially, thanks to the great complexity of optical measurements of this type.[25] Therefore their interpolation by a theoretical dependence for the above-listed parameters is quite complicated, and when more reliable experimental data are obtained it will be possible to refine the model medium parameters in system (5) defining n_2.

We supplement system (5) with Maxwell's equation

$$\Delta E-\frac{1}{c^2}\frac{\partial^2 E}{\partial t^2}=\frac{4\pi}{c^2}\frac{\partial^2}{\partial t^2}(P_e+P_i), \tag{6}$$

where c is the speed of light in vacuum.

Thus, the problem of the propagation of an ultrashort optical pulse with frequency spectrum falling within the transparency region of the dielectric medium reduces to a study of the closed nonlinear system consisting of the material equations (5) and the wave equation (6). Such a system, however, is hard to analyze. Therefore we will reduce it to something simpler using the nonresonant approximation, whose essence is laid out below.

3. WAVE EQUATION DESCRIBING THE NONRESONANT INTERACTION OF AN ULTRASHORT PULSE WITH A DIELECTRIC MEDIUM

In dielectrics the natural frequencies of the medium determining electronic and ionic absorption usually differ by orders of magnitude. In the given example of quartz glass $\omega_e/\omega_i\sim 10^2$. Therefore, if the frequency $\overline{\omega}$ corresponding to the center of the spectrum of an ultrashort pulse (it is no longer possible to introduce the concept of a carrier frequency for such short signals) satisfies the condition

$$\omega_v^2,\omega_i^2\ll\overline{\omega^2}\ll\omega_e^2,\omega_{e1}^2. \tag{7}$$

then even for pulses with spectral width $\Delta\omega\sim\overline{\omega}$ the interaction of the radiation with the medium in the linear optics approximation can be taken to be nonresonant. That is, in this paper we do not consider the situation of a single-photon resonance with an accompanying large linear absorption, but allow for the possibility of two-photon resonances of both an electronic and a Raman nature. The latter case is realized in a Raman-active dielectric automatically since the wide spectrum of an ultrashort pulse contains an infinite set of spectral components satisfying the conditions for stimulated Raman resonance.[28,33] Note that condition (7) includes within itself the two inequalities (3) and (4) used above.

The relation $\overline{\omega^2}\gg\omega_i^2$ [see Eq. (7)] implies that low-frequency components are almost completely absent from the spectrum of the ulatrashort pulse, i.e., it imposes the condition

$$\int_{-\infty}^{+\infty}E\,dt=0 \tag{8}$$

on the ultrashort pulse.

This means that self-action of half-wavelength pulses remains outside the scope of the present paper, i.e., self-action of solutions in the form of bell-shaped video pulses, which have attracted so much interest in the context of the interaction of ultrashort pulses with matter, when the natural frequencies of the medium are spanned by the pulse spectrum.[10,11,13,14,16,18]

Expanding in the small dynamical parameter $(\overline{\omega}/\omega_e)^2$ in the first of equations (5) in accordance with the nonresonant approximately (7), we find

$$P_e\simeq\frac{\alpha_e}{\omega_e^2}E-\frac{\alpha_e}{\omega_e^4}\frac{\partial^2 E}{\partial t^2}+\frac{\beta}{\omega_e^2}(R_e+R_v)E. \tag{9}$$

By virtue of $(\overline{\omega}/\omega_i)^2\gg 1$, we find from the second of equations (5)

$$\frac{\partial^2 P_i}{\partial t^2}\simeq\alpha_i E. \tag{10}$$

Comparing Eqs. (9) and (10), we obtain the estimate

$$P_i/P_e\sim(\alpha_i/\alpha_e)(\overline{\omega}/\omega_e)^2.$$

Usually $\alpha_i\ll\alpha_e$. Also taking conditions (7) into account, we find $P_i\ll P_e$. Therefore, in the last two equations of system (5) we may set $P_i=0$. Then from these equations and also Eq. (9) taking conditions (7) into account, we have

$$P_e\approx\frac{\alpha_e}{\omega_e^2}E-\frac{\alpha_e}{\omega_e^4}\frac{\partial^2 E}{\partial t^2}+\frac{\beta\alpha_e\gamma_e}{\omega_e^4\omega_{e1}^2}E^3+\frac{\beta\alpha_e\gamma_v}{\omega_e^4}E\int_{-\infty}^{t}dt'\int_{-\infty}^{t'}E^2dt''. \tag{11}$$

The simplified material equations (10) and (11), like the original system of equations (5), contain the main characteristics of the medium for estimating the evolution of ultrashort pulses. Thus, Eq. (10) takes account of the contribution to the anomalous group dispersion of the ionic (lattice) vibrations. Expansion (12) takes account of the normal group dispersion due to the electron subsystem of the dielectric

medium and also the polarization response nonlinearity, both electronic and Raman. As follows from Eq. (12), the latter type of nonlinearity has an inertial character. The first-order expansion in small dynamical parameters in Eqs. (10) and (11) does not take account of attenuation of the ionic and electronic contributions to the polarization. This attenuation defines the absorption of radiation in the medium, which in the case of the nonresonant interaction (7) we can take to be small. Relaxation of a Raman nature can also be neglected since the corresponding characteristic times in dielectrics significantly exceed the duration of an ultrashort pulse. For example, for quartz glass we have $T_v \simeq 70$ fs.

Next, substituting Eqs. (10) and (11) in Eq. (6) and employing the approximation of unidirectional wave propagation,[7] we obtain the following closed nonlinear equation for the pulse electric field:

$$\frac{\partial E}{\partial z} - a\,\frac{\partial^3 E}{\partial \tau^3} + b\int_{-\infty}^{\tau} E\,\alpha\tau' + gE^2\,\frac{\partial E}{\partial \tau} + q\,\frac{\partial}{\partial \tau}\left(E\int_{-\infty}^{\tau} d\tau' \int_{-\infty}^{\tau'} E^2 d\tau''\right) = \frac{c}{2n_0}\,\Delta_\perp \int_{-\infty}^{\tau} E\,d\tau'. \tag{12}$$

Here the pulse propagates in the z direction, $\Delta_\perp$ is the transverse Laplacian, $\tau = t - n_0 z/c$ is time in the comoving system of coordinates, and the coefficients a, b, g, and q are algebraic combinations of the medium parameters introduced above:

$$a = \frac{n_0^2 - 1}{2cn_0\omega_e^2}, \quad b = \frac{2\pi\alpha_i}{cn_0},$$

$$g = \frac{3n_2}{c}, \quad q = \frac{\gamma_v}{\gamma_e}\,\omega_{e1}^2\,\frac{n_2}{c}. \tag{13}$$

In relations (13) the low-frequency refractive index

$$n_0 = \sqrt{1 + 4\pi\alpha_e/\omega_e^2} \tag{14}$$

and the coefficient of the electronic nonlinear low-frequency refractive index

$$n_2 = \frac{2\pi\beta\alpha_e\gamma_e}{n_0\omega_e^4\omega_{e1}^2} \tag{15}$$

define the total refractive index corresponding to the subsystem of electronic transitions

$$n = n_0 + n_2 E^2. \tag{16}$$

In the reduced wave equation (12) the term on the right-hand side describes diffraction of the ultrashort pulse, and the second and third terms on the left-hand side describe dispersion of the electronic and Raman linear polarization response, respectively.

In the derivation of the reduced wave equation, the dielectric medium was assumed to be homogeneous. However, treating the coefficients α_e and α_i in the material equations (5) and, consequently, the parameters a, b, g, and q in Eq. (12) as independent of the transverse coordinates, we can also to analyze the self-action of ultrashort pulses in inhomogeneous media, e.g., waveguides (optical fibers).

4. ANALYSIS OF THE NONLINEAR WAVE EQUATION

Equation (12) allows us to compare the influence of both electronic and electronic–vibrational nonlinearity on the evolution of a light signal in a medium. Setting

$$\partial E/\partial\tau \sim \overline{\omega E} \quad \text{and} \quad \int_{-\infty}^{\tau} d\tau' \int_{-\infty}^{\tau'} E^2 d\tau'' \sim E^2\tau_p^2,$$

we obtain for the ratio of the nonlinear terms in Eq. (12)

$$\frac{q\,\dfrac{\partial}{\partial\tau}\left(E\int_{-\infty}^{\tau} d\tau' \int_{-\infty}^{\tau'} E^2 d\tau''\right)}{gE^2\,\dfrac{\partial E}{\partial\tau}} \sim \frac{\gamma_v}{3\gamma_e}\,(\omega_{e1}\tau_p)^2. \tag{17}$$

For quartz glass this ratio is equal to unity for $\tau_p = 35$ fs, while for pulses of duration $\tau_p = 10$ fs it is equal to only 0.08. Thus, it follows from (17) that as the duration of the ultrashort pulse decreases, the relative influence of the electronic–vibrational nonlinearity of the medium on the character of the self-action of the pulse decreases quadratically. For an ultrashort pulse with $\tau_p \lesssim 10$ fs, the nonlinearity can be neglected to first order. This conclusion, valid for quartz glasses and other media with moderate Raman activity, correlates well with the estimate of the inertial character of the contribution to n_2 for dielectrics with an electronic–vibrational nonlinearity mechanism.[25] Therefore we will analyze the wave equation

$$\frac{\partial E}{\partial z} - a\,\frac{\partial^3 E}{\partial \tau^3} + b\int_{-\infty}^{\tau} E\,d\tau' + gE^2\,\frac{\partial E}{\partial \tau} = 0, \tag{18}$$

i.e., we will take account only of the electronic nonlinearity of the medium, and also, guided by Eq. (12), we will restrict the discussion to the case of one-dimensional propagation of the pulse, taking the medium and the wave to be transversely homogeneous. For media with strong Raman activity the term describing the electronic–vibrational nonlinearity should be kept in the wave equation. In this case it is useful to refer to the results of Refs. 33–35 which analyze self-action of ultrashort pulses in model media with a purely Raman nonlinearity, i.e., they neglect all other effects considered in the present work even though these effects are usually important, as was shown above, for ultrashort pulses in dielectrics.

It is important to note that the nonlinear wave equation (18), which describes the dynamics of an ultrashort pulse field in the limiting case of ''long'' pulses (with duration greater than ten periods), transforms into the cubic, modified nonlinear Schrödinger equation (1) with higher orders of dispersion theory taken into account, which characterizes the variation of the pulse envelope. This is not hard to do if we substitute the field in the form (2) into Eq. (18) and differentiate in the usual way[7] for the slowly varying envelope and then integrate using multiple integration by parts:

$$\int_{-\infty}^{\tau} E d\tau' = \frac{1}{2}\left(-i\,\frac{\varepsilon}{\omega} + \frac{1}{\omega^2}\frac{\partial \varepsilon}{\partial \tau} + \frac{i}{\omega^3}\frac{\partial^2 \varepsilon}{\partial \tau^2} - \frac{1}{\omega^4}\frac{\partial^3 \varepsilon}{\partial \tau^3} + \ldots \right) \times e^{i(\omega\tau - kz)} + \text{c.c.}$$

The relations between the coefficients of the modified nonlinear Schrödinger equation (1) and the wave equation (18) have the form

$$\alpha_1 = -\frac{3a}{\omega^3}(\omega_c^4 - \omega^4), \quad \alpha_2 = -a(1 + 3\omega_c^4/\omega^4),$$

$$\beta_0 = -g\omega/4, \quad \beta_1 = g/4, \quad \omega_c^4 = b/3a,$$

$$T = \tau - 3a\omega^2[1 + (\omega_c/\omega)^4]z. \tag{19}$$

Thus, Eq. (18) contains Eq. (1) as a special case, being a generalization of the latter when the slowly-varying-envelope approximation is invalid.

As in the case of a quasi-monochromatic wave packet (2) self-action of ultrashort pulses in a dielectric medium varies, depending on whether the main part of its spectrum lies in the region of normal or anomalous dispersion.

In the first case, dispersion is defined mainly by the electronic linear polarization response, i.e., the second term in Eq. (18). But if the linear lattice response, i.e., the third term in the wave equation (18) can be neglected, then Eq. (18) takes the form of the modified Korteweg–de Vries equation

$$\frac{\partial E}{\partial z} - a\,\frac{\partial^3 E}{\partial \tau^3} + gE^2\,\frac{\partial E}{\partial \tau} = 0. \tag{20}$$

In this case, it is important that the coefficients a and g in Eq. (20) are positive. Therefore the self-action of ultrashort pulses in dielectrics for the case under consideration consists in their temporal defocusing added onto linear-dispersional pulse spreading. The duration of the pulse increases due to generation in the medium of new light fields.[36] Equation (20) has no solutions in the form of solitary waves (solitons and breathers).

In the case of anomalous group dispersion, the third term in Eq. (18) cannot be neglected, since it is specifically this term that defines anomalous group dispersion. The nature of the evolution of the ultrashort pulse changes qualitatively.

Figure 3 presents results of a numerical calculation of the nonlinear propagation of an ultrashort pulse whose spectrum belongs to the region of anomalous dispersion of the group velocity.[37] The parameters of Eq. (18) in this calculation correspond to quartz glass. The duration of the ultrashort pulse does not vary as the pulse propagates in the medium, and the dynamics consist in the periodic evolution of the internal structure of the pulse. This result correlates with the results of Ref. 38 in which the numerical calculation of the unreduced system (5)–(6) also demonstrates that an ultrashort pulse of soliton (breather) type can form in a dielectric.

Analytical solitonlike solutions of Eq. (18) are hard to find. This is because the nonlinear wave equation (18) for $b=0$, as previously noted, does not have soliton solutions. Therefore, for $b \neq 0$ the usual soliton perturbation theory,[39] which considers slow variations of the parameters of ''starter'' solutions of the equations being integrated, cannot

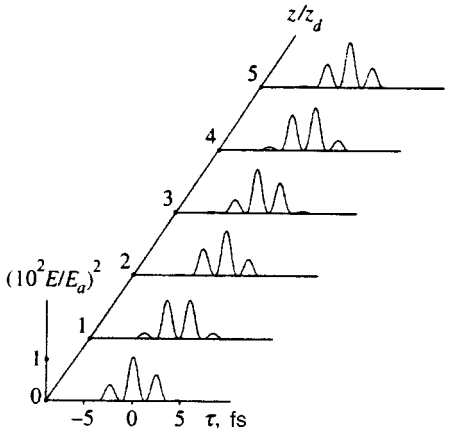

FIG. 3. Dynamics of an ultrashort pulse in a dielectric. The field E is scaled by the intra-atomic field $E_a = e/a_B^2$ (e is the charge of the electron, a_B is the Bohr radius), and the coordinate z is scaled by the dispersion spreading length $z_d = \tau_p^2/2|\alpha_1|$ (Ref. 8).

be applied to it. Thus, the presence of the integral term in Eq. (18) is fundamental for the existence of solitonlike solutions, and the term in question cannot be regarded as a small perturbation. Despite these difficulties, quantitative relations between the parameters of the breather can be found through analytic continuation of the dispersion parameters to the complex plane.[40–43] A detailed justification of this method applied to two-parameter solutions is given in Ref. 43. Its essence consists in the following. Let $f(\omega,k)=0$ be the dispersion relation of the linearized equation whose original nonlinear variant allows a solution in the form of solitary waves. Carrying out analytic continuations of the form

$$\omega \to \omega + i\gamma, \quad k \to k + i\text{k}$$

and then making these substitutions in the original relation $f(\omega,k)=0$, after separating the real and imaginary parts we obtain two equations linking the four parameters. Thus we obtain two free parameters. We may take as these two free parameters the filling frequency ω and the duration $\tau_p = 2/\gamma$ of the pulse. The factor of 2 in the latter relation arises because the field of a solitonlike pulse is exponentially localized on both sides of its ''center of mass.'' In this case, the group velocity of the pulse v_g is equal to γ/k and the phase velocity of the oscillations filling the pulse v_{ph} is equal to ω/k. A solitonlike solution (pulse) of Eq. (18) has two degrees of freedom: an external degree of freedom responsible for its translational motion as a solitary pulse, and an internal degree of freedom corresponding to pulsations of the profile of the breather in the comoving coordinate system. Therefore there are grounds to assume that any solitonlike solution of Eq. (18) is a two-parameter solution.

Linearizing Eq. (18), we find a dispersion relation for it of the form

$$k = a\omega^3 - b/\omega. \tag{21}$$

Hence it follows that the condition of anomalous group dispersion, when formation of optical solitons is possible for $n_2 > 0$,

$$\partial^2 k/\partial \omega^2 < 0 \tag{22}$$

can be rewritten as

$$\omega < \omega_c , \tag{23}$$

where the critical frequency is

$$\omega_c = \left(\frac{b}{3a} \right)^{1/4} = \left(\frac{\alpha_i}{3\alpha_e} \right)^{1/4} \omega_e . \tag{24}$$

Condition (23) is valid for envelope pulses having a narrow spectral component at the frequency ω. The spectral width of a pulse containing only a few periods depends substantially on its duration. Let us generalize the given condition to the case of ultrashort pulses.

Applying to Eq. (21) the above-proposed procedure of analytic continuation of the dispersion parameters to the complex plane, we obtain

$$k(\omega, \gamma^2) = a\omega^3 - 3a\omega\gamma^2 - b\,\frac{\omega}{\omega^2+\gamma^2}, \tag{25}$$

$$\frac{1}{v_{\rm ph}} = a\omega^2 - 3a\gamma^2 - \frac{b}{\omega^2+\gamma^2}, \tag{26}$$

$$\frac{1}{v_g} - \frac{1}{v_{\rm ph}} = 2\left[a(\omega^2+\gamma^2) + \frac{b}{\omega^2+\gamma^2} \right]. \tag{27}$$

As could be expected, for $b=0$ and $a<0$ expression (27) coincides with the corresponding expression for a MKdV breather,[39] which is an important argument on behalf of the proposed method. According to Eq. (8) the parameter ω is always nonzero for solution (18) in the form of a solitary pulse. Therefore the given solution cannot be a single-parameter solution. Since we have $a,\ b>0$, it must be the case that $v_g \neq v_{ph}$ [see Eq. (27)]. Consequently, Eq. (18) has no solutions in the form of traveling pulses with a steady-state profile.

Let us now determine the region of possible values of the parameters ω and $\gamma = 2/\tau_p$ of the solitonlike solution of Eq. (18). Broadening of the spectrum of an ultrashort pulse corresponds to entrainment of a continually increasing number of frequency components into the dynamics of the pulse. For the formation of a solitonlike pulse it is important that these components lie in the region of anomalous group dispersion. The mentioned broadening of the spectrum of an ultrashort pulse is taken into account in relation (25). Hence we arrive at the following generalization of condition (22) to the case of an ultrashort pulse:

$$\frac{\partial^2 k(\omega, \gamma^2)}{\partial \omega^2} < 0. \tag{28}$$

Substituting relation (25) here, we find the equation of the curve in the (ω, γ) plane enclosing the values of ω and γ corresponding to solitonlike pulses:

$$(W^2+G^2)^3 = W^2 - 3G^2, \tag{29}$$

where $W \equiv \omega/\omega_c > 0$ and $G \equiv \gamma/\omega_c > 0$.

The region of possible values of ω and γ for a solitonlike pulse is shown by the shaded area in Fig. 4. The curve bounding this region from above is defined by Eq. (29). It is easy to see from this equation that in the low-frequency region the given curve has the form of a straight line:

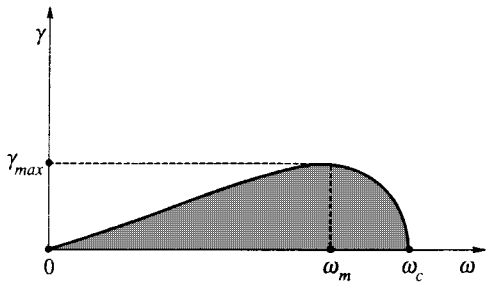

FIG. 4. Region of possible values of the pulse parameters $\omega \equiv 2\pi/T_p$ and $\gamma \equiv 2/\tau_p$ of Eq. (18) (shaded). The upper boundary of this region is described by Eq. (29). The value $\gamma_{\max} = 0.18\omega_c$ corresponds to the minimum duration $\tau_p^{\min} = 11.1\omega_c^{-1}$ of a pulse that can be formed in the dielectric. The ratio of the duration $\tau_p^{\min}$ of the given pulse to the period of the optical oscillations T_p filling it is equal to 1.33 for any solid dielectric in its transparency region. The critical frequency ω_c is determined by the concrete parameters of the dielectric.

$\gamma \simeq \omega/\sqrt{3}$. Hence it follows, in particular, that as $\omega \to 0$ the pulse duration $\tau_p = 2/\gamma \to \infty$. This circumstance is in line with the conclusion made above that the central frequency of the spectrum of an ultrashort pulse cannot be equal to zero [see condition (8)]. Near the critical frequency $\gamma \approx \sqrt{(\omega_c^2 - \omega^2)/3}$.

A numerical study of the transcendental equation (29) leads to the result (see Fig. 4) that

$$\gamma_{\max} = 0.18\omega_c , \quad \omega_m = 0.76\omega_c . \tag{30}$$

It should be especially stressed that relations (30) are universal for solid isotropic dielectrics and do not depend on their specific structure ''encoded'' in the parameter ω_c. The magnitude of $\gamma_{\max}$ corresponds to the minimum value of the pulse duration $\tau_p^{\min}$ that can be formed in a solid dielectric. Knowing $\tau_p^{\min}$ is important from the point of view of determining the maximum transmission rate of information in dielectric light-guides. The period of the oscillations filling the breather is $T_p = 2\pi/\omega$. Thus for a pulse of minimum duration we find $\tau_p^{\min}/T_p = \omega_m/\pi\gamma_{\max} \approx 1.33$. Thus, the result obtained here corresponds to the results of our numerical experiments with Eq. (18), namely, that the ultrashort pulse holds within itself roughly one and a half periods of the light wave. Using relations (30), let us obtain numerical estimates of the minimum pulse duration and its corresponding filling frequency for quartz glass. It follows from relation (24) and the numerical parameter values given above that for quartz glass $\omega_c = 0.07\omega_e = 1.47 \times 10^{15}\ \text{s}^{-1}$. Thus, the minimum pulse duration is $\tau_p^{\min} = 7$ fs and its filling frequency is $\omega_m = 1.06 \times 10^{15}\ \text{s}^{-1}$. The latter frequency corresponds to a wavelength of $\lambda_m = 2\pi c/\omega_m = 1.8\ \mu$m, lying in the region of the anomalous group dispersion. Let us now estimate the frequency of pulsations Ω of the profile of the electric field of the traveling pulse in the accompanying coordinate system. This estimate may be found from the formula[22]

$$\Omega \approx (c\omega/n_0)(1/v_g - 1/v_{\rm ph}).$$

Next employing relations (27), (13), and (30), for the shortest pulse corresponding to relations (30) we find

$$\Omega \approx 4.2\,\frac{n_0^2-1}{n_0^2}\left(\frac{\omega_c}{\omega_e}\right)^2 \omega_c .$$

Above we found $\omega_c = 0.07\omega_e = 1.47\times 10^{15}$ s^{-1} for quartz glass. Also substituting the value $n_0 = 1.45$ here,[25] we obtain $\Omega \approx 1.5\times 10^{13}$ s^{-1}, which is significantly smaller than the corresponding pulse filling frequency $\omega = 1.06\times 10^{15}$ s^{-1} (see above). Thus, the deformation of the profile of the pulse electric field in the comoving coordinate system varies quite slowly, so that the parameter Ω/ω can be taken to be small.

Let us estimate the intensity of an ultrashort solitonlike pulse. A soliton is the result of a balance between nonlinearity and dispersion. Equating the corresponding terms in Eq. (18), we obtain for the amplitude of the pulse electric field

$$E_m \sim \frac{1}{\tau_p}\sqrt{\frac{a}{g}\left(\frac{\omega_c^4}{\omega^4}-1\right)}.$$

Thus the estimate for its intensity, taking relations (30) and (13) into account, has the form

$$I \sim \frac{c}{n_2}\,(\omega_e \tau_p)^{-2}.$$

Substituting the characteristic values $n_2 \sim 10^{13}$ emu and $\omega_e = 2.1\times 10^{16}$ s (Ref. 25) for quartz glass, and also $\tau_p = 7$ fs (see above), we find $I \sim 10^{13}$ W/cm^2.

To conclude the present section, we note that the nonlinear wave equation (18) can be written in the form of a variational principle:

$$\delta \int_{-\infty}^{+\infty} \mathscr{L}\, d\tau = 0, \tag{31}$$

where the ''Lagrangian'' is equal to

$$\mathscr{L} = \frac{1}{2}\frac{\partial \Phi}{\partial z}\frac{\partial \Phi}{\partial \tau} + \frac{a}{2}\left(\frac{\partial^2 \Phi}{\partial \tau^2}\right)^2 - \frac{b}{2}\,\Phi^2 + \frac{g}{12}\left(\frac{\partial \Phi}{\partial \tau}\right)^4, \tag{32}$$

and the pulse electric field is $E = \partial\Phi/\partial\tau$.

The existence of a variational principle for Eq. (18) allows us to study the formation and propagation of an ultrashort pulse with the help of the approximate method of the ''average Lagrangian'' due to Ritz and Whitham.[44] A necessary condition for the application of this method is the presence of a slow dynamical variable. As was shown above, as such a variable we may choose the pulsation frequency Ω of the breather in the comoving coordinate system since $\Omega \ll \omega$, τ_p^{-1}. We propose to pursue this topic in future work.

5. CONCLUSION

In the present work we have derived a nonlinear wave equation (12) describing the propagation of an ultashort pulse in dielectrics in the case in which the pulse spectrum lies in the transparency range of the material. We have taken account of diffraction, dispersion, and the nonlinearity of the polarization response of the medium. We have discussed the properties of the solutions of this equation in the form of transversely homogeneous waves propagating in homogeneous dielectrics. We have shown that these properties differ qualitatively depending on whether the spectrum of the ultrashort pulse lies in the region of normal or anomalous dispersion of the medium. In the first case the pulse experiences both linear and nonlinear temporal defocusing, while in the second it can propagate in the form of solitons. We have presented results of numerical and analytical studies of the properties of ultrashort optical solitons. In this context, it is of special interest to determine the region of the parameters ω and τ_p^{-1} of the soliton that is independent of the specific structure of the dielectric. We also obtained relations (30), which define the minimum possible duration of an optical soliton in a dielectric and the corresponding filling frequency in terms of the critical frequency ω_c. These relations are valid for any isotropic solid dielectric and in this sense are universal, as is the conclusion that a minumum-duration pulse contains roughly one and a half periods of the optical oscillations. We have also shown that Eq. (18) has no solutions in the form of isolated video solitons, which, consequently, cannot form in an isotropic dielectric.

However, many questions of the nonresonant, nonlinear optics of ultashort pulses remain unanswered. Among these we note the following:

1. Even for an ultrashort pulse with a homogeneous planar wavefront only a general analysis has been attempted of the solutions of the wave equation. Self-action of an ultrashort pulse whose spectrum contains both normal and anomalous group dispersion has not been discussed. The nature of the evolution of an ultrashort pulse as a function of the duration and energy of the pulse has not been investigated. The interaction of ultrashort pulses with each other has not been analyzed.

2. A theoretical discussion of the nonlinear evolution of an ultrashort pulse in a dielectric medium with diffraction of real, transversely bounded signals taken into account still stands before us, both in homogeneous and inhomogeneous media (including optical fibers).

3. The model we have constructed of the propagation of an ultrashort pulse in a dielectric is valid only for linearly polarized radiation. Self-action of elliptically polarized ultrashort pulses will be qualitatively different since they induce not only inhomogeneity of the refractive index but also anisotropy of the medium in a nonlinear medium.[25]

4. The analysis presented here is valid in essence only for isotropic dielectrics in which the lowest-order nonlinearity is the cubic. In dielectric crystals without an inversion center the quadratic nonlinearity also plays an important role.

5. Dielectric media in an ultrashort pulse field are characterized by high optical strength. The maximum values of the intensity at which transparent glasses and crystals do not yet break down, according to the estimates in Ref. 8, can reach 10^{15} W/cm^2. Under these conditions nonlinearities of higher orders, including nonlinearities of a different nature from those considered here, will possibly play an important role.

6. A study of the mathematical properties of the nonlinear wave equation (18) is of no small interest because the presence of the integral term is fundamental for solitonlike solutions. This term, for this reason, cannot be thought of as a small addition to the modified KdV equation. Consequently, the standard perturbation theory for solitons is inap-

plicable here. In this case it may be helpful to use the variational principle (31), (32).

The answer to these and a number of other questions in addition to the results of the present work and the references we have cited lays a theoretical foundation for the nonlinear optics of ultrashort pulses for the case of non-resonant interaction of light with matter. Here we again note that we use the term ''non-resonant interaction'' here as above only in the sense of an approximation of linear optics, assuming linear absorption of light in dielectrics to be small because the spectrum of an ultrashort pulse belongs to the transparency region of the medium.

ACKNOWLEDGMENTS

This work was carried out with the support of the Russian Fund for Fundamental Research (Grants No. 96-02-19140a and No. 96-02-16228a), the State Committee for Higher Education (Grant No. 95-0-5.5-79), and the European Association INTAS within the framework of the program ''International Center for Fundamental Physics, Moscow'' (Grant No. 93-2492).

[1] D. N. Auston, K. P. Cheung, J. A. Vaidmanis, and D. A. Kleinman, Phys. Rev. Lett. **53**, 1555 (1984).
[2] J. A. Vaidmanis, R. L. Fork, and J. P. Gordon, Opt. Lett. **10**, 131 (1985).
[3] R. L. Fork, C. H. Brito-Cruz, P. C. Becker, and C. V. Shank, Opt. Lett. **12**, 483 (1987).
[4] P. C. Becker, H. L. Fragnito, J. Y. Bigot *et al.*, Phys. Rev. Lett. **63**, 505 (1989).
[5] J. T. Darrow, B. D. Hu, X. C. Zhang, and D. H. Auston, Opt. Lett. **15**, 323 (1990).
[6] V. L. Ginzburg, *The Propagation of Electromagnetic Waves in Plasmas*, 2nd ed. (Pergamon Press, Oxford, 1970).
[7] M. B. Vinogradova, O. V. Rudenko, and A. P. Sukhorukov, *Theory of Waves* [in Russian] (Nauka, Moscow, 1979).
[8] S. A. Akhmanov, V. A. Vysloukh, and A. S. Chirkin, *Optics of Femtosecond Laser Pulses*, Amer. Inst. Phys. New York, 1992.
[9] A. Kujawski, Z. Phys. B: Condens. Matter **66**, 271 (1987).
[10] É. M. Belenov, P. G. Kryukov, A. V. Nazarkin *et al.*, JETP Lett. **47**, 523 (1988).
[11] É. M. Belenov and A. V. Nazarkin, Pis'ma Zh. Éksp. Teor. Fiz. **51**, 252 (1990) [JETP Lett. **51**, 288 (1990)].
[12] A. I. Maĭmistov and S. O. Elyutin, Opt. Spektrosk. **70**, 101 (1991) [Opt. Spectrosc. **70**, 57 (1991)].
[13] É. M. Belenov, A. V. Nazarkin, and V. A. Ushapovskiĭ, Zh. Éksp. Teor. Fiz. **100**, 762 (1991) [Sov. Phys. JETP **73**, 422 (1991)].
[14] S. V. Sazonov, JETP Lett. **53**, 420 (1991).
[15] A. Kujawski, Z. Phys. B: Condens. Matter **85**, 129 (1991).
[16] S. V. Sazonov, Laser Physics **2**, 795 (1992).
[17] A. V. Vederko, O. B. Dubrovskaya, V. F. Marchenko, and A. P. Sukhorukov, Vestnik MGU [Moscow State Univ. Bulletin], Series 3: Phys. Astron. **33**, 4 (1992).
[18] S. V. Sazonov and E. V. Trifonov, J. Phys. B **27**, L7 (1994).
[19] S. V. Sazonov and L. S. Yakupova, J. Phys. B **27**, 369 (1994).
[20] A. I. Maĭmistov, Opt. Spektrosk. **76**, 636 (1994) [Opt. Spectrosc. **76**, 569 (1994).
[21] A. I. Maĭmistov, Opt. Spektrosk. **78**, 483 (1995) [Opt. Spectrosc. **78**, 435 (1995).
[22] S. V. Sazonov, Fiz. Tverd. Tela **37**, 1612 (1995) [Phys. Solid State **37**, 875 (1995)].
[23] A. V. Andreev, Zh. Éksp. Teor. Fiz. **108**, 796 (1995) [JETP **81**, 434 (1995)].
[24] S. V. Sazonov, Opt. Spektrosk. **79**, 282 (1995) [Opt. Spectrosc. **79**, 260 (1995)].
[25] A. N. Azarenkov, G. B. Al'tshuler, N. R. Belashenkov, and S. A. Kozlov, Kvant. Elektron. **20**, 733 (1993) [Quantum Electron. **23**, 633 (1993)].
[26] D. N. Klyshko, *Physical Foundations of Quantum Electronics* [in Russian] (Nauka, Moscow, 1986).
[27] A. N. Azarenkov, G. B. Al'tshuler, and S. A. Kozlov, Opt. Spektrosk. **71**, 334 (1991) [Opt. Spectrosc. **71**, 195 (1991)].
[28] A. N. Azarenkov, G. B. Al'tshuler, and S. A. Kozlov, Proceedings of SPIE, Vol. 1841, p. 2 (1991).
[29] A. N. Azarenkov, G. B. Al'tshuler, and S. A. Kozlov, Studies in Math. Phys. **3**, 429 (1992).
[30] A. N. Azarenkov, G. B. Al'tshuler, S. A. Kozlov *et al.*, Proceedings of SPIE, Vol. 1983, p. 879 (1993).
[31] N. Bloembergen, H. Lotem, and R. T. Lynch, Indian J. Pure Appl. Phys. **16**, 151 (1978).
[32] S. A. Kozlov, Opt. Spektrosk. **79**, 290 (1995) [Opt. Spectrosc. **79**, 267 (1995)].
[33] É. M. Belenov, P. G. Kryukov, A. V. Nazarkin, and I. P. Prokopovich, Zh. Éksp. Teor. Fiz. **105**, 28 (1994) [JETP **78**, 15 (1994)].
[34] É. M. Belenov, V. A. Isakov, A. P. Kanavin, and I. V. Smetanin, JETP Lett. **60**, 770 (1994).
[35] É. M. Belenov, V. A. Isakov, A. P. Kanavin, and I. V. Smetanin, Kvant. Elektron. **22**, 193 (1995) [Quantum Electron. **25**, (1995)].
[36] V. I. Karpman, *Non-Linear Waves in Dispersive Media* (Pergamon Press, Oxford, 1975).
[37] S. A. Kozlov and S. V. Sazonov, *Technical Digest of the Fifteenth International Conference on Coherent Nonlinear Optics*, St. Petersburg, Vol. 1, p. 370 (1995).
[38] A. N. Azarenkov, S. A. Kozlov, P. V. Kuznetsov, and G. A. Martsinovsky, Proceedings of SPIE, Vol. 1983, p. 865 (1993).
[39] A. M. Kosevich and A. S. Kovalev, *Introduction to Nonlinear Physical Mechanics* [in Russian] (Naukova Dumka, Kiev, 1989).
[40] E. Schlömann, Appl. Phys. Lett. **19**, 274 (1971).
[41] V. G. Bar'yakhtar, B. A. Ivanov, and A. L. Sukstanskiĭ, JETP Lett. **27**, 211 (1978).
[42] S. V. Sazonov, Izv. Akad. Nauk SSSR, Ser. Fiz. **58**, 129 (1994).
[43] S. V. Sazonov, Zh. Éksp. Teor. Fiz. **107**, 20 (1995) [JETP **80**, 10 (1995)].
[44] D. Anderson, Phys. Rev. A **27**, 3135 (1983).

Translated by Paul F. Schippnick

Multiphoton static and polarization bremsstrahlung in collisions of charged particles with multiply-charged ions in a strong laser field

V. A. Astapenko

Physicotechnical Institute, 141700 Dolgoprudnyĭ Moscow Province, Russia

A. B. Kukushkin

Kurchatov Institute, 123182 Moscow, Russia

(Submitted 23 May 1996)
Zh. Éksp. Teor. Fiz. **111**, 419–439 (February 1997)

A universal analytic description of multiphoton bremsstrahlung, including the static and polarization bremsstrahlung channels, in the collision of charged particles with multiply-charged ions is obtained on the basis of a specified quantum/classical current for arbitrary ''quantum/classical'' motion of the incident particle. For the description of stimulated polarization bremsstrahlung, the method of equivalent Fermi photons and the Kramers electrodynamics method [V. I. Kogan, A. B. Kukushkin, and V. S. Lisitsa, Phys. Rep. **213**, 1 (1992)] are generalized to multiphoton processes. The resulting description of stimulated polarization bremsstrahlung is valid over a broad range about resonance, where its contribution is the most significant. The regions of polarization predominance over the static channel are indicated, and examples of interaction between the static and polarization channels are given. © *1997 American Institute of Physics.* [S1063-7761(97)00302-8]

1. Stimulated bremsstrahlung in a laser field (otherwise known as free–free or continuous–continuous transitions in a laser field, or laser-assisted scattering) plays an important role in the physics of interaction between radiation and matter, and has been investigated by a number of authors in various physical situations and approximations.

The investigation of this category of phenomena began with calculations in the approximation of the static scattering potential, i.e., static bremsstrahlung, for two opposite limiting values of the Coulomb parameter $\xi \equiv Ze^2/\hbar v$ (Ze is the charge of the target, and v is the initial velocity of the incident charged particle). Bunkin and Fedorov[2] treated the Born case ($\xi \ll 1$), while Berson[3] studied the semiclassical case ($\xi \gg 1$). The theory of static multiphoton bremsstrahlung was further elaborated in Refs. 4–9. Kroll and Watson[4] calculated the stimulated bremsstrahlung effect in the low-frequency limit for the scattering of an electron by a short-lived potential for arbitrary values of ξ, and Rahman[5] gave a simple derivation of their result in Ref. 4 for the Born case. Lisitsa and Savel'ev[6] generalized Berson's work[3] to bremsstrahlung in an external electromagnetic field in the alternative cases of narrow (single-mode) and broad (Planck radiation field) spectra. Veniard *et al.*[7] analyzed two-photon stimulated and spontaneous static bremsstrahlung in a Coulomb potential, using a Green's function method developed in Ref. 8. We also mention the recent work of Korol,[9] in which two-photon static bremsstrahlung is calculated in the distorted partial wave formalism.

At the same time, it has been shown in a major series of papers[10–12] (see also the review monograph[13] and Amusia's survey[14]) for spontaneous bremsstrahlung (or one-photon bremsstrahlung) that it is important to treat both channels—static and polarization—in radiation processes associated with charge scattering by a structured target particle (the formalism of calculating the contributions of both channels for slow-electron atomic bremsstrahlung has been developed in Ref. 15). The latter case is concerned with the emission of so-called polarization bremsstrahlung (dynamic bremsstrahlung,[10] atomic bremsstrahlung[11]), for which a (real) photon is generated as a result of interaction between the polarization current induced in the target and fluctuations of the electromagnetic vacuum in the case of spontaneous bremsstrahlung, and its interaction with the laser field in the case of stimulated bremsstrahlung. Polarization radiation as a universal phenomenon subsuming not only the well-known processes of macroscopic electrodynamics (e.g., transition radiation), but also more recently cited processes (polarization recombination[16] and polarization bound–bound transitions[17]) is a burgeoning branch of the theory of radiative processes in media beginning with the work of Buĭmistrov[10] and Tsytovich.[18]

Polarization radiation is based on the conversion of a portion of the energy of the electric self-field of a particle into dynamic polarization of the medium with the subsequent emission of a photon by the compound system. The spatial scale of the induced polarization varies over a wide range, from macroscopic scale to polarization of the Debye cloud around a charged particle, as in the virtual excitation of an individual atom, an ion with core, and a nuclear particle (see Ref. 13 for details). For the whole wide-ranging class of polarization radiation processes, it is useful to describe it as ''scattering'' of the electric self-field (which is longitudinal for a nonrelativistic particle) of the particle by fluctuations of the charge density in the medium, specifically as the nonresonant scattering of equivalent Fermi photons[19] by the ion core (for polarization radiation in the plasma-frequency range, this is analogous to the ''transition radiation'' of virtual waves of colliding particles[13,18]). Such an approach permits the well-established results for radiative processes to be applied to calculations of collision processes (for more de-

tails see Refs. 1 and 16 and Chap. 4 in Lisitsa's book[20]).

Dubois and Maquet[21] detailed the theory of spontaneous polarization bremsstrahlung for the case in which the target—atomic hydrogen—is incorporated exactly in the Coulomb Green's function formalism for an incident Born electron. Amusia *et al.*[22,23] have calculated the total bremsstrahlung, including the polarization kind, beyond the scope of the Born approximation for the scattering of electrons by a neutral xenon atom.

Especially noteworthy is the work of Verkhovtsev *et al.*,[24] who investigated spontaneous total bremsstrahlung theoretically and experimentally for Xe atoms in the frequency range corresponding to the giant resonance in the photoabsorption of xenon due to the $4d$ subshell. They calculated the differential cross section of total bremsstrahlung in the Born approximation with respect to the incident electron, while acknowledging the inadequacy of this approximation. The total bremsstrahlung on the same target in the spectral range of the ionization threshold of the $4d$ subshell was studied experimentally in a more recent paper.[25] A theoretical interpretation of the results of this work is given in Ref. 26, based on the so-called low-frequency approximation, by which it is possible to extend the Born treatment.

To the best of our knowledge, polarization effects in the scattering of an electron by an atom in the presence of a weak, near-resonance laser field were first taken into account in Ref. 27 for small momentum transfer from the incident particles, within the framework of the time-dependent close-coupling method.

Calculations of total multiphoton stimulated bremsstrahlung within the framework of a ''dipole'' perturbation of the target (neutral hydrogen and helium atoms), and the Born approximation for the incident particles, were carried out in Refs. 28 and 29 without and with excitation of the target, respectively. These papers stress the importance of ''dressing'' of the target by the laser field for small momentum transfer from the incident particle, a strong laser field, and/or the near-resonance case, where the laser photon energy is close to one of the natural frequencies of the target.

A general expression for the multiphoton stimulated bremsstrahlung cross section of an atom in a strong laser field, in the Born approximation with respect to the motion of the incident particle, and taking into account the emission of an arbitrary number of photons by way of the polarization channel, has been derived[30] and calculated.[31] Stimulated bremsstrahlung in a laser field of relativistic intensity has been investigated with allowance for polarization and excitation of the target.[32]

Two-photon stimulated bremsstrahlung has been calculated for the scattering of a Born electron by a hydrogen atom in the presence of a weak laser field[33] with allowance for virtual one- and two-photon excitation of the target (i.e., polarization effects). The authors mention the importance of these effects for the special case in which the hydrogen atom remains in its ground state after electron scattering.

An analysis of experimental data on the energy losses of electrons in small-angle scattering by helium atoms in a laser field[34] suggests the need to take the polarization channel into account when the effect is investigated under the given conditions.

The method of equivalent photons as a means of describing multiphoton polarization stimulated bremsstrahlung was summarized in Ref. 35.

Note that polarization bremsstrahlung from the Debye cloud around an ion in a plasma, originally called transition bremsstrahlung, was first investigated in Refs. 18 and 36 for the spontaneous process (see also Chaps. 2 and 3 in Ref. 13) and later with allowance for the interference of atomic and plasma polarization bremsstrahlung.[37] Multiphoton stimulated bremsstrahlung in a plasma has been calculated with allowance for the polarization channel.[38]

It is evident from the foregoing survey of the literature that most of the results in the theory of stimulated bremsstrahlung have been obtained for the case of Born motion of the incident particle, which admits of relatively simple calculations and for which the parameter ξ is small. However, radiation in a plasma with multiply-charged ions usually falls in the alternative range of semiclassical electron motion ($\xi \gg 1$), where the methods and concepts of Kramers electrodynamics are found to be productive.[1]

The objective of the present article is to obtain a universal analytic description of the multiphoton stimulated bremsstrahlung, encompassing the static and polarization channels, that occurs when charged particles collide with multiply-charged ions for arbitrary ''quanticity/classicality'' of the motion of the incident particle. The result obtained here admits of direct application in calculations of energy transfer between a plasma and a strong nonresonant laser field; this has important bearing on a great many practical problems. The description of stimulated polarization bremsstrahlung requires generalizations of the method of equivalent Fermi photons[19] and Kramers electrodynamics[1] to multiphoton processes.

In Sec. 2 we summarize the method of a specified (not necessarily classical) current for multiphoton processes in collisions of charged particles with multiply-charged ions. In Sec. 3 we generalize the method of equivalent Fermi photons to multiphoton processes in order to describe polarization bremsstrahlung. In Sec. 4 we analyze the resulting general expression for the probability of multiphoton stimulated bremsstrahlung, taking both mechanisms—static and polarization—into account. Finally, in Sec. 5 we indicate the region in which the polarization channel dominates the static channel, and we give examples of interaction between the two channels.

2. SPECIFIED-CURRENT APPROXIMATION FOR MULTIPHOTON PROCESSES IN COLLISIONS OF CHARGED PARTICLES WITH MULTIPLY CHARGED IONS: MULTIPHOTON STIMULATED STATIC BREMSSTRAHLUNG FOR ARBITRARY ξ

Major mathematical difficulties are encountered in the systematic quantum electrodynamic solution of the stated problem assuming summation of an infinite diagram series. The approach developed below corresponds to the approximate summation of such a series in the case of interest to us:

collisions of a charged particle with multiply-charged ions. This approach is based on the feasibility of describing radiation processes associated with electron scattering in the field of a multiply-charged ion in the approximation of a specified (not necessarily classical) current. The given model has a broad domain of applicability for the case of stimulated bremsstrahlung in the collision of charged particles with multiply-charged ions. The main condition for the approach to be valid is that the motion of the incident particle in the spatial region responsible for the emission of photons in a laser mode be only slightly perturbed by either the laser field (in comparison with the perturbation of the motion by the field of multiply-charged ions) or by the emission or absorption of a photon in and of itself (a real photon in static bremsstrahlung or an equivalent photon in polarization bremsstrahlung).

The weakness of the laser field relative to the ion field in the spatial region responsible for emission imposes an upper bound on the amplitude of the electric field component in the laser beam:

$$E_0 < \frac{Ze}{r_\omega^2}.$$

Here r_ω is estimated to be the characteristic distance at which a photon of frequency ω is emitted in the field of multiply-charged ions:

$$r_\omega \approx \left[Z \left(\frac{\mathrm{Ry}}{\hbar\omega} \right)^2 \right]^{1/3} a_B$$

(here Ry is the Rydberg energy, and a_B is the Bohr radius) in the high-frequency asymptotic limit in the semiclassical case[1,39] ($\xi \gg 1$, $\omega \gg \overline{\omega}$, and $\overline{\omega} \equiv mv^3/Ze^2$ is the characteristic Coulomb frequency), and

$$r_\omega \approx \frac{v}{\omega}$$

for the Born case ($\xi \ll 1$) and the low-frequency asymptotic limit in the case of semiclassical motion of the incident particle ($\xi \gg 1, \omega \ll \overline{\omega}$).

We now give the results of Refs. 2 and 3 for the opposite limiting types of motion of the incident particle.

The equation for the probability $W(n)$ of an n-photon static process in the Born case ($\xi \ll 1$), first obtained in Ref. 2, has the form

$$W(n) = J_n^2(\mathbf{a}\cdot\mathbf{q}). \tag{1}$$

Here J_n is the nth-order Bessel function, and $\mathbf{a} = e\mathbf{E}_0/m\omega^2$ is the amplitude of the electron oscillations in a laser field of frequency ω and amplitude $\mathbf{E}_0$, and $\hbar\mathbf{q}$ is the change in momentum of the incident particle due to inelastic scattering by a multiply-charged ion.

In the case of semiclassical motion ($\xi \gg 1$) Berson[3] (see also Ref. 6) obtained the similar result

$$W(n) = J_n^2\left(\left| \frac{m\omega \mathbf{a}\cdot\mathbf{v}_\omega}{\hbar} \right| \right), \tag{2}$$

where $\mathbf{v}_\omega$ is the Fourier component of the classical trajectory of the incident particle in the ion field.

The relationship between the formalism of the semiclassical description of bremsstrahlung and the specified current method has been analyzed in Ref. 3 at the qualitative level for the radiative transition of an incident particle in a static central field. For the calculation of multiphoton transitions of incident particles in a static central field in the presence of laser radiation for an arbitrary transition operator (that depends only on the coordinates), the specified classical current method can be justified quantum mechanically within the framework of the two-dimensional semiclassical method[1,40] by passing to the limit $\hbar \to 0$ in the quantum formalism of multiphoton transitions. The result of passing to this limit, which yields the correspondence principle for multiquantum inelastic processes, is given in Appendix A.

In the fast collision limit ($\omega\tau_{\mathrm{coll}} \ll 1$), which corresponds to weak inelasticity of the process, both results are represented, as noted in Ref. 3 (see also Ref. 6), by a single equation of the form (1), in which the vector $\hbar\mathbf{q}$ is again the momentum change in the incident particle in scattering by a multiply-charged ion for both $\xi \ll 1$ and $\xi \gg 1$.

We find that Eq. (1) can be extended to the region of strong inelasticity in the sense that the ratio of the total energy of the emitted photons to the initial energy of the incident particle E_i is not small. In this case the validity of the equation is actually restricted to weak perturbation of the motion of the incident particle by an emission event in the spatial region responsible for photon emission. This generalization of Eq. (1) essentially covers (provided that it is applicable to the region just mentioned) the region of strong inelasticity in the case of semiclassical motion of the incident particle—an electron in particular. In the latter case, as shown by a generalization of the Kramers electrodynamics formalism[1,39,40] to multiphoton processes (a generalization of the result described in Appendix A for the leading term in the limiting process for $\hbar$ in the quantum probability of the multiquantum inelastic transition of an incident particle), the actual condition for weak perturbation of the motion of an electron, according to the main conclusions of Kramers electrodynamics, is weak local kinematic inelasticity:

$$\mu \equiv n\hbar\omega / E_{\mathrm{kin}}(r_\omega),$$

where r_ω is the characteristic radius of revolution of an electron about an ion near the point of closest approach, and $E_{\mathrm{kin}}(r_\omega)$ is the local kinetic energy of the incident particle. In the case of semiclassical electron motion, which is in fact typical of the important practical case of collisions between electrons and multiply-charged ions, the condition of small μ is satisfied over a wide range of frequencies. Indeed, $\mu \approx n(\hbar\omega/\mathrm{Ry})^{1/3} Z^{-2/3}$, so that for typical frequencies of the Coulomb bremsstrahlung spectrum $\omega \approx mv^3/Ze^2$ we have $\mu \approx n/\xi$, and at the short-wavelength bremsstrahlung limit we obtain $\mu \approx (n/\xi)^{2/3}$.

Equation (1) can be generalized to the case of strong inelasticity and any degree of quantization of the incident

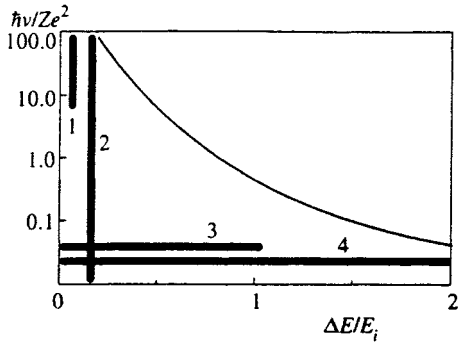

FIG. 1. ''Transition inelasticity vs. nonclassicality of motion'' diagram ($\Delta E = n\hbar\omega$). The region of validity of Eq. (3) lies above the curve. The numbers indicate the region of validity of the following results: *1*) multiphoton bremsstrahlung[2] and factorization of the multiphoton emission cross section in the first Born approximation, Jauch and Rohrlich (1956); see Ref. 42; *2*) two-photon bremsstrahlung in a Coulomb field, exact derivation[7,8] for arbitrary ζ, and multiphoton bremsstrahlung in the low-frequency approximation in a short-range potential[4]; *3*) multiphoton bremsstrahlung[3]; *4*) quantum derivation of equations for classical bremsstrahlung in a central field: one-photon[1,39,40] and multiphoton (the present study; see Appendix A).

particle motion by analyzing the matrix element of multiphoton transitions between the exact wave functions for motion of the incident particle in a static central ion field. This kind of generalization is based on matching the descriptions in the various regions of space $\{\hbar v/Ze^2,\ n\hbar\omega/E_i\}$. Here the first step is to demonstrate the validity of the description (1) in the low-frequency limit ($\hbar\omega \ll E_{ij}$, $\hbar\omega \ll E_f$) for arbitrary ξ. For the special case of the emission of two photons in a Coulomb field, this has been done[7] by elaborate calculations that expand upon the approach in Ref. 8 (we mention also that an equation for low frequencies and an arbitrary short-lived potential is given in Ref. 4). The second step is to extend the low-frequency description to the case of arbitrary inelasticity within the scope of classical motion of the incident particle in the rangle $\xi \gg 1$. This is achieved by the aforementioned justification of the specified classical current method (see Appendix A).

As a result of rigorous justification over the indicated ranges of parameters and interpolation over the intermediate range, we finally obtain the following universal representation for the probability of multiphoton bremsstrahlung in the static field of the target ion, covering the entire range of validity of the specific current approximation (see Fig. 1):

$$W_{\text{stat}}(n) = J_n^2\{(4n_{\mathbf{k}\lambda}^{\text{Las}} n_{\mathbf{k}\lambda}^{\text{stat}})^{1/2}\}, \tag{3}$$

where $n_{\mathbf{k}\lambda}^{\text{Las}}$ is the occupation number of photons in the laser mode ($n_{\mathbf{k}\lambda}^{\text{Las}} \gg 1$),

$$n^{\text{Las}} = (8\pi^3 c^2/\hbar\omega^3) I_{\text{Las}}, \tag{4}$$

I_{Las} is the spectral intensity of the laser radiation; $n_{\mathbf{k}\lambda}^{\text{stat}}$ is the occupation number of photons spontaneously emitted in the usual one-photon bremsstrahlung regime by an incident particle in the static ion field in laser mode $\{\mathbf{k},\lambda\}$, with wave vector $\mathbf{k}$ and polarization λ, during an inelastic (radiative) transition from a state with initial momentum $\mathbf{p}_i$ to a state with momentum in the same direction $\mathbf{n}_f \equiv \mathbf{p}_f/|\mathbf{p}_f|$ as that of the exact final quantum state (with momentum $\mathbf{p}_f$ and energy $E_f = E_i - n\hbar\omega$), and with an energy that differs from the initial energy by only one photon:

$$n_{\mathbf{k}\lambda}^{\text{stat}} = \frac{2\pi}{\hbar} \frac{|\omega(\mathbf{e}\cdot\mathbf{d}_{if1})|^2}{V d\sigma_{\text{scatt}}/d\Omega_{f1}}, \tag{5}$$

where $\mathbf{d}_{if1}$ is the matrix element for the emitting dipole moment of the incident electron between states $|i\rangle$ and $|f1\rangle$,

$$|i\rangle \equiv |\mathbf{p}_i\rangle \equiv |E_i \mathbf{n}_i\rangle \equiv |p_i^2/2m, \mathbf{p}_i/|\mathbf{p}_i|\rangle,$$
$$|f1\rangle \equiv |E_i - \hbar\omega, \mathbf{n}_f\rangle, \tag{6}$$

V is the quantization volume, and $d\sigma_{\text{scatt}}/d\Omega_f$ is the elastic scattering cross section of the incident particle in the ion field from state $|i\rangle$ to state $|f1\rangle$.

It is evident from Eq. (5) that the specified current method (in the region where it is valid; see Fig. 1) can be extended to the case of arbitrary quantum character of the motion of the incident property by replacing the classical Fourier transform $\mathbf{J}_\omega^{\text{proj}}$ of the current generated by the incident particles with the quantum-mechanical expression

$$\frac{m\langle f|\mathbf{j}^{\text{proj}}|i\rangle}{2\pi\hbar\sqrt{d\sigma_{\text{scatt}}/d\Omega_f}}. \tag{7}$$

In fact, by the correspondence principle[1,40] for one-quantum inelastic transitions of the incident particles in an arbitrary central field between the states described by the wave functions of the continuous spectrum (wave functions like $\Psi_{\mathbf{p}}^+$ and $\Psi_{\mathbf{p}'}^-$ in Ref. 41, Sec. 136), we obtain from (7) in the limit $\hbar \to 0$ the Fourier component of the classical trajectory in the argument of the Bessel function of Eq. (2). In the Born limit ($\xi \ll 1$), on the other hand, Eq. (7) coincides with the quantity $\mathbf{q}/\omega$ in Eq. (1) to within this same approximation, which is based on weak inelasticity of the transition (a change in the energy, i.e., the modulus of the momentum vector, provides $\mathbf{q}$ with a contribution of second-order smallness in comparison with the contribution of the angle of rotation of the momentum vector).

An equation for the cross section of the process can be obtained from (3) by summing over the statistical weights of the final state of the incident particle. This operation corresponds to multiplication of the emission probability by the Coulomb scattering cross section $d\sigma_{\text{Coul}}$ of the incident particle in the field of a multiply-charged ion:

$$d\sigma(n) = d\sigma_{\text{Coul}} W(n). \tag{8}$$

3. GENERALIZATION OF THE FERMI METHOD TO MULTIPHOTON PROCESSES: POLARIZATION BREMSSTRAHLUNG IN THE COLLISION OF A CHARGED PARTICLE WITH A MULTIPLY CHARGED ION IN A STRONG LASER FIELD

The ensuing generalization of the method of equivalent Fermi photons to the multiphoton case is based on the extension of the specified classical current approximation used in Refs. 3 and 6 as a means of describing multiphoton static stimulated bremsstrahlung for $\xi \gg 1$ to polarization stimulated bremsstrahlung, including arbitrary quantization of the motion of the incident particle.

Since, as mentioned previously,[1,16] the equivalent photon method is (within the scope of its validity discussed in the cited papers) insensitive to the quanticity/classicality of the motion of the charged particle producing the flux of equivalent photons, it is natural in the problem of multiphoton stimulated polarization bremsstrahlung to include the interaction of (quantized if necessary) the emitted/absorbed field of real photons not only directly via the incident particle current (as in ordinary, static bremsstrahlung), but also via the polarization current induced by the incident particle in the target ion/atom. For the case of a specified classical current (see below for the generalization to quantum motion of the incident particle), this adds an additional term to the Hamiltonian, so that the equation for the wave function χ of one mode of the laser field in the interaction picture assumes the form

$$i\hbar\ \frac{\partial\chi}{\partial t}=-e\left(\frac{2\pi\hbar}{\omega V}\right)^{1/2}(\mathbf{e}_{\mathbf{k}\lambda}\cdot\mathbf{j}^{\text{total}})[a_{\mathbf{k}\lambda}(t)+a^{+}_{\mathbf{k}\lambda}(t)]\chi. \quad (9)$$

Here a and a^{+} are the laser-mode photon annihilation and creation operators, $\mathbf{e}_{\mathbf{k}\lambda}$ is the unit polarization vector of the electric component of the laser radiation, e is the electron charge, and V is the quantization volume.

The Fourier transform of the total current, including the polarization current, is given by the expression

$$\mathbf{j}^{\text{total}}_{\omega}=\mathbf{j}^{\text{proj}}_{\omega}+\mathbf{j}^{\text{pol}}_{\omega}=\left[1-\left(\frac{m\omega^2}{Ze^2}\right)\alpha(\omega,\mathbf{E}_0)\right]\mathbf{j}^{\text{proj}}_{\omega}. \quad (10)$$

Here $\mathbf{j}^{\text{proj}}_{\omega}$ is the Fourier current of the incident-particle current, evaluated on the classical trajectory, and $\mathbf{j}^{\text{pol}}_{\omega}$ is the Fourier transform of the polarization current induced in the target.

Equation (10) corresponds to the dipole approximation, both in terms of the interaction of the laser radiation with multiply-charged ions and the incident electron, and with respect to interaction of the incident electron with multiply-charged ions. The first two conditions are expressed by the inequalities $\lambda>r_b$ and $\lambda>r(\omega)$, and the third condition is expressed by the inequality $r(\omega)>r_b$ (λ is the laser wavelength, r_b is the radius of the orbit of a bound electron in the multiply-charged ion, and $r(\omega)$ is the characteristic distance from the incident particle to the multiply-charged ion, which provides the main contribution to radiation of frequency ω). It is evident that the dipole approximation is valid over a wide range of emission frequencies.

The last condition, $r(\omega)>r_b$, also dictates that the field of the incident electron at the site of the bound electron is much lower than the field of the multiply-charged ion core. We can therefore assume that the following relation is approximately satisfied:

$$\mathbf{j}^{\text{pol}}\sim\chi(\mathbf{E}_0)\mathbf{j}^{\text{proj}}, \quad (11)$$

where $\chi(\mathbf{E}_0)$ is the total susceptibility operator of the electronic system of the multiply-charged ion (taking into account the influence of the laser field of amplitude $\mathbf{E}_0$), which includes the contribution of all harmonics of the incident particle field. This equation establishes a linear relation between the incident particle current and the current induced in the multiply-charged ion under the influence of the incident particle during scattering, justifying the choice of total current in the form (11).

For problems of energy transfer between the plasma and a strong laser field (but still, however, not greater than the Coulomb field of a multiply-charged ion in the effective zone of photon emission/absorption) due to the stimulated emission and absorption of radiation in the collision of plasma particles with multiply-charged ions, it is important to include the contribution of the polarization channel created in the presence of the electronic core of multiply-charged ions. This channel can be expected to play the greatest role when the main contribution to polarization stimulated bremsstrahlung is determined by the presence of one-photon near resonance of the laser field with the eigenfrequencies of multiply-charged ions. This case corresponds to the stimulated scattering of n equivalent photons of energy $\hbar\omega$, each ''emitted'' by the incident particle as it is scattered in the Coulomb field of a multiply-charged ion (under the influence of the laser field), by the core of the target ion and their subsequent conversion into n real photons. In a systematic QED analysis this process can be described by a sum of ''ladder'' diagrams (see Appendix B, which leads to near resonance of order n in the amplitudes of the n-photon processes. The indicated approach actually corresponds to a mechansim for the induced (stimulated, preferential) emission of quanta of energy at the frequency of the external field, not only for (real) photons, but also for virtual photons in anticipation of their coherent conversion to real photons.

The foregoing approach, however, overlooks contributions from resonances in the ion core with higher harmonics of the laser frequency. This would correspond to the inception of higher orders of polarizability (see Ref. 43) and, in particular, to a process such as the conversion of one virtual photon of energy $n\hbar\omega$, into n real photons, which in diagram language is represented by a single (for given n) ''comb'' diagram, and thus corresponds, first, to perturbation of the target ion over a considerably more restricted frequency range and, second, to the possibility of only first-order resonance in the amplitude of the process.

In our approximation we obtain

$$\mathbf{j}^{\text{total}}_{\omega}=\left[1-\left[\frac{m\omega^2}{Ze^2}\right]\alpha(\omega,\mathbf{E}_0)\right]\mathbf{j}^{\text{proj}}_{\omega}, \quad (12)$$

where $\alpha(\omega,\mathbf{E}_0)$ is the first-order polarizability at the frequency ω for the target ion, determined with allowance for the perturbation of the target by a laser field of amplitude $\mathbf{E}_0$.

4. PROBABILITY OF MULTIPHOTON STATIC+POLARIZATION INDUCED BREMSSTRAHLUNG

A consequence of Eqs. (9) and (10) is the following expression for the total probability of the n-photon emission/absorption process $W(n)$ in the case $n^{\text{Las}}\gg 1$ (n^{Las} is the occupation number of photons in the laser mode), which includes the static and polarization channels:

$$W_{\Sigma}(n)=J_n^2\{2(n^{\text{Las}}_{\mathbf{k}\lambda}n^{\text{stat}}_{\mathbf{k}\lambda})^{1/2}|1-\delta|\}. \quad (13)$$

Here J_n is the nth-order Bessel function, and

$$\delta = \frac{m\omega^2 \alpha(\omega, \mathbf{E}_0)}{Ze^2} \tag{14}$$

describes the contribution of the polarization radiation mechanism to the amplitude of the process. If radiation in the polarization channel is dominant, we obtain[35]

$$W_{\mathrm{pol}}(n) = J_n^2\{2(n_{\mathbf{k}\lambda}^{\mathrm{Las}} n_{\mathbf{k}\lambda}^{\mathrm{pol}})^{1/2}\}, \tag{15}$$

where $n_{\mathbf{k}\lambda}^{\mathrm{pol}} = \delta^2 n_{\mathbf{k}\lambda}^{\mathrm{stat}}$ is the occupation number of photons spontaneously emitted into the laser mode $\{\mathbf{k},\lambda\}$ by an incident particle in the polarization channel when it collides with a multiply-charged ion.[16]

Equation (13) is the result of summing the contributions of the two channels. The radiation contribution from either channel can be isolated in this sum by means of the addition formula for Bessel functions. Equation (13) can then be rewritten in the form

$$W_{\Sigma}(n) = \left| \sum_{v+m=n} (-1)^m J_v\left(\sqrt{4 n_{\mathbf{k}\lambda}^{\mathrm{Las}} n_{\mathbf{k}\lambda}^{\mathrm{stat}}}\right) J_m\left(\sqrt{4 n_{\mathbf{k}\lambda}^{\mathrm{Las}} n_{\mathbf{k}\lambda}^{\mathrm{pol}}}\right) \right|^2 . \tag{16}$$

The equation (13) for the probability of a multiphoton process is a generalization of equations previously derived by Bunkin and Fedorov[2] in the Born approximation and by Berson[3] in the semiclassical limit. First, they were applied to the case of a highly inelastic multiquantum transition over a broad range of quantum versus classical motion of the incident particle (Fig. 1), spanning not only the range of validity of the results of Refs. 2 and 3, but also the entire range of validity of the specified quantum/classical current approximation as well. Second, they were applied to the case in which the contributions of the static and polarization channels, including their interference, to the emission process are taken into account simultaneously in the approximation of a specified quantum/classical current generated by the incident particles.

It is important to note that the result (13) generalizes to the multiphoton case the well-known[10–14] phenomenon of ''stripping'' of a target ion, i.e., the partial (for an ion) or complete (for an atom) unscreening of the nucleus as a result of cancellation of the contributions from polarization radiation and the part of the incident-particle bremsstrahlung due to Coulomb interaction of this particle with core electrons. Such cancellation exactly corresponds to the vanishing of bremsstrahlung in the dipole approximation for the collision of particles having the same charge-to-mass ratio.

Another consequence of Eq. (13) is that the nature of the interference in our case of bremsstrahlung associated with scattering by a multiply-charged ion differs significantly from the case of a neutral atom. This contrast is aptly illustrated in the example of $\sigma_1(Z=0, \xi \ll 1)$, the cross section for one-photon bremsstrahlung by a neutral atom with allowance for both the static and the polarization channel in the case of Born scattering of the incident particle, which has already been studied in detail (see, e.g., Refs. 2 and 13). Indeed, even though the cross section $\sigma_1(Z=0,\ \xi \ll 1)$ initially has the same structure (of the type $|1-\delta|^2$) as Eq. (13) in our investigated region of dipole collisions (the parameter δ itself differs somewhat by virtue of the difference in the spectra of equivalent photons for scattering by a neutral atom and by a charged particle; more details can be found in an earlier paper[16] which appears in Ref. 13 pp. 288–289), we know that the interference term proportional to δ drops out after integration over the scattering angle of the incident particle, owing to the difference in the regions of significance of the static and polarization channels (specifically, interference is significant only over a rather narrow interval of angles). In the case of bremsstrahlung by a multiply-charged ion, on the other hand, the regions of significance of the static and polarization channels, subject to the condition that the collisions have a dipole character, simply coincide, so that interference becomes far more important.

The approach used in deriving Eq. (13) differs from the investigation in Refs. 30 and 31, which is framed in the Born approximation without second quantization of the emitted/absorbed field, in that it systematically incorporates interaction of the polarization current induced in a multiply-charged ion with a quantized laser field and is generalized to the case of arbitrary values of the parameter ξ in the region of validity of the specified current formalism (see Fig. 1).

Note, however, that the result of Refs. 30 and 31 has a rigorous physical analog. A direct comparison of (13) with Eq. (2) in Ref. 30 and Eq. (13) in Ref. 31 at the level of the corresponding process obtained by multiplying the probability and the Coulomb scattering cross section of the incident particle in the field of the multiply-charged ion indicates that their structures are similar. The main difference is the form of the factors representing the polarization channel, which in Refs. 30 and 31 are expressed in terms of the nonlinear susceptibilities of the target. This difference is attributable to the dissimilar models on which the description of the given phenomenon is based. For example, our result (13), as mentioned, corresponds to the stimulated scattering (under the influence of the laser field) of n equivalent photons of energy $\hbar\omega$, each ''emitted'' by the incident particle as it is scattered in the Coulomb field of the multiply-charged ion, by the core of the target ion, and their subsequent conversion into n real photons (here we encounter near resonance of order n; see Appendix B).

In contrast, the approach of Refs. 30 and 31 corresponds, in terms of the equivalent photon formalism, to the conversion of a single virtual phonon of energy $n\hbar\omega$ into n real photons, where only first-order resonance is possible. Our approximation is found to be more realistic for the multiphoton bremsstrahlung discussed in the present article, in connection with the collision of a charged particle with a multiply-charged ion in the presence of a strong laser field close to resonance, with respect to one-photon transitions in the core of the multiply-charged ion (see Sec. 3).

We note that the ''extra'' lines of virtual phonons in the ladder diagrams describing ''n-to-n'' conversion increase the number of diagram vertices, but do not necessarily decrease the amplitude of the process. Such a decrease takes place upon satisfaction of a condition that generalizes the familiar Born condition for the static scattering potential to the case of a time-dependent potential. For the investigated

n-photon emission process this condition can be written in the form

$$\left| \frac{[\alpha^{(1)}(\omega)]^n}{\alpha^{(n)}(n\omega)} \frac{[E_p(\omega)]^n}{E_p(n\omega)} \right| < 1.$$

Here $\alpha^{(n)}(n\omega)$ is the nth-order polarizability of the multiply-charged ion, and $E_p(n\omega)$ is the nth harmonic of the amplitude of the incident-particle field. Clearly, such an inequality does not hold in the near-resonance case.

The difference between Eq. (13) and the equations in Refs. 28 and 29 stems from the fact that the target wave function in the indicated situations was taken into account in the ''dipole perturbation'' approximation, which dictates that the emission of only one photon in the polarization channel is taken into account.

5. INTERACTION OF THE STATIC AND POLARIZATION CHANNELS IN STIMULATED BREMSSTRAHLUNG IN A STRONG LASER FIELD

The contribution of the polarization mechanism to the total probability of stimulated bremsstrahlung becomes dominant in the case of near-resonant laser radiation. In this kind of region, which is characterized in the general case by the condition

$$\gamma \ll |\omega - \omega_0| \ll \omega \tag{17}$$

(ω_0 is the natural frequency of the resonant electron transition in a multiply-charged ion, $\Delta = \omega - \omega_0$, and γ is the total width of the investigated transition), we need to take into account the influence of the laser field on electrons of the multiply-charged ion core, as it produces a certain modification of the polarizability of the ion, and the generalized Rabi frequency appears in the denominator of the expression for the near-resonance polarizability,

$$\Omega_R = \sqrt{\left(\frac{\mathbf{d} \cdot \mathbf{E}_0}{\hbar} \right)^2 + (\omega - \omega_0)^2}.$$

As for the near-resonance polarizability of a multiply-charged ion, it can be described by the expression

$$\alpha(\omega, \mathbf{E}_0) = d^2 \mathrm{sgn}(\omega_0 - \omega)/\hbar\Omega_R,$$

where d is the dipole matrix element of the near-resonance transition. Accordingly, the expression for the quantity δ describing the contribution of the polarization channel to the total amplitude of the process can be written in the form (the contribution of the lower level of the ''near-resonant'' transition in the core of the multiply-charged ion is tacitly understood from now on)

$$\delta = \frac{m\omega^2}{Ze^2} \frac{d^2}{\hbar\Omega_R} \mathrm{sgn}(\omega_0 - \omega). \tag{18}$$

From this expression we obtain the condition for dominance of the polarization channel over the static channel (in natural units):

$$\Delta^2 + \frac{f_0}{2\omega} E^2 < \left(\frac{f_0 \omega}{2Z} \right)^2, \tag{19}$$

where f_0 is the resonant-transition oscillator strength. From condition (19) we deduce an expression for the saturating amplitude of the laser field in the given near-resonance case:

$$E_{\mathrm{sat}} = \sqrt{\frac{2\omega}{f_0}} |\Delta|.$$

In soft x rays and at off-resonance laser frequencies with $|\Delta| \approx 10^{-2}$ (which exceeds the characteristic line broadening in the current case), we estimate $E_{\mathrm{sat}} > 10^{-2} - 10^{-1}$ a.u.

From this condition we obtain an upper bound for the laser field when polarization bremsstrahlung dominates the static kind in the near-resonance case:

$$E_* = \sqrt{\frac{2\omega}{f_0} \left[\left(\frac{\omega f_0}{2Z} \right)^2 - \Delta^2 \right]}, \quad E_{\mathrm{sat}} < E < E_*. \tag{20}$$

Hence, for $Z = 10$, $\omega \approx 3$ a.u., $\Delta = 0.03$ a.u., and $f_0 \sim 0.3$ we find $E_* \sim 0.15$ a.u.

In laser fields with $E < E_{\mathrm{sat}}$, we have the following condition governing the dominance of polarization over static bremsstrahlung:

$$|\Delta| < \frac{f_0}{2Z} \omega, \tag{21}$$

from which it follows that an extremely broad spectral range is covered in this case as well.

We illustrate the interaction of the static and polarization channels in stimulated bremsstrahlung over the range of parameter values that are relevant to the case of coherent radiation emitted in the soft x-ray range, and at the same time are attainable in present-day and planned experiments (see, e.g., Elton's book[44]). For example, the numerical estimation of the stimulated emission/absorption cross sections for the case of a recombination scheme is most appropriate in application to the ''Kramers'' frequency range $\omega \gg \overline{\omega} \equiv v^3/Z$. Here we obtain the expression for the total cross section (integrated over the impact parameter) of the n-photon stimulated process

$$\sigma_n(\alpha) = \frac{(2Z)^{4/3}}{v^2 \omega^{2/3}} \int_0^{2\pi} d\varphi \times \int \frac{dN}{N^{1/3}} J_n^2 \left[\frac{|1-\delta|}{\omega^{5/3} Z^{1/3}} \frac{2^{5/3}}{\sqrt{3}} N^{2/3} F(N, \alpha, \varphi) \right], \tag{22}$$

where

$$F(N, \alpha, \varphi) = \sqrt{\cos^2 \alpha K_{2/3}^2 \left(\frac{4}{3} N \right) + \cos^2 \varphi \sin^2 \alpha K_{1/3}^2 \left(\frac{4}{3} N \right)}, \tag{23}$$

and α is the angle between the (initial) velocity of the incident particle and the polarization vector of the laser field.

Figure 2 shows the cross section of the one-photon process σ_1, averaged over the angles α, as a function of the strength of a linearly polarized laser field for ionic charge $Z = 10$, electron velocity $v = 1.44$ a.u., laser frequency

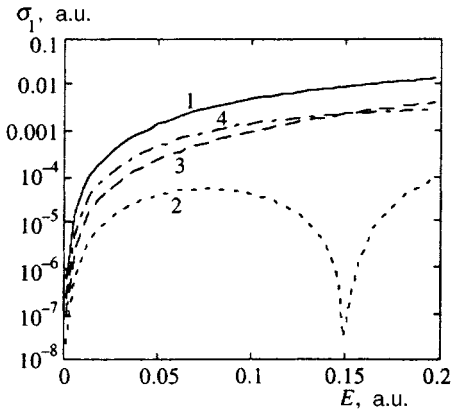

FIG. 2. Dependence of the cross section σ_1 of the one-photon process, averaged over angles α, on the strength of a linearly polarized laser field for an ion charge $Z=10$, an electron velocity $v=1.44$ a.u., a laser frequency $\omega=3$ a.u., an oscillator strength $f_0=0.3$, and a relative frequency deviation $|\Delta|/\omega\simeq 0.01$. The curves are given for equal moduli and opposite signs of the frequency deviation (curves *1* and *2*) and for cross sections with only one of the two channels taken into account (curve *3* corresponds to the static channel alone, and curve *4* to the polarization channel alone).

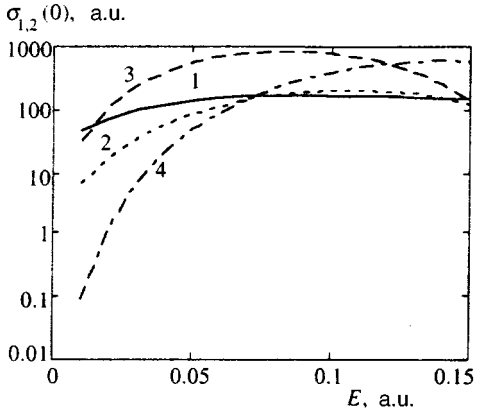

FIG. 3. Dependence of the differential bremsstrahlung cross sections for one-photon $[\sigma_1(0)$, curve *1*] and two-photon $[\sigma_2(0)$, curve *2*] processes on the strength of a linearly polarized laser field for the angle $\alpha=0$, ion charge $Z=4$, electron velocity $v=0.447$ a.u., laser frequency $\omega=0.37$ a.u., oscillator strength $f_0=0.69$, and relative frequency deviation $\Delta/\omega\simeq+0.014$. Also shown are curves corresponding to the static channel alone for one-photon (curve *3*) and two-photon (curve *4*) processes.

$\omega=3$ a.u. (near-resonance with transitions $\Delta n=0$ in the ion core), oscillator strength $f_0=0.3$, and relative frequency deviation $|\Delta|/\omega\approx 0.01$ (in the present case we have the semiclassicality parameter $\xi\approx 7$ and the ''Kramers'' parameter $\omega/\overline{\omega}\approx 10$). The curves are plotted for identical moduli and opposite signs of the frequency deviation (curves *1* and *2*) and also with only one channel taken into account (curve *3* corresponds to the static channel alone, and curve *4* to the polarization channel alone). The plotted cross section corresponds to the contribution of only one of the levels involved in a near-resonance (virtual) transition in the core of the multiply-charged ion. The upper curve *1* corresponds to a deviation $\Delta>0$ for the contribution of the lower level of a ''near-resonant'' transition in the core of the multiply-charged ion (or, equivalently, $\Delta<0$ for the contribution of the upper level of such a transition); the lower curve *2* corresponds to a deviation $\Delta<0$. The actual difference between these curves illustrates the degree of interference of the static and polarization channels. The dip in the lower curve is caused by the complete cancellation of the amplitudes of the two channels and, accordingly the vanishing of the argument of the Bessel function in (22) when $\delta=1$. We note that the curves describing the contribution of only one of the channels intersect precisely at this value of the laser field. Allowance for the contributions of the populations of the upper and lower levels smooth out the dip, but curve *2* is still not monotonic.

Over the range of parameters for Fig. 2, the contribution of multiphoton radiative transitions is small.

Figure 3 shows the dependence of the differential cross sections of bremsstrahlung for one-photon $[\sigma_1(0)$, curve *1*] and two-photon $[\sigma_2(0)$, curve *2*] processes on the strength of a linearly polarized laser field for the angle $\alpha=0$, ion charge $Z=4$, electron velocity $v=0.447$ a.u., laser frequency $\omega=0.37$ a.u. (near-resonance with transitions $\Delta n=0$ in the ion core), oscillator strength $f_0=0.69$, and relative frequency deviation $\Delta/\omega>+0.014$ (in this case we have the quasiclassicity parameter $\xi\approx 9$ and the ''Kramers'' parameter $\omega/\overline{\omega}=16.5$). The competition between the one-photon and two-photon processes with increasing strength of the laser field is evident. Also shown in the figure are curves corresponding to the contribution of the static channel alone (curves *3* and *4*). Clearly, when the polarization channel is taken into account, the cross section of the two-photon process becomes comparable with the one-photon cross section for weaker laser fields.

6. CONCLUSION

The universal analytic description obtained here for multiphoton stimulated bremsstrahlung, encompassing both the static and the polarization channel, can be used to calculate the cross sections of stimulated emission and absorption of photons in the collision of charged particles with multiply-charged ions for any degree of quantum versus classical motion (the ''quanticity/classicality'' criterion) of the incident particle, over a wide range of parameters such that the specified incident-particle current approximation is applicable to the stimulated emission/absorption of a photon by the composite system {incident particle+ion and core}. The approach developed here for the description of multiphoton polarization stimulated bremsstrahlung generalizes the method of equivalent Fermi photons,[19] to multiphoton processes elaborating the method of Ref. 16 for spontaneous polarization bremsstrahlung and the method of Kramers electrodynamics[1] for the semiclassical description of radiative collision processes involving multiphoton ions.

The foregoing numerical calculations of the stimulated bremsstrahlung cross sections over the range of parameters relevant to problems in the kinetics of a strong laser field in a multicomponent plasma with multiply-charged ions, under conditions in which nonresonant processes influence the

transfer of energy between the plasma and the laser beam, reveal the significance of interference effects between the static and polarization channels.

The authors are grateful to V. M. Buĭmistrov, G. Grimm, N. B. Delone, J. Davis, B. A. Zon, V. I. Kogan, V. P. Kraĭnov, V. S. Lisitsa, E. A. Manykin, R. H. Pratt, A. N. Starostin, and M. V. Fedorov for valuable discussions of the results.

This work received partial financial support from the International Science and Engineering Center (Grant No. 076-95), the Russian Fund for Fundamental Research (Grant No. 94-02-04261), and the International Science Foundation (Grant No. RLT-300).

APPENDIX A: SCHEME DEMONSTRATING THE CORRESPONDENCE PRINCIPLE FOR A MULTIQUANTUM TRANSITION MATRIX ELEMENT

We generalize the formalism of the limit $\hbar \to 0$ for a one-quantum inelastic transition[1,40] to the case of multiquantum transitions (including induced transitions) within the framework of the previously developed[40] two-dimensional semiclassical method in the theory of inelastic transitions of a particle in a central field.

The analysis is best carried out in general form for the most representative form of the correspondence principle. For the matrix element of scattering between states {particle+field}

$$\langle \mathbf{p}_f, m | \hat{T} \exp\left\{ \int_{-\infty}^{+\infty} \hat{\mathbf{Q}}(\mathbf{r},t) \cdot \hat{\mathbf{A}}(t) dt \right\} | \mathbf{p}_i, n \rangle \tag{A1}$$

(here $\hat{T}$ is the time ordering operator, the arbitrary operator $\hat{Q}(\mathbf{r},t)$ and the electromagnetic field vector potential operator $\hat{\mathbf{A}}(t)$ are defined in the interaction picture, m and n are the photon occupation numbers, and $\mathbf{p}_f$ and $\mathbf{p}_i$ are the momenta of the emitting particle in the initial and final states), the expression for a typical nonvanishing term in the expansion of the scattering matrix has the form

$$M_n = \langle \mathbf{p}_f, s+n | \hat{T} \left\{ \int_{-\infty}^{+\infty} \hat{a}^+(t) \hat{Q}(\mathbf{r},t) dt \right\}^n | \mathbf{p}_i, s \rangle, \tag{A2}$$

where the photon creation operator $a^+(t)$ is defined in the interaction picture. The introduction of $(n-1)$ unitary operators in the form of sums over the complete set of states,

$$\sum_{\mathbf{p}} \Psi^{(-)*}(\mathbf{p},\mathbf{r}') \Psi^{(-)}(\mathbf{p},\mathbf{r}) \propto \delta(\mathbf{r}'-\mathbf{r}),$$

where $\Psi^{(-)}(\mathbf{p},\mathbf{r})$ is taken from Ref. 41 (Sec. 136), leads to the factorization of (A2) into a product of n matrix elements mutually coupled in n time integrals. The application of the operators $\exp(\pm i/\hbar \int \hat{H} dt)$ contained in the operators Q in the interaction picture to $\Psi^{(-)}(\mathbf{p},\mathbf{r})$ and the subsequent computation of the time integrals produces $(n-1)$ resonance denominators (which, as the upper limit of the time integral exponentially approaches infinity, tend to the corresponding delta functions and thus ensure the approximate conservation of energy in each successive one-photon transition in the multiquantum transition event factorized in this way) and one exact delta function, which ensures the conservation of energy in a single multiquantum transition event. The combined influence of the indicated delta function and the overall limit $\hbar \to 0$ in (A2) brings the resonance denominators to the mass shell, yielding the following expression as a result:

$$\begin{aligned} M_n \propto \delta(E_f + n\hbar\omega - E_i)(M_n)_{\text{phot}} \int d\mathbf{r}_{n-1} \int d\mathbf{p}_{n-1} \\ \times \Psi^{(-)*}(\mathbf{p}_f, \mathbf{r}_{n-1}) Q(\mathbf{r}_{n-1}) \Psi^{(-)}(\mathbf{p}_{n-1}, \mathbf{r}_{n-1}) \delta(E_{n-1} \\ + (n-1)\hbar\omega - E_i) \ldots \int d\mathbf{r}_k \int d\mathbf{p}_k \Psi^{(-)*} \\ \times (\mathbf{p}_{k+1}, \mathbf{r}_k) Q(\mathbf{r}_k) \Psi^{(-)}(\mathbf{p}_k, \mathbf{r}_k) \delta(E_k + k\hbar\omega \\ - E_i) \ldots \int d\mathbf{r}_1 \int d\mathbf{p}_1 \Psi^{(-)*}(\mathbf{p}_2, \mathbf{r}_1) Q(\mathbf{r}_1) \\ \times \Psi^{(-)}(\mathbf{p}_1, \mathbf{r}_1) \delta(E_1 + \hbar\omega - E_i) \ldots \int d\mathbf{r} \Psi^{(-)*} \\ \times (\mathbf{p}_1, \mathbf{r}) Q(\mathbf{r}) \Psi^{(+)}(\mathbf{p}_i, \mathbf{r}), \end{aligned} \tag{A3}$$

where the photon part of the matrix element

$$(M_n)_{\text{phot}} = \left(\frac{(s+n)!}{s!} \right)^{1/2} \tag{A4}$$

is attributable to the matrix elements of successive one-quantum transitions in the presence of the initial and already emitted photons in the given mode.

We consider the simplest version of (A3), the case $n=2$, which corresponds to a two-quantum transition. Applying the formalism of the limit $\hbar \to 0$ to the matrix element $\langle \mathbf{p}_1 | Q | \mathbf{p}_i \rangle$, for the coordinate part M_2 we obtain

$$\begin{aligned} M_2 \propto \int d\Omega_1 \int d\mathbf{r}_1 \Psi^{(-)*}(\mathbf{p}_f, \mathbf{r}_1) Q(\mathbf{r}_1) \Psi^{(-)}(\mathbf{p}_1, \mathbf{r}_1) \\ \times \left[\left(\frac{d\sigma}{d\Omega} \right)^{1/2} Q_\omega \exp\left(\frac{i}{\hbar} S \right) \right]_{\{i \to 1^*\}}, \end{aligned} \tag{A5}$$

where Ω_1 is the solid angle of the vector $\mathbf{n}_1$, $\mathbf{n}_1 \equiv \mathbf{p}_1/|\mathbf{p}_1|$; here also the scattering cross section $d\sigma/d\Omega$, the Fourier component Q_ω of the function $Q(r)$, and the action S are evaluated for the trajectory $\mathbf{r}(t)$ corresponding to the scattering event $\{\mathbf{p}_i \to \{E_i, \mathbf{n}_1\}\} \equiv \{i \to 1^*\}$. It will be advantageous below to transform the integral over the solid angle Ω_1 into an integral with respect to the trajectory variables M_1 and φ_1 (see Refs. 1 and 40),

$$\int d\Omega_1 \propto \int \overline{M_1}\, d\overline{M_1}\, d\overline{\varphi_1} \left(\frac{d\sigma}{d\Omega} \right)^{-1}_{\{1^* \to i\}}, \tag{A6}$$

so that the integrals left in (A5) are grouped, as in Refs. 1 and 40, into a single time integral on trajectories departing (scattered) in the direction of the final momentum $\mathbf{p}_f$ and a quadruple integral in the doubly-reduced trajectory space $\{\overline{M_1}, \overline{\varphi_1}\} \otimes \{M_1, \varphi_1\}$. The latter integral is evaluated in the limit $\hbar \to 0$ by the stationary phase method in four-dimensional space. Here the stationary phase corresponds

to $\mathbf{n}_1=\mathbf{n}_f\equiv\mathbf{p}_f/|\mathbf{p}_f|$, and the phase factors (action functions) in the semiclassical wave functions $\Psi^{(-)*}(\mathbf{p}_f,\mathbf{r}_1)$ and $\Psi^{(-)}(\mathbf{p}_1,\mathbf{r}_1)$ are preserved (in contrast with their summation in the action function along the classical trajectory in $\langle\mathbf{p}_1|Q|\mathbf{p}_i\rangle$) to within their difference, due to the difference between the energies E_f and $E_1=E_i-\hbar\omega$, which yields the factor required for the Fourier component

$$\omega t_1\propto\frac{1}{\hbar}\frac{\partial S}{\partial E}\ (E_f-E_1)$$

in the exponential function. In the final analysis, the scattering cross section in (A6) cancels the product of the square roots of this quantity that emerge when the integrals (A5) are evaluated by the stationary phase method.

The generalization (by induction) of the conclusion briefly described here to the case of an arbitrary number of photons can be used in the generalization of Eq. (4.42) from Ref. 1 to find a correspondence principle for the n-quantum transition between wave functions of the scattering problem $\{\mathbf{p}_i\rightarrow\mathbf{p}_f\}$ with s photons present in the given mode (which do not perturb the particle motion):

$$\langle\mathbf{p}_f,s+n|\hat{T}\left\{\int_{-\infty}^{+\infty}\hat{a}^+(t)\hat{Q}(t)dt\right\}^n|\mathbf{p}_i,s\rangle_{\hbar\rightarrow 0}$$
$$\propto\left(\frac{d\sigma}{d\Omega_f}\right)^{1/2}(Q_\omega)^n\delta(E_i-E_f-n\hbar\omega)\left(\frac{(s+n)!}{s!}\right)^{1/2},$$

where $d\sigma/d\Omega_f$ is the classical particle scattering cross section from a state with initial momentum $\mathbf{p}_i$ to a state with momentum $\mathbf{p}_f|\mathbf{p}_i|/|\mathbf{p}_f|$, ($\mathbf{p}_f$ is the momentum of the final quantum state), and Q_ω is the Fourier component of $Q(\mathbf{r})$ along the trajectory $\mathbf{r}(t)$ corresponding to the indicated scattering event.

APPENDIX B: JUSTIFICATION OF THE SPECIFIED POLARIZATION CURRENT METHOD

This justification of the specified polarization current method (in the sense that this current is not perturbed by a photon emission/absorption event) is based on the possibility of ''cutting'' the corresponding diagrams along the lines of propagation of the electronic core of the multiply-charged ion (in Fig. 4 the double slash across the heavy line corresponding to the Green's function of the electronic core of the multiply-charged ion). We note here that the possibility of ''cutting'' (up to an elastic scattering contribution—the root of the scattering cross section—with but a single common factor) the diagram along the line of propagation of the incident particle (the single slash across the thin line in Fig. 4) follows from the validity of the specified current approximation. For example, in the limit of classical motion of the incident particle for the case of static bremsstrahlung, this corresponds to factorization of the probability of multiphoton emission (see the justification in Appendix A of the correspondence principle for multiquantum processes). And, finally, cutting along the photon Green's function corresponds to the method of equivalent Fermi photons.

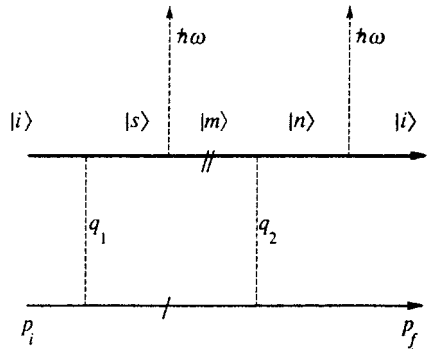

FIG. 4. Second-order ladder diagram describing the conversion of two virtual photons (4-momenta $q_{1,2}$) into two real photons (energy $\hbar\omega$) at the electronic core of a multiply-charged ion. The single slash represents the ''cutting'' of the diagram along the incident-electron line (see Sec. 3). The double slash indicates the cutting of the diagram along the line of the electronic core of the multiply-charged ion.

We wish to investigate the ladder diagrams describing multiphoton radiation in the polarization channel, which are the result of expanding the formal solution for the scattering matrix in powers of the interaction of the electronic subsystem of a multiply-charged ion with the laser field.

As an example, we discuss the elementary case of the conversion of n virtual photons into n real photons for $n=2$. One of the topologically similar diagrams is shown in Fig. 4. In this diagram the fine line corresponds to the incident particle scattered in the field of a multiply-charged ion from state $|p_i\rangle$ to state $|p_f\rangle$. The electronic subsystem of the multiply-charged ion does not change its state $|i\rangle$ and is represented by the heavy line; q_1 and q_2 are 4-vectors of equivalent Fermi photons, and $|n\rangle$, $|m\rangle$, and $|s\rangle$ are the intermediate states of the electronic subsystem of the multiply-charged ion.

In the dipole approximation (with respect to interaction with both real and virtual photons), the analytic expression corresponding to the given ladder diagram has the form

$$M_2\propto\int dq_1^0dq_2^0\delta(q_1^0+q_2^0-2\hbar\omega)E_a^*E_b^*E_c^{\mathrm{EPh}}$$
$$\times(q_1)E_d^{\mathrm{EPh}}(q_2)\mathfrak{R}_{ii}^{abcd}(-q_1^0,\omega,-q_2^0,\omega).\qquad\text{(B1)}$$

Here E is the vector representing the electric component of the laser field, E^{EPh} is the field of equivalent Fermi photons (we are assuming that the diagram has already been ''cut'' along the incident-particle line as represented by the single slash in Fig. 4), $\mathfrak{R}_{ii}^{abcd}$ is the diagonal matrix element of the nonlinear scattering tensor of the electromagnetic field by the electronic subsystem of the multiply-charged ion; in the given situation it is proportional to the third-order susceptibility, and is given by the expression

$$\Re_{ii}^{abcd}(-q_1^0,\omega,-q_2^0,\omega)$$

$$\propto \sum_{n,m,s} \frac{d_{in}^a d_{nm}^b d_{ms}^c d_{si}^d}{(\omega_{ni}+\omega-q_1^0-q_2^0-i\gamma_{ni}/2)(\omega_{mi}+\omega-q_1^0-i\gamma_{mi}/2)(\omega_{si}-q_1^0-i\gamma_{si}/2)}, \tag{B2}$$

where ω_{mn} and γ_{mn} are the eigenfrequencies and corresponding transition widths between states of the electronic subsystem of the multiply-charged ion, and d_{mn} denotes the matrix elements of the dipole moment operator.

This approximation of the specified polarization current corresponds to the $m=i$ term in the sum over m in Eq. (A2). Discarding terms with $m \neq i$ can be justified if the near-resonance condition (17) is satisfied; this is precisely the condition for which the polarization radiation mechanism plays a significant role.

The indicated term, which is responsible for the main contribution to $\Re_{ii}^{abcd}$ in the case of interest, is written in the form

$$\Re_{ii,m=i}^{abcd} \propto \frac{\alpha(\omega)\alpha(q_1^0)\delta^{ab}\delta^{cd}}{\omega-q_1^0-i\gamma_{ii}/2}. \tag{B3}$$

Here $\alpha(\omega)$ and $\alpha(q_1^0)$ are the dynamic polarizability of the multiply-charged ion at the frequencies ω and q_1^0, respectively, and δ_{mn} is the Kronecker delta. Noting that $\omega \gg \gamma_{ii}$, we can use the Sokhotskiĭ equation, which gives the sum of the delta function and the principal-value operator. Integration with respect to q_1^0 in Eq. (B1) cancels the contribution of the principal value, and the part that remains gives the leading contribution to the amplitude M_2:

$$M_2 \propto \{[\mathbf{E}^{\mathrm{Las}}\cdot\mathbf{E}^{\mathrm{EPh}}(\omega)]\alpha(\omega)\}^2 \propto \{\mathbf{E}^{\mathrm{Las}}\cdot\mathbf{j}^{\mathrm{pol}}(\omega)\}^2. \tag{B4}$$

Here $\mathbf{j}^{\mathrm{pol}} \propto \alpha(\omega)\mathbf{E}^{\mathrm{EPh}}(\omega)$ is the polarization current induced by equivalent photons of frequency ω in the multiply-charged ion, and E^{Las} is the amplitude of the laser field. Equation (B4) substantiates the ''cutting'' of the diagrams along the line of the electronic subsystem of the multiply-charged ion (as represented by the double slash in Fig. 4).

This cutting reduces the nth-order diagram to the nth power of the expression in braces in Eq. (B4). The resulting series of such multiplied diagrams (taking into account the series for the static radiation channel) can be convolved with an exponential function, the argument of which contains the total emitting current as a factor in accordance with Eq. (10).

[1] V. I. Kogan, A. B. Kukushkin, and V. S. Lisitsa, Phys. Rep. **213**, 1 (1992).
[2] F. V. Bunkin and M. V. Fedorov, Zh. Éksp. Teor. Fiz. **49**, 1215 (1965) [Sov. Phys. JETP **22**, 844 (1965)]; M. V. Fedorov, *The Electron in a Strong Light Field* [in Russian], Nauka, Moscow (1991), Chap. 1.
[3] I. Ya. Berson, Zh. Eksp. Teor. Fiz. **80**, 127 (1981) [Sov. Phys. JETP **53**, 63 (1981)].
[4] N. M. Kroll and K. M. Watson, Phys. Rev. A **8**, 804 (1973).
[5] N. K. Rahman, Phys. Rev. A **10**, 440 (1974).
[6] V. S. Lisitsa and Yu. A. Savel'ev, Zh. Éksp. Teor. Fiz. **92**, 484 (1987) [Sov. Phys. JETP **65**, 273 (1987)].
[7] V. Veniard, M. Gavrila, and A. Maquet, Phys. Rev. A **32**, 2537 (1985); **35**, 448 (1987).
[8] M. Gavrila, Phys. Rev. **163**, 147 (1967).
[9] A. V. Korol, J. Phys. B **26**, 3137 (1993).
[10] V. M. Buĭmistrov, Ukr. Fiz. Zh. **17**, 640 (1972); V. M. Buĭmistrov and L. I. Trakhtenberg, Zh. Éksp. Teor. Fiz. **69**, 108 (1975) [Sov. Phys. JETP **42**, 54 (1975)].
[11] M. Ya. Amus'ya, A. S. Baltenkov, and A. A. Paĭziev, JETP Lett. **24**, 332 (1976).
[12] B. A. Zon, Zh. Éksp. Teor. Fiz. **73**, 128 (1978) [Sov. Phys. JETP **46**, 65 (1978)].
[13] V. N. Tsytovich and I. M. Oĭringel' (eds.), *Polarization Bremsstrahlung of Atoms and Particles* [in Russian], Nauka, Moscow (1987).
[14] M. Ya. Amus'ya (Amusia), Phys. Rep. **162**, 249 (1988); M. Ya. Amus'ya, *Bremsstrahlung* [in Russian], Énergoatomizdat, Moscow (1990).
[15] V. Kas'yanov and A. N. Starostin, Zh. Éksp. Teor. Fiz. **48**, 295 (1965) [Sov. Phys. JETP **21**, 193 (1965)].
[16] A. B. Kukushkin and V. S. Lisitsa, in *Polarization Bremsstrahlung of Atoms and Particles* [in Russian], V. N. Tsytovich and I. M. Oĭringel' (Eds.), Nauka, Moscow (1987), Chap. 11.
[17] A. B. Kukushkin and V. S. Lisitsa, Phys. Lett. A **159**, 184 (1991).
[18] V. N. Tsytovich, Tr. Fiz. Inst. Akad. Nauk SSSR **66**, 191 (1973).
[19] E. Fermi, Z. Phys. **29**, 315 (1924).
[20] V. S. Lisitsa, *Atoms in Plasmas*, Springer-Verlag, Berlin–Tokyo (1994).
[21] A. Dubois and A. Maquet, Phys. Rev. A **40**, 4288 (1989).
[22] M. Ya. Amusy'ya (Amusia), L. V. Chernysheva, and A. V. Korol, J. Phys. B **23**, 2899 (1990).
[23] M. Ya. Amus'ya (Amusia) and A. V. Korol, J. Phys. B **25**, 2383 (1992).
[24] É. T. Verkhovtseva, E. V. Gnatchenko, B. A. Zon, A. A. Nekipelov, and A. A. Tkachenko, Zh. Éksp. Teor. Fiz. **98**, 797 (1990) [Sov. Phys. JETP **71**, 443 (1990)].
[25] É. T. Verkhovtseva, E. V. Gnatchenko, and A. A. Tkachenko, Opt. Spektrosk. **78**, 208 (1995) [Opt. Spectrosc. (Russia) **78**, 183 (1995)].
[26] B. A. Zon, Zh. Éksp. Teor. Fiz. **107**, 1176 (1995) [JETP **80**, 655 (1995)].
[27] J. I. Gersten and M. H. Mittleman, Phys. Rev. A **13**, 123 (1976).
[28] F. M. Byron, Jr., P. Francken, and C. J. Joachain, J. Phys. B **20**, 5487 (1987).
[29] P. Francken, Y. Attaourti, and C. J. Joachain, Phys. Rev. A **38**, 1785 (1988).
[30] E. L. Beilin and B. A. Zon, J. Phys. B **16**, L159 (1983).
[31] P. A. Golovinskiĭ, Zh. Éksp. Teor. Fiz. **94**(7) 87 (1988) [Sov. Phys JETP **67**, 1346 (1988)].
[32] P. A. Golovinskiĭ and M. A. Dolgopolov, Teor. Mat. Fiz. **95**, 418 (1993).
[33] G. Kracke, J. S. Briggs, A. Dubois, A. Maquet, and V. Veniard, Phys. Rev. B **27**, 3241 (1994).
[34] B. Wallbank and J. K. Holmes, Phys. Rev. A **48**, R2515 (1993); **27**, 1221 (1994).
[35] V. A. Astapenko and A. B. Kukushkin, in *Proceedings of the 12th International Conference on Spectral Line Shapes* (Toronto, 1994), Vol. 8, A. D. May, J. R. Drummond, and E. Oks (Eds.), AIP Press, New York (1994); Preprint IAE-5820/6, Kurchatov Institute, Moscow (1994).
[36] A. V. Akopyan and V. N. Tsytovich, Fiz. Plazmy **1**, 673 (1975) [Sov. J. Plasma Phys. **1**, 371 (1975)]; Zh. Éksp. Teor. Fiz. **71**, 166 (1977) [Sov. Phys. JETP **44**, 87 (1977)].
[37] V. A. Astapenko, V. M. Buĭmistrov, Yu. A. Krotov, and V. N. Tsytovich, Fiz. Plazmy **15**, 202 (1989) [Sov. J. Plasma Phys. **15**, 116 (1989)].
[38] P. A. Golovinskiĭ, M. A. Dolgopolov, and V. G. Khlebostroev, Fiz. Plazmy **20**, 558 (1994) [Plasma Phys. Rep. **20**, 500 (1994)].
[39] V. I. Kogan and A. B. Kukushkin, Zh. Éksp. Teor. Fiz. **87**, 1164 (1985) [Sov. Phys. JETP **60**, 665 (1985)].
[40] V. I. Kogan and A. B. Kukushkin, IAÉ Preprint No. IAÉ-3660/6 [in Russian], Kurchatov Institute of Atomic Energy, Moscow (1982).

[41] L. D. Landau and E. M. Lifshitz, *Quantum Mechanics*, Pergamon Press, New York–Oxford (1974), Sec. 136.
[42] V. B. Berestetskiĭ, E. M. Lifshitz, and L. P. Pitaevskii, *Quantum Electrodynamics*, 2nd ed., Pergamon Press, New York–Oxford (1982).
[43] N. B. Delone and V. P. Kraĭnov, *The Atom in a Strong Light Field* [in Russian], Energoatomizdat, Moscow (1984).
[44] R. Elton, *X-Ray Lasers*, Academic Press, Boston (1990).

Translated by James S. Wood

Quantum theory of the resonance interaction of an intense monochromatic electromagnetic wave with arbitrary polarization composition

A. A. Panteleev

Troitsk Institute of Innovational and Thermonuclear Research 142092 Troitsk, Moscow Region, Russia
(Submitted 24 July 1996)
Zh. Éksp. Teor. Fiz. **111**, 440-466 (February 1997)

A theory describing the absorption and emission spectra of an atomic transition in the field of an intense monochromatic wave with arbitrary polarization composition is developed. The theory includes a quantum description of forward-directed four-wave interaction processes. Expressions are obtained for describing the absorption and emission spectra in transitions adjacent to the working transition. The description developed includes the perturbation of the atomic subsystem by a constant magnetic field. The spectral characteristics, polarization composition, and angular distribution of the resonance fluorescence are investigated. The nonlinear Faraday effect and the properties of resonance fluorescence are investigated for the transition $J=1\rightarrow J=0$. © *1997 American Institute of Physics.* [S1063-7761(97)00402-2]

1. INTRODUCTION

The investigation of the properties of the interaction of intense radiation with resonant media is a fundamental problem of modern optics. It is well known that the absorption and emission spectra of atoms change substantially in the field of a strong electromagnetic wave. The basic theoretical and experimental investigations of these spectra concern the study of the spectra of a nondegenerate two-level system,[1–7] which presupposes that it is excited by a wave with fixed polarization. The resonance fluorescence of the transition $J=0\rightarrow J=1$ accompanying the excitation of atoms by intense linearly polarized radiation was investigated in Refs. 8 and 9 allowing for collisional mixing of the magnetic sublevels, and the emission and absorption spectra for the sodium D_2 lines were studied in Refs. 10 and 11. In Ref. 12 Mollow's theory of resonance fluorescence[13] was extended to a degenerate two-level atom in the field of a monochromatic linearly polarized wave.

In Refs. 14–16, an approach was developed for calculating the absorption and emission spectra of the magnetized transition $J=0\rightarrow J=1$ in the field of an electromagnetic wave of arbitrary intensity for the Faraday ($\mathbf{k}_L\| \mathbf{H}$) and Voigt ($\mathbf{k}_L\perp \mathbf{H}$) geometries, where $\mathbf{k}_L$ is the wave vector of the pump wave and $\mathbf{H}$ is the magnetic field vector. It was shown that the scattering spectrum, and in particular the Hanle signal characterizing the depolarization of the scattered radiation, can contain up to seven peaks.

In Ref. 17 the polarization, spectral, and angular (allowing for the thermal motion of the atoms) characteristics of the absorption coefficients for transitions with arbitrary J in the field of an intense electromagnetic wave with definite polarization (linear or circular) were investigated by the test-field method.

The propagation of an intense electromagnetic wave in a resonant medium is accompanied by the appearance of forward-directed nondegenerate four-wave mixing. Mathematically, the forward-directed nondegenerate four-wave mixing processes are determined by the same (second) order of the perturbation theory in the radiation–atom coupling constant as is absorption or amplification of fluorescence photons.[18,19] It should be noted that in Refs. 18 and 19 it was indicated that these are quantum processes: For the states of the electromagnetic field which correspond to them, there exist spontaneous sources similar to resonance fluorescence which determine the appearance of the scattered radiation field. It was found that a quantum description of these processes is fundamental for constructing a theory of the generation of squeezed states by means of resonant four-wave mixing[20,21] and for the interpretation of the first experimental observation of squeezed states of light.[22]

In Refs. 18, 19, and 23 it was proved that the radiation absorption coeffcicients and four-wave coupling constants describing induced processes are the same for quantum radiation and classical test fields. They can be calculated for the classical fields by perturbation theory using the standard atomic density matrix formalism.[17] A number of approaches have been used to calculate resonance fluorescence spectra. We mention the atom–photon wave function apparatus,[1,2] the quantum regression theorem,[24,13] Keldysh's diagrammatic technique for nonequilibrium Green's functions[23,25,26] Haken's method,[21,27] and the Scully–Lamb atom–photon density matrix apparatus.[28,29] The present paper employs the latter approach.

In this paper the results of Refs. 14 –16 are extended to the case of the interaction of an arbitrarily polarized monochromatic electromagnetic wave with a resonant atomic transition with an arbitrary angular momentum. The absorption and emission spectra associated with transitions adjacent to the working transition (see the level scheme in Fig. 1) are also investigated. This paper is organized as follows. In Sec. 2 the mathematical apparatus is developed and a modification of the formalism is given on the basis of the representation of nondegenerate polarization operators. In Sec. 3 the characteristic features of the polarization and angular distributions of the scattered radiation are investigated. Section 4 is devoted to an investigation of the resonance fluorescence spectra. In Sec. 5 the formalism developed is employed to study the fluorescence spectra of the transition $J=1\rightarrow J=0$. The characteristic features of the nonlinear

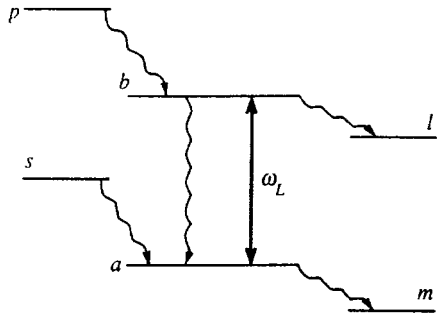

FIG. 1. Level scheme.

Faraday effect for this transition are also investigated. The basic results and a discussion of the limitations and limits of applicability of the formalism developed are presented in the concluding section.

2. BASIC EQUATIONS

2.1. Model

We shall study the interaction between a monochromatic wave, in resonance with the transition $a \rightarrow b$ (see Fig. 1), and an ensemble of atoms. Assuming arbitrary polarization of the electromagnetic wave, we represent the wave as a sum

$$\mathbf{E}=\sum_{\sigma=0,\pm 1} \mathbf{e}^{\sigma} E_{\sigma},$$

$$E_{\pm 1}=\mp\frac{1}{\sqrt{2}}(E_x \pm iE_y), \quad E_0=E_z, \tag{1}$$

where $\mathbf{e}^{\sigma}$ is a unit polarization vector. In the case when a constant magnetic field perturbing the atomic system is present, we assume that the field is oriented along the z axis. Using the dipole and resonance approximations, the Hamiltonian (in rad/s) of this system can be represented as a sum

$$\hat{H}=\hat{H}_0+\hat{H}_f+\hat{H}_{\mathrm{mag}}+\hat{V}_L+\hat{V}_q, \tag{2}$$

where

$$\hat{H}_0=\sum_{j=1}^{N}\sum_{\xi}\ \frac{\varepsilon_{\xi}}{\hbar}\hat{R}_{\xi\xi}^{(j)} \tag{3}$$

describes the unperturbed atomic subsystem. Here $\xi=\alpha JM=nM$ is the set of quantum numbers of the atomic state with energy ε_{ξ}, total angular momentum J, and projection M of the total angular momentum on the quantization axis (z); α represents the other quantum numbers; and, $\hat{R}_{\xi\xi'}=|\xi\rangle\langle\xi|$ is the atomic projection operator. In Eq. (2) $\hat{H}_f$ is the Hamiltonian of the quantum radiation field

$$\hat{H}_f=\sum_{k,\sigma}\ \omega_k \hat{a}_{k\sigma}^{+}\hat{a}_{k\sigma}, \tag{4}$$

where ω_k is the frequency of photons with wave vector $\mathbf{k}$ and polarization σ and $\hat{a}_{k\sigma}^{+}$ and $\hat{a}_{k\sigma}$ are the creation and annihilation operators of the photons. The perturbation of the atomic system by a magnetic field is described by the expression

$$\hat{H}_{\mathrm{mag}}=\sum_{j=1}^{N}\sum_{\xi}\ g_{\xi}M\Omega\hat{R}_{\xi\xi}^{(j)}, \tag{5}$$

where g_{ξ} is the Landé factor and $\Omega=-\mu_B H/\hbar$ is the Larmor frequency. The interaction of the pump wave with the transition $a \rightarrow b$ is described by the expression

$$\hat{V}_L=\sum_{j=1}^{N}\sum_{MM'}[V_{ba}(MM')\hat{R}_{MM'}^{+(j)}+V_{ba}^{*}(M'M)\hat{R}_{M'M}^{-(j)}], \tag{6}$$

$$V_{ba}(M'M)=\sum_{\sigma}\ -d_{ba}(M'M)E_{\sigma}U_L(r)\frac{\exp(i\omega_L t)}{2\hbar}, \tag{7}$$

where $d_{ba}(M'M)=d_{bM',aM}$ is the dipole moment matrix element and $U_L(r)$ is the spatial mode factor. Using the Wigner–Eckart theorem,[30] we represent the expression (7) in the form

$$V_{ba}(M'M)=\sum_{\sigma}\ V_{ba}(\sigma)(-1)^{J_a-M}C_{J_bM'J_a-M}^{1-\sigma}\exp(i\omega_L t), \tag{8}$$

$$V_{ba}(\sigma)=-\frac{(-1)^{\sigma}\|d_{ba}\|E_{\sigma}U_L(r)}{2\sqrt{3\hbar}},$$

where $C_{J_bM'J_a-M}^{1-\sigma}$ are the Clebsch–Gordan coefficients[30] and $\|d_{ba}\|$ is the irreducible value of the dipole moment matrix element. Here

$$V_{ba}(MM')=V_{ba}^{*}(M'M),$$
$$V_{ba}(\sigma)=(-1)^{J_a-J_b-\sigma}V_{ba}^{*}(-\sigma). \tag{9}$$

The operators satisfy $\hat{R}_{\xi\xi'}^{+}=|\xi\rangle\langle\xi'|$ for $\xi \neq \xi'$ and $\varepsilon_{\xi}<\varepsilon_{\xi'}$ and $\hat{R}_{\xi\xi'}^{-}=|\xi\rangle\langle\xi'|$ for $\varepsilon_{\xi}>\varepsilon_{\xi'}$. The superscripts + and – are introduced in connection with the resonance approximation. The operators $\hat{R}_{MM'}^{+}=|aM\rangle\langle bM'|$ and $\hat{R}_{MM'}^{-}=|bM'\rangle\langle aM|$ are specially distinguished for the transition $a \rightarrow b$.

The projection operators satisfy the following commutation relations:

$$[\hat{R}_{\xi\xi'}^{(j)},\hat{R}_{\zeta\zeta'}^{(j')}]=\delta_{jj'}(\hat{R}_{\xi\zeta'}^{(j)}\delta_{\zeta\xi'}-\hat{R}_{\xi'\zeta}^{(j)}\delta_{\xi\zeta'}). \tag{10}$$

where $\delta_{jj'}$ is the Kronecker delta function.

The interaction of atoms with a quantized radiation field is described by the expression

$$\hat{V}_q=\sum_{j=1}^{N}\sum_{k\sigma}\sum_{\xi\xi'}(g_{\xi\xi'}^{k\sigma},\hat{a}_{k\sigma}\hat{R}_{\xi'\xi}^{+(j)}+g_{\xi\xi'}^{k\sigma}\hat{a}_{k\sigma}^{+}\hat{R}_{\xi\xi'}^{-(j)}), \tag{11}$$

where $g_{\xi\xi'}^{k\sigma}=id_{\xi\xi'}U_{k\sigma}(r)\sqrt{2\pi\omega_k/\hbar W}$ and W is the quantization volume. Setting $d_{\xi\xi'}=d_{nn'}(MM')$, we employ the Wigner–Eckart theorem:

$$g_{\xi\xi'}^{k\sigma}=g_{nn'}^{k\sigma}(MM')=(-1)^{\sigma}C_{JMJ'-M'}^{1-\sigma}g_{nn'}/\sqrt{3}, \tag{12a}$$

$$g_{nn'}=i\|d_{nn'}\|U_k(r)\sqrt{2\pi\omega_k/\hbar W}. \tag{12b}$$

2.2. Basic formalism in the *M* representation

We shall employ the Scully–Lamb atom–photon density matrix formalism to describe the system under study.[28] The equation of motion for the atom–photon density matrix operator ρ_{a-ph} has the form

$$i\dot{\rho}_{a-ph}=[\hat{H},\rho_{a-ph}]+i\hat{\Gamma}(\rho_{a-ph}), \tag{13}$$

where the operator $\hat{\Gamma}_{a-ph}$ describes relaxation processes. The atomic density matrix ρ is determined from the operator ρ_{a-ph} by summing over the photon variables $\rho=\mathrm{Tr}(\rho_{a-ph})_{ph}$ and the photon field operator P is determined by contracting over the atomic variables $P=\mathrm{Tr}(\rho_{a-ph})_a$. In the zeroth approximation we neglect the effect of the quantum radiation field on the atomic subsystem. Then the equation of motion for the atomic density matrix ρ has the form

$$i\dot{\rho}=[\hat{H}_0+\hat{H}_{mag}+\hat{V}_L,\rho]+i\hat{r}+i\hat{S}+i\hat{Q}, \tag{14}$$

where the operator $\hat{r}$ describes the radiation relaxation processes, $\hat{S}$ describes the effect of collisions, and $\hat{Q}$ describes the pumping to the levels from other states. The components of the atomic density matrix are determined by the relation $\rho_{\xi\xi'}=\langle\rho\hat{R}_{\xi\xi'}\rangle$, which satsifies the equation

$$i\dot{\rho}_{\xi\xi'}=\Delta_{\xi\xi'}\rho_{\xi\xi'}+\sum_{\xi_1=a,b}(V_{\xi\xi_1}\rho_{\xi_1\xi'}-\rho_{\xi\xi_1}V_{\xi_1\xi'})+ir_{\xi\xi'}+iS_{\xi\xi'}+iQ_{\xi}\delta_{\xi\xi'}, \tag{15}$$

where $\Delta_{\xi\xi'}=(\varepsilon_n-\varepsilon_{n'})/\hbar+\Omega(g_nM-g_{n'}M')$.

Two terms can be distinguished in the operator $\hat{r}$ describing the radiation processes:

$$\hat{r}=-\hat{r}^{(1)}+\hat{r}^{(2)}, \tag{16}$$

where $\hat{r}^{(1)}$ corresponds to radiative loss processes and $\hat{r}^{(2)}$ corresponds to radiative arrival processes:

$$r^{(1)}_{\xi\xi'}=(\gamma_n+\gamma_{n'})\rho_{\xi\xi'}/2,\quad \gamma_n=\sum_{n''<n}A_{nn''}, \tag{17}$$

$$r^{(2)}_{\xi\xi'}=\delta_{nn'}\sum_{n_1M_1M_1'}A(nMnM'|n_1M_1n_1M_1')\rho_{n_1n_1}(M_1M_1'), \tag{18}$$

$$A(nMnM'|n_1M_1n_1M_1')=A_{n_1n}\sum C^{J_1M_1}_{JM1\sigma}C^{J_1M_1'}_{JM'1\sigma}, \tag{19}$$

and the coefficient $A_{nn''}$ determines the spontaneous relaxation rate in the transition $n\to n''$. One can see from the expressions (17) and (18) that the decay of the density matrix has a diagonal structure, and the arrival term $r^{(2)}$ describes not only the ''transfer'' of the population of the sublevels but also the coherence between the magnetic sublevels. The condition

$$M-M'=M_1-M_1'. \tag{20}$$

for Eq. (19) follows from the properties of the Clebsch–Gordan coefficients.[30] In the polarization operator representation (κq representation), which will be examined below, the arrival term is diagonal with respect to n and the degeneracy indices M. Allowance for the effect of collisions, which is described by the operator $\hat{S}$, is a complicated problem of quantum kinetics which depends strongly on the conditions of the gaseous medium. In the present paper the effect of collisions is taken into account purely phenomenologically. We note that, just as in the case of the operator $\hat{r}$, loss and arrival terms $\hat{S}^{(1)}$ and $\hat{S}^{(2)}$, respectively, can usually be distinguished in the operator $\hat{S}$. For the often employed model of isotropic collisions the loss term $\hat{S}^{(1)}$ in the M representation is diagonal, like the loss term $\hat{r}^{(1)}$, and the arrival term $\hat{S}^{(2)}$ possesses a similar structure under the condition (20).

Since the pump wave interacts only with the transition $a\to b$, the populations of the other levels are determined by the pump $Q_{\xi\xi}=Q_{nn}/\sqrt{2J_n+1}=\widetilde{Q}_n$, which we assume to be isotropic for all sublevels:

$$\rho_{nn}(MM')=\delta_{MM'}Q_{nn}/\Gamma_n\sqrt{2J_n+1},\quad n\neq a,b, \tag{21}$$

where $\Gamma_n=\gamma_n+v_n^{(c)}$ is the decay rate of the population of the state n and $v_n^{(c)}$ is the decay rate due to collisions. The dynamics of the transition $a\to b$ in the rotating-wave approximation is described by the standard equations:

$$\begin{aligned}i\dot{\rho}_{aa}(MM')=&[g_a(M-M')\Omega-i\Gamma_a(MM')]\rho_{aa}(MM')\\&+\sum_{M_1M_1',n=a,b}i\Gamma_a^n(M_1M_1')\rho_{nn}(M_1M_1')\\&+\sum_{M_1}[\widetilde{V}_{ab}(MM_1)\widetilde{\rho}_{ba}(M_1M')\\&-\widetilde{\rho}_{ab}(MM_1)\widetilde{V}_{ba}(M_1M')]+i\widetilde{Q}_a\delta_{MM'},\end{aligned} \tag{22}$$

$$\begin{aligned}i\dot{\rho}_{bb}(MM')=&[g_b(M-M')\Omega-i\Gamma_b(MM')]\rho_{bb}(MM')\\&+i\sum_{M,M'}v_b^{(c)}(MM'|bM_1M_1')\rho_{bb}(M_1M_1')\\&+\sum_{M_1}[\widetilde{V}_{ba}(MM_1)\widetilde{\rho}_{ab}(M_1M')\\&-\widetilde{\rho}_{ba}(MM_1)\widetilde{V}_{ab}(M_1M')]+i\widetilde{Q}_b\delta_{MM'},\end{aligned} \tag{23}$$

$$\begin{aligned}i\dot{\widetilde{\rho}}_{ba}(MM')=&[\Delta_L+\Omega(g_bM-g_aM')\\&-i\Gamma_{ba}(MM')]\widetilde{\rho}_{ba}(MM')\\&+\sum_{M_1}[\widetilde{V}_{ba}(MM_1)\rho_{aa}(M_1M')\\&-\rho_{bb}(MM_1)\widetilde{V}_{ba}(M_1M')],\end{aligned} \tag{24a}$$

$$\widetilde{\rho}_{ab}(M'M)=\widetilde{\rho}^*_{ba}(MM'), \tag{24b}$$

where

$$\widetilde{V}_{ba}(MM')=V_{ba}(MM')\exp(-i\omega_Lt),$$

$$\widetilde{\rho}_{ba}(MM')=\rho_{ba}(MM')\exp(-i\omega_Lt),$$

$$\Delta_L=\omega_{ba}-\omega_L,$$

$$\Gamma_{ba}(MM')=\frac{\gamma_a+\gamma_b}{2}+v_{ba}^{(c)}(MM'),\quad \Gamma_n(MM')=\gamma_n$$

$$+\sum_{M_1,M_1'} v_n^{(c)}(nM_1M_1'|MM'),$$

$$\Gamma_a^n(M_1M_1')=A(aMaM'|nM_1nM_1')$$

$$+v_a^{(c)}(MM'|nM_1M_1').$$

In the general case the constant $v_{ba}^{(c)}$ is complex, i.e., collisions result in not only depolarization of coherence between the states but also a shift of the levels. The quantity $v_n^{(c)}(MM'|n_1M_1M_1')$ describes arrivals, which are due to collisional mixing of the populations of the magnetic sublevels, or the coherence between them for states n with $n_1=n$, and for $n_1\neq n$ it describes arrivals from upper states. In the expressions (22) and (23), we assume that arrivals from the levels p and s (see Fig. 1) enter in the pumping Q_b and Q_a. For the case when the level a is the ground state and there is no pumping ($Q=0$), Eqs. (22) and (23) must be supplemented by the condition

$$\sum_{M,n=a,b} \rho_{nn}(MM)=1.$$

We represent the system of equations (22)–(24) in the matrix form

$$i\dot{\boldsymbol{\rho}}=\Lambda\boldsymbol{\rho}+i\mathbf{Q}, \tag{25}$$

where $\boldsymbol{\rho}$ is a column matrix of the components of the density matrix,

$$\boldsymbol{\rho}^T=(\rho_{aa}(-J_a,-J_a),\rho_{aa}(-J_a,-J_a+1),\ldots,\rho_{bb}(MM'),\ldots,\tilde{\rho}_{ba}(MM'),\ldots,\tilde{\rho}_{ab}(MM'),\ldots),$$

$$\mathbf{Q}^T=(\tilde{Q}_a,0,\ldots).$$

After contraction over the atomic variables in Eq. (13), we have

$$i\dot{P}=[H_{ph},P]+\left(\sum_{k\sigma,\xi\xi',j} g_{\xi\xi'}^{k\sigma}\hat{R}_{\xi'\xi}^{+(j)}\hat{\Phi}_{k\sigma}^{-}\right.$$

$$\left.+g_{\xi\xi'}^{k\sigma}\hat{R}_{\xi\xi'}^{-(j)}\hat{\Phi}_{k\sigma}^{+}-\text{H.c.}\right), \tag{26}$$

where $\hat{\Phi}_{k\sigma}^{+}=\hat{a}_{k\sigma}^{+}\rho_{a-ph}$ and $\hat{\Phi}_{k\sigma}^{-}=\hat{a}_{k\sigma}\rho_{a-ph}$ are auxiliary operators.

For the slow component of the operator P Eq. (2) reduces to the form

$$\dot{P}=-i\left\{\sum_{k\sigma,\xi\xi',j}[g_{\xi\xi'}^{k\sigma}\Phi_{\xi'\xi}^{-(j)}+g_{\xi\xi'}^{k\sigma}\Phi_{\xi\xi'}^{+(j)}-(g_{\xi\xi'}^{k\sigma}\Phi_{\xi'\xi}^{-(j)})^{+}\right.$$

$$\left.-(g_{\xi\xi'}^{k\sigma}\Phi_{\xi'\xi}^{+(j)})^{+}]\right\}. \tag{27}$$

The operator P makes it possible to determine the number of photons in a given mode: $n_{k\sigma}=\langle P\hat{a}_{k\sigma}^{+}\hat{a}_{k\sigma}\rangle$. A linear equation for $n_{k\sigma}$ follows from the equation for P in second-order perturbation theory in the coupling constant g. For this, we seek a solution for the operators $\hat{\Phi}$ to first order in g. Using Eq. (13), we obtain for the operators $\hat{\Phi}_{k\sigma}^{+}$ and $\hat{\Phi}_{k\sigma}^{-}$ the equations

$$i\dot{\hat{\Phi}}_{k\sigma}^{+}=[\hat{H}_0+\hat{H}_{mag}+\hat{V}_L,\hat{\Phi}_{k\sigma}^{+}]-\omega_k\hat{\Phi}_{k\sigma}^{+}+i\hat{\Gamma}[\hat{\Phi}_{k\sigma}^{+}]$$

$$+\sum_{\sigma'}(\hat{T}_{\sigma'}^{+}\rho^{(0)}\hat{a}_{k\sigma}^{+}\hat{a}_{k\sigma'}P-\hat{a}_{\sigma k}^{+}P\hat{a}_{k\sigma'}\rho^{(0)}\hat{T}_{\sigma'}^{+}$$

$$+\hat{a}_{k'\sigma'}^{+}\hat{a}_{k\sigma}^{+}\hat{T}_{\sigma'}^{-}\rho^{(0)}-\hat{a}_{k\sigma}^{+}P\hat{a}_{k\sigma'}^{+}\rho^{(0)}\hat{T}_{\sigma'}^{-}), \tag{28}$$

$$i\dot{\hat{\Phi}}_{k\sigma}^{-}=[\hat{H}_0+\hat{H}_{mag}+\hat{V}_L,\hat{\Phi}_{k\sigma}^{-}]+\omega_k\hat{\Phi}_{k\sigma}^{-}+i\hat{\Gamma}[\hat{\Phi}_{k\sigma}^{-}]$$

$$+\sum_{\sigma'}(\hat{a}_{k\sigma}\hat{a}_{k\sigma'}^{+}P\hat{T}_{\sigma'}^{-}\rho^{(0)}-\hat{a}_{k\sigma}P\hat{a}_{k\sigma'}^{+}\rho^{(0)}\hat{T}_{\sigma'}^{-}$$

$$+\hat{a}_{k'\sigma'}\hat{a}_{k\sigma}P\hat{T}_{\sigma'}^{+}\rho^{(0)}-\hat{a}_{k\sigma}P\hat{a}_{k'\sigma'}\rho^{(0)}\hat{T}_{\sigma'}^{+}), \tag{29}$$

where

$$\hat{T}_{\sigma}^{\pm}=\sum_{\xi\xi'} g_{\xi\xi'}^{k\sigma}\hat{R}_{\xi'\xi}^{\mp},$$

$\rho^{(0)}$ is the stationary solution of the system (22)–(24). The last two terms in Eqs. (28) and (29) describe the interaction of the pump wave with two quantum modes which are frequency-detuned from it:

$$\omega_k+\omega_{k'}=2\omega_L \tag{30a}$$

under the condition

$$\mathbf{k}_{\sigma}+\mathbf{k}_{\sigma'}'\approx\mathbf{k}_{L\sigma}+\mathbf{k}_{L\sigma'}. \tag{30b}$$

2.2.1. Scattering in the transition $a\rightarrow b$

To describe scattering in the transition $a\rightarrow b$, we shall study the projection of the operators $\hat{\Phi}^{+}$ and $\hat{\Phi}^{-}$ on the states a and b. We employ the rotating-wave approximation and separate the rapidly oscillating components:

$$\Phi_{aa}^{\pm}(MM')=\tilde{\Phi}_{aa}^{\pm}(MM')\exp(\pm i\omega_L t),$$

$$\Phi_{bb}^{\pm}(MM')=\tilde{\Phi}_{bb}^{\pm}(MM')\exp(\pm i\omega_L t),$$

$$\Phi_{ab}^{+}(MM')=\tilde{\Phi}_{ab}^{+}(MM')\exp(2i\omega_L t),$$

$$\Phi_{ba}^{-}(MM')=\tilde{\Phi}_{ba}^{-}(MM')\exp(-2i\omega_L t),$$

$$\Phi_{ba}^{+}(MM')\propto 1,\quad \Phi_{b}^{-}(MM')\propto 1.$$

We now introduce the column matrices $\boldsymbol{\Phi}_{k\sigma}^{+}$ and $\boldsymbol{\Phi}_{k\sigma}^{-}$ for the slow components of the atomic parts of the corresponding operators. Let the order of the components in these column matrices be the same as that of the components of the atomic density matrix in the column matrix $\boldsymbol{\rho}$ in Eq. (25). Then the equations for $\hat{\boldsymbol{\Phi}}^{+}$ and $\hat{\boldsymbol{\Phi}}^{-}$ can be represented in the form

$$i\dot{\boldsymbol{\Phi}}_{k\sigma}^{\pm}=(\Lambda\mp\nu_k\mathbf{I})\boldsymbol{\Phi}_{k\sigma}^{\pm}+\boldsymbol{\Sigma}_{k\sigma}^{\pm}, \tag{31}$$

where $\nu_k=\omega_k-\omega_L$, $\mathbf{I}$ is a unit matrix, and Λ is the matrix in Eq. (25). Taking account of the structure of Eqs. (28) and (29), we represent the column matrix $\boldsymbol{\Sigma}$ as a sum

$$\boldsymbol{\Sigma}={}^{(1)}\boldsymbol{\Sigma}+{}^{(4)}\boldsymbol{\Sigma}. \tag{32}$$

Here ${}^{(1)}\mathbf{\Sigma}$ corresponds to isotropic photon absorption and emission processes and ${}^{(4)}\mathbf{\Sigma}$ corresponds to four-wave processes under the condition (30). The explicit expressions for the components of the column matrices $(\Sigma^{+}_{k\sigma})_{jM,mM'} = \Sigma^{+}_{jm}(k\sigma|MM')$ (where $j,\ m = a,b$) are

$$
\begin{aligned}
{}^{(1)}\Sigma^{+}_{jm}(k\sigma|MM') = \sum_{M''\sigma'} [&\hat{a}^{+}_{k\sigma}\hat{a}_{k\sigma'} P g^{k\sigma'}_{ba}(MM'') \\
&\times \rho^{(0)}_{am}(M''M)\,\delta_{jb} \\
&- \hat{a}^{+}_{k\sigma} P \hat{a}_{k\sigma'} g^{k\sigma'}_{ba}(M''M') \\
&\times \rho^{(0)}_{jb}(MM'')\,\delta_{ma}],
\end{aligned} \tag{33}
$$

$$
\begin{aligned}
{}^{(4)}\Sigma^{+}_{jm}(k\sigma|MM') = \sum_{k'\sigma'M''} [&\hat{a}^{+}_{k'\sigma'}\hat{a}^{+}_{k\sigma} P g^{k'\sigma'}_{ab}(MM'') \\
&\times \rho^{(0)}_{bm}(M''M')\,\delta_{ja} \\
&- \hat{a}^{+}_{k\sigma} P \hat{a}^{+}_{k'\sigma'} g^{k'\sigma'}_{ab}(M''M') \\
&\times \rho^{(0)}_{ja}(MM'')\,\delta_{mb}].
\end{aligned} \tag{34}
$$

We find the stationary solution for the components of the operators $\mathbf{\Phi}^{\pm}_{k\sigma}$:

$$
\mathbf{\Phi}^{+}_{k\sigma} = -(\Lambda \mp \nu_k \mathbf{I})^{-1}\Sigma^{+}_{k\sigma}. \tag{35}
$$

We now substitute $(\Phi_{k\sigma})_{bM,aM'} = \Phi_{ba}(k\sigma|MM')$ into Eq. (27) and transform the equation for the photon field operator P into the form

$$
\begin{aligned}
\dot{P} = \sum_{\sigma\sigma',kk'} [&A^{(k)}_{\sigma\sigma'}(\hat{a}^{+}_{k\sigma} P \hat{a}_{k\sigma'} - P\hat{a}_{k\sigma'}\hat{a}^{+}_{k\sigma}) - B^{(k)}_{\sigma\sigma'} \\
&\times(\hat{a}^{+}_{k\sigma}\hat{a}_{k\sigma'} P - \hat{a}_{k\sigma} P \hat{a}^{+}_{k\sigma}) + C^{(k)}_{\sigma\sigma'}(\hat{a}^{+}_{k\sigma}\hat{a}^{+}_{k'\sigma'} P \\
&- \hat{a}^{+}_{k'\sigma'} P \hat{a}^{+}_{k\sigma}) - D^{(k)}_{\sigma\sigma'}(\hat{a}^{+}_{k\sigma} P \hat{a}^{+}_{k'\sigma'} - P\hat{a}^{+}_{k'\sigma'}\hat{a}^{+}_{k\sigma}) \\
&+ (k \leftrightarrow k') + \text{H.c.}],
\end{aligned} \tag{36}
$$

where the coefficients A, B, C, and D are determined by the expression

$$
\begin{aligned}
\sum_{MM'j} & i g^{k\sigma}_{ab}(M'M)\Phi^{+(j)}_{ba}(k\sigma k'\sigma'|MM') \\
&= (A^{(k)}_{\sigma\sigma'}\hat{a}^{+}_{k\sigma} P \hat{a}_{k\sigma'} - B^{+}_{\sigma\sigma'}\hat{a}^{+}_{k\sigma}\hat{a}_{k\sigma'} P + C^{(k)}_{\sigma\sigma'}\hat{a}^{+}_{k\sigma}\hat{a}^{+}_{k'\sigma'} P \\
&\quad - D^{(k)}_{\sigma\sigma'}\hat{a}^{+}_{k\sigma} P \hat{a}^{+}_{k'\sigma'}).
\end{aligned} \tag{37}
$$

Here $\Phi^{+}_{ba}(k\sigma k'\sigma'|MM')$ is found by solving Eq. (35) without summing over the index σ' in Eqs. (33) and (34). Using Eq. (36) for photons, we obtain the following equations of motion:

$$
\begin{aligned}
\frac{d}{dt}\langle a^{+}_{k\sigma'} a_{k\sigma}\rangle = -\sum_{\sigma''} &(\alpha^{(k)}_{\sigma\sigma''}\langle a^{+}_{k\sigma'} a_{k\sigma''}\rangle \\
&+ (\alpha^{(k)}_{\sigma'\sigma''})^{*}\langle a^{+}_{k\sigma''} a_{k\sigma}\rangle) - \sum_{k,k',\sigma''} (\beta^{(k)}_{\sigma\sigma''} \\
&\times\langle a^{+}_{k\sigma'} a^{+}_{k'\sigma''}\rangle + (\beta^{(k)}_{\sigma'\sigma''})^{*}\langle a_{k'\sigma''} a_{k\sigma}\rangle) \\
&+ (A^{(k)}_{\sigma\sigma'})^{*} + A^{(k)}_{\sigma'\sigma},
\end{aligned} \tag{38}
$$

$$
\begin{aligned}
\frac{d}{dt}\langle a_{k'\sigma'} a_{k\sigma}\rangle = -\sum_{\sigma''} &(\alpha^{(k)}_{\sigma\sigma''}\langle a_{k'\sigma'} a_{k\sigma''}\rangle + \alpha^{(k)}_{\sigma'\sigma''} \\
&\times\langle a_{k'\sigma''} a_{k\sigma}\rangle) - \sum_{\sigma''} (\beta^{(k)}_{\sigma\sigma''}\langle a^{+}_{k\sigma''} a_{k'\sigma'}\rangle \\
&+ \beta^{(k')}_{\sigma'\sigma''}\langle a^{+}_{k'\sigma''} a_{k\sigma}\rangle) + C^{(k)}_{\sigma'\sigma} + C^{(k')}_{\sigma\sigma'},
\end{aligned} \tag{39}
$$

$$
\langle a^{+}_{k'\sigma'} a^{+}_{k\sigma}\rangle = \langle a_{k'\sigma'} a_{k\sigma})^{+}, \tag{40}
$$

where $\langle a^{+}_{k\sigma'} a_{k\sigma}\rangle = \langle P\hat{a}^{+}_{k\sigma'}\hat{a}_{k\sigma}\rangle$, $\langle a_{k'\sigma'} a_{k\sigma}\rangle = \langle P\hat{a}_{k'\sigma'}\hat{a}_{k\sigma}\rangle$, $\langle a^{+}_{k'\sigma'} a^{+}_{k\sigma}\rangle = \langle P\hat{a}^{+}_{k'\sigma'}\hat{a}^{+}_{k\sigma}\rangle$, $\alpha^{(k)}_{\sigma\sigma'} = A^{(k)}_{\sigma\sigma'} - B^{(k)}_{\sigma\sigma'}$, and $\beta^{(k)}_{\sigma\sigma'} = C^{(k)}_{\sigma\sigma'} - D^{(k)}_{\sigma\sigma'}$.

The correlation functions $\langle a^{+}_{k\sigma'} a_{k\sigma}\rangle$ correspond to the well-known Fano polarization matrix. The correlation functions $\langle a_{k'\sigma'} a_{k\sigma}\rangle$ and $\langle a^{+}_{k'\sigma'} a^{+}_{k\sigma}\rangle$ describe forward-directed four-wave mixing processes under the condition (30), the coefficients $\alpha_{\sigma\sigma'}$ describe the absorption and dispersion of the radiation, and the coefficients $\beta_{\sigma\sigma'}$ describe four-wave coupling of the modes. A detailed interpretation of these correlation functions and coefficients is given in Ref. 16. The free terms in Eqs. (38) and (39) describe spontaneous sources for the corresponding correlation functions. For $\sigma = \sigma'$ in Eq. (38) the quantity $\mathscr{A}_{\sigma\sigma}$ ($\mathscr{A}_{\sigma\sigma'} = A_{\sigma\sigma'} + A^{*}_{\sigma'\sigma}$) characterizes the resonance fluorescence spectrum of σ-polarized photons.

The intensity of the electromagnetic field of the quantum modes can be described by $E_{k\sigma} = \langle \hat{a}_{k\sigma} P\rangle E_{\omega}$, where E_{ω} is the intensity of the field of a single photon. Using Eq. (36), we obtain the system of equations

$$
\frac{d}{dt} E_{k\sigma} = -\sum_{\sigma'} \alpha^{(k)}_{\sigma\sigma'} E_{k\sigma'} - \sum_{\sigma' k'} \beta^{(k)}_{\sigma\sigma'} E^{*}_{k'\sigma'}. \tag{41}
$$

This system is identical to the equations for classical test fields interacting with the transition $a \to b$ in the presence of a pump wave E_L. The coefficients α and β are identical to the polarizabilities calculated from the standard equations for the density matrix in first-order perturbation theory in E_{σ} and arbitrary order in E_L. In the general case the system (38)–(40) contains 36 equations. If the terms corresponding to forward-directed four-wave interaction, which are important only for describing forward scattering, are discarded, the system reduces to 9 equations. Then the system consisting of Eqs. (41) and (38)–(40) have the form

$$
\frac{d}{dt}\,\boldsymbol{\varepsilon} = -\mathbf{K}\boldsymbol{\varepsilon}. \tag{42}
$$

where

$$
\boldsymbol{\varepsilon} = \begin{pmatrix} E_{+} \\ E_{0} \\ E_{-} \end{pmatrix}, \quad \mathbf{K} = \begin{pmatrix} \alpha_{++} & \alpha_{+0} & \alpha_{+-} \\ \alpha_{0+} & \alpha_{00} & \alpha_{0-} \\ \alpha_{-+} & \alpha_{-0} & \alpha_{--} \end{pmatrix}
$$

$$
\frac{d}{dt}\,\mathbf{F} = -\mathbf{K}\cdot\mathbf{F} - \mathbf{F}\cdot\mathbf{K}^{+} + \mathbf{A}, \tag{43}
$$

where

$$\mathbf{A}=\begin{pmatrix} \mathscr{A}_{++} & \mathscr{A}_{+0} & \mathscr{A}_{+-} \\ \mathscr{A}_{0+} & \mathscr{A}_{00} & \mathscr{A}_{0-} \\ \mathscr{A}_{-+} & \mathscr{A}_{-0} & \mathscr{A}_{--} \end{pmatrix}, \tag{46}$$

$$\mathbf{F}=\begin{pmatrix} \langle a_+^+ a_+\rangle & \langle a_+^+ a_0\rangle & \langle a_+^+ a_-\rangle \\ \langle a_0^+ a_+\rangle & \langle a_0^+ a_0\rangle & \langle a_0^+ a_-\rangle \\ \langle a_-^+ a_+\rangle & \langle a_-^+ a_0\rangle & \langle a_-^+ a_-\rangle \end{pmatrix}.$$

To simplify the equations we drop the 1 in the indices ± 1. For the quantities $A_{\sigma\sigma'}$ and $\alpha_{\sigma\sigma'}$ we drop the upper index k, since the forward-directed four-wave mixing processes are neglected and the equations of motion include only a mode with the wave vector $\mathbf{k}$.

2.2.2. Scattering on adjacent transitions

To describe absorption and emission processes in the transitions $p\to b$ and $s\to a$, we apply the projection operators corresponding to these transitions to Eq. (28). Then

$$\begin{aligned} i\dot{\Phi}_{pb}^+(k\sigma|MM') =& [\Delta_{pb}+(g_pM-g_bM')\Omega \\ & -i\Gamma_{pb}(MM')]\Phi_{pb}^+(k\sigma|MM') \\ & +\sum_M \widetilde{\Phi}_{pa}^+(k\sigma|MM')\widetilde{V}_{ab}(M_1M') \\ & +\sum_{\sigma' M_1} g_{pb}(k\sigma'|MM_1)\hat{a}_{k\sigma}^+\hat{a}_{k\sigma'}P \\ & -g_{pb}(k\sigma|MM')\rho_{pp}^{(0)}(MM)\hat{a}_{\sigma k}^+P\hat{a}_{\sigma k}, \end{aligned} \tag{44}$$

$$\begin{aligned} i\dot{\Phi}_{pa}^+(k\sigma|MM_1) =& [\Delta_{pb}+\Delta_L+(g_pM-g_aM_1)\Omega \\ & -i\Gamma_{pa}(MM_1)]\Phi_{pa}^+(k\sigma|MM_1) \\ & +\sum_{M_2} \Phi_{pb}^+(k\sigma|MM_2)V_{ba}(M_2M_1) \\ & +\sum_{\sigma' M_2} g_{pb}(k\sigma'|MM_2)\tilde{\rho}_{ba}^{(0)} \\ & \times(M_2M_1)\hat{a}_{k\sigma}^+\hat{a}_{k\sigma'}P, \end{aligned} \tag{45}$$

where $\Delta_{pb}=\omega_{pb}-\omega_k$ and $\widetilde{\Phi}_{pa}^+=\Phi_{pa}^+\exp(i\omega_L t)$. The components of the density matrix $\tilde{\rho}_{ba}^{(0)}$ and $\rho_{bb}^{(0)}$ are the stationary solution of the system (22)–(24) and $\rho_{pp}^{(0)}(MM)$ is determined by the expression (21). The equations for the transition $s\to a$ are similar with the substitutions $p\to s$, $b\leftrightarrow a$, and $\Delta_L\to-\Delta_L$.

For the transition $b\to l$ Eq. (28) assumes the form

$$\begin{aligned} i\dot{\Phi}_{bl}^+(k\sigma|MM') =& [\Delta_{bl}+\Omega(g_bM-g_lM') \\ & +i\Gamma_{bl}(MM')]\Phi_{bl}^+(k\sigma|MM') \\ & +\sum_{M_1} \widetilde{V}_{ba}(MM_1)\widetilde{\Phi}_{al}^+(k\sigma|M_1M') \\ & +g_{bl}(k\sigma|MM')\hat{a}_{k\sigma}^+\hat{a}_{k\sigma}P\rho_{ll}^{(0)}(M'M') \\ & -\sum_{M_1\sigma'} \rho_{bb}^{(0)}(MM_1)g_{bl}^{k\sigma}\hat{a}_{k\sigma}^+P\hat{a}_{k\sigma'}. \end{aligned}$$

$$\begin{aligned} i\dot{\Phi}_{al}^+(k\sigma|M_1M') =& [\Delta_{bl}-\Delta_L+\Omega(g_aM_1-g_lM') \\ & -i\Gamma_{al}(MM')]\widetilde{\Phi}_{al} \\ & +\sum_{M_2} \widetilde{V}_{ab}(M_1M_2)\Phi_{bl}^+(k\sigma|M_2M') \\ & -\sum_{M_2\sigma'} \tilde{\rho}_{ab}^{(0)}(M_1M_2)g_{bl}(k\sigma'|M_2M') \\ & \times\hat{a}_{k\sigma}^+P\hat{a}_{k\sigma'}, \end{aligned} \tag{47}$$

where $\Phi_{al}^+=\widetilde{\Phi}_{al}^+\exp(-i\omega_L t)$. The equations for the transition $a\to m$ are similar to Eqs. (44) and (45) with the substitutions $b\leftrightarrow a$, $l\to m$, and $\Delta_L\to-\Delta_L$.

Substituting the stationary solutions of Eqs. (44), (45), (46), and (47) in Eq. (27), we obtain an equation for the photon field operator P that is similar to Eq. (36) but without the terms corresponding to forward-directed four-wave interaction processes ($C=D=0$). Equations (42) and (43) describe the dynamics of the photon field. For the transitions $p\to b$ and $s\to a$ $A_{\sigma\sigma'}=A_{\sigma\sigma}\delta_{\sigma\sigma'}$, i.e., ordinary spontaneous emission with no correlation between photons with different polarizations occurs. This means that there are no interference effects, but here interference effects occur in connection with absorption in these transitions: $B_{\sigma\sigma'}\neq 0$ for $\sigma\neq\sigma'$. This is due to the presence of coherence induced between the magnetic sublevels of the states a and b by the pump wave. Conversely, interference effects are absent in the photon absorption processes for the transitions $b\to l$ and $a\to m$, $B_{\sigma\sigma'}=B_{\sigma\sigma}\delta_{\sigma\sigma'}$, since there is no coherence between the sublevels of the states l and m. Interference effects are present in the spontaneous Raman spectrum (in the presence of different polarizations in the pump wave): $\mathscr{A}_{\sigma\sigma'}\neq 0$ for $\sigma\neq\sigma'$.

2.3. Application of the κq representation

It is evident from Eqs. (22) and (23) that terms describing relaxation processes are strongly nondiagonal. This is also true of Eq. (31) for the quantities $\Phi_{k\sigma}^{\pm}$. This drawback disappears when the polarization operator or κq representation is used.[30] This representation has wide application in problems of spectroscopy, atomic collisions, and others.[31,32]

In this representation the system of equations (22)–(24) assumes the form

$$\begin{aligned} i\dot{\rho}_{aa}(\kappa q) =& [q\Omega_a-i\Gamma_a(\kappa)]\rho_{bb}(\kappa q)+iA_{ba}(\kappa)\rho_{bb}(\kappa q) \\ & +iQ_a(\kappa)-\sum_{\kappa_1 q_1\sigma} U_{aa}^{b\sigma}(\kappa q|\kappa_1 q_1)[\\ & (-1)^{\kappa_1-\kappa}\widetilde{V}_{ab}(\sigma)\widetilde{\rho}_{ba}(\kappa_1 q_1) \\ & +\widetilde{\rho}_{ab}(\kappa_1 q_1)\widetilde{V}_{ba}(\sigma)], \end{aligned} \tag{48}$$

$$i\dot{\rho}_{bb}(\kappa q)=[q\Omega_b-i\Gamma_b(\kappa)]\rho_{bb}(\kappa q)+iQ_b(\kappa)$$

$$-\sum_{\kappa_1 q_1 \sigma} U_{ba}^{a\sigma}(\kappa q|\kappa_1 q_1)[(-1)^{\kappa_1-\kappa}\tilde{V}_{ba}$$

$$\times(\sigma)\tilde{\rho}_{ab}(\kappa_1 q_1)+\tilde{\rho}_{ba}(\kappa_1 q_1)\tilde{V}_{ab}(\sigma)], \quad (49)$$

$$i\dot{\tilde{\rho}}_{ba}(\kappa_1 q_1)=[\Delta_L+q_1(\Omega_b+\Omega_a)/2-i\Gamma_{ba}(\kappa_1)]\tilde{\rho}_{ba}(\kappa_1 q_1)$$

$$-\sum_{\kappa_2 q_2 \sigma} \tilde{V}_{ba}(\sigma)[(-1)^{\kappa_2-\kappa_1}U_{ba}^{a\sigma}$$

$$\times(\kappa_1 q_1|\kappa_2 q_2)\rho_{aa}(\kappa_2 q_2)$$

$$+U_{ab}^{a\sigma}(\kappa_1 q_1|\kappa_2 q_2)\rho_{bb}(\kappa_2 q_2)]$$

$$+\frac{\Omega_b-\Omega_a}{2}\Bigg[q_1\frac{J_a(J_a+1)-J_b(J_b+1)}{\kappa_1(\kappa_1+1)}\tilde{\rho}_{ba}$$

$$\times(\kappa_1 q_1)+f(\kappa_1,q_1)\tilde{\rho}_{ba}(\kappa_1-1,q_1)$$

$$+f(\kappa_1+1,q_1)\tilde{\rho}_{ba}(\kappa_1+1,q_1)\Bigg], \quad (50)$$

$$\tilde{\rho}_{ba}(\kappa,-q)=(-1)^{J_a-J_b+q}\tilde{\rho}_{be}^{*}(\kappa,q), \quad (51)$$

where

$$U_{\alpha\beta}^{\gamma\sigma}(\kappa q|\kappa_1 q_1)=(-1)^{J_\beta+J_\alpha+\kappa_1-q_1}$$

$$\times\sqrt{(2\kappa_1+1)(2\kappa_2+1)}C_{\kappa q \kappa_1-q_1}^{1-\sigma}$$

$$\times\begin{Bmatrix}\kappa & 1 & \kappa_1\\ J_\gamma & J_\alpha & J_\beta\end{Bmatrix}, \quad (52)$$

$$f(\kappa_1,q_1)=\frac{1}{\kappa_1}\Bigg\{[(J_a+J_b+1)^2-\kappa_1^2][\kappa_1^2-(J_a$$

$$-J_b)^2]\frac{\kappa_1^2-q_1^2}{4\kappa_1^2-1}\Bigg\}^{1/2}, \quad (53)$$

$$A_{ba}(\kappa)=(-1)^{J_a+J_b+\kappa+1}(2J_b+1)\begin{Bmatrix}J_b & J_a & \kappa\\ J_a & J_a & 1\end{Bmatrix}A_{ba}. \quad (54)$$

Here $\Omega_j=g_j\Omega$ and $A_{ba}=4\omega_{ba}^3\|d_{ba}\|^2/3\hbar c^3(2J_b+1)$.

The relaxation constants $\Gamma_n(\kappa)$ and $\Gamma_{ba}(\kappa)$ are determined in the standard manner.[31,32] We assume that the collisions are isotropic, and therefore the quantities Γ and Q do not depend on q. A great advantage of the system of equations (48)–(51), in contrast to Eqs. (22)–(24), is that they are diagonal with respect to the relaxation constants. However, as one can see from Eq. (50), this system becomes more complicated because of the coupling of the components of different rank with respect to κ. This direct coupling vanishes when the Landé factors of the levels a and b are equal ($\Omega_a=\Omega_b$) or for the transition $J_a=1\to J_b=0$ and, naturally, in the absence of a magnetic field.

Writing the system (48)–(51) as

$$i\dot{\boldsymbol{\rho}}=\Xi\cdot\boldsymbol{\rho}+\mathbf{Q}, \quad (55)$$

we represent the system of equations, similar to Eq. (31), for the auxiliary operator $\Phi_{k\sigma}^{\pm}(\kappa q)$ in the form

$$i\dot{\boldsymbol{\Phi}}_{k\sigma}^{\pm}=(\boldsymbol{\Xi}\mp\nu_k\mathbf{I})\boldsymbol{\Phi}_{k\sigma}^{\pm}+\boldsymbol{\Sigma}_{k\sigma}^{+}. \quad (56)$$

The components of the column matrix $\Sigma_{k\sigma}^{+}$ are determined by the expression

$$\Sigma_{jm}^{+}(k\sigma|\kappa q)=\sum_{\kappa_1 q_1 \sigma';d=a,b;k''}$$

$$\times\{(-1)^{\kappa_1-\kappa}U_{mj}^{d\sigma'}(\kappa q|\kappa_1 q_1)(1-\delta_{md})$$

$$\times[\hat{a}_{k\sigma}^{+}\hat{a}_{k\sigma'}Pg_{ba}(\sigma)\rho_{am}^{(0)}(\kappa_1 q_1)\delta_{jb}$$

$$+\hat{a}_{\sigma' k'}^{+}\hat{a}_{\sigma k}^{+}Pg_{ab}(\sigma)\rho_{bm}^{(0)}(\kappa_1 q_1)\delta_{ja}]$$

$$+U_{jm}^{d\sigma'}(\kappa q|\kappa_1 q_1)\rho_{jd}^{(0)}(\kappa_1 q_1)$$

$$\times[\hat{a}_{\sigma k}^{+}P\hat{a}_{\sigma' k}g_{ba}(\sigma')\delta_{db}\delta_{ma}$$

$$+g_{ab}(\sigma')\hat{a}_{\sigma k}^{+}P\hat{a}_{\sigma' k'}^{+}\delta_{da}\delta_{mb}]\}. \quad (57)$$

The equation for the operator of the density of the photon field resonant with the transition $a\to b$ has the form, taking account of the κq representation of the operators $\Phi^{\pm}$,

$$\frac{d}{dt}P=-i\sum_{k\sigma,q}[\Phi_{ba}^{+}(k\sigma|1q)g_{ba}^{*}(\sigma)$$

$$+\Phi_{ab}^{-}(k\sigma|1q)g_{ab}^{*}(\sigma)-\text{H.c.}], \quad (58)$$

where the values of the components of the operators $\Phi^{\pm}(k\sigma|1q)$ are found from Eq. (56). The equation ultimately obtained for the operator P is completely identical to Eq. (36) derived from the M representation.

The application of the κq representation for describing scattering in transitions adjacent to the transition $a\to b$ reduces to applying this representation to Eqs. (44)–(47).

3. PROPERTIES OF THE SCATTERED RADIATION: ANGULAR AND POLARIZATION CHARACTERISTICS

In our system the intensity of the radiation scattered by large angles is determined by the correlation functions $\langle a_{k\sigma}^{+}a_{k\sigma'}\rangle$ whose dynamics is described by the system (43). In the chosen coordinate system, it was assumed that they have the same polarization vectors as the pump wave. To interpret the experimental observations and describe theoretically the propagation of radiation in an extended medium, the modification of these quantities in a rotated coordinate system is of interest. The coupling between the correlation functions $\langle a_\lambda^{+}a_{\lambda'}\rangle$ and $\langle a_\sigma^{+}a_{\sigma'}\rangle$, where $\hat{a}_\lambda^{+}$ and $\hat{a}_\lambda$ are the photon creation and annihilation operators in the coordinate system rotated by the Euler angles α, β, and γ, is determined by the expression (for simplicity, we drop the superscript)

$$\langle a_\lambda^{+}a_{\lambda'}\rangle=\sum_{\sigma\sigma'}\varepsilon_{\lambda\lambda'}^{\sigma\sigma'}\langle a_\sigma^{+}a_{\sigma'}\rangle,$$

$$\varepsilon_{\lambda\lambda'}^{\sigma\sigma'}(\alpha,\beta,\gamma)=(D_{\sigma\lambda}^{1})^{*}D_{\sigma'\lambda'}^{1}, \quad (59)$$

where $D_{\sigma\lambda}^{1}(\alpha,\beta,\gamma)$ are the Wigner functions.[30] The equations for the correlation functions $\langle a_\lambda^{+}a_{\lambda'}\rangle$ are similar to the system (43) with the corresponding replacement of the coefficients A and B; for example,

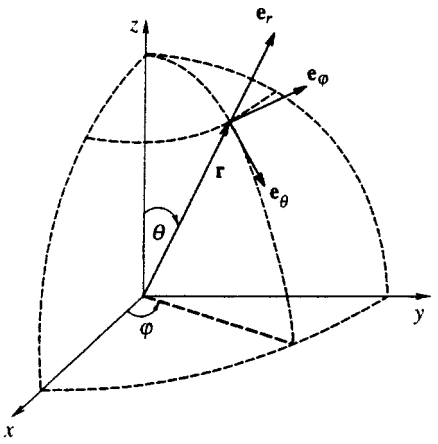

FIG. 2. Spherical coordinate system.

$$\mathscr{A}_{\lambda\lambda'}=\sum_{\sigma\sigma'}\varepsilon_{\lambda\lambda'}^{\sigma\sigma'}\mathscr{A}_{\sigma\sigma'}\,. \tag{60}$$

The quantity $\mathscr{A}_{\sigma\sigma'}$ can be regarded as a spectral characteristic. We note that using the relation[30]

$$D^{J_1}_{M_1N_1}(\alpha,\beta,\gamma)D^{J_2}_{M_2N_2}(\alpha,\beta,\gamma)=\sum_{J=|J_1-J_2|}^{J_2+J_1}\sum_{M,N}C^{JM}_{J_1M_1}D^{J}_{MN}(\alpha,\beta,\gamma)C^{JN}_{J_1N_1J_2N_2},$$

we obtain the well-known polarization–angular dependence of the spontaneous radiation[33]

$$\mathscr{A}_{\lambda\lambda'}=\sum_{\substack{\sigma\sigma'\\L=0,1,2}}(-1)^{\lambda'+\sigma'}(2L+1)\begin{pmatrix}1&1&L\\ \sigma'&-\sigma&\chi\end{pmatrix}\times\begin{pmatrix}1&1&L\\ \lambda'&-\lambda&-\mu\end{pmatrix}D^{L}_{\chi\mu}\mathscr{A}_{\sigma\sigma'} \tag{61}$$

where according to the properties of the $3jm$ symbols we have $\mu=\lambda'-\lambda$ and $\chi=\sigma'-\sigma$.

Neglecting dispersion, we introduce the tensor of intense scattered radiation:

$$J_{\lambda\lambda'}=c\int\langle a^+_{k\lambda}a_{k\lambda'}\rangle\hbar\omega\,\delta(\omega-\omega_k)\,\frac{d\mathbf{k}\,d\omega}{(2\pi)^4}\,. \tag{62}$$

Scattering in the direction of the unit vector $\mathbf{e}$ is determined by the expression

$$J_{\lambda\lambda'}(\mathbf{e})=\int\frac{\hbar\omega_k^3 d\omega_k}{4\pi^2c^2}\langle a^+_{k\lambda}a_{k\lambda'}\rangle\delta(O-O_e)dO, \tag{63}$$

where O is the solid angle. For the spectral intensity tensor we have

$$J_{\lambda\lambda'}(\omega_k,\lambda)=\frac{\hbar\omega_k^3}{4\pi^2c^2}\langle a^+_\lambda a_{\lambda'}\rangle=Q_\omega\langle a^+_\lambda a_{\lambda'}\rangle. \tag{64}$$

We now consider the case of a spherical geometry (see Fig. 2), which is important for practical applications, and we introduce for photons with polarization vectors $\mathbf{e}_\varphi$ and $\mathbf{e}_\theta$ the correlation functions $\langle a^+_\varphi a_\varphi\rangle$ and $\langle a^+_\theta a_\theta\rangle$, where $\hat{a}_\varphi$ and $\hat{a}_\theta$ are the corresponding photon annihilation operators. Using the expression (59), we obtain

$$\langle a^+_\theta a_\theta\rangle=\frac{1}{2}\sum_{\sigma\sigma'}(D^1_{\sigma-1}-D^1_{\sigma1})^*(D^1_{\sigma'-1}-D^1_{\sigma'1})\times\langle a^+_\sigma a_{\sigma'}\rangle, \tag{65}$$

$$\langle a^+_\varphi a_\varphi\rangle=\frac{1}{2}\sum_{\sigma\sigma'}(D^1_{\sigma-1}+D^1_{\sigma1})^*(D^1_{\sigma'-1}+D^1_{\sigma'1})\times\langle a^+_\sigma a_{\sigma'}\rangle. \tag{66}$$

Here $D^1_{\sigma\pm1}=D^1_{\sigma\pm1}(\varphi,\theta,0)$. Using the explicit form of the D function,[30] we write the expression (66) in the compact form

$$\langle a^+_\varphi a_\varphi\rangle=\frac{1}{2}[\langle a^+_+a_+\rangle+\langle a^+_-a_-\rangle+\cos(2\varphi)(\langle a^+_+a_-\rangle+\langle a^+_-a_+\rangle)+i\,\sin(2\varphi)(\langle a^+_-a_+\rangle-\langle a^+_+a_-\rangle)]. \tag{67}$$

In the case of scattering along the r axis (see Fig. 2) Stokes parameters can be introduced as follows:

$$\eta_1=(J_\theta(45,0)-J_\varphi(45,0))/J_t\,, \tag{68a}$$

$$\eta_2=(J_{++}-J_{--})/J_t\,, \tag{68b}$$

$$\eta_3=(J_\theta(0,0)-J_\varphi(0,0))/J_t\,, \tag{68c}$$

where $J_{\theta(\varphi)}(\varphi,\theta)$ is the intensity, which is defined similarly to the expression (64), of photons linearly polarized along the vector $\mathbf{e}_\theta$ ($\mathbf{e}_\varphi$) and J_t is the total intensity. Using the expressions (64) and (67), we obtain

$$\eta_1=\frac{i(\langle a^+_-a_+\rangle-\langle a^+_+a_-\rangle)}{\langle a^+_+a_+\rangle+\langle a^+_-a_-\rangle}\,, \tag{69a}$$

$$\eta_2=\frac{\langle a^+_+a_+\rangle-\langle a^+_-a_-\rangle}{\langle a^+_+a_+\rangle+\langle a^+_-a_-\rangle}\,. \tag{69b}$$

$$\eta_3=-\frac{\langle a^+_+a_-\rangle+\langle a^+_-a_+\rangle}{\langle a^+_+a_+\rangle+\langle a^+_-a_-\rangle}\,. \tag{69c}$$

For observation along the z axis the number of equations reduces to four, and in this case the system (43) is determined for the quantity

$$\mathbf{F}=\begin{pmatrix}\langle a^+_+a_+\rangle&\langle a^+_+a_-\rangle\\ \langle a^+_-a_+\rangle&\langle a^+_-a_-\rangle\end{pmatrix}\,. \tag{70}$$

Here one can see that if the scattered radiation is collected in a cavity, then the system of equations (43) is mathematically completely equivalent to the equations from Ref. 20, where the production of squeezed states was investigated. In our system the correlation functions $\langle a^+_+a_-\rangle$ and $\langle a^+_-a_+\rangle$ are the analogs of the correlation functions $\langle a_1a_3\rangle$ and $\langle a^+_1a^+_3\rangle$ from Refs. 18–20. The question arises of whether or not the production of squeezed states is possible in the present case. A numerical analysis which we performed of this system for the transitions $J_a=0\rightarrow J_b=1$ and

$J_a=1\rightarrow J_b=0$ in a wide range of values of the basic quantities (detuning from resonance, pump wave intensity, magnetic field intensity, cavity Q) did not reveal such a possibility. Apparently, the impossibility of the appearance of squeezed states is due not simply to the behavior of the spectral characteristics in the equations of motion, which is determined by the properties of the transitions in question. This is connected with the properties of the photon states, as follows. The biphoton state $\hat{b}=\mu\hat{a}_1+v\hat{a}_3^+$, which was investigated in Refs. 20 and 21, presumes that the commutation relation $[\hat{b},\ \hat{b}^+]=1$ holds, whence follows a condition on the coefficients μ and v: $|\mu|^2-|v|^2=1$. This means that the solution $\hat{a}_1\propto\cosh\chi$ and $\hat{a}_3\propto\sinh\chi$ (χ is a dynamical variable), which is well-known[34] to lead to the production of a squeezed state, is possible for the operators $\hat{a}_1$ and $\hat{a}_3^+$. In our case, the commutation relation for the biphoton state $\hat{b}=v\hat{a}_+ +\mu\hat{a}_-$ implies the condition $|\mu|^2+|v|^2=1$ and a possible solution of the form $\hat{a}_+\propto\cos\chi$ and $\hat{a}_-\propto\sin\chi$ for the operators $\hat{a}_+$ and $\hat{a}_-$. A solution of this type does not lead to the production of squeezed states.

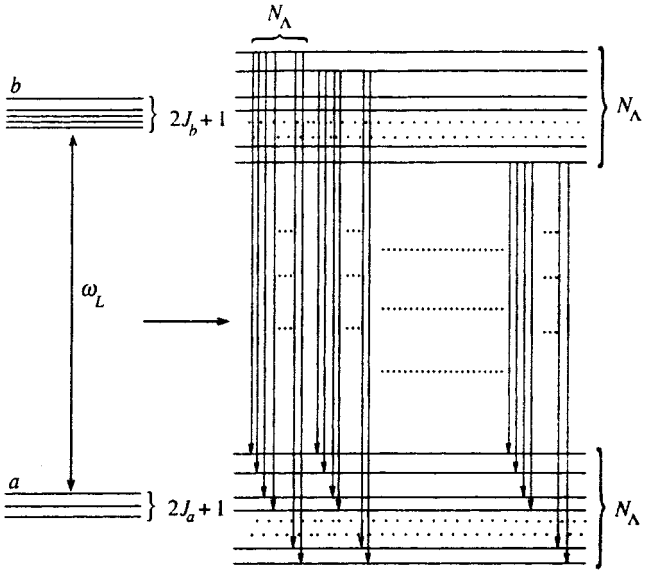

FIG. 3. Scheme of quasienergy states of a resonant transition in the field of an intense electromagnetic wave.

4. PROPERTIES OF THE SCATTERED RADIATION: RESONANCE FLUORESCENCE

The study of the properties of resonance fluorescence is of great practical value in laser spectroscopy and its applications. When laser radiation interacts with an optically thin medium, i.e., when absorption is weak, one of the main characteristics is resonance fluorescence. In this case it follows from Eqs. (43) that the correlation functions $\langle a_{\sigma'}^+ a_\sigma\rangle$ are determined by the quantities $\mathscr{A}_{\sigma'\sigma}$ which describe the resonance fluorescence spectra. The quantities $\mathscr{A}_{\sigma'\sigma}$ with $\sigma'\neq\sigma$ characterize the interference effects in the emission of photons with different polarization as a result of the coherence between magnetic sublevels.

Let us consider the properties of resonance fluorescence for the transition $a\rightarrow b$. In sufficiently strong fields the spectrum possesses a multiplet structure and can be approximated by a set of Lorentzians:

$$\mathscr{A}_{\sigma\sigma}\propto\sum_{j=1}^{N_\Lambda^2}\left(\frac{f_j^{(\sigma)}}{\nu+\Omega_j^R+i\Gamma_j}+\text{c.c.}\right), \tag{71}$$

where $\Omega_j^R+i\Gamma_j$ are the eigenvalues of a matrix whose dimension is determined by the quantity $\dim\Lambda=4(I_a+I_b+1)^2=N_\Lambda^2$ and $f_j^{(\sigma)}$ is a constant determining the contribution of this term. The number of peaks is determined by the quantity $Z_\Lambda=N_\Lambda^2-N_\Lambda+1$. This result can be interpreted from the standpoint of the states of a dressed atom: In a strong field this transition splits into N_Λ quasienergy levels at the top and bottom (see Fig. 3). Transitions between them determine the resonance fluorescence spectrum. In some cases, for example, at exact resonance of the pump wave with the transition frequency ($\Delta_L=0$) or in the presence of a magnetic field, the quasienergy spectrum becomes equidistant and the number of peaks decreases (Z_Λ is the maximum number of peaks). In the general case, for arbitrary pump wave intensity, detuning of the pump wave from resonance, and magnetic field strngth, it follows from the expression (37) that $\mathscr{A}_{\sigma'\sigma}(\nu)$ is determined by the ratio of two polynomials in ν: the dimension N_Λ^2 in the denominator and N_Λ^2-1 in the numerator (we recall that $\mathscr{A}_{\sigma'\sigma}$ is determined by the sum $A_{\sigma'\sigma}+A_{\sigma'\sigma}^*$). Using the expressions (33) and (35), we find from Eq. (37) that the total resonance fluorescence signal, i.e., the signal integrated over the spectrum, is determined by the expression

$$S_{\sigma'\sigma}=N\sum_{M,M',M''}g_{ab}^{k\sigma}(M'M)g_{ba}^{k\sigma'}(M''M')\rho_{bb}^{(0)}(MM''). \tag{72}$$

We note that the M representation was employed here. Of course, the results do not depend on the type of representation. We note that the dimension of the matrix Ξ equals the dimension of Λ. An expression for $S_{\sigma'\sigma}$ in the κq representation is obtained by the corresponding transformation (72). To describe the Hanle effect,[35] characterizing the depolarization of the scattered radiation in a magnetic field, in the optically thin medium we employ the expressions (64) and (67). Then

$$S_\varphi=\frac{1}{2}\left[S_{++}+S_{--}+\cos(2\varphi)(S_{+-}+S_{-+})\right.$$
$$\left.+i\,\sin(2\varphi)(S_{-+}-S_{+-})\right], \tag{73}$$

where S_φ is the Hanle signal of radiation linearly polarized along the vector $\mathbf{e}_\varphi$. The expressions (73) and (72) generalize the results of Ref. 36.

We now consider the case when the lower level is the ground state. This case is important for practical applications. The spectrum can be represented in the form

$$\mathscr{A}_{\sigma'\sigma}=\mathscr{A}_{\sigma'\sigma}^{\text{el}}+\mathscr{A}_{\sigma'\sigma}^{\text{inel}}, \tag{74}$$

where $\mathscr{A}_{\sigma'\sigma}^{\text{el}}=\lim_{\nu\rightarrow0}\nu\mathscr{A}_{\sigma'\sigma}(\nu)$ describes scattering with no change in the photon frequency, $\mathscr{A}_{\sigma'\sigma}^{\text{el}}\propto\delta(\nu)$ is the Ray-

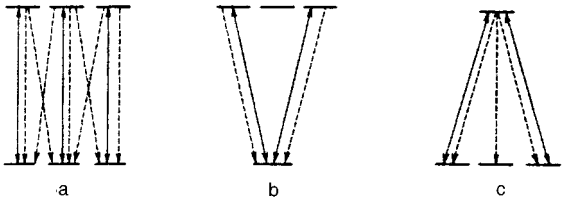

FIG. 4. Transition scheme in the case of excitation of the atoms by linearly polarized light (a), of the V type (b), and of the Λ type (c) with excitation by left- and right-circularly polarized radiation. The dashed lines represent spontaneous emission.

leigh scattering, and $\mathscr{A}^{\text{inel}}$ is the inelastic scattering, i.e., scattering with a change in the photon frequency.

In the M representation $\mathscr{A}^{\text{el}}_{\sigma'\sigma}$ is determined by the expression

$$\mathscr{A}^{el}_{\sigma'\sigma}(\nu)=2\pi N\sum_{MM'M_1M_2} g^{k\sigma}_{ab}(MM')g^{k\sigma'}_{ba}(M_1M_2)\tilde{\rho}^{\,(0)}_{ab} \times(M_2M_1)\tilde{\rho}^{\,(0)}_{ba}(M'M)\,\delta(\nu). \tag{75}$$

We note that the contribution of the elastic component is very small in the presence of strongly depolarizing collisions. In a purely radiative relaxation regime its contribution is determined by the parameters

$$\tilde{V}_{ab}(MM')/|\Delta_L+(g_bM-g_aM')\Omega+iA_{ba}/2|.$$

If at least one of these parameters is large, then the inelastic component will be determining, but if not all are small, then the elastic component will dominate.

For spontaneous radiation on transitions which are adjacent to $a\to b$, the maximum number of peaks in the spectrum is $(2J_n+1)N_\Lambda$, $n=l$, m, s, and p. The radiation is incoherent, even if one of the levels is the ground state. In Sec. 2.2 it was noted from Eqs. (44) and (45) that the interference terms $\mathscr{A}_{\sigma'\sigma}=\delta_{\sigma'\sigma}\mathscr{A}_{\sigma\sigma}$ will be absent in the emission spectrum for the transitions $p\to b$ and $s\to a$.

5. INTERACTION AND SCATTERING OF A MONOCHROMATIC ELECTROMAGNETIC WAVE IN THE TRANSITION $J_a=1\to J_b=0$

Three basic types of transitions between atomic sublevels can be distinguished in the description of the interaction between an electromagnetic wave, possessing arbitrary polarization composition, and a resonance transition. They are shown schematically in Fig. 4. The simplest type is shown in Fig. 4a: transitions between two-level subsystems. Schemes referring to the Λ and V types of interaction of radiation with sublevels are displayed in Figs. 4b and 4c. Their combinations make it possible to describe all possible transitions.

Recently, a description was developed in Refs. 12 and 37 and the resonance fluorescence spectra of a degenerate two-level system (with arbitrary J_a and J_b neglecting the effect of a magnetic field, i.e., $H=0$) in the field of a monochromatic, linearly polarized, electromagnetic wave of arbitrary intensity (see Fig. 4a) were investigated. Here there are no interference effects: $\mathscr{A}_{\sigma'\sigma}=0$ $(\sigma'\neq\sigma)$ in our description.

The simplest system describing V-type transitions is the interaction of an electromagnetic wave with the transition $J_a=0\to J_b=1$ (Fig. 4b). The resonance fluorescence spectrum and the interference phenomena for this system, as well as the effect of degenerate processes on their properties, were recently investigated in Refs. 15 and 16. The Faraday and optical alignment effects have been well studied for this transition.[14,38]

Both the interaction and scattering spectra of intense electromagnetic waves in the transition $J_a=1\to J_b=0$ (see Fig. 4c) have been investigated in much less detail. This transition is the simplest system describing Λ-type transitions. The investigation of this transition is of interest in itself and it is important for understanding the interaction of an electromagnetic wave with atomic transitions which have a complicated structure.

5.1. Nonlinear Faraday effect for the transition $J_a=1\to J_b=0$

In the Faraday geometry the rotation angle of the polarization plane of a monochromatic electromagnetic wave which has passed through an optically thin gaseous medium is determined by the expression

$$\varphi=(n_+-n_-)\omega_L l/2c, \tag{76}$$

where l is the length of the medium and n_σ is the index of refraction, which for a medium with the working transition $J_a=1\to J_b=0$ equals $n_\sigma=1+2\pi N\,\mathrm{Re}(d_{\sigma b}\rho_{b\sigma}/E_{L\sigma})$, where N is the density of atoms. In the present section we adopt the notation $\rho^{(0)}_{bb}(00)=\rho_{bb}$, $\tilde{\rho}^{(0)}_{ba}(0\sigma)=\rho_{b\sigma}$ and $\rho^{(0)}_{aa}\times(\sigma\sigma')=\rho_{\sigma\sigma'}$. We find the value of $\rho_{b\sigma}$ from the stationary solution of Eqs. (22)–(24) for the given transition. Figure 5 displays φ as a function of the detuning of the electromagnetic wave from resonance for different values of the parameters $V_\sigma=\tilde{V}_{ba}(0\sigma)$. Here and below we assume in the calculations that $\Gamma_a(\sigma\sigma)=\gamma$, $\Gamma_a(\sigma\sigma')=6\gamma$ $(\sigma\neq\sigma')$, $\Gamma_b=3\gamma$, $\Gamma_{ba}=9\gamma$, and $A_{ba}\ll\gamma$. One can see from Fig. 5 that the dependence of φ on the detuning changes substantially as the intensity increases. This modification of the line shape $\varphi(\Delta_L)$ is qualitatively identical to the results for this dependence in a medium with the working transition $J_a=0\to J_b=1$.[14] Therefore similar results should be expected for transitions with a more complicated structure of the atomic sublevels. We note that this agrees with the experimental results of Ref. 39.

Assuming that at the entrance into the medium the electromagnetic wave was linearly polarized along the y axis, it should be expected that the appearance of an orthogonal component, due to the rotation of the polarization plane by a small angle φ, will be described by the expression

$$I_x\propto I_L\varphi^2. \tag{77}$$

where I_L is the intensity of the radiation at the entrance into the medium and $I_x=|E_+-E_-|^2$. This expression is correct only far from resonance, where radiation absorption can be neglected. Near resonance, the appearance of an orthogonal component will be due to both the different magnitude of the

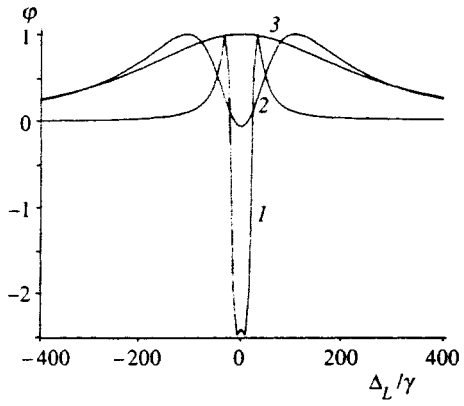

FIG. 5. Angular rotation of the polarization plane of the radiation versus the detuning of the radiation from resonance with $\Omega/\gamma=20$, $V_\pm/\gamma=0.1$ (curve *1*), 20 (curve *2*), and 50 (curve *3*). The curve is normalized to 1.

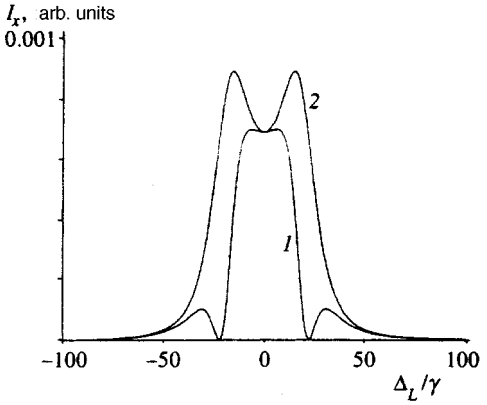

FIG. 7. $I_x(\Delta_L)$ calculated according to Eqs. (77) (curve *1*) and (79) (curve 2) with $V_\pm/\gamma=1$ and $\Omega/\gamma=20$.

dispersion for left- and right-hand circularly polarized waves and the difference of the absorption of these waves. From Maxwell's equations it follows that for the slowly varying amplitude

$$\frac{\partial I_x}{\partial z}=P_x^*(E_+-E_-)+\text{c.c.}, \tag{78}$$

where $P_x \propto i(d_{b+}\rho_{+b}-d_{b-}\rho_{-b})$. In the optically thin case $E_+-E_-\propto P_x$. Then

$$I_x\propto|d_{b+}\rho_{+b}-d_{b-}\rho_{-b}|^2. \tag{79}$$

The expressions (77) and (79) are identical only at exact resonance. The difference in the dependences $I_x(\Delta L)$ and $I_x(\Omega)$ calculated according to Eqs. (77) and (79) is demonstrated in Figs. 6 and 7. The expressions (77) and (79) are almost identical in a strong pump-wave field $V_\pm>\Delta_L$ or in a strong magnetic field $\Omega\gg\Delta_L$. They differ most in the region of the parameters $\Omega\sim\Delta_L$ and $V_\pm\ll\Delta_L$ (see Figs. 6 and 7).

We point out that for intense radiation characteristic features can be observed in the transverse distribution I_x. Let the radiation intensity at the entrance have a Gaussian distribution:

$$U_L=\exp[-(r_\perp/r_0)^2], \tag{80}$$

where $r_\perp$ is the transverse coordinate and r_0 is the size of the beam. The function $I_x(r_\perp)$, calculated from the expression (79) allowing for the dependence (80), is displayed in Fig. 8. The distribution $I_x(r_\perp)$ is reminiscent of the well-known conical radiation,[40–42] but it is of a completely different nature. This distribution is determined by two main factors: the decrease in the rotation angle of the polarization plane as a result of saturation and the transverse distribution of the entering radiation. The result obtained explains qualitatively the experimental results of Ref. 43, where the Faraday effect for the transition $J_a=1\to J_b=0$ in neon atoms was investigated. A quantitative analysis should take account of the thermal motion of the atoms, which we neglect in the present work and which is important for the conditions of the experiment in Ref. 43.

5.2. Spontaneous emission spectra for the transition $J_a=1\to J_b=0$

Using the formalism developed in Sec. 2 above for the transition $J_a=1\to J_b=0$, we shall investigate its spontaneous emission spectra in the field of a strong electromagnetic wave. The scattering spectra of atoms in the Voigt geometry ($\mathbf{k}_L\perp\mathbf{H}$) with the same parameters of the atomic subsystem

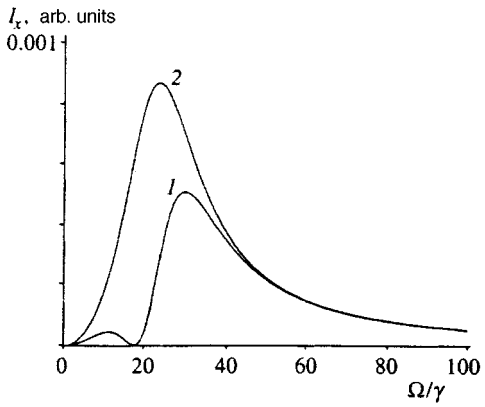

FIG. 6. $I_x(\Omega)$ calculated according to Eqs. (77) (curve *1*) and (78) (curve *2*) with $V_\pm/\gamma=1$ and $\Delta_L/\gamma=20$.

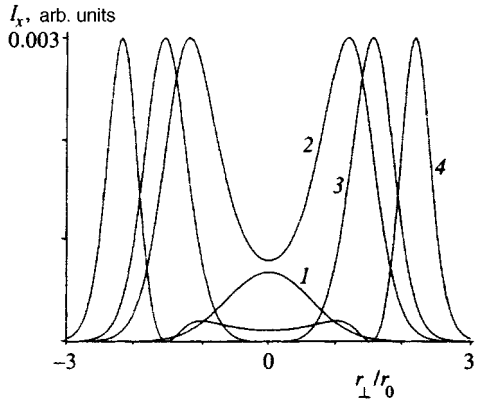

FIG. 8. Transverse distribution I_x with a Gaussian pump wave over the cross section of the beam for $\Delta_L=0$ and $\Omega/\gamma=20$ and the parameters $V_\pm/\gamma=1$ (curve *1*), 10 (curve *2*), 20 (curve *3*), and 50 (curve *4*).

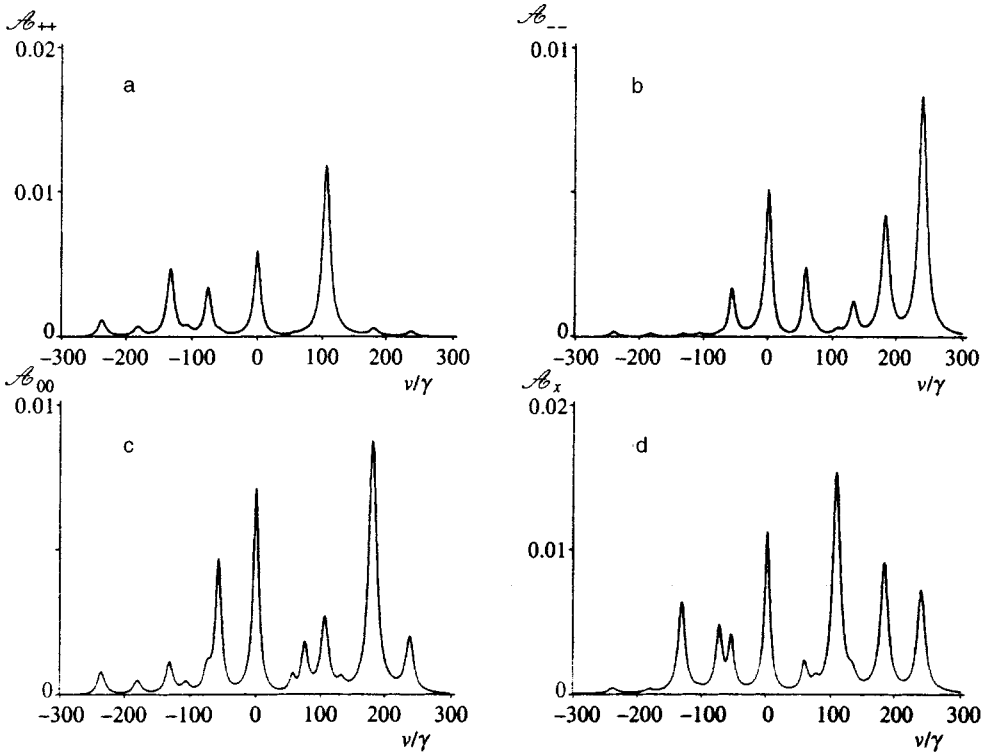

FIG. 9. Resonance fluorescence spectra with different polarization for the parameters $V_{\pm}/\gamma=50$, $\Delta_L/\gamma=80$, $V_0/\gamma=70$, and $\Omega/\gamma=60$.

as in the preceding section are displayed in Fig. 9. Explicit expressions for the scattering spectra are given in Ref. 44. One can see from Fig. 9 that in accordance with the results of Sec. 4, up to 13 peaks can be observed in the scattering spectrum. An important distinction of the transition under study from the transition $J_a=0\to J_b=1$ is that the scattered radiation contains π and $\sigma_{\pm}$ components, irrespective of the polarization composition of the exciting radiation. The quantity $\mathscr{A}_x$ describes the spectra of fluorescence which is linearly polarized along the x axis and scattered along the y axis. Figure 10a displays the spectrum $\mathscr{A}_x$ for the pump wave, whose linear polarization vector $\mathbf{e}_L$ is orthogonal to the direction of the magnetic field, $\mathbf{e}_L\|\mathbf{e}_y$. It follows from Eqs. (60) and (67) that $\mathscr{A}_x$ is determined by the expression

$$\mathscr{A}_x=\mathscr{A}_{++}+\mathscr{A}_{--}+\mathscr{A}_{+-}+\mathscr{A}_{-+}. \tag{81}$$

The complete scattering signal S_x is determined by the population of the upper level:

$$S_x=\int \mathscr{A}_x \frac{d\nu}{2\pi}\propto\rho_{bb}. \tag{82}$$

This is associated with the structure of the transition $J_a=1\to J_b=0$, for which it follows from (72) that

$$S_{\sigma'\sigma}\propto\delta_{\sigma'\sigma}\rho_{bb}. \tag{83}$$

Comparing the results obtained (for $\mathbf{e}_L\|\mathbf{e}_y$, i.e., $V_0=0$) with the results of Refs. 15 and 36, where for the same geometry the scattering of a monochromatic wave on the transition $J_a=0\to J_b=1$ was investigated, we shall indicate the most important differences. First, there is no π component (there is no collisional mixing of the magnetic sublevels) in the scattered radiation for the transition $J_a=0\to J_b=1$. Second, the interference processes differ substantially: The properties of the corresponding quantities $\mathscr{A}_{\sigma'\sigma}$ and $S_{\sigma'\sigma}$ $(\sigma\neq\sigma')$ differ substantially. The spectral dependence of $\mathscr{A}_{\pm}$ is presented in Fig. 10b, c; one can see from these plots that it changes sign. Moreover, it follows from the expression (83) that $S_{\sigma'\sigma}=0$ for $\sigma\neq\sigma'$. This means that the Hanle effect (change in the polarization characteristics of the scattered radiation under the influence of a magnetic field) for the transition $J_a=0\to J_b=1$, in contrast to the transition $J_a=1\to J_b=0$, is manifested primarily as a change in the emission spectra. Figure 11 displays S_x as a function of the magnetic field intensity. Comparing it with the analogous dependence S_x for the transition $J_a=0\to J_b=1$,[36] we can see that there is no interference dip at $\Omega=0$. The effect of a magnetic field reduces to the effect of the magnetic field on the population: The maximum of S_x is reached at $\Omega=\pm\Delta_L$, and for $\Omega\gg\Delta_L$, V_σ, Γ_{ba} the population of the upper level (and therefore S_x) decreases as a result of an increase in the detuning of the radiation from resonances.

In the case when a transition is excited by a wave with a single polarization type V_σ $(V_{\sigma'}=0,\ \sigma'\neq\sigma)$, the fluorescence spectrum $\mathscr{A}_{\sigma\sigma}$ corresponding to this transition will be described by the well-known expressions for a nondegenerate open two-level system.[17] In sufficiently strong fields it has the form of a triplet. The spectra of the other two components of $\mathscr{A}_{\sigma'\sigma'}$ will have the form of doublets and will be described by the expressions

$$\mathscr{A}_{\sigma'\sigma'}(\nu)\propto i\,\frac{\rho_{bb}(\nu+\widetilde{\Delta}_{\sigma'\sigma})+V_\sigma^*\rho_{b\sigma}}{(\nu-\widetilde{\Delta}_{\sigma'})(\nu+\widetilde{\Delta}_{\sigma'\sigma})-|V_\sigma|^2}+\text{c.c.}, \tag{84}$$

where

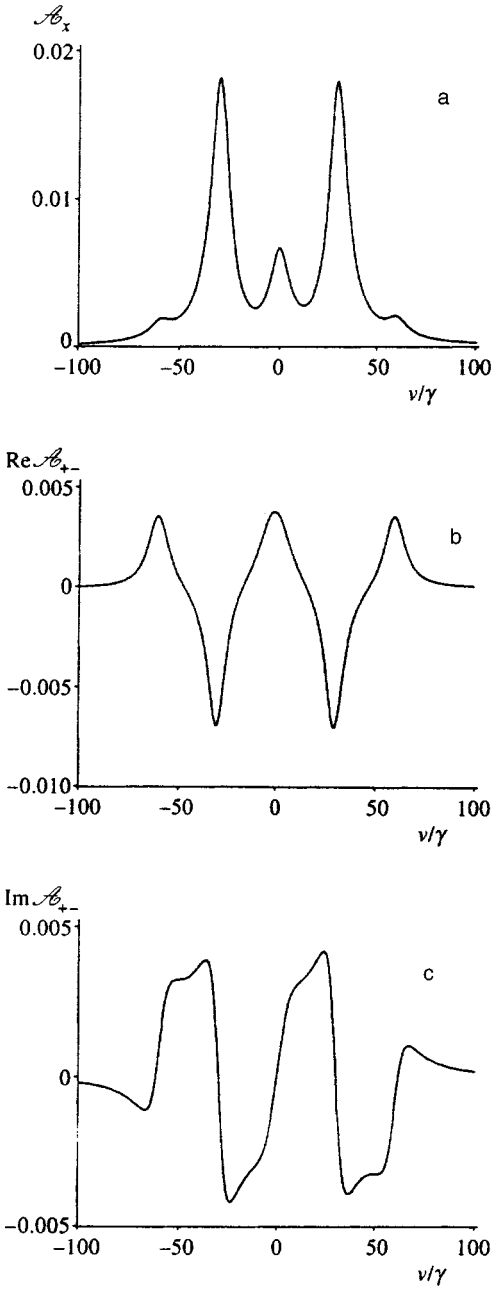

FIG. 10. Spectral dependence of $\mathscr{A}_x$ (a) and the real (b) and imaginary (c) parts of the quantity $\mathscr{A}_{+-}$ with the parameters $V_\pm/\gamma=20$, $\Delta_L=V_0=0$, and $\Omega/\gamma=10$.

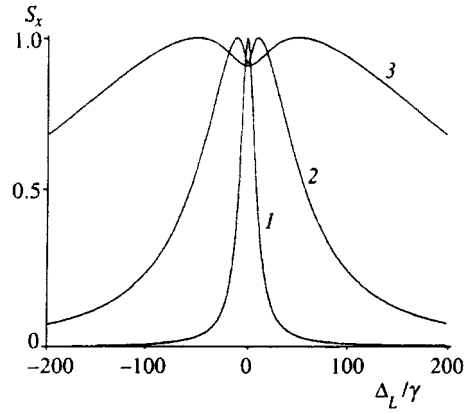

FIG. 11. Dependence of the quantity S_x, normalized to unity, on the magnetic field for $\Delta_L=V_0=0$ and the parameters $V_\pm/\gamma=0.1$ (curve *1*), 10 (curve *2*), and 50 (curve *3*).

$$\tilde{\Delta}_\sigma=\Delta_L-\Omega\sigma+i\Gamma_{ba},\quad \tilde{\Delta}_{\sigma'\sigma}=\Omega(\sigma'-\sigma)-i\Gamma_a(\sigma'\sigma),$$

$$V_\sigma^*\rho_{b\sigma}=-(\Gamma_b\rho_{bb}-Q_b)\tilde{\Delta}_\sigma/2\Gamma_{ba}. \tag{85}$$

For $Q_b=0$

$$\rho_{bb}=\frac{2\Gamma_{ba}|V_\sigma|^2Q_\sigma}{|\tilde{\Delta}_\sigma|^2\Gamma_b\Gamma_a+2\Gamma_{ba}|V_\sigma|^2(\Gamma_b+\Gamma_a-A_{ba}/3)}. \tag{86}$$

Using Eq. (85) with $Q_b=0$, Eq. (84) can be put into the form

$$\mathscr{A}_{\sigma'\sigma'}(\nu)\propto\mathrm{Im}\left(\rho_{bb}\frac{\nu+\tilde{\Delta}_{\sigma'\sigma}-\tilde{\Delta}_\sigma\Gamma_b/2\Gamma_{ba}}{(\nu-\tilde{\Delta}_{\sigma'})(\nu+\tilde{\Delta}_{\sigma'\sigma})-|V_\sigma|^2}\right). \tag{87}$$

Let us consider the limit when the lower level is the ground state and the relaxation regime is radiative: $\Gamma_b=2\Gamma_{ba}=A_{ba}$ and $\Gamma_a(\sigma'\sigma)=0$. This system is open. Therefore, in order for a stationary solution to exist formally, we assume the presence of a pump at the lower level of the working transition. Then

$$\mathscr{A}_{\sigma'\sigma}(\nu)\propto\frac{\rho_{bb}}{2}\frac{|V_\sigma|^2A_{ba}}{|(\nu+\Delta_{\sigma'\sigma})(\nu+\tilde{\Delta}_{\sigma'})-|V_\sigma|^2|^2}. \tag{88}$$

where $\Delta_{\sigma'\sigma}=\Omega(\sigma'-\sigma)$. As expected, the total intensity of the σ' component satisfies

$$\int\mathscr{A}_{\sigma'\sigma'}d\nu\propto\rho_{bb}$$

and therefore is linear in the intensity $I_{L\sigma}$ of the pump wave (see Eq. (86)). In weak fields $V_\sigma\ll A_{ba}$ the spontaneous emission spectrum of the σ' component consists of a very narrow peak with a width of order $|V_\sigma|^2/|\tilde{\Delta}_\sigma|$. Substituting the expression (86) for ρ_{bb}, we find from Eq. (88) that $\mathscr{A}_{\sigma'\sigma'}(\nu)\propto O(V_\sigma^4)$ or proportional to $I_{L\sigma}^2$. The result obtained is similar to the spectral composition of the resonance fluorescence of a two-level atom in the field of a weak electromagnetic wave:[13] The elastic (or Rayleigh) component is proportional to $I_{L\sigma}$ and the inelastic (or mixed) component is proportional to $I_{L\sigma}^2$. In the case of a degenerate two-level atom irradiated by a weak, σ-polarized wave, Mollow's result[13] generalizes as follows:

$$\mathscr{A}_{\sigma'\sigma'}\propto\delta(\nu)I_{L\sigma}\delta_{\sigma'\sigma}+f^{\mathrm{inel}}_{\sigma'\sigma'}(\nu)I_{L\sigma}^2, \tag{89}$$

where $f^{\mathrm{inel}}_{\sigma'\sigma'}(\nu)$ is the form of the linear inelastic component (see Eq. (88)). This analysis was performed for the transition $J_a=1\to J_b=0$. However, the result (89) can be extended to transitions with arbitrary values of the angular momentum provided that the lower level is the ground state and the relaxation regime is radiative.

The foregoing investigation of the polarization–Raman scattering spectra for the transition $J_a=1\to J_b=0$ pertains to scattering in the transition $b\to l$ (see Fig. 1) for nondegenerate states, the case investigated in Ref. 45. The expressions (84) and (89) agree with the results of Ref. 45.

6. CONCLUSIONS

In the present paper a technique was developed for describing nondegenerate resonant scattering of a monochromatic electromagnetic wave with arbitrary polarization composition. Expressions were obtained for describing the resonance fluorescence spectra, the absorption (amplification) coefficients, and the forward-directed four-wave interaction of the scattered photons. A technique was developed for calculating the polarization-spectral characteristics of the absorption and emission of radiation in transitions between laser-coupled and other states. This result extends the description developed in Ref. 45.

It was shown that in the general case the dynamics of the scattered radiation, accompanying the propagation of an electromagnetic wave, is determined by a system of 36 equations. In the description of the scattering of the radiation by large angles, when the forward-directed four-wave mixing processes become inconsequential, this system reduces to 9 equations.

In an optically thin medium the resonance fluorescence of the atoms determines the characteristics of the scattered radiation. In the present paper, the polarization, spectral, and angular characteristics of the resonance fluorescence were investigated. It is well known that if the lower level is the ground state, then the scattering spectrum contains both the Rayleigh (elastic) and mixed (inelastic) components. Explicit expressions were obtained for the elastic component, which include interference effects between the fluorescence photons with different polarization. A possible influence of a constant magnetic field on the atoms is taken into account in this work. Expressions were obtained for describing the depolarization of the radiation (Hanle effect) in a magnetic field accompanying scattering of an electromagnetic wave with arbitrary intensity. Expressions that make it possible to describe the spectral properties of the Hanle effect and its total intensity and extend previously obtained results in some particular cases[15,16,36] were obtained.

In the general case the dynamics of a laser-coupled transition (with arbitrary J) is determined by a set of configurations of transitions between two- and three-level systems of the V and Λ types (see Fig. 4). In this paper the properties of the transition $J_a=1\rightarrow J_b=0$ were studied in order to investigate the properties of the scattering of radiation by Λ-type systems. The investigation of the nonlinear Faraday effect for this transition showed that the shape of the line of the rotation angle of the polarization plane of the pump wave is qualitatively and quantitatively identical with respect to the parameter $I_L/I_{\rm sat}$ (here $I_{\rm sat}$ is the saturation intensity) to the results for the transition $J_a=0\rightarrow J_b=1$. This suggests that the results obtained for these transitions can be extended to transitions with arbitrary values of the angular momentum (in the dipole approximation). The resonance fluorescence spectra and the properties of the Hanle signal were investigated for the transition $J_a=1\rightarrow J_b=0$. We shall indicate the main difference in the properties of the interference effects for the transitions $J_a=1\rightarrow J_b=0$ and $J_a=0\rightarrow J_b=1$. This difference is due to the fact that in the case of the scattering of waves with different polarization on the transition $J_a=0\rightarrow J_b=1$ the atomic system ultimately arrives at one state, and in the case of the transition $J_a=1\rightarrow J_b=0$ it arrives in different states. In the first case, substantial interference effects are present, and in the second case only spectral nonlinear effects occur. For the complete signal (integral over the spectrum) these effects are completely absent, since according to the laws of quantum mechanics interference phenomena are present only for processes with the same final states.

We note that the model investigation of the resonance fluorescence spectrum of the transition $J_a=1\rightarrow J_b=0$, where the lower state is the ground state, with a radiative relaxation regime excited by radiation with fixed σ polarization revealed a characteristic feature in the spontaneous σ-polarized radiation ($\sigma' \neq \sigma$). This feature is manifested for weak fields $I_{L\sigma}\ll I_{\rm sat}$: The spectral emission line becomes narrower, almost a delta function. The spectral density of the scattered σ' component is proportional to $I_{L\sigma}^2$. This result is correct for transitions with arbitrary values of the angular momentum.

The description developed in this paper neglects the thermal motion of the atoms, i.e., the results are valid when Doppler broadening is much less than the broadenings due to other phenomena. A substantial thermal motion of the atoms not only changes in the absorption (amplification) and emission spectra of the atoms, but also makes them more anisotropic with respect to the direction of propagation of the pump wave. A formal kinematic extension to the case of the thermal motion of atoms does not present any difficulty. However, to take into account correctly the change in the number of particles with a fixed velocity as a result of collisions, photoexcitation, and so on,[17,32] a separate analysis and a careful investigation are required.

In the present paper it was assumed that the intensity of the pump wave can be arbitrary. The change in the relaxation constants as a result of the effect of a strong field was neglected (see, for example, Ref. 46). This phenomenon may be important in the study of radiation in optically dense media, where induced processes become determining, since in this case the absorption (amplification) and four-wave interaction spectra can be substantially modified in a definite range of the parameters.[47–49] The change in the relaxation constants of an atom in a strong field will have a much smaller effect on the resonance fluorescence spectra.[47] This phenomenon could strongly influence interference effects, but this requires a separate investigation.

I thank A. M. Starostin, F. A. Lomaya, and D. I. Chekhov for helpful discussions and their interest in this work and N. I. Kurchatova for assisting in the composing this paper. This work was supported by the Russian Fund for Fundamental Research grant No. 96-02-17390.

[1] S. G. Rautian and I. I. Sobel'man, Zh. Éksp. Teor. Fiz. **41**, 456 (1961) [Sov. Phys. JETP **14**, 328 (1962)].
[2] B. R. Mollow, Prog. Optics **19**, 3 (1981).
[3] B. R. Mollow, Phys. Rev. A **5**, 2217 (1972).
[4] F. Y. Wu, S. Ezekiel, M. Ducloy, and B. R. Mollow, Phys. Rev. Lett. **38**, 1077 (1977).
[5] W. Harting, W. Rasmussen, R. Shieder, and H. Walther, Z. Phys. A **278**, 205 (1976).
[6] Y. Zhu, O. Wu, A. Lezama, D. J. Gauthier, and T. W. Mossberg, Phys. Rev. A **41**, 6574 (1990).

[7] G. S. Agarwal, Y. Zhu, D. J. Gautheir, and T. W. Mossberg, J. Opt. Soc. Amer. B **8**, 1163 (1991).
[8] J. Cooper, R. J. Ballagh, and K. Burnet, Phys. Rev. A **22**, 535 (1980).
[9] P. D. Kleiber, K. Burnet, and J. Cooper, Phys. Rev. Lett. **47**, 1595 (1981).
[10] A. G. Leonov, A. A. Panteleev, A. N. Starostin, and D. I. Chekhov, Zh. Éksp. Teor. Fiz. **105**, 1536 (1994) [JETP **78**, 827 (1994)].
[11] D. V. Gaidarenko, A. G. Leonov, A. A. Panteleev, A. N. Starostin, and D. I. Chekhov, Laser Phys. **3**, 151 (1993).
[12] M. Trippenbach, B. Gao, and J. Cooper, Phys. Rev. A **45**, 6555 (1992).
[13] B. R. Mollow, Phys. Rev. **188**, 1969 (1969).
[14] A. A. Panteleev, Zh. Éksp. Teor. Fiz. **99**, 1684 (1991) [Sov. Phys. JETP **72**, 939 (1991)].
[15] F. A. Lomaya and A. A. Panteleev, Zh. Éksp. Teor. Fiz. **103**, 1970 (1993) [JETP **76**, 976 (1993)].
[16] F. A. Lomaya and A. A. Panteleev, Zh. Éksp. Teor. Fiz. **106**, 886 (1994), **108** 23 (1995) [JETP **79**, 486 (1994); **81**, 12 (1995)].
[17] S. G. Rautian, G. I. Smirnov, and A. I. Shalagin, *Nonlinear Resonances in Atomic and Molecular Spectra* [in Russian], Nauka, Novosibirsk (1979).
[18] M. Sargent III, D. A. Holm, and M. S. Zubary, Phys. Rev. A **31**, 3112 (1985).
[19] S. Stenholm, D. A. Holm, and M. Sargent III, Phys. Rev. A **31**, 2124 (1985).
[20] D. A. Holm and M. Sargent III, Phys. Rev. A **35**, 2150 (1987).
[21] M. D. Reid and D. F. Walls, Phys. Rev. A **34**, 4929 (1986).
[22] R. E. Slusher, L. W. Hollberg, B. Yurke, J. C. Mertz, and J. F. Valley, Phys. Rev. Lett. **55**, 2409 (1985).
[23] A. A. Panteleev, V. A. Roslyakov, A. N. Starostin, and M. D. Taran, Zh. Éksp. Teor. Fiz. **97**, 1777 (1990) [Sov. Phys. JETP **70**, 1003 (1990)].
[24] M. Lax, Phys. Rev. **129**, 2342 (1963).
[25] L. V. Keldysh, Zh. Éksp. Teor. Fiz. **47**, 1515 (1964) [Sov. Phys. JETP **20**, 1018 (1965)].
[26] H. R. Zaidi, Can. J. Phys. **59**, 737 (1981).
[27] H. Haken in *Handbuch der Physik*, Springer-Verlag, Berlin, 1970, Vol. 25/2c.
[28] M. O. Scully and W. E. Lamb Jr., Phys. Rev. **159**, 208 (1967).
[29] E. V. Baklanov, Zh. Éksp. Teor. Fiz. **65**, 2203 (1973) [Sov. Phys. JETP **38**, 1100 (1974)].
[30] D. A. Varshalovich, A. P. Moskalev, and V. K. Khersonskiĭ, *Quantum Theory of Angular Momentum*, World Scientific, Singapore, 1988.
[31] K. Blum, *Density Matrix Theory and Applications*, Plenum Press, New York, 1981.
[32] A. Omont, Prog. Quant. Electron. **5**, 69 (1977).
[33] E. M. Lifshitz and L. P. Pitaevskiĭ, *Quantum Electrodynamics*, Pergamon Press, N. Y. [Russian original, Nauka, Moscow, 1989].
[34] D. F. Walls, Nature **306**, 141 (1983).
[35] Z. Phys. D **18**(1) (1991) (special edition dedicated to W. Hanle on his 90th birthday).
[36] P. Avan and C. Cohen-Tannoudji, J. de Phys. Lett. **36**, L85 (1975).
[37] B. Gao, Phys. Rev. A **50**, 4139 (1994).
[38] E. B. Aleksandrov, G. I. Khvostenko, and M. P. Chaĭka, *Interference of Degenerate Atomic States* [in Russian], Nauka, Moscow, 1991.
[39] O. É. Buevich, A. F. Grigor'ev, A. F. Semerok, and B. A. Firsov, JETP Lett. **45**, 407 (1987).
[40] J. Opt. Soc. Am. B **7** (6) (1990) (special edition dedicated to transverse effects in nonlinearly optical systems).
[41] J. F. Valley, G. Khitrova, H. M. Gibbs, J. W. Grantham, and J. Xu, Phys. Rev. Lett. **64**, 2362 (1990).
[42] A. N. Starostin, A. A. Panteleev, V. I. Lebedev, S. V. Rotin, A. G. Leonov, and D. I. Chekhov, Zh. Éksp. Teor. Fiz. **108**, 1203 (1995) [JETP **81**, 660 (1995)].
[43] P. Junger, A. Lindberg, and B. Stahlberg, Phys. Rev. A **48**, 1369 (1993).
[44] A. A. Panteleev, TRINITI Preprint [in Russian], Moscow (1996).
[45] B. R. Mollow, Phys. Rev. A **8**, 1949 (1973).
[46] É. G. Pestov, Trudy FIAN **187**, 60 (1988).
[47] A. A. Panteleev and A. N. Starostin, Zh. Éksp. Teor. Fiz. **106**, 1606 (1994) [JETP **79**, 866 (1994)].
[48] É. G. Pestov, Kratkie soobshcheniya po fizike FIAN, No. 12, 20 (1989).
[49] A. N. Oraevskiĭ and É. G. Pestov, Kvant. Élektron. **16**, 1422 (1989) [Sov. J. Quantum Electron. **19**, 917 (1989)].

Translated by M. E. Alferieff

Highly nonideal classical thermal plasmas: experimental study of ordered macroparticle structures

V. E. Fortov, A. P. Nefedov, O. F. Petrov, A. A. Samaryan, and A. V. Chernyshev

Scientific Research Center for the Thermophysics of Pulsed Interactions, Russian Academy of Sciences, 127412 Moscow, Russia

(Submitted 25 April 1996)
Zh. Éksp. Teor. Fiz. **111**, 467–477 (February 1997)

The formation of spatially ordered CeO_2 particle structures in a thermal plasma at atmospheric pressure and temperatures of 1700–2200 K is studied. The spatial structure of the particles in the plasma is analyzed using laser time-of-flight counting of individual particles. Probe and optical diagnostics are used to determine the parameters of the thermal plasma. The CeO_2 particles were positively charged (about 10^3 electronic charges). The resulting Coulomb interaction parameter for the particles is $\gamma_p > 120$, which corresponds to a highly nonideal plasma. © *1997 American Institute of Physics.* [S1063-7761(97)00502-7]

1. INTRODUCTION

A thermal plasma with macroscopic particles is a low-temperature plasma that contains small sized liquid or solid material particles.[1,2] The macroparticles interact efficiently with the charged species in the plasma, and therefore, have a major effect on its properties. Thus, particles that emit electrons can raise the electron density of the gaseous phase, as well as its electrical conductivity. If, on the other hand, the particles capture electrons, then the opposite effect occurs. In the limiting case of an unionized gas, the macroparticles fully determine the electrical properties of the plasma. Effects associated with the presence of particles were observed in early experiments[3,4] on the plasma of hydrocarbon flames.

The conditions for the existence of a plasma with macroparticles can vary considerably. Because of the high macroscopic charges that the particles can acquire (on the order of 10^2-10^4e), the entire range of plasma states, from a Debye plasma to a highly nonideal system of charged particles, can be realized in typical thermal plasmas ($T_g=1700-3000$ K, $n_e=10^9-10^{12}$ cm^{-3}), depending on the concentration, size, and electron work function of the particles, as well as on the concentrations of electrons and ions.[2] Therefore, the interparticle interaction parameter γ_p, defined as the ratio of the Coulomb interaction energy of the particles to their energy of thermal motion, can greatly exceed unity, which means that the plasma is highly nonideal. Theoretical calculations of the equilibrium properties of these plasmas show that under certain conditions, strong interparticle interaction leads to ordered structure in the locations of the macroscopic particles analogous to structures in liquids or solids.[5]

A detailed examination of the ordered structures, including the conditions for their formation, has been carried out using a single-species plasma model and a Yukawa model.[5–7] We note that these models were for a classical, quasineutral, spatially unbounded plasma, for which critical values of the interparticle interaction parameter corresponding to phase transitions were obtained by numerical simulation.[8,9]

A single-species plasma consists of an idealized system of ions against a compensating uniform background of neutralizing particles, so that the system is electrically neutral overall. The interaction potential of the particles $\Phi(r)$ is the Coulomb potential in this case, and the thermodynamics of the plasma is characterized by the parameter γ_p, which has the form

$$\gamma_p=(Z_pe)^2/\langle r\rangle kT_g.$$

Here Z_p is the charge on a particle, T_g is the plasma temperature, $\langle r\rangle=(4\pi n_p/3)^{-1/3}$ is the average distance between particles, and n_p is the plasma density. It was found that a three-dimensional system forms a regular crystalline structure for γ_p greater than $\gamma_c=171$.[8] For small γ_p ($\gamma_p<4$), the plasma is in a ''gaseous'' state.[2,5]

In the Yukawa model one examines the effect of shielding by the background charges, which leads to a Debye–Hückel type interaction potential.[9,10] When shielding, whose effect is determined by the ratio $\langle r\rangle/r_D$ (r_D is the Debye radius), is taken into account, the new parameter

$$\Gamma_s=\frac{(Z_pe)^2\ \exp(-\langle r\rangle/r_D)}{\langle r\rangle kT_g}$$

is introduced. The limiting cases in the Yukawa model are the single-species plasma (for $\langle r\rangle/r_D\to 0$) and the hard sphere model (for $\langle r\rangle/r_D\to\infty$).[10]

One of the first observations of crystalline structures was in a system of charged, micron-sized, iron and aluminum particles confined by a certain configuration of alternating and static electric fields.[11] Later, Coulomb crystals were observed for atomic ions in various types of traps, such as the Penning trap.[12] For macroscopic particles with high negative charge ($\sim 10^4e$), crystalline states have been observed when they were introduced into a space-charge boundary layer[13] in which equilibrium was established between gravitational and electrostatic forces.[14–17]

In most published experimental work, ordered structures have been observed in a cloud of space charge containing hundreds to several thousand charged particles.[12] The interaction potential of the particles (the form of the potential has a significant effect on phase transitions in the plasma), can then differ considerably from the interaction potential in a

classical quasineutral plasma.[7] For plasma formations of this type, the boundary conditions have been predicted theoretically to have a major effect on the phase state of the plasma.[18] Thus, for example, in a spherical trap, the cloud of particles separates into spherical layers. Instead of sharp phase transitions, there is a gradual evolution of the system from a liquid state with close ordering to an intermediate state characterized by the existence of liquid and solid phases, and finally to a solid state.[19]

Under quasineutrality conditions for large aggregations of macroparticles (more than 10^7 particles in the plasma volume), ordered structures have been observed in a stream of thermal plasma at $T_g \approx 1700$ K and with electron and macroparticle densities on the order of 10^{10} and 10^7 cm^{-3}, respectively.[20]

In this paper we present the results of an experimental study of the formation of macroscopic ordered structures in a classical quasineutal thermal plasma at atmospheric pressure and temperatures of 1700−2200 K. The rather large plasma dimensions (its volume is ~ 10 cm^3, which corresponds to a particle number on the order of 10^8 at a particle density of 10^7 cm^{-3}), its uniformity, and the absence of external electric and magnetic fields made it possible to eliminate the effect of boundary conditions on phase transitions in the plasma.

2. EXPERIMENTAL APPARATUS

2.1. Source of thermal plasma with macroparticles

The test stand includes a plasma generator and the diagnostic means for determining the parameters of the particles and gas.[21] The main part of the plasma source consists of a two-flare Maecker burner with propane and air fed into its inner and outer flares. The diameter of the inner flare is 25 mm and that of the outer, 50 mm. Particles are introduced into the inner flare of the burner. This burner design makes it possible to create a laminar stream of plasma with uniform parameter distributions (temperature, electron and ion densities) in the region. During operation, the velocity V_g of the plasma stream was varied over 2–3 m/s and the electron density in the flame, over 10^9-10^{11} cm^{-3}. The temperatures of the electrons and ions were equal and were varied over the range $T_i = T_e = T_g = 1700-2200$ K. Spectroscopic measurements of the temperature T_p of the particles[22] showed that it was close to the gas temperature ($T_p \cong T_g$). The combustion products were at atmospheric pressure.

In our experiments we studied a thermal plasma with two types of chemically inert particles, Al_2O_3 and CeO_2. The particles of powder contain an admixture of alkali metal compounds. Spectral measurements in the plasma stream revealed the presence of alkali metal atoms (sodium and potassium) with low ionization potentials. Thus, the main components of the plasma in one case were charged CeO_2 particles, electrons, and singly charged Na^+ ions, and, in the other, charged Al_2O_3 particles, electrons, and Na^+ and K^+ ions.

In order to study Coulomb ordered structures in the plasma, it is necessary to have data on the charge of the particles, as well as on the basic plasma parameters. The important feature of this plasma source is that it creates a large plasma volume. As a result, various diagnostic measurements of the plasma can be made. Various parameters of the gas and macroscopic particles were determined, such as the electron and alkali ion densities, the gas temperature, and the size and density of the macroparticles.

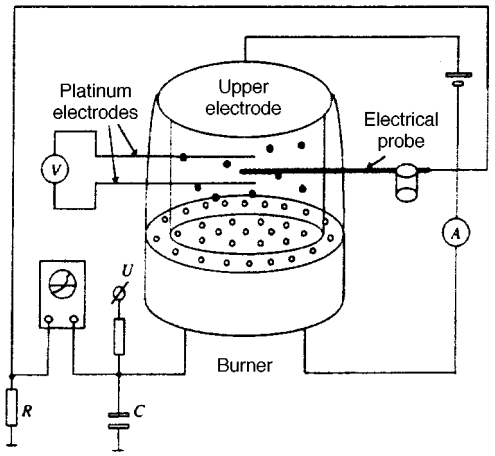

FIG. 1. The arrangement of the probe measurements.

2.2. Plasma diagnostics

The plasma was diagnosed by probe and optical techniques. The arrangement of the probe measurements is shown in Fig. 1. The density n_i of the positive alkali metal ions was measured with an electrical probe.[23,24] The rms error in the density determination was 20%. The local electron density n_e was determined by a method based on measuring the current I and longitudinal electric field E in the plasma.[23] An electrode at constant voltage relative to the burner was placed in the plasma flow to determine the current I. Two platinum probes were introduced into the plasma to determine the tangential component E of the electric field. The electrical conductivity of the plasma, $\sigma = n_e e \mu_e$, was determined on the basis of Ohm's law $j = \sigma E$ (j is the current density and μ_e is the mobility of the electrons). The electron density was found from known μ_e. The error in n_e was less than 30%.

The gas temperature and alkali metal concentration were measured by traditional methods: a generalized inversion method and a total absorption method[21] (the rms errors were less than 1% and 30%, respectively).

2.3. Particle diagnostics

A novel laser technique was used to determine the mean (Sauter) diameter D_p and density n_p of the macroparticles.[25] This technique is based on measurements of the extinction (attenuation of light) in a dispersive medium at small scattering angles, and is intended for determining the characteristics of particles with sizes of 0.5–15 μm.

The setup for measuring the extinction of optical radiation includes a rotating disk with aperture stops of various diameters located in front of a photodetector (Fig. 2). A He–Ne laser ($\lambda = 0.633$ μm) is used as the light source. For

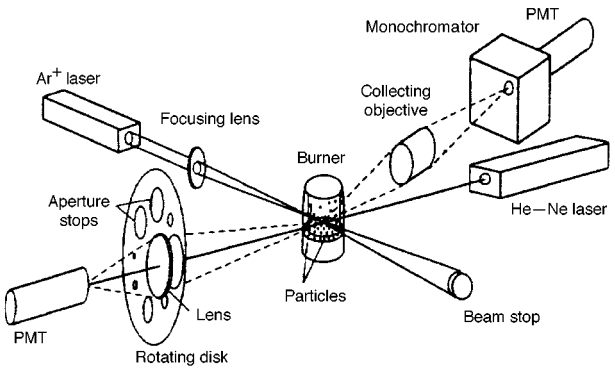

FIG. 2. The setup for the optical measurements of the sizes, density, and spatial structures of the macroparticles

an error in the measurement of the extinction of about 2%, the errors in recovering the particle sizes and density were about 3%, 10%, respectively.

The ordered structures were analyzed using the binary correlation function[5] obtained with a laser time-of-flight counter (Fig. 2). The measurement volume is formed by focusing the beam of an Ar^+ laser ($\lambda = 0.488$ μm) onto the axial region of the plasma stream. Radiation scattered by individual particles at an angle of 90° when they cross the waist of the laser beam is collected by a lens and directed onto the 15-μm-wide monochromator entrance slit. The diameter of the measurement volume was less than 10 μm. The resulting pulsed signals were then processed to calculate the binary correlation function $g(r)$, which characterizes the probability of finding a particle a distance $r = V_p t$ from a given particle. Here t is time and V_p is the average particle velocity ($V_p \sim V_g$ for micron sized particles[26]). An analysis of $g(r)$ makes it possible to describe the spatial structure and interparticle correlations of the particles.

3. RESULTS AND DISCUSSION

Plasma diagnostics were performed in the temperature stabilized zone $h = 25-40$ mm above the top of the burner at various plasma temperatures and particle densities. The plasma temperature was changed by varying the propane/air ratio over 0.95–1.47. Thus, it is was possible to change the Debye radius, the distance between particles, and the charge of particles in the plasma. Measurements of the spatial structures of the macroparticles were compared with data for an aerosol stream at room temperature. In the latter case, only air with particles of Al_2O_3 or CeO_2 was fed into the inner flare of the burner. This system simulates a plasma with a random spatial disposition of the macroparticles (a ''gaseous'' plasma).

In measurements with CeO_2 particles, the particle density n_p was varied over the range $(0.2-5.0)\cdot 10^7$ cm^{-3} and the plasma temperature T_g over 1700–2200 K. As a consequence, the ion density n_i varied from $0.42\cdot 10^{10}$ to $4.0\cdot 10^{10}$ cm^{-3} and the electron density, over $(2.5-7.2)\cdot 10^{10}$ cm^{-3}. The CeO_2 particles are polydisperse, with a distribution half-width of less than 30% according to our measurements. The average Sauter diameter of the particles was about 0.8 μm.

Based on these data, the quasineutrality condition $Z_p n_p + n_i = n_e$ implies that the CeO_2 particles are positively charged at $10^3 e$ to with a factor of 2. The observed magnitude and sign of the charge on the particles can be explained by thermal emission of electrons from the surface of heated CeO_2 particles,[1,2] which are characterized by a low electron work function (~ 2.75 eV[27]). In the following analysis of the data, we use the lower limit for the measured particle charge ($Z_p \approx 500$).

To analyze the state of the plasma with CeO_2 particles, we first estimate the relaxation times in the plasma: the characteristic time τ_R to establish an ordered particle structure, and the thermalization time τ_T over which the kinetic energy of the particles approaches the kinetic energy of those of the ambient gas. The estimate of τ_T addresses the validity of using a particle interaction parameter in the form $\gamma_p = Z_p^2 e^2/\langle r \rangle kT$, where $T = T_g$.

3.1. Relaxation processes in thermal plasmas with macroparticles

Relaxation processes in plasmas can be related to the times for ionization and the changes in the relative locations of the macroparticles. Estimates show that the ionization relaxation times in the plasma are short. The equilibration controlled by the dynamics of the particles' motion in a highly nonideal plasma is characterized by very much longer times.

Let us estimate the time to establish an ordered structure in a thermal plasma. This process occurs when initially randomly oriented particles are introduced into a plasma flow. In the Wigner–Seitz cell model, the relaxation time τ_R is[2]

$$\tau_R = \left(4 + \frac{1}{2}\pi\right) \frac{R_p^2 u n_g m_g}{Z_p^2 n_p}, \tag{1}$$

where $u = \sqrt{kT_g/2\pi m_g}$ and m_g and n_g are the mass and density of the gas molecules.

In the experiments with CeO_2 particles ($n_g = 2.7\cdot 10^{18}$ cm^{-3}, $m_g = 5.0\cdot 10^{-23}$ g, $T_g = 2000$ K, $R_p = 0.4$ μm, $Z_p \approx 500$, and $n_p = 5.0\cdot 10^7$ cm^{-3}), the estimated relaxation time is $\tau_p \cong 10$ ms. In order to establish spatial ordering in the particle positions, the plasma lifetime must be much longer than τ_R. Under our conditions, τ_R is much longer than the relaxation time of the particle charge and electron density to their equilibrium values and is shorter than the plasma lifetime, which is characterized by $\tau_f = h/V_p$. For $h \cong 40$ mm and $V_p \cong 2$ m/s, we have $\tau_f \cong 20$ ms, which yields $\tau_f \cong 2\tau_R$.

3.2. Thermalization of particles in the plasma

For an approximate estimate of the thermalization time τ_T we use the equation

$$D_p \approx V_T^2 \tau_T \approx (kT_g/M_p)\tau_T, \tag{2}$$

where D_p is the diffusion coefficient of the particles, V_T is their thermal speed, and M_p is their mass.

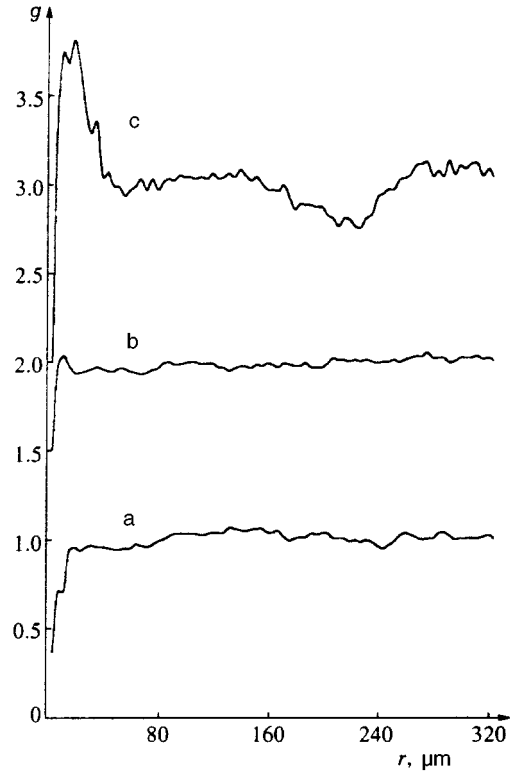

FIG. 3. The binary correlation function $g(r)$ for CeO_2 particles in an air stream at room temperature $T_g \cong 300$ K with $\gamma_p = 0$ (a), in plasmas ($Z_p \approx 500$) at temperature $T_g = 2170$ K with $\gamma_p = 40$ ($\Gamma_s \approx 1$) (b) and at temperature $T_g = 1700$ K with $\gamma_p = 120$ ($\Gamma_s \approx 40$) (c).

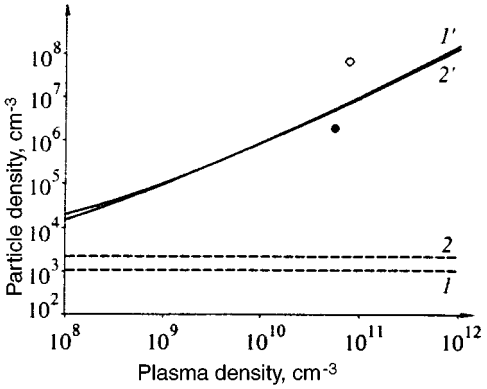

FIG. 4. The range of plasma ($n_e + n_i$) and particle (n_p) densities within which an ordered structure is formed for $Z_p = 500$. Curves *1* (*1′*) and *2* (*2′*) refer to $\gamma_p = 4$ ($\Gamma_s = 4$) with $T_g = 1700$ and 2200 K, respectively; $\gamma_p = 40$ ($\Gamma_s = 1$) (●) and $\gamma_p = 120$ ($\Gamma_s = 40$) (○) for plasmas with CeO_2 particles.

Under conditions such that a thermal plasma exists (the transition from a free molecular flow to a hydrodynamic flow), the following interpolation formula is usually used for the diffusion coefficient:[28]

$$D_p = \left(\frac{kT_g}{6\pi\eta R_p} \right) \left[1 + \frac{l}{R_p} \left(1.257 + 0.400 \exp \frac{-1.10 R_p}{l} \right) \right], \tag{3}$$

where l is the mean free path in the gas and η is the viscosity of the gas.

Finally, we find

$$\tau_T \approx \frac{2\rho_p R_p^2}{9\eta} \left[1 + \frac{l}{R_p} \left(1.257 + 0.400 \exp \frac{-1.10 R_p}{l} \right) \right]. \tag{4}$$

For the typical conditions of the experiments with CeO_2 particles ($T_g = 2000$ K, $R_p = 0.4$ μm, $l \approx 0.4$ μm, $\rho_p = 7.3$ g/cm^{-3}, and $\eta = 7.0 \cdot 10^{-5}$ Pa·s), we obtain $\tau_T \approx 10$ μs, or much less than the characteristic plasma lifetime $\tau_f = h/V_p$. Thus confirms the validity of our assumption that the kinetic energy of the particles is close to the kinetic energy of the ambient gas particles.

3.3. Spatially ordered structures in thermal plasmas

Figures 3a, b, and c show typical binary correlation functions $g(r)$ for CeO_2 particles in an aerosol stream at room temperature ($T_g \cong 300$ K) and in plasmas ($T_g = 2170$ and 1700 K). It is quite evident that the correlation functions $g(r)$ for the plasma with temperature $T_g = 2170$ K and particle density $n_p = 2.0 \cdot 10^6$ cm^{-3} and for the aerosol stream are essentially the same. Thus, the particles in the plasma interact weakly and formation of ordered structures is impossible. This is also confirmed by the plasma diagnostic measurements. The optical and probe measurements showed that the average interparticle distance ($\langle r \rangle = 50$ μm) is roughly 3.5 times the Debye radius ($r_D = 14$ μm), while the interaction parameter γ_p is about 40. Then an estimate of Γ_s, which accounts for Debye shielding, yields $\Gamma_s \cong 1$.

Figure 4 shows the range of n_e and n_p within which ordered structures can develop. Curves *1* (*1′*) ($T_g = 1700$ K) and *2* (*2′*) ($T_g = 2200$ K) correspond to $\gamma_p = 4$ ($\Gamma_s = 4$). Near ordering in the particle positions is established in the region above curves *1* and *2* (single-species plasma model) or curves *1′* and *2′* (Yukawa model). The Yukawa model predicts higher γ_p for the observed interparticle separations and Debye radii. The experimental point ($T_g = 2170$ K and $n_p = 2.0 \cdot 10^6$ cm^{-3}, corresponding to the correlation function shown in Fig. 3b) denoted by a solid circle lies below the boundary between the weakly and strongly nonideal plasma states according to the Yukawa model.

For the lower plasma temperature $T_g = 1700$ K and a particle density of $n_p = 5.0 \cdot 10^7$ cm^{-3}, Fig. 3c shows that the binary correlation function $g(r)$ exhibits the near ordering characteristic of a liquid. Under these conditions, as the diagnostic measurements showed, the ion density ($n_i \sim 10^9$ cm^{-3}) is roughly an order of magnitude lower than the electron density ($n_e \sim 10^{10}$ cm^{-3}), while the particle charge Z_p is determined by the quasineutrality condition in the form $Z_p n_p = n_e$ ($n_i \ll n_e$). The calculated values of γ_p and Γ_s are ~ 120 and 40, respectively, which correspond to a system of strongly interacting particles. Therefore, the particles form an ordered structure, in accord with the phase diagram for the plasma (Fig. 4). The corresponding experimental point (the hollow circle) lies above the theoretical curves for the Yukawa model.

An analysis of the distributions of the relative interpar-

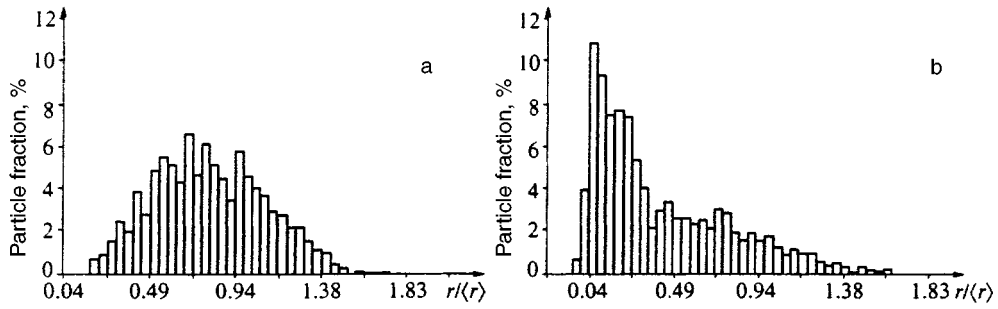

FIG. 5. Distributions over the parameter $r/\langle r\rangle$ for CeO_2 particles in an air stream at room temperature $T_g \cong 300$ K, $\gamma_p = 0$ (a) and in a plasma ($Z_p = 500$) at $T_g = 1700$ K and $\gamma_p = 120$ ($\Gamma_s = 40$) (b).

ticle distances $r/\langle r\rangle$ obtained under the same conditions as the correlation functions showed that both regions with ordered structures (domains) and regions with random particle positions exist.[29] Figures 5a and b show histograms for the aerosol ($T_g \cong 300$ K) (the ''gaseous'' plasma) and the plasma ($T_g = 1700$ K). The distributions were measured for 1500–2000 particles using the laser time-of-flight counter described above and are normalized in area. For a plasma temperature of 1700 K the histogram becomes substantially narrower (by a factor of 4–5), its peak shifts toward smaller interparticle separations $r/\langle r\rangle = 0.3$, and the maximum value rises from 6–7% to 10–11%. In this case the observed structure of the particles differs sharply from the ''gaseous'' case, which suggests the development of strong correlation in the positions of the particles. At the same time, the presence of randomly oriented particles leads to the appearance of the broad pedestal characteristic of the ''gaseous'' plasma in the histogram.

The development of domains can be explained by the polydisperse nature of the CeO_2 particles, which results in the finer particles forming regions of ordered structure (domains) with small interparticle distances,[29] while the coarser particles, which lie at large distances, are positioned randomly.

The formation of ordered structures was observed only at sufficiently high ($\sim 10^7$ cm^{-3}) particle densities. Lowering the concentration of CeO_2 particles increases the average distance between particles and leads to a reduction in the Coulomb interaction energy. Then an ordered structure does not develop, as shown in Fig. 3b ($n_p = 2.0 \cdot 10^6$ cm^{-3}).

Plasmas with Al_2O_3 particles were studied at temperatures $T_g = 1900 - 2200$ K. The higher concentration of Na^+ and K^+ ions (by ~ 10 times) should be noted in this case. The measured ranges of the densities of the ions, electrons, and particles were, respectively, $(0.35 - 12.0) \cdot 10^{10}$ cm^{-3}, $(0.85 - 18.0) \cdot 10^{10}$ cm^{-3}, and $(0.7 - 1.0) \cdot 10^6$ cm^{-3}. The average particle diameter was about 1.5 μm. The high density of alkali metal ions leads to strong shielding of the Coulomb interaction of the macroparticles. Thus, as an example, for $T_g = 2035$ K, $n_i = 8.6 \cdot 10^{10}$ cm^{-3}, $n_e = 1.3 \cdot 10^{11}$ cm^{-3}, and $n_p = 1.0 \cdot 10^6$ cm^{-3}, we obtain $r_D = 6.5$ μm and $\langle r\rangle = 60$ μm. Since $\langle r\rangle \cong 9 r_D$, the particles are strongly shielded and cannot form a spatially ordered structure.

4. CONCLUSION

In this paper a way of finding the binary correlation function for a system of macroparticles has been proposed, based on a laser time-of-flight method. An analysis of correlation functions obtained in this way has demonstrated the existence, under certain conditions, of spatially ordered particle structures in thermal plasmas. The existence of these structures is also confirmed by diagnostic (probe and optical) measurements. The formation of ordered structures was observed for micron-sized particles in a plasma consisting of positively charged CeO_2 particles, the electrons emitted by them, and singly-charged sodium ions. When the density of the particles was reduced and the density of alkali metals was increased, the particles were positioned randomly. Experimental data have been obtained on the plasma parameters (particle, ion, and electron densities, and temperature) at which the structures are formed. This occurs at a particle density of $\sim 10^7$ cm^{-3} and a temperature of about 1700 K. The CeO_2 particles were positively charged at about 10^3 electron charges. The Coulomb interaction parameter for the particles is $\gamma_p > 120$, which corresponds to a highly nonideal plasma.

This work was partially supported by the Russian Fund for Fundamental Research (Grant No. 95-02-06456) and the International Science Foundation (Grant No. JCN100).

[1] M. S. Sodha and S. Guha, Adv. Plasma Phys. **4**, 219 (1971).
[2] V. E. Fortov and I. T. Yakubov, *Nonideal Plasmas [in Russian]*, Énergoizdat, Moscow (1994), p. 282.
[3] T. M. Sugden and B. A. Thrush, Nature **168**, 703 (1951).
[4] K. E. Shuler and J. Weber, J. Chem. Phys. **22**, 491 (1954).
[5] S. Ichimaru, Rev. Mod. Phys. **54**, 1017 (1982).
[6] H. Ikezi, Phys. Fluids **29**, 1764 (1986).
[7] M. O. Robbins, K. Kremer, and G. S. Crest, J. Chem. Phys. **88**, 3286 (1988).
[8] W. L. Slattery, G. D. Doolen, and H. E. DeWitt, Phys. Rev. A **21**, 2087 (1980).
[9] R. T. Farouki and S. Hamaguchi, Appl. Phys. Lett. **61**, 2973 (1992).
[10] M. J. Stevens and M. O. Robbins, J. Chem. Phys. **98**, 2319 (1992).
[11] R. F. Wuerker, H. Shelton, and R. V. Langmuir, J. Appl. Phys. **30**, 342 (1959).
[12] S. L. Gilbert, J. J. Bollinger, and D. J. Wineland, Phys. Rev. Lett. **60**, 2022 (1988).
[13] T. Trottenberg, A. Melzer, and A. Piel, Plasma Sources Sci. Technol. **4**, 450 (1995).
[14] J. H. Chu and L. I., Phys Rev. Lett **72**, 4009 (1994).
[15] H. Thomas, G. E. Morfill, V. Demmel *et al.*, Phys. Rev. Lett. **73**, 652 (1994).

[16] Y. Hayashi and K. Tachibana, Japan. J. Appl. Phys. **33**, L804 (1994).
[17] A. Melzer, T. Trottenberg, and A. Piel, Phys. Lett. A **191**, 301 (1994).
[18] A. Rahman and J. P. Schiffer, Phys. Rev. Lett. **57**, 1133 (1986).
[19] D. H. E. Dubin and T. M. O'Neil, Phys. Rev. Lett. **60**, 511 (1988).
[20] V. E. Fortov, A. P. Nefedov, O. F. Petrov *et al.*, JETP Lett. **63**, 181 (1996).
[21] A. B. Kondrat'ev, A. P. Nefedov, O. F. Petrov, and A. A. Samaryan, Tepl. Vys. Temp. **32**, 452 (1994).
[22] A. P. Nefedov, O. F. Petrov, and O. S. Vaulina, J. Quant. Spectrosc. and Radiat. Transfer **54**, 453 (1995).
[23] V. F. Kosov, V. I. Molotkov, and A. P. Nefedov, Tepl. Vys. Temp. **29**, 633 (1991).
[24] M. S. Benilov, Tepl. Vys. Temp. **26**, 993 (1988).
[25] O. S. Vaulina, A. P. Nefedov, O. F. Petrov, and A. V. Chernyshev, Zhurn. Prikl. Spectrosk. **63**, 133 (1996).
[26] G. L. Grodzovskiĭ, Uchenye zapiski TsAGI **5**, 80 (1974).
[27] V. S. Fomenko, *Emission Properties of Materials [in Russian]*, Naukova Dumka, Kiev (1981), p. 164.
[28] M. R. Zachariah, D. Chin, H. G. Semerjian, and J. L. Katz, Appl. Opt. **28**, 530 (1989).
[29] J. H. Chu, J.-B. Du, and L. I, J. Phys. D.: Appl. Phys. **27**, 296 (1994).

Translated by D. H. McNeill

Anomalous kinetics of plasmas in high-power radiation fields

V. P. Silin

P. N. Lebedev Physics Institute, Russian Academy of Sciences, 117333 Moscow, Russia
(Submitted 17 June 1996)
Zh. Éksp. Teor. Fiz. **111**, 478–495 (February 1997)

Transport equations are obtained in the nine-moment approximation for plasmas in intense radiation fields where the amplitude of the electron oscillations in the electromagnetic field exceeds the thermal speed. It is shown that for plasmas with a high degree of ionization, Z, the electron thermal conductivity is higher by approximately a factor of Z. The change in the frictional force on electrons colliding with ions owing to the effect of the radiation field leads to the possibility of electron acceleration and to a change in the sign of the dc and low-frequency electrical conductivities. © *1997 American Institute of Physics.* [S1063-7761(97)00602-1]

1. INTRODUCTION

Advances in short-pulse laser technology[1] have made the development of plasma kinetic theory in high-power electromagnetic fields essential, both at microwave and laser frequencies. Collisional kinetic theory is not adequately developed for fully ionized plasmas in which high-power radiation is absorbed by electrons in collisions with ions or, as one still says, through inverse bremsstrahlung absorption.[2] Usually, when the radiation power is low, the kinetic coefficients characterizing the plasma properties are independent of the electric field,[3,4] while the contribution of the radiation to the nonequilibrium fluxes is determined by expanding in powers of bilinear combinations of the radiation field strength.[5] This situation occurs when the electron thermal speed v_T is substantially higher than the amplitude v_E of the velocity of the electron oscillations in the electromagnetic field of the radiation. In the case of plasma ions with a high degree of ionization,

$$Z=|e_i/e|, \tag{1.1}$$

the condition for applicability of this sort of ordinary theory is more restrictive, i.e.,

$$Zv_E^2 \ll v_T^2, \tag{1.2}$$

otherwise the electron distribution differs greatly from Maxwellian, as predicted theoretically[6–8] and confirmed experimentally.[9] The reason the distribution differs from Maxwellian is that when Eq. (1.2) is violated, i.e., for

$$Zv_E^2 > v_T^2 > v_E^2, \tag{1.3}$$

electron–electron collisions are comparatively rare and the electron distribution cannot relax to Maxwellian. Some steps toward constructing a theory of transport under conditions (1.3) have been taken in local[10] and nonlocal[11] treatments of transport. At the same time, we note the self-similar, spatially nonuniform and time-dependent distribution obtained analytically by Uryupin *et al.*[12] for the parameter range (1.3). That distribution differs substantially from the standard distribution of Balescu[7] at high electron velocities and may have important consequences.

As the intensity of the radiation heating a plasma is increased, when the right-hand side of the inequality (1.3) is violated, electron–ion collisions will be suppressed, since the frequency of these collisions falls off as v_E^{-3} (Ref. 13). However, when the condition

$$Zv_T > v_E > v_T \tag{1.4}$$

is satisfied, it has been shown[14] that the electron distribution in the heated plasma is not only time-dependent, it is also anisotropic.

We shall be interested in even higher fields, such that[1)]

$$v_E > Zv_T. \tag{1.5}$$

Then electron–ion collisions are so strongly suppressed compared to electron–electron collisions, that a Maxwellian distribution can be used for the electrons. This is assumed in the theory of nonlinear high frequency plasma conductivity[13] under the condition (1.5). These results[13] have been confirmed to a great extent, and this has led to a large number of successor articles.[15,16] Considerable attention has been devoted to modifications of the Coulomb logarithm, which determines the electron–ion collisions. These studies have been summarized by Silin and Uryupin,[17] who clarified the conditions for various effects controlled by the Coulomb logarithm. This is also discussed by Polishchuk and Meyer-Ter-Vehn,[18] who examined an important property of plasmas in intense radiation fields, the relaxation of the electron and ion temperatures under condition (1.5). Here, in particular the electron heating owing to the absorption of intense radiation was also discussed. With regard to other transport processes in fully ionized plasmas located in high-power, high-frequency radiation fields whose frequency greatly exceeds the electron collision frequency, the theory is not yet adequately developed. In this paper we fill in this gap. We shall use Grad's moment method.[19] We emphasize also that the foundations of kinetic theory for plasmas in the case of the rapidly varying processes of interest to us were laid previously.[19–21]

In Sec. 2 we introduce a basic kinetic equation for averaging the electron distribution function over the period of a high-frequency radiation field which can be used to construct a theory for slow transport processes. In Sec. 3 we write down the transport equations in Grad's nine-moment approximation. In Sec, 4 an approximate approach is formulated that is realized under condition (1.5) and can be used to

describe, rigorously and comparatively simply, the effect of electron–ion collisions. It is shown that both the frictional force and the variation in the heat released in the plasma owing to ordered electron motion are determined by the effective collision frequency tensor. In Section 5 it is shown that the anisotropy in the effect of the radiation on the plasma, which is characterized by its polarization, shows up in such a way that the frictional force can either slow down or accelerate the electrons. This sort of acceleration can cause the spontaneous generation of currents (and, therefore, magnetic fields), as well as the generation of currents induced by a quasi-dc electric field and pressure gradient. Section 6 is devoted to an anomaly in the dc and low-frequency conductivities, which are negative in directions lying in a plane perpendicular to the beam of radiation. This phenomenon is similar to a high-frequency anomaly that has been predicted elsewhere.[22–24] In Section 7 it is shown that the electron thermal conductivity increases by roughly a factor of Z under high-power irradiation owing to the suppression of electron–ion collisions when condition (1.5) is satisfied.

Formulas needed to characterize the dependence of the averages over the oscillation period of the radiation on its polarization are given in Appendix 1 and a detailed derivation of the features of the transition[24] from low power to the limit of high power radiation is given in Appendix 2 for extending the basic material in this article to the case of circularly polarized radiation. Finally, a summary is given in Section 8.

2. BASIC KINETIC EQUATION

We consider a fully ionized plasma in a high-frequency electric field

$$\mathscr{E}(\mathbf{r},t)=\frac{1}{2}\left[\mathbf{E}(\mathbf{r},t)e^{-i\omega t}+\mathbf{E}^*(\mathbf{r},t)e^{i\omega t}\right], \tag{2.1}$$

$$\mathscr{B}(\mathbf{r},t)=\frac{1}{2}\left[\mathbf{B}(\mathbf{r},t)e^{-i\omega t}+\mathbf{B}^*(\mathbf{r},t)e^{i\omega t}\right]. \tag{2.2}$$

Here the amplitudes of the electric $\mathbf{E}(\mathbf{r},t)$ and magnetic $\mathbf{B}(\mathbf{r},t)$ fields are slowly varying functions of time over the period $2\pi/\omega$ of the high-frequency field. With the Maxwell equation

$$\operatorname{curl}\mathscr{E}=-\frac{1}{c}\frac{\partial\mathscr{B}}{\partial t} \tag{2.3}$$

this allows us to write the following approximate formula:

$$\mathbf{B}=\frac{c}{i\omega}\operatorname{curl}\mathbf{E}-\frac{c}{\omega^2}\frac{\partial}{\partial t}\operatorname{curl}\mathbf{E}. \tag{2.4}$$

With Eq. (2.4) the kinetic equation for the electron distribution function $f(\mathbf{v},\mathbf{r},t)$ can be written in the following form:

$$\frac{\partial f}{\partial t}+\mathbf{v}\frac{\partial f}{\partial\mathbf{r}}+\frac{\partial f}{\partial\mathbf{v}}\frac{e}{m}\left(\mathbf{E}_0+\frac{1}{2}\{\mathbf{E}e^{-i\omega t}+\mathbf{E}^*e^{i\omega t}\}+\frac{1}{2i\omega}\left[\mathbf{v}\operatorname{curl}(\mathbf{E}e^{-i\omega t}-\mathbf{E}^*e^{i\omega t})\right]-\frac{1}{\omega^2}\left[\mathbf{v}\operatorname{curl}\left(\frac{\partial\mathbf{E}}{\partial t}e^{-i\omega t}+\frac{\partial\mathbf{E}^*}{\partial t}e^{i\omega t}\right)\right]\right)=J_{ee}[f,f]+J_{ei}[f,f]. \tag{2.5}$$

Here $\mathbf{E}_0$ is the quasi-dc or low-frequency electric field, e and m are the charge and mass of the electron, and J_{ee} and J_{ei} are the electron–electron and electron–ion collision frequencies, respectively.

Under the influence of the high-frequency field the electron distribution function varies rapidly in time and becomes anisotropic, since this sort of field causes rapid oscillations in the electron velocity,

$$\mathbf{u}_E(t)=\frac{ei}{2m\omega}\{\mathbf{E}e^{-i\omega t}-\mathbf{E}^*e^{i\omega t}\}. \tag{2.6}$$

In this regard, it is convenient to use the new function

$$F(\mathbf{u},\mathbf{r},t)=f(\mathbf{v},\mathbf{r},t), \tag{2.7}$$

where

$$\mathbf{u}=\mathbf{v}-\mathbf{u}_E(t). \tag{2.8}$$

Equations (2.7) and (2.8) can be used to transform the kinetic equation (2.5) to the following:

$$\frac{\partial F}{\partial t}+\mathbf{u}\frac{\partial F}{\partial\mathbf{r}}+\left(\frac{e}{m}\mathbf{E}_0-\frac{e^2}{4m^2\omega^2}\frac{\partial|\mathbf{E}|^2}{\partial\mathbf{r}}\right)\frac{\partial F}{\partial\mathbf{u}}+e^{-i\omega t}\frac{e}{2m\omega i}\left\{-\mathbf{E}\frac{\partial F}{\partial\mathbf{r}}+\frac{\partial F}{\partial\mathbf{u}}\left(\frac{\partial\mathbf{E}}{\partial t}+\frac{\partial}{\partial\mathbf{r}}(\mathbf{u}\mathbf{E})-\frac{i}{\omega}\left[\mathbf{u}\operatorname{curl}\frac{\partial\mathbf{E}}{\partial t}\right]\right)\right\}+e^{i\omega t}\frac{e}{2m\omega i}\left\{\mathbf{E}^*\frac{\partial F}{\partial\mathbf{r}}-\frac{\partial F}{\partial\mathbf{u}}\left(\frac{\partial\mathbf{E}^*}{\partial t}+\frac{\partial}{\partial\mathbf{r}}(\mathbf{u}\mathbf{E}^*)+\frac{i}{\omega}\left[\mathbf{u}\operatorname{curl}\frac{\partial\mathbf{E}^*}{\partial t}\right]\right)\right\}+e^{-2i\omega t}\frac{e^2}{4m^2\omega^2}\left\{\frac{1}{2}\frac{\partial(\mathbf{E})^2}{\partial\mathbf{r}}-\frac{i}{\omega}\left[\mathbf{E}\operatorname{curl}\frac{\partial\mathbf{E}}{\partial t}\right]\right\}\times\frac{\partial F}{\partial\mathbf{u}}+e^{2i\omega t}\frac{e^2}{4m^2\omega^2}\left\{\frac{1}{2}\frac{\partial(\mathbf{E}^*)^2}{\partial\mathbf{r}}+\frac{i}{\omega}\left[\mathbf{E}^*\operatorname{curl}\frac{\partial\mathbf{E}^*}{\partial t}\right]\right\}\frac{\partial F}{\partial\mathbf{u}}=J_{ei}[\mathbf{u}+\mathbf{u}_E(t),F(\mathbf{u})]+J_{ee}[F(\mathbf{u}),F(\mathbf{u})]. \tag{2.9}$$

Note that, since the electron–electron collision integral depends on the relative velocity of the two colliding electrons, Eq. (2.8) does not introduce a dependence on the high-frequency field into J_{ee}. On the other hand, the electron–ion collision integral in Eq. (2.9) does depend on $\mathbf{u}_E(t)$.

It can be seen from Eq. (2.9) that if the amplitude $a_E=eE/m\omega^2$ of the oscillations in the high frequency field is sufficiently small compared to the scale lengths of the inhomogeneities in the field L_E and in the electron distribution L, then a comparatively simple equation can be obtained for the distribution function $\langle F\rangle=F_0$ averaged over the period of the fast oscillations. Here we shall assume that the following inequalities are satisfied:[13]

$$\frac{u}{\omega L}\ll 1, \quad \frac{eE_0}{m\omega u}\ll 1, \quad \frac{u_E a_E}{L_E u}\ll 1. \tag{2.10}$$

Then, on averaging Eq. (2.9) we can neglect the contribution of the harmonics of F. As a result, we obtain

$$\frac{\partial F_0}{\partial t}+\mathbf{u}\,\frac{\partial F_0}{\partial \mathbf{r}}+\left(\frac{e}{m}\,\mathbf{E}_0-\frac{e^2}{4m^2\omega^2}\,\frac{\partial|\mathbf{E}|^2}{\partial \mathbf{r}}\right)\frac{\partial F_0}{\partial \mathbf{u}} =\langle J_{ei}[\mathbf{u}+\mathbf{u}_E(t),F_0(\mathbf{u})]\rangle+J_{ee}[F_0(\mathbf{u}),F_0(\mathbf{u})]. \tag{2.11}$$

We shall use this equation below to elucidate the unique features of transport in plasmas caused by a strong high-frequency electromagnetic field.

3. THE NINE-MOMENT APPROXIMATION

In the following we shall use Grad's method, with the distribution in the nine-moment approximation represented by[19]

$$F_0(\mathbf{u},\mathbf{r},t)=\frac{n(\mathbf{r},t)}{(2\pi)^{3/2}v_T^3}\exp\left\{-\frac{m[\mathbf{u}-\mathbf{u}^e(\mathbf{r},t)]^2}{2\kappa_B T(\mathbf{r},t)}\right\} \times\left\{1-\frac{\mathbf{q}(\mathbf{r},t)m[\mathbf{u}-\mathbf{u}^e(\mathbf{r},t)]}{n(\mathbf{r},t)[\kappa_B T(\mathbf{r},t)]^2} \times\left(1-\frac{m[\mathbf{u}-\mathbf{u}^e(\mathbf{r},t)]^2}{5\kappa_B T(\mathbf{r},t)}\right)\right\}. \tag{3.1}$$

Here κ_B is Boltzmann's constant, $n(\mathbf{r},t)$ is the electron number density, $\mathbf{u}^e$ and $T(\mathbf{r},t)$ are the average velocity of the electrons and their temperature, given by

$$\mathbf{u}^e(\mathbf{r},t)=\frac{1}{n}\int d\mathbf{u}\,\mathbf{u}F_0,$$

$$T(\mathbf{r},t)=\frac{2}{3\kappa_B n}\int d\mathbf{u}\,\frac{m}{2}\,[\mathbf{u}-\mathbf{u}^e(\mathbf{r},t)]^2F_0, \tag{3.2}$$

$v_T=\sqrt{\kappa_B T/m}$ is the electron thermal speed, and the electron thermal flux is given by

$$\mathbf{q}=\int d\mathbf{u}[\mathbf{u}-\mathbf{u}^e(\mathbf{r},t)]\cdot\,\frac{1}{2}\,m[\mathbf{u}-\mathbf{u}^e(\mathbf{r},t)]^2F_0(\mathbf{u},\mathbf{r},t). \tag{3.3}$$

The kinetic equation (2.11) yields the following system of transport equations:[2)]

$$\frac{\partial n}{\partial t}+\mathrm{div}(n\mathbf{u}^e)=0, \tag{3.4}$$

$$mn\left(\frac{\partial \mathbf{u}^e}{\partial t}+\left(\mathbf{u}^e\,\frac{\partial}{\partial \mathbf{r}}\right)\mathbf{u}^e\right)+\frac{\partial n\kappa_B T}{\partial \mathbf{r}}-n\left(e\mathbf{E}_0-\frac{e^2}{4m\omega^2}\,\frac{\partial|\mathbf{E}|^2}{\partial \mathbf{r}}\right)=\mathbf{R}^{ei}, \tag{3.5}$$

$$\frac{\partial T}{\partial t}+\mathbf{u}^e\,\frac{\partial T}{\partial \mathbf{r}}+\frac{2}{3}\,T\ \mathrm{div}\ \mathbf{u}^e+\frac{2}{3n\kappa_B}\,\mathrm{div}\ \mathbf{q}=\frac{2}{3n\kappa_B}\,Q^{ei}, \tag{3.6}$$

$$\frac{\partial \mathbf{q}}{\partial t}+\left(\mathbf{u}^e\,\frac{\partial}{\partial \mathbf{r}}\right)\mathbf{q}+\frac{1}{5}\left(7\mathbf{q}\ \mathrm{div}\ \mathbf{u}^e+7\left(\mathbf{q}\,\frac{\partial}{\partial \mathbf{r}}\right)\mathbf{u}^e+2\mathbf{q}_s\,\frac{\partial \mathbf{u}_s^e}{\partial \mathbf{r}}\right) +\frac{5}{2}\,\frac{n\kappa_B T}{m}\,\frac{\partial \kappa_B T}{\partial \mathbf{r}}=\Delta\mathbf{Q}_{ee}+\Delta\mathbf{Q}_{ei}-\frac{5\kappa_B T}{2m}\,\mathbf{R}^{ei}. \tag{3.7}$$

Here, in the usual terminology for Grad's method, we write the frictional force as

$$\mathbf{R}^{ei}=\int d\mathbf{u}\ m(\mathbf{u}-\mathbf{u}^e)\langle J_{ei}[\mathbf{u}+\mathbf{u}_E(t),F_0(\mathbf{u})]\rangle, \tag{3.8}$$

the heat delivered to the electron component owing to collisions with ions as

$$Q^{ei}=\int d\mathbf{u}\cdot\,\frac{1}{2}\,m(\mathbf{u}-\mathbf{u}^e)^2\langle J_{ei}[\mathbf{u}+\mathbf{u}_E(t),F_0(\mathbf{u})]\rangle \tag{3.9}$$

and finally,

$$\Delta\mathbf{Q}_{ee}=\int d\mathbf{u}(\mathbf{u}-\mathbf{u}^e)\cdot\,\frac{1}{2}\,m(\mathbf{u}-\mathbf{u}^e)^2J_{ee}[F_0,F_0], \tag{3.10}$$

and

$$\Delta\mathbf{Q}_{ei}=\int d\mathbf{u}(\mathbf{u}-\mathbf{u}^e)\cdot\,\frac{1}{2}\,m(\mathbf{u}-\mathbf{u}^e)^2\langle J_{ei}[\mathbf{u}+\mathbf{u}_E(t),F_0(\mathbf{u})]\rangle. \tag{3.11}$$

In the following we find a form of Eqs. (3.8)–(3.11) that closes the system of transport equations (3.4)–(3.7). Information will be obtained on the qualitative changes in electron transport produced by the electromagnetic fields of high-power radiation.

4. ELECTRON–ION COLLISIONS

The electron–ion collision integral in a radiation field has been obtained classically.[13,20,21] The required quantum mechanical treatment has been described elsewhere.[17] It should be emphasized that Refs. 17 and 13 show that the Landau collision integral with needed refinements in the expression for the Coulomb logarithm $\Lambda_{e,i}$ can be used in the kinetic theory of plasmas in high-power radiation fields. We shall use the Landau collision integral in the following, referring the reader to Refs. 17 and 13 for the form of the Coulomb logarithm, which is always large compared to unity in low-density plasmas.

We shall not be interested further in quantities that are small compared to the electron–ion mass ratio in accordance with a study[18] of temperature relaxation of plasma species in a high-power radiation field. Then[19] we have

$$J_{ei}[\mathbf{u}+\mathbf{u}_E(t),F(\mathbf{u})]=\frac{2\pi e^2e_i^2n_i\Lambda_{ei}}{m^2} \times\frac{\partial}{\partial u_k}\,D_{kj}(\mathbf{u}+\mathbf{u}_E(t))\,\frac{\partial F}{\partial u_j}, \tag{4.1}$$

where

$$D_{kj}(\mathbf{u}+\mathbf{u}_E)=\{(\mathbf{u}+\mathbf{u}_E)^2\delta_{kj}-(\mathbf{u}+\mathbf{u}_E)_k \times(\mathbf{u}+\mathbf{u}_E)_j\}|\mathbf{u}+\mathbf{u}_E|^{-3}. \quad (4.2)$$

For simplicity and, at the same time, generality, we avoid the special case of plane polarized radiation, where the velocity of the electron oscillations, $\mathbf{u}_E$ can go to zero, and consider elliptically polarized radiation. Here we shall assume that the minimum velocity $u_E(t)$ is high compared to the electron thermal velocity. This makes it possible to expand Eq. (4.2) in powers of u_E^{-1}:

$$D_{lj}=u_E^{-3}\Big\{u_E^2\delta_{lj}-u_{El}u_{Ej}+[-3(\mathbf{u}_E\mathbf{u})u_E^{-2}(\delta_{lj}u_E^2 -u_{El}u_{Ej})+2(\mathbf{u}_E\mathbf{u})\delta_{lj}-u_{El}u_j-u_{Ej}u_l]+u^2\delta_{lj} -u_lu_j-6(\mathbf{u}_E\mathbf{u})^2u_E^{-2}\delta_{lj}+3u_{El}u_j(\mathbf{u}_E\mathbf{u})u_E^{-2} +3u_{Ej}u_l(\mathbf{u}_E\mathbf{u})u_E^{-2}-\frac{3}{2}u^2u_E^{-2}(\delta_{lj}u_E^2-u_{El}u_{Ej}) +\frac{15}{2}(\mathbf{u}_E\mathbf{u})^2u_E^{-4}(\delta_{lj}u_E^2-u_{El}u_{Ej})+\ldots\Big\}. \quad (4.3)$$

We use the approximation (4.3) to find the frictional force. Given Eqs. (4.1)–(4.3), Eq. (3.8) can be written in the following form:

$$(\mathbf{R}^{ei})_k=\frac{2\pi e^2e_i^2n_i\Lambda_{ei}}{m}\int d\mathbf{u}\,F_0\left\langle\frac{\partial}{\partial u_j}D_{kj}\right\rangle, \quad (4.4)$$

where, according to Eq. (4.3),

$$\frac{\partial}{\partial u_j}D_{kj}=\frac{1}{u_E^3}\left\{-2u_{Ek}-2u_k+6\frac{u_{Ek}u_{Ej}}{u_E^2}u_j\right\}. \quad (4.5)$$

In conformity with the Fourier expansion Eq. (A.1.4), we have

$$\langle u_{El}/u_E^3\rangle=0, \quad \langle u_{El}u_{Ej}u_{Ei}/u_E^5\rangle=0. \quad (4.6)$$

Thus, according to Eq. (3.1) the frictional force can be written in the form

$$(\mathbf{R}^{ei})_k=-mn\nu_{kj}u_j^e, \quad (4.7)$$

where

$$\nu_{kj}=\frac{4\pi e^2e_i^2n_i\Lambda_{ei}}{m^2}\left\{\left\langle\frac{1}{u_E^3(t)}\right\rangle\delta_{kj}-3\left\langle\frac{u_{Ek}(t)u_{Ej}(t)}{u_E^5(t)}\right\rangle\right\} \quad (4.8)$$

is the effective electron–ion collision frequency tensor. In the following we examine the unique properties of this tensor, which are determined by the polarization of the radiation and might be expected because the trace of the tensor (4.8) is zero.

We now consider the heat Q^{ei} released in collisions between electrons and ions. In accordance with Eq. (4.1), Eq. (3.9) takes the form

$$Q^{ei}=\frac{2\pi e^2e_i^2n_i\Lambda_{ei}}{m}\int d\mathbf{u}\,F_0\left\langle D_{jj}+(\mathbf{u}-\mathbf{u}^e)_k\frac{\partial D_{kj}}{\partial u_j}\right\rangle. \quad (4.9)$$

In the approximation (4.3) we have

$$D_{jj}=\frac{2}{u_E}-\frac{2\mathbf{u}\mathbf{u}_E}{u_E^3}-\frac{u^2}{u_E^3}+3\frac{(\mathbf{u}_E\mathbf{u})^2}{u_E^5}. \quad (4.10)$$

Given Eq. (4.6), in the nine-moment approximation (3.1) this expression, together with Eq. (4.5), yields

$$Q^{ei}=Q_{IB}+\frac{1}{2}\mathbf{R}^{ei}\mathbf{u}^e, \quad (4.11)$$

where the first term

$$Q_{IB}=\frac{4\pi e^2e_i^2nn_i\Lambda_{ei}}{m}\left\langle\frac{1}{u_E}\right\rangle \quad (4.12)$$

represents the heat released through inverse bremsstrahlung absorption, neglecting the ordered motion of the electrons. The second term originates, first, in the work performed by the frictional force, $-\mathbf{u}_e\mathbf{R}^{ei}$, as is customary in plasmas, including those without high-power radiation, and second, in the effect of the ordered motion of the electrons on inverse bremsstrahlung absorption, $(3/2)\mathbf{u}^e\mathbf{R}^{ei}$.

Finally, we consider the contribution of electron–ion collisions to the right hand side of Eq. (3.7). In the approximation of Eq. (4.3), Eq. (3.11) reduces to

$$(\Delta\mathbf{Q}_{ei})_j=\frac{2\pi e^2e_i^2n_i\Lambda_{ei}}{m^2}\int d\mathbf{u}\,F_0m\Big\{\frac{1}{2}(\mathbf{u}-\mathbf{u}^e)^2\frac{\partial\langle D_{jk}\rangle}{\partial u_k}+(\mathbf{u}-\mathbf{u}^e)_k(\mathbf{u}-\mathbf{u}^e)_j\frac{\partial\langle D_{kl}\rangle}{\partial u_l} +(\mathbf{u}-\mathbf{u}^e)_j\langle D_{ll}\rangle+2(\mathbf{u}-\mathbf{u}^e)_k\langle D_{jk}\rangle\Big\}. \quad (4.13)$$

Using the explicit expressions (4.3), (4.5), and (4.9), we obtain

$$(\Delta\mathbf{Q}_{ei})_j=-\frac{1}{2}\nu_{jk}\left\{11n\kappa_BTu_k^e+\frac{34}{5}q_k\right\}. \quad (4.14)$$

The contribution to the right hand side of Eq. (3.7) from electron–ion collisions takes the form

$$(\Delta\mathbf{Q}_{ei})_j-\frac{5\kappa_BT}{2m}(\mathbf{R}^{ei})_j=-\nu_{jk}\left(3n\kappa_BTu_k^e+\frac{17}{5}q_k\right). \quad (4.15)$$

We shall obtain some physical consequences of these equations below.

5. GENERATION OF CURRENTS BY ACCELERATED ELECTRONS

The equations obtained in Appendix 1 make it possible to write the effective electron–ion collision frequency tensor (4.9) in the form

$$\nu_{lj}=\nu(E)N_{lj}, \quad (5.1)$$

where the tensor N_{lj} is defined by Eqs. (A1.9) and

$$\nu(E)=8\sqrt{2}\pi e^2e_i^2n_i\Lambda_{ei}m^{-2}v_E^{-3}, \quad (5.2)$$

where $v_E^2=(e^2E^2/m^2\omega^2)$. In order of magnitude, the effective frequency (5.2) is a factor of $(v_E/v_T)^3$ smaller than the ordinary electron–ion collision frequency in the absence of

high-power radiation.[13] According to Eq. (A1.10), for circularly polarized radiation the frictional force (4.7) takes the form

$$\mathbf{R}^{ei}=(R_x^{ei},R_y^{ei},R_z^{ei})=-mn\nu(E)\left(-\frac{1}{2}u_x^e,-\frac{1}{2}u_y^e,u_z^e\right). \tag{5.3}$$

Whereas the z component of this formula corresponds to a reduction in the averaged z component of the velocity, the other two components of Eq. (5.3) correspond to acceleration of the electrons owing to the work performed by the high-power radiation field.

A similar situation occurs in the other limiting case of nearly plane polarization. Thus, in the case of Eq. (A1.13), we have

$$\mathbf{R}^{ei}=-mn\nu(E)(N_{xx}u_x^e,N_{yy}u_y^e,N_{zz}u_z^e). \tag{5.4}$$

Equation (A1.3) shows that, approximately,

$$N_{zz}=\frac{1}{\pi\sqrt{2}}\frac{E^2}{E_y^2}=-N_{yy},\quad N_{xx}=-\frac{1}{\pi\sqrt{2}}\ln\frac{4E}{E_y}, \tag{5.5}$$

so that, first, the effective collision frequency is much higher than that for circular polarization, since $E\gg E_y$, and, second, the electrons are slowed down, as in the case of circular polarization, along the z axis, while they are accelerated along the other two axes. In fact, if we neglect the spatial inhomogeneity and slowly varying electric field in Eq. (3.5), then according to Eq. (5.1) we obtain

$$\frac{du_k^e}{dt}=-\nu(E)N_{kj}u_j^e. \tag{5.6}$$

In the case of Eqs. (5.4) and (5.5), the acceleration is most intense along the y axis, i.e., perpendicular to the plane of polarization. Then, assuming $E=\text{const}$, we have

$$u_y^e(t)=u_y^e(0)\exp(t/t_{ac}), \tag{5.7}$$

where we obtain

$$t_{ac}=\pi\sqrt{2}E_y^2/E^2\nu(E) \tag{5.8}$$

for the characteristic acceleration time. This sort of electron acceleration leads to the generation of spontaneous currents by high-power heating radiation and, therefore, to the generation of spontaneous magnetic fields.

The presence of a quasi-dc field $\mathbf{E}_0$ (or pressure gradient) in the plasma makes the process of accelerating the electrons as they collide with ions and simultaneously absorb radiation an induced process. Here in place of Eq. (5.6) we have

$$\frac{du_k^e}{dt}+\nu(E)N_{kj}u_j^e=\frac{e}{m}E_{0k}. \tag{5.9}$$

In the case of Eqs. (5.4) and (5.5) with $E_0=\text{const}$, for acceleration along the y by a high-power radiation pulse of duration t_0 we obtain

$$u_y^e=\frac{eE_{0y}}{m}t_{ac}\left\{\exp\left(\frac{t_0}{t_{ac}}\right)-1\right\}, \tag{5.10}$$

where the acceleration time is given by Eq. (5.8).

To conclude this section we use Eq. (A1.5) to write down the dependence of the heat released in the plasma, (4.1), on the polarization of the radiation:

$$Q_{IB}=\frac{8\sqrt{2}e^2e_i^2nn_i\Lambda_{ei}}{mv_E\sqrt{1+\rho^2}}\mathbf{K}\left(\sqrt{\frac{2\rho^2}{1+\rho^2}}\right). \tag{5.11}$$

In nearly plane-polarized radiation, when ρ^2 is close to unity, we have

$$\mathbf{K}\left(\sqrt{\frac{2\rho^2}{1+\rho^2}}\right)\approx\frac{1}{4}\ln\left[\frac{32}{1-\rho^2}\right].$$

The resulting large logarithm is similar to that derived in the theory of the absorption of high-power plane polarized radiation[13,15] and shown to depend on the ratio v_T^2/v_E^2. A suitable comparison shows that the approximation (4.3) is applicable in the limit $1-\rho^2\gg v_T^2/v_E^2$. Note that in the case of nearly plane polarization, the plasma heating time is $\sim[\nu(E)\ln(E/E_y)]^{-1}$, substantially longer than the acceleration time (5.8).

6. ANOMALOUS CONDUCTIVITY

We now use Eq. (3.5) to determine the dc conductivity. In doing this we neglect the inertial term. Then this equation gives

$$\mathbf{R}^{ei}=\frac{\partial n\kappa_BT}{\partial\mathbf{r}}-ne\mathbf{E}_{\text{eff}}, \tag{6.1}$$

where

$$\mathbf{E}_{\text{eff}}=\mathbf{E}_0-\frac{e}{4m\omega^2}\frac{\partial|\mathbf{E}|^2}{\partial\mathbf{r}}. \tag{6.2}$$

For the subsequent discussion it is convenient to use the electron–ion collision mean free time tensor τ_{kj}, which is defined by

$$\tau_{kj}\nu_{kl}=\delta_{jl}. \tag{6.3}$$

According to Eq. (5.1) and using the tensor T_{kj} introduced in Appendix 1, we can write

$$\tau_{kj}=\frac{1}{\nu(E)}T_{kj}. \tag{6.4}$$

These formulas allow us to derive the following from Eq. (4.7):

$$mnu_j^e=-\tau_{jk}R_k^{ei}=-\frac{1}{\nu(E)}T_{kj}R_k^{ei}. \tag{6.5}$$

Since the electric current density is $\mathbf{j}=en\mathbf{u}^e$, Eqs. (6.1) and (6.5) imply that

$$j_i=\sigma_{ik}\left[\mathbf{E}_{\text{eff}}-\frac{1}{en}\frac{\partial n\kappa_BT}{\partial\mathbf{r}}\right]_k, \tag{6.6}$$

where the dc conductivity tensor has the form

$$\sigma_{ik}=\frac{e^2n}{m}\tau_{ik}=\frac{e^2n}{m\nu(E)}T_{ik}. \tag{6.7}$$

In the case of circular polarization, the tensor T_{ik} is diagonal with $T_{xx}=T_{yy}=-2$ and $T_{zz}=1$. This means that the com-

ponent σ_{zz} of the conductivity tensor is positive and corresponds to ordinary dissipation. On the other hand, in the plane perpendicular to the beam of radiation heating the plasma, the components of the conductivity tensor are negative. In the case of nearly plane polarization, the components of the tensor T_{ik} are given by Eqs. (A.1.14). In the special case $\varphi_x-\varphi_y=\pi/2$ and $E_y^2 \ll E_x^2$, the conductivity tensor is diagonal with

$$\sigma_{zz}=\frac{e^2 n\pi\sqrt{2}E_y^2}{m\nu(E)E_x^2}=-\sigma_{yy},$$

$$\sigma_{xx}=-\frac{e^2 n\pi\sqrt{2}}{m\nu(E)[\ln(4E/E_y)-1]}. \tag{6.8}$$

Here the components of the conductivity tensor perpendicular to the beam are again negative. The anomaly is especially strong in the direction of the electric field vector of the radiation that is heating the plasma.

Equation (3.5) can also be used in the case of an alternating field

$$E_0(t)=E_0\ \exp(-i\omega_0 t). \tag{6.9}$$

Neglecting the spatial inhomogeneity, when we have $\mathbf{u}^e(t)=\mathbf{u}^e\exp(-i\omega_0 t)$, Eq. (3.5) yields

$$-i\omega_0 u_k^e+\nu(E)N_{kj}u_j^e=\frac{e}{m}E_{0k}. \tag{6.10}$$

In the simplest case, when the tensor N_{kj} is diagonal, we have $j_i=\sigma_{ii}(\omega_0)E_{0i}$. Here no sum is taken over the subscript i and the conductivity at frequency ω_0 is given by

$$\sigma_{ii}(\omega_0)=\frac{e^2 n}{m}\frac{i\omega_0+\nu(E)N_{ii}}{\omega_0^2+[\nu(E)N_{ii}]^2}. \tag{6.11}$$

The negative real conductivities for $N_{ii}<0$ correspond to the possibility of generating and amplifying an alternating electric field under the influence of the high-power radiation that is heating the plasma. This sort of phenomenon has been predicted theoretically[22–24] for a high-frequency alternating field ($\omega_0>\omega_{Le}=\sqrt{4\pi e^2 n/m}$). If we take $\omega_0 \gg \nu(E)N_{ii}$ in Eq. (6.11), then in the special case of circularly polarized radiation we obtain the corresponding result of Ref. 24 on using Eqs. (A2.5).

7. ELECTRON–ELECTRON COLLISIONS AND THERMAL CONDUCTIVITY

We now consider the contribution of electron–electron collisions to the right hand part of Eq. (3.7). The collision integral has the form

$$J_{ee}[F_0,F_0]=\frac{2\pi e^4\Lambda_{ee}}{m^2}\times\frac{\partial}{\partial u_k}\int d\mathbf{u}'\,\frac{(\mathbf{u}-\mathbf{u}')^2\delta_{kj}-(\mathbf{u}-\mathbf{u}')_k(\mathbf{u}-\mathbf{u}')_j}{|\mathbf{u}-\mathbf{u}'|^3}\times\left(\frac{\partial}{\partial u_j}-\frac{\partial}{\partial u_j'}\right)F_0(\mathbf{u})F_0(\mathbf{u}'). \tag{7.1}$$

The effect of the field on the Coulomb logarithm Λ_{ee} can be neglected. Simple calculations[19] give

$$\Delta\mathbf{Q}_{ee}=-\frac{16}{15}\frac{v_T}{l_{ee}}\mathbf{q}, \tag{7.2}$$

where $l_{ee}=m^2v_T^4/\sqrt{\pi}e^4 n\Lambda_{ee}$ is the electron mean free path. Using Eq. (4.14), for the right-hand side of Eq. (3.7) we obtain

$$\left(\Delta\mathbf{Q}_{ee}-\frac{5\kappa_B T}{2m}\mathbf{R}^{ei}+\Delta\mathbf{Q}_{ei}\right)_j=\frac{3\kappa_B T}{m}(\mathbf{R}^{ei})_j-\frac{16}{15}\frac{v_T}{l_{ee}}q_j-\frac{17}{5}\nu_{jk}q_k. \tag{7.3}$$

Thus, the system of equations for the nine-moment approximation (3.4)–(3.7) has been closed. In this article we shall neglect the last term on the right-hand side of Eq. (7.3) since $v_T/l_{ee}\gg|\nu_{jk}|$.

We now determine the thermal conductivity with the aid of Eq. (3.7). To do this, as is customary in the moment approximation, we neglect all terms on the left-hand side of Eq. (3.7) except the last. We then obtain

$$\mathbf{q}=-\frac{75}{32}n\kappa_B v_T l_{ee}\left\{\frac{\partial T}{\partial\mathbf{r}}-\frac{6}{5}\frac{\mathbf{R}^{ei}}{\kappa_B n}\right\}, \tag{7.4}$$

where R^{ei} is given by Eq. (6.1). In the simplest case, where $\mathbf{u}^e=0$, Eq. (7.4) gives Fick's law

$$\mathbf{q}=-\chi\frac{\partial T}{\partial\mathbf{r}}, \tag{7.5}$$

where χ is the thermal conductivity. Equation (7.4) corresponds to the approximation

$$\chi_1=\frac{75}{32}n\kappa_B v_T l_{ee}. \tag{7.6}$$

In the absence of high-power plasma heating radiation, the same nine-moment approximation leads to a thermal conductivity of the form[19]

$$\chi_0=\chi_1\left[1+\frac{13Z}{4\sqrt{2}}\right]^{-1}. \tag{7.7}$$

Thus, applying a high-power radiation field to a plasma with highly charged ions ($Z\gg1$) increases the thermal conductivity by roughly a factor of $2Z$.

The thermal conductivity χ_1 is the same as that calculated by the Hilbert–Chapman–Enskog method in the approximation of a single Sonine–Laguerre polynomial. In the approximation of two polynomials we obtain

$$\chi_2=\frac{375}{128}\frac{\kappa_B v_T^5 m^2}{\sqrt{\pi}e^4\Lambda_{ee}}, \tag{7.8}$$

which exceeds the first approximation by 25%.

8. CONCLUSION

The results on the kinetics of fully ionized plasmas in high-power electromagnetic radiation fields presented in the preceding sections make it possible to obtain the equations

for generalized electron hydrodynamics in the nine-moment approximation. Here we note the consequences of this hydrodynamics. First of all, we discuss the consequences of Eq. (4.11) for the heat released in a plasma by electron–ion collisions. This formula consists, first of all, of a term (4.12) that is similar to that discussed previously for several polarizations of the radiation and which corresponds to ordinary collisional absorption. Second, Eq. (4.11) includes a contribution owing to the presence of an ordered average motion of the electrons. The formal difference between the expression for this contribution and the ordinary expression for a plasma without a high-power radiation field lies in the opposite sign and the factor (1/2) in front of the product $\mathbf{u}^e\mathbf{R}^{ei}$. However, the actual difference is more important, since according to Eqs. (4.7) and (5.1) this expression can be written in the form

$$\frac{1}{2}\,\mathbf{R}^{ei}\mathbf{u}^e=-\frac{1}{2}\,mnu_k^e\nu_{kj}u_j^e=-\frac{1}{2}\,\nu(E)mnu_k^eN_{kj}u_j^e\,. \tag{8.1}$$

The properties of the electron–ion collision tensor are such that, depending on the orientation of the velocity $\mathbf{u}^e$ of the average electron motion relative to the polarization of the radiation, Eq. (8.1) can be either positive or negative. Here, when the quadratic form

$$u_k^e\nu_{kj}u_j^e \tag{8.2}$$

which determines Eq. (8.1) is positive definite, we have a situation corresponding to the ordinary role of collisions as the cause of dissipation. Then the contribution of the heat to Eq. (8.1) is negative. This means that the correction (8.1) to the energy flux (4.12) absorbed by the plasma decreases the total absorbed power. The opposite situation occurs when the quadratic form (8.2) can be nonpositive definite.

An opposite situation of this type is discussed in Section 5. It is shown there that the dependence of the signs of the diagonal elements of the electron–ion collision frequency tensor on the polarization properties of the radiation makes it possible for the electrons to be accelerated collisionally by a high-power high-frequency field. This kind of acceleration leads both to spontaneous and to induced generation of currents by the electric field. During the heating time, in which the thermal velocity of an electron changes from $v_T(0)$ to a value on the order of v_E, the velocity of electrons accelerated as a result of the presence of a quasi-dc electric field can reach a magnitude on the order of $(eE_0/m\nu(E))v_E/v_T(0)$. The possibility of a negative electron–ion collision frequency demonstrated here will show up as a negative dc electrical conductivity for the plasma. In an alternating electric field, a negative real part of the complex electrical conductivity corresponds both to acceleration and to the generation of such a field.[22–24]

As for heat transport,[3)] we have identified some behavior which is important for the practically interesting case of high-power radiation acting on a plasma with a high degree of ionization Z. There, because the high-power radiation suppresses electron–ion collisions and essentially has no effect on electron–electron collisions, the electron thermal conductivity of a plasma in an intense radiation field is higher by a factor of Z.

All the phenomena discussed here can be attributed to a direct nonlinear manifestation of the inverse bremsstrahlung absorption of high-power electromagnetic radiation in the kinetic properties of the plasma.

This work was completed as part of project No. 96-02-17002-a of the Russian Fund for Fundamental Research and partially supported by the Program on Optics and Laser Physics.

APPENDIX I

The heat released in electron–ion collisions and the frictional force are determined by taking the averages, over the period of the field, of the expressions

$$\left\langle\frac{1}{u(t)}\right\rangle \quad\text{and}\quad \left\langle\frac{1}{u^3(t)}\right\rangle\delta_{kj}-\left\langle\frac{u_{Ek}(t)u_{Ej}(t)}{u_E^5(t)}\right\rangle. \tag{A1.1}$$

We shall examine the dependence of these quantities on the polarization of the radiation that is heating the plasma. Write $E=(E_xe^{i\varphi_x},E_ye^{i\varphi_y},0)$, where E_x and E_y are the real amplitudes and the difference $\varphi_x-\varphi_y$ determines the phase shift of the components of the polarized radiation. Then, using the notation $E_x=E\cos\alpha$ and $E_y=E\sin\alpha$, we can write

$$u_E(t)=(u_{Ex}(t),u_{Ey}(t),0),$$

where

$$u_{Ex}(t)=v_E\cos\alpha\,\sin(\omega t-\varphi_x),$$

$$u_{Ey}(t)=v_E\sin\alpha\,\sin(\omega t-\varphi_y),$$

and $v_E^2=(eE/m\omega)^2$. Thus, we can write

$$u_E^2(t)=\frac{1}{2}\,v_E^2\{1-\rho^2\cos(\omega t-2\psi)\}, \tag{A1.2}$$

where

$$\tan 2\psi=\frac{\cos^2\alpha\,\sin 2\varphi_x+\sin^2\alpha\,\sin 2\varphi_y}{\cos^2\alpha\,\cos 2\varphi_x+\sin^2\alpha\,\cos 2\varphi_y},$$

$$\rho^4=1-\sin^2 2\alpha\,\sin^2(\varphi_x-\varphi_y). \tag{A1.3}$$

Using the Fourier series expansion

$$\left(\frac{v_E}{\sqrt{2}u_E(t)}\right)^n=\frac{1}{[1-\rho^2\cos(\omega t-2\psi)]^{n/2}}=A_0^{(n/2)}(\rho^2)+2\sum_{m=1}^{\infty}A_m^{(n/2)}(\rho^2)\cos[2m(\omega t-\psi)]. \tag{A1.4}$$

it is easy to see that Eq. (4.6) is satisfied.

In accordance with the expansion (A1.4), we have

$$\left\langle\frac{1}{u(t)}\right\rangle=\frac{\sqrt{2}}{v_E}\,A_0^{(1/2)}(\rho^2)=\frac{2^{3/2}}{v_E\pi\sqrt{1+\rho^2}}\,\mathbf{K}\left(\sqrt{\frac{2\rho^2}{1+\rho^2}}\right). \tag{A1.5}$$

Here $\mathbf{K}(k)$ is the complete elliptic integral of the first kind (Eq. (8.111.2) of Gradshtein and Ryzhik[25]). Similarly,

$$\left\langle \frac{1}{u_E^3(t)} \right\rangle = \frac{2^{3/2}}{v_E^3} A_0^{(3/2)}(\rho^2) = \frac{2^{3/2} a_0}{v_E^3}$$

$$= \frac{2^{5/2}}{v_E^3 \pi (1-\rho^2)\sqrt{1+\rho^2}} \mathbf{E}\left(\sqrt{\frac{2\rho^2}{1+\rho^2}} \right), \quad \text{(A1.6)}$$

where $\mathbf{E}(k)$ is the complete elliptic integral of the second kind (Eq. (2.574.4) of Gradshtein and Ryzhik[25]). According to the expansion (A.1.4), for the nonzero elements of the tensor $\langle u_{E_k}(t) u_{E_j}(t)/u^5(t) \rangle$ we obtain

$$\left\langle \frac{u_{Ex}^2(t)}{u_E^5(t)} \right\rangle = \frac{2^{3/2}}{v_E^3} (a_1 \cos^2 \alpha + a_2),$$

$$\left\langle \frac{u_{Ey}^2(t)}{u_E^5(t)} \right\rangle = \frac{2^{3/2}}{v_E^3} (a_1 \sin^2 \alpha + a_2),$$

$$\left\langle \frac{u_{Ex}(t) u_{Ey}(t)}{u_E^5(t)} \right\rangle = \frac{2^{3/2}}{v_E^3} a_1 \sin \alpha \cos \alpha \cos(\varphi_x - \varphi_y), \quad \text{(A1.7)}$$

where

$$a_1 = A_0^{(5/2)}(\rho^2) - \frac{1}{\rho^2} A_1^{(5/2)}(\rho^2), \quad a_2 = \frac{1-\rho^4}{2\rho^2} A_1^{(5/2)}(\rho^2). \quad \text{(A1.8)}$$

In these last formulas the coefficients of the expansion (A1.4) have the form

$$A_0^{(5/2)}(\rho^2) = \frac{2}{3\pi(1+\rho^2)^{1/2}(1-\rho^2)} \left\{ \frac{4}{1-\rho^2} \mathbf{E}\left(\sqrt{\frac{2\rho^2}{1+\rho^2}} \right) - \mathbf{K}\left(\sqrt{\frac{2\rho^2}{1+\rho^2}} \right) \right\},$$

$$A_1^{(5/2)}(\rho^2) = \frac{2}{3\pi(1+\rho^2)^{3/2}(1-\rho^2)} \left\{ \frac{1+3\rho^4}{1-\rho^2} \mathbf{E}\left(\sqrt{\frac{2\rho^2}{1+\rho^2}} \right) - \mathbf{K}\left(\sqrt{\frac{2\rho^2}{1+\rho^2}} \right) \right\}.$$

If we denote the tensor (A1.1) by $2^{3/2} v_E^{-3} N_{kj}$, then for the nonzero elements of the tensor N_{kj} we have

$$N_{xx} = a_0 - 3a_2 - 3a_1 \cos^2 \alpha,$$

$$N_{yy} = a_0 - 3a_2 - 3a_1 \sin^2 \alpha,$$

$$N_{xy} = N_{yx} = 3a_1 \sin \alpha \cos \alpha \cos(\varphi_x - \varphi_y), \quad N_{zz} = a_0. \quad \text{(A1.9)}$$

In the special case of circularly polarized radiation, where $\alpha = \pi/4$ and $\varphi_x - \varphi_y = \pi/2$, we have

$$\langle u_E^{-1}(t) \rangle = \sqrt{2}/v_E \quad \text{and} \quad N_{kj} = -\frac{1}{2} [\delta_{kx}\delta_{jx} + \delta_{ky}\delta_{jy}] + \delta_{kz}\delta_{jz}. \quad \text{(A1.10)}$$

Things are a little more complicated in the other limiting case of nearly plane polarization, where ρ^2 is close to unity. Then, in particular, we have

$$A_0^{(1/2)}(\rho^2) \simeq \frac{1}{\pi\sqrt{2}} \ln \frac{32}{1-\rho^2}. \quad \text{(A1.11)}$$

For the quantities determined by the tensor N_{kj} (A1.9), we obtain

$$a_0 = \frac{\sqrt{2}}{\pi} \left\{ \frac{1}{1-\rho^2} + \frac{1}{8} \ln \frac{32}{1-\rho^2} + \frac{1}{8} \right\},$$

$$3a_1 = \frac{\sqrt{2}}{\pi} \left\{ -\frac{1}{1-\rho^2} + \frac{3}{8} \ln \frac{32}{1-\rho^2} + \frac{17}{8} \right\},$$

$$a_0 - 3a_2 = \frac{\sqrt{2}}{\pi} \left\{ -\frac{1}{1-\rho^2} + \frac{1}{8} \ln \frac{32}{1-\rho^2} - \frac{9}{8} \right\}. \quad \text{(A1.12)}$$

In particular, for $\varphi_x - \varphi_y = \pi/2$ and $E_y \ll E_x$, we have $1-\rho^2 = 2\sin^2 \alpha$ and the tensor N_{kj} is diagonal with

$$N_{xx} = -\frac{1}{\pi\sqrt{2}} \left\{ \ln \frac{4}{\sin \alpha} - 1 \right\},$$

$$N_{yy} = -\frac{1}{\pi\sqrt{2}} \left\{ \frac{1}{\sin^2 \alpha} - \frac{1}{2} \ln \frac{4}{\sin \alpha} + \frac{5}{4} \right\},$$

$$N_{zz} = \frac{1}{\pi\sqrt{2}} \left\{ \frac{1}{\sin^2 \alpha} + \frac{1}{2} \ln \frac{4}{\sin \alpha} + \frac{1}{4} \right\}. \quad \text{(A1.13)}$$

For an arbitrary phase difference $\varphi_x - \varphi_y$ but with ρ^2 close to unity, the tensor inverse to N_{kj}, $T_{lj} = (N_{lj})^{-1}$, has the following nonzero elements:

$$T_{xx} = \frac{\pi\sqrt{2}}{d} \left\{ -\cos^2 \alpha + \frac{1}{8}(1-\rho^2) \left[(1 - 3\sin^2 \alpha) \ln \frac{32}{1-\rho^2} - 9 + 17 \sin^2 \alpha \right] \right\},$$

$$T_{yy} = \frac{\pi\sqrt{2}}{d} \left\{ -\sin^2 \alpha + \frac{1}{8}(1-\rho^2) \left[(1 - 3\cos^2 \alpha) \ln \frac{32}{1-\rho^2} - 9 + 17 \cos^2 \alpha \right] \right\},$$

$$T_{zz} = \frac{\pi}{\sqrt{2}} (1-\rho^2). \quad \text{(A1.14)}$$

Note that the relatively small terms in Eqs. (A1.12) determine the expression

$$d = \frac{1}{2} \ln \frac{32}{1-\rho^2} - 1. \quad \text{(A1.15)}$$

which, according to Eq. (6.8), characterizes the large negative component of the dc electrical conductivity tensor.

APPENDIX 2

As a supplement to the main text, here we examine the transition from a relatively weak field, for which $v_E \ll v_T$, to the limit of high-power radiation, for which $v_T \ll v_E$, for the part of the frictional force determined by the ordered motion of the electrons, $\mathbf{u}^e$, in the special case of circular polarized

radiation. We first note that after linearization with respect to the velocity $\mathbf{u}^e$ of the ordered motion, Eq. (3.8) can be written in the form

$$(\mathbf{R}^{ei})_k = -\frac{4\pi e^2 e_i^2 n_i \Lambda_{ei}}{m} \int d\mathbf{v}\, \frac{v_k}{v^3} \frac{n}{(2\pi)^{3/2} v_T^5} \langle (\mathbf{u}^e, \mathbf{v}+\mathbf{u}_E(t)) \rangle. \tag{A2.1}$$

Given that $v_x = v\ \sin\theta \cos\varphi$ and $v_y = v\ \sin\theta \sin\varphi$, in the case of circular polarization we obtain

$$\exp\left\{ -\frac{(\mathbf{v}+\mathbf{u}_E(t))^2}{2v_T^2} \right\} = \exp\left\{ -\frac{v^2}{2v_T^2} - \frac{v_E^2}{4v_T^2} \right\} \exp\left(-\frac{v v_E}{\sqrt{2} v_T^2} \sin\theta \cos(\omega t - \varphi) \right). \tag{A2.2}$$

Using the expansion (Eq. (9.6.34) of Abramowitz and Stegun[26])

$$\exp\left(-\frac{v v_E}{\sqrt{2} v_T^2} \sin\theta \cos(\omega t - \varphi) \right) = I_0\left(\frac{v v_E}{\sqrt{2} v_T^2} \sin\theta \right) + 2 \sum_{n=1}^{\infty} (-1)^n I_n\left(\frac{v v_E}{\sqrt{2} v_T^2} \sin\theta \right) \times \cos(n(\omega t - \varphi)). \tag{A2.3}$$

we obtain

$$\left\langle \exp\left\{ -\frac{[\mathbf{v}+\mathbf{u}_E(t)]^2}{2v_T^2} \right\} (\mathbf{u}^e, \mathbf{v}+\mathbf{u}_E(t)) \right\rangle = \exp\left\{ -\frac{v^2}{2v_T^2} - \frac{v_E^2}{4v_T^2} \right\} \left\{ (\mathbf{u}^e \mathbf{v}) I_0\left(\frac{v v_E}{\sqrt{2} v_T^2} \sin\theta \right) - I_1\left(\frac{v v_E}{\sqrt{2} v_T^2} \sin\theta \right) \frac{v_E}{\sqrt{2}} (u_x^e \cos\varphi + u_y^e \sin\varphi) \right\}. \tag{A2.4}$$

Using Ref. 26 (Eqs. (6.618.4) and (10.2.13)), we have

$$\int_0^\infty dv\ \exp\left(-\frac{v^2}{2v_T^2} \right) I_1\left(\frac{v v_E}{\sqrt{2} v_T^2} \sin\theta \right) = \frac{\sqrt{2} v_T^2}{v_E \sin\theta} \left[\exp\left(\frac{v_E^2 \sin^2\theta}{4 v_T^2} \right) - 1 \right]$$

and finally obtain a diagonal effective collision frequency tensor ν_{kj} with the following elements:[24]

$$\nu_{xx} = \nu_{yy} = \nu(E) F_\perp\left(\frac{v_E}{2 v_T} \right), \quad \nu_{zz} = \nu(E) F_\parallel\left(\frac{v_E}{2 v_T} \right). \tag{A2.5}$$

Here $\nu(E)$ is defined by Eq. (5.2) and

$$F_\perp(x) = \frac{1}{2} \left\{ -\mathrm{erf}(x) + \frac{2}{\sqrt{\pi}} (x + 2x^3) e^{-x^2} \right\}, \tag{A2.6}$$

$$F_\parallel(x) = \mathrm{erf}(x) - \frac{2}{\sqrt{\pi}} x e^{-x^2}, \tag{A2.7}$$

where

$$\mathrm{erf}(x) \equiv \Phi(x) = \frac{2}{\sqrt{\pi}} \int_0^x e^{-t^2} dt$$

is the probability integral.

In the limit $v_E \ll v_T$ we have $F_\perp(x) = F_\parallel(x) = (8/3\sqrt{\pi}) x^3$, which yields the usual[3,4,19] expression for the effective collision frequency,

$$\nu_{xx} = \nu_{yy} = \frac{4\sqrt{2\pi} e^2 e_i^2 n_i \Lambda_{ei}}{3 m^2 v_T^3} = \nu_{zz}.$$

In the opposite case of $v_E \gg v_T$, we have $F_\parallel = 1$ and $F_\perp = -1/2$ and obtain Eq. (5.3).

Equations (A2.5)–(A2.7) describe the transition from the ordinary case of low-intensity radiation to the case of high-power radiation. The signs of the components ν_{xx} and ν_{yy} of the effective collision frequency tensor change at $v_E = 3.02 v_T$.[24]

[1)] Condition (1.5) is satisfied if the energy flux of the radiation, $q_R = cE^2/4\pi$ obeys the condition $\lambda^2 q_R > Z^2 (\pi m c^3/e^2) \kappa_B T$, where λ is the wavelength of the radiation. If the electron temperature is measured in electron volts ($\kappa_B T = \Theta_e$), the wavelength in microns, and the energy flux in W/cm^2, then this condition reduces to $\lambda^2[\mu\mathrm{m}] q_R[\mathrm{W/cm^2}] \geqslant Z^2 \Theta_e[\mathrm{eV}] \cdot 10^{13}$.

[2)] In Eq. (3.7) the repeated subscript s denotes summation.

[3)] We note that the neglect of the nonlocal nature of heat transfer corresponding to our examination of this system is natural, in particular, when the wavelength of the radiation is much greater than the electron mean free path in electron–electron collisions.

[1] G. Mourout and D. Umstadter, Phys. Fluids B **4**, 2315 (1992).
[2] V. P. Silin, Usp. Fiz. Nauk **145**, 225 (1985) [Sov. Phys. Uspekhi **28**, 136 (1985)].
[3] S. I. Braginskii, in: M. A. Leontovich, ed., *Reviews of Plasma Physics*, Vol. 1, Consultants Bureau, NY (1963).
[4] A. F. Alexandrov, L. S. Bogdankevich, and A. A. Rukhadze, *Principles of Plasma Electrodynamics*, Springer–Verlag, Berlin 1984.
[5] A. V. Maksimov, V. P. Silin, and M. V. Chegotov, Fiz. Plazmy **16**, 575 (1990) [Sov. Phys. Plasma Phys. **16**, 331 (1990)].
[6] A. B. Langdon, Phys. Rev. Lett. **44**, 575 (1980).
[7] R. Balescu, J. Plasma Phys. **27**, 553 (1982).
[8] J. P. Matte, M. Lemoureux, C. Moeller, R. Y. Yin, J. Delettrez, J. Virmont, and T. W. Johnston, Plasma Phys. and Contr. Fusion **30**, 1665 (1988).
[9] J. M. Liu, J. S. De Groot, J. P. Matte, T. W. Johnston, and R. P. Drake, Phys. Plasmas **1**, 3570 (1994).
[10] P. Mora and H. Yahi, Phys. Rev. A **26**, 2259 (1982).
[11] V. P. Silin, Zh. Éksp. Teor. Fiz. **108**, 193 (1995) [JETP **81**, 103 (1995)].
[12] S. A. Uryupin, S. Kato, and K. Mima, Phys. Plasmas **2**, 3100 (1995).
[13] V. P. Silin, Zh. Éksp. Teor. Fiz. **47**, 2254 (1964) [Sov. Phys. JETP **20**, 1510 (1965)].
[14] B. N. Chichkov, S. A. Shumsky, and S. A. Uryupin, Phys. Rev. A **45**, 7475 (1992).
[15] C. D. Decker, W. B. Mori, J. M. Dawson, and T. Kattsouleas, Phys. Plasmas **1**, 4043 (1994).
[16] A. Djaoui and A. A. Offenberger, Phys. Rev. E **50**, 4961 (1994).
[17] V. P. Silin and S. A. Uryupin, Zh. Éksp. Teor. Fiz. **81**, 910 (1981). [Sov. Phys. JETP **54**, 485 (1981)].

[18] A. Ya. Polishchuk and J. Meyer-Ter-Vehn, Phys. Rev. E **49**, 663 (1994).
[19] V. P. Silin, *Introduction to the Kinetic Theory of Gases [in Russian]*, Nauka, Moscow (1971).
[20] V. P. Silin, Zh. Éksp. Teor. Fiz. **38**, 1771 (1960) [Sov. Phys. JETP **11**, 1277 (1960)].
[21] V. P. Silin, Zh. Éksp. Teor. Fiz. **41**, 861 (1961) [Sov. Phys. JETP **14**, 617 (1962)].
[22] M. V. Fedorov and R. V. Karapetyan, J. Phys. A **9**, L103 (1976).
[23] R. V. Karapetyan and M. V. Fedorov, Kvant. Elektronika **4**, 2203 (1977) [Sov. J. Quantum Electronics **7**, 1260 (1977)].
[24] B. N. Chichkov and S. A. Uryupin, Phys. Rev. E **48**, 4659 (1993).
[25] I. S. Gradshtein and I. M. Ryzhik, *Table of Integrals, Series, and Products*, Academic Press, NY (1965).
[26] M. Abramowitz and I. Stegun, eds., *Handbook of Mathematical Functions*, National Bureau of Standards, Washington (1965).

Translated by D. H. McNeill

Average-ion model for calculating the state of a multicomponent transient nonequilibrium highly charged ion plasma

S. A. Bel'kov, P. D. Gasparyan, Yu. K. Kochubeĭ, and E. I. Mitrofanov

(Submitted 28 June 1996)
Zh. Éksp. Teor. Fiz. **111**, 496–513 (February 1997)

The ionization kinetics of a transient nonequilibrium highly charged ion plasma are investigated in the average-ion approximation. Approximations of a hydrogenic ion, whose energy levels depend either on the principal quantum number alone or on the principal and orbital angular momentum quantum numbers, are considered as atom models. The results of calculations of various plasma characteristics performed within this model are presented, and a comparison with previously published data, as well as with calculations in the chemical-bond approximation, is performed. It is shown that the average-ion model satisfactorily describes the spectral characteristics of a nonideal plasma. © *1997 American Institute of Physics.*
[S1063-7761(97)00702-6]

1. INTRODUCTION

Investigations of the radiation and thermodynamic properties of a high-temperature highly charged ion plasma are based on separation of the plasma into weakly interacting subsystems, whose kinetics can be described by transfer equations for single-particle distribution functions. In the region of a high-temperature plasma these subsystems are the ion, electron, and photon subsystems. In some cases a plasma can be in a state of partial thermodynamic equilibrium among the components. As the plasma density increases, its degree of nonideality increases, but the time for the establishment of equilibrium between its components simultaneously decreases. Since the time for the establishment of equilibrium in the photon subsystem has the largest value, numerous problems are described quite accurately by an approximation in which the deviation of only the photon subsystem from equilibrium is taken into account (the local thermodynamic equilibrium approximation). One special feature of a nonequilibrium high-temperature highly charged ion plasma is the role of radiation processes in the plasma kinetics, which increases relative to that of collisional processes as Z increases. This is why for small plasma dimensions and large values of Z, a deviation of the photon subsystem from equilibrium causes the electron subsystem to deviate from equilibrium at very high (up to solid-state) densities of a high-temperature highly charged ion plasma, at which the plasma is very nonideal. A nonideal high-temperature highly charged ion plasma forms in experiments devised to investigate targets for laser thermonuclear fusion and inertial confinement fusion, in experiments set up to investigate the interaction of ultrashort powerful pulses of laser radiation with solids, etc. A description of the state of such a plasma with consideration of its gas-dynamic motion and energy transfer is possible only within a kinetic approach.

2. EQUATIONS OF IONIZATION KINETICS IN THE AVERAGE-ION APPROXIMATION

A detailed description of a multicomponent highly charged ion plasma requires determination of the concentration distribution of a large number of states of the ions, which are characterized not only by their charge, but also by the configuration of occupation numbers of the electronic orbitals of each ion in an assigned state, at each moment in time. A large system of kinetic equations describing the transitions among all possible states of the ions must be solved. Such a description of a plasma is called the chemical-bond model.[1] However, the feasibility of taking into account the ionization kinetics in the chemical-bond approximation in radiation gas-dynamic programs, especially two-dimensional and three-dimensional ones, is very limited, since a large number of kinetic equations must be solved at each moment in time and at each point in space. The number of equations increases rapidly when we move to the description of a plasma with a large value of Z ($Z>10$), and can reach hundreds and even thousands.

Assuming that the charge of an ion varies continuously, we can replace a set of ions in different charge states by one ion in some average charge state. The state of such an average ion is described completely by assigning the occupation numbers of the ion's various electronic orbitals, which can also vary continuously. In this case the complete system of equations of the ionization kinetics of a plasma in the average-ion approximation can be reduced to the equations describing the kinetics of the average populations of the electronic states:[2,3]

$$\begin{aligned}\frac{d}{dt}(P_\xi N)=&R_\xi N_e N Q_\xi - I_\xi N_e N P_\xi + N\\ &\times\left[\sum_{\substack{\xi'\\(E_{\xi'}>E_\xi)}} A_{\xi'\xi}P_{\xi'}Q_\xi - \sum_{\substack{\xi'\\(E_{\xi'}<E_\xi)}} A_{\xi\xi'}P_\xi Q_{\xi'}\right]\\ &+NN_e\left[\sum_{\substack{\xi'\\(E_{\xi'}>E_\xi)}} C^D_{\xi'\xi}P_{\xi'}Q_\xi - \sum_{\substack{\xi'\\(E_{\xi'}<E_\xi)}} C^D_{\xi\xi'}P_\xi Q_{\xi'}\right]\\ &+NN_e\left[\sum_{\substack{\xi'\\(E_{\xi'}<E_\xi)}} C^U_{\xi'\xi}P_{\xi'}Q_\xi - \sum_{\substack{\xi'\\(E_{\xi'}>E_\xi)}} C^U_{\xi\xi'}P_\xi Q_{\xi'}\right],\end{aligned} \tag{1}$$

where P_ξ is the average population of the electronic orbital

of the ion characterized by the quantum numbers ξ. In the average-ion model without consideration of the distribution over orbital angular moment, ξ is specified by the principal quantum number n, and in the model that takes into account the distribution over orbital angular momentum it is specified by the pair of quantum numbers (n,l). In addition, in (1) $Q_\xi = 1 - P_\xi / g_\xi$ is the number of vacancies in state ξ, g_ξ is the statistical weight of state ξ, $N = \rho N_A / A$ is the ion density, ρ is the plasma density, A is the atomic weight of the ion, N_A is Avogadro's number,

$$N_e = N\langle Z\rangle = N\left[Z_0 - \sum_\xi P_\xi\right]$$

is the free electron density, $\langle Z\rangle$ is the charge of the average ion, Z_0 is the nuclear charge, I_ξ and R_ξ are, respectively, the ionization and recombination rate coefficients in state ξ, and $A_{\xi'\xi}$, $C^D_{\xi'\xi}$ and $C^U_{\xi'\xi}$ are the rates of the transitions between the states (ξ',ξ) as a result of spontaneous radiative decay, impact quenching, and excitation processes.

The rate constants of the atomic processes appearing on the right-hand side of the system of equations (1) are functions of the temperature and the plasma density, as well as the binding energies of electrons in state ξ, in the general case. The binding energies, in turn, depend on the populations of the levels and the ion density (so-called pressure ionization). Thus, an atom model that makes it possible to calculate the binding energy of an electron in state ξ from the known values of the populations of all the states must be employed to close the system of equations (1).

The simplest models of an atom are various versions of the Slater model.[4] However, all of these models have one serious drawback: they faithfully describe the states of an isolated free ion, but are inapplicable to a fairly dense plasma, where the influence of adjacent ions can no longer be neglected and their presence can significantly alter both the energies of bound states of a particular ion and the statistical weight of each state.

Self-consistent-field models of the Hartree–Fock type[5] make it possible to take the influence of the surroundings into account, but their application in practice entails enormous additional computational expenditures, which are unacceptable when the necessary kinetic calculations are performed together with gas-dynamic calculations of plasma flow.

It was suggested in Ref. 2 that the dependence of the statistical weight of a state on the plasma density should be introduced in such a manner that the statistical weight of the state of an isolated ion would be obtained at low densities, and would tend to zero at high densities. This simulates removal of the degeneracy of state ξ due to its interaction with the surrounding ions (for example, due to Stark splitting of the level), as a result of which some of the bound states move into the continuum. The simplest function having these properties is a function of the form

$$g_\xi = \frac{g^0_\xi}{1 + a(R^0_\xi / R_0)^b}, \tag{2}$$

where $R_0 = (3A/4\pi\rho N_A)^{1/3}$ is the mean distance between ions in the plasma, and R^0_ξ and g^0_ξ are the effective radius of the orbital and the statistical weight of level ξ of an isolated ion.

When a function like (2) is chosen and the effective radius of the orbital is properly determined, highly excited states disappear first as the plasma density increases. The dependence of the extent of ionization $\langle Z\rangle$ of the cold substance on the density ρ then has the form

$$\langle Z\rangle = \sum_\xi P^0_\xi \left(1 - \frac{g_\xi}{g^0_\xi}\right), \tag{3}$$

where the P^0_ξ are the populations of the levels of a neutral isolated $(\rho = 0)$ atom.

The parameters a and b can be found from the condition that the dependence of the extent of ionization of the cold substance on the density obtained, for example, within the Thomas–Fermi model,[6] is most closely approximated by Eq. (3). The specific values of the constants a and b depend on the atom model and will be presented below.

An equation of the ionization kinetics of the form (1) does not contain terms that describe photoionization and photoexcitation processes, which are the reverse processes of photorecombination and radiative decay. Such a model, in which only collisional processes (collisional ionization and recombination, as well as collisional excitation and quenching) and radiation processes (photorecombination and radiative decay) are taken into account, is called the collisional–radiative model. It describes an optically thin plasma, in which the radiation density is low, and therefore photoionization and photoexcitation can be neglected. The stationary solution obtained within the collisional–radiative model does not correspond to thermodynamic equilibrium in the general case, since not all the direct processes are balanced by reverse processes. However, at high densities, where collisional processes are dominant, the stationary solution of the collisional–radiative model should proceed to thermodynamic equilibrium. At low densities, three-particle recombination processes can be neglected, and the collisional–radiative approximation transforms into the so-called coronal approximation.

3. ION MODEL NEGLECTING SPLITTING WITH RESPECT TO THE ORBITAL ANGULAR MOMENTUM QUANTUM NUMBER (H MODEL)

The simplest ion model that permits determination of the energy levels of the bound states is the model proposed in Ref. 7. In this model the state of the ion is determined by the occupation numbers of orbitals with different values of the principal quantum number n. States with identical principal quantum numbers but different orbital angular momenta are assumed to be degenerate (hence it is called the hydrogenic (H) atom model).

Let there be P_n electrons in the state with principal quantum number n. Then the effective nuclear charge, which determines the Coulomb interaction of an electron in an orbital with quantum number n, is calculated with consider-

TABLE I. Coefficients of the screening matrix σ_{nm}.

	n									
m	1	2	3	4	5	6	7	8	9	10
1	0.3125	0.9380	0.9840	0.9954	0.9980	0.9990	0.9995	0.9999	0.9999	0.9999
2	0.2345	0.6038	0.9040	0.9722	0.9880	0.9979	0.9985	0.9990	0.9999	0.9999
3	0.1093	0.4018	0.6800	0.9155	0.9796	0.9820	0.9860	0.9900	0.9920	0.9999
4	0.0622	0.2430	0.5150	0.7100	0.9200	0.9600	0.9750	0.9830	0.9860	0.9900
5	0.0399	0.1381	0.3527	0.5888	0.7320	0.8300	0.9000	0.9500	0.9700	0.9800
6	0.0277	0.1109	0.2455	0.4267	0.5764	0.7248	0.8300	0.9000	0.9500	0.9700
7	0.0204	0.0808	0.1811	0.3184	0.4592	0.6098	0.7374	0.8300	0.9000	0.9500
8	0.0156	0.0624	0.1392	0.2457	0.3711	0.5062	0.6355	0.7441	0.8300	0.9000
9	0.0123	0.0493	0.1102	0.1948	0.2994	0.4222	0.5444	0.6558	0.7553	0.8300
10	0.0100	0.0400	0.0900	0.1584	0.2450	0.3492	0.4655	0.5760	0.6723	0.7612

ation of its screening by the inner electrons (relative to the electron under consideration) from the formula

$$Z_n = Z_0 - \sum_{m \leqslant n} P_m \sigma_{nm} \left(1 - \frac{1}{2} \delta_{nm} \right), \tag{4}$$

where σ_{nm} is the matrix of screening constants, which was first proposed in Ref. 7 and whose coefficients are presented in Table I.

The total energy of an ion is calculated from the formula[7]

$$E = -\sum_m \frac{P_m Z_m^2}{m^2} I_{\mathrm{H}}, \tag{5}$$

where $I_{\mathrm{H}} = e^2/2a_0$ is the ionization potential of the hydrogen atom and a_0 is the Bohr radius.

The binding energy for a level is found by differentiating (5) with respect to the population P_n:

$$E_n^0 = \frac{\partial E}{\partial P_n} = I_{\mathrm{H}} \left[-\frac{Z_n^2}{n^2} + \sum_{m \geqslant n} 2 P_m \frac{Z_m}{m^2} \sigma_{nm} \left(1 - \frac{1}{2} \delta_{nm} \right) \right]. \tag{6}$$

The radius of an orbital is calculated from the familiar expression for the radius of an orbital in the hydrogen atom:

$$R_n^0 = a_0 n^2 / Z_n. \tag{7}$$

The constants in (2), accordingly, have the values $a = 3.5$ and $b = 1.75$.

In the general case of a dense plasma, lowering of the ionization potential of the orbital due to the influence of the Coulomb fields of the surrounding ions occurs in addition to the removal of the degeneracy, so that Eq. (6) can be written in the form $E_n = E_n^0 + \Delta E$, where $\Delta E = e^2 \langle Z \rangle / 2R_0$ is the displacement of the level due to pressure ionization.[2]

4. ION MODEL WITH CONSIDERATION OF THE SPLITTING WITH RESPECT TO THE ORBITAL ANGULAR MOMENTUM QUANTUM NUMBER (*L* MODEL)

A further development of the simple hydrogenic-ion model takes into account the l splitting of the levels (we call it the L model). According to this model, the effective nuclear charge Z_n in the nth orbital of an atom is written with consideration of the screening by the inner electrons in the form[8]

$$Z_n = Z_0 - \sum_{m \leqslant n} P_m \sigma_{nm} \left(1 - \frac{1}{2} \delta_{nm} \right) + \sum_m P_m q_{mn} \sum_{l=0}^{n-1} \frac{P_{nl}}{P_n} G_{nl}, \quad P_m = \sum_{l'=0}^{m-1} P_{ml'}.$$

The values of v_n and q_{nn} are presented in Table II, and the values of q_{nm} and G_{nl} are calculated using the formulas

$$q_{nm} = \begin{cases} \dfrac{1}{\pi} \left(\dfrac{m}{n} \right)^5 \left[2 - \left(\dfrac{m}{n} \right)^2 \right]^{1/2}, & 2n^2 > m^2, \\ 0, & 2n^2 \leqslant m^2, \end{cases}$$

$$G_{nl} = \frac{1}{4n^2} [n^2 - 2l(l+1) - 1] + v_n.$$

The total energy of the ion is calculated just as in the H model from Eq. (5). Then the energy levels E_{nl} are calculated from the formula

$$E_{nl} = E_n^0 - 2I_{\mathrm{H}} \left[\sum_m P_m (q_{nm} S_m - q_{mn} S_n) + \frac{Z_n}{n^2} G_{nl} \sum_m P_m q_{mn} \right] + \Delta E,$$

where

$$S_n = \frac{Z_n}{n^2} \sum_{l=0}^{n-1} \frac{P_{nl}}{P_n} G_{nl},$$

TABLE II. Numerical values of the constants q_{nn} and v_n used in the L model.

n	q_{nn}	v_n
1	0.270672	0.000
2	0.366310	0.070
3	0.371802	0.020
4	0.329523	0.012
5	0.295072	−0.100
6	0.296580	−0.400
7	0.320910	−0.420
8	$1/\pi$	0
9	$1/\pi$	0
10	$1/\pi$	0

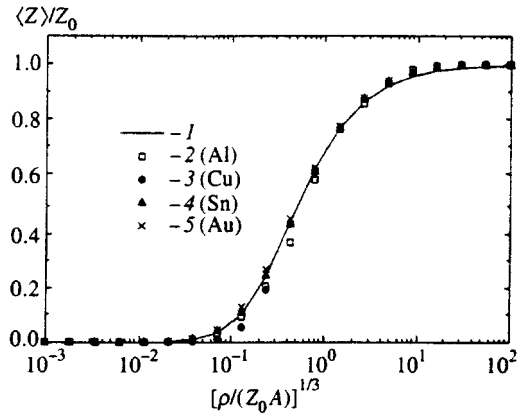

FIG. 1. Dependence of the extent of ionization of the cold substance on the density: *1* — the Thomas–Fermi model, *2–5* — calculation using Eq. (3) with $a=12.0$ and $b=2.7$ for Al, Cu, Sn, and Au.

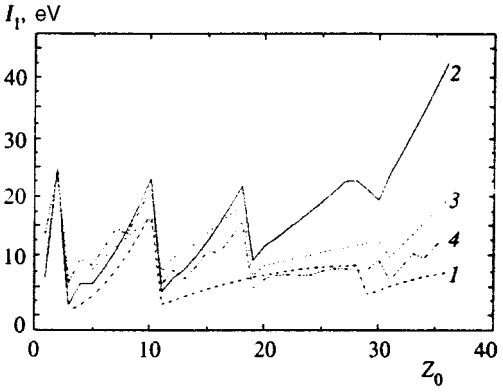

FIG. 2. Ionization potentials I_1 of neutral ions calculated on the basis of the H model (curve *1*), the L model (curve *2*), and the model in Ref. 10 (curve *3*); *4* — experimental curve.

and E_n^0 is the energy of the level neglecting l splitting (6).

This model was used in Ref. 9 to calculate the characteristics of a plasma in the local thermodynamic equilibrium approximation. However, the expression proposed in Ref. 9 for the radius of an orbital in the nl subshell is inconsistent when the statistical weight in (2) is calculated, since it causes the orbitals with small l, which are more symmetric and have larger binding energies, to begin to disappear first as the plasma density increases. The use of the mean dipole interaction radius $R_{nl}\sim\langle 1/r^2\rangle^{-1/2}$, rather than the mean distance between an electron and the nucleus $R_{nl}\sim\langle r\rangle$ (Ref. 9) is more easily justified. Thus, orbitals with large l have an effectively larger radius, or, more specifically,

$$R_{nl}=\frac{a_0 n^{3/2}}{Z_n}\sqrt{l+\frac{1}{2}}. \tag{8}$$

The use of (8) instead of (7) in (2) results in alteration of the values of the constants: $a=12.0$, $b=2.7$. Figure 1 presents the dependence of the mean extent of ionization for aluminum, copper, tin, and gold on the density of the cold ($T=0$) plasma for the constants just presented, and compares them with the results for the Thomas–Fermi model.

A somewhat different atom model which takes into account l was considered in Ref. 10. Faussurier, Blancard, and Decoster[10] proposed using an expression similar to (4) with replacement of the screening matrix σ_{mn} by a matrix which depends not only on the principal quantum number, but also on the orbital angular momentum quantum number to calculate the screened nuclear charge. Unfortunately, complete testing of this model over a broad range of nuclear charges was not possible, since the new screening matrix was specified only for values of n not exceeding 4.

Figure 2 presents the first ionization potentials of elements with the nuclear charges $Z_0=1,\ldots,36$ calculated using the H and L models, as well as the matrix in Ref. 10. The figure also presents an experimental curve.[11] As seen from the figure, the L model greatly overestimates the first ionization potentials for elements with $Z_0\geqslant 20$. However, there are classes of problems (for example, the interaction of laser radiation with matter), in which the range of temperatures and densities is such that the plasma is ionized sufficiently strongly. In this case the decisive role in the calculation, for example, of the spectral characteristics of the plasma, is played by the higher ionization potentials, rather than the first. Figure 3 presents the dependence of the ionization potential of copper on the extent of ionization calculated using the models described here, as well as the experimental values from Ref. 11. As a whole, both models agree well with the literature data. Consideration of the l splitting produces additional jumps in the ionization potentials, which appear upon passage from one ionized subshell to another.

5. RATE CONSTANTS OF ATOMIC PROCESSES

There are presently a multitude of expressions for the collisional ionization rate constant. The approximations proposed in Refs. 12–16 are the most widely used. They can all be written in the form

$$I_\xi=CT^{-3/2}\,\frac{\exp(-u)}{u^\zeta}F(u,Z_n), \tag{9}$$

where $u=-E_\xi/T$ and T is the electron temperature. The constants ζ and C, as well as the function $F(u,Z_n)$, are presented in Table III.

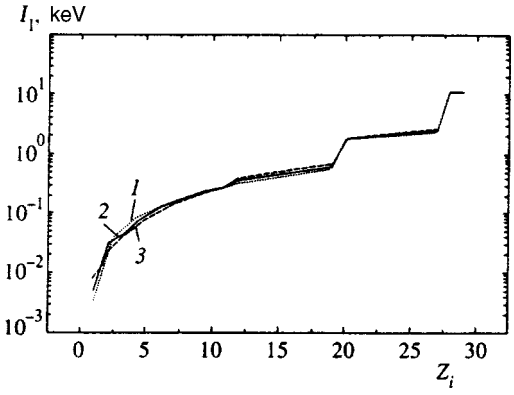

FIG. 3. Dependence of the ionization potential I_Z of copper on the extent of ionization Z_i: curves *1* and *2* are the results of calculations based on the H and L models, and curve *3* was constructed on the basis of data from Ref. 11.

TABLE III. The parameters C and ζ and the function $F(u,Z_n)$ appearing in the approximating formula (9) for the collisional ionization rate constant.

No.	Source	C, $\mathrm{cm^3 s^{-1} keV^{1.5}}$	ζ	$F(u,Z_n)$
1	Ref. 12	3.44×10^{-11}	2	$12.18[1-\exp(-u)](1+0.0335n)\times(1-0.622/Z_n-0.0745/Z_n^2)\lvert f(y)\rvert$, $y=0.25\ln u$, $f(y)=0.23+0.46y+0.1074y^2-0.045y^3-0.01505y^4$
2	Ref. 13	9.516×10^{-11}	1	$E_1(u)\exp u$
3	Ref. 14	6.82×10^{-11}	2	1
4	Ref. 15	7.399×10^{-12}	7/4	1
5	Ref. 16	3.92×10^{-11}	2	$0.915(1+0.64/u)^{-2}+0.42(1+0.5/u)^{-2}$

Note: $E_1(u)=\int_u^\infty e^{-t}\frac{dt}{t}$ is an exponential integral.

Two processes, namely three-particle recombination and photorecombination, were taken into account in the recombination rate constant:

$$R_\xi = R_\xi^{3b} + R_\xi^R .$$

The rate R_ξ^{3b} of three-particle recombination to state ξ is calculated from the principle of detailed balance:

$$R_\xi^{3b} = \frac{1}{2}\left(\frac{2\pi\hbar^2}{m_e T}\right)^{3/2} N_e \exp(u) g_\xi I_\xi .$$

The rate R_ξ^R of the photorecombination of electrons to state ξ is given by the expression

$$R_\xi^R = \frac{8\sqrt{2\pi}\, e^{10} g_\xi Z_n^4}{3\sqrt{3m_e}\,\hbar^3 c^3 n^5 T^{3/2}} \exp(u) E_1(u),$$

where

$$E_1(u) = \int_u^\infty e^{-t}\frac{dt}{t}$$

is the exponential integral.

The rate of spontaneous radiative decay from state ξ' to state ξ was calculated from the formula[17]

$$A_{\xi',\xi} = \frac{2e^2}{m_e c^3 \hbar^2}(E_{\xi',\xi})^2\left(\frac{g_\xi}{g_{\xi'}}\right) f_{\xi,\xi'}, \quad l' = l \pm 1,$$

where $E_{\xi',\xi}=E_{\xi'}-E_\xi$ is the transition energy and $f_{\xi,\xi'}$ is the oscillator strength for the transition under consideration.

In the H model we calculated the oscillator strengths using the expression obtained for transitions between levels with the principal quantum numbers m and n of a hydrogenic ion:[2]

$$f_{nm} = 1.96\,\frac{Z_n^4 Z_m^2}{n^5 m^3 E_{\xi',\xi}^3}.$$

In the L model the oscillator strength of the transition from level nl to level ml' was calculated using the formula[18]

$$f_{nl,ml'} = \frac{1}{3}\,\frac{\max(l,l')}{2l+1}\,\frac{E_{\xi',\xi}}{I_\mathrm{H}}\left(\frac{\mathscr{R}_{nl}^{ml'}}{a_0}\right)^2,$$

$$\mathscr{R}_{nl}^{ml'} = \int_0^\infty R_{nl}(r) R_{ml'}(r) r^3 dr,$$

where $R_{nl}(r)$ is the radial part of the wave function of an electron in the Coulomb field of a nucleus with the charge Z_n. The analytic expression for $\mathscr{R}_{nl}^{ml'}$ can be found in Ref. 6.

The formulas for the rate constants of collisional excitation from level nl to level ml' has the form[17]

$$C_{\xi,\xi'}^U = 24\pi\,\frac{\hbar^4}{m_e^2 e^4}\left(\frac{I_\mathrm{H}}{E_{\xi',\xi}}\right)^2 f_{\xi,\xi'}\sqrt{\frac{2T}{\pi m_e}}\beta_{\xi',\xi} \times \exp(-\beta_{\xi',\xi})\Gamma_{\xi,\xi'},$$

where $\beta_{\xi',\xi}=E_{\xi',\xi}/T$, and

$$\Gamma_{\xi,\xi'} = 0.19\left\{1+0.9\,\exp(\beta_{\xi',\xi})E_1(\beta_{\xi',\xi}) \times\left[1+\frac{m(m-n)}{20}\left(1+\beta_{\xi',\xi}\left\{1-\frac{2}{Z}\right\}\right)\right]\right\}$$

is the Gaunt factor.[2]

The transition rate from excited state ξ' to state ξ in an impact quenching process is found from the principle of detailed balance:

$$C_{\xi',\xi}^D = C_{\xi,\xi'}^U \frac{g_\xi}{g_{\xi'}}\,\exp(\beta_{\xi',\xi}).$$

6. CALCULATION RESULTS

The model of ionization kinetics described above was investigated numerically over a broad range of plasma temperatures and densities and was used to calculate the spectral characteristics. The system of differential equations (1) was solved by the implicit Euler method, and at each time step the system of algebraic equations obtained was solved by Newton's method.[19]

We performed comparative calculations using the H and L average-ion models for various plasma compositions, temperatures, and densities. The collisional ionization rate was calculated using constants No. 2 in Table III. Figure 4 presents the mean charge of an aluminum plasma at $T=100$ eV versus the density for the stationary solution of Eqs. (1). The calculations were performed both in the local thermodynamic equilibrium approximation (curves *2*), in which only the collisional processes were taken into account in Eqs. (1), and in the collisional–radiative approximation (curve *1*). As

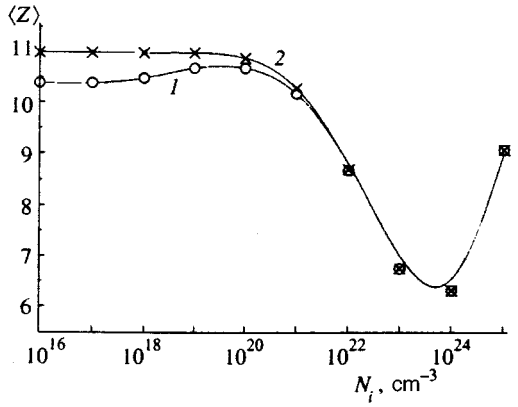

FIG. 4. Dependence of the extent of ionization of an Al plasma at $T=100$ eV on the density for the average-ion model without consideration of the l splitting (solid curves) and with consideration of the l splitting (points): *1* — collisional–radiative approximation; *2* — local thermodynamic equilibrium approximation.

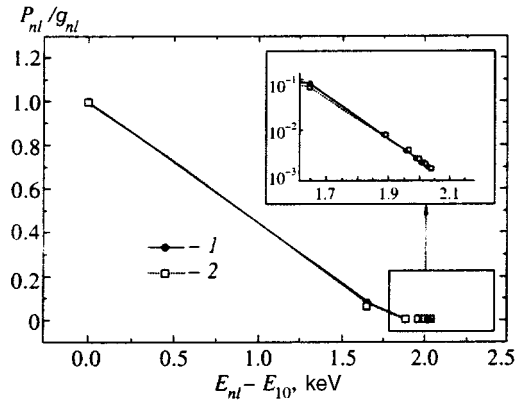

FIG. 6. Dependence of the occupation numbers of the levels on their binding energy in the average-ion model with consideration of the l splitting for an Al plasma with an electron temperature $T=100$ eV and a density $N_i=10^{21}$ cm^{-3}: *1* — collisional–radiative approximation; *2* — local thermodynamic equilibrium approximation.

seen from this figure, the differences between the plots of the mean charge for the two average-ion models are very small and do not exceed fractions of a percent. The calculations in the local thermodynamic equilibrium approximation at low densities give higher values of the mean charge than do the calculations in the collisional–radiative approximation. As the density increases, the collisional–radiative approximation goes over to the local thermodynamic equilibrium approximation, as was postulated. At ion densities $N_i>10^{21}$ cm^{-3}, the two approximations give essentially identical solutions not only for the mean charge, but also for the populations.

Figures 5 and 6 show plots of the occupation numbers P_{nl}/g_{nl} of level nl versus the energy of the level for two density values. At the low density the collisional–radiative approximation gives an occupation number distribution that differs significantly from the Boltzmann distribution. The states closer to the ground state are more populated, while the highly excited states are depleted. At the density corresponding to the merging of the two curves in Fig. 4 the populations also coincide.

Figures 7 and 8 show plots of the temperature dependence of the mean charge of Al and Ag plasmas calculated in the average-ion approximation and the chemical-bond model at various densities. About 150 different ion states were taken into account in the calculations based on the chemical-bond model. Pressure ionization was not taken into account, and this is possibly the reason for the discrepancy between the results at 10 g/cm^3. As a whole, satisfactory agreement between the temperature dependences obtained using the different models of the kinetics is observed.

The influence of the various processes taken into account in the ionization kinetics on the mean charge was studied in an aluminum plasma at a temperature of 0.1 keV. Figure 9 presents the mean charge versus the density for the stationary solution of Eqs. (1) when different processes were disregarded in the calculation of the right-hand side.

It is seen from a comparison of curves *2* and *3* that the influence of the collisional excitation and collisional quenching processes becomes significant at 10^{-6}–10^{-5} g/cm^3. Ow-

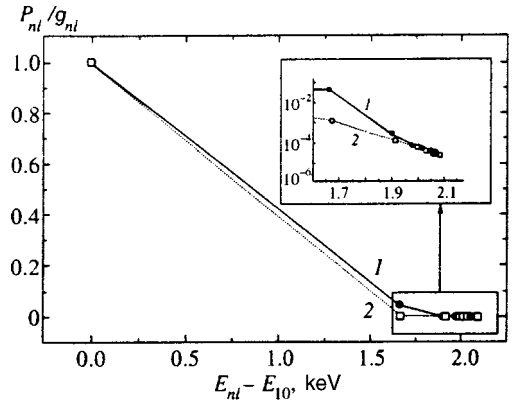

FIG. 5. Dependence of the occupation numbers of the levels on their binding energy in the average-ion model with consideration of the l splitting for an Al plasma with an electron temperature $T=100$ eV and a density $N_i=10^{19}$ cm^{-3}: *1* — collisional–radiative approximation; *2* — local thermodynamic equilibrium approximation.

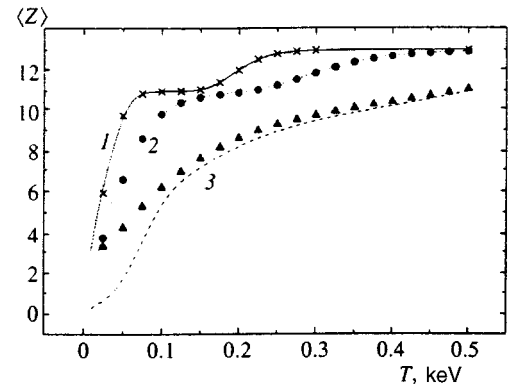

FIG. 7. Dependence of the mean charge of an Al plasma on the temperature T: calculations performed using the chemical-bond model (lines) and in the average-ion approximation (points) for densities equal to 10^{-3} (*1*), 10^{-1} (*2*), and 10 g/cm^3 (*3*).

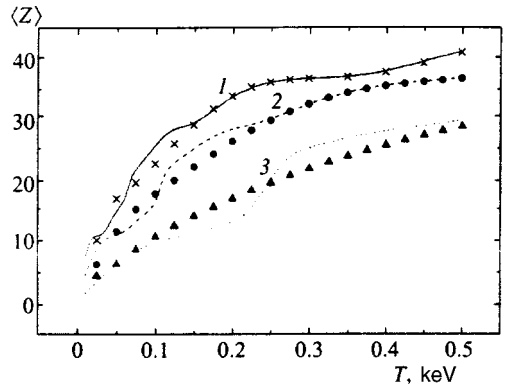

FIG. 8. Dependence of the mean charge of a Ag plasma on the temperature T: calculations performed using the chemical-bond model (lines) and in the average-ion approximation (points) for densities equal to 10^{-3} (*1*), 10^{-1} (*2*), and 10 g/cm^3 (*3*).

ing to the occurrence of cascade ionization processes, they cause an increase in the mean charge (curve *2*) as the density increases in the range 10^{-6}–10^{-3} g/cm^3. At densities greater than 10^{-3} g/cm^3, three-particle recombination becomes the dominant process, and the mean charge begins to decrease. Curves *1*, *2*, and *4* show that radiative decay prevents the establishment of equilibrium (curve *1* essentially coincides with curve *4* by the time the density is 10^{-6} g/cm^3, and curve *2* does so only at a density of 10^{-1} g/cm^3).

7. CALCULATION OF THE SPECTRAL EMISSION AND ABSORPTION COEFFICIENTS

The expressions for the spectral coefficients for the bremsstrahlung and photoabsorption of quanta with the energy $\varepsilon_\nu = 2\pi\hbar\nu$ have the form[17]

$$k_\nu^{ff} = \frac{16\pi^2}{3}\sqrt{\frac{2\pi}{3m_eT}}\,\frac{e^6\hbar^2N_A^2\rho^2\langle Z\rangle^3}{cm_eA^2\varepsilon_\nu^3},$$

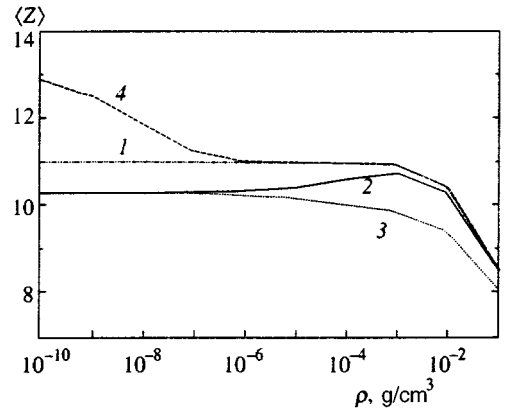

FIG. 9. Dependence of the mean charge of an Al plasma at $T=100$ eV on the density for the stationary solution of Eqs. (1) when the following processes were taken into account on the right-hand side of these equations: *1* — collisional ionization, three-particle recombination, photorecombination, collisional excitation, and collisional quenching; *2* — collisional ionization, three-particle recombination, photorecombination, collisional excitation, collisional quenching, and radiative decay; *3* — collisional ionization, three-particle recombination, photorecombination, and radiative decay. Curve *4* was obtained in the local thermodynamic equilibrium approximation.

$$k_\nu^{bf} = \frac{32\pi}{3\sqrt{3}}\,\frac{e^2\hbar N_A\rho}{m_ecA\varepsilon_\nu^3}\sum_\xi P_\xi\frac{I_{\rm H}^2Z_n^4}{n^5}\theta(\varepsilon_\nu-|E_\xi|),$$

$$\theta(x)=\begin{cases}1, & x\geqslant 0,\\ 0, & x<0.\end{cases}$$

The line absorption coefficient is given by the expression[2]

$$k_\nu^{{\rm abs},bb} = \frac{2\pi^2\hbar e^2N_A\rho}{m_ecA}\times\sum_{\xi'}\sum_\xi P_\xi\left(1-\frac{g_\xi P_{\xi'}}{g_{\xi'}P_\xi}\right)f_{\xi,\xi'}\psi_{\xi,\xi'}\delta_{l,l'\pm1},$$

where $\psi_{\xi,\xi'}$ is the line profile.

The total spectral absorption coefficient with consideration of the induced emission equals

$$k_\nu^{\rm abs} = (k_\nu^{ff}+k_\nu^{bf})\left[1-\exp\left(-\frac{\varepsilon_\nu}{T}\right)\right]+k_\nu^{{\rm abs},bb}.$$

For the emission coefficient in a line and the recombination emission coefficient we used the expressions

$$k_\nu^{{\rm em},bb} = \frac{2\pi^2\hbar e^2N_A\rho[\exp(\varepsilon_\nu/T)-1]}{m_ecA\varepsilon_\nu^3}\sum_\xi\sum_{\xi'}(g_\xi-P_\xi)\times(E_{\xi'}-E_\xi)^3\frac{P_{\xi'}}{g_{\xi'}}f_{\xi,\xi'}\psi_{\xi,\xi'}\delta_{l,l\pm1},$$

$$k_\nu^{fb} = \frac{8\pi^2\sqrt{2\pi}}{3\sqrt{3m_e}}\,\frac{e^{10}N_A^2\rho^2\langle Z\rangle}{T^{3/2}cA^2\varepsilon_\nu^3}\times\sum_\xi(g_\xi-P_\xi)\exp\left(\frac{E_\xi}{T}\right)\frac{Z_n^4}{n^5}\theta(\varepsilon_\nu-|E_\xi|).$$

The total spectral emission coefficient equals

$$k_\nu^{\rm em} = (k_\nu^{ff}+k_\nu^{fb})\left[1-\exp\left(-\frac{\varepsilon_\nu}{T}\right)\right]+k_\nu^{{\rm em},bb}.$$

The spectral emission coefficient thus determined is related to the spectral radiated power J_ν per unit volume of the substance by

$$J_\nu = ck_\nu^{\rm em}U_\nu^{\rm Pl},$$

where

$$U_\nu^{\rm Pl} = \frac{\varepsilon_\nu^3}{\pi^2\hbar^3c^3}\,\frac{1}{\exp(\varepsilon_\nu/T)-1}$$

is the Planck distribution.

Figure 10 presents the results of calculations of the spectral absorption coefficients for aluminum at a temperature $T=0.01$ keV and density $\rho=2.7$ g/cm^3. The spectral absorption coefficients of cold dense aluminum obtained in Ref. 20 are presented for comparison. Close agreement between the results is observed over the entire portion of the spectrum where the calculations were performed (10 eV$<\varepsilon_\nu<$30 keV).

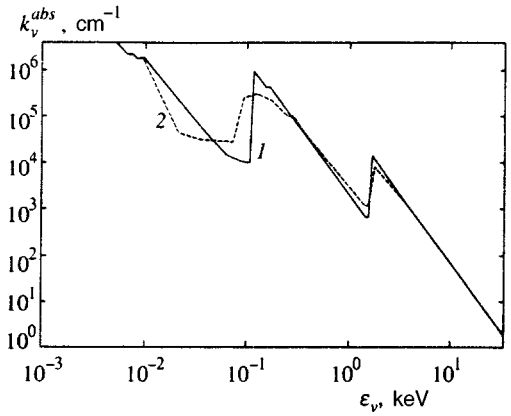

FIG. 10. Spectral absorption coefficients $k_\nu^{\rm abs}$ in cold dense aluminum (curve *1* was constructed on the basis of calculations in the average-ion approximation, and curve *2* was constructed on the basis of data from Ref. 20).

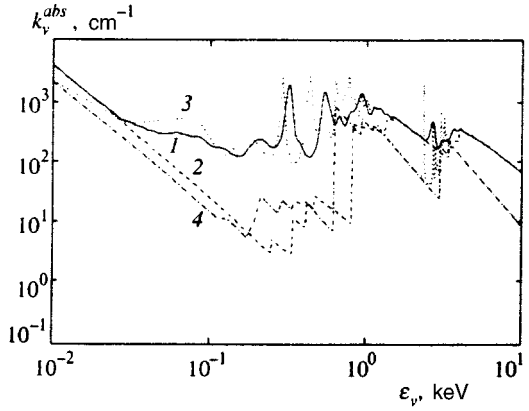

FIG. 11. Spectral absorption coefficients $k_\nu^{\rm abs}$ in gold at a temperature $T=0.1$ keV and a density $\rho=0.1$ g/cm^3: *1*, *2* — absorption coefficients calculated with consideration of lines and without consideration of lines in the local thermodynamic equilibrium approximation (results from Ref. 9); *3*, *4* — corresponding results of the calculations in the present work with the line shape (10).

In calculations of the spectral characteristics of a hot plasma, the line profile and linewidth are of great importance. The simplest line profile, which was used in Ref. 9, is the Lorentzian

$$\psi_{\xi,\xi'}=\frac{1}{\pi}\frac{\gamma_{\xi,\xi'}}{(E_{\xi'}-E_\xi-\varepsilon_\nu)^2+\gamma_{\xi,\xi'}^2}, \tag{10}$$

$$\gamma_{\xi,\xi'}=\sqrt{(\gamma_{\xi,\xi'}^N)^2+(\gamma_{\xi,\xi'}^D)^2+(\gamma_{\xi,\xi'}^C)^2},$$

where $\gamma_{\xi,\xi'}$ is the total linewidth, and $\gamma_{\xi,\xi'}^N$, $\gamma_{\xi,\xi'}^D$, and $\gamma_{\xi,\xi'}^C$ are, respectively, the radiative, Doppler, and collisional linewidths.

Figure 11 presents the results of calculations of the spectral absorption coefficients using the average-ion model described above with consideration of the l splitting for a gold plasma at a temperature $T=0.1$ keV and density $\rho=0.1$ g/cm^3. The figure also presents the results from Ref. 9. Qualitative agreement between our calculations and the data from Ref. 9 is observed on the whole. The differences between the positions of the jumps in absorption and the lines can be attributed to the fact that at the density and temperature indicated, the rate of collisional processes is insufficient for establishing local thermodynamic equilibrium. As was shown above, the calculation in Ref. 9, which was performed in the local thermodynamic equilibrium approximation, yields higher values for the mean charge of the plasma and, therefore, leads to displacement of the levels in the stiffer direction.

The characteristic values of the linewidth at a temperature $T\approx 0.1$ keV and plasma density $\rho\approx 0.1$ g/cm^3 amount to several electron volts. Nevertheless, in a high-Z plasma thermodynamic fluctuations of the occupation numbers lead to level shifts comparable to the binding energy.[21] If we assume that the fluctuations of the occupation numbers of different levels are statistically independent, this leads to effective broadening of the line. As shown in Refs. 21 and 22, in this case the line has a Doppler line shape:

$$\psi_{\xi,\xi'}=\frac{1}{\sqrt{2\pi(\Delta E_{\xi,\xi'})^2}}\exp\left[-\frac{(E_{\xi'}-E_\xi-\varepsilon_\nu)^2}{2(\Delta E_{\xi,\xi'})^2}\right],$$

where the linewidth $\Delta E_{\xi,\xi'}$ is related to the root-mean-square values of the energy fluctuations δE_ξ of the levels by

$$(\Delta E_{\xi,\xi'})^2=\langle(\delta E_{\xi'}-\delta E_\xi)^2\rangle. \tag{11}$$

In the average-ion approximation under consideration here we can express the linewidth (11) in terms of derivatives of the energies of the respective states with respect to the population:

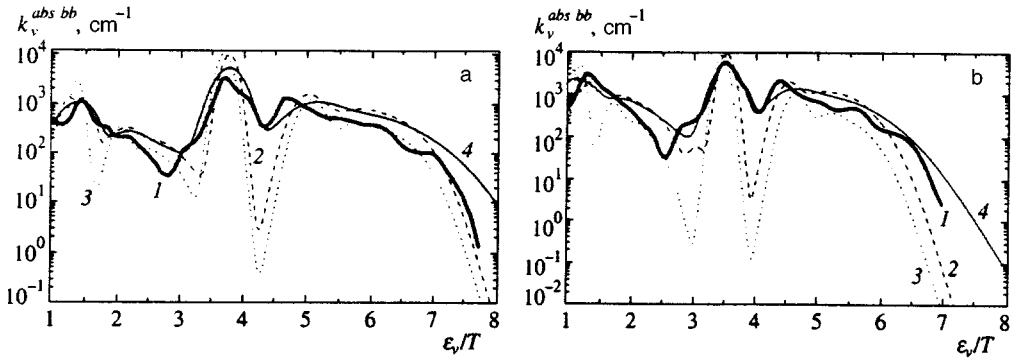

FIG. 12. Spectral absorption coefficient in lines for a gold plasma at a temperature $T=750$ eV and densities $\rho=1.9$ g/cm^3 (a) and $\rho=19$ g/cm^3 (b): *1* — calculated results from Ref. 21, *2*, *3* — calculation using the average-ion model with and without consideration of the l splitting with linewidths (12) and (13), respectively; *4* — calculation using the average-ion model with consideration of the l splitting and doubled linewidths.

TABLE IV. Transition parameters calculated by different methods.

Transition	Transition energy, eV		$\Delta E_{\xi,\xi'}$, eV	
	Ref. 22	(6)	Ref. 22	(12), (13)
1→2	6339	6454	57.7	24.8
1→3	7128	7272	97.3	50.4
1→4	7307	7459	117.6	67.8
2→3	886.5	819	41.4	26.2
2→4	1066	1006	67.7	44.9
3→4	210.8	187.3	27.8	19.5

$$(\Delta E_{\xi,\xi'})^2=\sum_{\xi''}\left(\frac{\partial E_{\xi'}}{\partial P_{\xi''}}-\frac{\partial E_{\xi}}{\partial P_{\xi''}}\right)^2\langle(\delta P_{\xi''})^2\rangle$$
$$=\sum_{\xi''}\left(\frac{\partial E_{\xi'}}{\partial P_{\xi''}}-\frac{\partial E_{\xi}}{\partial P_{\xi''}}\right)^2 P_{\xi''}\left(1-\frac{P_{\xi''}}{g_{\xi''}}\right). \qquad (12)$$

Thus, differentiating (6), for the average-ion model without consideration of the splitting with respect to the orbital angular momentum quantum numbers (the H model) we obtain

$$\frac{\partial E_n}{\partial P_m}=2I_{\mathrm{H}}\begin{cases}\dfrac{Z_n}{n^2}\sigma_{nm}-\displaystyle\sum_{k\geqslant n}\sigma_{kn}\left(1-\frac{1}{2}\delta_{kn}\right)\\ \quad\times\sigma_{km}\left(1-\dfrac{1}{2}\delta_{km}\right)\dfrac{P_k}{k^2}, & m\leqslant n,\\ \dfrac{Z_m}{m^2}\sigma_{mn}-\displaystyle\sum_{k\geqslant m}\sigma_{kn}\left(1-\frac{1}{2}\delta_{kn}\right)\\ \quad\times\sigma_{km}\left(1-\dfrac{1}{2}\delta_{km}\right)\dfrac{P_k}{k^2}, & m\geqslant n.\end{cases} \qquad (13)$$

The expression for the linewidth (11) in the case in which the l splitting is taken into account (the L model), which has a fairly cumbersome form, can be obtained in a similar manner.

Table IV presents the energies of various transitions, as well as the values of the linewidths, calculated from Eqs. (6), (12), and (13) for an iron plasma at a temperature $T=200$ eV and density $\rho=7.8$ g/cm^3. For comparison, the table also presents the energies of the corresponding transitions and linewidths from Ref. 22, which were obtained in the Thomas–Fermi model. It can be seen from a comparison that the calculations of the transition energy in the average-ion model are in satisfactory agreement with the quantum-mechanical calculations. The difference in the transition energy does not exceed 2% for most transitions, and it amounts to about 10% only for the 3→4 transition. However, the linewidth values differ by almost twofold, although linewidth differences among the various transitions agree qualitatively with the data in Ref. 22.

Figure 12 presents the spectral absorption coefficients in lines for a gold plasma at a temperature $T=0.75$ keV and densities $\rho=1.9$ and 19 g/cm^3. Curves *2* and *3* correspond to an exact calculation of the linewidth from Eqs. (12) and (13), while curve *4* was obtained for the case in which the exact widths were doubled. For comparison, the figure also presents the results from Ref. 21 (curve *1*), where the calculations were performed using the Hartree–Fock model.

This study has shown that the use of the average-ion approximation to calculate the ionization kinetics of a high-temperature highly charged ion plasma gives satisfactory results when the thermodynamic and spectral characteristics of such a plasma are determined. This approach can be used in comprehensive calculations of the kinetics and the radiative gas dynamics.

In conclusion, we thank the International Scientific-Technical Center for supporting this work as Project No. 76.

[1] W. Ebeling, W. D. Kraeft, and D. Kremp, *Theory of Bound States and Ionization Equilibrium in Plasmas and Solids*, Akademie-Verlag, Berlin, (1976).
[2] M. Itoh, T. Yabe, and S. Kiyokawa, Phys. Rev. A **35**, 233 (1987).
[3] S. A. Bel'kov and G. V. Dolgoleva, Vopr. At. Nauki Tekh., Ser. Mat. Modelirovanie Fiz. Protsessov, (1) 59 (1992).
[4] J. C. Slater, Phys. Rev. **36**, 57 (1930).
[5] A. F. Nikiforov, V. G. Novikov, and V. B. Uvarov, Vopr. At. Nauki Tekh., Ser. Metodiki Programmy Chislennogo Resheniya Zadach Mat. Fiz., 2(6) 16 (1979).
[6] L. D. Landau and E. M. Lifshitz, *Quantum Mechanics: Non-Relativistic Theory*, 2nd ed., Pergamon Press, Oxford–New York (1965)
[7] R. M. More, J. Quant. Spectrosc. Radiat. Transfer **27**, 345 (1982).
[8] F. Perrot, Phys. Scr. **39**, 332 (1989).
[9] A. Rickert and J. Meyer-ter-Vehn, Laser Part. Beams **8**, 715 (1990).
[10] G. Faussurier, C. Blancard, and A. Decoster, in *Laser Interaction with Matter (Proceedings of the 23rd European Conference, St. John's College, Oxford, 19–23 September 1994)*, S. J. Rose (ed.), Rutherford Laboratory, Chilton, Didcot, Oxfordshire, UK (1995), p. 239.
[11] C. W. Allen, *Astrophysical Quantities*, 3rd ed., Athlone Press, London (1973).
[12] W. A. Lokke and D. E. Post, At. Data Nucl. Data Tables **20**, 397 (1977).
[13] W. Lotz, Z. Phys. **216**, 241 (1968).
[14] M. J. Seaton, in *Atomic and Molecular Processes*, D. R. Bates (ed.), Academic Press, New York (1962), p. 375.
[15] R. W. P. McWhirter, in *Plasma Diagnostics*, R. H. Huddlestone and S. L. Leonard (eds.), Academic Press, New York (1965).
[16] R. K. Landshoff and J. D. Perez, Phys. Rev. A **13**, 1619 (1976).
[17] I. A. Zel'dovich and Yu. P. Raizer, *Physics of Shock Waves and High-Temperature Hydrodynamic Phenomena*, Academic Press, New York (1966–1967).
[18] H. A. Bethe and E. Salpeter, *Quantum Mechanics of One- and Two-Electron Atoms*, Springer-Verlag, Berlin; Academic Press, New York (1957)
[19] N. S. Bakhvalov, *Numerical Methods: Analysis, Algebra, Ordinary Differential Equations*, Mir, Moscow (1977).
[20] B. L. Henke, E. M. Gullikson, and J. C. Davis, At. Data Nucl. Data Tables **54**, 181 (1993).
[21] V. V. Dragalov, A. F. Nikiforov, V. G. Novikov, and V. B. Uvalov, Fiz. Plazmy **16**, 77 (1990) [Sov. J. Plasma Phys. **16**, 44 (1990)].
[22] T. Blenski and B. Cichocki, Phys. Rev. A **41**, 6973 (1990).

Translated by P. Shelnitz

On the dynamics of a curved deflagration front

V. V. Bychkov

Department of Plasma Physics, Umea University, S-90187 Umea, Sweden

M. A. Liberman

Department of Physics, Uppsala University, Box 530, S-75121 Uppsala, Sweden; P. Kapitsa Institute for Physical Problems, 117334 Moscow, Russia

(Submitted 25 June 1996)
Zh. Éksp. Teor. Fiz. **111**, 514–527 (February 1997)

An equation describing evolution of a curved deflagration front of finite thickness is obtained for the case of an arbitrary equation of state of the ''fuel'', an arbitrary type of energy release and an arbitrary type of thermal conduction. The equation is complemented by conservation laws for the mass flux and the momentum flux through the deflagration front of finite thickness. As an illustration of the method, the growth rates and the cutoff wavelengths for the linear stage of the flame instability are calculated for the case of a flame in an ideal gaseous fuel and for the case of a thermonuclear deflagration propagating in a strongly degenerate matter of white dwarfs. © *1997 American Institute of Physics*. [S1063-7761(97)00802-0]

1. INTRODUCTION

The dynamics of a deflagration wave is a key problem in many physical phenomena from industrial problems of burning in engines to astrophysical problems of stellar evolution. A deflagration wave (flame) is a front of energy release propagating due to thermal conduction with a subsonic velocity.[1] An ordinary flame supported by chemical reactions of a gaseous or liquid fuel is a typical example of a deflagration wave. Other examples are waves of laser ablation in inertial fusion,[2,3] fronts of thermonuclear reaction in supernova events,[4,5] evaporation waves in a superheated fluid,[6] etc. A deflagration wave may propagate as a planar stationary front separating cold initial matter (fresh ''fuel'') from heated products of deflagration. It was shown by Landau and by Darrieus[1,7] that a planar flame front is hydrodynamically unstable against perturbations which bend the front on length scales large compared to the flame front thickness. Similar instability is inherent to all waves of the deflagration type. The instability leads to a cellular structure of a deflagration front[8,9] or to self-turbulization of the combustion flow,[1,9,10] which may cause considerable increase of the velocity of the deflagration front. Because of the Landau–Darrieus instability the configuration of a curved deflagration front is much more common than the configuration of a planar front. Besides, some external effects like turbulence may wrinkle a deflagration front as well.

To study propagation of a deflagration wave one has to consider the complete system of hydrodynamic equations, taking into account thermal conduction and the kinetics of the energy release. This is a rather complicated problem even for numerical solution and any simplification of the problem is of great interest. The problem may be simplified considerably if the region of thermal conduction and energy release can be replaced by a surface of discontinuity, separating the fuel and the products of deflagration. In this case one must specify the evolution equation for the deflagration front and the boundary conditions at the front. Such a model was employed first by Landau and Darrieus[1,7] to study stability of a planar flame front of zero thickness. However further investigation of the flame front stability showed that the finite thickness of the front has to be taken into account.[9,10] The influence of thermal conduction and finite flame thickness remains important even on the scales exceeding the flame thickness by several orders of magnitude. At the same time introduction of a discontinuity surface for a flame front does not necessarily imply that the front has zero thickness: the flame thickness may enter the boundary conditions and the evolution equation as an external parameter, depending on the fuel properties. The evolution equation for a flame front of finite thickness and the boundary conditions at the front were obtained first by Matalon and Matkowsky[11] (though misprints in the final results somewhat spoil the excellent work). Matalon and Matkowsky considered the case of an ordinary laboratory flame propagating in an ideal gas with a large activation energy of the chemical reaction. The same evolution equation for a flame in an ideal gaseous fuel was obtained independently in Ref. 12. However, the diversity of deflagration waves and their properties require development of more general theory of curved deflagration fronts, including the case of an arbitrary fuel with an arbitrary type of energy release.

In the present paper we obtain the conservation laws at a deflagration front and the evolution equation for a curved deflagration front of finite thickness propagating in a fuel with an arbitrary equation of state, an arbitrary type of thermal conduction and an arbitrary type of energy release. To illustrate the method, the growth rates and the cut-off wavelengths for the linear stage of the flame instability are calculated for a flame in an ideal gaseous fuel and for a thermonuclear deflagration propagating in the strongly degenerate matter of white dwarfs. For the particular case of a flame in an ideal gas with large activation energy of the reaction the equations obtained agree with the results of Ref. 11.

2. A PLANAR STATIONARY DEFLAGRATION FRONT

As usual the deflagration velocity is essentially subsonic, so that the flow caused by a deflagration wave can be treated as incompressible. The equations describing propagation of a deflagration wave are

$$\frac{\partial \rho}{\partial t}+\nabla\cdot(\rho\mathbf{v})=0, \tag{1}$$

$$\rho\,\frac{\partial \mathbf{v}}{\partial t}+(\rho\mathbf{v}\cdot\nabla)\mathbf{v}+\nabla P=\mu_F\Delta\mathbf{v}+\left(\mu_S+\frac{\mu_F}{3}\right)\nabla\cdot(\nabla\mathbf{v}), \tag{2}$$

$$\rho\,\frac{\partial H}{\partial t}+\rho\mathbf{v}\cdot\nabla H=\nabla\cdot(\kappa\nabla T)+\frac{\rho-Q}{\tau_R}\,W(T), \tag{3}$$

where H is the enthalpy per unit mass, κ is the coefficient of thermal conduction, μ_F and μ_S are the coefficients of the first and second viscosity respectively, which may be taken constant for the majority of physical problems. For incompressible matter the density, enthalpy, and thermal conduction depend only upon temperature: $\rho=\rho(T)$, $H=H(T)$, $\kappa=\kappa(T)$. The last term in Eq. (3) describes the energy release in the deflagration wave, τ_R is a constant with dimension time and Q is the energy release per unit mass. For a given enthalpy of the fuel (label ''$-$'') the enthalpy of deflagration products (label ''$+$'') is computed through the conservation of energy: $H_+=H_-+Q$. Then the equation of state gives the final temperature of the deflagration products $T_+=T(H_+)$, and the final density $\rho_+=\rho(H_+)$. The dimensionless function $W(T)$ gives the temperature dependence of the reaction rate; this function vanishes for the initial matter and for the deflagration products $W(T_-)=0$, $W(T_+)=0$. Strictly speaking, the process of energy release should be described by a separate kinetic equation: the chemical kinetic equation, the equation of laser light absorption, etc. However in many cases the kinetic equation together with the equation of energy transfer may be reduced to an equation of the form of Eq. (3). This is an exact result for a flame in an ordinary gaseous fuel with Lewis number equal to unity, when the coefficients of mass diffusion and thermal diffusivity are equal.[9,10] This simplification can be made also for the case of negligible mass diffusion, when electron thermal conduction or thermal conduction of radiation is the dominant process, as it is for the thermonuclear reaction fronts in supernovae,[13] for laser ablation[3] and for many other physical processes.

Equations (1)–(3) have a stationary solution which is a planar deflagration front propagating along z-axis. In the reference frame comoving with the deflagration front the stationary solution consists of the upstream homogeneous flow of cold matter, the transition region of heating and energy release, and the homogeneous downstream flow of the deflagration products. For the stationary flow we have $\rho u=\rho_- U_f=$const and the speed of a stationary deflagration is determined as an eigenvalue of the energy transfer equation (3)

$$\rho_- U_f\,\frac{dH}{dz}=\frac{d}{dz}\left(\kappa\,\frac{dT}{dz}\right)+\frac{\rho-Q}{\tau_R}\,W(T) \tag{4}$$

with the boundary conditions $T=T_-$ ahead of the deflagration front and $T=T_+$ behind the front.

It is convenient to introduce the dimensionless variables and parameters $r=\rho/\rho_-$, $\Theta=T/T_-$, $h=H/H_-$, $\Pi=(P-P_-)/\rho_- U_f^2$, $\chi=\kappa/\kappa_-$, $P\tau_{F,S}=\mu_{F,S}H_-/T_-\kappa_-$, $\Lambda=QL/(H_- U_f\tau_R)$, and the dimensionless coordinate $\xi=z/L$, where U_f is the velocity and $L=\kappa_- T_-/(H_-\rho_- U_f)$ is the thickness of the planar stationary deflagration front. The parameter Λ is an eigenvalue of the dimensionless equation of heat transfer

$$\frac{d}{d\xi}\left(\chi\,\frac{d\Theta}{d\xi}\right)-\frac{dh}{d\xi}+\Lambda W(\Theta)=0, \tag{5}$$

with the boundary conditions $\Theta=1$ for $\xi\to-\infty$ and $\Theta=\Theta_+$ for $\xi\to\infty$.

Let us consider the approximate analytical solution of Eq. (5) for the case of negligible thickness of the zone of energy release using the method proposed by Zel'dovich and Frank-Kamenetskii.[10] Outside the reaction zone $W\approx 0$ holds and the temperature obeys the equation

$$\chi\,\frac{d\Theta}{d\xi}=h-1. \tag{6}$$

Neglecting the second term in Eq. (5) inside the thin zone of energy release and using Eq. (6) as a boundary condition upstream from the zone we obtain the following approximate value of Λ

$$\Lambda\approx\frac{(h_+-1)^2}{2\chi_+}\left(\int_1^{\Theta_+}W(\Theta)d\Theta\right)^{-1}. \tag{7}$$

Equation (7) makes it possible to obtain the deflagration velocity depending on the particular function of the energy release as $U_f=\sqrt{Q\kappa_- T_-/\Lambda H^2-\rho-=\tau_R}$.

3. EVOLUTION EQUATION FOR AN INFINITELY THIN DEFLAGRATION FRONT

Let the curved deflagration front be described by a function $z=Rf(\mathbf{x},t)$, so that the evolution of the front is characterized by the length scale $R\gg L$ and by the time scale R/U_f. It is convenient to introduce the dimensionless time $\tau=U_f t/R$, the transverse coordinate $\boldsymbol{\eta}=\mathbf{x}/R$ and the small parameter $\varepsilon=L/R\ll 1$. In a coordinate system comoving with the flame front

$$\zeta=\xi-f(\boldsymbol{\eta},\tau)/\varepsilon,\quad \boldsymbol{\eta}=\boldsymbol{\eta},\quad \tau=\tau \tag{8}$$

the hydrodynamic equations take the form

$$\varepsilon\,\frac{\partial r}{\partial\tau}+\frac{\partial m}{\partial\zeta}+\varepsilon\nabla_\perp(r\boldsymbol{v})=0, \tag{9}$$

$$\varepsilon r\,\frac{\partial \boldsymbol{v}}{\partial\tau}+m\,\frac{\partial \boldsymbol{v}}{\partial\zeta}+\varepsilon r(\boldsymbol{v}\nabla_\perp)\boldsymbol{v}$$
$$=-\varepsilon\nabla_\perp\Pi+\nabla_\perp f\,\frac{\partial\Pi}{\partial\zeta}+Pr_F\Delta_\zeta\boldsymbol{v}+\left(Pr_S+\frac{Pr_F}{3}\right)$$
$$\times\left(\varepsilon\nabla_\perp-\nabla_\perp f\,\frac{\partial}{\partial\zeta}\right)\left(\frac{\partial}{\partial\zeta}\left(\frac{m}{r}\right)+\varepsilon\nabla_\perp\boldsymbol{v}\right), \tag{10}$$

$$\varepsilon r\,\frac{\partial u}{\partial \tau}+m\,\frac{\partial u}{\partial \zeta}+\varepsilon r(\boldsymbol{v}\nabla_\perp)u$$
$$=-\frac{\partial \Pi}{\partial \zeta}+Pr_F\Delta_\zeta u+\left(Pr_S+\frac{Pr_F}{3}\right)\frac{\partial}{\partial \zeta}$$
$$\times\left(\frac{\partial}{\partial \zeta}\left(\frac{m}{r}\right)+\varepsilon\nabla_\perp \boldsymbol{v}\right), \tag{11}$$

$$\varepsilon r\,\frac{\partial h}{\partial \tau}+m\,\frac{\partial h}{\partial \zeta}+\varepsilon r\,\boldsymbol{v}\nabla_\perp h$$
$$=N^2\,\frac{\partial}{\partial \zeta}\left(\chi\,\frac{\partial \Theta}{\partial \zeta}\right)+\varepsilon\nabla_\perp\left[\chi\left(\varepsilon\nabla_\perp\Theta-\nabla_\perp f\,\frac{\partial \Theta}{\partial \zeta}\right)\right]$$
$$-\varepsilon\nabla_\perp f\,\frac{\partial}{\partial \zeta}\,(\chi\nabla_\perp\Theta)+W(\Theta), \tag{12}$$

where the mass flux m is given by the expression

$$m=ru-r\,\frac{\partial f}{\partial \tau}-r\,\boldsymbol{v}\nabla_\perp f, \tag{13}$$

$u=v_z/U_f$, $\boldsymbol{v}=\mathbf{v}_x/U_f$ are the components of the dimensionless velocity, and $\nabla_\perp$ is the part of the operator ∇ related to the coordinate $\boldsymbol{\eta}$ along the front surface. The Laplace operator in these variables takes the form

$$\Delta_\zeta=N^2\,\frac{\partial^2}{\partial \zeta^2}-\varepsilon\nabla_\perp^2 f\,\frac{\partial}{\partial \zeta}-2\varepsilon\,\frac{\partial}{\partial \zeta}\,(\nabla_\perp f\nabla_\perp)+\varepsilon^2\nabla_\perp^2, \tag{14}$$

where $N=\sqrt{1+(\nabla_\perp f)^2}$. It is convenient to rewrite Eqs. (10) and (11) in another form, putting the expression for the momentum flux in the left-hand side

$$m\,\frac{\partial}{\partial \zeta}\,(\boldsymbol{v}+u\nabla_\perp f)=-\varepsilon r\left(\frac{\partial}{\partial \tau}+\boldsymbol{v}\nabla_\perp\right)(\boldsymbol{v}+u\nabla_\perp f)$$
$$+\varepsilon r u\left(\frac{\partial}{\partial \tau}+\boldsymbol{v}\nabla_\perp\right)\nabla_\perp f-\varepsilon\nabla_\perp\Pi+Pr_F$$
$$\times(\Delta_\zeta\boldsymbol{v}+\nabla_\perp f\Delta_\zeta u)+\varepsilon\left(Pr_S+\frac{Pr_F}{3}\right)\nabla_\perp$$
$$\times\left(\frac{\partial}{\partial \zeta}\left(\frac{m}{r}\right)+\varepsilon\nabla_\perp \boldsymbol{v}\right), \tag{15}$$

$$N^2\,\frac{\partial}{\partial \zeta}\left(\Pi+\frac{m^2}{N^2 r}\right)$$
$$=-\varepsilon\,\frac{\partial m}{\partial \tau}-\varepsilon\nabla_\perp(m\boldsymbol{v})-\varepsilon r\,\frac{\partial^2 f}{\partial \tau^2}-2\varepsilon r\,\boldsymbol{v}\nabla_\perp\,\frac{\partial f}{\partial \tau}$$
$$-\varepsilon r\,\boldsymbol{v}(\boldsymbol{v}\nabla_\perp)\nabla_\perp f+\varepsilon\nabla_\perp f\nabla_\perp\Pi+Pr_F\Delta_\zeta\left(\frac{m}{r}\right)$$
$$+Pr_F\,\boldsymbol{v}\Delta_\zeta\nabla_\perp f+Pr_F\Delta_\zeta\,\frac{\partial f}{\partial \tau}+\left(Pr_S+\frac{Pr_F}{3}\right)\left(N^2\,\frac{\partial}{\partial \zeta}\right.$$
$$\left.-\varepsilon\nabla_\perp f\nabla_\perp\right)\left(\frac{\partial}{\partial \zeta}\left(\frac{m}{r}\right)+\varepsilon\nabla_\perp \boldsymbol{v}\right). \tag{16}$$

We expand a solution of Eqs. (9)–(12) in power series of the small parameter ε: $m=m_0+\varepsilon m_1+O(\varepsilon^2)$, $\Theta=\Theta_0+\varepsilon\Theta_1+O(\varepsilon^2)$, etc. Then with accuracy $O(\varepsilon)$ Eqs. (9), (12), (15), and (16) take the form

$$\frac{\partial m}{\partial \zeta}=0, \tag{17}$$

$$m\,\frac{\partial}{\partial \zeta}\,(\boldsymbol{v}+u\nabla_\perp f)=Pr_F N^2\,\frac{\partial^2}{\partial \zeta^2}\,(\boldsymbol{v}+u\nabla_\perp f), \tag{18}$$

$$N^2\,\frac{\partial}{\partial \zeta}\left(\Pi+\frac{m^2}{N^2 r}\right)=\left(\frac{4}{3}\,Pr_F+Pr_S\right)N^2\,\frac{\partial^2}{\partial \zeta^2}\left(\frac{m}{r}\right), \tag{19}$$

$$m\,\frac{\partial h}{\partial \zeta}=N^2\,\frac{\partial}{\partial \zeta}\left(\chi\,\frac{\partial \Theta}{\partial \zeta}\right)+W(\Theta). \tag{20}$$

It follows from Eq. (17) that $m=m_0(\boldsymbol{\eta},\tau)+O(\varepsilon)$. Similar to Eq. (5), the solution of Eq. (20) can be presented in the form:

$$\Theta_0=\Theta_p(\zeta/N),\quad m_0(\boldsymbol{\eta},\tau)=N\equiv\sqrt{1+(\nabla_\perp f)^2}, \tag{21}$$

where $\Theta=\Theta_p(\xi)$ is the temperature profile for a planar deflagration front, which is a solution of the ordinary differential equation (5). The equation of state of the fuel gives us immediately

$$r_0=r(\Theta_0)=r_p(\zeta/N),\quad h_0=h(\Theta_0)=h_p(\zeta/N). \tag{22}$$

Equations (18) and (19) integrated across the deflagration front supply the conservation laws for the momentum flux at the infinitely thin surface of discontinuity. In particular, we find from Eq. (18)

$$\boldsymbol{v}+u\nabla_\perp f=\boldsymbol{v}_-+u_-\nabla_\perp f+O(\varepsilon). \tag{23}$$

Equations (13) and (23) give the solution for the velocity components

$$u=u_--\frac{1}{N}\,\frac{r-1}{r}+O(\varepsilon), \tag{24}$$

$$\boldsymbol{v}=\boldsymbol{v}_-+\frac{\nabla_\perp f}{N}\,\frac{r-1}{r}+O(\varepsilon). \tag{25}$$

The expression for pressure follows from Eq. (19)

$$\Pi=\Pi_-+\frac{r-1}{r}+\left(\frac{4}{3}\,Pr_F+Pr_S\right)N\,\frac{\partial}{\partial \zeta}\left(\frac{1}{r}\right)+O(\varepsilon). \tag{26}$$

Equations (13) and (21) give the evolution equation for an infinitely thin deflagration front

$$\frac{\partial f}{\partial \tau}+\boldsymbol{v}_-\nabla_\perp f+\sqrt{1+(\nabla_\perp f)^2}-u_-=O(\varepsilon). \tag{27}$$

The evolution equation (27) and the relations (24)–(26) determine the dynamics of an infinitely thin deflagration front, which is, in fact, the Landau–Darrieus model of a deflagration front.

4. INFLUENCE OF THE FINITE THICKNESS OF A DEFLAGRATION FRONT ON FRONT EVOLUTION

The evolution of a deflagration front depends essentially upon the finite thickness of the front even on the length scales which exceed the front thickness by several orders of

magnitude.[9,10] The next terms of the expansion in ε describe the influence of the finite thickness of the deflagration front. The equation for the mass flux, Eq. (9), with accuracy ε^2 may be written in the form

$$\frac{\partial m_1}{\partial \zeta}=N^{-1}\left(\frac{\partial N}{\partial \tau}+\boldsymbol{v}_-\nabla_\perp N+\frac{\nabla_\perp f\nabla_\perp N}{N}\right)\frac{\partial}{\partial \zeta}\left((r_0-1)\zeta\right)$$
$$-\frac{r_0-1}{N}\left(\frac{\partial N}{\partial \tau}+\nabla_\perp(N\boldsymbol{v}_-)+\nabla_\perp^2 f\right)-\nabla_\perp \boldsymbol{v}_- . \tag{28}$$

The solution of Eq. (28) is

$$m_1=m_{1-}-\zeta\nabla_\perp \boldsymbol{v}_-+\left(\frac{\partial N}{\partial \tau}+\boldsymbol{v}_-\nabla_\perp N+\frac{\nabla_\perp f\nabla_\perp N}{N}\right)$$
$$\times\frac{\zeta}{N}(r_0-1)-\left(\frac{\partial N}{\partial \tau}+\nabla_\perp(N\boldsymbol{v}_-)+\nabla_\perp^2 f\right)J\left(\frac{\zeta}{N}\right), \tag{29}$$

where

$$J\left(\frac{\zeta}{N}\right)=\int_{-\infty}^{\zeta/N}(r_p(\nu)-1)\,d\nu. \tag{30}$$

Substituting the expression (29) for the mass flux into the thermal conduction equation (12) and extracting the terms of order of $O(\varepsilon)$ we have

$$m_{1-}\frac{\partial h_0}{\partial \zeta}-\left(\frac{\partial N}{\partial \tau}+\nabla_\perp(N\boldsymbol{v}_-)\right)\frac{\zeta}{N}\frac{\partial h_0}{\partial \zeta}-\left(\frac{\partial N}{\partial \tau}+\nabla_\perp(N\boldsymbol{v}_-)\right.$$
$$\left.+\nabla_\perp^2 f\right)J\left(\frac{\zeta}{N}\right)\frac{\partial h_0}{\partial \zeta}+\nabla_\perp^2 f\chi\frac{\partial \Theta_0}{\partial \zeta}$$
$$-2\nabla_\perp f\frac{\nabla_\perp N}{N}\frac{\partial}{\partial \zeta}\left(\zeta\chi\frac{\partial \Theta_0}{\partial \zeta}\right)$$
$$=N^2\frac{\partial^2}{\partial \zeta^2}(\chi\Theta_1)-N\frac{\partial}{\partial \zeta}\left(\frac{dh}{d\Theta}\Theta_1\right)+\frac{dW}{d\Theta}\Theta_1. \tag{31}$$

One can check by simple substitution and comparison with Eq. (5) that the right-hand side of Eq. (31) is zero for $\Theta_1=\partial\Theta_0/\partial\zeta$:

$$\hat{F}\left(\frac{\partial \Theta_0}{\partial \zeta}\right)\equiv N^2\frac{\partial^2}{\partial \zeta^2}\left(\chi\frac{\partial \Theta_0}{\partial \zeta}\right)-N\frac{\partial}{\partial \zeta}\left(\frac{dh}{d\Theta}\frac{\partial \Theta_0}{\partial \zeta}\right)$$
$$+\frac{dW}{d\Theta}\frac{\partial \Theta_0}{\partial \zeta}=0. \tag{32}$$

The operator $\hat{F}(\Theta_1)$ can be reduced to a Hermitian form $\hat{F}_H(\psi)$ by the substitution

$$\Theta_1=\frac{\psi}{\chi}\exp\left(\frac{1}{2}\int_{\zeta_-/N}^{\zeta/N}\chi_p^{-1}\frac{dh_p}{d\Theta_p}\,d\nu\right), \tag{33}$$

where ζ_- is an arbitrary position since the operator $\hat{F}(\Theta_1)$ is linear. The expression $\hat{F}_H(\psi)$ becomes zero for

$$\psi_0=\chi\frac{\partial \Theta_0}{\partial \zeta}\exp\left(-\frac{1}{2}\int_{\zeta_-/N}^{\zeta/N}\chi_p^{-1}\frac{dh_p}{d\Theta_p}\,d\nu\right). \tag{34}$$

If we write the right-hand side of Eq. (31) in Hermitian form, multiply it by ψ_0 and integrate, we obtain the relation

$$m_{1-}=\left(\frac{\partial N}{\partial \tau}+\nabla_\perp(N\boldsymbol{v}_-)+\nabla_\perp^2 f\right)\left\langle(\xi+J(\xi))\frac{dh_p}{d\xi}\right\rangle$$
$$-\nabla_\perp^2 f\left\langle\xi\frac{dh_p}{d\xi}+\chi\frac{d\Theta_p}{d\xi}\right\rangle+2\frac{\nabla_\perp f\nabla_\perp N}{N}$$
$$\times\left\langle\frac{d}{d\xi}\left(\xi\chi\frac{d\Theta_p}{d\xi}\right)\right\rangle, \tag{35}$$

where

$$\langle\Phi\rangle=\left(\int_{-\infty}^{\infty}\Phi\Psi^2 d\xi\right)\left(\int_{-\infty}^{\infty}\frac{dh_p}{d\xi}\Psi^2 d\xi\right)^{-1} \tag{36}$$

and

$$\Psi^2=\chi\frac{d\Theta_p}{\partial \xi}\exp\left(-\int_{\xi_-}^{\xi}\chi_p^{-1}\frac{dh_p}{d\Theta_p}\,d\nu\right). \tag{37}$$

The profiles of temperature, enthalpy and density $\Theta_p=\Theta_p(\xi)$, $h_p=h_p(\xi)$, $\rho_p=\rho_p(\xi)$ for a planar stationary deflagration front follow from Eq. (5) and the equation of state. Taking into account Eq. (35) we obtain the evolution equation for a deflagration front of finite thickness with the accuracy $O(\varepsilon^2)$

$$\frac{\partial f}{\partial \tau}+\boldsymbol{v}_-\nabla_\perp f-u_-+N$$
$$=-\varepsilon\left(\frac{\partial N}{\partial \tau}+\nabla_\perp(N\boldsymbol{v}_-)+\nabla_\perp^2 f\right)\left\langle(\xi+J)\frac{dh_p}{d\xi}\right\rangle$$
$$+\varepsilon\nabla_\perp^2 f\left\langle\xi\frac{dh_p}{d\xi}+\chi\frac{d\Theta_p}{d\xi}\right\rangle$$
$$-2\varepsilon\frac{\nabla_\perp f\nabla_\perp N}{N}\left\langle\frac{d}{d\xi}\left(\xi\chi\frac{d\Theta_p}{d\xi}\right)\right\rangle, \tag{38}$$

where $N=\sqrt{1+(\nabla_\perp f)^2}$. Equation (38) is obtained for the case of an arbitrary equation of state of the fuel, an arbitrary type of the thermal conduction and an arbitrary type of energy release.

Let us consider a deflagration wave, for which energy is released in a zone of negligible thickness compared to the total thickness of the deflagration front. For an ordinary flame this case corresponds to a reaction with large activation energy. In this case we have from Eq. (6) $\Psi^2=1$ for $\xi<0$ and $\Psi^2=0$ for $\xi>0$, so that the average of Eq. (36) becomes

$$\langle\Phi\rangle=\frac{1}{h_+-1}\int_{-\infty}^{0}\Phi\,d\xi. \tag{39}$$

Calculating the coefficients in Eq. (38) we can write the evolution equation for the deflagration front in the form

$$\frac{\partial f}{\partial \tau}+\boldsymbol{v}_-\nabla_\perp f-u_-+N=\varepsilon\alpha\left(\frac{\partial N}{\partial \tau}+\nabla_\perp(N\boldsymbol{v}_-)+\nabla_\perp^2 f\right). \tag{40}$$

Equation (40) describes the influence of front stretching and the finite thickness of the deflagration wave on the velocity of the front. The numerical factor depends on the fuel properties

$$\alpha=\frac{h_+}{h_+-1}\int_1^{\Theta_+} r\chi d\Theta+\int_1^{\Theta_+}\frac{1-rh}{h-1}\,\chi d\Theta. \tag{41}$$

For many physical problems the dimensionless equation of state for an isobaric flow has the form $rh=1$. This holds when pressure is determined for an ideal gas, a nonrelativistic, or ultra-relativistic fermi-gas, by radiation pressure, etc. In this case the numerical factor becomes

$$\alpha=\frac{h_+}{h_+-1}\int_1^{\Theta_+} r\chi d\Theta. \tag{42}$$

For the particular case of an ideal gas ($r\Theta=1$) with a constant coefficient of thermal conduction ($\chi=1$) the evolution equation obtained by Matalon and Matkowsky[11] is recovered from Eq. (40).

5. CONSERVATION LAWS AT A DEFLAGRATION FRONT OF FINITE THICKNESS

The evolution equation (40) should be complemented by conservation laws at the deflagration front which take into account the finite thickness of the front. These conservation laws follow from Eqs. (9), (15) and (16) integrated with accuracy $O(\varepsilon^2)$. The conservation law for the mass flux follows immediately from Eq. (29):

$$\left(ru-r\boldsymbol{v}\nabla_\perp f-r\frac{\partial f}{\partial\tau}\right)\Bigg|_-^+=\varepsilon J_1\left(\frac{\partial N}{\partial\tau}+\nabla_\perp(N\boldsymbol{v})+\nabla_\perp^2 f\right), \tag{43}$$

where the numerical factor is given by the formula

$$J_1=\int_{-\infty}^{\infty}\xi\frac{dr_p}{d\xi}\,d\xi. \tag{44}$$

To obtain conservation laws for the momentum flux we need to integrate Eqs. (15) and (16), which to $O(\varepsilon^2)$ have the form

$$\begin{aligned}
&m\frac{\partial}{\partial\zeta}(\boldsymbol{v}+u\nabla_\perp f)\\
&\quad=-\varepsilon r\left(\frac{\partial}{\partial\tau}+\mathbf{v}_-\nabla_\perp\right)\boldsymbol{v}_--\varepsilon r\nabla_\perp f\left(\frac{\partial}{\partial\tau}+\boldsymbol{v}_-\nabla_\perp\right)\\
&\quad\times u_--\varepsilon\frac{r-1}{N}(\nabla_\perp f\nabla_\perp)\boldsymbol{v}_--\varepsilon\frac{r-1}{N}\nabla_\perp f(\nabla_\perp f\nabla_\perp)u_-\\
&\quad-\varepsilon\nabla_\perp\Pi_--\varepsilon\frac{r-1}{N}\left(\frac{\partial}{\partial\tau}+\boldsymbol{v}_-\nabla_\perp+\frac{\nabla_\perp f}{N}\nabla_\perp\right)\nabla_\perp f\\
&\quad+\varepsilon\frac{\nabla_\perp N}{N}\frac{\partial}{\partial\zeta}\left(\zeta\frac{r-1}{r}\right)+Pr_F N^2\frac{\partial^2}{\partial\zeta^2}(\boldsymbol{v}+u\nabla_\perp f)\\
&\quad-\varepsilon Pr_F\nabla_\perp N\frac{\partial}{\partial\zeta}\left(\frac{r-1}{r}\right),
\end{aligned} \tag{45}$$

$$\begin{aligned}
&N^2\frac{\partial}{\partial\zeta}\left(\Pi+\frac{m^2}{N^2r}\right)\\
&\quad=\left(\frac{4}{3}Pr_F+Pr_S\right)N^2\frac{\partial^2}{\partial\zeta^2}\left(\frac{m}{r}\right)-\varepsilon\frac{\partial N}{\partial\tau}-\varepsilon\nabla_\perp(N\boldsymbol{v}_-)\\
&\quad-\varepsilon r\frac{\partial^2 f}{\partial\tau^2}-2\varepsilon r\boldsymbol{v}_-\nabla_\perp\frac{\partial f}{\partial\tau}-2\varepsilon(r-1)\left(\frac{\partial}{\partial\tau}-\boldsymbol{v}_-\nabla_\perp\right)\\
&\quad\times N-\varepsilon\frac{(r-1)^2}{r}\frac{\nabla_\perp f\nabla_\perp N}{N}-\varepsilon rv_-(\boldsymbol{v}_-\nabla_\perp)\nabla_\perp f\\
&\quad+\varepsilon\nabla_\perp f\nabla_\perp\Pi_--\varepsilon\frac{r-1}{r}\nabla_\perp^2 f+\varepsilon\left(\frac{4}{3}Pr_F\right.\\
&\quad\left.+Pr_S\right)N^2\nabla_\perp\left(\frac{\nabla_\perp f}{N}\right)\frac{\partial}{\partial\zeta}\left(\frac{r-1}{r}\right).
\end{aligned} \tag{46}$$

Integrating Eqs. (45) and (46) and taking into account asymptotic behavior outside the deflagration front we obtain the jump of the components of the momentum flux across the deflagration front of finite thickness:

$$\begin{aligned}
(\boldsymbol{v}+u\nabla_\perp f)\Big|_-^+&=Pr_F N\left(\frac{\partial\boldsymbol{v}}{\partial\zeta}+\nabla_\perp f\frac{\partial u}{\partial\zeta}\right)\Bigg|_-^+\\
&\quad-\varepsilon Pr_F\frac{r_+-1}{r_+}\frac{\nabla_\perp N}{N}+\varepsilon J_1(\hat{D}\boldsymbol{v}_-\\
&\quad+\nabla_\perp f\hat{D}u_-+N^{-1}\hat{D}\nabla_\perp f),
\end{aligned} \tag{47}$$

$$\begin{aligned}
\left(\Pi+\frac{m^2}{N^2r}\right)\Bigg|_-^+&=\varepsilon J_2\nabla_\perp\left(\frac{\nabla_\perp f}{N}\right)+\frac{\varepsilon J_1}{N}\left(\frac{\partial^2 f}{\partial\tau^2}\right.\\
&\quad+2\boldsymbol{v}_-\frac{\partial}{\partial\tau}\nabla_\perp f+\boldsymbol{v}_-(\boldsymbol{v}_-\nabla_\perp)\nabla_\perp f\\
&\quad\left.+2\hat{D}N-\frac{\nabla_\perp f\nabla_\perp N}{N}\right)+\left(\frac{4}{3}Pr_F+Pr_S\right)\\
&\quad\times\left(\frac{\partial}{\partial\zeta}\left(\frac{m}{r}\right)\Bigg|_-^+\right.+\varepsilon\left.\frac{r_+-1}{r_+}\nabla_\perp\left(\frac{\nabla_\perp f}{N}\right)\right),
\end{aligned} \tag{48}$$

where the coefficient J_2 is

$$J_2=\int_{-\infty}^{\infty}\frac{\xi}{r_p^2}\frac{dr_p}{d\xi}\,d\xi \tag{49}$$

and the differential operator $\hat{D}$ is introduced for convenience:

$$\hat{D}=\frac{\partial}{\partial\tau}+\boldsymbol{v}_-\nabla_\perp+N^{-1}\nabla_\perp f\nabla_\perp. \tag{50}$$

From the hydrodynamic equations (9)–(11) outside the deflagration front,[11]

$$\begin{aligned}
\left(\frac{\partial\boldsymbol{v}}{\partial\zeta}+\nabla_\perp f\frac{\partial u}{\partial\zeta}\right)\Bigg|_-^+&=-\varepsilon\frac{r_+-1}{N}\left(\hat{D}\boldsymbol{v}_-+\nabla_\perp f\hat{D}u_-\right.\\
&\quad\left.+\frac{1}{N}\hat{D}\nabla_\perp f\right)+\varepsilon\frac{r_+-1}{r_+}\frac{\nabla_\perp N}{N^2},
\end{aligned} \tag{51}$$

$$\frac{\partial}{\partial\zeta}\left(\frac{m}{r}\right)\Bigg|_{-}^{+}=-\varepsilon\,\frac{r_{+}-1}{r_{+}}\,\nabla_{\perp}\left(\frac{\nabla_{\perp}f}{N}\right). \tag{52}$$

Taking into account Eqs. (51)–(52), we can rewrite the conservation laws (47) and (48) in the form

$$(\boldsymbol{v}+u\nabla_{\perp}f\,)\big|_{-}^{+}=\varepsilon(J_1-Pr_F(r_{+}-1))(\hat{D}\,\boldsymbol{v}_{-}+\nabla_{\perp}f\hat{D}u_{-}+N^{-1}\hat{D}\nabla_{\perp}f\,), \tag{53}$$

$$\left(\Pi+\frac{m^2}{N^2r}\right)\Bigg|_{-}^{+}=\varepsilon J_2\nabla_{\perp}\left(\frac{\nabla_{\perp}f}{N}\right)+\frac{\varepsilon J_1}{N}\left(\frac{\partial^2 f}{\partial\tau^2}+2\,\boldsymbol{v}_{-}\nabla_{\perp}\,\frac{\partial f}{\partial\tau}+\boldsymbol{v}_{-}(\boldsymbol{v}_{-}\nabla_{\perp})\nabla_{\perp}f+2\hat{D}N-\frac{\nabla_{\perp}f\nabla_{\perp}N}{N}\right). \tag{54}$$

Equations (43), (53) and (54) represent the conservation laws for the mass flux and the tangential and normal components of the momentum flux for a deflagration front of finite thickness for the case of an arbitrary fuel. The left-hand sides of these equations represent the conservation laws for an infinitely thin deflagration front, the right-hand sides describe the influence of the transport processes and the finite thickness of the deflagration front. The dependence upon the equation of state of the fuel and the particular form of the energy release enters the conservation laws through the coefficients J_1, J_2. For the common case of a thin zone of energy release the coefficients take the form

$$J_1=\int_1^{\Theta_{+}} r\chi\,d\Theta+\int_1^{\Theta_{+}}\frac{1-rh}{h-1}\,\chi\,d\Theta, \tag{55}$$

$$J_2=\int_1^{\Theta_{+}}\chi\,d\Theta+\int_1^{\Theta_{+}}\frac{1-rh}{h-1}\,\frac{\chi}{r}\,d\Theta. \tag{56}$$

The evolution equation (38) and the conservation laws (43), (53) and (54) determine the dynamics of a curved deflagration front in a fuel with an arbitrary equation of state and an arbitrary type of energy release. It should be mentioned that second viscosity does not enter either the evolution equation or the conservation laws, though this process has been taken into account in calculations.

6. SUMMARY OF THE RESULTS AND DISCUSSION

In the present paper we have obtained the evolution equation for a curved deflagration front of finite thickness propagating in a fuel with an arbitrary equation of state and an arbitrary type of energy release. The evolution equation is complemented by the boundary conditions: the conservation laws for the mass flux and for the momentum flux through the deflagration front. Let us write the results in dimensional units in a coordinate free form. For a deflagration front described by a function $F(z,\mathbf{x},t)=0$ (for example, $F=z-Rf(\mathbf{x},t)=0$) we have $N=|\nabla F|$ and so the evolution of a deflagration front is described by the equation

$$\mathbf{n}\cdot\mathbf{v}_{-}+\frac{1}{N}\,\frac{\partial F}{\partial t}=U_f-\alpha LK, \tag{57}$$

where $\mathbf{v}_{-}$ is the flow velocity at the cold boundary of the deflagration front, $\mathbf{n}=\nabla F/|\nabla F|$ is the unit normal vector directed towards the products of deflagration, K is the front stretch, which may be written in a coordinate-free form as[11]

$$K=\frac{1}{N}\,\frac{\partial N}{\partial t}+\frac{1}{N}\,\nabla\cdot(N(\mathbf{v}_{-}-U_f\mathbf{n})), \tag{58}$$

and the numerical factor for the case of a narrow zone of energy release is given by

$$\alpha=\frac{Q+H_{-}}{Q}\int_{T_{-}}^{T_{+}}\frac{\rho\kappa\,dT}{\rho_{-}\kappa_{-}T_{-}}+\int_{T_{-}}^{T_{+}}\frac{\rho_{-}H_{-}-\rho H}{H-H_{-}}\,\frac{\kappa\,dT}{\rho_{-}\kappa_{-}T_{-}}. \tag{59}$$

Taking into account Eqs. (57) and (58) we can write the conservation laws in the following coordinate-free form

$$\rho\left(\mathbf{n}\cdot\mathbf{v}+\frac{1}{N}\,\frac{\partial F}{\partial t}\right)\Bigg|_{-}^{+}=\rho_{-}LJ_1K, \tag{60}$$

$$[\mathbf{n}\cdot\mathbf{v}]\big|_{-}^{+}=\frac{L}{U_f}\left(J_1+Pr_F\,\frac{\rho_{-}-\rho_{+}}{\rho_{-}}\right)\mathbf{n}\times\hat{D}(\mathbf{v}_{-}-U_f\mathbf{n}), \tag{61}$$

$$(P+\rho(\mathbf{v}\cdot\mathbf{n})^2)\big|_{-}^{+}=-L\rho_{-}U_f^2J_2\nabla\cdot\mathbf{n}+L\rho_{-}J_1\times\left(\frac{U_f}{N}\,\hat{D}N+\mathbf{n}\cdot\,\frac{\partial\mathbf{v}}{\partial t}+\mathbf{n}\cdot(\mathbf{v}_{-}\cdot\nabla)\mathbf{v}_{-}\right), \tag{62}$$

where the dimensional form of the operator $\hat{D}$ is

$$\hat{D}=\frac{\partial}{\partial t}+\mathbf{v}_{-}\cdot\nabla-U_f\mathbf{n}\cdot\nabla \tag{63}$$

and the coefficients J_1, J_2 for the common case of a deflagration wave with a thin zone of energy release are given by the formulas

$$J_1=\int_{T_{-}}^{T_{+}}\frac{\rho\kappa}{\rho_{-}\kappa_{-}T_{-}}\,dT+\int_{T_{-}}^{T_{+}}\frac{\rho_{-}H_{-}-\rho H}{H-H_{-}}\,\frac{\kappa\,dT}{\rho_{-}\kappa_{-}T_{-}}, \tag{64}$$

$$J_2=\int_{T_{-}}^{T_{+}}\frac{\kappa}{\kappa_{-}T_{-}}\,dT+\int_{T_{-}}^{T_{+}}\frac{\rho_{-}H_{-}-\rho H}{\rho(H-H_{-})}\,\frac{\kappa\,dT}{\kappa_{-}T_{-}}. \tag{65}$$

The evolution equation Eq. (57) and the conservation laws Eqs. (60)–(62) determine the dynamics of a deflagration front in the flow of a fuel with an arbitrary equation of state and arbitrary type of thermal conduction and energy release. An essential advantage of the present model is the possibility of applying it to physical problems of different nature, i.e., flame propagation in a chemical of thermonuclear fuel, propagation of an ablation front in a laser target, the evaporation front in a superheated fluid, etc.

Let us apply the results to some particular physical situations. In the simplest case of a flame in an ideal gaseous fuel with a large activation energy and equal coefficients of thermal conductivity and fuel diffusion the evolution equation (57) and the conservation laws (60)–(62) coincide with the equations derived in Ref. 11. The well known

expression[14–16] for the instability growth rate σ of perturbations at a planar flame front of finite thickness may also be derived directly from these equations. The linearized equations (57), (60)–(62) couple the amplitudes of the perturbation modes generated by an unstable flame front in the upstream and the downstream flows. Taking into account the explicit expressions for the perturbation modes[16] one finds the instability growth rate from the consistency condition of the linearized equations (57), (60)–(62):

$$\sigma = SU_f k(1 - k\lambda_c/2\pi), \tag{66}$$

where $S = (1 + r_+)^{-1}(\sqrt{1+1/r_+ - r_+} - 1)$ is the coefficient obtained in the Landau–Darrieus theory of the flame front instability. The instability is suppressed by thermal conduction for perturbations with wavelength shorter than the cut-off wavelength

$$\lambda_c = \frac{\pi L r_+}{2S(S(r_+ + 1) + r_+)} \left(1 - r_+ - \frac{\ln r_+}{1 - r_+} \times (2Sr_+ + 1 + r_+) \right). \tag{67}$$

Because of the large numerical coefficient in Eq. (67) the cut-off wavelength λ_c for typical laboratory flames ($r_+ = 0.1-0.2$) exceeds the flame thickness L substantially, $\lambda_c \approx 20L$. For this reason smooth planar flames are observed much more often than was expected from the Landau–Darrieus theory.[1,7,10]

Another interesting application of the obtained nonlinear model is to the dynamics of a thermonuclear deflagration in supernova events. It is generally believed that the observed spectrum of a supernova of type Ia is determined mostly by the first deflagration stage of white dwarf burning.[4,17] At the same time investigation of the deflagration stage is greatly complicated by the huge range of the length scales which have to be taken into account. The hydrodynamic length scale of the deflagration dynamics in supernovae is about the white dwarf radius ~ 100 km, which exceeds the flame thickness ($\sim 10^{-5}$ cm) by 12 orders of magnitude. By this reason a direct numerical simulation of white dwarf burning is impossible and a simplified model is required. The most probable scenario of the deflagration dynamics in white dwarfs is development of a fractal structure, which implies many cascades of cells of different sizes growing because of the Landau–Darrieus instability.[18] The velocity of a fractal flame increases with the flame radius R as[18,19]

$$U = r_+^{-1} U_f \left(\frac{2\pi R}{n_c \lambda_c} \right)^d, \tag{68}$$

where $2+d$ is the fractal dimension and n_c is the critical number of a spherical function for a fractal accelerating flame found in Ref. 19, which determines the upper limit of the fractal structure. The cutoff wavelength λ_c gives the low limit of the fractal structure of the deflagration in white dwarfs. This value may be calculated on the basis of the model equations (57), (60)–(62), taking into account the properties of the white dwarf fuel. In the dense central layers of a white dwarf with $\rho = 3 \cdot 10^9$ g/cm^3 the equation of state is determined by degenerate ultrarelativistic electrons, so that[20]

$$H = \frac{4P}{\rho}, \tag{69}$$

$$P = 0.77\hbar c \left(\frac{\rho Z}{M_i} \right)^{4/3} \left(1 + 2.06 \left(\frac{M_i}{\rho Z} \right)^{2/3} \frac{T^2}{\hbar^2 c^2} \right), \tag{70}$$

where eZ and M_i are the average electrical charge and the average mass of the ions. Because of the relatively low temperature the thermal conduction of the degenerate electrons dominates in a white dwarf over the radiation thermal conduction, therefore[21]

$$\kappa = \frac{0.81\hbar c^2}{e^4 Z \Lambda_{ei}} \left(\frac{\rho Z}{M_i} \right)^{1/3} T, \tag{71}$$

where Λ_{ei} is the Coulomb logarithm. Using the equation of state and the expression for the thermal conduction we calculate the coefficients of the nonlinear model Eqs. (59), (64) and (65). Then similar to the case of a flame in an ideal gaseous fuel, we find the cutoff wavelength of the Landau–Darrieus instability of a deflagration front in white dwarfs

$$\lambda_c = \frac{2\pi L}{Sr_+} \frac{b_1 + Sb_2}{(1 + r_+)S + 1} \tag{72}$$

with the coefficients depending upon the ratio of densities r_+ of the fuel and the products of the thermonuclear reaction

$$b_1 = \frac{3 - 2r_+^{1/3} - r_+^{4/3}}{6(1 - r_+^{4/3})} + \frac{r_+ + 1}{12 r_+^{4/3}(1 - r_+)(1 + r_+^{4/3})} \times (3 - 3r_+^{2/3} + 4r_+^{4/3} + r_+^{6/3} + r_+^{8/3}), \tag{73}$$

$$b_2 = \frac{1}{2r_+^{4/3}(1 - r_+)} - \frac{1 - r_+^{2/3}}{6r_+^{2/3}(1 + r_+^{4/3})} (3 + 2r_+^{2/3} + r_+^{4/3}). \tag{74}$$

The fuel close to the white dwarf center is strongly degenerate so that energy release in the reaction causes only a slight decrease of density of the burning matter, $r_+ = 0.85-0.9$. For such small expansion the Landau–Darrieus instability is rather weak, while the thermal stabilization is strong and the cutoff wavelength exceeds the flame thickness by almost three orders of magnitude, $\lambda_c = 410L$. This value differs considerably from the crude estimate of the cutoff wavelength made in,[22] where the stabilization of the hydrodynamic instability was expected on length scales of about $10L$.

The developed model may be useful as well for investigation of the fractal dimension of the deflagration fronts in white dwarfs, which up to now has been estimated with rather low accuracy ($\sim 50\%$)[18] not acceptable in the theory of thermonuclear supernovae.

This work was supported in part by the Swedish National Board for Industrial and Technical Development (NUTEK), Grant P2204-1 and in part by the Swedish Natural Science Research Council (NFR), Grant F-AA/Fu-10297-307.

[1] L. D. Landau and E. M. Lifshitz, *Fluid Mechanics*, Pergamon, Oxford (1987).
[2] W. H. Manheimer, D. G. Colombant, and G. H. Gardner, Phys. Fluids **25**, 1644 (1982).

[3] V. V. Bychkov, S. M. Golberg, and M. A. Liberman, Phys. Plasmas **1**, 2976 (1994).
[4] S. E. Woosley and T. A. Weaver, Ann. Rev. Astron. Astroph. **24**, 20 (1986).
[5] V. V. Bychkov and M. A. Liberman, Astron. Astroph. **302**, 727 (1995).
[6] J. E. Shepherd and B. Sturtevant, J. Fluid Mech. **121**, 379 (1982).
[7] L. D. Landau, Zh. Éksp. Teor. Fiz. **14**, 240 (1944).
[8] G. I. Sivashinsky, Ann. Rev. Fluid. Mech. **15**, 179 (1983).
[9] F. A. Williams, *Combustion Theory*, 2nd ed., Benjamin, Reading, MA (1985).
[10] Ya. B. Zel'dovich, G. I. Barenblatt, V. B. Librovich, and G. M. Makhviladze, *The Mathematical Theory of Combustion and Explosion*, Consultants Bureau, New York (1985).
[11] M. Matalon and B. J. Matkowsky, J. Fluid Mech. **124**, 239 (1982).
[12] P. Clavin and G. Joulin, J. Physique Lettres **44**, L1 (1983).
[13] V. V. Bychkov and M. A. Liberman, Astroph. J. **451**, 711 (1995).
[14] P. Pelce and P. Clavin, J. Fluid Mech. **124**, 219 (1982).
[15] M. L. Frankel and G. I. Sivashinsky, Comb. Sci. Tech. **29**, 207 (1982).
[16] M. A. Liberman and V. V. Bychkov, S. M. Golberg, and D. L. Book, Phys. Rev. E **49**, 445 (1994).
[17] A. M. Khokhlov, Astron. Astroph. **245**, 114 (1991).
[18] S. I. Blinnikov and P. V. Sasorov, Phys. Rev. E **53**, 4827 (1996).
[19] V. V. Bychkov and M. A. Liberman, Phys. Rev. Lett. **76**, 2814 (1996).
[20] L. D. Landau and E. M. Lifshitz, *Statistical Physics*, Pergamon, Oxford (1959).
[21] F. X. Timmes and S. E. Woosley, Astroph. J. **396**, 649 (1992).
[22] A. M. Khokhlov, Astrophys. J. **449**, 695 (1995).

Published in English in the original Russian journal. Reproduced here with stylistic changes by the Translation Editor.

Distribution of the electric field and current in a turbulent conducting fluid for small magnetic Reynolds numbers

V. A. Bityurin and A. L. Tseskis

Institute of High Temperatures, Russian Academy of Sciences, 127412 Moscow, Russia
(Submitted 17 April 1996; resubmitted 5 September 1996)
Zh. Éksp. Teor. Fiz. **111**, 528–535 (February 1997)

Various aspects of the influence of an external magnetic field on turbulent flow of a conducting fluid are investigated. The distributions of electric variables are determined for weak magnetic fields (both the electric field and the current have nonzero values in this case). For very strong magnetic fields it is shown that turbulent motion acquires a two-dimensional character. The emergence of an electric current component perpendicular to the flow and to the magnetic field is described in the case of a temperature-stratified medium in the presence of turbulent heat flux. © *1997 American Institute of Physics.* [S1063-7761(97)00902-5]

1. INTRODUCTION

The description of magnetohydrodynamic turbulent motion encompasses two types of problems. On the one hand, it concerns (for example) the generation of magnetic fields in the turbulent motion of a conducting fluid (phenomena of this kind are of utmost importance for a variety of astrophysical applications). The corresponding mathematical apparatus reduces to a system of equations that embody the hydrodynamic equations of motion (including the Lorentz $\mathbf{j}\times\mathbf{B}$ force) and discontinuities, along with all the Maxwell equations.[1] On the other hand, the investigation of MHD turbulent motion in the channels of various MHD devices and the extremely important problem of how the properties of turbulent motion *per se* change under the influence of an external field lead to situations in which the fluctuating magnetic field can be disregarded. This possibility is associated with the smallness of the magnetic Reynolds number

$$\mathrm{Re}_m \ll 1,$$

where $\mathrm{Re}_m = vL/\nu_m$ (v is the order of the hydrodynamic velocity, L is a characteristic length of the problem, and ν_m is the magnetic viscosity of the fluid). In this so-called noninductive approximation the Maxwell equation

$$\mathrm{curl}\ \mathbf{E} = -\frac{\partial \mathbf{B}}{\partial t}$$

reduces to $\mathrm{curl}\ \mathbf{E}=0$ in the case of a static external $\mathbf{B}$ field, so that the electric field is a potential field:

$$\mathbf{E} = -\nabla\varphi.$$

Accordingly, taking into account Ohm's law $\mathbf{j}=\sigma(\mathbf{E}+\mathbf{v}\times\mathbf{B})$ and the condition of continuity of the electric current $\mathrm{div}\ \mathbf{j}=0$, we arrive at the equation (for a constant conductivity of the fluid)

$$\nabla^2\varphi = \mathbf{B}\cdot\mathrm{curl}\ \mathbf{v}. \tag{1}$$

Equation (1) in conjunction with the hydrodynamic equations of motion and continuity (we assume that the fluid is incompressible, $\mathrm{div}\ \mathbf{v}=0$) thus forms a complete system of five equations for the determination of five unknown functions: the three components of the velocity, the pressure, and the electric potential φ. If necessary, the components of the electric current can be determined from Ohm's law.

Since a solution of these equations cannot be obtained in any reasonably general form,[1)] it is customary to rely on additional semiempirical hypotheses or formal assumptions to investigate the corresponding phenomena. It is important to note at this point that such modifications are often incorrect; for example, in the literature we sometimes encounter the notion that it is permissible to set $\mathbf{E}=0$ for $\mathrm{Re}_m \ll 1$ (Refs. 2 and 4). The lack of substance in this condition can be clearly demonstrated with the aid of Eq. (1): the solution of the problem in this case reduces to the trivial case of a fluid at rest.[5] On the other hand, experimental data show that the application of an external magnetic field to initially isotropic turbulence (in a conducting fluid) produces a multitude of nontrivial phenomena. In this paper we investigate the electric current (and field) distribution for a small value of B, the formation of two-dimensional (2D) turbulence in the opposite case of strong magnetic fields, and a certain ''odd'' effect that occurs in a temperature-inhomogeneous conducting fluid in the presence of turbulent heat flux.

2. WEAK MAGNETIC FIELDS

The ''weakness'' of the magnetic field must be characterized by a dimensionless quantity; in our case it corresponds to smallness of the ratio of the magnitude of the Lorentz force jB to the term nonlinear in v in the hydrodynamic equation of motion, $\rho v^2/L$, so that

$$\frac{\sigma B^2 L}{\rho v} \ll 1,$$

where σ and B have nonzero values; of course, the inequalities $\sigma L/c\varepsilon_0 \gg 1$ and especially $\sigma L/v\varepsilon_0 \gg 1$ must be satisfied in this case to ensure that the electromagnetic field is quasistationary (see Ref. 1, Sec. 58). Looking at the distribution of the electric field, we can completely disregard the influence of the Lorentz force on the motion, because it is readily apparent that the corresponding corrections to the electric field would merely add higher-order corrections in the small quantity B to the expansion of $\langle \mathbf{E}^2 \rangle$ in powers of B (angle brackets are used everywhere to signify statistical

averaging). Inasmuch as the distribution of **E** must be uniform in a homogeneous field **B** applied to isotropic turbulence, and since the statistical averages must coincide with the volume averages (see Ref. 6 regarding the ergodicity of hydrodynamic fields), on the basis of the well-known relation

$$(\nabla\varphi)^2=\mathrm{div}(\varphi\nabla\varphi)-\varphi\nabla^2\varphi,$$

and with allowance for the transformation of the volume integral of div(. . .) into a surface integral, we have

$$\langle\mathbf{E}^2\rangle=\langle(\nabla\varphi)^2\rangle=-\langle\varphi\nabla^2\varphi\rangle. \tag{2}$$

The solution of Eq. (1) has the form

$$\varphi(\mathbf{x})=-\frac{1}{\pi}\int\mathbf{B}\cdot\boldsymbol{\omega}(\mathbf{x}+\mathbf{r})\ \frac{d^3r}{r},$$

$$\boldsymbol{\omega}=\mathrm{curl}\ \mathbf{v}, \tag{3}$$

so that from Eqs. (1)–(3) we obtain

$$\langle\mathbf{E}^2\rangle=\frac{B_iB_j}{4\pi}\left\langle\int\omega_i(\mathbf{x})\omega_j(\mathbf{x}+\mathbf{r})\ \frac{d^3r}{r}\right\rangle \tag{4}$$

(summation over repeated lower-case Latin indices is tacitly understood throughout the article). Considering a homogeneous magnetic field directed along one of the coordinate axes, $\mathbf{B}=(0,0,B_3)$, $B_3\equiv B$, and making use of the well-known relations for the average values of the products of the derivatives of the velocity with respect to the coordinates,[7] we can reduce Eq. (4) to the form (with obvious interchangeability of the averaging and integration operations)

$$\begin{aligned}\langle\mathbf{E}^2\rangle&=\frac{B^2}{4\pi}\left\langle\int\omega_3(\mathbf{x})\omega_3(\mathbf{x}+\mathbf{r})\ \frac{d^3r}{r}\right\rangle\\&=\frac{B^2}{4\pi}\int\left[-\Delta b_{ii}(\mathbf{r})+\frac{\partial^2b_{ii}(\mathbf{r})}{\partial r_3^2}+\Delta b_{33}(\mathbf{r})\right]\frac{d^3r}{r}.\end{aligned} \tag{5}$$

In the isotropic case, the two-point velocity correlation tensor b_{ij} can be expressed in terms of the longitudinal scalar b_{LL} and the transverse scalar b_{NN}, which depend on r (Ref. 7):

$$b_{ij}(\mathbf{r})=[b_{LL}(r)-b_{NN}(r)]\ \frac{r_ir_j}{r^2}+b_{NN}\delta_{ij},$$

where δ_{ij} is the Kronecker delta. Taking the latter expression in to account, we have

$$b_{ii}=b_{LL}+2b_{NN},$$

$$b_{33}=(b_{LL}-b_{NN})\ \frac{r_3^2}{r^2}+b_{NN},$$

so that the bracketed expression in Eq. (5) is transformed to $(-1/3)\nabla^2(b_{LL}+2b_{NN})$. Consequently,

$$\langle\mathbf{E}^2\rangle=-\frac{B^2}{12\pi}\int\frac{d^3r}{r}\left(\frac{\partial^2}{\partial r^2}+\frac{2}{r}\frac{\partial}{\partial r}\right)(b_{LL}+2b_{NN}).$$

After integration over angles, this expression yields (for brevity we set $b_{LL}+2b_{NN}=A$)

$$\begin{aligned}\langle\mathbf{E}^2\rangle&=-\frac{B^2}{3}\int\left(r\ \frac{\partial^2A}{\partial r^2}+2\frac{\partial A}{\partial r}\right)dr\\&=-\frac{B^2}{3}\left(2A|_0^\infty+r\frac{\partial A}{\partial r}|_0^\infty-\int_0^\infty\frac{\partial A}{\partial r}\ dr\right).\end{aligned} \tag{6}$$

To calculate the corresponding quantities in Eq. (6), we need to take account of the fact that as $r\to\infty$ the correlation functions decay in any case as r^{-5} or faster (as a consequence of the finiteness of the Loĭtsyanskiĭ invariant associated with the conservation of angular momentum[8]); the final result therefore has the form

$$\langle\mathbf{E}^2\rangle=\frac{B^2}{3}\ A(0)=\frac{B^2}{3}\ \langle\mathbf{v}^2\rangle, \tag{7}$$

since $b_{LL}(0)+2b_{NN}(0)$ is simply the mean-square velocity of the turbulent motion. It is evident from Eq. (7) that the energy of the electric field is proportional to the kinetic energy of the fluid and in the given situation is not related to the mean-square vorticity in the sense that Eq. (7) does not contain any factor with units of length (otherwise the right-hand side of (7) would include some characteristic length corresponding to the relation between $\langle(\mathrm{curl}\ \mathbf{v})^2\rangle$ and $\langle\mathbf{v}^2\rangle$)), contrary to the oft-encountered notion that $\langle\mathbf{E}^2\rangle$ is determined by small-scale motions, which provide the main contribution to $\langle(\mathrm{curl}\ \mathbf{v})^2\rangle$ (see Ref. 9).

Calculating the average values of $(\mathbf{v}\times\mathbf{B})^2$ and $\mathbf{E}\cdot(\mathbf{v}\times\mathbf{B})$ analogously, we readily verify that the mean-square current differs from (7) by a constant factor, so that both the electric field and the current density **j** are nonzero in the given situation. We also recognize that, generally speaking, these assertions are equally valid for arbitrary (but not too large) values of B. We have already mentioned that to choose the trivial solution of the Maxwell equations, $\mathbf{E}=0$, lacks any kind of logical foundation for the turbulent motion of a conducting fluid. In the next section, however, we intend to show that for sufficiently high values of B, another special case arises, $\mathbf{j}=0$, which reduces to 2D turbulent motion.

3. STRONG MAGNETIC FIELDS: TWO-DIMENSIONAL TURBULENCE

For sufficiently large values of B, such that the inequality $\sigma B^2L/\rho v\ll 1$ is not satisfied, the influence of the magnetic field on turbulence in a conducting fluid can no longer be ignored, and all the corresponding quantities become more or less anisotropic. In a homogeneous magnetic field there is only one preferred direction in space, and the two-point velocity correlation function must be axisymmetric:

$$b_{ij}(\mathbf{r})=a_1r_ir_j+a_2\lambda_i\lambda_j+a_3\delta_{ij}+a_4r_i\lambda_j+a_5r_j\lambda_i,$$

where $\boldsymbol{\lambda}=\mathbf{B}/B$ is the unit vector in the direction of **B**, and $a_1,\ldots,a_5$ are functions of r^2 and $\mathbf{r}\cdot\boldsymbol{\lambda}$. Of course, the equations containing b_{ij} (and the corresponding three-point moments) and the generalizing Karman–Howarth equations are also relatively easy to obtain in the given situation, but their solution is even more difficult than the solution of the Karman–Howarth equation. On the other hand, the most important issue from a physical standpoint is to ascertain the

character of the anisotropy of turbulence for magnetic fields of sufficient strength as to satisfy the opposite of the inequality given in Sec. 2:

$$\frac{\sigma B^2 L}{\rho v} \gg 1. \tag{8}$$

This problem is important in that experimental data[10] have shown that when this inequality holds and $\mathrm{Re}_m \ll 1$, the turbulent motion becomes 2D, with the velocity perpendicular to the magnetic field; such motion has a great many nontrivial features that distinguish it from the three-dimensional kind (see Refs. 11 and 12). In addition, it should be noted here that, as shown previously,[1] 2D turbulent motion perpendicular to the external field also occurs in the opposite limiting case $\mathrm{Re}_m \gg 1$, because now the field-generating equation holds identically. Obviously the ideal way to achieve these results theoretically would be to incorporate the corresponding equations into the solution. This being impossible, some sort of additional considerations[11,13] or numerical experiments (see, e.g., Ref. 14) are brought into the picture. As a rule, these considerations rest on an analogy with fluid motion in a rotating reference frame, for which the so-called Proudman–Taylor theorem holds.[15]

On the other hand, qualitative ''mechanical'' considerations suggest in any case how MHD interaction can lead to two-dimensionality. Indeed, an examination of a nondeformable, planar, closed electric current line in an external magnetic field quickly reveals that interaction rotates the plane of the current loop until it rests perpendicular to the magnetic field. It is clear, however, that nondeformable current loops do not exist in the fluid, and the indicated considerations cannot be regarded as proof of the result in question. Such a proof might be based on the derivation of some kind of local relations resulting from hydrodynamic and electrodynamic equations and leading to two-dimensionality.

To assist in the selection of these relations, and bearing condition (8) in mind, we can disregard the term $\rho(\mathbf{v}\cdot\nabla)\mathbf{v}$ in comparison with the Lorentz force in the equation of motion. Assuming that the derivative $\partial\mathbf{v}/\partial t$ is also small and ignoring it, we obtain

$$-\nabla p + \mathbf{j}\times\mathbf{B} = 0, \tag{9}$$

which is exactly analogous to the basic relation used to derive the Proudman–Taylor relation (the only difference being that the latter contains a term proportional to $\mathbf{v}\times\boldsymbol{\Omega}$ instead of $\mathbf{j}\times\mathbf{B}$). We note here that as in the case of the Proudman–Taylor theorem, to write expression (9) without $\partial\mathbf{v}/\partial t$ cannot be rigorously justified and is essentially an assumption. Applying the curl operator to (9) and taking into account the homogeneity of $\mathbf{B}$ and the continuity of the current, we obtain

$$(\mathbf{B}\cdot\nabla)\mathbf{j} = 0. \tag{10}$$

In the case of the Proudman–Taylor theorem we would have $(\boldsymbol{\Omega}\cdot\nabla)\mathbf{v} = 0$, and the two-dimensionality of the motion would be guaranteed; for the case investigated here Eq. (10) requires further consideration. Assuming that $\mathbf{B}$ is directed along the z axis and noting that Eq. (10) is satisfied by all components of the current density, we have

$$\frac{\partial j_z}{\partial z} = 0. \tag{11}$$

Since $\mathbf{v}\times\mathbf{B}$ contributes absolutely nothing to the z-component of the current density, this component is related only to the strength of the electric field $\mathbf{E}$ (or, more precisely, to its z-component). Consequently, without a potential difference in the z-direction, according to (11), we have simply $E_z = 0$ (or, equivalently, $j_z = 0$), and the distribution of the current and the electric field is 2D. For this reason the vector curl $\mathbf{j}$ is directed along z, so that from the potential character of $\mathbf{E}$ and Ohm's law we infer that

$$(\mathbf{B}\cdot\nabla)\mathbf{v} = \mathbf{k}\psi(x,y,t),$$

where $\mathbf{k}$ is the unit vector along z, and ψ is a function that does not depend on z. It follows from the latter relation that

$$\frac{\partial v_x}{\partial z} = 0, \quad \frac{\partial v_y}{\partial z} = 0, \quad \frac{\partial v_z}{\partial z} = \psi(x,y,t).$$

Inasmuch as the velocity v_z must be bounded in any case, the function $\psi(x,y,t)$ vanishes, so that we have

$$\mathbf{v} = (v_x, v_y), \quad \mathrm{div}\ \mathbf{v} = 0,$$

and it is at once obvious that the equations of motion revert to 2D equations. Since in fact curl $\mathbf{j} = 0$ and the current distribution in this case corresponds to minimum Joule heat loss (see Problem 3 in Sec. 21 of Ref. 1), it is reasonable to state that the transition to a 2D turbulence structure in a conducting fluid under the influence of a homogeneous field is equivalent to requiring minimization of the Joule heat loss.

Finally, looking at the physically relevant case of nonconducting boundaries (zero current at the boundary), we also infer from div $\mathbf{j} = 0$ and curl $\mathbf{j} = 0$ in accordance with the Liouville theorem that $\mathbf{j} = 0$. This relation simply implies that the electric field is related to the velocity by $\mathbf{E} = -\mathbf{v}\times\mathbf{B}$, so that the magnetic field no longer interacts with the resulting 2D motion.

We conclude this section with the stipulation that the foregoing results are naturally valid in situations where allowed by the boundary conditions. In real life, this means that the corresponding phenomena must be treated at large distances from any boundary whose normal is parallel to the field; these distances must be at least much greater than the primary space scale of the turbulent motion.

4. AVERAGING OF OHM'S LAW IN THE PRESENCE OF TURBULENT HEAT FLUX

The results described in the preceding sections are valid in a temperature-homogeneous medium, but if the temperature distribution is nonuniform, its fluctuations induced by the turbulence of the fluid can be correlated with the velocity fluctuations. It will be shown below that the existence of such a correlation with allowance for the temperature dependence of the conductivity of the medium leads to a nontrivial effect, which can be observed in appropriate experiments.

In describing the motion of a conducting fluid, it is usually necessary to use certain averaged values of the corresponding quantities. For small magnetic Reynolds numbers in the noninductive approximation this refers specifically to

quantities involved in Ohm's law, in which the conductivity is replaced by an effective value that depends on the distribution of the space–time inhomogeneities. In the case of turbulent fluid motion, the averaged Ohm's law has the form

$$\langle \mathbf{j} \rangle = \langle \sigma \rangle \langle \mathbf{E} \rangle + \langle \sigma \rangle [\langle \mathbf{v} \rangle \times \mathbf{B}] + \langle \sigma' \mathbf{E}' \rangle + \langle \sigma' (\mathbf{v}' \times \mathbf{B}) \rangle \tag{12}$$

(the primes in this expression refer to fluctuations of the corresponding quantities, and the Hall effect is disregarded for simplicity).

The quantity $\langle \sigma' \mathbf{E}' \rangle$ also includes the component $\langle \sigma' \mathbf{E}'_{\sigma'} \rangle$ associated with the presence of inhomogeneity in the electric field in a medium with inhomogeneous conductivity even when it is not in motion (in some cases the corresponding effective values of the conductivity can be calculated in their entirety[16]). Since the value of σ' is small in the given situation (see below), the quantity $\mathbf{E}'_{\sigma'}$ is also small and can be neglected in relation to the fluctuations of the field $\mathbf{E}'$ due to turbulent motion for a homogeneous conductivity. Thus, when the conductivity has a small inhomogeneity, the corresponding perturbation of the electric field $\mathbf{E}'_{\sigma'}$ is a certain functional of σ' such that it does not contain any zeroth-order terms in σ'. In any case, therefore, the quantity $\sigma' \mathbf{E}'_{\sigma'}$ is of higher than first order in σ'; on the other hand, the turbulence-dependent quantity $\mathbf{E}'$ is not small, so that $\sigma' \mathbf{E}'$ is first-order in σ'.

Naturally, it is impossible to calculate $\langle \sigma' \mathbf{E}' \rangle$ and $\langle \sigma' (\mathbf{v}' \times \mathbf{B}) \rangle$ for arbitrary values of the corresponding quantities. However, it follows from the preceding sections that for B not too large, these are quantities of the same order, and in general they are of the same order as their sum. In the presence of turbulent heat flux $\mathbf{q}$ the component $\langle \sigma' (\mathbf{v}' \times \mathbf{B}) \rangle$ can then be expressed exactly in terms of the magnitude of this flux.

The form of the expression for this component of the current makes it clear that it can only fail to vanish when the mean of $\sigma' \mathbf{v}'$ is nonzero. Since the conductivity of a plasma, for example, depends on the temperature (neglecting nonequilibrium effects and weak pressure dependence[17]), we must write $\sigma' \equiv \sigma'(T')$, where σ' and T' have the same sign.

Consequently, for a nonzero value of $\langle T' \mathbf{v}' \rangle$ the quantity $\langle \sigma' \mathbf{v}' \rangle$ is also nonzero in general. When $T' \ll \overline{T}$ (average temperature), as is usually the case in practice, this assertion becomes exact, because $\sigma' = (d\sigma/dT) T'$, and

$$\langle \sigma' \mathbf{v}' \rangle = \left\langle \frac{\sigma'}{T'} \; T' \mathbf{v}' \right\rangle = \frac{d\sigma}{dT} \langle T' \mathbf{v}' \rangle. \tag{13}$$

Recalling now that $\langle T' \mathbf{v}' \rangle$ is none other (to within some factor) than the turbulent heat flux,[6]

$$\mathbf{q} = \rho c_p \langle T' \mathbf{v}' \rangle,$$

for the additional contribution to the current density we have

$$\mathbf{j}_{\sigma'} \sim \langle \sigma' (\mathbf{v}' \times \mathbf{B}) \rangle = \frac{d\sigma}{dT} \frac{1}{\rho c_p} (\mathbf{q} \times \mathbf{B}). \tag{14}$$

The emf corresponding to this current density is

$$\mathscr{E} \sim \frac{1}{\sigma} \frac{d\sigma}{dT} \frac{Bq}{\rho c_p}.$$

The indicated effect can be demonstrated in the laboratory using, for example, an aqueous NaCl solution, for which $(1/\sigma)(d\sigma/dT)$ is of the order of 10^{-2} K^{-1}. Then for $q \sim 10$ W/cm^2 and $B \sim 1$ T we have an induced electric field $\sim 10^{-3}$ V/cm, which is easily measurable.

We also note that formally analogous conclusions can be drawn for the case $\mathrm{Re}_m \gg 1$, so that we actually have a certain mechanism, over and above the α-effect,[18] for the generation of large-scale fields in turbulent motion. However, its analysis is far more complex than for $\mathrm{Re}_m \ll 1$, because in the presence of nonzero fluctuations of the magnetic field $\mathbf{B}'$ it would be necessary to augment Eq. (12) with ternary correlation, specifically to include the quantity $\langle \sigma' (\mathbf{v}' \times \mathbf{B}') \rangle$, which is not small for $\mathrm{Re}_m \gg 1$.

[1)]Except for situations that are reducible to laminar flow stability problems and the onset of turbulence[2] or are associated with the degeneracy of turbulence, in which case the nonlinear terms in the hydrodynamic equations can be neglected.[3]

[1] L. D. Landau and E. M. Lifshitz, *Electrodynamics of Continuous Media*, 2nd ed. (rev. and enl., with L. P. Pitaevskiĭ), Pergamon Press, New York (1984).
[2] T. Cowling, *Magnetohydrodynamics*, Interscience, New York (1957).
[3] B. V. Eliseev, Dokl. Akad. Nauk SSSR **161**, 560 (1965) [Sov. Phys. Dokl. **10**, 239 (1965)].
[4] S. P. Pikelner, *Fundamentals of Cosmic Electrodynamics*, NASA, Washington, D.C. (1964).
[5] A. L. Tseskis, Teplofiz. Vys. Temp. **33**, 496 (1995).
[6] A. S. Monin and A. M. Yaglom, *Statistical Fluid Mechanics* [in Russian], Part I, Nauka, Moscow (1965).
[7] A. S. Monin and A. M. Yaglom, *Statistical Fluid Mechanics* [in Russian], Part II, Nauka, Moscow (1967).
[8] L. D. Landau and E. M. Lifshitz, *Fluid Mechanics*, 2nd ed., Pergamon Press, New York (1987).
[9] R. Moreau, Magn. Gidrodin., No. 4, 31 (1970).
[10] L. G. Kit and A. B. Tsinober, Magn. Gidrodin., No. 3, 37 (1972).
[11] R. H. Kraichnan and D. Montgomery, Rep. Prog. Phys. **4**, 547 (1980).
[12] A. L. Tseskis, Zh. Éksp. Teor. Fiz. **83**, 176 (1982) [Sov. Phys. JETP **56**, 95 (1982)].
[13] J. Sommeria and R. Moreau, J. Fluid Mech. **118**, 507 (1982).
[14] J. Verron and J. Sommeria, Phys. Fluids **30**, 732 (1987).
[15] H. Greenspan, *The Theory of Rotating Fluids*, Cambridge Univ. Press, New York (1968).
[16] A. M. Dykhne, Zh. Éksp. Teor. Fiz. **59**, 110 (1970) [Sov. Phys. JETP **32**, 63 (1971)].
[17] D. A. Frank-Kamenetskiĭ, *Lectures in Plasma Physics*, Atomizdat, Moscow (1968).
[18] S. I. Vaĭnshteĭn and Ya. B. Zel'dovich, Usp. Fiz. Nauk **106**, 432 (1972) [Sov. Phys. Usp. **15**, (1972)].

Translated by James S. Wood

Phenomenological theory of the magnetoelectric effect in some boracites

D. G. Sannikov

Institute of Crystallography, Russian Academy of Sciences, 117333 Moscow, Russia
(Submitted 28 May 1996)
Zh. Éksp. Teor. Fiz. **111**, 536–546 (February 1997)

An explanation is given for the narrow peak in the temperature dependence of the component α_{32} of the magnetoelectric effect tensor near the transition at $T=T_c$ to the $m'm2'$ phase observed in the boracites. A phenomenological approach is used which is based on the symmetry of the cubic phase of the crystals. The change in the sign of α_{23} and α_{32} observed in some of the boracites as the temperature is lowered is attributed to the low value of T_c. © *1997 American Institute of Physics.* [S1063-7761(97)01002-0]

The boracites are a large family of crystals with the general formula $M_3B_7O_{13}X$, where M is the ion of a doubly valent metal and X is a halogen. In the Co–Br, Co–I, Ni–Cl, and several other boracites, as the temperature T is reduced, a sequence of phase transitions is observed from the cubic phase $T_d'=43m1'$ (the C_0 phase) into the orthorhombic phase: first $C_{2v}'=mm21'$ (the C_1 phase) and then $C_{2v}(C_s)=m'm2'$ (the C_2 phase). The higher temperature first-order transition at $T=T_0$ ($T_0=466$ K for Co–Br boracite) is a nonintrinsic ferroelectric ferroelastic transition, and involves a change in the translational symmetry of the crystal. The lower second-order transition at $T=T_c$ is simultaneously a nonintrinsic ferroelectric ferroelastic transition and a weak ferromagnetic transition. In the C_2 phase, the components α_{32} and α_{23} of the magnetoelectric effect tensor α_{ik} are observed to have a temperature dependence.[1–3] The characteristic features of this dependence are a sharp peak in $\alpha_{32}(T)$ near $T=T_c$ and a change in the sign of $\alpha_{32}(T)$ or $\alpha_{23}(T)$ at some distance from T_c in some individual cases (see Fig. 1).

The purpose of this paper is to examine the dependences $\alpha_{32}(T)$ and $\alpha_{23}(T)$ theoretically in the framework of a phenomenological approach (see the earlier work of Chupis,[4] as well). Consistent with experimental data,[5] we assume that the translational symmetry of the crystal does not change during the C_1-C_2 phase transition. This means that the order parameter transforms according to one of the irreducible representations of the point symmetry group of the crystal. The symmetry of the cubic C_0 phase will serve as the basis for subsequent analysis. This makes it possible, in particular, to compare the values of the coefficients in the resulting expressions for α_{32}, α_{23}, and other quantities.

The two three dimensional representations of the T_d' point group reduce to the $C_{2v}(C_s)$ group. The magnetic moment vector M_i transforms according to one of them (F_{1m}). Then the C_2 phase is the usual (exchange) ferromagnetic phase. An analysis shows that this case is inconsistent with the experimental data, so it will not be examined here.

The toroidal momentum vector T_i transforms according to the other representation (F_{2m}) (a discussion of the third dipole moment T_i in electrodynamics can be found elsewhere[6]). We regard T_i as the order parameter for the C_1-C_2 phase transition, and construct the invariants of the lowest powers in T_i, as well as in the polarization vectors P_i and magnetization M_i.

It must be kept in mind that the coordinate systems of the cubic and orthorhombic systems are different. One is rotated relative to the other by an angle of 45° about the z axis. The coordinates in the cubic phase (x,y,z) and orthorhombic phase (x_1,x_2,x_3) are related by

$$x=\frac{1}{\sqrt{2}}(x_1+x_2),\quad y=\frac{1}{\sqrt{2}}(-x_1+x_2),\quad z=x_3,$$

$$x_1=\frac{1}{\sqrt{2}}(x-y),\quad x_2=\frac{1}{\sqrt{2}}(x+y),\quad x_3=z. \tag{1}$$

We shall write down the invariants in both coordinate systems.

The order parameter of the C_0-C_1 phase transition has six components. It transforms according to the six dimensional representation of the $T_d^5=F\bar{4}3c$ space group of the C_0 phase.[7] We denote the square of the order parameter by R^2. This quantity is all that is needed in the following, since the C_0-C_1 phase transition, as such, is of no interest to us.

The part of the thermodynamic potential that depends on R^2 and P_i can be represented in the form

$$\alpha R^2+\frac{1}{2}\beta R^4+\frac{1}{2}\kappa P^2-\sigma P_z R^2-\mathbf{P}\cdot\mathbf{E},$$

$$P^2=P_x^2+P_y^2+P_z^2=P_1^2+P_2^2+P_3^2,$$

$$\mathbf{P}\cdot\mathbf{E}=P_xE_x+P_yE_y+P_zE_z=P_1E_1+P_2E_2+P_3E_3. \tag{2}$$

The fact that the C_0-C_1 transition is a first-order phase transition is not important, and we treat it as if it were a second-order transition, i.e., set $\beta>0$ and neglect the invariant γR^6 in Eq. (2). This does not affect the final results. In the mixed invariant P_zR^2 only one component, P_z, of the vector P_i has been retained. It is assumed for concreteness that in the C_1 phase the crystal has a single domain and the spontaneous polarization is directed along the z axis. The fact that the component P_z is actually related to some quadratic combination of the components of the order parameter is not important, i.e., this combination can be replaced by R^2, as has been done in Eq. (2).

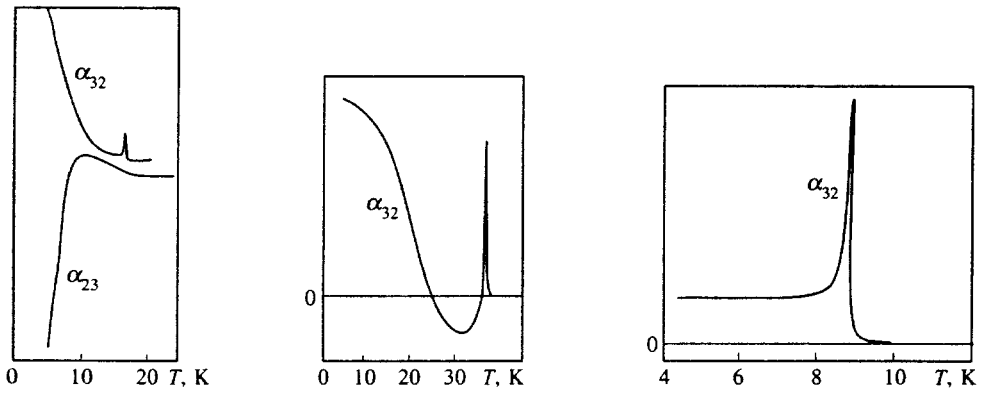

FIG. 1. Temperature variations in the components α_{32} and α_{23} of the magnetoelectric tensor in the $m'm2'$ phase of Co–Br[1] (*1*), Co–I[2] (*2*), and Ni–Cl[3] (*3*) boracites.

The part of the potential that depends on T_i, as well on R^2 and P_i, can be written in the form

$$\frac{1}{2}AT^2+\frac{1}{4}CT^4-DR^2T^2. \tag{3}$$

Note that using the same notation for the absolute magnitude of the vector T_i and the temperature cannot lead to confusion. There is yet another independent invariant of the fourth degree in T_i:

$$cI_{T^4}=c(T_x^2T_y^2+T_z^2T_x^2+T_y^2T_z^2)$$
$$=\frac{1}{4}c(T_1^2-T_2^2)^2+c(T_1^2+T_2^2)T_3^2.$$

This invariant, however, is relativistic and is small compared to the exchange invariant CT^4, so it can be neglected.

Yet another relativistic invariant has the form

$$dI_{PT^2}=d(P_xT_yT_z+P_yT_zT_x+P_zT_xT_y)$$
$$=-d(P_1T_1-P_2T_2)T_3-\frac{1}{2}dP_3(T_1^2-T_2^2). \tag{4}$$

Although it can be neglected compared to the exchange invariant DR^2T^2, we can use it to see how the three-dimensional representation of the cubic C_0 phase splits up into three one-dimensional representations of the rhombic C_1 phase.

The invariant (4) renormalizes the coefficient A of T^2 in Eq. (3):

$$\frac{1}{2}(A-dP_3)T_1^2+\frac{1}{2}(A+dP_3)T_2^2+\frac{1}{2}AT_3^2. \tag{5}$$

In order for a C_1-C_2 phase transition to take place, the coefficient A must decrease with temperature and pass through zero. As can be seen from Eq. (5), one of the coefficients $A\mp dP_3$ goes to zero before the others, since P_3 has a spontaneous value in the C_1 phase. Let us assume that it is the coefficient of T_1^2, i.e., $dP_3>0$. Then a spontaneous value T_1 arises in the C_2 phase and the component T_1 is the order parameter for the C_1-C_2 transition. The choice of T_1 as an order parameter ensures that the component M_2 will have a spontaneous value in the C_2 phase (see below).

The part of the potential that depends on M_1 can be written in the form

$$\frac{1}{2}BM^2+aI_{PMT}-2bI_{MT^3}-\mathbf{M}\cdot\mathbf{H},$$

$$I_{PMT}=[PM]T=(P_yM_z-P_zM_y)T_x$$
$$+(P_zM_x-P_xM_z)T_y+(P_xM_y-P_yM_x)T_z$$
$$=(P_2M_3-P_3M_2)T_1+(P_3M_1-P_1M_3)T_2$$
$$+(P_1M_2-P_2M_1)T_3,$$

$$I_{MT^3}=M_xT_x(T_y^2-T_z^2)$$
$$+M_yT_y(T_z^2-T_x^2)+M_zT_z(T_x^2-T_y^2)$$
$$=\frac{1}{2}(M_2T_1-M_1T_2)(T_1^2-T_2^2)$$
$$-(M_2T_1+M_1T_2)T_3^2+2M_3T_1T_2T_3. \tag{6}$$

The form of the invariant $I_{MT'}$ implies that a spontaneous $M_2\propto T_1^3$ develops in the C_2 phase.

We have not considered invariants containing the deformation tensor u_{ik} in the above discussion. In the meantime, the components u_{yz}, u_{zx}, and u_{xy} transform as P_x, P_y, and P_z, so that they play an equally important role. However, if we include these components and then eliminate them from the potential by taking derivatives with respect to them, we then obtain the same expressions (2)–(6), but with renormalized coefficients β, κ, σ, d, a, and b. Thus, we may assume that this sort of operation eliminating u_{ik} has already been carried out and that the coefficients in Eqs. (2)–(6) are renormalized.

If we express P_i and M_i in terms of E_i and H_i from Eqs. (2) and (6),

$$\mathbf{P}=\frac{1}{\kappa}\mathbf{E},\quad \mathbf{M}=\frac{1}{B}\mathbf{H} \tag{7}$$

and substitute Eq. (7) in Eq. (6), then we obtain the invariant

$$\frac{\alpha}{\kappa B}(\mathbf{E}\times\mathbf{H})\cdot\mathbf{T}. \tag{8}$$

Equation (8) implies that the vector product $\mathbf{E}\times\mathbf{H}$ can be treated as a generalized force conjugate to the generalized coordinate $\mathbf{T}$, the toroidal momentum. In crossed fields with $E_3\neq 0$ and $H_2\neq 0$ or $E_2\neq 0$ and $H_3\neq 0$, the second-order

C_1-C_2 phase transition is smeared out, since these fields induced a toroidal ordering in the C_1 phase, removing the symmetry difference between the C_1 and C_2 phases. The presence of the invariant (8) leads to the existence of off-diagonal components of the magnetoelectric effect tensor α_{ik} in a phase with spontaneous toroidal momentum. It may be said that the appearance of off-diagonal components of the tensor α_{ik} in the low-temperature phase during the phase transition is the most characteristic feature of the (ferro) toroidal phase transition. Note that the phase transition in the Ni–I boracite has been treated as a (ferro) toroidal transition before.[8]

The thermodynamic potential, therefore, consists of three parts: (2), (3), and (6). We retain only one component T_1 of the vector T_i, setting $T_2=T_3=0$. Let us first consider only the components P_3 and M_2 of the vectors P_i and M_i. The components P_2 and M_3 will be considered separately (see below). Thus, we have

$$\Phi(R^2,P_3,M_2,T_1)=\alpha R^2+\frac{1}{2}\beta R^4+\frac{1}{2}\kappa P_3^2-6P_3R^2+\frac{1}{2}(A-dP_3)T_1^2+\frac{1}{4}CT_1^4-DR^3T_1^2+\frac{1}{2}BM_2^2-aP_3M_2T_1-bM_2T_1^3-P_3E_3-M_2H_2. \tag{9}$$

Let us consider the C_1 phase, in which $T_1=0$ and $M_2=0$. Differentiating the potential (9) with respect to the variables R^2 and P_3 and setting $T_1=0$, we obtain

$$\Phi_{R^2}=\alpha+\beta R^2-\sigma P_3=0,$$
$$\Phi_{P_3}=\kappa P_3-\sigma R^2-E_3=0. \tag{10}$$

Here and in the following the derivatives are denoted by subscripts, e.g., $\Phi_{R^2}=\partial\Phi/\partial(R^2)$.

Solving the system of Eqs. (10) with $E_3=0$, we obtain

$$P_3=\frac{\sigma}{\kappa}R^2,\quad R^2=-\frac{\alpha}{\widetilde{\beta}},\quad \widetilde{\beta}\equiv\beta-\frac{\sigma^2}{\kappa},\quad \widetilde{\kappa}\equiv\kappa-\frac{\sigma^2}{\beta}. \tag{11}$$

Recall that the C_0-C_1 phase transition is, in fact, a first-order transition, so that the second expression in Eq. (11) yields a false dependence $R^2(T)$. However, it is possible to use only the first expression in Eq. (11), assuming that the dependence $R_3(T)$ is known from experiment.

We now consider the C_2 phase, in which all the variables R^2, P_3, M_2, and T_1 are nonzero, i.e., have spontaneous values. The variable R^2, which is of no intrinsic interest, can be conveniently eliminated from the potential (9). Differentiating Eq. (9) with respect to R^2, we obtain

$$\Phi_{R^2}=\alpha+\beta R^2-\sigma P_3-DT_1^2=0,$$
$$R^2=R_0^2+\frac{\sigma}{\beta}P_3+\frac{D}{\beta}T_1^2,\quad R_0^2\equiv-\frac{\alpha}{\beta}. \tag{12}$$

Substituting Eq. (12) into Eq. (9), we find

$$\Phi=\Phi_0+\frac{1}{2}\widetilde{\kappa}P_3^2-\sigma R_0^2P_3+\frac{1}{2}\overline{A}T_1^2+\frac{1}{4}\overline{C}T_1^4-\frac{\sigma D}{\beta}P_3T_1^2+\frac{1}{2}BM_2^2-aP_3M_2T_1-bM_2T_1^3-P_3E_3-M_2H_2,\quad \Phi_0\equiv-\frac{1}{2}\beta R_0^4,$$
$$\overline{A}\equiv A-2DR_0^2,\quad \overline{C}\equiv C-\frac{2D^2}{\beta}. \tag{13}$$

In Eq. (13) the invariant $dP_3T_1^2$ is neglected, being relativistically small compared to the invariant $(\sigma D/\beta)P_3T_1^2$. The advantage of the potential (13) compared to (9) is not only that it has fewer variables (three instead of four), but also that there is a direct relationship between P_3 and T_1^2 (and not indirectly in terms of R^2, as in Eq. (9)).

Differentiating Eq. (13) with respect to P_3, M_2, and T_1, we obtain

$$\Phi_{P_3}=\widetilde{\kappa}P_3-\sigma R_0^2-\frac{\sigma D}{\beta}T_1^2-aM_2T_1-E_3=0,$$
$$\Phi_{M_2}=BM_2-aP_3T_1-bT_1^3-H_2=0,$$
$$\Phi_{T_1}=\overline{A}T_1+\overline{C}T_1^3-\frac{2\sigma D}{\beta}P_3T_1-aP_3M_2-3bM_2T_1^2=0. \tag{14}$$

Solving the system formed by the first two of Eqs. (14), which are linear in P_3 and M_2, with $E_3=0$ and $H_2=0$, we obtain

$$P_3=P_0+\frac{\sigma D}{\beta\widetilde{\kappa}}T_1^2,\quad M_2=\frac{aP_0}{B}T_1+\frac{1}{B}\left(\frac{\sigma D}{\beta\widetilde{\kappa}}a+b\right)T_1^3. \tag{15}$$

In Eq. (15), the quantity R_0^2 that shows up in Eqs. (12)–(14) has been replaced by P_0, which is given by

$$P_0\equiv\frac{\sigma}{\widetilde{\kappa}}R_0^2=\frac{\sigma}{\widetilde{\kappa}}\frac{(-\alpha)}{\beta}=\frac{\sigma}{\kappa}\frac{(-\alpha)}{\beta},$$

where the last expression coincides with Eq. (11) for P_3 in the C_1 phase. Thus, the first term P_0 in Eq. (15) for P_3 in the C_2 phase can be regarded as part of the P_3 obtained by extrapolating the experimental $P_3(T)$ curve from the C_1 phase into the C_2 phase.

Substituting the solutions (15) into the third of Eqs. (14) and solving it, we obtain

$$T_1^2=\frac{-\widetilde{A}}{\widetilde{C}},\quad \widetilde{A}\equiv\overline{A}-\frac{2\sigma D}{\beta}P_0-\frac{a^2}{B}P_0^2=A-\frac{2\kappa D}{\sigma}P_0-\frac{a^2}{B}P_0^2,\quad \widetilde{C}\equiv\overline{C}-\frac{2\sigma^2D^2}{\beta^2\widetilde{\kappa}}=C-\frac{2D^2}{\widetilde{\beta}}. \tag{16}$$

We have retained all terms in the coefficient $\widetilde{A}$, since $\widetilde{A}$ goes to zero at the C_1-C_2 transition point. Even the last, smallest, term in $\widetilde{A}$ is important for subsequent calculations.

We now find the susceptibilities: dielectric $\chi_{33}=P_{3E_3}$, magnetic $k_{22}=M_{2H_2}$, and magnetoelectric $\alpha_{32}=P_{3H_2}=M_{2E_3}$, where the subscripts, as before, denote derivatives, e.g., $P_{3H_2}\equiv\partial P_3/\partial H_2$. We take the total derivatives of Eq. (14) with respect to E_3 and H_2. As a result we obtain a system of three plus three equations, which we write in the consistent form

$$\Phi_{P_3P_3}P_{3E_3(H_2)}+\Phi_{P_3M_2}M_{2E_3(H_2)}+\Phi_{P_3T_1}T_{1E_3(H_2)}=1(0),$$

$$\Phi_{M_2P_3}P_{3E_3(H_2)}+\Phi_{M_2M_2}M_{2E_3(H_2)}+\Phi_{M_2T_1}T_{1E_3(H_2)}=0(1),$$

$$\Phi_{T_1P_3}P_{3E_3(H_2)}+\Phi_{T_1M_2}M_{2E_3(H_2)}+\Phi_{T_1T_1}T_{1E_3(H_2)}=0(0). \tag{17}$$

According to Eq. (13) or (14),

$$\Phi_{P_3P_3}=\widetilde{\kappa},\quad \Phi_{P_3M_2}=\Phi_{M_2P_3}=-aT_1,$$

$$\Phi_{P_3T_1}=\Phi_{T_1P_3}=-\frac{2\sigma D}{\beta}T_1,\quad \Phi_{M_2M_2}=B,$$

$$\Phi_{M_2T_1}=\Phi_{T_1M_2}=-aP_3-3bT_1^2,$$

$$\Phi_{T_1T_1}=\overline{A}-3\overline{C}T_1^2-\frac{2\sigma D}{\beta}P_3, \tag{18}$$

where P_3, M_2, and T_1 are taken from Eqs. (15) and (16). The determinant of the system of linear equations (17) reduces to the form $2\widetilde{\kappa}B\widetilde{C}T_1^2$. It must be assumed (see Eqs. (11) and (15)–(18)) that $\widetilde{\beta}>0$, $\widetilde{\kappa}>0$, $B>0$, and $\widetilde{C}>0$. The remaining coefficients σ, D, a, and b have arbitrary signs.

Solving Eq. (17) for P_{3E_3}, M_{2H_2}, and $P_{3H_2}=M_{2E_3}$, we obtain

$$\chi_{33}=\frac{1}{\widetilde{\kappa}}+\frac{2\sigma^2D^2}{\beta^2\widetilde{\kappa}^2\widetilde{C}},\quad k_{22}=\frac{(aP_0)^2}{2B^2\widetilde{C}}\frac{1}{T_1^2}+\frac{1}{B},$$

$$\alpha_{32}=\frac{\sigma DaP_0}{\beta\widetilde{\kappa}B\widetilde{C}}\frac{1}{T_1}+\frac{1}{\widetilde{\kappa}B}\left(a+\frac{3\sigma^2D^2}{\beta^2\widetilde{\kappa}\widetilde{C}}a+\frac{3\sigma D}{\beta\widetilde{C}}b\right)T_1. \tag{19}$$

The susceptibilities χ_{33} and k_{22} in the C_1 phase can be obtained from Eqs. (17) and (18) by setting $T_1=0$ and $M_2=0$:

$$\chi_{33}=\frac{1}{\widetilde{\kappa}},\quad k_{22}=\frac{(aP_0)^2}{B^2\widetilde{A}}+\frac{1}{B}, \tag{20}$$

where P_0 is the polarization in the C_1 phase. In accordance with Eq. (7), in the C_0 phase we have

$$\chi_{33}=\frac{1}{\kappa},\quad k_{22}=\frac{1}{B}.$$

Let us examine the temperature dependences of Eqs. (15), (16), (19), and (20) for P_3, M_2, χ_{33}, k_{22}, and α_{32}. We assume, as usual, that only one coefficient, $\widetilde{A}$, depends linearly on the temperature:

$$\widetilde{A}=A_T(T-T_c). \tag{21}$$

The remaining coefficients are assumed constant and equal to their values at the transition point $T=T_c$. Then, according to Eq. (16), we obtain

$$T_1^2=\frac{A_TT_c}{\widetilde{C}}\frac{T_c-T}{T_c}. \tag{22}$$

The dependence of these quantities on T in the C_2 phase is determined by their dependence on T_1.

The second term in Eq. (16) for P_3 is the spontaneous polarization, which appears in the C_2 phase as a supplement to the polarization $P_0(T)$ that existed in the C_1 phase (see above). It can be said that the C_1-C_2 phase transition is a nonintrinsic ferroelectric (and ferroelastic) transition with an index $f=2$: $\Delta P_3\sim T_1^f$. During a C_1-C_2 transition, the dielectric susceptibility χ_{33} undergoes an upward jump, which is the characteristic feature of nonintrinsic ferroelectric phase transitions (see the review by Levanyuk and Sannikov,[9] for example).

If the C_0-C_1 phase transition did not exist, the C_0-C_2 transition would be a nonintrinsic ferromagnetic transition with $f=3$: $M_2\sim T_1^3$; see Eq. (15) (a latent antiferromagnetism in the terminology of Dzyaloshinskiĭ and Man'ko[10]). Because of the C_0-C_1 transition and, therefore, the existence of spontaneous polarization P_0 in the C_1 phase, C_2 is a weak ferromagnetic phase: $M_2\sim T_1$; see Eq. (15). The coupling constant aP_0/B is proportional to two small quantities, a/B and P_0. The distortion of the C_1 phase relative to the C_0 phase is considered small, i.e., it is assumed that P_0 is small even far from the temperature T_0 of the C_0-C_1 transition.

Because of the linear relationship between M_2 and T_1, the susceptibility k_{22} in the potential (13) obeys the Curie–Weiss law in both phases C_2 and C_1 (compare Eqs. (19) and (20)). The Curie constant, which is proportional to the square of the coupling constant aP_0/B, is very small. Thus, the peak in k_{22} near the transition point $T=T_c$ must be very narrow. Outside a narrow neighborhood of the transition point $T=T_c$ the susceptibility k_{22} is the same in both phases, and equals $1/B$.

The component α_{32} of the magnetoelectric tensor, which differs from zero only in the C_2 phase, contains a term inversely proportional to T_1 (see Eq. (19)). The coefficient of T_1^{-1} is proportional to the two small quantities a/B and P_0. Thus, the peak in the $\alpha_{32}(T)$ curve near the transition point $T=T_c$ is narrow (but not so narrow as the peak in $k_{22}(T)$). If we define the width ΔT of the peak in terms of its width at the temperature for which the first term in Eq. (19) equals the second term, then we obtain $\Delta T\sim P_0$ for α_{32} and $\Delta T\sim(aP_0/B)^2$ for k_{22}.

A peak in $\alpha_{32}(T)$ in the neighborhood of $T=T_c$ has been observed in the boracites (see the Fig. 1). Since the signs of the coefficients σ, D, a, and b are arbitrary, the first term in Eq. (19) for α_{32}, which determines the peak in $\alpha_{32}(T)$, and the second term, which determines the subsequent variation in $\alpha_{32}(T)$, can have either the same or opposite signs (compare the dependences for the Co–I boracite and the Co–Br

and Ni–Cl boracites in the figure).

We now consider the variables P_2 and M_3 in the thermodynamic potential constructed from the invariants (2), (3), and (6):

$$\Phi(P_2,M_3)=\frac{1}{2}\,\kappa P_2^2+\frac{1}{2}\,BM_3^2+aP_2M_3T_1 - P_2E_2-M_3H_3. \tag{23}$$

Differentiating this part of the potential with respect to P_2 and M_3, we obtain a system of equations in addition to the system (14):

$$\Phi_{P_2}=\kappa P_2+aT_1M_3-E_2=0,$$

$$\Phi_{M_3}=BM_3+aT_1P_2-H_3=0. \tag{24}$$

Solving Eq. (24) with $E_2=0$ and $H_3=0$, we obtain

$$P_2=0, \quad M_3=0. \tag{25}$$

Since P_2 and M_3 are equal to zero in all phases, the part of the potential (23) added to the potential (9) does not change the previous analysis, and all the previous results remain valid.

Taking the total derivatives of Eq. (24) with respect to E_2 and H_3, we obtain the system of equations (cf. Eq. (17)):

$$\Phi_{P_2P_2}P_{2E_2(H_3)}+\Phi_{P_2M_3}M_{3E_2(H_3)}=1(0),$$

$$\Phi_{M_3P_2}P_{2E_2(H_3)}+\Phi_{M_3M_3}M_{3E_2(H_3)}=0(1), \tag{26}$$

where, according to Eqs. (23) or (24),

$$\Phi_{P_2P_2}=\kappa \quad \Phi_{P_2M_3}=\Phi_{M_3P_2}=aT_1, \quad \Phi_{M_3M_3}=B. \tag{27}$$

The expressions for the susceptibilities $\chi_{22}=P_{2E_2}$, $k_{33}=M_{3H_3}$, and $\alpha_{23}=P_{2H_3}=M_{3E_2}$ obtained from Eqs. (26) and (27) have the form

$$\chi_{22}=\frac{1}{\kappa}, \quad k_{33}=\frac{1}{B}, \quad \alpha_{23}=-\frac{a}{\kappa B}\,T_1, \tag{28}$$

where T_1 is taken from Eq. (16). The expressions for χ_{22} and k_{33} in Eq. (28) are valid in all phases C_2, C_1, and C_0, while α_{23} is nonzero only in the C_2 phase, where $T_1 \neq 0$.

The components α_{23} and k_{33} in Eq. (28), in contrast to α_{32} and k_{22} in Eq. (19), have no terms that diverge at the transition point $T=T_c$. Note that if the C_0-C_1 phase transition did not exist, then we would have $\alpha_{32}=-\alpha_{23}=aT_1/\kappa B$. Note also that all three terms in α_{32} proportional to T_1 in Eq. (19) have arbitrary signs and, generally, are comparable in magnitude. Obviously, the change in sign of α_{23} observed in Co–Br boracite (see Fig. 1) cannot be explained on the basis of Eq. (28). Thus, we find the subsequent terms in the expansion of α_{23} in powers of T_1^2 (this is much harder to do for α_{32}).

Let us examine invariants in higher powers of T_1^2 in the potential (23) than those included in Eqs. (2), (3), and (6). One part of these invariants has the form

$$-\frac{1}{2}FP^2T^2-\frac{1}{2}\,\kappa' P^2R^2-\tau I_{P^3},$$

$$I_{P^3}=P_xP_yP_z=-\frac{1}{2}\,(P_1^2-P_2^2)P_3. \tag{29}$$

There are two other independent invariants of the form P^2T^2: $f(\mathbf{P}\cdot\mathbf{T})^2$ and

$$f'I_{P^2T^2}=f'(P_xP_yT_xT_y+P_zP_xT_zT_x+P_yP_zT_yT_z) =\frac{1}{4}\,f'(P_1^2-P_2^2)(T_1^2-T_2^2) +f'(P_1T_1+P_2T_2)P_3T_3.$$

Both of these invariants are relativistic, and can be neglected compared to the exchange invariant FP^2T^2 in Eq. (29).

Yet another part of the invariants has the form

$$-\frac{1}{2}\,GM^2T^2-\frac{1}{2}\,G'(\mathbf{M}\cdot\mathbf{T})^2-\frac{1}{2}\,B'M^2R^2. \tag{30}$$

The invariant $(\mathbf{M}\times\mathbf{T})^2=M^2T^2-(\mathbf{M}\cdot\mathbf{T})^2$ is not independent, while the two further invariants,

$$gI_{PM^2}=g(P_xM_yM_z+P_yM_zM_x+P_zM_xM_y) =-g(P_1M_1-P_2M_2)M_3+\frac{1}{2}\,gP_3(M_1^2-M_2^2),$$

$$g'I_{M^2T^2}=g'(M_xM_yT_xT_y+M_zM_xT_zT_x+M_yM_zT_yT_z) =\frac{1}{4}\,g'(M_1^2-M_2^2)(T_1^2-T_2^2) +g'(M_1T_1+M_2T_2)M_3T_3,$$

which are of the same order in T_1^2 as the invariants in Eq. (30), are relativistic and can be neglected.

Part of the invariants in addition to Eq. (29) and (30) has the form

$$-a_1'I_{PMT}T^2-a''I_{PMT}R^2-a'''I_{P^2MT} -a_2'(I_{PMT^3}+I'_{PMT^3}),$$

$$I_{P^2MT}=P_xP_y(M_xT_y-M_yT_x)+P_zP_x(M_zT_x-M_xT_z) +P_yP_z(M_yT_z-M_zT_y) =-\frac{1}{2}\,(P_1^2-P_2^2)(M_1T_2-M_2T_1)-P_1P_3(M_2T_3 -M_3T_2)+P_2P_3(M_3T_1-M_1T_3),$$

$$I_{PMT^3}=(P_yM_z+P_zM_y)T_x(T_y^2-T_z^2) +(P_zM_x+P_xM_z)T_y(T_z^2-T_x^2) +(P_xM_y+P_yM_x)T_z(T_x^2-T_y^2) =\frac{1}{2}\,(P_2M_3+P_3M_2)T_1(T_1^2-T_2^2-2T_3^2) +\frac{1}{2}\,(P_3M_1+P_1M_3)T_2(T_1^2-T_2^2+2T_3^2)$$

$$-2(P_1M_1-P_2M_2)T_1T_2T_3,$$

$$I'_{PMT^3}=(P_yM_z-P_zM_y)T_x(T_y^2+T_z^2)$$
$$+(P_zM_x-P_xM_z)T_y(T_z^2+T_x^2)$$
$$+(P_xM_y-P_yM_x)T_z(T_x^2+T_y^2)$$
$$=\frac{1}{2}(P_2M_3-P_3M_2)T_1(T_1^2-T_2^2+2T_3^2)$$
$$-\frac{1}{2}(P_3M_1-P_1M_3)T_2(T_1^2-T_2^2-2T_3^2)$$
$$+(P_1M_2-P_2M_1)(T_1^2+T_2^2)T_3. \quad (31)$$

Still another invariant

$$I'_{P^2MT}=P_x^2(M_yT_y-M_zT_z)+P_y^2(M_zT_z-M_xT_x)$$
$$+P_z^2(M_xT_x-M_yT_y)$$
$$=-\frac{1}{2}(P_1^2+P_2^2-2P_3^2)(M_1T_2+M_2T_1)$$
$$+P_1P_2(M_1T_1+M_2T_2-2M_3T_3),$$

and the invariant $I_{PMT^3}-I'_{PMT^3}$ do not contribute to the potential (23), only to the potential (9).

As a result of this analysis, the part of the potential in addition to Eq. (24) can be written in the form

$$\Delta\Phi(P_2,M_3)=-\frac{1}{2}FP_2^2T_1^2-\frac{1}{2}\kappa'P_2^2R^2-\frac{1}{2}\tau P_2^2P_3$$
$$-\frac{1}{2}GM_3^2T_1^2-\frac{1}{2}B'M_3^2R^2-a'P_2M_3T_1^3$$
$$-a''P_2M_3T_1R^2-a'''P_2M_3T_1P_3, \quad (32)$$

where $a'\equiv a'_1+a'_2$. The solution (25) is unchanged if we add Eq. (32) to Eq. (23). We use Eqs. (12) and (15) to eliminate the variables R^2 and P_3 from Eq. (32). Substituting Eqs. (12) and (15) into Eq. (32) and neglecting terms proportional to P_0, we obtain

$$\Delta\Phi(P_2,M_3)=-\frac{1}{2}\left(F+\frac{k'D}{\tilde{\beta}}+\frac{\tau\sigma D}{\tilde{\beta}\kappa}\right)P_2^2T_1^2$$
$$-\frac{1}{2}\left(G+\frac{B'D}{\tilde{\beta}}\right)M_3^2T_1^2$$
$$-\left(a'+a''\frac{D}{\tilde{\beta}}+a'''\frac{\sigma D}{\tilde{\beta}\kappa}\right)P_2M_3T_1^3. \quad (33)$$

Repeating the same calculations with the sum of the potentials (23) and (33) as have been done with Eq. (23), instead of Eq. (27) we obtain

$$\Phi_{P_2P_2}=\kappa-\left(F+\frac{k'D}{\tilde{\beta}}+\frac{\tau\sigma D}{\tilde{\beta}\kappa}\right)T_1^2,$$

$$\Phi_{P_2M_3}=\Phi_{M_3P_2}=aT_1-\left(a'+a''\frac{D}{\tilde{\beta}}+a'''\frac{\sigma D}{\tilde{\beta}\kappa}\right)T_1^3,$$

$$\Phi_{M_3M_3}=B-\left(G+\frac{B'D}{\tilde{\beta}}\right)T_1^2. \quad (34)$$

From Eqs. (26) and (34) we obtain

$$\alpha_{23}=\frac{-aT_1+(a'+a''D/\tilde{\beta}+a'''\sigma D/\tilde{\beta}\kappa)T_1^3}{[\kappa-(F-\kappa'D/\tilde{\beta}+\tau\sigma D/\tilde{\beta}\kappa)T_1^2][B-(G-B'D/\tilde{\beta})T_1^2]}. \quad (35)$$

The stability condition $\Phi_{P_2P_2}>0$ and $\Phi_{M_3M_3}>0$ implies (see Eq. (34)) that the denominator of Eq. (35) is always positive. In the numerator of Eq. (35) the coefficients of T_1 and T_1^3 generally are of the same order of magnitude with arbitrary signs. Thus, the numerator can go to zero when $(T_c-T)/T_c$, which determines the value of T_1^2 (Eq. (22)), is of order unity. This can happen far from the transition point $T=T_c$, but the boracites being considered are characterized by a low T_c (see the figure). Thus, even for comparatively small values of T_c-T, the sign of α_{23}, like that of α_{32}, might change (see the figure). Obviously, the above discussion is qualitative and is not changed if higher-order terms in the expansion in T_1^2 are taken into account.

It is well known that in the phenomenological theory of phase transitions the physical significance of the order parameter is unimportant. Only its transformation properties are important, i.e., the irreducible representation of the symmetry group of the initial phase of the crystal according to which it transforms. In this sense, the toroidal momentum can be regarded as a special case of the antiferromagnetism vector in which off-diagonal components of the magnetoelectric effect tensor develop in the low-symmetry phase of the crystal. Toroidal spin ordering assumes the formation of a closed annulus of spins (in the simplest case, three) and of a toroidal momentum perpendicular to the plane in which the spins lie. This sort of structure should be looked for in the low-symmetry phase of these boracites. That task, however, lies beyond the scope of this paper.

In conclusion, we emphasize that the first feature of the α_{ij} curves for the boracites (the narrow peak in $\alpha_{32}(T)$), in contrast to the second feature (the sign change in α_{23} or α_{32}), can be explained rigorously in terms of the present approach based on the sole assumption that the C_1-C_2 transition is equitranslational.

The author thanks H. Schmidt and J.-P. Rivera for useful and stimulating discussions that have aided greatly in completing this work.

[1] M. Clin, J.-P. Rivera, and H. Schmidt, Ferroelectrics **79**, 173 (1988).
[2] M. Clin, J.-P. Rivera, and H. Schmidt, Ferroelectrics **108**, 213 (1990).
[3] J.-P. Rivera, and H. Schmidt, J. Appl. Phys. **70**, 6410 (1991).
[4] N. E. Chupis, Fiz. Nizk. Temp. **9**, 56 (1983) [Sov. J. Low Temp. Phys. **9**, 28 (1983)].
[5] M. Clin, H. Schmidt, P. Schobinger, and P. Fischer, Phase Transitions **33**, 149 (1991).
[6] V. M. Dubovik and L. A. Tosunyan, Fiz. Élem. Chast. Atomn. Yad. **14**, 1193 (1983).
[7] V. Dvořak and J. Petzelt, Czech J. Phys. B **21**, 1141 (1971); V. Dvořak,

Czech J. Phys. B **21**, 1250 (1971)
[8] D. G. Sannikov and I. S. Zheludev, Fiz. Tverd. Tela **27**, 1369 (1985) [Sov. Phys. Solid State **27**, 826 (1985)].
[9] A. P. Levanyuk and D. G. Sannikov, Usp. Fiz. Nauk **112**, 561 (1974) [Sov. Phys. Uspekhi **17**, 199 (1974)].
[10] I. E. Dzyaloshinskiĭ and V. I. Man'ko, Zh. Éksp. Teor. Fiz. **46**, 1352 (1964) [Sov. Phys. JETP **19**, 915 (1964)].

Translated by D. H. McNeill

The phase diagram of the superconducting state of superconductor–band -antiferromagnet superlattices

V. N. Krivoruchko

A. A. Galkin Donetsk Physicotechnical Institute, Ukrainian National Academy of Sciences, 340144 Donetsk, Ukraine

(Submitted 7 June 1996)
Zh. Éksp. Teor. Fiz. **111**, 547–561 (February 1997)

The formation of the superconducting phase in short-period proximity-effect layered superlattices of the superconductor–band-antiferromagnetic-metal (SC/AF) type is studied. The exact solution of the Usadel equations is used to discuss the possibility of formation in such structures of a ground state in which the order parameters of the adjacent superconducting layers have opposite signs (the ''π-phase''). The dependence of the superconducting transition temperature and the upper critical field normal to the layers on the lattice period, the intensity of magnetic interaction in the antiferromagnetic layer, and the state of the interface between the layers is examined. It is found that there exists a nonlinear dependence of the conditions for the appearance of the superconducting state in a layered SC/AF system on the system's parameters. Finally, the conditions for the appearance of the superconducting phase in proximity-effect superlattices consisting of a superconductor with nonmagnetic, ferromagnetic, and antiferromagnetic metals are compared. © *1997 American Institute of Physics.*
[S1063-7761(97)01102-5]

1. INTRODUCTION

Among artificial layered systems the structures formed by alternating layers of superconducting and magnetic metals constitute ideal objects for studying the relationship between superconductivity and magnetism. There exists a vast body of experimental and theoretical work devoted to studying the properties of superlattices that consist of layers of superconducting and ferromagnetic metals (SC/FM superlattices).[1–9] The remarkable properties of these objects, such as the coexistence of bulk superconductivity and ferromagnetic ordering in the layers and the nonlinear temperature dependence of the critical fields (to name just some), have been predicted theoretically and in some cases have been observed in experiments.[4–9]

Alternating systems of a superconductor and an antiferromagnetic metal (SC/AF superlattices) have been investigated to a considerably smaller extent (see, e.g., Ref. 1 and 10–12). At the same time, for example, most high-T_c superconducting materials are obtained by doping layered antiferromagnets, and the strong antiferromagnetic correlations of the copper spins in the CuO planes are their characteristic feature. The question of how closely related are the magnetic and superconducting properties of high-T_c superconductors still remains open. At present this and other aspects of the interrelationship between magnetism and superconductivity are being actively discussed in connection with the problem of the symmetry type of the order parameter in high-T_c systems (see, e.g., Refs. 13 and 14 and the literature cited therein).

Recently the present author derived[15] a system of Usadel equations for antiferromagnetic superconductors in which electrons of the same type are carriers of the magnetic and superconducting properties of the system and the dispersion law of electrons and holes has the property of nesting. This system of equations was used to study the formation of the superconducting phase in proximity-effect layered SC/AF structures, where it was assumed that the thickness of the AF layer is much greater than the corresponding superconducting correlation length. At the same time, the technology of fabricating superlattices has become so advanced[16,17] that it is quite possible to fabricate lattices from layers with a thickness of several lattice periods. Already the first theoretical[6,7,18] and experimental[2,9] studies of lattices with small periods demonstrated the unusual properties of such structures, properties caused by the overlap of condensate wave functions of neighboring superconducting layers. In particular, for SC/N lattices this leads to quantitative changes in the properties of the system,[18] and for SC/FM lattices to the appearance of entirely new states. For instance, states with a nontrivial phase difference between the superconducting layers can exist in the system (the ''π-phase''),[19] and oscillations of the superconducting transition temperature across the ferromagnetic layer can be observed.[2,6,7,9]

Note that the properties of a superlattice in the ''π-phase'' are in many respects similar to those of superconductors with d-pairing.[7,9] In connection with the discussion concerning the type of pairing in high-T_c superconductivity systems and the presence in such systems of layers with strong antiferromagnetic correlations, solving the problem of a ''π-phase'' appearing in thin SC/AF lattices becomes very important. Bearing all this in mind, we will analyze the conditions for the appearance of the superconducting phase in proximity-effect superlattices consisting of a low-temperature superconductor (SC) and a band antiferromagnetic metal (AF) with periods that are smaller than or comparable to the characteristic scale of the problem, the superconducting correlation lengths.

Section 2 gives the basic equations describing the transition to the superconducting state in small-period proximity-

effect SC/AF superlattices. In Sec. 3 the exact solution of the Usadel equations for an SC layer is used to study the possibility of the system passing into a ground state with a nontrivial phase difference between the closest SC layers. Section 4 is devoted to a discussion of the results of calculations, for SC/AF systems, of the upper critical field normal to the layers. In the same section we will also discuss the conditions for the existence of proximity-effect superconductivity for SC/AF, SC/N, and SC/FM superlattices. The theoretical results obtained in this paper are compared with the existing experimental data in Sec. 5. Finally, Sec. 6 discusses the main conclusions.

2. FORMATION OF THE SUPERCONDUCTING PHASE IN THIN SC/AF SUPERLATTICES: BASIC EQUATIONS

We assume that both metals, SC and AF, are ''dirty,'' i.e., they satisfy the condition $l_{S(\mathrm{AF})} \ll \xi_{S(\mathrm{AF})}$, with $l_{S(\mathrm{AF})}$ the mean free path and $\xi_{S(\mathrm{AF})}$ the correlation length in the SC(AF) layer. As we know,[20,21] in describing the superconducting states of such metals it is convenient to use Green's functions that have been integrated with respect to the energy and averaged over the Fermi surface.

The SC layer

For the SC layer we have the usual system of Usadel equations for the Green's functions $G_S(\mathbf{r},\omega)$ and $F_S(\mathbf{r},\omega)$ describing normal excitations in the system and the Cooper-pair condensate, respectively. Writing only independent relationships, we have

$$-\frac{D_S}{2}\,\mathbf{\Pi}(G_S(\mathbf{r},\omega)\mathbf{\Pi}F_S(\mathbf{r},\omega)-F_S(\mathbf{r},\omega)\mathbf{\nabla}G_S(\mathbf{r},\omega))$$

$$=\frac{\Delta_S(\mathbf{r})}{\hbar}\,G_S(\mathbf{r},\omega)-\omega F_S(\mathbf{r},\omega),$$

$$G_S^2(\mathbf{r},\omega)+F_S(\mathbf{r},\omega)F_S^+(\mathbf{r},\omega)=1. \tag{1}$$

Here $\mathbf{\Pi}=\mathbf{\nabla}+2\pi i\mathbf{A}/\Phi_0$ is the gradient-invariant momentum operator, $\mathbf{A}$ is the vector potential, Φ_0 is the flux quantum, D_S is the diffusion coefficient in the SC layer, and $\hbar\omega=\pi T(2n+1)$, with $n=0,\pm1,\pm2,\ldots$. The self-consistency equation for the order parameter $\Delta_S(\mathbf{r})$ and the function $F_S(\mathbf{r},\omega)$ has the standard form

$$\Delta_S(\mathbf{r})=\pi T\lambda\sum_{\omega}\,F_S(\mathbf{r},\omega), \tag{2}$$

where λ is the constant of the electron–electron interactions forming the superconducting electron correlations, and the summation is limited by the Debye frequency Ω_D (the Boltzmann constant k_B is set equal to unity).

Near the phase transition to the normal state we have $G_S(\mathbf{r},\omega)\simeq\mathrm{sgn}(\omega)$, while for the anomalous Green's function we have the linearized equation

$$-\frac{D_S}{2}\,\mathbf{\Pi}^2F_S(\mathbf{r},\omega)=\frac{\Delta_S(\mathbf{r})}{\hbar}-\omega F_S(\mathbf{r},\omega). \tag{3}$$

At this point it is convenient to introduce the characteristic superconducting correlation length in the SC layer, $\xi_S=(\hbar D_S/2\pi T_{c0})^{1/2}$, where T_{c0} is the superconducting transition temperature of the bulk SC material. The parameter ξ_S is related to the correlation length in the Ginzburg–Landau theory by the following formula:

$$\xi_{\mathrm{GL}}(T)=\frac{\pi}{2}\,\xi_S\left(1-\frac{T}{T_c}\right)^{-1/2}.$$

The AF layer

The magnetic properties of many band antiferromagnets are closely related to the special features of the band structure of these materials.[22] More precisely, the Fermi surface of such metals exhibits a nesting property, i.e., consists of electron and hole sections that almost coincide under a translation by a wave vector $\mathbf{Q}$, known as the nesting vector. The transition to a magnetically ordered state is accompanied by the appearance of a spin-triplet insulator gap on the Fermi surface. Typical representatives of band antiferromagnets are Cr and Cr-based alloys.[23] These compounds were used in all the experimental studies of metallic superlattices of the SC/AF type. For this reason, when we estimate the parameters of the AF layer we have in mind chromium-based magnetic materials. Extensive experimental data on the magnetic properties of Cr and its compounds have been assembled in the review by Fawcett *et al.*[23]

As we know,[24] the contact of a metal and a superconductor results in the appearance of proximity-induced superconductivity in a thin layer of the normal metal. The induced superconducting state of the AF metal is described by the following system of independent equations:[15]

$$-\frac{D_n}{2}\,\mathbf{\Pi}(G_{11}(\mathbf{r},\omega)\mathbf{\Pi}F_{11}(\mathbf{r},\omega)-F_{11}(\mathbf{r},\omega)\mathbf{\nabla}G_{11}(\mathbf{r},\omega))$$

$$=\frac{\Delta_{1n}(\mathbf{r})}{\hbar}\,G_{11}(\mathbf{r},\omega)-\omega F_{11}(\mathbf{r},\omega), \tag{4}$$

$$-\frac{D_n}{2}\,\mathbf{\Pi}(G_{22}(\mathbf{r},\omega)\mathbf{\Pi}F_{22}(\mathbf{r},\omega)-F_{22}(\mathbf{r},\omega)\mathbf{\nabla}G_{22}(\mathbf{r},\omega))$$

$$=\frac{\Delta_{2n}(\mathbf{r})}{\hbar}\,G_{22}(\mathbf{r},\omega)-\omega F_{22}(\mathbf{r},\omega), \tag{5}$$

$$D_n\mathbf{\nabla}(G_{11}(\mathbf{r},\omega)\mathbf{\nabla}G_{12}(\mathbf{r},\omega)-G_{12}(\mathbf{r},\omega)\mathbf{\nabla}G_{22}(\mathbf{r},\omega))$$

$$-2\omega G_{12}(\mathbf{r},\omega)-i\,\frac{H_{\mathrm{exc}}}{\hbar}\,(G_{11}(\mathbf{r},\omega)+G_{22}(\mathbf{r},\omega))=0, \tag{6}$$

$$D_n\mathbf{\nabla}(G_{12}(\mathbf{r},\omega)\mathbf{\nabla}G_{11}(\mathbf{r},\omega)-G_{22}(\mathbf{r},\omega)\mathbf{\nabla}G_{21}(\mathbf{r},\omega))$$

$$+2\omega G_{21}(\mathbf{r},\omega)-i\,\frac{H_{\mathrm{exc}}}{\hbar}\,(G_{11}(\mathbf{r},\omega)+G_{22}(\mathbf{r},\omega))=0. \tag{7}$$

Here the anomalous Green's functions $F_{11(22)}$, as usual, describe the Cooper-pair condensate, $G_{11(22)}$ and $G_{12(21)}$ describe normal excitations in the system, D_n is the diffusion coefficient in the AF layer, Δ_{1n} and Δ_{2n} are the band superconducting order parameters, and the magnetic parameter

$H_{\rm exc}$ (the antiferromagnetic exchange energy) can be assumed real.[25,26] The following normalization condition also holds:

$$G_{ii}^2(\mathbf{r},\omega)+F_{ii}(\mathbf{r},\omega)F_{ii}^+(\mathbf{r},\omega)+G_{ij}(\mathbf{r},\omega)G_{ij}^+(\mathbf{r},\omega)=1,$$

where $i\neq j=1,2$, and there is no summation over repeated indices.

The following fact concerning the system of equations (4)–(7) must be mentioned. As we know, in the absence of interactions that violate the invariance under time reversal, the system Hamiltonian commutes with the time reversal operator $\hat{T}$. As a result the energy of the time-reversed one-electron states is the same and Cooper pairing of states $(\mathbf{k},\sigma)$ and $(-\mathbf{k},-\sigma)$ becomes possible. For (antiferro)magnetic interactions of the form

$$H_{\rm int}=H_{\rm exc}\sum_{\sigma}\ [\psi_\sigma^+(\mathbf{r})\varphi_{-\sigma}(\mathbf{r}+\mathbf{a})+\varphi_\sigma^+(\mathbf{r}+\mathbf{a})\psi_{-\sigma}(\mathbf{r})],$$

where $\psi_\sigma^+(\mathbf{r})$ and $\psi_\sigma(\mathbf{r})$, and $\varphi_\sigma^+(\mathbf{r})$ and $\varphi_\sigma(\mathbf{r})$ are the creation and annihilation operators of electrons and holes in the first and second bands, respectively, and $\mathbf{a}$ is the translation vector linking the magnetic sublattices, the invariance is broken: $[H_{\rm int},\hat{T}]\neq 0$. (The transformation of the operators $(\psi_\sigma^+\varphi_{-\sigma})$ under the operation $\hat{T}$ is similar to the transformation of the spin operators $S^{\pm}=S^x\pm iS^y$.) The total system Hamiltonian now commutes with the operator $\hat{Y}=\hat{T}\hat{R}$, where $\hat{R}$ is the operator of translation by vector $\mathbf{a}$. This fact is unimportant in the superconducting pairing of electrons belonging to the same band (sublattice). But when there are interband superconducting correlations, the triplet type rather than the singlet type of electron convolutions proves to be compatible with AF ordering (here a certain analogy can be drawn between the superconducting phases of systems with heavy fermions[27] and ^{3}He (Ref. 28; see also Chap. 9 in Ref. 29). We will assume that the superconducting properties of the SC layer are caused by the ordinary (singlet) type of pairing. Since the superconductivity of the AF layer is induced, we should not expect (say, from symmetry considerations) triplet correlations to appear in this layer. If we allow for this fact, the system of equations (4)–(7) contains only intraband superconducting correlation functions of the s-type.

Band antiferromagnets based on chromium have fairly high Néel temperatures $T_N\sim 200-300$ K (see Ref. 23). Taking this circumstance into account, we restrict ourselves to a treatment of the situation of greatest current interest, in which the magnetic ordering temperature T_N significantly exceeds the superconducting transition temperature of the SC/AF superlattice: $T_c\leqslant T_{c0}\ll T_N$. Actually this means that in studying the conditions for the formation of the superconducting phase we ignore the temperature-induced variations of the magnetic properties of the AF layer. In addition, in Sec. 4 we will assume that the upper critical field of the superconducting state does not exceed the fields for the transition of the AF layer from the antiferromagnetic phase to a phase with another magnetic configuration.

It is now convenient to pass from the band variables to the total variables $F_{\rm AF}(\mathbf{r},\omega)=F_{11}(\mathbf{r},\omega)+F_{22}(\mathbf{r},\omega)$ and $\Delta_{\rm AF}(\mathbf{r})=\Delta_{1n}(\mathbf{r})+\Delta_{2n}(\mathbf{r})$. Then the linearized equation for the anomalous Green's function $F_{\rm AF}$ assumes the form[15]

$$\frac{D_n}{2}\ G_{\rm AF}(\mathbf{r},\omega)\mathbf{\Pi}^2F_{\rm AF}(\mathbf{r},\omega)$$

$$=\omega F_{\rm AF}(\mathbf{r},\omega)-\frac{\Delta_{\rm AF}(\mathbf{r})}{\hbar}\ G_{\rm AF}(\mathbf{r},\omega),\qquad(8)$$

where $G_{\rm AF}(\mathbf{r},\omega)=\hbar\omega\ {\rm sgn}(\omega)((\hbar\omega)^2+H_{\rm exc}^2)^{-1/2}$. Next we use the substitution $F_{\rm AF}(\mathbf{r},\omega)=\Delta_{\rm AF}G_{\rm AF}(\mathbf{r},\omega)(\hbar\omega-\pi T)^{-1}$ and transform Eq. (8) to the standard form

$$\mathbf{\Pi}^2F_{\rm AF}(\mathbf{r},\omega)=k_{\rm AF}^2F_{\rm AF}(\mathbf{r},\omega),\quad k_{\rm AF}^2=\frac{2\pi T}{\hbar D_nG_{\rm AF}(\mathbf{r},\omega)}.\qquad(9)$$

The typical superconducting transition temperature T_c for the systems considered here is lower than 10 K (see Refs. 10–12), i.e., the characteristic frequencies satisfy $\hbar\omega\sim T_c\ll T_N$. In the adopted approximation of ignoring the temperature-induced variations in the properties of the AF layer we can write the following expression for $k_{\rm AF}$:

$$k_{\rm AF}=\frac{2}{\xi_{\rm AF}},\quad \xi_{\rm AF}=\left(\frac{2\hbar D_n}{H_{\rm exc}}\right)^{1/2}.\qquad(10)$$

Here we have introduced the characteristic damping length $\xi_{\rm AF}$ for superconducting correlations in the AF layer. Note that the destruction of Cooper pairs in an AF layer is much more intense than in a normal nonmagnetic layer of the same thickness: $\xi_{\rm AF}$ is much smaller than the corresponding damping length $\xi_N=(\hbar D_n/2\pi T)^{1/2}$ (see Ref. 30) in a normal metal with the same diffusion coefficient. In this the action of the antiferromagnetic exchange field coincides with the action of the ferromagnetic exchange field. The difference is that for an FM layer the equation of the form (10) contains a complex-valued parameter; the characteristic wave vector for an FM metal is[4,6]

$$k_{\rm FM}=\frac{2(1+i)}{\xi_{\rm FM}},\quad \xi_{\rm FM}=\left(\frac{4\hbar D_n}{H_{\rm exc}}\right)^{1/2},\qquad(11)$$

where $H_{\rm exc}$ is the ferromagnetic exchange field. This fact, as we will shortly see, is important and leads to a qualitative difference in the properties of SC/FM and SC/AF systems with a small lattice period.

Equations (3) and (9) should be supplemented by boundary conditions at the interface between the layers. We use relations of the form[31,32]

$$F_S(\mathbf{r},\omega)=F_{\rm AF}(\mathbf{r},\omega),\quad \frac{d}{d\mathbf{r}}\ F_S(\mathbf{r},\omega)=\eta\ \frac{d}{d\mathbf{r}}\ F_{\rm AF}(\mathbf{r},\omega).\qquad(12)$$

The phenomenological parameter η depends on the nature of electron scattering on the interface and the properties of the materials comprising the layers; its value in the general case is unknown. Under mirror reflection at the interface it satisfies $\eta=\sigma_{\rm AF}/\sigma_S$, where $\sigma_{\rm AF}$ (σ_S) is the conductivity of the AF (SC) layer in the normal state.

We also note that the when the normal electrons of the AF layer penetrate the SC layer they induce magnetic properties in the latter, which constitutes what is known as the

magnetic proximity effect. For ''clean'' superconductors magnetic proximity effects play an important role up to distances of order ξ_S, and allowing for this fact is important in examining the properties of superlattices consisting of ''clean'' metals.[33] In the ''dirty'' limit ($l_S \ll \xi_S$), magnetic correlations inside the SC layer manifest themselves over a distance of the order of the mean free path l_S and for this reason can be ignored.

3. THE SUPERCONDUCTING TRANSITION TEMPERATURE. STATES WITH A NONTRIVIAL PHASE DIFFERENCE BETWEEN SC LAYERS

As noted earlier, for superlattices consisting of thin normal-metal layers the overlap of the wave functions of the condensate from the next layers following the nearest-neighbor layers is important. This fact can be taken into account by solving the Usadel equations for the SC layer exactly and satisfying the boundary conditions for each value of ω.

Let us require that the function $F_{S,\mathrm{AF}}(\mathbf{r},\omega)$ satisfy the periodicity condition in the form

$$F_{S,\mathrm{AF}}(z+L,\omega)=\exp(-i\varphi)F_{S,\mathrm{AF}}(z,\omega), \tag{13}$$

where $L=d_S+d_{\mathrm{AF}}$ is the lattice period, and φ is the phase difference between the nearest SC layers. We select the x,y plane of the coordinate system to be the interface between the layers and direct the z axis perpendicular to the planes. In this section we assume that the magnetic field satisfies $\mathbf{H}=\mathrm{curl}\ \mathbf{A}=0$.

We define the superconducting transition temperature as the maximum value of $T(\varphi)$, i.e., the value at which the Green's function of the Cooper-pair condensate satisfies Eqs. (3) and (9) and the boundary conditions (13). Allowing for a situation in which states with a nontrivial phase difference φ between SC layers can be realized, we seek a solution for the function $F_{\mathrm{AF}}(z,\omega)$ asymmetric with respect to the middle of the AF layer:

$$F_{\mathrm{AF}}(z,\omega)=C_1\ \exp(k_{\mathrm{AF}}z)+C_2\ \exp(-k_{\mathrm{AF}}z),$$

$$d_S \leqslant z \leqslant d_S+d_{\mathrm{AF}}.$$

The coefficients C_1 and C_2 can be found explicitly from the boundary conditions and the periodicity condition. We have

$$2\ \sinh(k_{\mathrm{AF}}d_{\mathrm{AF}})C_1=F_S(0,\omega)\exp(-i\varphi-k_{\mathrm{AF}}d_S) - F_S(d_S,\omega)\exp(-k_{\mathrm{AF}}L),$$

$$2\ \sinh(k_{\mathrm{AF}}d_{\mathrm{AF}})C_2=F_S(d_S,\omega)\exp(k_{\mathrm{AF}}L)-F_S(0,\omega)\exp(-i\varphi+k_{\mathrm{AF}}d_S).$$

Now it is convenient to introduce the Fourier transform in the variable z and reduce the differential equation (3) to the algebraic equation

$$-\frac{\hbar D_S}{2d_S}\ [(-1)^m F_S'(d_S,\omega)-F_S'(0,\omega)]+\frac{\hbar D_S q_m^2}{2} \times F_S(q_m,\omega)=\Delta_S(q_m)-\hbar|\omega|F_S(q_m,\omega) \tag{14}$$

with $q_m=\pi m/d_S$, $m=0,\pm1,\pm2,\ldots$. The values of the derivatives $F_S'(d_S,\omega)$ and $F_S'(0,\omega)$ can be expressed in terms of the values of the function proper if we plug the explicit values of the coefficients C_1 and C_2 into the Fourier transform of the boundary condition (12). We get

$$F_S'(0,\omega)\sinh(k_{\mathrm{AF}}d_{\mathrm{AF}})=\eta k_{\mathrm{AF}}\sum_{m'}\ \{F_S(q_{m'},\omega) \times\cosh(k_{\mathrm{AF}}d_{\mathrm{AF}})-(-1)^{m'} \times\exp(i\varphi)F_S(d_S,\omega)\}, \tag{15a}$$

$$F_S'(d_S,\omega)\sinh(k_{\mathrm{AF}}d_{\mathrm{AF}})=-\eta k_{\mathrm{AF}}\sum_{m'}\ \{(-1)^{m'}F_S(q_{m'},\omega) \times\cosh(k_{\mathrm{AF}}d_{\mathrm{AF}})-\exp(i\varphi) \times F_S(q_{m'},\omega)\}. \tag{15b}$$

Using the above relationships, we can write the function $F_S(q_m,\omega)$ in the following compact form:

$$F_S(q_m,\omega)=\frac{\Delta_S(q_m)}{A(q_m,\omega)} - \frac{1}{A(q_m,\omega)}\sum_{m'}\ B_{mm'}(\omega)F_S(q_{m'},\omega). \tag{16}$$

The following notation has been introduced:

$$A(q_m,\omega)=\hbar|\omega|+\frac{1}{2}\ \hbar D_S q_m^2,$$

$$B_{mm'}(\omega)=\frac{\hbar\eta D_S k_{\mathrm{AF}}}{2d_S\ \sinh(k_{\mathrm{AF}}d_{\mathrm{AF}})}\{[1+(-1)^{m+m'}] \times\cosh(k_{\mathrm{AF}}d_{\mathrm{AF}})-[(-1)^m \times\exp(-i\varphi)+(-1)^{m'}\ \exp(i\varphi)]\}. \tag{17}$$

The values of the sums

$$\sum_m\ F_S(q_m,\omega),\quad \sum_m\ (-1)^m F_S(q_m,\omega)$$

in (16) can easily be found by employing Eq. (16) proper. Finally, plugging (16) into the Fourier transform of the self-consistency condition (2) and performing simple but somewhat lengthy calculations, we arrive at a system of linear equations for the Fourier transform of the order parameter $\Delta_S(q_m)$ of the SC layer:

$$\sum_{m'=-\infty}^{\infty} A_{mm'}(\omega)\Delta_S(q_{m'})=0,$$

$$A_{mm'}(\omega)=\left[1-\pi T\lambda\sum_{\omega}\ A^{-1}(q_m,\omega)\right]\delta_{mm'} + \pi T\lambda\sum_{\omega}\ \gamma_{mm'}A^{-1}(q_m,\omega)A^{-1}(q_{m'},\omega). \tag{18}$$

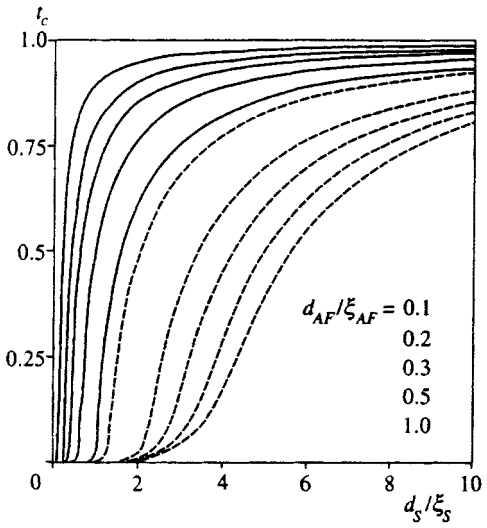

FIG. 1. Dependence of the reduced superconducting transition temperature of an SC/AF superlattice, $t_c = T_c/T_{c0}$, on the reduced thickness of the SC layer, d_S/ξ_S, and the parameter ε characterizing the state of the interface. Solid curves depict the results for $\varepsilon = 10$ and dashed curves the results for $\varepsilon = 1$.

The explicit form of $\gamma_{mm'}$ is given in the Appendix (Eq. (A1)).

The system of equations (18) has a nontrivial solution if

$$\det|A_{mm'}(\omega)| = 0. \tag{19}$$

The greatest value of $T(\varphi)$ at which this is still true is the superconducting transition temperature of the SC layer. Equation (19) was solved numerically; some details of the numerical method are given in the Appendix. Figures 1–3 depict the results of calculations of the superconducting transition temperature for SC/AF superlattices. We will now discuss the results.

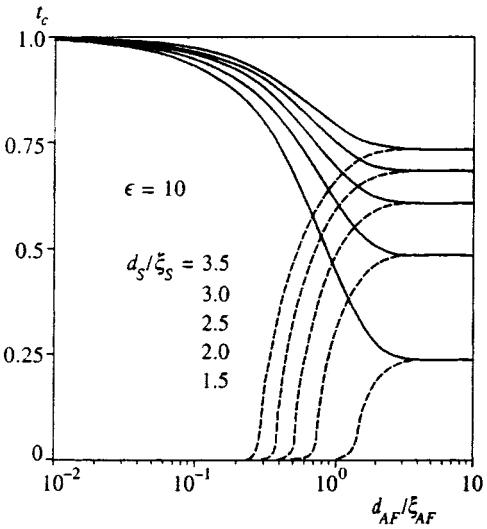

FIG. 2. The reduced superconducting transition temperature of an SC/AF superlattice, $t_c = T_c/T_{c0}$, as a function of the reduced thickness of the AF layer, d_{AF}/ξ_S, with weak magnetic effects at the interface between layers ($\varepsilon = 10$). Here and in Fig. 3 solid curves represent the results for a zero phase difference between SC layers, $T_c(\varphi = 0)$, and dashed curves the results for a finite phase difference, $T_c(\varphi = \pi)$.

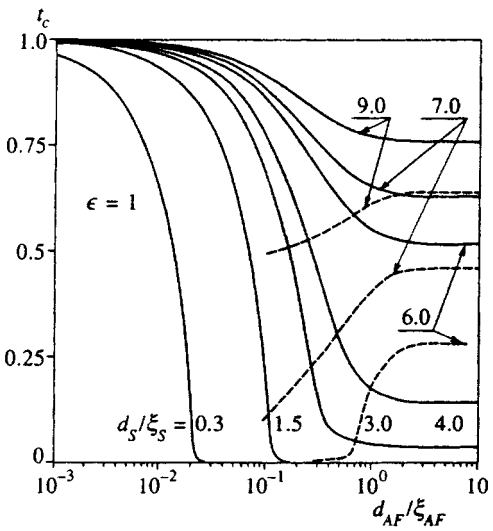

FIG. 3. The same as in Fig. 2 but at $\varepsilon = 1$. The values for $T_c(\varphi = \pi)$ are given only in the two-dimensional superconductivity region.

First we note that the properties of an SC/AF superlattice are extremely sensitive to the value of the parameter $\epsilon = \xi_{AF}(\eta\xi_S)^{-1}$, which characterizes the intensity with which the exchange field acts on the Cooper pairs near the interface between the layers. Here the values $\epsilon \gg 1$ correspond to a weak exchange field (Figs. 1 and 2), while $\epsilon \sim 1$ corresponds to a strong exchange field (Figs. 1 and 3). In general we see that, as with large-period sublattices,[15] for each value of d_{AF} the superconducting state is realized if the thickness of the SC layer is greater than a certain critical value. For systems with sufficiently thick SC layers, an increase in d_{AF} may initiate a transition to the two-dimensional (2D) superconductivity mode, when the transition temperature does not depend on d_{AF} (see the results represented in Figs. 2 and 3 by solid curves). When the effect of the exchange field is weak, this mode is observed even in thin SC layers: $d_S < \xi_S$ (Fig. 2); when the effect is strong, the mode is observed in thick AF layers (Fig. 3). The value of d_{AF} for the transition to the 2D state in both limiting cases is approximately the same, $d_{AF} \approx 2\xi_{AF}$, but the values of the critical temperature of 2D superconductivity are drastically different. In these properties the behavior of SC/AF superlattices is similar to the behavior of SC/FM structures.[3,6]

The most dramatic differences between SC/AF and SC/FM systems concern the transition to a state with a finite phase difference between the SC layers and the change of the phase transition to the normal state from one type to the other. In Figs. 2 and 3 the solid curves depict the dependence of T_c on the lattice period for a zero phase difference between neighboring SC layers, and the dashed curves the same dependence for a finite phase difference $\varphi = \pi$. We see that the critical temperature of the ground state, at which the order parameters of neighboring SC layers have opposite signs, is always lower than the temperature of the transition to the state with $\varphi = 0$. Interestingly, while for weak mag-

netic effects the values $T_c(0)$ and $T_c(\pi)$ in the 2D superconductivity mode are equal (see Fig. 2), at $\epsilon \sim 1$ the value $T_c(\pi)$ is strongly suppressed even in this region (see the results for $d_S > 3\xi_S$ in Fig. 3).

Thus, the ''π-phase'' is not realized in SC/AF superlattices, and in this respect their properties are similar to those of SC/N systems.[18] The physical origin of such behavior lies in the fact that in an AF layer, just as in an N layer, the wave function of a Cooper pair monotonically decays as a function of distance into the layer, while for an FM layer this decay is, in addition, oscillatory. Note that similar conclusions concerning the energy disadvantage of the ground state with a finite phase difference between neighboring SC layers have been obtained for lattices made of ''clean'' SC and AF layers.[7] A microscopic analysis based on the Gor'kov equations shows[7] that for structures with Josephson coupling between the SC and AF layers there is no ''π-phase'' for all reasonable ratios of $H_{\rm exc}$ and the Fermi energy.

An earlier paper of Sarma[34] discussed the effect of the change in the phase transition into the superconducting state from second-order to first-order as the strength of the exchange magnetic field acting on the electron spins increases. Not long ago the existence of a phenomenon of this type was predicted for SC/FM superlattices.[6] As the results of the present study imply, the antiferromagnetic exchange field does not change the type of phase transition of thin SC/AF superlattices into the normal state.

4. THE UPPER CRITICAL FIELD $H_{c2\perp}$

We find the values of the upper critical field normal to the layers by solving the Usadel equations for the SC layer exactly. However, in view of the results of Sec. 3, we restrict our discussion to states with $\varphi = 0$.

A magnetic field perpendicular to the layers penetrates the lattice in the form of Abrikosov vortices modulated along the field. Separating variables in the usual manner, i.e., writing $F_{S,\rm AF}(\mathbf{r},\omega) = f(x,y) g_{S,\rm AF}(z,\omega)$, and using Eq. (8) for the AF layer, we find that

$$\frac{d^2}{dz^2}\, g_{\rm AF}(z,\omega) = g_N^2 g_{\rm AF}(z,\omega),$$

$$-(\Pi_x^2 + \Pi_y^2) f(x,y) = (q_N^2 - k_{\rm AF}^2) f(x,y) = \frac{2\pi H}{\Phi_0}\, f(x,y). \tag{20}$$

As with bulk superconductors,[35] the smallest eigenvalue of Eq. (20) yields the largest value $H = H_{c2\perp}$, so that

$$q_N^2 = k_{\rm AF}^2 + \frac{2\pi H_{c2\perp}}{\Phi_0}. \tag{21}$$

We seek the function $g_{\rm AF}(z,w)$ in a form symmetric with respect to the middle of the AF layer:

$$g_{\rm AF}(z,\omega) = C_N \cosh\left[q_N \left(\frac{d_{\rm AF}}{2} - |z| \right) \right].$$

Equations of the form (14)–(16) also become much simpler because of the condition $F_S(0,\omega) = F_S(d_S,\omega)$. As a result,

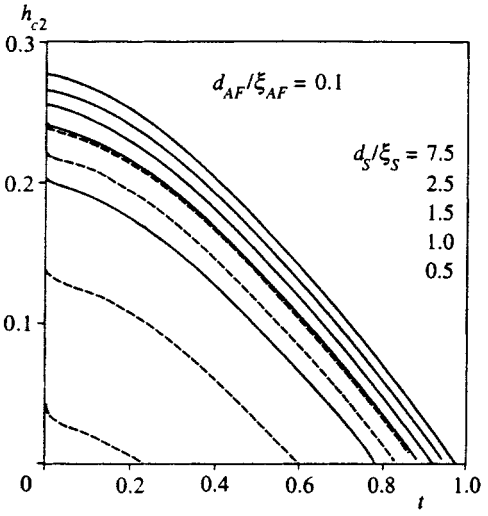

FIG. 4. Dependence of the upper critical field perpendicular to layers of the SC/AF lattice, $h_{c2} = H_{c2\perp}/H_{c2\rm GL}$, on the reduced temperature $t = T/T_{c0}$ for different conditions for electron scattering on the interface between the layers, i.e., values of ε, and a fixed thickness of the SC and AF layers. Here and in Figs. 5 and 6 solid curves represent the results for $\varepsilon = 10$ and dashed curves the results for $\varepsilon = 1$.

repeating the calculations of Sec. 3, we arrive at equations similar to (18) and (19), where, however, the coefficient $A(q_m,\omega)$ specified in (17) has the form

$$A(q_m,\omega) = \hbar|\omega| + \frac{\hbar D_S}{2}\left(q_m^2 + \frac{2\pi H_{c2\perp}}{\Phi_0} \right), \tag{22}$$

and the parameter $\gamma_{mm'} = \gamma_{mm'}(H)$ is given by Eq. (A2). The values of $H_{c2\perp}$ were found by numerically solving Eqs. (19) with $A(q_m,\omega)$ given by (22) and $\gamma_{mm'}(H)$ given by (A2). The results are depicted in Figs. 4–6.

At this point it is convenient to introduce into the picture the upper critical field of the Ginzburg–Landau theory,

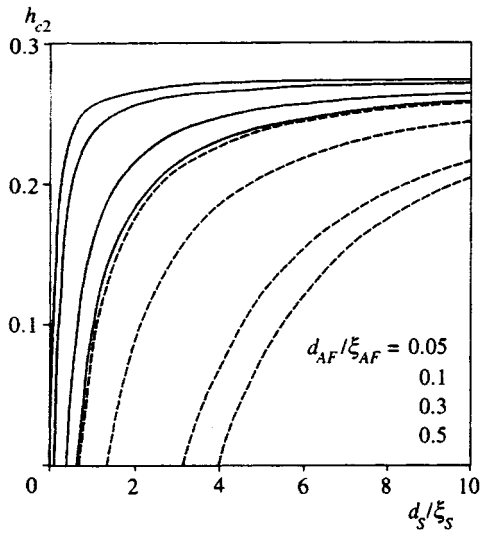

FIG. 5. Dependence of the upper critical field perpendicular to the lattice layers, h_{c2}, on the reduced thickness of the SC layer for different thicknesses of the AF layer and different conditions for electron scattering on the interface between the layers; $T = 0.1T_c$.

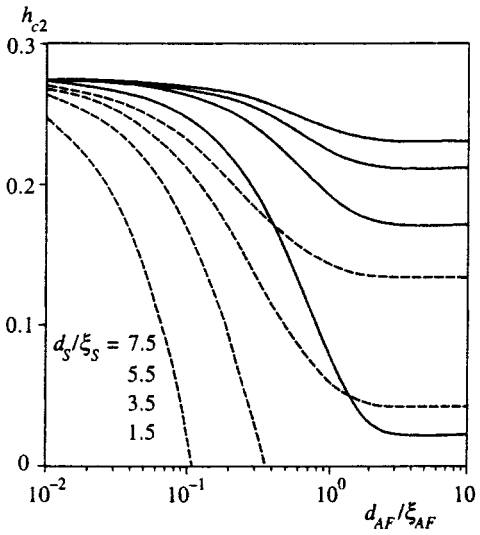

FIG. 6. Dependence of the upper critical field perpendicular to the lattice layers, h_{c2}, on the reduced thickness of the AF layer for different thicknesses of the SC layer and different conditions for electron scattering on the interface between the layers; $T=0.1T_c$.

$H_{c\mathrm{GL}}=\Phi_0/2\pi\xi_S^2$, and the reduced critical field $h_{c2}=H_{c2\perp}/H_{c2\mathrm{GL}}$. Figure 4 depicts the dependence of the reduced critical field h_{c2} on the reduced temperature $t=T/T_{c0}$ for different conditions of electron scattering on the interface between the layers, i.e., values of ϵ, and a fixed lattice period. The dependence of the critical field for different values of d_S and fixed ϵ, T, and d_{AF} is shown in Fig. 5 and for different values of d_{AF} and fixed ϵ, T, and d_S in Fig. 6. Note the absence of publications in which the upper critical field of thin SC/FM superlattices are calculated. For this reason below we will compare the results only with those obtained for SC/N systems.

As usual, when the magnetic field is perpendicular to the layers, its critical value $H_{c2\perp}$ is shown to vary linearly with temperature in a broad vicinity of T_c, with saturation at low temperatures (see Fig. 4). This behavior of $H_{c2\perp}$ corresponds to the three-dimensional nature of the superconducting state of the lattices. Note that the value of $H_{c2\perp}$ at $T=0$ depends significantly on the thickness of the SC layer. At the same time, when the SC layer in superlattices consisting of a superconductor and a nonmagnetic metal is not excessively thin, $H_{c2\perp}(T)$ tends to a unique value $H_{c2\perp}(0)$.[36,5] Depairing effects of a magnetic nature, rather than the state of the interface, are decisive for the value of $H_{c2\perp}$.

The results depicted in Figs. 5 and 6 show that for each given value of d_{AF} the field $H_{c2\perp}\neq 0$ is finite if the thickness of the SC layer is greater than a certain critical value. This value, d_{Scr}, increases with d_{AF} and strongly depends on the parameter ϵ. In the 2D superconductivity mode the upper critical field is independent of the lattice period (see Fig. 6); however, $H_{c2\perp}(2\mathrm{D})$ is strongly dependent on the intensity of scattering of Cooper pairs on the interface between the layers.

Equation (21) can be written in a different form if we use the characteristic parameters of the problem ξ_S, ξ_{AF}, and $H_{c2\mathrm{GL}}$:

$$q_N=\frac{2}{\xi_{\mathrm{AF}}}\left[1+\frac{H_{c2\perp}}{4H_{c2\mathrm{GL}}}\left(\frac{\xi_{\mathrm{AF}}}{\xi_S}\right)^2\right]^{1/2}.$$

We see that applying a magnetic field also makes it possible to study the dependence of the properties of the system on the parameter $\kappa=\xi_{\mathrm{AF}}/\xi_S$. Note that at $H=0$ the ratio of correlation lengths of the layers enters into the formulas only together with the parameter η, which characterizes the state of the interface between the layers. The results depicted in Figs. 4–6 were obtained at $\kappa=1$; varying κ by a factor of ten in both directions was found to change the numerical results no more than by one percentage point. This, we believe, supports the hypothesis of Deutscher and de Gennes[37] that suppression of the superconducting order parameter in proximity-effect junctions of a superconductor and a magnetic material is caused chiefly by destruction of Cooper pairs on the magnetic defect in the interface between the layers, rather than by the type of magnetic order in the bulk of the normal layer.

5. COMPARISON WITH EXPERIMENTAL DATA

Because there exists no systematic experimental study of SC/AF systems with a small lattice period, only qualitative comparison of the theoretical results of the theory with the experimental data was possible. For instance, both the first experimental studies of the proximity effect in SC/AF junctions[1] and the later investigations of SC/AF superlattices[11,12] have revealed a sharp drop in the superconducting transition temperature with increasing thickness of the AF layer for fairly thin SC layers as well as the fact that T_c becomes saturated for large values of d_S. But there are still a number of problems and discrepancies. The ambiguity in interpreting the results for Nd/Cr lattices[12] is caused by the large thickness of the transition layer between the SC and AF metals. The thickness of this layer (≈ 20 Å) is comparable to the thickness of the Cr layer (30 Å). Actually, the investigated objects consisted of three alternating layers, a fact also supported by the two-stage nature of the transition into the superconducting state of such lattices observed by Cheng and Stearns.[12]

The most thorough investigations of SC/AF systems have apparently been conducted by Devis *et al.*[11] The researchers studied the conditions needed for the appearance of a superconducting state in V/Cr superlattices by varying the thickness of the SC layer from 98 to 197 vanadium atomic layers and the thickness of the AF layer from 3 to 100 chromium atomic layers. They found that starting at $d_{\mathrm{Cr}}\cong 80$ atomic layers the superconductivity is quasi-two-dimensional. The transition temperature monotonically decreases with increasing AF-layer thickness in the 3D superconductivity region and tends to become saturated in the 2D superconductivity region, which agrees with our results. At the same time, with one set of samples (prepared under conditions differing from those in which other samples were prepared, however) nonmonotonic behavior of $T_c(d_{\mathrm{Cr}})$ was discovered in the 2D superconductivity region.

Yetter *et al.*[10] studied the dependence of the upper critical fields of multilayered Pb–Bi/Cr systems on the thickness of the SC layer at fixed temperatures. Note that the system

data are in better agreement with the requirements of the model: Cr does not mix with Pb and Bi, and the interface between the layers is apparently fairly sharp. Moreover, in the lattices investigated by Yetter *et al.*[10] the normal layers were fairly thin: $d_{\rm AF}=20$ Å and 75 Å. One can expect, therefore, that for systems with $d_S<5\xi_S$ ($\xi_S\approx 200$ Å for the Pb–Bi alloy) interference effects become important. For lattices with a thickness of the SC layer in the interval $1.5\xi_S\leqslant d_S\leqslant 10\xi_S$, $H_{c2\perp}$ was observed to increase with d_S. This dependence of the behavior of $H_{c2\perp}$ on the thickness of the SC layer is also characteristic of the results depicted in Figs. 5 and 6. However, the reason why the critical field for superlattices with $10\xi_S\leqslant d_S\leqslant 15\xi_S$ is much higher than that for the bulk sample of the Pb–Bi alloy, $H_{c2}^{\rm bulk}$, remains unclear. In the range $d_S>15\xi_S$, the experimental values of the field $H_{c2\perp}$ are approximately equal to $H_{c2}^{\rm bulk}$, as physical considerations suggest.

6. CONCLUSION

The results of the present investigation suggest that the general dependence of the superconducting transition temperature and the upper critical field $H_{c2\perp}$ on the system parameters is qualitatively the same for a thin SC/AF superlattice and a thin SC/N superlattice. More precisely, T_c rapidly drops as the thickness of the normal layer in fairly thin SC layers increases, and becomes saturated when the SC layers are thick. As in SC/N systems, the transition to a ground state with a nonzero coherent-phase difference between the layers is energetically disadvantageous; the type of transition remains unchanged. Quantitatively, however, the conditions for the formation of a superconducting phase in SC/AF systems may differ drastically from those in SC/N systems because of magnetic effects of scattering on the interface between layers. We established the qualitative differences existing between SC/AF and SC/FM small-period lattices. These differences manifest themselves primarily in the change of the type of phase transition into the normal state and in the transition to a superconducting state with a finite coherent-phase difference between the SC layers.

As for the discrepancies (mentioned in Sec. 5) between the theoretical results and the experimental data, in addition to the possible explanations given by Yetter *et al.*[10] and Devis *et al.*[11] one more should be mentioned. These results were interpreted in Refs. 10 and 11 on the assumption that Cr has only one (antiferro)magnetic phase. But chromium and its alloys are known to have many magnetic phases, including those with a magnetic cell incommensurate with the crystal lattice.[23] An external agent can easily transform one phase into another. In the vicinity of magnetic phase transitions one should expect a nonmonotonic dependence of the transition temperature and the upper critical fields of the superconducting state of the system on the lattice period. These problems were not discussed here, but, we believe, they merit a separate study.

The author would like to thank A. D'yachenko and Yu. Medvedev for reading the manuscript of this paper and for valuable remarks, and V. Tarenkov for useful discussions concerning the experimental work of Jiang *et al.*[9] and Devis *et al.*[11]

APPENDIX

The coefficient $\gamma_{mm'}$ is given by the following expression:

$$\gamma_{mm'}=\{[1+(-1)^{m+m'}][c_\omega a_\omega\ \coth(k_{\rm AF}d_{\rm AF})]-[(-1)^m+(-1)^{m'}]c_\omega b_\omega-[(-1)^m\ \exp(i\varphi)+(-1)^{m'}\times\exp(-i\varphi)]\sinh^{-1}(k_{\rm AF}d_{\rm AF})\}\left\{c_\omega^{-1}+\frac{2d_S c_\omega}{\hbar^2 D_S|\omega|}+2\left[a_\omega\ \coth(k_{\rm AF}d_{\rm AF})-b_\omega\ \frac{\cos\ \varphi}{\sinh(k_{\rm AF}d_{\rm AF})}\right]\right\}^{-1}. \quad \text{(A1)}$$

Here we have introduced the notation $c_\omega=\hbar D_S\eta k_{\rm AF}/2d_S$, $a_\omega=a_\omega(H=0)$, and $b_\omega=b_\omega(H=0)$, with the explicit form of the coefficient $a_\omega(H)$ and $b_\omega(H)$ given in Eqs. (A3) and (A4) below.

Note that although formally the matrix $\hat{A}$ given by Eq. (18) is infinite, we have $A_{mm'}\to\delta_{mm'}$ as $m,m'\to\pm\infty$, as the expression for $A_{mm'}$ implies. As a rule, even a 5-by-5 matrix provides an accuracy of about one percentage point, which is sufficient for our purposes. Simple sums over frequencies were evaluated using the formula (see, e.g., Ref. 31)

$$\pi T\sum_n^{\hbar\Omega_D/T_{c0}}\frac{1}{\hbar|\omega|+x}=\lambda^{-1}-\ln\frac{T}{T_{c0}}-\Psi\left(\frac{1}{2}+\frac{x}{2\pi T}\right)+\Psi\left(\frac{1}{2}\right),$$

which is valid for $\hbar|\omega|\gg T,x$; here $\Psi(x)$ is the digamma function. In more complicated cases the summation was done explicitly, with $\hbar\Omega_D/T_{c0}=200$ and $\lambda^{-1}=\ln(1.134\hbar\Omega_D/T_{c0})$.

The expression for $\gamma_{mm'}(H)$ has the form

$$\gamma_{mm'}(H)=[1+(-1)^{m+m'}]\xi_\omega\times\frac{1+\xi_\omega a_\omega(H_{c\perp})-(-1)^{m'}\xi_\omega b_\omega(H_{c2\perp})}{[1+\xi_\omega a_\omega(H_{c2\perp})]^2-\xi_\omega^2 b_\omega^2(H_{c2\perp})}, \quad \text{(A2)}$$

where the following notation has been introduced:

$$\xi_\omega=\frac{\hbar D_S}{2d_S}\ \eta q_N\ \tanh\frac{q_N d_{\rm AF}}{2},$$

$$a_\omega(H)=2d_S\ \coth\left[d_S\left(\frac{2|\omega|}{D_S}+\frac{2\pi H}{\Phi_0}\right)^{1/2}\right]\times\left[\hbar D_S\left(\frac{2|\omega|}{D_S}+\frac{2\pi H}{\Phi_0}\right)^{1/2}\right]^{-1}, \quad \text{(A3)}$$

$$b_\omega(H) = 2d_S \sinh^{-1}\left[d_S \left(\frac{2|\omega|}{D_S} + \frac{2\pi H}{\Phi_0} \right)^{1/2} \right] \times \left[\hbar D_S \left(\frac{2|\omega|}{D_S} + \frac{2\pi H}{\Phi_0} \right)^{1/2} \right]^{-1}. \quad \text{(A4)}$$

[1] J. J. Hauser, H. C. Theyerer, and N. R. Werthamer, Phys. Rev. **142**, 118 (1966).
[2] H. K. Wong, B. Y. Jin, H. Q. Yang, J. B. Ketterson, and J. E. Hilliard, J. Low Temp. Phys. **63**, 307 (1986).
[3] L. Dobrosavljevic-Grujic and Z. Radovic, Jpn. J. Appl. Phys. **26**, Suppl. 26-3, 1463 (1987).
[4] Z. Radovic, L. Dobrosavljevic-Grujic, A. I. Buzdin, and J. R. Clem, Phys. Rev. B **38**, 2388 (1988).
[5] B. Y. Jin and J. B. Ketterson, Adv. Phys. **38**, 189 (1989).
[6] Z. Radovic, M. Ledvij, L. Dobrosavljevic-Grujic, A. I. Buzdin, and J. R. Clem, Phys. Rev. B **44**, 759 (1991).
[7] A. V. Andreev, A. I. Buzdin, and R. M. Osgood, Phys. Rev. B **43**, 10 124 (1991).
[8] P. Koorevaar, Y. Suzuki, R. Coehoorn, and J. Aarts, Phys. Rev. B **49**, 441 (1994).
[9] J. S. Jiang, D. Davidovic, D. H. Reich, C. L. Chien, Phys. Rev. Lett. **74**, 314 (1995).
[10] W. E. Yetter, E. J. Kramer, and D. G. Ats, J. Low Temp. Phys. **49**, 227 (1982).
[11] B. Devis, J. Q. Zheng, P. R. Ketterson, and J. E. Hilliarg, Superlatt. Microstruct. **4**, 465 (1988).
[12] Y. Cheng and M. B. Stearns, J. Appl. Phys. **67**, 5038 (1990).
[13] A. Liechtenstein, I. I. Mazin, and O. K. Anderson, Phys. Rev. Lett. **74**, 2303 (1995).
[14] A. A. Golubov and I. I. Mazin, Physica C **243**, 153 (1995).
[15] V. N. Krivoruchko, Zh. Éksp. Teor. Fiz. **109**, 649 (1995) [JETP **82**, 347 (1995)].
[16] I. Bozovic, J. N. Eckstein, G. F. Virshup *et al.*, J. Supercond. **7**, 187 (1994).
[17] I. Bozovic, J. N. Eckstein, G. F. Virshup *et al.*, Bull. Electrotechn. Labor. **58**, 117 (1994).
[18] Z. Radovic, M. Ledvij, and L. Dobrosavljevic-Grujic, Phys. Rev. B **43**, 8613 (1991).
[19] L. N. Bulaevskiĭ, V. V. Kuziĭ, and A. A Sobyanin, JETP Lett. **25**, 290 (1977).
[20] K. Usadel, Phys. Rev. Lett. **25**, 507 (1970).
[21] A. V. Svidzinskiĭ, *Spatially Inhomogeneous Problems of Superconductivity Theory* [in Russian], Nauka, Moscow (1982), p. 312.
[22] N. I. Kulikov and V. V. Tugushev, Usp. Fiz. Nauk **144**, 643 (1984) [Sov. Phys. Usp. **27**, 954 (1984)].
[23] E. Fawcett, H. L. Alberts, V. Yu. Galkin *et al.*, Rev. Mod. Phys. **66**, 25 (1994).
[24] E. L. Wolf, *Principles of Electron Tunneling Spectroscopy*, Oxford Univ. Press, New York (1985), p. 454.
[25] A. M. Ismagilov and Yu. V. Kopaev, Zh. Éksp. Teor. Fiz **96**, 1492 (1989) [JETP **69**, 846 (1989)].
[26] Yu. V. Kopaev, Usp. Fiz. Nauk **159**, 567 (1989) [Sov. Phys. Usp. **32**, 1033 (1989)].
[27] G. E. Volovik and L. P. Gor'kov, Zh. Éksp. Teor. Fiz. **88**, 1412 (1985) [Sov. Phys. JETP **61**, 843 (1985)].
[28] V. P. Mineev, Usp. Fiz. Nauk **139**, 303 (1983) [Sov. Phys. Usp. **26**, 160 (1983)].
[29] *Superconductivity in Ternary Compounds II: Superconductivity and Magnetism*, edited by M. P. Maple and O. Fisher, Mir Publishers, Moscow (1985), p. 392 [English original edition: Springer, Berlin (1982)].
[30] K. R. Biagi, V. G. Kogan, and J. R. Clem, Phys. Rev. B **32**, 7165 (1985).
[31] P. G. de Gennes, Rev. Mod. Phys. **36**, 225 (1964).
[32] A. V. Zaĭtsev, Zh. Éksp. Teor. Fiz. **86**, 1742 (1984) [Sov. Phys. JETP **59**, 1015 (1984)].
[33] T. Tokuyasi, J. A. Sauls, and D. Rainer, Phys. Rev. B **38**, 8823 (1988).
[34] G. Sarma, J. Phys. Chem. Solids **24**, 1029 (1963).
[35] A. A. Abrikosov, *Fundamentals of the Theory of Metals*, Nauka, Moscow (1987), p. 520 [English transl.: Elsevier, New York (1988)].
[36] I. Banerjee and I. K. Schuller, J. Low Temp. Phys. **54**, 501 (1984).
[37] G. Deutscher and P. G. de Gennes, in *Superconductivity*, Vol. 2, edited by R. D. Parks, Marcel Dekker, New York (1969), p. 1005.

Translated by Eugene Yankovsky

Realization of a heavily doped and fully compensated semiconductor state in a crystalline semiconductor with a deep impurity band

M. I. Daunov, I. K. Kamilov, and A. B. Magomedov

Institute of Physics, Dagestan Science Center, Russian Academy of Sciences, 367003 Makhachkala, Russia
(Submitted 18 October 1995; resubmitted 2 August 1996)
Zh. Éksp. Teor. Fiz. **111**, 562–574 (February 1997)

We use the data on the pressure (up to $P=1.5$ GPa) and field (up to $H=17$ kOe) dependence of the Hall coefficient and the resistivity at 77.6 and 300 K in p-$CdSnAs_2\langle Cu\rangle$ to calculate the effective kinetic characteristics of the charge carriers, the density and mobility of the conduction electrons and the holes of the deep acceptor and valence bands, in an interval of excess-acceptor densities N_{ext} ranging from 10^{10}–10^{17} cm^{-3}. We establish that in a heavily doped semiconductor with a deep impurity band at the tail of the density of states of the intrinsic band, with unequal donor and acceptor densities, a a heavily doped and fully compensated semiconductor state is realized under hydrostatic compression. The threshold value of the pressure that initiates the transition into such a state, P_c, depends on the extent to which the impurity band is populated. In p-$CdSnAs_2\langle Cu\rangle$ at $N_{ext}=N_A$, where N_A is the density of deep acceptors, and $T\leqslant 77.6$ K the value of P_c amounts to 10^{-4} GPa. As the population of the deep acceptor band grows, P_c increases and in the limit becomes infinite. We discuss the special features of the electrophysical properties of p-$CdSnAs_2\langle Cu\rangle$ arising from the absence of an energy gap between the states of the conduction band and those of the deep acceptor band.
 [S1063-7761(97)01202-X]

1. INTRODUCTION

The analogy of the properties of a heavily doped and fully compensated semiconductor and those of an amorphous semiconductor, which is caused by the presence of a random large-scale potential in both systems, has been emphasized in Refs. 1–3. In this connection, Shklovskiĭ and Éfros[1] developed a theory of a heavily doped and fully compensated semiconductor and suggested using this theory as a model in describing amorphous semiconductors. It was also suggested that a model of an amorphous semiconductor could be constructed by introducing, in various ways, compensatory impurities in a heavily doped crystalline semiconductor. This idea has been implemented, for instance, in heavily doped n-Ge samples irradiated by fast neutrons[2] and in heavily doped n-$CdSnAs_2$ samples diffusion-doped by copper from the electrolytic layer on the sample surface.[4,5]

In earlier work (see Ref. 6) the present authors discovered a deep acceptor level (band) of the intrinsic defect of the cadmium vacancy in $CdSnAs_2\langle Cu\rangle$ crystals. The level was found to be closely related to the valence band and was situated at a distance

$$\varepsilon_A=\varepsilon_A^0+\alpha T-\beta P \tag{1}$$

(where $\varepsilon_A^0=-30$ meV, $\alpha=4.6\times10^{-2}$ meV/K, and $\beta=120$ meV/GPa) from the unperturbed edge of the conduction band ($\beta=\partial\varepsilon_g/\partial P$, and $\varepsilon_g=0.28$ eV is the bandgap[6]). Here and in what follows the energy is measured from the unperturbed edge of the conduction band, and for the positive direction we take the one pointing into the band. The behavior of the density of states for the model being discussed in the case $K_A=N_A^-/N_A\approx0$ is depicted in Fig. 1 (N_A^- is the density of ionized deep acceptors). The temperature dependence of the effective mobilities of localized charge carriers has been discussed in detail in Refs. 4, 5, and 7. It was found that from 2 K to 40–50 K the temperature dependence of the effective mobilities of electrons from the conduction band and holes from the acceptor band obeys the Mott law

$$\mu_{c,A}\propto\exp\{-(T_{0c,A}/T)^{1/4}\}, \tag{2}$$

which is characteristic of systems with large-scale fluctuations and of amorphous systems. Here μ_c and μ_A are, respectively, the effective mobilities of the electrons of the conduction band and the holes of the acceptor band, and T_{0c} and T_{0A} are constant parameters that increase with pressure; in the limit $P\to\infty$ we have $T_{0c}\to\infty$ and $\mu_c\to0$, while T_{0A} and μ_A tend to fixed values. It has also been found[4] that in samples for which the population coefficient K_A of the deep acceptor band is larger than 0.9 the state of a heavily doped and fully compensated semiconductor emerges at liquid-helium temperatures when the hydrostatic compression P is greater than 0.1 GPa.

We introduce the following notation: n, $p_A=N_A-N_A^-$, and p_v are the densities of, respectively, the electrons of the conduction band, of the holes of the deep acceptor band, and of the holes of the valence band; $N_a^-=N_a-p_A$ and $N_d^+=N_{d\mu}^+-N_{dr}^+$ are the total densities of the ionized acceptor and donor centers, where $N_a=N_{ar}^++N_{a\mu}^-+N_A$, $N_{a\mu}^-$ and $N_{d\mu}^+$ are the densities of the shallow impurity centers, and N_{ar}^- and N_{dr}^+ are the densities of possible ionized deep acceptor and donor centers whose energy levels are much lower or much higher than the Fermi level $\varepsilon_F=\varepsilon_A$ (because of their position with respect to the Fermi level such centers do not affect the behavior of the electron system); and $N=N_d^+-(N_{a\mu}+N_{ar}^-)$. The condition for electrical neutrality of the system,

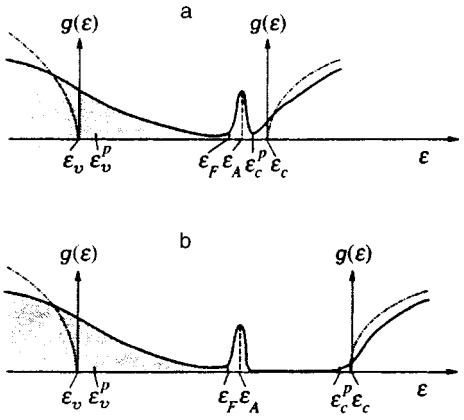

FIG. 1. The (schematic) behavior the density of states of p-$CdSnAs_2\langle Cu\rangle$, a heavily doped and compensated semiconductor with a deep acceptor band whose population coefficient K_A is approximately zero, at atmospheric pressure (a) and under hydrostatic compression (b). Here ε_v and ε_c are the unperturbed energies of the top of the valence band and the bottom of the conduction band, ε_A and ε_F are the energies of the deep acceptor level and the Fermi level, and ε_v^p and ε_c^p are energies of the percolation levels for the holes of the valence band and the electrons of the conduction band. The dot–dash curve describes the behavior of the density of states in a perfect crystal. The shaded areas correspond to populated states.

$$N_a^- + n = p_v + N_d^+ , \tag{3}$$

yields the following expression for the density of excess acceptors: $N_{\text{ext}} = N_a - N_d^+ = N_A - N = p_v + p_A - n$. With this notation we can write $K_A = (N + p_v - n)/N_A$. Note that when $0 \leqslant N \leqslant N_A$, in the limit of $T \to 0$ and $P \to \infty$ the population coefficient of the deep acceptor band satisfies the inequality $0 \leqslant K_A = N/N_A \leqslant 1$, and $\varepsilon_F \approx \varepsilon_A$.

Obviously, if $K_A \approx 0$, holds i.e., the states of the acceptor band are neutral, the conductivity in this band is zero. In the absence of a random potential, near absolute zero, and at

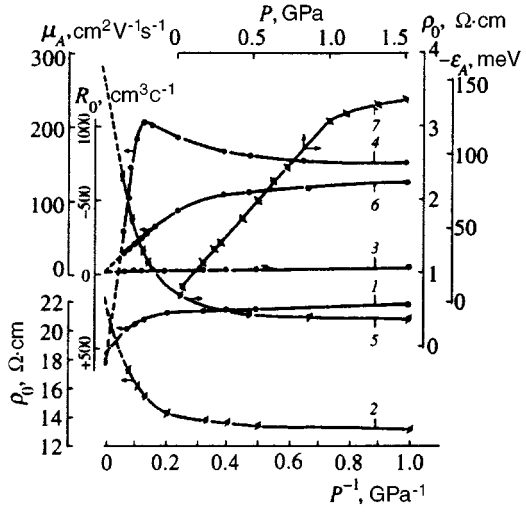

FIG. 2. Pressure dependence of the Hall coefficient R_0 in a very weak magnetic field (curves *1* and *4*), the resistivity ρ_0 (curves *2* and *5*), the mobility μ_A of the holes of the acceptor band (curves *3* and *6*) at 77.6 K (*1–3*) and 280 K (*4–6*), and the deep-acceptor energy level ε_A at 280 K (curve *7*) in sample 10.

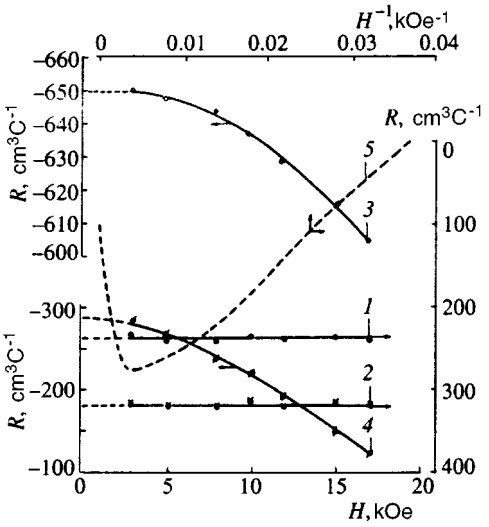

FIG. 3. Magnetic field dependence of the Hall coefficient R in sample 10 at 77.6 K (curves *1* and *2*) and 280 K (curves *3–5*) at different pressures P (measured in GPa): curve *1* — 0.02; curve *2* — 1.09 curve *3* — 10^{-4}; and curves *4* and *5* — 1.51. The dashed curve represents the results of theoretical calculations.

$N_{\text{ext}} = N_A$, the Fermi level is situated between the top of the valence band and the acceptor band. In this case $n = p_v = N_a^- = 0$. However, large-scale fluctuations of the density of ionized impurities and the corresponding random potential, which are sure to be present in a heavily doped semiconductor, bend the edges of the conduction and valence bands so that these edges cross the acceptor band, changing the energy by a quantity of order ε_g (Fig. 1). As a result the Fermi level gets shifted to the acceptor band, while the electrons and hole that have condensed into droplets screen the random potential. In this way, for $N_a \neq N_d$, even at atmospheric pressure a state of the type of a heavily doped and

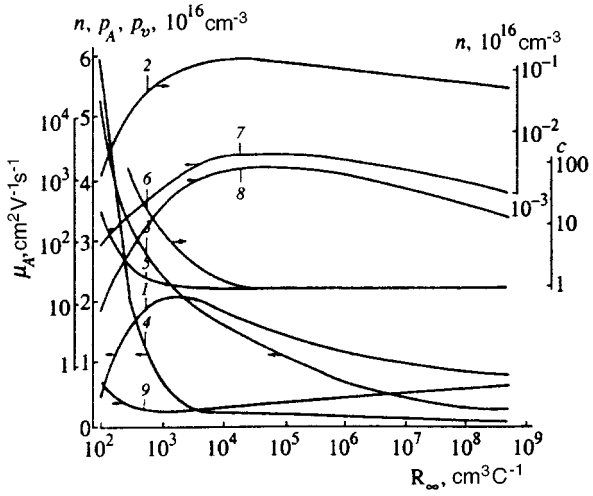

FIG. 4. Curves representing the calculated dependence of the density n of the conduction electrons (curves *1* and *2*), the density p_A of the holes of the acceptor band (curves *3* and *4*), the parameter $c = (p_A + p_v)/n$ (curves *5* and *6*), the mobility μ_A of the holes of the acceptor band (curves *7* and *8*), and the density p_v (*9*) of the holes of the valence band at atmospheric pressure and at 300 K (odd-numbered curves) and 77.6 K (even-numbered curves) on $R_\infty = (N_{\text{ext}} e)^{-1}$ in p-$CdSnAs_2\langle Cu\rangle$.

TABLE I. Parameters of samples under atmospheric pressure.

No. of sample	N_{ext}, 10^{16} cm^{-3}	N_A, 10^{16} cm^{-3}	$-R_0$, cm^3 C^{-1}	ρ_0^{-1} $\Omega^{-1}\cdot$cm^{-1}	μ_c, cm^2 V^{-1} s^{-1}	K_A	R_0, cm^3 C^{-1}	ρ_0^{-1}, $\Omega^{-1}\cdot$cm^{-1}	μ_c, cm^2 V^{-1} s^{-1}	K_A
			$T=300$ K				$T=77.6$ K			
1	1.2×10^{-6}	0.28	781	12.3	8000	0.190	−9600	0.71	7070	0.80
2	4.6×10^{-3}	1.38	331	31.1	12300	0.285	−2290	1.20	4040	0.90
3	6.9×10^{-3}	1.50	320	21.5	8020	0.280	−2130	1.00	3170	0.90
4	1.25×10^{-2}	1.70	280	25.2	8540	0.300	−1800	1.70	5010	0.91
5	5.90×10^{-2}	2.35	220	25.0	7040	0.330	−1100	1.29	3060	0.90
6	0.245	3.16	206	38.1	9780	0.350	−930	0.94	2440	0.87
7	0.275	3.20	210	32.0	8160	0.355	−920	0.83	2200	0.86
8	1.040	4.20	286	23.0	6980	0.360	−850	0.58	2260	0.73
9	1.980	4.77	405	8.84	3160	0.315	−795	0.25	1300	0.56
10	5.94	6.03	650	3.50	3890	0.077	212	0.08	520	0.02
11	6.25	6.08	530	3.70	–	0.060	260	0.07	–	~0
12	11.1	6.80	225	35	–	–	770	0.17	–	–

fully compensated semiconductor could be realized. Our goal was to verify this assumption in experiments. To this end we performed a complex investigation of transfer phenomena using a series of single-crystal p-$CdSnAs_2\langle Cu\rangle$ samples with a total impurity center density of order 10^{18} cm^{-3} in a broad interval of excess-acceptor densitys ranging from 10^{10} to 10^{17} cm^{-3}, with acceptor-band population coefficients $0\leqslant K_A<1$ and compensation coefficients $0.9<K=Nd^+/N_a<1$. The study, which was started in Ref. 6 and was conducted in magnetic fields up to $H=17$ kOe, under hydrostatic compression up to $P=1.5$ GPa, and at 77.6 and 300 K, was aimed at determining the density dependence of the various kinetic characteristics, examining the characteristic features of the gapless state induced by impurity centers, and selecting samples with $N_{ext}\approx N_A$.

2. EXPERIMENTAL RESULTS

Figures 2–4 and Tables I and Tables II depict and list some characteristic results of experimental studies and data gathered by quantitative interpretation. The notation is given above and in the figure captions. For $N_{ext}\approx N_A$ the measurements were done on two identical samples, 10 and 11 (Table I), and reference measurements on sample 11 produced results that for all practical purposes coincided with those involving sample 10.

To generate pressure we used a nonmagnetic stand-alone low-temperature chamber of the piston–cylinder type with a fixed clamp and a liquid as the agent for transferring the pressure. The measurement method is described in Ref. 8. The maximum relative errors in measuring the resistivity, the Hall coefficient, and the Hall mobility amounted to 4%, 2%, and 5%, respectively. The errors in measuring hydrostatic pressure with a Manganin transducer were less than 1.5% at room temperature and 3% at $T\approx100$ K. In experiments with hydrostatic compression, the maximum relative errors in measuring the resistivity and the Hall coefficient were less than 5%. The accuracy of measuring relative variations of the kinetic coefficient under variations of pressure was higher by a factor of ten.

As in Refs. 4–6, the samples were prepared by diffusion doping by copper impurities from the surface layers of n-$CdSnAs_2$ crystals with a donor density of order 10^{18} cm^{-3}. Introduction of compensating acceptors, which are apparently substitutional impurities (a copper atom in an arsenic vacancy[6,9]), lowers the Fermi level to the energy level of a deep acceptor of a cadmium-vacancy intrinsic defect, and because of this the states of the acceptor band become electrically active.[6] The extremely high compensation of p-$CdSnAs_2\langle Cu\rangle$ crystals agrees with the Reis–Fuller theory, which attributes the high solubility of diffused copper in cadmium–tin diarsenide to the effect of donor impurities.[9]

To analyze the density dependence of the Hall constant and the resistivity at $T_1=300$ K and $T_2=77.6$ K qualitatively, we used the curves representing the dependencies of $R_0(T_1)$, $R_0(T_2)$ and $\rho_0(T_1)$, $\rho_0(T_2)$ on $R_0(T_2)/R_0(T_1)$. The appropriateness of such constructions, which make it possible even before calculations to determine the characteristic features of the functions $R_0(N_{ext})$ and $\rho_0(N_{ext})$ and

TABLE II. Parameters of sample 10.

T, K	P, GPa	R_0, cm^3 C^{-1}	ρ_0, $\Omega\cdot$cm	$p_A\times10^{16}$, cm^{-3}	μ_A, cm^2 V^{-1} s^{-1}	p_A/n	p_v/p_A	μ_c/μ_A	μ_v/μ_A	K_A
	10^{-4}	−650	0.286	5.6	130	16.5	0.13	30	1.6	0.08
280	1.5	−300	2.50	5.4	22	1450	0.10	180	9.5	–
	∞	530	3.80	5.4	10	∞	0.10	0	21	0.10
	10^{-4}	212	12.7	5.9	7.9	3×10^4	3×10^{-3}	67	27	0.2
77.6	1.0	320	16.8	5.9	6.1	–	–	–	–	0.2
	∞	507	22.0	5.9	4.4	∞	–	0	–	0.02

TABLE II. (*Continued*)

	ε_A, meV	ε_F, meV	$\partial\varepsilon_A/\partial P$,	$\partial\varepsilon_F/\partial P$,
K	$T=280$ K	$P=10^{-4}$ GPa	meV/GPa	meV/GPa
0.98	−11	−70	−120	−110

carry out a meaningful selection of samples to obtain the density dependence of the kinetic characteristics, was demonstrated on the gapless semiconductor p-HgTe (Ref. 10). The similarity of the kinetic properties of p-$CdSnAs_2\langle Cu\rangle$ and p-HgTe has been noted in Ref. 6 (see Sec. 4).

As the excess-acceptor density grows, the ratio $R_0(T_2)/R_0(T_1)$ is found to decrease from positive values to negative (from 12 to −4.5 in the studied p-$CdSnAs_2\langle Cu\rangle$ crystals). A feature characteristic of p-$CdSnAs_2\langle Cu\rangle$, caused by the fact that a gapless state in this compound appears because the conduction band and the impurity (acceptor) band merge, was discovered in the process; namely, $|R_0|$ was found to increase with the ratio $R_0(T_2)/R_0(T_1)$ from 5 to 12. This feature can be explained by the narrowing of the acceptor band as N_{ext} decreases (see Sec. 4).

3. DETERMINING THE PARAMETERS OF THE CHARGE CARRIERS

The procedure of calculating the effective kinetic characteristics, the charge-carrier densities and mobilities, from the data on the Hall coefficient $R(T,P,H)$ and the resistivity $\rho(T,P,H)$ has been thoroughly discussed in Refs. 4–6. But in contrast to Refs. 4–6, in addition to allowing for the contributions of the conduction electrons and acceptor-band holes, we took into account the contribution of valence-band holes to conductivity, which that cannot be ignored in p-$CdSnAs_2\langle Cu\rangle$ crystals with $N_{\text{ext}}\approx N_A$. Thus, the calculations have been carried out using well-known phenomenological relationships in terms of a theory that allows for three types of charge carriers with parameters (densities and mobilities) independent of the magnetic field strength and assumes that the contribution of each type of charge carrier to the conductivity tensor is additive. The effective densities and mobilities of the charge carrier were found from the formulas $n_j=(|R_j|e)^{-1}$ and $\mu_j=|R_j|\sigma_j$, where R_j and σ_j are the partial values of the Hall coefficient and the resistivity. Determining the characteristic parameters in this case in a reliable manner is not a trivial problem. Mathematical analysis of the $R(T,H)$ and $\rho(T,H)$ dependences, including computer models needed for determining whether there is enough data to estimate the unknown parameters, as well as the results of physical modeling, can be found in Refs. 11–13. We also used the electroneutrality equation, the known values of the band parameter, and the Kildal–Bodnar (KB) four-band model for the dispersion law.[6]

The fact that $N_A^-=N_A[1+\gamma_{\text{exp}}(\varepsilon_A^*-\eta)]^{-1}$ implies

$$\ln\ \gamma+\varepsilon_A^{0}{}^*-\beta^*P=\eta+\ln\frac{1-K_A}{K_A}, \tag{4}$$

where γ is the parameter of the acceptor-level spin degeneracy, $\varepsilon_A^{0}{}^*=\varepsilon_A^0/k_BT$, $\beta^*=\beta/k_BT$, and $\eta=\varepsilon_F/k_BT$, with k_B the Boltzmann constant. Equation (4) was used in calculating the characteristic charge-carrier parameters when the variation of the average charge-carrier energy caused by a random potential is small compared to the energy proper and when acceptor-level broadening can be ignored.[6,14] At $N_{\text{ext}}\approx N_A$ at room temperature and with allowance for the fact that the acceptor-level baric coefficient $\partial\varepsilon_A/\partial P$ is independent of pressure, at least up to $P=1.5$ GPa,[6,8] we used Eq. (4) in the pressure interval from atmospheric to $P=1.5$ GPa, where $f(P)=\eta+\ln(1-K_A)/K_A$ is a linear function (Fig. 2). Here we allowed for the fact that the parameter η was estimated by n in the KB dispersion-law approximation, which used the known values of band parameters, while n and K_A were determined directly from the experimental data. Hence the deviation of $f(P)$ from a linear function suggests that the random potential affects the density of conduction-band states. Since in semiconductors the baric coefficients of the energy gaps $\Delta\varepsilon$ are usually pressure-independent (or are weakly dependent on pressure[15]), in cases where hydrostatic compression has a strong effect on electron statistics, expressions of type (4) can usually be used as a condition for the applicability of the dispersion law for impurity-free semiconductors in a semiconductor with a random potential.

In other words, applying the dispersion law for a perfect semiconductor to a semiconductor with a random potential is meaningful as long as the pressure dependence of $\Delta\varepsilon(P)$ calculated using experimental data and relations of type (4) remains linear, as is the case with $CdSnAs_2\langle Cu\rangle$ for samples with $N_{\text{ext}}\approx N_A$ at room temperature and at pressures up to $P\approx 1$ GPa (Fig. 2) and for samples with $N_{\text{ext}}<N_A$ at room temperature and at pressures up to at least 1.5 GPa, as well as at 77.6 K and nearly atmospheric pressure.[6]

With allowance for adjustments in graph plotting, physical models, and a satisfactory agreement between the thermoelectric power measured in experiments[16] and the one calculated with the use of certain values of the characteristic parameters, the maximum relative error in determining the characteristic charge-carrier parameters, including the excess acceptor density, is 15%.

The compensation coefficient of the samples was estimated by the formula

$$1-K=\frac{N_{\text{ext}}}{n^{in}}\frac{2(1-K^{in})}{1+K^{in}}. \tag{5}$$

Here $n^{in}=(|R_0^{in}|e)^{-1}$ and K^{in} are, respectively, the electron density and the compensation coefficient for crystal prior to diffusion doping. The parameter K^{in} was calculated by the Bruns–Herring formula for electron mobility in heavily doped degenerate n-$CdSnAs_2$ crystals at 77.6 K when electron scattering on ionized impurities dominates.[17] Here the

error in determining the total density of ionized impurities, caused by using measured values of R_0^{in} and ρ_0^{in} was found to be no higher than 10%. In deriving Eq. (5) we allowed for the fact that the appearance of a $Cu \rightarrow V_{As}$ defect (V_{As} is an arsenic vacancy) is accompanied by the disappearance of a V_{As} defect,[9] and used the simplifying assumption that defect charges are equal to unity. We also assumed that $n^{in} \gg N_{ext}$.

Equation (5) made possible a qualitative suggestion that compensation in the p-$CdSnAs_2\langle Cu\rangle$ crystals studied is extremely strong.

Within the range of variation of N_{ext} studied here (see Table I), a decrease in N_{ext} leads to a decrease in the parameter $1-K$ from 10^{-1} to 10^{-6}.

4. DISCUSSION

Within the range of variation of N_{ext} studied here we have the following empirical formula:

$$N_A = 4.2 \times 10^{16} (10^{-16} N_{ext})^{1/5}, \tag{6}$$

where N_A and N_{ext} are measured in units of cm^{-3}. Thus, as N_{ext} decreases, the acceptor band narrows. Such correlation between the parameters N_A and N_{ext}, as we will shortly see, has a strong effect on the density dependence of electrophysical properties.

The dependence of the Hall coefficient in an extremely weak magnetic field, R_0, on N_{ext} (Table I) is characteristic of p-type semiconductors with an electron-to-hole mobility ratio much larger than unity. However, the quasi-intrinsic conductivity region, where $c=(p_A+p_v)/n=1$ (Fig. 4), contains a characteristic feature, an increase in $|R_0|$ with decreasing N_{ext}, caused by a narrowing of the acceptor band. As $N_{ext} \rightarrow 0$, the Hall coefficient tends to the value R_i for intrinsic $CdSnAs_2$ ($R_i = -830$ cm^3 C^{-1} at room temperature; see Ref. 18). Naturally, a transition to quasi-intrinsic conductivity at 77.6 K occurs for lower values of N_{ext}. Of certain interest here is the dependence of the acceptor-band hole mobility on the excess acceptor density (Fig. 4). As N_{ext} decreases from a value of order 10^{16} cm^{-3} ($K_A \approx 0$), μ_A grows (the coefficient K_A increases) and passes through a maximum. Further decrease in μ_A can be linked to the decrease in the deep-acceptor density, i.e., to the narrowing of the acceptor band. The explanation for the temperature and baric dependence of K_A is equally straightforward. The fact that in crystals with $N_{ext} > 2 \times 10^{16}$ cm^{-3} (samples 10 and 11) K_A decreases as the temperature drops from 300 to 77.6 K (Table I) is caused by the freezing of electrons into the valence band.

The similarity between p-$CdSnAs_2\langle Cu\rangle$ and the gapless semiconductor p-HgTe (Ref. 19) in their electrophysical properties was noted in Ref. 6. A characteristic feature here is that the mixed-conductivity region is ''extended'' in temperature, even down to liquid-helium temperatures when the excess-acceptor density is lower than the threshold value ($R_0 < 0$) (for p-$CdSnAs_2\langle Cu\rangle$ $N_{ext} < 10^{15}$ cm^{-3}; see Ref. 4). Moreover, the temperature dependence of the intrinsic (or quasi-intrinsic $[n(p_A+p_v)]^{1/2}$ in $CdSnAs_2\langle Cu\rangle$) density ($n_i$) in both compounds is close to the $n_i \propto T^{3/2}$ law, and the reduced Fermi energy (η_i) is weakly temperature-dependent. For instance, in the quasi-intrinsic sample 3 of p-$CdSnAs_2\langle Cu\rangle$ (Table I and Fig. 4), $|\eta_i|$ grows from 1.5 to 1.7 as the temperature rises from 77.6 to 300 K. The Fermi energy was estimated from the electron density (Fig. 3) with the use of the known values of the band parameter and the KB four-band model for the dispersion law.[6]

The baric and magnetic-field dependence of the kinetic coefficients and the baric dependence of the characteristic parameters, with the exception of μ_A, in p-$CdSnAs_2\langle Cu\rangle$ crystals with $N_{ext} \approx N_A$ at room temperature are typical of p-type semiconductors in the mixed-conductivity range, with a tendency toward a transition to impurity conductivity as the pressure rises (Figs. 2 and 3 and Table II). On the other hand, the rapid decrease in μ_A with increasing pressure is caused by the separation of the states of the band continuum from those of the deep acceptor band, since, as noted in Ref. 5, the effective mobility of the impurity-band carriers depends on the density of states $g(\varepsilon_A)$ of the band continuum in its vicinity. As the conduction band moves away from the acceptor band, i.e., as $g(\varepsilon_A)$ decreases, the rate of the decrease of μ_A with increasing pressure drops. The extremely weak dependence of p_A and p_v on pressure explains the almost linear dependence of ε_F on pressure up to $P=1$ GPa, as long as the random-potential effect is insignificant. Nevertheless, in contrast to the acceptor band, whose position is fixed in relation to the top of the valence band, because the electrons become ''frozen'' into the lower states the Fermi level slowly moves away, as the pressure grows, from the top of the valence band, approaching the acceptor band with a rate of 10 meV/GPa (Table II). The satisfactory agreement between the values of ε_A^0 and $\partial \varepsilon_A / \partial P$ found in our investigation and the earlier estimates[4,6] suggests that the present calculations of the values of the kinetic characteristics of the charge carrier using the $R(H,P)$ and $\rho(P)$ dependences are reliable.

As the temperature is lowered, the Hall coefficient changes sign. At 77.6 K $R_0 > R_\infty = (N_{ext} e)^{-1}$ (see Tables I and II and Fig. 3), which suggests that two types of holes, from the valence and acceptor band, participate in transport processes[11–13] (see Eq. (7) below). This is also evident from the calculated dependence of R on the magnetic field strength in the high-field range at room temperature (Fig. 3). The fact that at 77.6 K the Hall constant is independent of H implies that the limit of an extremely weak field holds for the charge carriers. As the temperature drops from room temperature to 77.6 K and the pressure remains atmospheric, both p_v and n decrease by one to three orders of magnitude. The Fermi level moves toward the acceptor band and is pinned there. Also, the acceptor-band hole mobility decreases by a factor greater than ten. The observed tendency toward localization of acceptor-band holes is caused not only by the decrease in the average thermal energy but also by the fact that, in accordance with (1), the conduction band moves away from the acceptor band, i.e., by the decreases in $g(\varepsilon_A)$, as in the case of growing hydrostatic compression.

The values of the coefficients R_0 and ρ_0 at 77.6 K are determined by the kinetic characteristics of the holes of the valence and acceptor bands. The hole density, the valence-band hole mobility, the Fermi energy, and the gap $\varepsilon_A - \varepsilon_v$

between the bands are pressure-independent. But the acceptor-band hole mobility decreases with increasing pressure because of the decrease in $g(\varepsilon_A)$. This means that the density of states of the conduction band at the Fermi level frozen into the acceptor band is nonzero starting at atmospheric pressure (although the electron contribution to the formation of R_0 and ρ_0 is unessential). The increase in the Hall coefficient and the resistivity $\rho_0 \approx (ep_A\mu_A)^{-1}$ with pressure is determined by the decrease in μ_A. Indeed, a simple phenomenological calculation of the Hall coefficient for two types of carrier of the same sign and the inequality

$$R_v=(p_ve)^{-1} \gg R_0 > R_A=(p_Ae)^{-1} \approx R_\infty=(N_{\text{ext}}e)^{-1} \quad (7)$$

(Table II) imply that R_0 increases with decreasing μ_A (as μ_A decreases to zero, R_0 tends to R_v). Just as at room temperature, as the pressure increases the effective acceptor-band hole mobility decreases to several $\text{cm}^2\ \text{V}^{-1}\ \text{s}^{-1}$ as $P\to\infty$ (Table II), approaching values obtained in p-$\text{CdSnAs}_2\langle\text{Cu}\rangle$ samples with $K_A>0.9$ at liquid-helium temperatures,[4,5] i.e., a pronounced tendency toward localization of acceptor-band holes with increasing pressure can be observed.

Thus, the presence of a large number of valence-band holes and conduction electrons ($g(\varepsilon_A)>0$) at 77.6 K in p-$\text{CdSnAs}_2\langle\text{Cu}\rangle$ with $N_{\text{ext}}\approx N_A$ suggests strong deformation of the band edges and formation of heavily doped and fully compensated semiconductor states even at atmospheric pressure.

5. CONCLUSION

In p-$\text{CdSnAs}_2\langle\text{Cu}\rangle$ crystals with $K_A\to 0$ and $N_A\to N_{\text{ext}}$, a heavily doped and fully compensated semiconductor state is realized at $T\leqslant 77.6$ K even at atmospheric pressure, in contrast to the case with $K_A\to 1$ (see Refs. 4 and 5). For semiconductors with a deep impurity band, the equality of donor and acceptor densities is not a necessary condition for the formation of a state of a heavily doped and fully compensated semiconductor, in contrast to the model suggested in Ref. 1.

The unique possibility of continuously controlling the height of potential barriers by applying hydrostatic compression in such systems is of certain interest to studies of the specific phenomena in disordered semiconductors, such as the state of ''frozen'' photoconductivity of nonequilibrium carriers, which can be retained indefinitely. Possible objects for such investigations are the heavily doped and strongly compensated $\text{Ge}\langle\text{Au,Sb}\rangle$, $\text{InSb}\langle\text{Cr}\rangle$, and n-InAs crystals with an excess donor density of order $10^{15}\ \text{cm}^{-3}$. The importance of these substances cannot be overestimated, since they can serve as an effective model for a disordered semiconductor (an amorphous semiconductor, in particular) controllable by compensation and hydrostatic compression.

The authors are grateful to the Russian Fund for Fundamental Research for financial support (Project No. 95-02-03653a).

APPENDIX

To increase the reliability of estimates of the characteristic parameters of the charge carrier, i.e., their density and mobility, we employed the transformations that linearized Eq. (4) (Ref. 6):

$$\begin{aligned} &L[\gamma\exp(\varepsilon_A^{*0}-\eta^0)]^{-1}=M+N(n^0-p_v^0)^{-1},\\ &L=[1-(n-p_v)/(n^0-p_v^0)](1-\exp\ \xi)^{-1},\\ &M=-[1-\{(n-p_v)/(n^0-p_v^0)\}\exp\ \xi](1-\exp\ \xi)^{-1}, \end{aligned} \quad (A1)$$

with $\xi=\eta^0-\eta-\beta^*P$ (the superscript 0 correspond to atmospheric pressure), and the expression for the Hall coefficient for three types of charge carriers when $R\neq 0$ (Ref. 11):

$$R=R_0\,\frac{1+\varphi H^2+\theta H^4}{1+\psi H^2+\nu H^4}. \quad (A2)$$

The coefficients R_0, φ, ψ, θ, and ν are determined by the densities (n, p_A, and p_v) and mobilities (μ_c, μ_A, and μ_c) of the charge carriers, and in the adopted approximation are independent of the magnetic field strength. In the mixed conductivity range, where the dependence of R on H is expressed most vividly, the ratio p_A/n is much larger than unity, and $\mu_vH\ll 1$ in fields up to 20 kOe (μ_v is a quantity of the order of several hundred $\text{cm}^2\ \text{V}^{-1}\ \text{s}-1$). In this case we have

$$(\varphi H^2+\theta H^4)(\varphi H^2)^{-1}\approx 1, \quad (\psi H^2+\upsilon H^4)(\psi H^2)^{-1}\approx 1$$

to within one percent, and Eq. (A2) becomes

$$R=R_0\,\frac{1+\varphi H^2}{1+\psi H^2}. \quad (A3)$$

This implies that

$$\frac{R_0}{R}=\frac{1-R_0/R}{\varphi H^2}+\frac{\psi}{\varphi}, \quad (A4)$$

$$(R-R_\infty^{\text{eff}})^{-1}=(R_0-R_\infty^{\text{eff}})^{-1}+\psi(R_0-R_\infty^{\text{eff}})^{-1}H^2. \quad (A5)$$

Note that

$$R_\infty^{\text{eff}}=R_0\left(\frac{\varphi}{\psi}\right)>R_\infty=R_0\left(\frac{\theta}{\nu}\right)=\lim_{H\to\infty} R=(N_{\text{ext}}e)^{-1}.$$

Allowing for the fact that $(\mu_c/\mu_v)^2\gg 1$, we obtain

$$\varphi=\mu_c^2\left(1-\frac{\mu_c^2}{R_cR_0\sigma_0^2}\right), \quad \psi=\mu_c^2\left(1-\frac{\mu_c}{R_c\sigma_0}\right)^2, \quad (A6)$$

with $|R_c|=(ne)^{-1}$. Thus, in weak fields the R vs H dependence is determined primarily by the characteristic parameters of the highly mobile charge carriers, the electrons of the conduction band, and n and μ_c can be found directly from (A6). Equations (A6) also lead directly to the following equations:

$$\begin{aligned} &R_A\sigma_A^2\left[1+\left(\frac{\mu_v}{\mu_A}\right)^2\frac{p_v}{p_A}\right]=R_0\sigma_0^2-R_c\sigma_c^2,\\ &\sigma_A\left(1+\frac{\mu_v}{\mu_A}\frac{p_v}{p_A}\right)=\sigma_0-\sigma_c, \end{aligned} \quad (A7)$$

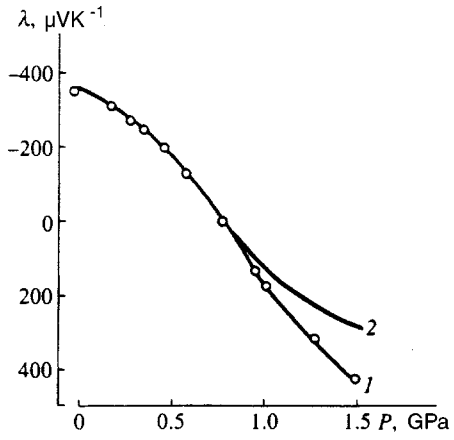

FIG. 5. Experimentally measured (curve *1*) and theoretically calculated (curve *2*) dependencies of the thermoelectric power λ on the pressure in sample 10 of p-$CdSnAs_2\langle Cu\rangle$ at room temperature.

with $\sigma_c = n\mu_c e$. Then, using n, the known band parameters, and the approximation of the KB dispersion law, we estimated η and p_v. Finally, we used Eqs. (4), (A1), and (A7) to determine the other characteristic parameters of the charge carriers.

To determine the errors in estimating the characteristic parameters by formulas (A4) and (A5) we used differentiation. We introduce the notation

$$y = \frac{R_0}{R}, \quad l = \frac{1 - R_0/R}{\varphi}, \quad b = \frac{\psi}{\varphi}$$

to be used in Eq. (A4), and the notation

$$y = (R - R_\infty^{\text{eff}})^{-1}, \quad l = \psi(R_0 - R_\infty^{\text{eff}}), \quad b = (R_0 - R_\infty^{\text{eff}})^{-1}$$

to be used in Eq. (A5).

The maximum relative errors in determining the coefficients l and b by (A4) are

$$\frac{|\Delta l|}{|l|} = \frac{|\Delta y|}{|y|}\left|1 - \frac{R}{R_\infty^{\text{eff}}}\right|^{-1}, \quad \frac{|\Delta b|}{|b|} = \frac{|\Delta y|}{|y|}\left|\frac{R}{R_\infty^{\text{eff}}}\right|^{-1}, \tag{A8}$$

while largest relative errors in determining the coefficients l and b by (A5) are

$$\frac{|\Delta l|}{|l|} = \frac{|\Delta y|}{|y|}\left|\frac{1 - R_\infty^{\text{eff}}/R_0}{1 - R/R_0}\right|,$$

$$\frac{|\Delta b|}{|b|} = \frac{|\Delta y|}{|y|}\left|1 - \frac{R - R_\infty^{\text{eff}}}{R_0 - R_\infty^{\text{eff}}}\,\beta H^2\right|^{-1}. \tag{A9}$$

In our calculations we usually used (A4), while (A5) was used if two types of charge carriers were involved, when the contribution of the valence-band holes could be ignored ($K_A > 0.5$, at low temperatures and high pressures) and when $R > 0$. This made it possible to determine R_∞ by graphical methods by extrapolating the R_0 vs P^{-1} dependence to $P \to \infty$ (Ref. 4) and by formula (A5).

According to (A8), the maximum relative error of determining the ratio ψ/φ in Eq. (A4) exceeds $|\Delta R_0/R||R_0/R|^{-1}$ by a factor of $|R_\infty^{\text{eff}}/R|$, while according to (A8) the maximum relative error of determining the quantity $(1 - R_0/R)/\varphi H^2$ in Eq. (A4) is smaller than $|\Delta R_0/R||R_0/R|^{-1}$ by a factor of $|1 - R/R_\infty^{\text{eff}}|$ ($R < 0$) and does not exceed 4%.

All this reasoning and the above relationships suggest that the method of calculation and the estimates of the errors in determining the characteristic parameters are determined by the properties of the specific sample (more precisely, by R_0, R_∞^{eff}, R_∞ and the range of variation of $R(H,P)$). The case of two types of charge carriers is fairly simple and has been discussed in detail in Refs. 4–6 and 9. We examine the case of three types of charge carriers[11–13] using sample 10 of p-$CdSnAs_2\langle Cu\rangle$ with $N_A \approx N_{\text{ext}}$ as an example. For room temperatures we used Eqs. (A4) and (A6) to estimate n and μ and to derive two independent equations (A7) containing the characteristic parameters p_A, μ_A, p_v, and μ_v. The value of n and the known band parameters were used to estimate η and p_v. After this we employed Eqs. (4), (A1), and (A7) to estimate the remaining parameters. There were aspects that facilitated the calculations and made the results more reliable: the value of the baric coefficient $\partial\varepsilon_A/\partial P$ was known *a priori*,[6] while the parameters p_A and μ_v at a fixed temperature and $N_A \approx N_{\text{ext}}$ are practically pressure-independent.

Moreover, the reliability of the results of calculations was increased by adjusting the estimates via a comparative analysis of the curves reflecting the dependence of R_∞, N, and N_A on $R_0(77.6\ \text{K})/R_0(300\ \text{K})$, by extrapolating R_0 to the point $P^{-1} = 0$ (i.e., $P \to \infty$), etc.

Finally, for crystals with $N_{\text{ext}} \approx N_A$, in the present work (Fig. 5) and earlier in other cases,[16] additional verification of the results was performed; namely, the value of the thermoelectric power λ calculated using the values of the parameters of the charge carriers and the approximation in which scattering of charge carriers on ionized impurities is predominant, was compared with the experimental value. Up to $P = 1$ GPa at room temperature and $N_{\text{ext}} \approx N_A$ the agreement was satisfactory (Fig. 5). The observed discrepancy in the λ vs P curves at pressures above 1 GPa is caused by the growing importance of the random potential with increasing pressure, a fact mentioned in the discussion of the ε_A vs P dependence (Fig. 2).

On the whole, with allowance for adjustments in plotting and for physical models and according to what has been said earlier, the error in determining the characteristic parameters of charge carriers, including N_{ext}, is at most 15%.

[1] B. I. Shklovskiĭ and A. L. Éfros, Zh. Éksp. Teor. Fiz. **62**, 1156 (1972) [Sov. Phys. JETP **35**, 610 (1972)].
[2] A. R. Gadzhiev, S. M. Ryvkin, and I. S. Shlimak, JETP Lett. **15**, 428 (1972).
[3] S. M. Ryvkin and I. S. Shlimak, Phys. Status Solidi A **16**, 515 (1973).
[4] I. K. Kamilov, M. I. Daunov, V. A. Elizarov, and A. B. Magomedov, Zh. Éksp. Teor. Fiz. **104**, 2436 (1993) [JETP **77**, 92 (1993)].
[5] I. K. Kamilov, M. I. Daunov, V. A. Elizarov, and A. B. Magomedov, JETP Lett. **54**, 594 (1991).
[6] M. I. Daunov, A. B. Magomedov, and V. I. Danilov, Fiz. Tekh. Poluprovodn. **25**, 467 (1991) [Sov. Phys. Semicond. **25**, 282 (1991)].
[7] M. I. Daunov, I. K. Kamilov, R. I. Bashilov *et al.*, High Pressure Research **9**, 361 (1992).
[8] M. I. Daunov and A. B. Magomedov, Fiz. Tekh. Poluprovodn. **8**, 45 (1974).

[9] V. G. Voevodin and O. V. Voevodina, *Cadmium–Tin Diarsenide* [in Russian], Tomsk Univ. Press, Tomsk (1988).
[10] M. I. Daunov, Dokl. Akad. Nauk Azerb. SSR **23**, No. 3, 10 (1967).
[11] M. I. Daunov and A. S. Aronson, manuscript deposited at the All-Union Institute of Scientific and Technical Information, No. 2662-79, Moscow (1979) [in Russian].
[12] M. I. Daunov, I. M. Abdurakhmanov, A. B. Magomedov, and A. É. Ramazanova, in *Photo- and Electric Phenomena in Semiconductors* [in Russian], Dagestan Science Center of the Russian Academy of Sciences, Makhachkala (1985), p. 110.
[13] M. I. Daunov, I. M. Abdurakhmanov, and A. B. Magomedov, in *Transfer of Charge and Heat Carriers in Semiconductors* [in Russian], Dagestan Science Center of the Russian Academy of Sciences, Makhachkala (1986), p. 49.
[14] M. I. Daunov, A. B. Magomedov, and V. I. Danilov, Ukr. Fiz. Zh. (Russ. Ed.) **37**, 103 (1992).
[15] A. Matulenis, Yu. Pozhela, E. Shimulite, and V. Yutsene, in *Semiconductor Transducers* [in Russian], Mokslas, Vilnius (1980), p. 141.
[16] M. I. Daunov, A. B. Magomedov, and V. I. Danilov, Izv. Vyssh. Uchebn. Zaved. No. 9, 116 (1991).
[17] T. A. Polyanskaya and Yu. V. Shmartsev, Fiz. Tekh. Poluprovodn. **4**, 727 (1970) [Sov. Phys. Semicond. **4**, 615 (1970)].
[18] M. I. Daunov and A. B. Magomedov, in *Transport and Magnetic Phenomena in Semiconductors and Metal Oxides* [in Russian], Dagestan Branch of the USSR Academy of Sciences, Makhachkala (1989), p. 10.
[19] I. M. Tsidil'kovskiĭ, G. I. Harus, and N. S. Shelushinina, Adv. Phys. **34**, 43 (1985).

Translated by Eugene Yankovsky

The Landauer resistance of a one-dimensional metal with periodically spaced random impurities

D. M. Sedrakyan, D. A. Badalyan, V. M. Gasparyan, and A. Zh. Khachatryan

Erevan State University, 375049 Erevan, Republic of Armenia
(Submitted 14 February 1996)
Zh. Éksp. Teor. Fiz. **111**, 575–584 (February 1997)

We find the dependence of the ensemble-averaged resistance, $\langle \rho_L \rangle$, of a one-dimensional chain consisting of periodically spaced random delta-function potentials of the chain length L, the incident-electron energy, and the chain disorder parameter w. We show that generally the $\langle \rho_L \rangle$ vs L dependence can be written as a sum of three exponential functions, two of which tend to zero as $L \to \infty$. Hence the asymptotic expression for $\langle \rho_L \rangle$ is always an exponential function of L. Such an expression for $\langle \rho_L \rangle$ means that the electronic states are indeed localized and makes it possible (which is important) to find the dependence of the localization radius on the incident-electron energy and the force with which an electron interacts with the sites of the chain. We also derive a recurrence representation for $\langle \rho_L \rangle$, which proves convenient in numerical calculations. © *1997 American Institute of Physics.* [S1063-7761(97)01302-4]

1. INTRODUCTION

It is well known that the procedure of averaging and calculating the averages of the physical properties for disordered systems is difficult primarily from the mathematical viewpoint. The phenomenon of electron localization in systems with random interaction potentials makes it possible occasionally to draw certain conclusions about the nature of the possible solutions without actually solving the problem. For instance, in the one-dimensional case, as shown in Refs. 1–4, the dependence of the average resistance of a metal with fixed impurities, where all the electronic states are localized , on the length L of the impurity chain can be expressed, for $L \to \infty$ at absolute zero, by the following formula ($\hbar = e^2 = 1$):

$$\langle \rho_L \rangle = \tfrac{1}{2}(e^{L/\xi} - 1),$$

where ξ is the electronic-state localization radius, which is independent of L. Here the ''nonideal region'' is assumed to exist between two semi-infinite electrodes in which electrons move freely. It is the fraction of electrons that have passed through the ''nonideal region'' from one electrode to the other that determines the transmissivity of the system, which is inversely proportional to $\langle \rho_L \rangle$. Thus, such a one-to-one correspondence between the Landauer resistance $\langle \rho_L \rangle$ with $L \to \infty$ and the localization radius ξ of one-electron states, the latter depending only on the electron energy and the force of the electron–impurity interaction, reduces the problem of finding ξ to that of finding $\langle \rho_L \rangle$ with $L \to \infty$, and vice versa.

For instance, for the entire class of random potentials in which the average potential is zero, i.e., potentials of the white-noise type, the localization radii have been calculated both in the presence of an external field and in the absence of such a field.[5] The well-known method of transfer matrices, when applied to the model of short-range potentials,[6] has made it possible to effectively perform numerical calculations but proved ineffective in obtaining analytic results. The determinant method, suggested in Refs. 7 and 8 for one-dimensional systems consisting of random single barriers, made it possible to obtain analytic results only under the assumption of weak or strong scattering of an electron by a single barrier and in the event of resonant passage. Calculations of the localization radius from the behavior of $\langle \rho_L \rangle$ as $L \to \infty$ were also done in Refs. 9–11.

In Ref. 12 it was shown that for the model of periodically spaced delta-function potentials whose amplitudes are independent random quantities with a zero average value, the average Landauer resistance $\langle \rho_L \rangle$ can be represented by a series expansion. In Ref. 13 we were able to sum this series and to derive a finite-difference equation for determining $\langle \rho_L \rangle$. There we also gave solutions for this equation in particular cases, i.e., for electron energies corresponding to the edge and center of the energy band.

In the present paper we find the analytic solution of the finite-difference equation for $\langle \rho_L \rangle$ in the general case. This solution actually gives $\langle \rho_L \rangle$ as a function of the chain length L, the energy of the impinging electron, and the intensity of electron scattering on a single barrier. We show that the solution for $\langle \rho_L \rangle$ with $L \to \infty$ can always be reduced to the form $\langle \rho_L \rangle \propto \exp(L/\xi)$, with ξ independent of L. We also calculate the localization radius.

In Sec. 2 we formulate the problem and give the results obtained in Ref. 13 that are needed for our present study. In Sec. 3 we find the general solution of the finite-difference equation that the unknown function $\langle \rho_L \rangle$ satisfies. Here we also derive a recurrence relation for $\langle \rho_L \rangle$. Section 4 is devoted to an analysis of the characteristic equation whose roots are used, as shown in Sec. 3, to express the dependence of $\langle \rho_L \rangle$ on L. We also find the solution of the equation for $\langle \rho_L \rangle$, with $L \to \infty$, from which we derive an expression for the electron localization radius. In Sec. 5 we analyze the results.

2. STATEMENT OF THE PROBLEM

We take a chain of N delta-function potentials with arbitrary amplitudes V_n and corresponding coordinates x_n:

 1063-7761/97/020317-05$10.00

$$V(x)=\sum_{n=1}^{N} V_n\delta(x-x_n), \quad n=1, 2, \ldots, N.$$

Let the solution of the Schrödinger equation for an electron with an energy $E=k^2$ ($\hbar=2m_0=1$, with m_0 the electron mass) outside the structure be

$$\psi(k,x)=\begin{cases} e^{ikx}+r_N(k)e^{-ikx}, & x\leqslant x_1, \\ t_N(k)e^{ikx}, & x\geqslant x_N, \end{cases}$$

where $r_N(k)$ and $t_N(k)$ are, respectively, the electron reflection and transmission amplitudes. The Landauer resistance can be expressed in terms of $r_N(k)$ and $t_N(k)$ by the well-known formula

$$\rho_N=\frac{1}{|t_N(k)|^2}-1, \quad |r_N(k)|^2=1-|t_N(k)|^2. \tag{1}$$

This formula holds for any type of scattering potential. In Ref. 13 we found that the quantity ρ_N averaged over the different realizations of the random field for a model in which N delta-function potentials occupy arbitrary points $x_1, x_2, \ldots, x_N$ can be expressed as

$$\langle\rho_N\rangle=1+\sum_{p=1}^{N}\sum_{1\leqslant j_1\leqslant\cdots\leqslant j_p}^{N} 2^{p-1}\alpha^p \times\prod_{l=1}^{p-1}\{1-\cos[2k(x_{j_{l+1}}-x_{j_l})]\}, \tag{2}$$

where

$$\alpha=\frac{1}{w}\int_{-w/2}^{w/2} f(V_j)\frac{V_j^2}{4k^2}dV_j, \quad \frac{1}{w}\int_{-w/2}^{w/2} f(V_j)dV_j=1.$$

Here $f(V_j)$ is the distribution function of the potentials V_j, which is defined in the interval $[w/2,-w/2]$, is assumed equal for all the V_j ($j=1,2,\ldots,N$), and is an arbitrary even function of V_j. In particular, for $f(V_j)=1$ we have $\alpha=w^2/48k^2$.

Direct summation of the series (2), even assuming that the scatterers are positioned equidistantly, runs into unsurmountable difficulties. Equation (2) can be summed only in some particular cases, when the electron energy corresponds either to the center of the energy band or to the edge ($ka=\pi/2$ or $ka=\pi$, where a is the chain period).[12,13] However, as shown in Ref. 13, we can sum over the inner indices in (2). The result is a finite-difference equation for the unknown quantity $\langle\rho_N\rangle$. This equation has the form

$$\langle\rho_N\rangle=\alpha N+\sum_{n=1}^{N} c_{N-n}\langle\rho_n\rangle, \tag{3}$$

where

$$\rho_1=1, \quad c_n=2\alpha[1-\cos(2kan)].$$

Note that Eq. (3) can be interpreted as a system of linear algebraic equations in the unknowns $\langle\rho_1\rangle,\langle\rho_2\rangle,\ldots,\langle\rho_N\rangle$, with the result that $\langle\rho_N\rangle$ can be written in the form of a determinant.

The solution of Eq. (3) for the particular case of $ka=\pi$ can be obtained immediately because $c_n=0$ for all n:

$$\langle\rho_N\rangle=\alpha N. \tag{4}$$

This result corresponds to resonant passage of electrons and was first derived in Ref. 6. In Ref. 13 we found the solution of Eq. (3) for another particular case, where the incident electron energy corresponds to the center of the energy band, $ka=\pi/2$. The solution is

$$\langle\rho_N\rangle=\frac{1}{2}\left[\frac{(a+b)^N+(a-b)^N}{2}+\frac{(a+b)^N-(a-b)^N}{2b}\right], \tag{5}$$

where

$$a=2\alpha, \quad b=\sqrt{1+4\alpha^2}.$$

As the solution (5) shows, for any α and $N\to\infty$ we can write $\langle\rho_N\rangle$ in the form $\langle\rho_N\rangle\propto\exp\{Na/\xi\}$, where ξ is independent of N and is the electron localization radius.

Below we show, however, that Eq. (3) can also be solved in the general case, i.e., for any values of the incident-electron energy and the parameter α.

3. SOLVING THE FINITE DIFFERENCE EQUATION FOR $\langle\rho_N\rangle$

Let us now solve Eq. (3) in the general case. We seek the solution in the following form:

$$\langle\rho_N\rangle=\sum_{j=1}^{p} A_j x_j^N+A_0, \tag{6}$$

where the x_j, A_j, and A_0 are assumed independent of N. The quantity p, determining the number of terms in (6), will be left undefined for the time being. Substituting the solution (6) in Eq. (3) and requiring that the latter hold for all values of N, we arrive at the necessary relationships determining x_j, A_j, and A_0. These conditions are

$$\sum_{j=1}^{p} A_j x_j=\frac{1}{2}+\alpha, \tag{7}$$

$$\sum_{j=1}^{p}\frac{A_j}{1+x_j}=\frac{1-\alpha}{4}, \tag{8}$$

$$\sum_{j=1}^{p} A_j=\frac{1}{2}, \quad A_0=\frac{1}{2}. \tag{9}$$

Here the x_j are the roots of the characteristic equation

$$x^3-x^2(l+m)+x(l-m)-1=0, \tag{10}$$

where

$$l=1+2\cos(2ka), \quad m=2\alpha[1-\cos(2ka)]. \tag{11}$$

Note that Eq. (10) implies, among other things, that $p=3$ in Eqs. (7)–(9). Simultaneous solution of Eqs. (7)–(9) and Eq. (10) determines the coefficients A_j ($j=1,2,3$):

$$A_1=\frac{1}{2}\frac{(1-\alpha)(1+l)-(1+x_1)(l+m-x_1-2\alpha)}{(x_2-x_1)(x_3-x_1)}. \tag{12}$$

A_2 and A_3 can be obtained from (12) via cyclic permutation of x_1, x_2, and x_3. The quantities x_j, which are the roots of the cubic equation (10), are given by the standard formulas

$$x_1 = C + D + \frac{l+m}{3},$$
$$x_{2,3} = -\frac{C+D}{2} \pm i\sqrt{3}\,\frac{C-D}{2} + \frac{l+m}{3}. \tag{13}$$

Here

$$C = \sqrt[3]{-\frac{q}{2} + \sqrt{Q}}, \quad D = \sqrt[3]{-\frac{q}{2} - \sqrt{Q}},$$
$$Q = \frac{2l}{3}\,\frac{l^2+3m^2}{9} - \frac{1}{12}\left(\frac{l^2-m^2}{3}\right)^2 - \frac{l^2-m^2}{6} + \frac{1}{4}, \tag{14}$$
$$q = -2\left(\frac{l+m}{3}\right)^3 + \frac{l^2-m^2}{3} - 1.$$

From the general solution given by (6), (12), and (13) we can easily find the particular solution for electrons with an energy corresponding to the center of the energy band. Indeed, for $ka = \pi/2$ Eqs. (11) yield $l = -1$ and $m = 4\alpha$. Then the solutions of Eq. (10) are

$$x_1 = -1, \quad x_{2,3} = 2\alpha \pm \sqrt{1+4\alpha^2}. \tag{15}$$

Plugging (15) into (6) and (12) and noting that the coefficient A_1, corresponding to the root $x_1 = -1$, is zero, we arrive at the solution (5) found in Ref. 13.

Combining (6) and the characteristic equation (10), we obtain the following recurrence equation for $\langle \rho_N \rangle$:

$$\langle \rho_N \rangle = (l-m)\langle \rho_{N-1} \rangle - (l+m)\langle \rho_{N-2} \rangle + \langle \rho_{N-3} \rangle + m, \tag{16}$$

where the initial values $\langle \rho_1 \rangle$, $\langle \rho_2 \rangle$, and $\langle \rho_3 \rangle$ for (16) can be found from (3):

$$\langle \rho_1 \rangle = \alpha, \quad \langle \rho_2 \rangle = 2\alpha + 2\alpha^2[1 - \cos(2ka)],$$
$$\langle \rho_3 \rangle = 3\alpha + 2\alpha^2[3 - 2\cos(2ka) - \cos(4ka)]$$
$$+ 4\alpha^3[1 - \cos(2ka)]^3.$$

The recurrence equation (16) can be used for numerical calculations and for studying $\langle \rho_N \rangle$ for moderate values of N.

We note that, as solution (6) shows, the dependence of the average Landauer resistance of a chain of periodically spaced random delta-function potentials on the chain length $L = Na$ generally has the form of a sum of three exponential functions.

4. LOCALIZATION OF ONE-ELECTRON STATES

Now let us discuss the behavior of $\langle \rho_L \rangle$, the solution (6), as $L \to \infty$. We wish to demonstrate that for all reasonable values of the parameters l and m the quantity $\langle \rho_L \rangle$ increases in the limit $L \to \infty$ according to an exponential law. This means that in our model all the one-electron states are localized. The only exceptions are the edges of the energy bands ($ka = \pi m$, $m = 1,2, \ldots$), for which the $\langle \rho_L \rangle$ vs L dependence is linear.[5]

To prove the above statement we must first establish certain properties of the real roots of the characteristic equation (10). This requires writing Eq. (10) in the form

$$l = \frac{x^2+x+1}{x} - \frac{x+1}{x-1}m. \tag{17}$$

Here we allowed for the fact that $x_j \neq 0$ and excluded the solution $x_j = 1$, $j = 1, 2, 3$, which corresponds to the edges of the energy bands (see above). If we substitute any real solution x_j of Eq. (10) in (17), then in the plane specified by the coordinates l and m Eq. (17) specifies a straight line containing all the pairs l and m for which x_j is a solution of Eq. (10). This statement provides the key to establishing whether or not a fixed real x_j is a solution of Eq. (10). To this end we need only to plug x_j into Eq. (17) and see whether the straight line (17) passes through the range of possible values of the parameter l and m. If it does, x_j is a solution of Eq. (10).

As the definitions (11) of the parameters l and m imply, the ranges of their allowed values are

$$-1 \leqslant l \leqslant 3, \quad m \geqslant 0. \tag{18}$$

Examining the various straight lines in the l, m plane for a fixed x_j, we can easily see that these straight lines pass through the region specified in (18) only if

$$-1 \leqslant x_j < 0, \quad x_j \geqslant 1. \tag{19}$$

Hence the conditions (19) determine the range of values of the real roots of Eq. (10) for arbitrary values of the electron energy (or ka) and the parameter α.

As is well known, for $Q > 0$ Eq. (10) has only one real root. Then the other two roots are complex-valued and $x_2 = x_3^*$. This means that we can always write

$$x_2 = \rho e^{i\varphi}, \quad x_3 = \rho e^{-i\varphi}, \tag{20}$$

where ρ and φ are real numbers. According to Viete's theorem, we have the following relationship for the roots of Eq. (10):

$$x_1 x_2 x_3 = 1. \tag{21}$$

Plugging (20) into (21) yields

$$x_1 \rho^2 = 1. \tag{22}$$

Since by definition ρ^2 is positive, Eq. (22) implies that the only real root x_1 is positive, so that according to (19) we have

$$x_1 \geqslant 1. \tag{23}$$

Then from (22) it follows that $0 < \rho^2 \leqslant 1$. The real root x_1 in the given case ($Q > 0$) can be found from (13). Using (20) and (22), we write the solution (6) in the following form:

$$\langle \rho_N \rangle = A_1 x_1^N + 2a x_1^{-N/2} \cos(N\varphi + \psi) - \tfrac{1}{2}. \tag{24}$$

The coefficients A_2 and A_3 of the solution (6) can be written as

$$A_2 = a e^{i\psi}, \quad A_3 = a e^{-i\psi},$$

since $A_3=A_2^*$. If we let N go to infinity and allow for the condition (23), from (24) we obtain the following asymptotic expression for $\langle\rho_N\rangle$:

$$\langle\rho_N\rangle=A_1x_1^N-\tfrac{1}{2}. \tag{25}$$

Reducing this expression to the form $\langle\rho_L\rangle\propto\exp\{L/\xi\}$, we arrive at a simple formula for the localization radius ξ:

$$\xi=\frac{a}{\ln x_1}. \tag{26}$$

Let us now examine another case, where $Q\leqslant 0$. Equation (10) then has three real roots. As Eq. (21) shows, all three roots cannot be greater than unity simultaneously, since in this case their product would be greater than unity, which contradicts (21). The case where all three roots are equal to unity, $x_1=x_2=x_3=1$ $(Q=0)$, corresponds to the edge of the energy band and is a feature of this model; it has been repeatedly discussed in the literature.[8,9] The case when one of the roots is negative and the other two are positive is also impossible, since $x_1x_2x_3$ would be negative, which contradicts condition (21). Hence the only variant that does not contradict conditions (19)–(21) is the one in which $x_1\geqslant 1$ and $-1\leqslant x_{2,3}<0$. In this case one of the negative roots, say x_3, can be found from (13) by using the formula

$$x_3=C+D+\frac{l+m}{3}, \tag{27}$$

with $C=D^*$. The other two roots are also determined by (13) and can be written as

$$x_{1,2}=a\pm b, \tag{28}$$

with a and b expressed in terms of x_3 in the following manner:

$$\begin{aligned} a&=\frac{l+m-x_3}{2},\\ b&=\sqrt{\frac{3}{4}\left(\frac{l+m}{2}+x_3\right)(l+m-x_3)+m-l}. \end{aligned} \tag{29}$$

Instead of a and b we introduce other variables, ρ and x, by the formulas

$$a=\rho\,\sinh x,\quad b=\rho\,\cosh x. \tag{30}$$

Then $b^2-a^2=\rho^2=-x_3^{-1}$. Plugging (30) and (29) into the solution (6) for $\langle\rho_N\rangle$, we arrive at the following expressions:

$$\langle\rho_N\rangle=\begin{cases} \tfrac{1}{2}\{(-1)^NA_3\rho^{-2N}+\rho^N\big[K_1\sinh(xN)\\ \quad+K_2\cosh(xN)\big]-1, \quad N=2n+1,\\ \tfrac{1}{2}\{(-1)^NA_3\rho^{-2N}+\rho^N\big[K_1\cosh(xN)\\ \quad+K_2\sinh(xN)\big]-1, \quad N=2n, \end{cases} \tag{31}$$

where

$$K_{1,2}=\frac{A_1\pm A_2}{2},\quad n=1,2,\ldots.$$

As noted earlier, for the electron energy corresponding to the center of the energy band, $ka=\pi/2$, we have $A_3=0$. For this particular case we can easily see that $K_1=\rho=1$ and $K_2=1/\cosh x$ hold, and the solutions (31) become the solutions (53) and (54) of Ref. 13. If we take N to infinity, as in the case $Q>0$, the solutions (31) become the solutions (25), in which $x_1=a+b>1$. Hence in this case too the localization radius is determined by formula (26).

We have proved that the solution (6) with $L\to\infty$ always leads to an exponential dependence of the average Landauer resistance $\langle\rho_L\rangle$ on L. This means, in particular, that all the one-electron states are localized, with the localization radius given by formula (26).

5. THE LOCALIZATION RADIUS OF ONE-ELECTRON STATES

Before proceeding with the calculation of the localization radius of one-electron states we would like to mention several general properties of the solution obtained for $\langle\rho_N\rangle$.

As noted earlier, the average Landauer resistance $\langle\rho_N\rangle$, expressed by (24) and (31), in the asymptotic case $N\to\infty$ is a power function of N, i.e., $\langle\rho_N\rangle\propto x_1^N$, with $x_1>1$, and is independent of N. The nature of the transition to such a dependence is determined by the values of the roots x_2 and x_3 of the characteristic equation (10). The farther the electron energy is from the edges of the energy bands, the closer the absolute values of x_2 and x_3 are to zero, and hence the more rapidly the solutions (24) and (31) acquire the form (25) as N grows. The dependence of $\langle\rho_L\rangle$ on L is oscillatory for any electron energy, but such behavior becomes less and less evident as L increases. The average Landauer resistance $\langle\rho_L\rangle$ depends on the incident-electron energy in a similar way, provided that L and w are fixed.

We calculated the dependence of ξ on ka and w numerically, with the results depicted in Fig. 1. Clearly, at a fixed w the value of the localization radius increases as a function of the electron energy within the first energy band $(0\leqslant ka\leqslant\pi)$, tending to infinity as $ka\to\pi$. Note that the localization radius has a minimum when the electron energy varies within the second band $(\pi\leqslant ka\leqslant 2\pi)$, and the value of this minimum tends to the center of the energy band as w increases. The diagram in Fig. 1 clearly demonstrates a natural physical result: at fixed electron energies the localization radius monotonically decreases as the chain disorder parameter w increases. Figure 1 also depicts the curves of equal values of the localization radius of electronic states. The universal result obtained here is that the electron energy must grow with w for the localization radius to remain unchanged.

In conclusion we note that in the cases of weak and strong electron scattering, simple analytic expressions can be obtained for the dependence of the localization radius on the electron energy and the chain disorder parameter w.

Let us start with weak electron scattering, i.e., $\alpha\ll 1$. In this limit the root of Eq. (10) determining the localization radius can be found in the form

$$x_1=1+\Delta x, \tag{32}$$

where $0<\Delta x\ll 1$. Plugging (32) into (10) and keeping only terms linear in α, we arrive at the following expression for Δx:

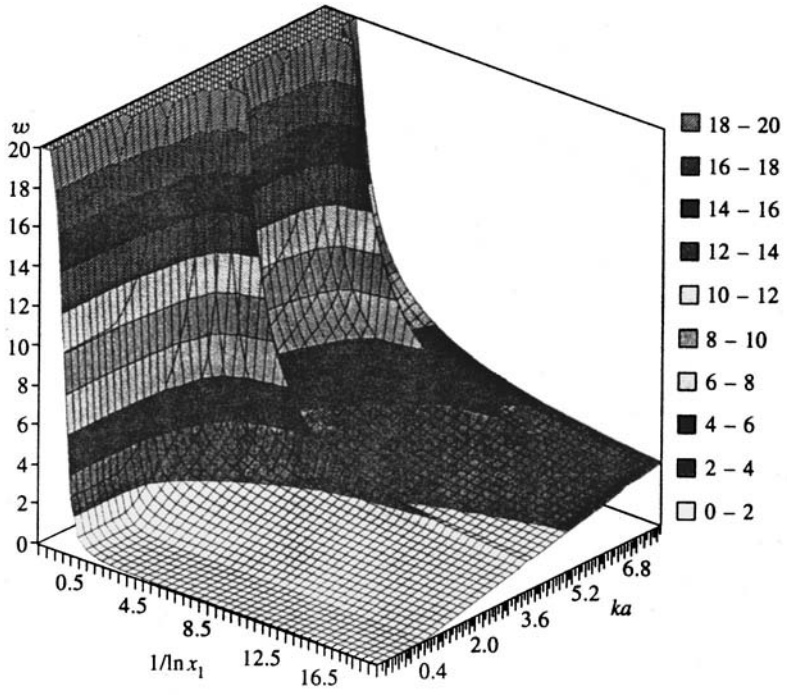

FIG. 1. Dependence of the electron localization radius $\xi/a = 1/\ln x_1$ on ka and w.

$$\Delta x = \frac{3m}{3-l} = 2\alpha. \tag{33}$$

Plugging (32) and (33) into (26) and taking $\ln(1+2\alpha) \approx 2\alpha$, we finally obtain

$$\xi = 96\left(\frac{k}{w}\right)^2 a. \tag{34}$$

Here the value of ξ exceeds by a factor of two the value obtained by Perel' and Polyakov.[9] The reason is that in Ref. 9 the localization radius was determined from the value of $\langle \ln \rho \rangle$, which for $\alpha \ll 1$ is two times the value of $\ln\langle\rho\rangle$.

In the limit of strong electron scattering, i.e., $\alpha \gg 1$, and with the additional requirement that

$$\alpha \sin^2(ka) \gg 1, \tag{35}$$

we arrive at the following simple expression for the electron localization radius:

$$\xi = \frac{a}{\ln[4\alpha \sin^2(ka)]}. \tag{36}$$

The same result was obtained in Ref. 13 for $\alpha \gg 1$. We see that to derive formula (36) we need a stronger requirement than $\alpha \gg 1$, namely, condition (35) must be met.

One of the authors (D. M. S.) is grateful to the Department of Theoretical Physics of the P. N. Lebedev Physics Institute of the Russian Academy of Sciences for hospitality shown at the final stage in preparing this paper. The results listed in the paper have been obtained thanks in part to the financial support of the International Science Foundation (Grant No. MVL000).

[1] R. Landauer, Philos. Mag. **21**, 863 (1970).
[2] P. W. Anderson, D. J. Thouless, E. Abraham, and D. S. Fisher, Phys. Rev. B **22**, 3519 (1980).
[3] A. A. Abrikosov, Solid State Commun. **37**, 997 (1981).
[4] N. Kumer, Phys. Rev. B **31**, 5513 (1985).
[5] I. M. Lifshits, S. A. Gredeskul, and L. A. Pastur, *Introduction to the Theory of Disordered Systems*, Wiley, New York (1985).
[6] M. Ya. Azbel, Phys. Rev. B **43**, 6847 (1991).
[7] V. M. Gasparian, B. L. Altshuler, A. G. Aronov, and Z. A. Kasamanian, Phys. Lett. A **132**, 201 (1988).
[8] A. G. Aronov, V. M. Gasparian, and Ute Commuch, J. Phys.: Condens. Matter **3**, 3023 (1991).
[9] V. I. Perel' and D. G. Polyakov, Zh. Éksp. Teor. Fiz. **86**, 352 (1984) [Sov. Phys. JETP **59**, 204 (1984)].
[10] G. M. Soukoulis, I. V. Jose, E. N. Economou, and Ping Shing, Phys. Lett. **50**, 764 (1983).
[11] E. Cota, I. V. Jose, and M. Ya. Azbel, Phys. Rev. B **32**, 6157 (1985).
[12] V. M. Gasparian and Ash. G. Khachatrian, Solid State Commun. **12**, 1061 (1993).
[13] D. M. Sedrakyan, D. A. Badalyan, V. M. Gasparyan, and A. Zh. Khachatryan, Zh. Éksp. Teor. Fiz. **109**, 243 (1996) [JETP **82**, 129 (1996)].

Translated by Eugene Yankovsky

High-temperature transition of uranium dioxide to the super-ion state

L. V. Matveev and M. S. Veshchunov

Institute for Problems of the Safe Development of Atomic Energy, Russian Academy of Sciences, 113191 Moscow, Russia

(Submitted 7 March 1996)
Zh. Éksp. Teor. Fiz. **111**, 585–599 (February 1997)

A microscopic model of the high-temperature ($T \approx 2670$ K) phase transition of uranium dioxide to the super-ion state is developed. It is shown that accounting for the interaction of the point defect subsystem with the electron subsystem in the mean-field approximation (where this interaction leads to significant additional screening of the charge of some of the defects) and then calculating the configurational entropy of the point defects with allowance for the actual symmetry of the UO_2 crystalline lattice affords satisfactory agreement with the available experimental data on the degree of disorder of the anion sublattice and the behavior of the specific heat of uranium dioxide in the given temperature range. [S1063-7761(97)01402-9]

1. INTRODUCTION

The last ten years have seen active experimental and theoretical studies of the high-temperature behavior of uranium dioxide. This question is interesting both from a practical point of view—the behavior of nuclear fuel during an accidental temperature increase—and for purely theoretical reasons. In particular, the question of a microscopic description of the anomaly of the thermodynamic properties of uranium dioxide in the vicinity of $0.8T_m$ still remains open. The significant peak in the specific heat and the abrupt growth of disorder of the anion sublattice over a temperature interval on the order of 100 degrees about the given peak have acquired the name ''Bredig transition'' in the literature are usually compared with the transition to the super-ion conducting state observed in crystals of fluorite type over approximately the same temperature range (near $0.8T_m$).

In earlier work (e.g., Ref. 1) the growth of the specific heat was linked with the behavior of the electron subsystem of the crystal and was considered to be a result of electronic excitation, on the basis of the fact that uranium dioxide is a semiconductor with a wide band gap on the order of 2 eV. Later the given anomaly was linked mainly with disordering of the anion subsystem by studying the interaction of the defects within the framework of the lattice gas model. Thus, one of the most interesting and important studies in this regard is that of Tam, Fink, and Leibowitz,[2] which takes account of the fact that UO_2 is an ionic crystal and, consequently, the nascent defects are charged. In this case the interaction energy of the defects is determined by the long-range Coulomb interaction so that an important contribution to the free energy comes from charge screening by the Debye–Hückel mechanism. When a critical defect concentration is reached with rising temperature, the Debye–Hückel interaction strongly lowers the initial energy of Frenkel pair formation, and as a result can lead to a spontaneous rise in defect generation. Such a mechanism of the transition to the super-ion conducting state was first proposed for crystals of fluorite type by March *et al.*[3]

A more detailed treatment of this mechanism should allow for the fact that the Coulomb repulsion between homotypic defects is not screened at interatomic distances and is very large, so that in the calculation of the number of states in the configurational entropy it is necessary to take account of ''blocking'' of neighboring sites occupied by homotypic defects. Taking account of these factors in Ref. 2 leads to abrupt growth of the equilibrium defect concentration when a sufficiently high temperature is reached.

Despite the fact that the given model is able to provide a qualitative explanation of the mechanism of the phase transition, the quantitative description does not accord with the available experimental data. Thus, the defect concentration calculated by Tam *et al.*,[2] which determines the onset of the transition to the super-ion state $n \approx 3 \times 10^{-3}$, turns out to be substantially lower than the value $n \approx 0.1$ measured by Hutching[4] by neutron scattering.

For a more accurate quantitative description of the super-ion transition in crystals with fluorite structure a number of microscopic models of lattice-gas type have been proposed, as have models which treat the problem in the mean-field approximation. These models describe the Frenkel defect distribution over the two sublattices with allowance for their long-range action and differ among themselves by the introduction of various terms (with varying degree of justification), describing the entropy contribution of the defects to the free energy functional. For the right choice of terms it is possible to explain the specific heat anomaly that arises; however, such a procedure often has an artificial character.

Thus, Hiernaut *et al.*[5] added a term to the free energy functional that is connected with the vibrational entropy of the defect sites, which is proportional to $\ln(\omega_i/\omega_0)$, where ω_i and ω_0 are the vibration frequencies of the oxygen atom at an interstitial position and at a lattice site, respectively. However, the ratio of these two frequencies, while providing good agreement between the results of analysis (Ref. 5) and the experimental data on the behavior of the equilibrium defect concentration in the vicinity of the transition, turns out to be unjustifiably high: $\omega_i/\omega_0 \approx 10^2$ (cf. Ref. 6). To account for the above-mentioned blocking of neighboring sites by charged defects, Oberschmidt[7] expressed the number of pos-

sible positions in the sublattices for the defects by a function of the defect concentration including fitting parameters, and so on.

This being the case, a more general (phenomenological) treatment of the problem would seem apt, one that would allow one to correctly describe the symmetry and form of the free energy functional in the vicinity of the transition. Two papers by one of the authors of the present paper[8,9] are dedicated to constructing such a model within the framework of the Landau theory of phase transitions that enables one to determine from general symmetry arguments the nature of the observed transformation and classify its order (and form), thereby narrowing down the possible choice of microscopic models. These papers showed that the given transition can be considered to result from disordering of oxygen atoms over the two sublattices: the anion sublattice, in which the O atoms initially find themselves, and the cation sublattice, whose sites are located at the centers of the cubes of the anion sublattice in such a way that half of these sites are occupied by uranium atoms. As follows from the experimental data, the position of the cations is essentially fixed all the way to the melting temperature, so that disordering of the anions over the two sublattice takes place in the ''external'' crystal field of the fixed cations. The concrete form of the free energy functional obtained in Ref. 8 is connected with a peculiarity of the spatial group (O_h^5) of crystals with fluorite structure that ensures preservation of the spatial symmetry even for complete disordering of the anions over the two sublattices. As a result, the given functional describes a transition which can be characterized as a second-order phase transition in an external field and, consequently, is accompanied by the appearance of a ''smeared'' anomaly in the specific heat over some finite temperature range.

The results of this analysis impose rigorous constraints on the form of the entropy term in the construction of the microscopic model, and require a more detailed and consistent description of the configurational distribution of the atoms and defects over the sites of the crystalline lattice (in particular, a more exact treatment, to the extent this is possible in the mean-field approximation, of ''blocking'' of nearby sites with the real symmetry of the fluorite crystalline lattice taken into account).

Thus, the problem posed in the present paper consists of two parts: 1) a calculation of the configurational entropy of the distribution of defects over crystalline lattice sites in fluorites with a correct account of blocking of neighboring sites reflecting the real (special) symmetry of the crystal, and 2) a consistent description of the interaction of charged defects within the framework of the Debye–Hückel mechanism, which probably requires an account of their interaction with the electron subsystem of the semiconductor crystal UO_2.

The sense of the first problem has already been spelled out in sufficient detail. In addition it may be mentioned that the problem of ''blocking'' of nearest sites was first considered by Pauling[10] in the mean-field approximation, who explained the nonzero value of the residual entropy of ice as $T\to 0$ by the degree of disorder of the protons on the double-minimum H-bonds. Later, within the framework of this approach, in order to account for strong correlations in the nearest-neighbor interaction (including ''blocking'') more accurate cluster methods were developed,[10,11] whose applicability, however, was limited to short-range potentials and which in the case under consideration are not directly applicable.

In regard to the second problem some additional explanations are necessary. The point is that although the very idea[3] of spontaneous formation of charged defects when a certain concentration is reached (with increasing temperature) at which mutual screening of charges self-consistently lowers the effective formation energy of these defects is undoubtedly valid, actual calculations within the framework of the Tam–Fink–Leibowitz model[2] lead to a value of the spontaneous defect disordering concentration that substantially exceeds the value measured in experiment. Analysis of the Tam–Fink–Leibowitz model shows that the main reason for such high values of the spontaneous defect disordering concentration has to do with the large charge of the defects ($Z=\pm 2$ respectively for the positively charged oxygen vacancies and the negatively charged oxygen interstitials). However, a more detailed treatment of the charge state of the vacancy defects shows that as a result of the interaction of the crystal defects with the electron subsystem of the semiconducting UO_2 crystal, the charge of these defects can vary considerably with increasing temperature. Indeed, according to the microscopic calculations based on the shell model[12] the vacancies of the oxygen sublattice are F-centers, so their electron level ε_a lies in the band gap (≈ 2 eV) near the position of the chemical potential for a defect-free crystal (i.e., approximately in the center of the gap). With increasing defect concentration they begin to influence the position of the chemical potential in the crystal, which in turn can lead to a self-consistent change in the degree of excitation of the electron subsystem and the occupancy of the ε_a level. Since the ''correlation'' energy determined by the Coulomb interaction heavily depends on the charges Z forming the defect ''plasma''

$$E_{\rm corr}\propto\left(\sum_\alpha Z_\alpha^2 N_\alpha\right)^{3/2},$$

allowance for defect ''recharging,'' which is related to changes in the occupancy of the defect levels ε_a, significantly affects the behavior of the system and, as will be shown below, ultimately leads to a substantial rise in the critical defect concentration at which the phase transition takes place.

A self-consistent solution of the two parts of the stated problem would consist of a correct description of the Coulomb interaction of the charged defects (allowing for charge exchange with the electron subsystem of the semiconductor crystal UO_2) and the defect configurational entropy (allowing for blocking by the charged defects of the nearest sites of the specific (fluorite) crystalline lattice, i.e., reflecting the special symmetry of the system). Such a solution would enable us to develop a microscopic model on the basis of which it is possible to obtain a valid quantitative description of the structural transition in the UO_2 crystal in the region of $T_{\rm crit}$ (essentially without resorting to fitting parameters).

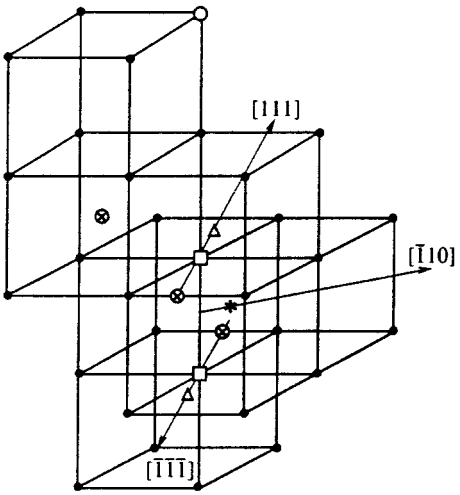

FIG. 1. Clusters (3:1:2) of defects, formed by the disordering of the anion lattice of UO_2 at high temperature. ●—oxygen atoms, ⊗—uranium atoms. Frenkel pair: ∗—interstitial, ○—vacancy. Relaxing atoms: △—interstitial, □—vacancy. The interstitial ∗ is displaced relative to the center of the edge connecting two vacancies □ in the direction [1,1,0].

2. DESCRIPTION OF MODEL

To describe the behavior of the point defect system in a UO_2 crystal, we write the free energy in the lattice-gas approximation in the standard form[13]

$$F = wN + F_{DH} - kTS. \tag{1}$$

The first term on the right-hand side of Eq. (1) is the energy of Frenkel pair formation ($N_i = N_v + N$). Here, on the basis of microscopic calculations of the formation of nascent complexes of defects,[4] we will assume that at high temperatures the defects are short-lived clusters (3:1:2) consisting of a Frenkel pair and two relaxing atoms at sites of the anion sublattice neighboring the interstitial (see Fig. 1). The relaxing atoms are displaced toward the center of the uranium-free cube of the anion sublattice by a distance of 0.25 to 0.5 times the length of the diagonal. The vacancies formed by the relaxation of the vacancy atoms also contribution to the total number of defects as measured by neutron scattering.[4] On the other hand, the displacement of the relaxing atoms is rigidly fixed both relative to the anion lattice sites and to the position of the initial interstitial (see Fig. 1). Therefore, they do not make an additional contribution beyond the contribution of the interstitials forming the ''current'' Frenkel pair to either the correlation energy (F_{DH}) or the configurational entropy. Proceeding from what has been said, we denote by N the number of ''current'' Frenkel pairs or, in other words, the number of clusters, which, as follows from the (3:1:2) cluster model, is three times smaller than the total number of interstitials (vacancies) measured in experiment.

According to the measurements reported in Ref. 14 of the degree of disorder of the anion sublattice at temperatures of the order of 2000 K, the formation energy of an oxygen Frenkel pair is equal to 3.67 eV. The measurements were carried out in a temperature interval lying quite far from the transition region (a few hundred degrees below T_{crit}) and, consequently, the defect concentration was small ($n \ll 0.01$). In this case, in the calculation of the equilibrium defect concentration n according to formula (1) the contribution F_{DH}, conditioned by the correlation interaction, can be neglected, yielding the standard temperature dependence of the equilibrium defect concentration, valid for small concentrations, $n \propto \exp(-w/kT)$, where w is the defect formation energy. Therefore, in the following calculations we may use the value 3.67 eV for w, measured in Ref. 14.

The point defect subsystem is a lattice gas of charged particles electrostatically interacting with each other. Consequently, for the interaction energy in the mean-field approximation we may use the formula describing the correlation interaction in a solid-state plasma (see Refs. 13 and 15):

$$F_{DH} = -\frac{2\sqrt{\pi}e^3}{3\varepsilon^{3/2}\sqrt{kTV}}\left(\sum_{\alpha} N_\alpha Z_\alpha^2\right)^{3/2}, \tag{2}$$

where e is the charge of the electron, T is the temperature, k is the Boltzmann constant, V is the volume, ε is the permittivity, N_α is the number of particles of type α, and Z_α is their charge. In the simplest case the index $\alpha = 1, 2$ corresponds respectively the positively charged vacancies and negatively charged interstitials. In the case under consideration, as will be shown below, the partially electron-screened vacancies and the holes formed as a result of excitation of the electron subsystem will also contribute to expression (2). In the given model we do not take account of formation of uranium vacancies by the Schottky mechanism in light of their high formation energy ($7-10$ eV).

The calculations carried out in Ref. 12 show that the vacancies and interstitials forming the Frenkel pairs in the anion sublattice at low temperatures possess effective charge $Z = \pm 2$. The same values were adopted in Ref. 2, which led, however, to too high a correlation energy (see the Introduction). Reference 12 also calculates the electron spectrum of UO_2, from which it follows that UO_2 is a semiconductor with a wide band gap ≈ 2 eV, which has been confirmed many times over in experiment (e.g., Ref. 16). Here the nascent oxygen vacancies are F-centers, and are capable of attaching themselves to an electron at the free electron level of the F-center located approximately in the middle of the band gap, i.e., near the position of the chemical potential for the defect-free crystal. The upper filled level of the interstitial O_i^{2-} lies below the valence band and therefore hardly participates in the excitation of the electron subsystem.

The presence of an vacancy electron level in the band gap can lead to important consequences in the behavior of the system of interacting defects and electrons which have been considered in numerous works in the literature. By way of an example we may mention the phenomenon of self-compensation in doped semiconductors, which consists in the following.[17] To increase the number of charge carriers (e.g., electrons in the conduction band), the semiconductor is doped with a high-valence impurity. However, in a number of cases, formation of vacancies containing the electron level (F-center) with trapping of the ''impurity'' electrons at this level turns out to be statistically more favorable for such a system than the transition of the ''impurity'' electron to the conduction band. As a result of such a process, the number

of carriers in the conduction band does not increase and, accordingly, conduction does not grow. Similarly, in the case under consideration, the presence of a vacancy electron level near the middle of the band gap can lead to strong screening of these vacancies by the electrons appearing as a result of thermal excitation and, consequently, to a lowering of the effective charge of some of the point defects (anion vacancies). In this case, allowing for the interaction of the electron and vacancy subsystems can lead to a substantial amplification of the excitation of the electron subsystem.

For nonzero temperature T, the distribution of the electrons over the energy levels ε_i obeys Fermi–Dirac statistics:

$$f(\varepsilon_i)=\left(1+\exp\left(\frac{\varepsilon_i-\mu}{kT}\right)\right)^{-1}. \tag{3}$$

The position of the chemical potential μ is determined self-consistently by the electrical neutrality of the system,

$$n_e+n_a=n_h, \tag{4}$$

where n_e is the electron concentration in the conduction band, n_a is the electron concentration at the F-center level, and n_h is the hole concentration in the valence band. Here $n_a=nf(\varepsilon_a)$, where n is the anion vacancy concentration. It is not hard to show that in the case under consideration

$$\left|\frac{\mu}{kT}\right|\gg 1, \quad \left|\frac{\varepsilon_g-\mu}{kT}\right|\gg 1$$

($\mu\approx 1$ eV, $\varepsilon_g\approx 2$ eV, $kT\approx 0.25$ eV) so that to describe the electron population of the conduction band and the hole population of the valence band we can use the standard formulas for a non-degenerate semiconductor:[18]

$$n_e=\frac{2}{m}\left(\frac{m_e kT}{2\pi\hbar}\right)^{3/2}\exp\left(\frac{\mu-\varepsilon_g}{kT}\right),$$

$$n_h=\frac{2}{m}\left(\frac{m_h kT}{2\pi\hbar}\right)^{3/2}\exp\left(-\frac{\mu}{kT}\right), \tag{5}$$

where m_e and m_h are the effective masses of the electrons and the holes, m is the concentration of the anion sublattice sites, and ε_g is the width of the band gap.

It is clear from Eq. (5) that the degree of excitation of the electron subsystem and the degree of screening of the vacancies are determined by the position of the chemical potential. At low temperatures, when the defect concentration is not large ($n\approx\exp(-w/kT)$, where $w\approx 4$ eV), the solution of system (3)–(5) yields an estimate for the chemical potential $\mu\approx\varepsilon_g/2$, whereupon

$$n_a\ll n_e\approx n_h\approx\exp\left(-\frac{\varepsilon_g}{2kT}\right). \tag{6}$$

With rising temperature and increasing defect concentration, the contribution n_a to the balance (4) grows, and in the region of $T_{\text{crit}}\approx 2670$ K it is decisive, so that the chemical potential is of order $\mu\approx\varepsilon_a/2$, and instead of relation (6) we have

$$n_e\ll n_a\approx n_h\approx\exp\left(-\frac{\varepsilon_a}{2kT}\right). \tag{7}$$

Hence, neglecting n_e in Eq. (4), we easily obtain an expression linking n and n_h:

$$n_h=2n\left\{1+\left(1+\frac{n\,\exp(\varepsilon_a/kT)}{2(kT)^{3/2}}\right)^{-1/2}\right\}^{-1}. \tag{8}$$

In calculations with (5) we take $m_h\approx 10m_0$, where m_0 is the mass of the free electron, and $m\approx 2.24\times 10^{22}$ cm^{-3}, where m is the density of the cation sublattice sites.[2] Substituting the values $n\approx 0.07$ and $kT\approx 0.3$ eV into Eq. (8), these values being characteristic of the region of the phase transition, we easily obtain the estimate $n_h\approx n$, which is self-consistent with Eq. (7).

Thus, in the temperature range of the phase transition, the lattice gas of charged particles forms the following defects: oxygen interstitials with charge $Z_i=-2$ and concentration $n_i=n$; fully ionized oxygen vacancies $Z_v=+2$, $n_v=(1-f)n$; oxygen vacancies with filled electron level $Z_a=+1$, $n_a=nf$; holes with $Z_h=+1$ and concentration n_h. Finally, the sum in expression (2) takes the form

$$\sum_\alpha N_\alpha Z_\alpha^2=(8n-2n_h)M, \tag{9}$$

where M is the number of anion sublattice sites. As can be seen from Eq. (9), as a result of screening of vacancies by electrons the variation of the total charge in the expression for the correlation energy is governed by the term $-2n_h$, which is comparable in order of magnitude with the first term $8n$. This latter fact is a consequence of the back effect of the vacancy subsystem on the behavior of the electron subsystem leading to the relation $n_h\approx n$.

Thus, taking account of the interaction of the electron subsystem and the point defect subsystem leads to a substantial decrease in the correlation energy of the interaction of the charged defects (in comparison with the calculated results of Ref. 2).

Note that the opinion exists (see, e.g., Ref. 19) that the holes in the valence band can be localized and form small polarons U^{5+}. In this case, expression (7) takes the form

$$n_h=\frac{2n}{1+(1+8n\,\exp(\varepsilon_a/kT))^{1/2}}. \tag{10}$$

Below we will also consider this case.

To calculate the entropy contribution to the free energy functional (1) it is necessary to allow for the fact that the Coulomb interaction of the charged defects, which is screened at large distances, leads to a strong repulsion of the charged defects with like sign at close distances (of the order of interatomic). Therefore, following Ref. 2, we will assume in the calculation of the number of states that the addition of one oxygen vacancy leads to a decrease in the number of remaining free sites over which to distribute subsequent vacancies by a factor of seven (one site is occupied by the defect itself and it blocks its six nearest neighbors). When the defect concentration is high enough, vacancies located near each other can block the same sites, which leads to a decrease in the effective number of sites blocked by one vacancy in comparison with the case of a tenuous vacancy gas (in which their concentration tends to zero). The Appen-

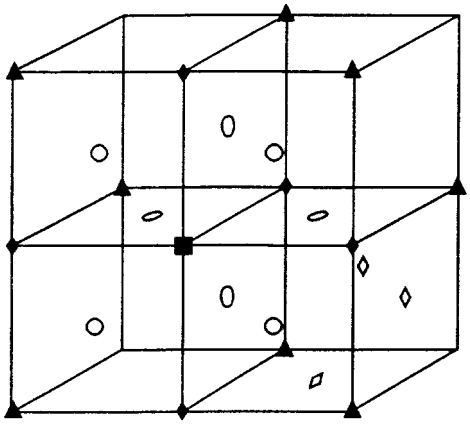

FIG. 2. Arrangement of different types of sites around a test defect in the sublattice formed by the interstitials. ■—test defect (*0*), ○—blocked sites (*1*), ◆, ▲, ◇—sites (*2*), (*3*), and (*4*), capable of blocking sites (*1*).

dix considers the possible configurations of interacting defects in a crystalline lattice with fluorite structure and on this basis calculates the contribution to the configurational entropy due to the vacancies (Eq. (A1)).

Let us consider the contribution to the entropy from the distribution of the interstitials O_i^{2-} To start with, we assume that the O_i^{2-} ions can be located at identical positions inside the uranium-free cubes of the oxygen sublattice (e.g., at their centers, from among the possible O_i^{2-} sites inside the cube), where these positions form a face-centered cubic (*fcc*) lattice with edge length equal to twice the interatomic distance of the oxygen sublattice. A test defect located at a site of such a lattice (see Fig. 2) blocks 12 nearest neighbors–the sites (1). To find the mean number of sites blocked by the test defect, it is necessary, as in the previous case (see the Appendix), to consider the possible configurations of the interstitials at sites (2), (3), and (4) and calculate their probabilities. However, in the given case the problem is complicated by the fact that the arrangement of particles at sites (2), (3), and (4) is not independent. Therefore, to calculate the number of states, we will use the following approach. Consider the case in which the concentration of interstitials is so high that they occupy all possible sites, provided their nearest neighbors are free as a result of blocking. In this case, the defects will completely occupy sites of one of the four simple cubic sublattices into which the initial *fcc* lattice is subdivided. We take this configuration as the new ground state (quadruply degenerate). The number of sites of the new sublattice K equals $M/8$, where M is the number of sites of the anion sublattice. If the number of interstitials N is less than K, then $K-N$ unoccupied sites is formed in the sublattice, and as a result the number of states corresponding to the given number of interstitials is

$$C_K^{K-N}=C_K^N.$$

As follows from the calculations in Ref. 4, in reality an O_i^{2-} interstitial is located not at the center of a cube of the anion sublattice, but near one of its edges (see Fig. 1). Consequently, each interstitial has 12 different positions inside the cube. Moreover, the relaxing atoms of the (3:1:2) clusters can shift in two different directions, so that the total number of states of a cluster associated with the given sublattice site is 24. Finally, the total number of states corresponding to the configurational entropy of the interstitial subsystem is

$$\Gamma=24^N C_K^N.$$

The contribution to the configurational entropy from the interstitial distribution correspondingly takes the form

$$S=n\ \ln 24-n\ \ln n-(0.125-n)\ln(0.125-n). \tag{11}$$

Reference 6 calculates the entropy of formation of a Frenkel pair due to the change in the phonon spectrum from the formula

$$\Delta S=-k\ \ln\left(\prod_i^{3N}\ \omega_i'/\prod_i^{3N}\ \omega_i\right), \tag{12}$$

which is valid at high temperatures (above the Debye temperature). Here ω_i is the spectrum of the ideal crystal, ω_i' is the spectrum of the crystal with a defect. The value obtained as a result of these calculations, $\Delta S\approx 4k$, is the contribution of the nonconfigurational entropy to the general expression (1).

Substituting the expression for the correlation energy (2) in Eq. (1) taking Eq. (9) into account and also Eqs. (A1), (11), and (12), which define the various contributions to the entropy, and using the values of the numerical parameters entering here and indicated above, we finally obtain the following expression for the free energy functional:

$$F=3.67n-\frac{0.09(8n-2n_h)^{3/2}}{\sqrt{kT}}+kT(2n\ \ln n$$
$$+(0.125-n)\ln(0.125-n)-S_v(n)-7.1n), \tag{13}$$

(the free energy per site of the anion sublattice), where the free energy and the quantity kT are expressed in units of electron volts, and the hole concentration is given by Eq. (8) or (10).

Also note (see, e.g., Ref. 14) that the term in the formula for the free energy proportional to nkT is usually dictated by the contribution of the non-configurational entropy, e.g., the change in the phonon spectrum associated with the appearance of defects. It follows in our model, then, that part of the configurational entropy defined by Eq. (11) also contributes to the free energy proportional to nkT. In summary, the coefficient of nkT is equal approximately to 7, which accords with the results of experiments[16] in which the given quantity was estimated from specific heat measurements in the temperature range from 300 to 1500 K.

3. RESULTS AND DISCUSSION

To describe the high-temperature behavior of uranium dioxide, specifically, that is, to find the degree of disorder of the anion sublattice and describe the temperature dependence of the specific heat, it is necessary to examine the derived system of equations (8) and (13). The equilibrium concentration of the vacancies in the oxygen sublattice is found by minimizing the free energy function (13) under the condition that the hole concentration is given by Eq. (8). In light of the

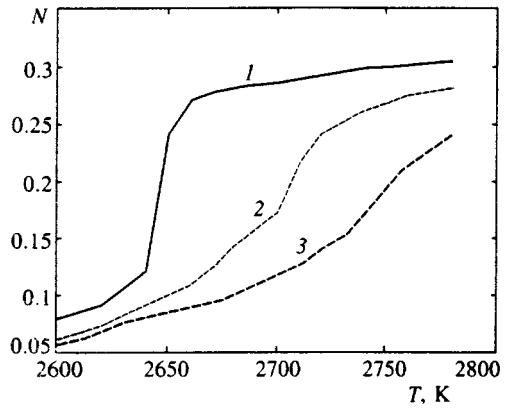

FIG. 3. Temperature dependence of the equilibrium defect concentration for various values of ε_a: *1*—$\varepsilon_a = 1.05$ eV, *2*—$\varepsilon_a = 0.97$ eV, and *3*—$\varepsilon_a = 0.9$ eV.

fact that at present the position of the electron level of the F-center ($\varepsilon_a \approx 1$ eV) is a calculated quantity and not an experimentally measured one, the temperature dependence of the defect concentration can be constructed by varying ε_a in some neighborhood of its indicated value 1 eV. The dependences so obtained are plotted in Fig. 3 for three values of ε_a. Here the experimentally measured quantity $N(T)$ is the total vacancy concentration, formed both by the vacancies corresponding to the current Frenkel pairs and by vacancies resulting from a shift of the relaxing atoms in the (3:1:2) cluster. In line with this, the quantity plotted in the graph is $N(T) = 3n(T)$, where $n(T)$ corresponds to the minimum of F at the given temperature.

Best agreement of the calculated curve $N(T)$ and the experimentally measured quantity in the vicinity of T_{crit} is obtained for $\varepsilon_a \approx 0.97$ eV. With increasing ε_a the transition region (i.e., the temperature range over which a substantial change in the equilibrium concentration takes place and abrupt growth of the specific heat is observed) shifts toward lower temperatures and lower concentrations. Physically, this means that an increase in ε_a corresponds to a decrease in the degree of excitation of the electron subsystem at a given temperature and, consequently, in the degree of screening of the vacancies by the electrons, so that the value of the correlation energy at the given concentrations grows. At higher values of ε_a ($\geqslant 1.05$ eV) the hole concentration becomes negligible in comparison with the vacancy concentration, $n_h \ll n$, and excitation of the electron subsystem ceases to influence the behavior of the point defect subsystem. This case in fact corresponds to the model of Ref. 2, in which the electron subsystem was generally ignored. Moreover, at high values of ε_a, growth of the equilibrium concentration of the vacancies with increasing temperature becomes very abrupt, so that for $\varepsilon_a \geqslant 1.05$ eV the equilibrium concentration in the vicinity of the transition does not vary continuously but by a jump, which contradicts the results of the general phenomenological treatment of this transition[8] and experimental observations.[4]

In light of the above analysis, a few critical remarks are appropriate regarding the expressions for the configurational entropy used in some other models. The account of blocking of nearest sites in Ref. 2 led to the result that the term in the free energy due to the configurational entropy has approximately the form

$$S_{\text{conf}} \approx -2n\ \ln(n) + (0.5 - 13n)\ln(0.5 - 13n) + (1 - 7n)\ln(1 - 7n), \tag{14}$$

where the numbers 13 and 7 control the decrease in the number of vacant sites upon the addition of one defect for the interstitial and vacancy subsystems, respectively. The number of defects to be distributed over the possible sites cannot exceed the total number of sites, as the arguments of the logarithms in Eq. (14) must be positive. Hence it follows at once that in the given model the defect concentration n cannot exceed $1/(2 \cdot 13) \approx 0.04$. Consequently, the region of the phase transition characterized by concentration values $n \approx 0.1$ according to the measurements of Ref. 4 in general within the frame cannot be described by the given model.

An effort to account for the fact that different defects can block the same sites (so that the effective number of blocked sites decreases with growth of the concentration) was made in Ref. 5, and led to an expression for the configurational entropy, $\ln(C_N^{\alpha M} C_N^{2\beta M})$, where α and β themselves depend on N, and, in particular, $\alpha = (1 + 18N/M)^{-1}$. Analogous arguments give for the maximum possible defect concentrations $n = N/M$ values on the order of 0.11, which are inconsistent with the concentration values $n \approx 0.2$ obtained in Ref. 5 from numerical calculations for temperatures above the transition temperature.

The temperature dependence of the equilibrium vacancy concentration can also be constructed for the case in which the hole concentration is given by Eq. (10), i.e., assuming that the holes are localized on the uranium atoms. In this case good quantitative agreement of the dependence $N(T)$ with the experimentally measured values[4] was achieved for smaller values of $\varepsilon_a \approx 0.88$ eV, which is also not in bad agreement with the calculated value $\varepsilon_a \approx 1$ eV.

It should be pointed out that the value of the nonconfigurational entropy (which in our model defines the coefficient of nkT in the expression for the free energy) is also an approximate quantity. Therefore we also studied the behavior of $N(T)$ for weak variation of ε_a within the limits $\pm 5\%$. Variations in the behavior of the concentration obtained in this way proved to be negligible.

The specific heat was calculated in accordance with the thermodynamic formula $C = -T\partial^2 F/\partial T^2$, where in the calculation of the temperature derivative in the expression for the free energy functional (13) we substituted the equilibrium concentration $n(T)$. Within the accuracy of the calculations, this did not result in any difference between the values of C_V and C_P. Comparison of the calculated results with the experimental data[4] shows that the proposed model provides a good description of the behavior of the specific heat and together with the transition temperature satisfactorily reproduces the height of the specific heat peak ($\delta C_{\max} \approx 100$ J/mole·K) and the width of the temperature interval of smearing ($\delta T \approx 80$ K) of the peak (see Fig. 4).

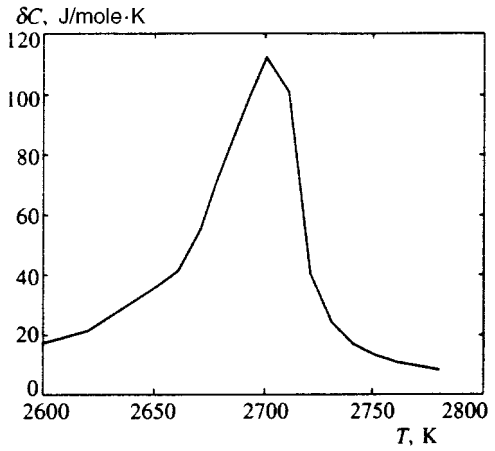

FIG. 4. Temperature dependence of the excess specific heat δC for $\varepsilon_a = 0.97$ eV.

4. CONCLUSIONS

In the present paper we have proposed a model which makes it possible, on the basis of the available calculated and experimental data, to achieve a satisfactory quantitative description of the disordering of the oxygen subsystem and the anomalous behavior of the specific heat of uranium dioxide in the region of its high-temperature phase transition. As a point of departure we chose the model proposed in Ref. 2, which takes account of the fact that UO_2 is an ionic crystal and, consequently, the nascent defects possess charge. When some critical defect concentration is reached with increasing temperature, screening of the charges of the nascent defects via the Debye–Hückel mechanism strongly lowers the energy of Frenkel pair formation, which can lead to an abrupt growth of their equilibrium concentration. Here the Coulomb repulsion between homotypic defects at interatomic distances is not screened and is very large, so that in the calculation of the number of states in the configurational entropy it is necessary to allow for blocking of neighboring sites occupied by homotypic defects. Allowance for these factors in Ref. 2 permits a qualitative explanation of the mechanism of the phase transition; however, the defect concentration defining the onset of the transition to the super-ion state $n \approx 3 \times 10^{-3}$ calculated in this model turned out to be two orders of magnitude lower than the value $n \approx 0.1$ measured in Ref. 4 by neutron scattering.

In the present work we have achieved satisfactory quantitative agreement with the experimental data thanks to allowing for the following two factors.

1. An important parameter defining the magnitude of the correlation energy in a system of electrostatically interacting defects is the charge of these defects. For defects of the crystalline lattice of uranium dioxide, which play a major role in the description of the phase transition, the magnitudes of the charges Z are usually taken to be equal to ± 2 for the positively charged oxygen vacancies and the negatively charged oxygen interstitials, respectively. However, a more detailed treatment of the charge state of the vacancy defects shows that as a result of the interaction of the crystal defects with the electron subsystem of the semiconducting crystal UO_2 the charge of these defects can vary substantially with growth of temperature. This has to do with the fact that the vacancies of the oxygen sublattice form F-centers whose electron level ε_a lies in the band gap (width ≈ 2 eV) near the position of the chemical potential for the defect-free crystal. With growth of the defect concentration as the temperature is raised the position of the chemical potential in the defect-containing crystal begins to be affected by their presence, which in turn can lead to self-consistent variation of the occupancy of the ε_a level and the degree of excitation of the electron subsystem. Taking this interaction into account has a significant influence on the effective charge of the vacancies and, consequently, on the behavior of the system as a whole.

2. The strong Coulomb repulsion of homotypic defects at close distances leads to blocking of the sites nearest a given defect. Taking this phenomenon into account leads to the result that the number of available sites for defects of one kind is decreased and the expression for the configurational entropy changes. The general phenomenological treatment presented earlier in Refs. 8 and 9 of the behavior of the system at the investigated transition imposes rigid constraints on the form of the free energy and, in particular, on the form of the configurational entropy. This requires a more detailed and consistent description description of the configurational distribution of the atoms and defects over the crystal lattice sites—in particular, a more accurate treatment of blocking of nearby sites with allowance for the actual symmetry of the fluorite crystalline lattice.

Taking these two factors into account has allowed us to develop a microscopic model within the framework of which it has been possible to obtain a quantitative description of the structural transition in the UO_2 crystal in the region of T_{crit}, that is consistent with the following experimental observations: 1) as the temperature is raised from 2650 to 2730 K, a substantial growth of disorder of the anion sublattice is observed, so that the equilibrium defect concentration in this range grows from 0.02 to 0.25 in the calculation per oxygen sublattice site; 2) the corresponding anomaly in the behavior of the specific heat has the form of a smeared peak with maximum height $\delta C_{\max} \approx 100$ J/mole·K and smearing width $\delta T \approx 80$ K.

Finally, on the basis of this model we have carried out a critical review of models previously proposed to describe the super-ion transition in uranium dioxide.

ACKNOWLEDGMENTS

In conclusion, we would like to express our sincere gratitude to A. M. Dykhne for helpful discussions of this paper.

This work was carried out with the financial support of the International Science Foundation (Project No. N6P000).

APPENDIX A

We calculate the mean number of sites blocked by one vacancy in the case when the vacancy concentration is nonzero. Let a test defect be located at the site (*0*) (Fig. 5), blocking the six neighboring sites (*1*) of the first coordination

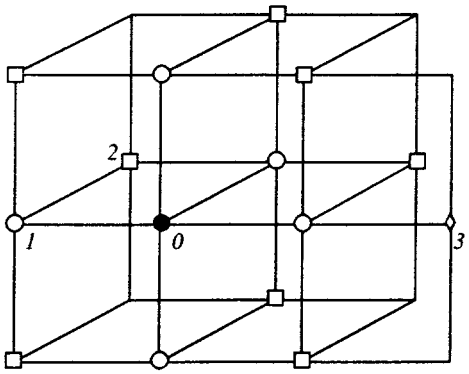

FIG. 5. Arrangement of various types of sites about a test defect in the anion sublattice. Markers denote the test defect (*0*) (●), blocking sites (*1*) (○), and sites on the second (*2*) and third (*3*) coordination spheres, respectively (□ and ◇).

sphere. The (*1*) sites may already be blocked if there are already other defects on the sites (*2*) of the second coordination sphere or (*3*) of the third coordination sphere. In this case, by virtue of the fact that the (*2*) and (*3*) sites are not nearest neighbors, the probabilities of finding defects at each of them are assumed to be independent and equal to $P=n$, where n is the mean defect concentration. The total number of (*2*) and (*3*) sites by which the (*1*) sites can be blocked is equal to 18.

The probability that all the (*2*) and (*3*) sites are free is

$$P_6=(1-n)^{18},$$

where the subscript 6 indicates that the test defect blocks six sites.

The probability that one of the (*1*) sites is already blocked and the test defect blocks five sites is

$$P_5=6(1-n)^{17}n.$$

The probability that two (*1*) sites are already blocked is

$$P_4=12(1-n)^{17}n+15(1-n)^{16}n^2+24(1-n)^{16}n^2,$$

where the first term is the probability that one defect is found at the (*2*) sites, the second term is the probability that two defects are found at the (*3*) sites, and the third term is the probability that the defects occupy a (*2*) site and a (*3*) site situated next to each other so that two (*1*) sites are blocked. Similarly, with terms out to n^2 we calculate

$$P_3=48(1-n)^{16}n^2+30(1-n)^{16}n^2,$$

$$P_2=36(1-n)^{16}n^2.$$

Finally, for the mean number of sites blocked by the test defect we obtain

$$\alpha(n)=\sum_{k=2}^{6} kP_k(n)\left(\sum_{k=2}^{6} P_k(n)\right)^{-1}=6-30n-867n^2.$$

Let us now calculate the number of states Γ for a system of N defects occupying M possible sites. In analogy with the simple system in which one particle occupies one site, we write

$$\Gamma=\frac{1}{N!}M\left(M-\left(1+\alpha\left(\frac{1}{M}\right)\right)\right)\left(M-\left(2+\alpha\left(\frac{1}{M}\right)+\alpha\left(\frac{2}{M}\right)\right)\right)\ldots\left(M-\left(N-1+\sum_{1}^{N-1}\alpha\left(\frac{k}{M}\right)\right)\right)$$

or, replacing the sume in each term by an integral

$$\sum_{k=1}^{K}\left(1+\alpha\left(\frac{k}{M}\right)\right)=M\int_0^{K/M}(1+\alpha(x))dx=M\beta\left(\frac{K}{M}\right)=M\left(7\left(\frac{K}{M}\right)-15\left(\frac{K}{M}\right)^2-286\left(\frac{K}{M}\right)^3\right),$$

we obtain the following expression for the entropy:

$$S_v=\ln\left(\prod_{K=0}^{N}\left(M-M\beta\left(\frac{K}{M}\right)\right)\right)-N\ln\left(\frac{N}{e}\right)=\sum_{K=0}^{N}\ln\left(1-\beta\left(\frac{K}{M}\right)\right)-N\ln\left(\frac{N}{Me}\right).$$

Again replacing the sum by an integral, we obtain the final expression for the contribution of vacancies to the configurational entropy:

$$S_v=M\left\{\int_0^n \ln(1-7n+15n^2+286n^3)dn-n\ln n+n\right\}. \tag{A.1}$$

[1] K. A. Young, J. Nucl. Mater. **84**, 283 (1979).
[2] S. W. Tam, T. K. Fink, and L. Leibowitz, J. Nucl. Mater. **130**, 199 (1985).
[3] N. H. March, D. D. Richardson, and M. P. Tosi, Solid State Commun. **35**, 903 (1980).
[4] M. T. Hutching, J. Chem. Soc. Faraday Trans. **83**, 1121 (1987).
[5] T. P. Hiernaut, G. T. Hyland, and C. Ronchi, Int. J. Thermophys. **14**, 259 (1993).
[6] R. A. Jackson, A. D. Murray, J. H. Harding, and C. R. A. Catlow, Phil. Mag. A **53**, 27 (1986).
[7] J. Oberschmidt, Phys. Rev. B **23**, 5038 (1981).
[8] M. S. Veshchunov, Fiz. Tverd. Tela **33**, 1297 (1991) [Sov. Phys. Solid State **33**, 735 (1991)].
[9] M. S. Veshchunov, J. Nucl. Mater. **175**, 184 (1990).
[10] V. G. Vaks, V. I. Zinenko, and V. E. Shneĭder, Usp. Fiz. Nauk **141**, 629 (1983) [Sov. Phys. Usp. **26**, 1059 (1983)].
[11] V. G. Vaks, N. E. Zeĭn, V. I. Zinenko, and V. G. Orlov, Zh. Éksp. Teor. Fiz. **87**, 2030 (1984) [Sov. Phys. JETP **60**, 1171 (1984)].
[12] C. R. A. Catlov, Proc. R. Soc. London A **353**, 531 (1977).
[13] Yu. Ya. Gurevich and Yu. I. Kharkats, *Super-Ion Conductors* [in Russian], Nauka, Moscow (1992).
[14] K. N. Clausen, M. A. Hackett, W. Hayes *et al.*, Physica B **156/157**, 103 (1989).
[15] L. D. Landau and E. M. Lifshitz, *Statistical Physics* Pt. 1 [in Russian], Nauka, Moscow (1976), p. 267 [English translation: *Statistical Physics*, 3rd. Ed., Pergamon Press, Oxford, (1980)].
[16] T. Matsui, Yu. Arita, and K. Naito, J. Nucl. Mater. **188**, 205 (1992).
[17] V. L. Vinnetskiĭ and G. A. Kholodar', *Statistical Interaction of Electrons and Defects in Semiconductors* [in Russian], Naukova Dumka, Kiev (1969).
[18] V. L. Bonch-Bruevich and S. G. Kalashnikov, *Physics of Semiconductors* [in Russian], Nauka, Moscow (1990).
[19] C. R. A. Catlov, J. Chem. Soc. Faraday Trans. **83**, 1065 (1987).

Translated by Paul F. Schippnick

Spin-density wave in a Kondo lattice

E. A. Zhukovskiĭ and V. V. Tugushev

Kurchatov Institute Russian Scientific Center, 123182 Moscow, Russia
(Submitted 27 March 1996; resubmitted 2 August 1996)
Zh. Éksp. Teor. Fiz. **111**, 600–614 (February 1997)

An Anderson model with N-fold degeneracy in the Kondo regime is considered. It is presumed that the electron–electron correlations in the system of f electrons have their maximum strength. A criterion for instability against the formation of a weakly antiferromagnetic phase superposed on the Kondo state is obtained by the auxiliary-boson method using the $1/N$ expansion. An effective interaction leading to the formation of magnetic ordering appears because of the spin fluctuations in the system of localized electrons. The phase diagram of the system is constructed. © *1997 American Institute of Physics.* [S1063-7761(97)01502-3]

1. INTRODUCTION

The influence of Kondo impurities on the formation of weak antiferromagnetic ordering in a system of band electrons [which is also called a spin-density wave (SDW)] was previously discussed in Refs. 1 and 2. In the limit of a small concentration of Kondo centers the principal effect is the incoherent scattering of the band electrons on these centers, which gives rise to antiferromagnetism. It was assumed in this case that the mechanism for forming the SDW is based on the exchange interaction in the system of band electrons, which thus competes with the mechanism for destroying the SDW.

The present work is concerned with a system having a regular arrangement of Kondo centers (i.e., a Kondo lattice), in which the interaction of the band electrons with one another is totally disregarded. As we know, in the Kondo regime the spin of a strongly correlated local center is shielded as a result of the redistribution of the spin density of the band electrons, and a nonmagnetic coherent state appears, which competes with magnetic states of various types.

The possibility of magnetic instability of a specific type in a heavy-fermion system is a question that was posed and actively studied a long time ago.[3–10] Several heavy-fermion systems experimentally exhibit weak antiferromagnetic ordering at low temperatures. The recent attempts to analytically describe the magnetic instability in such systems were generally based on the use of pseudofields. The latter are introduced either according to Barnes' procedure,[11] in which different kinds of auxiliary particles obey Fermi and Bose statistics,[10] or by the method of Kotliar and Ruckenstein,[12] in which the pseudoparticles introduced are bosons.[7,8]

In most cases the problem of a doubly degenerate f level is investigated in connection with magnetic solutions (see, for example, Refs. 7, 9, and 10). The results are obtained either in the boson mean-field approximation (i.e., by replacing the boson operators by c-numbers) or in first order with respect to the fluctuations of the boson field. It should be noted that the absence of a small parameter in the theories of this type causes the higher-order corrections to the (essentially variational) solutions to be comparable to the solutions themselves. This circumstance precludes drawing confident conclusions regarding the behavior of a heavy-fermion system with presumed magnetic ordering.

The situation is different in the case of strong orbital degeneracy of the f level. Although it is known that an increase in this degeneracy renders a heavy-fermion system more stable with respect to magnetic ordering, the presence of the small parameter $N^{-1} \ll 1$ (N is the degree of degeneracy of the level) makes it possible to devise a more systematic theory.

Below we investigate a situation in which a weakly antiferromagnetic state of localized and band electrons appears as a result of quantum fluctuations of the spin density in a system with an N-fold degenerate seed f level on a background of a Kondo state. We assume that $N \gg 1$. This allows us to utilize the $1/N$ expansion and the diagram technique developed for it[13–15] by introducing auxiliary Barnes fields. Miura, Matsurura, and Kuroda[15] pointed out the possibility of considering different types of ordering in a Kondo lattice within the $1/N$ diagram technique, but concentrated on calculating the lifetime of the quasiparticles and the response functions to an external field in a general form with consideration of vertex corrections.

An attempt to extend the Kotliar–Ruckenstein scheme[12] to the case of orbital degeneracy was made by Dorin and Schlottmann in Ref. 8. These workers did not study the tendency for antiferromagnetism in a Kondo lattice, but they thoroughly treated the case of $N=2$ in the mean-field approximation.

We stress that in the mean-field approximation with respect to boson operators there are no magnetic solutions at all in the Hamiltonian under investigation here (see below), and there is only a solution of the Kondo type. We take into account the fluctuations of the boson field in the lowest approximation with respect to $1/N$, and we derive a Stoner criterion as a necessary condition for the existence of antiferromagnetism in just this approximation. Naturally, the antiferromagnetism in our scheme is found to be weak (the effective exchange is small, of order N^{-2}, since the boson propagator itself contains the small parameter $1/N \ll 1$), and we proceed so as not to exceed the range of applicability of the $1/N$ expansion. The Néel temperature T_N and the antiferromagnetic gap Σ in the spectrum of the band electrons in this situation are small in comparison with the Kondo tem-

perature T_K and the Kondo energy ϵ_f, i.e., $\Sigma, T_N \ll \epsilon_f, T_K$. Thus, we are concerned with the coexistence of antiferromagnetism and a Kondo state, which is possible when certain conditions are satisfied. We shall discuss them in this paper, bearing in mind the case of a zero temperature $T=0$.

A transition to finite $N \sim 2$ is impossible in our scheme, since it requires consideration of correlators that are higher with respect to $1/N$, which cannot be done correctly in the absence of a small parameter.

2. MODEL HAMILTONIAN

We write an N-fold degenerate Anderson Hamiltonian for a lattice in the pseudofermion and pseudoboson field representation:[16]

$$H = H_b + H_f + H_{bf}, \tag{1}$$

where

$$H_b = \sum_{\mathbf{k}m} \epsilon(\mathbf{k}) a^+_{\mathbf{k}m} a_{\mathbf{k}m}, \quad H_f = \sum_{im} E_0 f^+_{im} f_{im},$$

$$H_{bf} = \sum_{\mathbf{k}mi} V(\mathbf{k},m) \exp(i\mathbf{k}\cdot\mathbf{R}_i) a^+_{\mathbf{k}m} f_{im} b^+_i + \text{H.c.}$$

Here $a^+_{\mathbf{k}m}$ is the creation operator of a band electron with ''spin'' projection m, quasimomentum $\mathbf{k}$, and energy $\epsilon(\mathbf{k})$; f^+_{im} is the creation operator of a pseudofermion at site i with ''spin'' projection m; and b^+_i is the creation operator of a pseudoboson at site i. The position of the Fermi level corresponding to half filling of the band is taken as the zero level of all the energies in the problem. The Kondo regime of the two-band model (1) is considered. This corresponds to the following conditions: $E_0 < 0$ and $|E_0| \gg N(0)V^2$, where the latter quantity is an estimate of the broadening of the f level due to the hybridization V, and $N(0)$ is the density of the band states at the Fermi level. It is assumed that the correlations of the f electrons have their maximum values, and, thus, the f sites are singly occupied at most. As usual, we express this condition in the form

$$\sum_m f^+_{im} f_{im} + b^+_i b_i = 1. \tag{2}$$

We shall assume below that the multiplicity of the degeneracy of the E_0 level is high, i.e., $N = 2J+1 \gg 1$ $(-J \leqslant m \leqslant J)$, which allows us to use the $1/N$ expansion.[13,14,16] Following Ref. 16, we assume that the Kondo regime is characterized by the appearance of an anomalous pseudoboson average

$$\frac{1}{\sqrt{N}} \langle b_{\mathbf{k}} \rangle = a\, \delta_{\mathbf{k},0}; \tag{3}$$

and the appearance of a resonant pseudofermion level ϵ_f near the Fermi level.

The mean-field part of the Hamiltonian (1) has the form

$$H_{mf} = \sum_{\mathbf{k},m} \epsilon(\mathbf{k}) a^+_{\mathbf{k},m} a_{\mathbf{k},m} + \sum_{\mathbf{k},m} \epsilon_f f^+_{\mathbf{k},m} f_{\mathbf{k},m}$$

$$+ \sum_{\mathbf{k},m} [a V(\mathbf{k}) a^+_{\mathbf{k}m} f_{\mathbf{k}m} + \text{H.c.}]$$

$$+ N \sum_{\mathbf{k}} (\epsilon - E_0) A^+_{\mathbf{k}} A_{\mathbf{k}}, \tag{4}$$

where we went over to a new parameter scale:

$$V \to V/\sqrt{N}, \quad b^+_i = \sqrt{N} A^+_i.$$

The Hamiltonian (4) can be diagonalized by the standard procedure of going over to new quasiparticles having a spectrum with two branches:

$$\epsilon_{1,2}(\mathbf{k}) = \frac{\epsilon(\mathbf{k}) + \epsilon_f \mp \sqrt{[\epsilon(\mathbf{k}) - \epsilon_f]^2 + 4(Va)^2}}{2}. \tag{5}$$

Here and below we use the notation $V^2 = \langle V^2(\mathbf{k}) \rangle$, where the angle brackets denote averaging over the directions of the vector $\mathbf{k}$ on the Fermi surface.

The Fourier transforms of the Green's functions of the band electrons, the pseudofermions, and the pseudobosons, respectively, for the Hamiltonian (4) have the following form:[16]

$$G_{aa,m}(\mathbf{k}, i\omega) = \frac{i\omega - \epsilon_f}{(i\omega - \epsilon_f)[i\omega - \epsilon(\mathbf{k})] - V^2 a^2},$$

$$G_{ff,m}(\mathbf{k}, i\omega) = \frac{i\omega - \epsilon(\mathbf{k})}{(i\omega - \epsilon_f)[i\omega - \epsilon(\mathbf{k})] - V^2 a^2}, \tag{6}$$

$$G_{af,m}(\mathbf{k}, i\omega) = \frac{V(\mathbf{k}) a}{(i\omega - \epsilon_f)[i\omega - \epsilon(\mathbf{k})] - V^2 a^2},$$

$$D(\mathbf{k}, i\nu) = \frac{1}{N(\epsilon_f - E_0)},$$

where $i\omega = i\pi T(2n+1)$, $i\nu = 2in\pi T$, and $n = 0, \pm 1, \pm 2, \ldots$ are the fermionic and bosonic Matsubara frequencies.

The interaction between the band and localized electrons in the Kondo regime is introduced by the fluctuational part of the Hamiltonian H_{bf}:

$$H_{\text{int}} = \sum_{\mathbf{k}m} V(\mathbf{k}) a^+_{\mathbf{k},m} f_{\mathbf{k}+\mathbf{q},m} b^+_{\mathbf{q}} + \text{H.c.} \tag{7}$$

As will be shown below, the appearance of antiferromagnetic ordering on a background of a Kondo state is possible specifically within H_{int}.

3. CRITERION FOR THE EXISTENCE OF WEAK ANTIFERROMAGNETISM

The antiferromagnetic ordering in the system under consideration is characterized by the appearance of self-energy parts of the Green's functions on a certain wave vector $\mathbf{Q}$ that are antisymmetric with respect to the spin index m: $\Sigma_{aa,m}$, $\Sigma_{ff,m}$. Henceforth we confine ourselves to consideration of the simplest case of a linearly polarized structure with $\mathbf{Q} = \mathbf{G}/2$, where $\mathbf{G}$ is a reciprocal-lattice vector. This corresponds to antiferromagnetic ordering with period doubling. The simplest diagrams which contribute to Σ_{aa} and Σ_{ff} in the lowest order with respect to $1/N$ are shown in Fig. 1. We note that the self-energy part $\Sigma_{af,m}$ which is off-

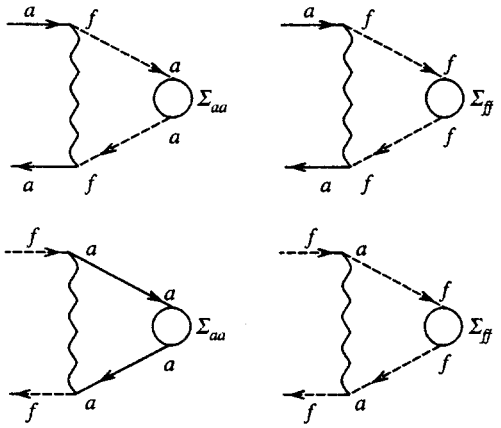

FIG. 1. Diagrams for the self-energy parts of the pseudofermions and band electrons.

diagonal with respect to the band indices vanishes because of the symmetry condition $\langle V_m(\mathbf{k})\rangle = 0$ upon integration over the directions of the vector $\mathbf{k}$ in the Brillouin zone. We assume that the quantization axis is directed along the polarization vector of the SDW. In this case, for simplicity, we write the dependence of Σ_m on the spin index in the form

$$\Sigma_m = \mathrm{sgn}(m)\Sigma. \tag{8}$$

Thus, to first order in Σ we obtain the following system of self-consistency equations:

$$\begin{aligned}\Sigma_{aa}(\mathbf{k},\mathbf{k}+\mathbf{Q}) = T\sum_{i\omega\mathbf{q}} &\frac{V^2}{N(\epsilon_f - E_0)} G_{ff,m}(\mathbf{q},i\omega)\\ &\times G_{ff,m}(\mathbf{q}+\mathbf{Q},i\omega)\Sigma_{ff}(\mathbf{q},\mathbf{q}+\mathbf{Q})\\ &+ T\sum_{i\omega\mathbf{q}} \frac{V^2}{N(\epsilon_f - E_0)} G_{fa,m}(\mathbf{q},i\omega)\\ &\times G_{af,m}(\mathbf{q}+\mathbf{Q},i\omega)\Sigma_{aa}(\mathbf{q},\mathbf{q}+\mathbf{Q}),\end{aligned} \tag{9}$$

$$\begin{aligned}\Sigma_{aa}(\mathbf{k},\mathbf{k}+\mathbf{Q}) = T\sum_{i\omega\mathbf{q}} &\frac{V^2}{N(\epsilon_f - E_0)} G_{aa,m}(\mathbf{q},i\omega)\\ &\times G_{aa,m}(\mathbf{q}+\mathbf{Q},i\omega)\Sigma_{aa}(\mathbf{q},\mathbf{q}+\mathbf{Q})\\ &+ T\sum_{i\omega\mathbf{q}} \frac{V^2}{N(\epsilon_f - E_0)} G_{af,m}(\mathbf{q},i\omega)\\ &\times G_{fa,m}(\mathbf{q}+\mathbf{Q},i\omega)\Sigma_{ff}(\mathbf{q},\mathbf{q}+\mathbf{Q}).\end{aligned} \tag{10}$$

It follows from Eqs. (9) and (10) that Σ_{aa} and Σ_{ff} do not depend on the quasimomentum and the frequency. In this case we have the following equations:

$$\Sigma_{aa} = \frac{V^2}{N(\epsilon_f - E_0)}[\Pi_{af}(\mathbf{Q})\Sigma_{aa} + \Pi_{ff}(\mathbf{Q})\Sigma_{ff}], \tag{11}$$

$$\Sigma_{ff} = \frac{V^2}{N(\epsilon_f - E_0)}[\Pi_{af}(\mathbf{Q})\Sigma_{ff} + \Pi_{aa}(\mathbf{Q})\Sigma_{aa}], \tag{12}$$

where

$$\Pi_{ff}(\mathbf{Q}) = T\sum_{i\omega\mathbf{q}} G_{ff,m}(\mathbf{q},i\omega)G_{ff,m}(\mathbf{q}+\mathbf{Q},i\omega),$$

$$\Pi_{aa}(\mathbf{Q}) = T\sum_{i\omega\mathbf{q}} G_{aa,m}(\mathbf{q},i\omega)G_{aa,m}(\mathbf{q}+\mathbf{Q},i\omega), \tag{13}$$

$$\Pi_{af}(\mathbf{Q}) = T\sum_{i\omega\mathbf{q}} G_{af,m}(\mathbf{q},i\omega)G_{fa,m}(\mathbf{q}+\mathbf{Q},i\omega).$$

Setting the determinant of the system of equations (11) and (12) equal to zero, we can obtain the criterion for antiferromagnetic instability

$$\begin{aligned}&\left[1 - \frac{V^2}{N(\epsilon_f - E_0)}\Pi_{af}(\mathbf{Q})\right]^2\\ &\quad - \frac{V^4}{N^2(\epsilon_f - E_0)^2}\Pi_{ff}(\mathbf{Q})\Pi_{aa}(\mathbf{Q}) = 0,\end{aligned} \tag{14}$$

which can be written in a different form:

$$\begin{aligned}1 = &\frac{V^2}{N(\epsilon_f - E_0)}\Pi_{af}(\mathbf{Q})\\ &\pm \sqrt{\frac{V^4}{N^2(\epsilon_f - E_0)^2}\Pi_{ff}(\mathbf{Q})\Pi_{aa}(\mathbf{Q})}.\end{aligned} \tag{15}$$

It is easy to show that only the plus sign should be chosen in (15), since in the system under consideration

$$\sqrt{\Pi_{ff}(\mathbf{Q})\Pi_{aa}(\mathbf{Q})} \gg |\Pi_{af}(\mathbf{Q})|,$$

so that we can omit the first term in (15) (the details are presented below).

To elucidate the physical meaning of the condition (14) we set $\Pi_{af} = 0$ and consider a more realistic model with the Hamiltonian

$$H_{\mathrm{int}} = \sum_{\mathbf{k}m\alpha} V_{m,\alpha}(\mathbf{k})a^+_{\mathbf{k},\alpha}f_{\mathbf{k}+\mathbf{q},m}b^+_{\mathbf{q}} + \mathrm{H.c.}, \tag{16}$$

where $\alpha = \pm 1$ is the spin index of the band electrons. To second order with respect to the fluctuations of the boson field two types of diagrams appear for the self-energy part Σ_α, which is antisymmetric with respect to the spin index (Fig. 2):

$$\begin{aligned}\Sigma^{(a)}_\alpha(\mathbf{k},\mathbf{k}+\mathbf{Q}) = -T^2 \sum_{i\omega' i\omega''} \sum_{\mathbf{k}'\mathbf{k}''} \sum_{mm'\alpha'} &|V_{m\alpha}|^2 |V_{m'\alpha'}|^2 D(k''\\ &- k)D(k'' - k + Q)G_{ff,m}(k'')G_{ff,m'}(k'' + k'\\ &- k)G_a(k')G_a(k' + Q)\Sigma^{(a)}_{\alpha'}(\mathbf{k}',\mathbf{k}'+\mathbf{Q}),\end{aligned} \tag{17}$$

where $k = (\mathbf{k}, i\omega)$, $k' = (\mathbf{k}', i\omega')$, $k'' = (\mathbf{k}'', i\omega'')$, and $Q = (\mathbf{Q}, 0)$;

$$\begin{aligned}\Sigma^{(b)}_\alpha(\mathbf{k},\mathbf{k}+\mathbf{Q}) = T^2 \sum_{i\omega' i\omega''} \sum_{\mathbf{k}'\mathbf{k}''} \sum_{mm'\alpha} &V^*_{m\alpha}V_{m\alpha'}V^*_{m'\alpha}V_{m'\alpha'}\\ &\times D(k'' - k)D(k'' - k')G_{ff,m}(k'')\\ &\times G_{ff,m'}(k'' + Q)G_a(k')\\ &\times G_a(k' + Q)\Sigma^{(b)}_{\alpha'}(\mathbf{k}',\mathbf{k}'+\mathbf{Q}).\end{aligned} \tag{18}$$

Expressions (17) and (18) contain mean-field Green's functions that are symmetric with respect to the indices m and

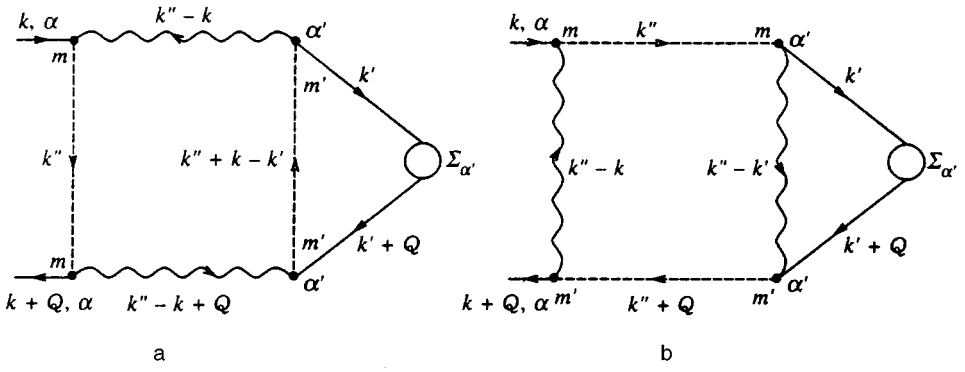

FIG. 2. Diagrams for the self-energy parts of the band electrons.

α. In the general case we can represent G_{ff} and G_{aa} in a simple form like (6), and the calculations in (17) and (18) become far more complicated than in (9) and (10). Nevertheless, for a qualitative analysis we take the simplest form of the dependence of $V_{m\alpha}$ on the indices in the approximation of an isotropic scattering potential:

$$V_{m\alpha}=Vg_{m\alpha}, \quad g_{m\alpha}=\sqrt{\frac{J+m\alpha}{2J}},$$

where the $g_{m\alpha}$ are the Clebsch–Gordan coefficients. The dependence of Σ_α on the spin index has the form

$$\Sigma_\alpha=\alpha\Sigma, \quad \alpha=\pm 1. \tag{19}$$

It can be shown that the diagram in Fig. 2a is proportional to the quantity

$$A=\sum_{\alpha' mm'} \alpha' g_{m\alpha}^2 g_{m'\alpha'}^2=0, \tag{20}$$

while the contribution of the diagram in Fig. 2b to Σ is finite as long as B is finite:

$$B=\frac{1}{2}\sum_{mm'}\left(\sum_\alpha \alpha g_{m\alpha}g_{m'\alpha}\right)^2\neq 0. \tag{21}$$

It can be concluded from an analysis of the diagrams in Fig. 2 that diagram 2a actually represents the self-energy part of the band electrons, in which the functional corrections to the boson propagator are taken into account. Such corrections do not give rise to a pseudofermion Green's function that depends on two different magnetic indices. At the same time, diagram 2b contains a fluctuational correction to G_{ff}, which leads to such a dependence (i.e., the pseudofermion propagator $G_{ff,mm'}$ with $m\neq m'$ effectively shows itself). This allows us to conclude that antiferromagnetic ordering appears simultaneously in the subsystems of the band and localized electrons.

From (17)–(21) we can obtain the instability condition

$$1\leqslant\frac{BV^4}{N^2(\epsilon_f-E_0)^2}\Pi_{ff}(\mathbf{Q})\Pi_{aa}(\mathbf{Q}), \tag{22}$$

which is similar to (14), if we set $B=1$ and $\Pi_{af}(\mathbf{Q})=0$.

We note that the condition (22) exhibits definite similarity to the generalized Stoner criterion[17]

$$1\leqslant\tilde{U}\chi_0(\mathbf{Q}), \tag{23}$$

where $\tilde{U}$ is the effective interaction and $\chi_0(\mathbf{Q})$ is the static magnetic susceptibility of a noninteracting system on the vector $\mathbf{Q}$. When the equality in (23) holds, the magnetic susceptibility calculated in the random-phase approximation has a pole:

$$\chi(\mathbf{Q})=\frac{\chi_0(\mathbf{Q})}{1-\tilde{U}\chi_0(\mathbf{Q})},$$

which signals the appearance of antiferromagnetic ordering with the wave vector $\mathbf{Q}$ in the system.

If we consider (22) [or its analog (14)] from the standpoint of the band electrons, the role of χ_0 is played here by $\Pi_{aa}(\mathbf{Q})$, and the role of the effective exchange interaction is played by the quantity $BV^4(\epsilon_f-E_0)^{-2}N^{-2}\Pi_{ff}(\mathbf{Q})$ [in (14) $B=1$]. Criterion (22) can also be interpreted from the standpoint of localized electrons coupled by the effective RKKY interaction $BV^4(\epsilon_f-E_0)^{-2}N^{-2}\Pi_{aa}(\mathbf{Q})$. In this case the role of $\chi_0(\mathbf{Q})$ is played by $\Pi_{ff}(\mathbf{Q})$.

In the general case the polarization loops in (14) can be calculated only numerically. To analyze them we use a model spectrum of band electrons with a constant density of states $N(0)$, which allows us to go easily from summation over the quasimomentum to integration over the energy $\epsilon(\mathbf{k})$. We assume that the Fermi level is located in the band corresponding to the branch $\epsilon_1(\mathbf{k})$ of the spectrum (5). Our calculations show that the main contribution to the polarization operator of the band electrons is made by states with energies from the bottom of the band to energies on the order of the width of the hybridization gap $\Delta=Va$, where the seed spectrum of the band electrons is modified significantly because of the hybridization with the f level. At the same time, the main contribution to $\Pi_{ff}(\mathbf{Q})$ is made by states in an energy range of width Δ below ϵ_f. Outside this range the Green's functions of the pseudofermions do not differ strongly from the Green's functions of dispersionless particles and make a nearly zero contribution to $\Pi_{ff}(\mathbf{Q})$.

Below we present the results of our calculations at $T=0$ for the most interesting case $\Delta/\epsilon_f\gg 1$. To simplify the calculations we consider the case of an almost half-filled seed band $\epsilon(\mathbf{k})$, which has the property of ideal nesting: $\epsilon(\mathbf{k})=-\epsilon(\mathbf{k}+\mathbf{Q})$. In principle, this condition is not critical for the existence of antiferromagnetism, as demonstrated below, although it is exceptionally favorable for its appearance.

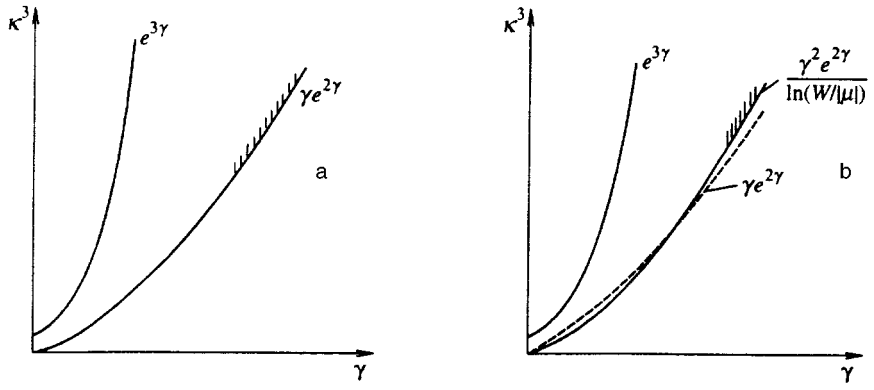

FIG. 3. Phase diagram in κ^3 versus γ coordinates. The regions of the antiferromagnetic phase are hatched: a – in a system with ideal nesting; b – in a system with imperfect nesting.

The spectrum (5), of course, does not have the property of nesting in the Kondo phase. The main terms of the polarization operators in order of importance are

$$\Pi_{aa}(\mathbf{Q}) \sim -N(0)\ln\frac{W}{\Delta},$$

$$\Pi_{af}(\mathbf{Q}) \sim -N(0)\ln\frac{\Delta}{\epsilon_f}, \tag{24}$$

$$\Pi_{ff}(\mathbf{Q}) \sim -\frac{\Delta^2}{\epsilon_f^2}N(0),$$

where W is an energy on the order of the half-width of the band ($W \gg \Delta$). We note that, according to (24), $\Pi_{ff}(\mathbf{Q})\Pi_{aa}(\mathbf{Q}) \gg \Pi_{af}^2(\mathbf{Q})$, since $\Delta/\epsilon_f \gg 1$.

Substituting (24) into (14) and taking into account that $\epsilon_f \ll |E_0|$, we obtain the following instability criterion:

$$1 \leqslant \frac{V^4 N^2(0)}{N^2 E_0^2}\frac{\Delta^2}{\epsilon_f^2}\ln\frac{W}{\Delta}. \tag{25}$$

As was shown in Ref. 16, the quantity Δ^2/ϵ_f^2, specifies the increase in the effective mass:

$$\frac{\Delta^2}{\epsilon_f^2} = \frac{m^*}{m} \sim \frac{W}{\epsilon_f N} = \frac{\exp[|E_0|/V^2 N(0)]}{N}. \tag{26}$$

Let us consider the criterion (25) in the heavy-fermion phase. It is convenient to introduce the following notation: $\kappa \equiv m^*/m$, $\gamma \equiv |E_0|/V^2 N(0)$. The Kondo regime corresponds to the limit $\gamma \gg 1$. In the new notation we obtain the following inequality from (25) and (26):

$$\frac{\kappa^3 e^{-2\gamma}}{\gamma^2}\left(\gamma - \frac{1}{2}\ln\kappa\right) \geqslant 1. \tag{27}$$

We also require fulfillment of the condition $N \gg 1$, which ensures applicability of the $1/N$ expansion and takes on the following form in the new notation:

$$\frac{e^\gamma}{\kappa} \gg 1. \tag{28}$$

Employment of the $1/N$ expansion allows us to omit the logarithmic term in (27). We ultimately have

$$\gamma e^{2\gamma} \leqslant \kappa^3 \ll e^{3\gamma}, \tag{29}$$

where it is assumed that $\gamma \gg 1$.

The region for the existence of antiferromagnetism in a Kondo lattice is qualitatively shown on the $\kappa^3 - \gamma$ phase diagram in Fig. 3a.

As we have already noted, the quantity in front of the logarithmic factor in (25) can be regarded as an effective interaction of the band electrons through the fluctuations of pseudofields. According to (25), this interaction is a decreasing function of N, which corresponds to the disappearance of the fluctuations in the limit $N \to \infty$. Using (25) and (26), we can show that N has an upper bound in the heavy-fermion phase with antiferromagnetic ordering:

$$1 \ll N < \frac{e^{\gamma/3}}{\gamma^{1/3}}. \tag{30}$$

We have hitherto assumed that the spectrum of the band electrons obeys the condition of exact nesting $\epsilon(\mathbf{k}) = -\epsilon(\mathbf{k}+\mathbf{Q})$. The expressions (24) were presented for just this case. If the nesting is imperfect [for example, when the filling of the band deviates from half, we have $\epsilon(\mathbf{k}) = -\epsilon(\mathbf{k}+\mathbf{Q}) + \mu$, where μ is the displacement of the Fermi level from the position in the half-filled band], the factor $\ln(W/\max[|\mu|,\Delta])$ appears instead of $\ln(W/\Delta)$ in $\Pi_{aa}(\mathbf{Q})$ (24). At the same time, the expression for $\Pi_{ff}(\mathbf{Q})$ in first order with respect to ϵ_f/Δ remains unchanged.

When $\mu > \Delta$ holds, instead of (29) we obtain

$$\frac{\gamma^2 e^{2\gamma}}{\ln(W/|\mu|)} \leqslant \kappa^3 \ll e^{3\gamma}. \tag{31}$$

As follows from this inequality, the deviation from ideal nesting narrows the region of antiferromagnetism (Fig. 3b), and when $|\mu|$ is sufficiently large, the parameter of the $1/N$ expansion must have an upper bound specified by the condition

$$1 \ll N^3 < \frac{e^\gamma}{\gamma^2}\ln\frac{W}{|\mu|}. \tag{32}$$

4. AMPLITUDE OF THE SPIN DENSITY

Let us turn to the calculation of the amplitude S of the spin density in the ground state near the boundary of the region where the antiferromagnetic phase exists. As an ex-

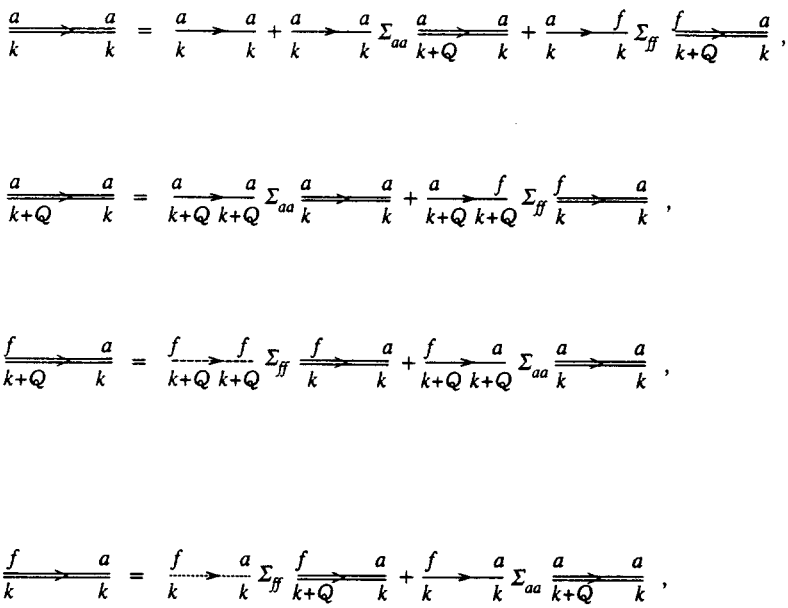

FIG. 4. System of equations for the Green's functions in the antiferromagnetic phase.

ample, we consider the band component S_a, which is defined in terms of the anomalous Green's function $\mathcal{G}_m^{aa}(k,\ k+Q)$ in the following manner:

$$S_a=\frac{T}{N}\sum_{i\omega}\ \sum_{m}\ \sum_{\mathbf{k}}\ \mathrm{sgn}(m)\mathcal{G}_m^{aa}(k,k+Q), \tag{33}$$

where the self-energy parts $\Sigma_{aa,m}$ and $\Sigma_{ff,m}$ appear in $\mathcal{G}_m^{aa}(k,k+Q)$ in a complicated manner along with the already known parameters of the problem. The self-energy parts, in turn, are determined from the self-consistency equations

$$\begin{aligned}&\Sigma_{aa,m}\frac{V^2}{(\epsilon_f-E_0)N}T\sum_{i\omega}\ \sum_{\mathbf{k}}\ \mathcal{G}_m^{ff}(k,k+Q),\\ &\Sigma_{ff,m}\frac{V^2}{(\epsilon_f-E_0)N}T\sum_{i\omega}\ \sum_{\mathbf{k}}\ \mathcal{G}_m^{aa}(k,k+Q).\end{aligned} \tag{34}$$

To calculate the functions $\mathcal{G}_m^{aa,ff}(k,k+Q)$ we must solve two fourth-order systems of linear equations: the first contains $\mathcal{G}_m^{aa}(k,k)$, $\mathcal{G}_m^{aa}(k,k+Q)$, $\mathcal{G}_m^{af}(k,k)$, and $\mathcal{G}_m^{af}(k,k+Q)$, and the second system is obtained from the first by the replacement of indices $a\leftrightarrow f$. To illustrate this, we present the diagram representation of such a system of equations in Fig. 4. The expressions for the Green's functions $\mathcal{G}_m^{ij}(i,j=a,f)$ are exceedingly cumbersome, forcing us to resort to numerical methods to solve the system of self-consistency equations (34). Nevertheless, near the line of instability with respect to the transition to the phase with an SDW (the hatched area in Fig. 3), where $\Sigma_{aa,m}$ is small, we can find an analytic solution using an expansion in $\Sigma_{aa,m}/\Delta\ll 1$.

We use the ansatz (8) to describe the dependence of $\Sigma_{aa,ff,m}$ on m. Leaving the terms with powers of $\Sigma_{aa,ff,m}$ no higher than cubic in (34) and antisymmetrizing with respect to m, we obtain the following system of equations:

$$\begin{aligned}&\Sigma_{aa}=L_f\Sigma_{ff}+A_3\Sigma_{aa}^3+A_0\Sigma_{ff}^3+A_2\Sigma_{aa}^2\Sigma_{ff}+A_1\Sigma_{ff}^2\Sigma_{aa},\\ &\Sigma_{ff}=L_a\Sigma_{aa}+F_3\Sigma_{ff}^3+F_0\Sigma_{aa}^3+F_2\Sigma_{ff}^2\Sigma_{aa}+F_1\Sigma_{aa}^2\Sigma_{ff},\end{aligned} \tag{35}$$

where all the coefficients are expressed in terms of the Green's functions (6):

$$\begin{aligned}L_{a,f}&=\frac{V^2}{(\epsilon_f-E_0)N}\Pi_{aa,ff}(\mathbf{Q}),\\ A_3&=\frac{V^2}{(\epsilon_f-E_0)N}T\sum_{i\omega}\ \sum_{\mathbf{k}}\ G_{aa}(k)G_{aa}(k+Q)\\ &\quad\times G_{af}(k)G_{af}(k+Q),\\ A_0&=\frac{V^2}{(\epsilon_f-E_0)N}T\sum_{i\omega}\ \sum_{\mathbf{k}}\ G_{ff}^2(k)G_{ff}^2(k+Q),\\ A_2&=\frac{V^2}{(\epsilon_f-E_0)N}T\sum_{i\omega}\ \sum_{\mathbf{k}}\ [2G_{aa}(k)G_{ff}(k)G_{af}^2(k+Q)\\ &\quad+G_{af}^2(k)G_{af}^2(k+Q)],\\ A_1&=\frac{V^2}{(\epsilon_f-E_0)N}T\sum_{i\omega}\ \sum_{\mathbf{k}}\ 3G_{af}(k)G_{af}(k+Q)\\ &\quad\times G_{ff}(k)G_{ff}(k+Q).\end{aligned} \tag{36}$$

Here $\Pi_{aa}(\mathbf{Q})$ and $\Pi_{ff}(\mathbf{Q})$ are given by (13). The expressions for the F_j $(j=0,1,2,3)$ in terms of the Green's functions (6) can be obtained from the corresponding expressions for the A_j in (36) after performing the interchange of indices $a\leftrightarrow f$ in the latter.

Expressing Σ_{ff} in terms of Σ_{aa} in (35) up to cubic terms, we have

$$\begin{aligned}\Sigma_{aa}=L_aL_f\Sigma_{aa}+[&L_f(L_a^3F_3+F_0+L_a^3F_2+L_aF_1)+A_3\\ &+L_a^3A_0+L_aA_2+L_f^2A_1]\Sigma_{aa}^3.\end{aligned} \tag{37}$$

According to (36), each of the coefficients in (37) contains the multiplier $N^{-1}\ll 1$. Leaving the terms no higher than N^{-2} in (37), we have

$$\Sigma_{aa}^2=\frac{1-L_aL_f}{L_fF_0+L_aA_2+A_3}. \tag{38}$$

Our calculations, which were performed using a model seed dispersion law of band electrons with a constant density of states for the case of ideal nesting, leads to the following results for the dominant terms in F_0 and $A_{2,3}$ ($\Delta/\epsilon_f\gg 1$, $\epsilon_f\ll|E_0|$, $\mu=0$) at $T=0$:

$$\begin{aligned} F_0&\sim-\frac{V^2N(0)}{E_0N\Delta^2},\\ A_2&\sim-\frac{V^2N(0)}{E_0N\Delta^2}\ \ln\frac{\Delta^2}{\epsilon_f^2},\\ A_3&\sim-\frac{V^2N(0)}{E_0N\Delta^2}. \end{aligned} \tag{39}$$

Substituting (13), (36), and (39) into (38), we obtain

$$\Sigma_{aa}^2=-\frac{1}{Z}\left[1-\frac{V^4N^2(0)\Delta^2}{N^2E_0^2\epsilon_f^2}\ \ln\frac{W}{\Delta}\right], \tag{40}$$

where

$$Z=\frac{V^2N(0)}{E_0N\Delta^2}\left[\frac{V^2N(0)}{E_0N}\left(\ln\frac{W}{\Delta}\ \ln\frac{\Delta^2}{\epsilon_f^2}+\frac{\Delta^2}{\epsilon_f^2}\right)+1\right]. \tag{41}$$

To analyze (40) and (41), we go over to the parameters κ and γ introduced above. In the region where the antiferromagnetic phase exists, which is specified by the condition (29), the numerator in (40) is negative, i.e., $\Sigma_{aa}^2>0$. The denominator Z (41) in the region (29) has the following form:

$$Z=\frac{\kappa e^{-\gamma}}{\gamma\Delta^2}\left[\kappa e^{-\gamma}\left(\ln\kappa+\frac{\kappa}{\gamma}\right)-1\right]. \tag{42}$$

We note that near the transition to the antiferromagnetic phase

$$\kappa=\gamma^{1/3}e^{2\gamma/3}+\alpha, \tag{43}$$

where α is a small parameter compared with the first term. The ratio between the terms in the round brackets in (42) is

$$\frac{\gamma\ \ln\kappa}{\kappa}\sim\gamma^{5/3}e^{-2\gamma/3}\ll 1,$$

so that the second term is dominant (we recall that $\gamma\gg 1$). Using (43), we now compare the second term in (42) with unity:

$$\frac{\kappa^2e^{-\gamma}}{\gamma}\sim\gamma^{-1/3}e^{\gamma/3}\gg 1.$$

Thus, near the line of the transition to the antiferromagnetic phase the second term is dominant in (42); therefore,

$$\Sigma_{aa}^2=\frac{g\ \ln(W/\Delta)-1}{g}\Delta^2, \tag{44}$$

where

$$g=\frac{V^4N^2(0)\Delta^2}{E_0^2N^2\epsilon_f^2}.$$

Near the line of the transition to the antiferromagnetic phase

$$\frac{g\ \ln(W/\Delta)-1}{g}\ll 1,$$

so that the expansion in $\Sigma_{aa}/\Delta\ll 1$ is justified. We note that the antiferromagnetic phase appears in the system under consideration at large, but finite N [see the inequality (30)]. The presence of such a restriction also makes it possible for the term proportional to $1/N^2$ to dominate the terms proportional to $1/N$ in the expression (41) for Z in the region where an SDW exists.

Substituting (44) into (33), in the linear approximation with respect to Σ_{aa}/Δ we obtain

$$S_a=N(0)\Delta\ \ln\frac{W}{\Delta}\sqrt{\ln\frac{W}{\Delta}-\frac{1}{g}}. \tag{45}$$

The result (45) was obtained for the system with exact nesting ($\mu=0$). In the case of a substantial deviation from ideal nesting ($|\mu|\gg\Delta$), the quantity Δ in the logarithmic terms in (44) should be replaced by $|\mu|$ with a resultant decrease in the amplitude S_a of the spin density. The amplitude S_f of the spin density of the localized electrons, which we shall not write out here, is calculated similarly.

5. CONCLUSIONS

Thus, we have demonstrated the possibility of satisfying the criterion for the existence of antiferromagnetic ordering in a Kondo lattice within the $1/N$ expansion. The interaction which leads to the formation of the magnetically ordered phase appears because of the fluctuations of the boson field. The appearance of an SDW in the system of band electrons is accompanied by antiferromagnetic alignment of the partially shielded spins in the localized system. The interaction between the localized electrons through polarization of the band electrons has the character of an effective RKKY interaction that has been renormalized by Kondo shielding. This state of the Kondo lattice can be regarded as an antiferromagnetic state of a system containing several sublattices with significantly different localization of the magnetic moments in them.

We described the state with magnetic ordering in the lowest order with respect to the fluctuations of the boson field within the $1/N$ expansion. The solutions that we obtained claim to describe only weak antiferromagnetism and cannot be extended to strong antiferromagnets. We are actually dealing with systems with $g<1$ [see (44)]. As we move into the region of the phase diagram with $g>1$, which corresponds to strong antiferromagnetism, consideration of the fluctuations of higher orders (i.e., terms that are higher in $1/N$) becomes essential for determining $\Sigma_{aa,ff}$. Now the system of equations (34) should be reformulated in the spirit of the self-consistency scheme for fluctuations in Ref. 18.

Within our approach it was assumed that the influence of antiferromagnetic ordering on the Kondo state is very weak ($T_N\ll T_K$). This allowed us to disregard the renormalization of the pseudoboson propagator in the magnetic phase. Such an approach seems justified in any case from the standpoint

of the $1/N$ expansion, since all normalizations of the pseudoboson Green's function will contain corrections that are higher in $1/N$. In the case of $N=2$ (which we did not consider in the present work), of course, the problem of the coexistence of a Kondo state and antiferromagnetism must be solved within a different self-consistency scheme. Significant modification of the phase diagram in Fig. 3 is then possible.

In conclusion, we wish to comment on the temperature of the transition to the antiferromagnetic phase in the system under consideration. The renormalization of the effective exchange interaction in the magnetic phase remains weak, i.e., bearing in mind the inequality $T_N \ll \Delta$, we can calculate the Néel temperature using the same effective coupling constant $g=\tilde{U}N(0)$ as in the case of $T=0$. In this case the quantity $\chi_0(\mathbf{Q}) \propto \ln(W/\Delta)$ is also weakly dependent on the temperature. Such a situation is known in the Moriya-Kawabata theory of self-consistent spin fluctuations,[19] where the temperature of the transition to the magnetic phase is determined not by the weak temperature dependence of $\chi_0(\mathbf{Q})$, but by corrections due to the thermodynamic spin fluctuations. According to Ref. 19, we then have

$$T_N \sim \Delta[g\ \ln(W/\Delta)-1]^{4/3}.$$

In the theory of self-consistent spin fluctuations[19] an energy of the order of the Fermi energy appears as the first factor in the analogous expression for the Néel temperature. This corresponds to the energy range in which the interaction forming the magnetic state takes place. In our case this quantity is specified by the energy parameter of the Kondo regime.

We thank B. A. Volkov, L. V. Keldysh, and the participants in the seminar on solid state physics of the theoretical physics department of the P. N. Lebedev Physics Institute of the Russian Academy of Sciences for discussing the results of this work. This research was partially supported by the Russian Fund for Fundamental Research (Grant No. 96-02-19693).

[1] E. E. Slyadnikov and V. V. Tugushev, Zh. Éksp. Teor. Fiz. **102**, 271 (1992) [Sov. Phys. JETP **75**, 142 (1992)].
[2] V. V. Tugushev, Zh. Éksp. Teor. Fiz. **106**, 269 (1994) [JETP **79**, 147 (1994)].
[3] S. Doniach, Physica B (Amsterdam) **91**, 231 (1977).
[4] C. Lacroix and M. Cyrot, Phys. Rev. B **20**, 1969 (1979).
[5] N. Read, D. M. Newns, and S. Doniach, Phys. Rev. B **30**, 3844 (1984).
[6] S. Doniach, Phys. Rev. B **35**, 1814 (1987).
[7] V. Dorin and P. Schlottmann, Phys. Rev. B **46**, 10 800 (1992).
[8] V. Dorin and P. Schlottmann, Phys. Rev. B **47**, 5095 (1993).
[9] Y. Kuramoto and K. Miyake, Prog. Theor. Phys. Suppl. **108**, 199 (1992).
[10] F. J. Ohkawa, Prog. Theor. Phys. Suppl. **108**, 209 (1992).
[11] S. E. Barnes, J. Phys. F **6**, 1375 (1976).
[12] G. Kotliar and A. E. Ruckenstein, Phys. Rev. Lett. **57**, 1362 (1986).
[13] N. F. Bickers, Rev. Mod. Phys. **59**, 845 (1978).
[14] P. Coleman, Phys. Rev. B **29**, 3035 (1984).
[15] R. Miura, T. Matsurura, and Y. Kuroda, Physica C (Amsterdam) **179**, 411 (1991).
[16] A. J. Millis and P. A. Lee, Phys. Rev. B **35**, 3394 (1987).
[17] C. Herring, in *Magnetism IV*, C. T. Rado and H. Suhl (eds.), Academic Press, New York (1966).
[18] E. A. Zhukovskiı and V. V. Tugushev, Zh. Éksp. Teor. Fiz. **103**, 568 (1993) [JETP **76**, 286 (1993)].
[19] T. Moriya, *Spin Fluctuations in Itinerant Electron Magnetism*, Springer-Verlag, Berlin (1985) [Russ. transl., Mir, Moscow (1988)].

Translated by P. Shelnitz

Magnetoplastic effect in irradiated NaCl and LiF crystals

V. I. Al'shitz, E. V. Darinskaya, and O. L. Kazakova

Institute of Crystallography, Russian Academy of Sciences, 117333 Moscow, Russia
(Submitted 9 April 1996)
Zh. Éksp. Teor. Fiz. **111**, 615–626 (February 1997)

The effect of low *x*-ray irradiation doses ($\approx 10^2$ rad) on the magnetoplastic effect — the detachment of dislocations from paramagnetic centers under the action of an external magnetic field B — in alkali-halide crystals has been investigated. The measurements were performed on LiF crystals and three types of NaCl crystals, differing in impurity content. The dependence of the mean free path l of the dislocations on the rotational frequency ν of a sample in a magnetic field was especially sensitive to low irradiation doses. In unirradiated crystals this dependence is a single-step dependence and is characterized by a critical frequency $\nu_c \propto B^2$ above which the magnetoplastic effect is not observed. The frequency ν_c depends only on the type of paramagnetic centers, and not on their density. Even the lowest irradiation dose employed (<100 rad) leads to a sharp restructuring of the dependence $l(\nu)$, converting it into a two-step dependence (for edge dislocations) with an additional critical frequency ν_{c2}, that is insensitive to the irradiation dose, and that corresponds to the appearance of magnetically sensitive stoppers of a new type under irradiation. The initial critical frequency ν_{c1}, as a rule, also varies with the dose, reflecting the change in state of the impurity complexes (Ca in NaCl and Mg in LiF). Specifically, it is shown for NaCl(Ca) crystals that as the irradiation dose increases, the frequency ν_{c1} increases, gradually approaching the value ν_{c2}, so that by the time the dose is ≈ 300 rad, the dependence $l(\nu)$ once again becomes a single-step dependence, dropping sharply only for $\nu \geqslant \nu_{c2}$. It is shown that the addition of a small number of Ni atoms to a NaCl crystal makes the Ca complexes radiation resistant, and the critical frequency ν_{c1} corresponding to them initially equals ν_{c2} for crystals with no Ni. The recombination kinetics of radiation defects in the case in which the samples are irradiated under a tungsten lamp was investigated. A possible physical model of the observed dependences is discussed. [S1063-7761(97)01602-8]

1. INTRODUCTION

It is well known that electronic excitations with a wide range of energies and lifetimes arise in alkali-halide crystals under the action of ionizing radiation of different nature and intensity. High-energy electronic excitations decay, transforming into very simple structural defects like electron–hole pairs and excitons, which in turn can form more complicated radiation-induced lattice defects.[1,2] This process, though not completely understood, has nonetheless been studied quite well in alkali-halide crystals at moderate and high irradiation doses ($D = 10^3 - 10^{17}$ rad).

In practice, however, existing methods are too insensitive for investigations at low irradiation doses. In a recent paper,[3] we proposed a fundamentally new method for studying weak radiation actions ($\approx 10^2$ rad).[1)] The method is based on the observed high sensitivity of the so-called magnetoplastic effect, investigated in Refs. 4–19, to x-ray irradiation of the crystals.

In many nonmagnetic crystals (alkali-halide crystals, Al, Zn), the magnetoplastic effect shows up experimentally as a displacement of dislocations under a constant magnetic field in the absence of a mechanical load. The mean free path l of dislocations increases as the magnetic treatment time t_m of the samples and the squared magnetic induction B ($l \propto B^2 t_m$), and decreases as the concentration C of the paramagnetic impurity increases ($l \propto 1/\sqrt{C}$). In crystals where diamagnetic impurities predominate, no effect of a magnetic field on dislocation mobility has been observed. The magnetoplastic effect is very insensitive to temperature: the mean free path at 4 K is essentially identical to that at 77 K, and is only 20% less than the mean free path at room temperature.

Essentially all basic features of the phenomenon can be explained on the basis of spin-dependent electronic transitions in an external magnetic field. It is assumed that the magnetic field engenders an evolution of the spin state in the dislocation–paramagnetic center system, which is completed by the removal of the spin-forbiddenness of a certain electronic transition. As a result, the configuration of the system changes radically. This change results in detachment of the dislocation from a point defect, and motion under existing internal stresses. The total energy in the system remains essentially unchanged, although the interaction energy can even change sign. A similar rationale lies at the root of the theoretical interpretation of an entire group of magnetically sensitive phenomena.[20] The corresponding theory has been developed in greatest detail to describe the magnetic effect on the rate of chemical reactions.[21]

All such effects are due to the spin selectivity of certain transitions or reactions. For example, the process proceeds only from the singlet state of the spin system, being forbidden in the triplet state. In this case the evolution of the system in a magnetic field from the triplet state to the singlet state ($T_0 - S$ transition) completely determines the kinemat-

ics of the magnetic effect on the process. The most important mechanisms of T_0-S transitions are considered to be the Δg mechanism and paramagnetic phase relaxation.[21]

The first mechanism arises if the Larmor precession frequencies of interacting spins in a magnetic field are different (for example, as a result of a small difference in the corresponding Landé g factors). As a result, in the course of precession, the spins must periodically be antiparallel, which corresponds to a T_0-S transition. The frequency of such transitions is obviously linear in the magnetic field, and should equal $\nu_{\Delta g}\sim 10^7$ s^{-1} for $B\sim 1$ T and $\Delta g\sim 10^{-3}$.

The second mechanism, determined by stepwise relaxation (decay) of the precession of the spin magnetization components perpendicular to the magnetic field yields a T_0-S transition when the spins are aligned parallel (or antiparallel) to the magnetic induction B. This process is ordinarily much slower than the Δg effect (for reasonable values of the parameters — by several orders of magnitude). It is important that the corresponding phase relaxation time be proportional to B^{-2}.

It is now considered to be well established that the Δg mechanism plays the main role in the magnetic sensitivity of chemical reactions. On the other hand, considering the fact that according to our data the detachment time τ_{dp} of a dislocation from a paramagnetic stopper at $B\sim 1$ T is of the order of 10^{-4} s and is proportional to B^{-2}, we are inclined to assume that the magnetoplastic effect is limited by paramagnetic phase relaxation.

Definite predictions follow from the proposed physical model of the magnetoplastic effect. Specifically, no process of the type being considered is impossible when the required spin evolution time τ is much longer than the average spin–lattice relaxation time τ_{sl} and thermal fluctuations in the system actively mix the spin states. Under the present conditions $\tau\sim\tau_{dp}\propto B^{-2}$, so there should exist a threshold magnetic field B_c below which the magnetoplastic effect vanishes. On the other hand, for $B>B_c$ the temperature dependence of the effect should be very weak. In recent work[11] we observed such a threshold field. The new method for determining the spin–lattice relaxation time in the dislocation–paramagnetic center system gives $\tau_{sl}\cong\tau_{dp}(B_c)$.

Another consequence of the model under consideration should be the existence of a critical rotation frequency ν_c of a sample in a magnetic field, above which the mean free path l of dislocations decreases sharply. Indeed, in order for the mechanism under discussion to operate in a rotating crystal, the change $\Delta\varphi=2\pi\nu\tau_{dp}$ in the orientation of the magnetic field with respect to the crystal over the spin evolution time $\tau\sim\tau_{dp}$ should obviously be quite small (for $\nu\gg\nu_c$ the spins simply ''do not know'' the direction in which they should relax).

Such a critical frequency is indeed observed experimentally.[5–10] According to our data

$$\nu_c\tau_{dp}\sim 10^{-2}-10^{-3}.$$

The frequency ν_c depends only on the magnetic field intensity ($\nu_c\propto B^2$) and the type of paramagnetic centers, and it is also different for screw and edge dislocations. Being proportional to the probability of an elementary event consisting of dislocation detachment from a point defect, the frequency ν_c is a fundamental characteristic of the process. Therefore the type of paramagnetic stoppers at a dislocation can be judged according to the position of the step ($\nu=\nu_c$) in the curve $l(\nu)$. The dislocation plays the role of a measuring tool with exemplary sensitivity.

The interaction of dislocations with paramagnetic centers, which consisted of impurity complexes in the crystal, was investigated in Refs. 4–11. It is well known that some defects formed in the crystal during irradiation exhibit paramagnetic properties.[22] Together with impurity paramagnetic centers, they form a spectrum of magnetically sensitive stoppers with which a dislocation interacts in a magnetic field. The method that we proposed in Ref. 3 , based on measurements of the dependence $l(\nu)$ for different irradiation doses, makes it possible to distinguish the contributions of different stoppers in dislocation retardation. As a result of our investigations, we were able to follow the detachment of dislocations from different types of impurity centers that were modified as a result of irradiation.

Our objective in the present work is to study further the effect of preliminary low dose x-ray irradiation on the magnetoplastic effect in NaCl and LiF crystals. We present the results of an experimental investigation of the magnetoplastic effect in irradiated crystals with differing impurity composition. As we shall see, the interaction of screw and edge dislocations with impurity–radiation defects is distinctive.

2. EXPERIMENTAL PROCEDURE

The investigations were performed on three types of NaCl crystals and on LiF crystals: NaCl-1, with yield stress $\tau=150$ kPa and Ca impurity concentration $C_{\mathrm{Ca}}=0.5$ ppm; NaCl-2, with $\tau=500$ kPa and $C_{\mathrm{Ca}}\cong 10$ ppm; NaCl-3 (modification of NaCl-2 crystals with additional Ni impurity), with $\tau=360$ kPa and $C_{\mathrm{Ni}}\cong 0.06$ ppm and LiF, with $\tau=300$ kPa and total impurity concentration 0.5 ppm.

Preannealed $3\times 4\times 7$ mm^3 samples were irradiated in an IRIS-M x-ray apparatus by a Mo source with wavelength $\lambda=0.7$ Å. The tube voltage and current were $U=45$ kV and $I=35$ mA, respectively, and the irradiation time $t_r=5-30$ s. The irradiation dose acquired by a sample per unit time was approximately 10 rad/s. The experimentally measured coefficient of through transmission of x-rays was 70–80% for the NaCl samples and 60–70% for LiF. Irradiation did not produce any coloring of the samples.

After irradiation, fresh dislocations were introduced into a sample by impact and the sample was positioned in a dc ($B=0.3-0.6$ T) field, or an ac magnetic field produced by rotating the sample at frequency $\nu=0-200$ Hz in a constant magnetic field. The magnetic treatment time varied over the range $t_m=5-40$ min. The crystals were held in the magnetic field in the dark in order to prevent de-excitation of the radiation defects. In experiments on the decay of radiation defects, an irradiated sample was de-excited under a tungsten incandescent lamp in a time $t_l=15-300$ min, after which dislocations were introduced into the sample and the sample was placed in a magnetic field.

The initial and final positions of the dislocations were determined by selective chemical etching. In the course of

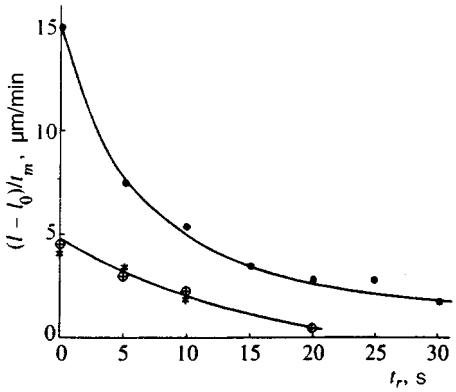

FIG. 1. Effective dislocation velocity $(l-l_0)/t_m$ versus sample irradiation time t_r; $B=0.5$ T, ● — NaCl-1, * — LiF (edge dislocations), ⊕ — LiF (screw dislocations).

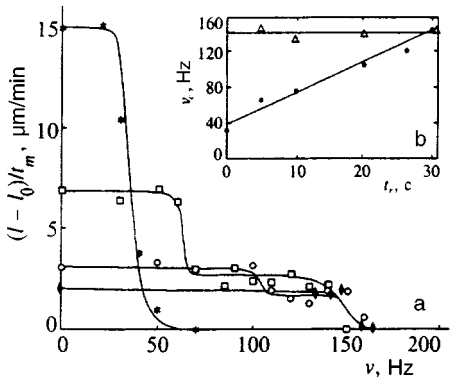

FIG. 2. a — Effective dislocation velocity $(l-l_0)/t_m$ versus sample rotation frequency ν in a magnetic field in NaCl-1 crystals for different irradiation times t_r; $B=0.5$ T, * — $t_r=0$, □ — $t_r=5$ s, ○ — $t_r=20$ s, ◆ — $t_r=30$ s. b — Critical frequencies ν_{c1} (●) and ν_{c2} (△)in NaCl-1 crystals versus the irradiation time t_r; $B=0.5$ T.

control experiments, the mean free path of dislocations on different faces of the sample was recorded. It was found to be approximately the same on the front (closest to the radiation source), back, and lateral surfaces of the crystal. Since it was impossible to construct representative histograms for screw dislocations in NaCl, in these crystals observations were performed only on edge dislocations. In LiF crystals, all dependences were obtained for both edge and screw dislocations.

The investigations of the transmission spectra of the irradiated samples were performed with an IFS-113v Fourier spectrometer in the IR ($\lambda=2-25$ μm), and with a Hitachi spectrometer in the visible ($\lambda=364-2500$ nm) and UV ($\lambda=185-360$ nm).

3. EXPERIMENTAL RESULTS

The optical investigations performed on the samples over a wide range of wavelengths (from IR to UV) showed that the apparatus was insensitive to the low irradiation doses that we employed. The absorption bands corresponding to *F*-centers and an increase in the transmission (by 5–20%) in the IR could be observed only by increasing the irradiation dose for the sample by two orders of magnitude (up to 10^4 rad). However, the magnetoplastic effect was found to be sensitive to small structural changes caused by irradiation doses of the order of 10^2 rad.

Our investigations showed that a linear growth of the mean dislocation free path l with magnetic treatment time t_m and the squared magnetic induction remains in the irradiated crystals: $l=l_0+kB^2t_m$, where l_0 is the background free path value, which also exists at $B=0$ and is associated with the etching out of near-surface stoppers.[23] The coefficient of proportionality k decreases monotonically with increasing irradiation dose; this is shown in Fig. 1, where the curves of the effective dislocation velocity $V=(l-l_0)/t_m=kB^2$ versus the irradiation time t_r with a fixed magnetic field $B=0.5$ T are constructed for NaCl-1 and LiF crystals. Such dependences reflect a gradual change in the spectrum of point defects under irradiation, but yield no information about the possible types of point defects.

As we have already noted, according to Ref. 3 such information is best obtained from measurements of the mean free path l in samples rotating in a magnetic field as a function of the rotation frequency ν. Such measurements, which were performed on all types of crystals indicated above, showed that x-ray irradiation of samples, even for several seconds, radically changes the dependence $l(\nu)$. Figure 2a displays the effective velocity $V=(l-l_0)/t_m$ versus the frequency ν for unirradiated and irradiated NaCl-1 crystals. As one can see from the figure, irradiation not only decreases the path length, but it also converts the one-step curve $V(\nu)$ into a two-step curve. The appearance of a second step indicates irradiation-induced production of a new, magnetically active, type of stopper. It is important that the first and second steps react differently to an increase in dose. It is shown in Fig. 2 that increasing the irradiation time for NaCl-1 crystals from $t_r=5$ s to $t_r=30$ s has no effect on the position of the second critical frequency $\nu_{c2}\approx 150$ Hz with $B=0.5$ T. At the same time, as the irradiation dose increases, the first step gradually expands and the critical frequency ν_{c1} corresponding to this step increases, reaching $\nu_{c1}\approx\nu_{c2}$ at $t_r=30$ s (Fig. 2a, b). A similar picture is observed in NaCl-2 crystals.

The situation is somewhat different in NaCl-3 crystals. According to Refs. 9 and 10 , even unirradiated, these crystals are much more magnetically sensitive than NaCl-2. The magnetoplastic effect in them, under otherwise identical conditions, is characterized by higher relative densities of mobile dislocations, larger dislocation travel distances, and a shorter delay time on paramagnetic stoppers, i.e. a higher critical frequency (by approximately a factor of 6–7). This is probably due to the alignment of Ni atoms in Ca complexes that occurs during the growth of the NaCl crystal, which can intensify the magnetic properties of the complexes, as well as changing their characteristic size (and hence their concentration).

In irradiated NaCl-3 crystals, two steps also appear in the curve $V(\nu)$ (Fig. 3). But this time, not only the second but also the first critical frequency are insensitive to the irradiation dose, i.e. $\nu_{c1}=\nu_c$ (Fig. 3a). It is significant that the

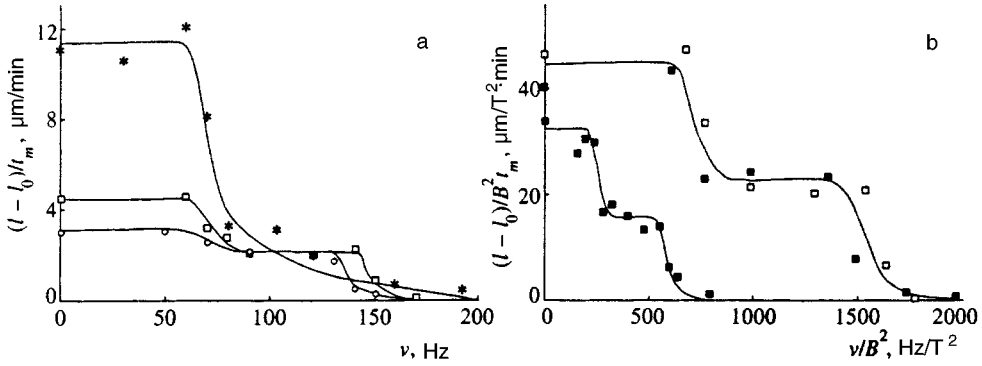

FIG. 3. a) Effective dislocation velocity $(l-l_0)/t_m$ versus sample rotation frequency ν in a magnetic field in NaCl-3 crystals for different irradiation times t_r; $B=0.3$ T. * — $t_r=0$, □ — $t_r=5$ s, ○ — $t_r=20$ s. b) Frequency dependence of the effective dislocation velocity, normalized to the squared magnetic field, in NaCl-2 and NaCl-3 crystals; $t_r=5$ s, ⊠ — NaCl-2, $B=0.2$ T; ■ — NaCl-3, $B=0.2$ T; □ — NaCl-3, $B=0.3$ T.

frequency ν_{c1} for NaCl-3 is essentially identical to the frequency ν_{c2} for NaCl-2 (Fig. 3b) and NaCl-1. The second critical frequency ν_{c2} for NaCl-3 is almost three times the first, and has no analog in NaCl-1 and NaCl-2 crystals. Therefore the spectrum of paramagnetic stoppers in NaCl is very sensitive to small additions of Ni impurity.

To study the effect of different types of dislocations on the interaction of the dislocations with magnetically sensitive stoppers, the magnetoplastic effect was investigated in LiF crystals, for which it is possible to construct complete histograms of the travel distances for both edge and screw dislocations. In the case of edge dislocations, a number of general laws typical for NaCl are observed in the irradiated LiF crystals ($t_r=5$ s): $V(\nu)$ is a two-step curve, and the critical frequencies satisfy $\nu_c<\nu_{c1}<\nu_{c2}$ (Fig. 4a). The second critical frequency does not change as the irradiation dose increases (just as in the case of NaCl) and is $\nu_{c2}\cong 115$ Hz for $B=0.5$ T. The first critical frequency is essentially identical for irradiation times of 5 and 10 s ($\nu_{c1}=55$ Hz), but increasing the irradiation time to $t_r=20$ s increases ν_{c1} to approximately 85 Hz. Unfortunately, measurements were not performed for $t_r>20$ s, since as one can see from Fig. 1, as the irradiation dose increases further, the dislocation travel distances in these crystals essentially decrease to the background values.

In LiF, screw dislocations react to irradiation completely differently (Fig. 4b): $V(\nu)$ remains a single-step curve, in the irradiated crystals the critical frequency ν_{c1} is less than ν_c, and no appreciable sensitivity of ν_{c1} to the irradiation dose is observed over the experimental range of irradiation times $t_r=5-20$ s, i.e. the entire dynamics of the transition from ν_c to ν_{c1} is played out at doses corresponding to $t_r<5$ s.

Experiments on the de-excitation of radiation-induced defects were conducted on NaCl-1 and LiF crystals. Irradiated samples of NaCl-1 were illuminated with a tungsten lamp for $t_r=5$ s (Ref. 3) and $t_r=20$ s (Fig. 5). Qualitatively the same pattern of decay of the radiation defects is observed in both cases. Initially, illumination causes the second step to vanish, and the first step has a very long ''tail'' whose center lies between ν_c and ν_{c1}. Further illumination of the samples restores the critical frequency ν_c corresponding to the unirradiated crystal. In the NaCl-1 samples irradiated for $t_r=5$ s, complete restoration of ν_c occurs over a de-excitation time $t_l=60$ min.[3] After irradiation for 20 seconds, the critical frequency is restored over a time $t_l=300$ min (Fig. 5). It was noted that in both cases, the travel distance of dislocations on the plateau (for $\nu<\nu_c$) does not return to the level corresponding to the travel distance in the unirradiated crystals, remaining approximately half the initial value. The maximum travel distance of dislocations on the plateau is reached long before the critical frequency is restored, and a further increase in the de-excitation time has essentially no effect on it.

Experiments on the de-excitation of irradiated LiF crystals (with $t_r=5$ s) show that in contrast to NaCl, illumination with light from a tungsten lamp for one hour is inadequate for de-excitation of all magnetically sensitive radiation defects (Fig. 6). The critical frequency of the unirradiated crystal is restored for edge (Fig. 6a) and screw (Fig. 6b) dislocations only if the de-excitation time increases to $t_l=120$ min. It is significant that for both edge and screw dislocations, continuation of illumination of the crystal (up to $t_l=180$ min) restores not only the step width but also the initial mean free path l for $\nu<\nu_c$. Recall that in NaCl-1, under the

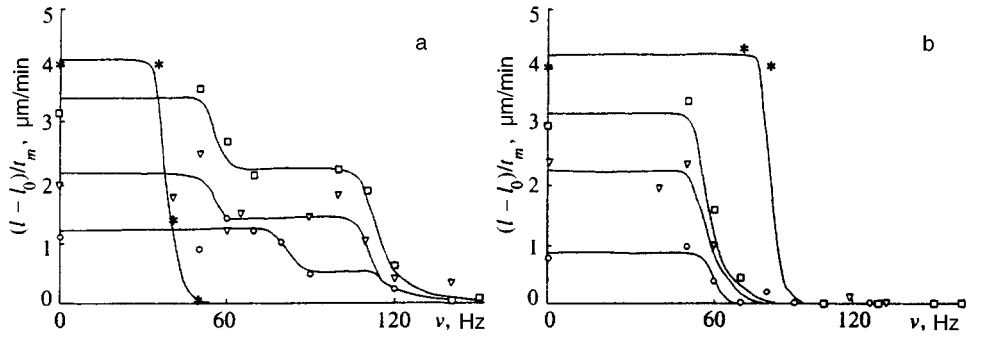

FIG. 4. Effective dislocation velocity $(l-l_0)/t_m$ versus sample rotation frequency ν in LiF crystals in a magnetic field for various irradiation times t_r; $B=0.5$ T,* — $t_r=0$, □ — $t_r=5$ s; ∇ — $t_r=10$ s; ○ — $t_r=20$ s; a) edge dislocations; b) screw dislocations.

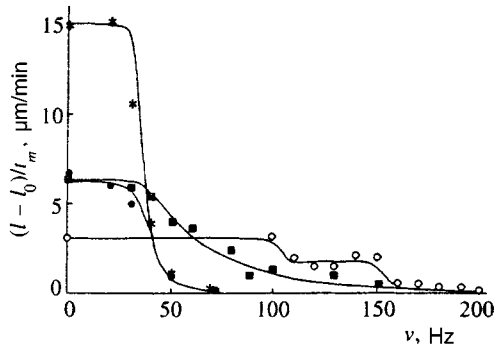

FIG. 5. Effective dislocation velocity $(l-l_0)/t_m$ versus sample rotational frequency ν in irradiated NaCl-1 crystals in a magnetic field for various de-excitation times t_l; $B=0.5$ T, *—$t_r=0$, $t_l=0$; ○ — $t_r=20$ s, $t_l=0$; ⊠ — $t_r=20$ s, $t_l=60$ min; ● — $t_r=20$ s, $t_l=300$ min.

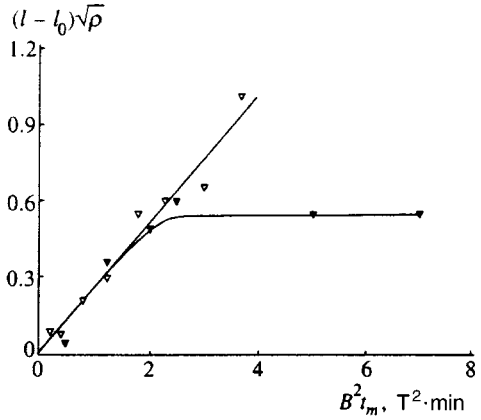

FIG. 7. Average dislocation travel distance, normalized to the density of dislocations in a forest, versus B^2t_m in NaCl-1 crystals: $t_r=10$ s; ∇ — $\nu<\nu_{c1}$, ▼ — $\nu_{c1}<\nu<\nu_{c2}$.

present illumination conditions, the mean free path of dislocations after de-excitation did not exceed half its value in the unirradiated crystal (Fig. 5).

4. DISCUSSION

The frequency dependence of the dislocation travel distances in irradiated samples rotating in a magnetic field is indeed a very sensitive indicator of weak radiation effects on a crystal. Experiments with edge dislocations are yet more informative. In any case, a second step is not formed in the curves $V(\nu)$ (Fig. 4b and 6b) for screw dislocations in irradiated LiF crystals. If it is assumed that each step corresponds to a particular type of stopper that pins dislocations, then the two-step curves $V(\nu)$ measured for edge dislocations in all experimental crystals attest to irradiation-induced generation of pinning centers (''transparent'' in LiF for screw dislocations).

We now discuss the kinematics of the dislocation motion in a way that admits the appearance of a second step in the curve $V(\nu)$ after irradiation. We note that the fresh dislocations introduced into the unirradiated crystal, and on which all measurements were performed, stop only at locations where long-range stresses are too weak to detach dislocations from impurity complexes. As follows from Refs. 5–10, in these crystals, for $\nu_c<\nu$, the spin-dependent transitions in impurity complexes, which pin dislocations, cease, and the dislocation motion ceases with them. Fresh dislocations in the irradiated crystals can also stop in more highly stressed locations, since they are pinned together with the impurity complexes, by new radiation defects. For $\nu_{c1}<\nu<\nu_{c2}$ only the new stoppers are ''turned off'' in a magnetic field. This is sufficient for depinning of some dislocations from the most stressed locations in the crystal. As the dislocations move, the distribution of long-range stresses changes, which can result in other dislocations being entrained into the motion as well. In this manner, a second plateau appears in the curve $V(\nu)$. Only for $\nu>\nu_{c2}$ are all magnetic depinning effects eliminated, and dislocation motion stops.

If the proposed scheme is correct, then it can be expected that for $\nu_{c1}<\nu<\nu_{c2}$ the saturation travel distance (for large values of B and t_m), corresponding to relaxation not of an entire dislocation structure but only some dislocations which started from the most stressed locations, should be much less than the average dislocation travel distance for $\nu<\nu_{c1}$ (for the same values of B^2t_m), whereupon essentially all freshly introduced dislocations participate in the motion. This behavior of the dislocations is demonstrated in Fig. 7, which displays the mean free path versus B^2t_m, measured for a NaCl-1 crystal for the two cases mentioned and normalized to the average distance $1/\sqrt{\rho}$ between dislocations in a ''forest'' (ρ is their density). This is also reflected in the experimental histograms of the dislocation travel distances, which for otherwise identical parameters are much wider on

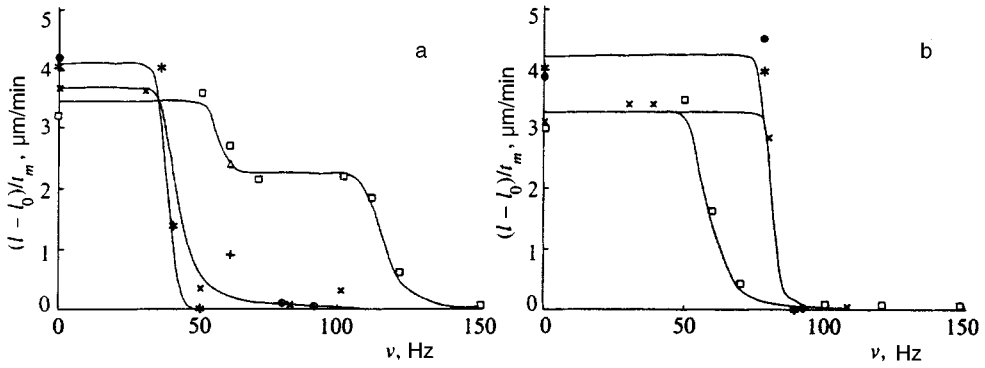

FIG. 6. Effective dislocation velocity $(l-l_0)/t_m$ versus sample rotation frequency ν in LiF crystals in a magnetic field for different de-excitation times t_l; $B=0.5$ T, *—$t_r=0$, $t_l=0$. a) Edge dislocations, $t_r=5$ s: □ — $t_l=0$; △ — $t_l=30$ min; + — $t_l=60$ min; × — $t_l=120$ min; b) screw dislocations, $t_r=5$ s: □ — $t_l=0$; × — $t_l=120$ min; ⊗ — $t_l=180$ min.

the first than on the second plateau of the curve $l(\nu)$.

The nature of the new type of stopper arising under irradiation cannot be unequivocally interpreted solely on the basis of the experimental data presented above. However, the information accumulated thus far about the formation of radiation defects in alkali-halide crystals under low irradiation doses suggests a number of plausible conjectures explaining the measurement results presented above.

It is well known[24] that rare-earth and alkaline-earth metal impurities, which have a low second ionization potential, form complicated radiation defects under the action of irradiation — Z-centers, which contain, besides an impurity ion, a cationic vacancy and a F-center. According to Ref. 25, as a result of irradiation of alkali-halide crystals containing such impurities, the complex consisting of Me^{2+} and a cationic vacancy $[C]^-$ can be restructured, and a Z-center and interstitial halogen molecule Hal_2^0 form in the process:

$$Me^{2+}[C]^- \rightarrow Me^+ + Hal^0 + [C]^- + [A]^+ \rightarrow Me^+ + [C]^- + [Hal_2^- + [A]^+ \rightarrow Me^+ + [C]^- + \text{F-center} + Hal_2^0,$$

where $[A]^+$ is an anionic vacancy. Ca and Mg, being the main impurities in NaCl-1, 2 and LiF crystals, respectively, are such centers. In contrast to Ca and Mg atoms, Ni impurity in NaCl-3 has quite a high second ionization potential, and ordinarily does not form a Z-center. It is also well known that the formation of F-centers at low irradiation doses is suppressed in crystals with Ni impurity.[26,27] The Ni impurity plays the role of an electron trap, i.e., the valence state of Ni changes under irradiation:[26–30]

$$Ni^{2+} \rightarrow Ni^+ \rightarrow Ni^0. \quad (1)$$

It is natural to conjecture that in the experimental NaCl-1, 2 and LiF crystals, stoppers of the new type, which are responsible for the second step in the curve $l(\nu)$, are Z-centers formed on isolated impurity atoms. In the ordinary state, these obstacles are too weak for dislocation motion, as compared with impurity complexes. Under irradiation, the latter complexes also gradually become ''packed'' with Z-centers; this is reflected in an expansion of the first step ($\nu_{c1} \rightarrow \nu_{c2}$), which ultimately results in merging of this step with the second step (Fig. 2a, b).

In NaCl-3 crystals, the first step is characterized, even in the initial state (prior to irradiation), by a critical frequency ν_{c1} that is approximately equal to the frequency ν_{c2} for NaCl-2 (Fig. 3b) and NaCl-1 crystals. We are not prepared to discuss now the mechanism of such a strong ''catalytic'' effect of Ni atoms on the state of Ca complexes, in which the Ni atoms are probably present. It can only be stated that its result is equivalent to the longest irradiation of NaCl-1 crystals in our experiments ($t_r = 30$ s). At the same time, it is obvious that Z-centers formed on isolated Ca-atoms by irradiation of NaCl-3 crystals cannot be manifested as a separate step, because the critical frequency corresponding to them is essentially identical to the frequency of radiation-resistant impurity complexes. The second step in the curve $l(\nu)$ in NaCl-3 crystals is probably due to isolated Ni impurity atoms whose valence changes under irradiation.

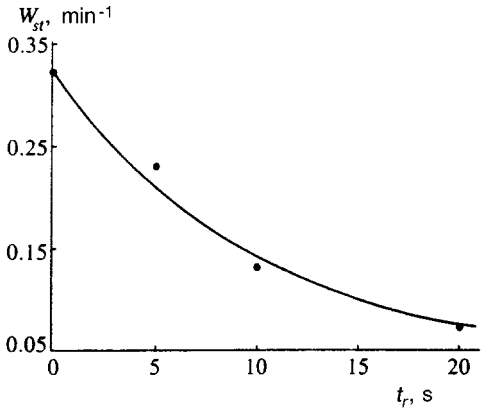

FIG. 8. Dislocation start probability W_{st} in NaCl-1 crystals versus sample irradiation time t_r.

Note for edge dislocations formed under irradiation, the new stoppers and the old complexes whose state changes are characterized by an increase in critical frequency, i.e., a decrease in the delay time on a stopper compared with the initial time. For screw dislocations in LiF, we observed exactly the opposite trend: under irradiation, the critical frequency decreases, together with the probability of detachment of a dislocation from a paramagnetic complex (Fig. 4b).

Despite the decrease in the delay time of edge dislocations on individual paramagnetic stoppers in irradiated crystals, the average velocity of the dislocations $V = (l - l_0)/t_m$ decreases as the irradiation dose increases (see Fig. 1). There is nothing paradoxical in this: first, additional paramagnetic centers appear and are responsible for the second step in the curve $V(\nu)$, and second, magnetically insensitive radiation defects, which slow the dislocation motion, also form under irradiation. This is especially clear in Fig. 4b, which refers to screw dislocations, where as the irradiation dose increases from 5 to 20 s, ν_{c1} remains unchanged and the velocity on the plateau ($\nu_c < \nu_{c1}$) decreases by a factor of 3. The same magnetically insensitive defects, which were not de-excited for our crystal illumination times, are responsible in NaCl-1 (Fig. 5) for the incomplete restoration of the height of the first step, in contrast to its width.

One of the quantitative characteristics directly associated with the density of such defects is the dislocation start probability W_{st},[5,7] which can be obtained from the experimental data on the dependence of the mobile dislocation density ρ_m in irradiated crystals on the magnetic treatment time t_m on the basis of the simple formula[5] $\rho_m/\rho_0 = 1 - \exp(-W_{st}t_m)$, where ρ_0 is the density of freshly introduced dislocations. The quantity W_{st} is inversely proportional to the characteristic time t_{st} up to detachment of a dislocation from nonmagnetic stoppers after it is depinned from paramagnetic centers. In Fig. 8 one can see that the dislocation start probability was four times lower in NaCl-1 crystals irradiated for 20 s than in the unirradiated sample.

In summary, our experimental investigations showed that the magnetoplastic effect can be used to distinguish the contribution of different types of stoppers, both newly formed and altered as a result of irradiation, to dislocation

retardation, and to follow the main stages in the changes of the state of stoppers as the irradiation dose increases or in the course of de-excitation of irradiated samples. The investigations demonstrated that the magnetoplastic effect is uniquely sensitive to low irradiation doses.

We thank V. L. Indenbom, A. A. Urusovskaya, and A. V. Shul'diner for useful discussions of the results, V. P. Kisel', E. B. Rudneva, I. L. Smol'skiĭ, and V. M. Chernov for technical assistance, and L. M. Soĭfer for providing the LiF crystals. This work was supported in part by the Russian Fund for Fundamental Research, Grant No. 95-02-03920-a.

[1)]Unfortunately, as a result of a misunderstanding, the irradiation dose indicated in Ref. 3 is an order of magnitude higher than that employed in the experiment.

[1] N. Itoh, Adv. Phys. **31**, 491 (1982).
[2] Ch. B. Lushik and A. Ch. Lushik, *Decay of Electronic Excitations with Formation of Defects in Solids* [in Russian], Nauka, Moscow (1989), p. 263.
[3] V. I. Al'shits, E. V. Darinskaya, and O. L. Kazakova, JETP Lett. **62**, 375 (1995).
[4] V. I. Al'shits, E. V. Darinskaya, T. M. Perekalina, and A. A. Urusovskaya, Fiz. Tverd. Tela (Leningrad) **29**, 467 (1987) [Sov. Phys. Solid State **29**, 265 (1987)].
[5] V. I. Al'shits, E. V. Darinskaya, and E. A. Petrzhik, Fiz. Tverd. Tela (Leningrad) **33**, 3001 (1990) [Sov. Phys. Solid State **33**, 1694 (1990)].
[6] V. I. Al'shits, R. Voska, E. V. Darinskaya, and E. A. Petrzhik, Fiz. Tverd. Tela (St. Petersburg) **35**, 70 (1993) [Phys. Solid State **35**, 37 (1993)].
[7] V. I. Al'shits, E. V. Darinskaya, and E. A. Petrzhik, Fiz. Tverd. Tela (St. Petersburg) **35**, 320 (1993) [Phys. Solid State **35**, 162 (1993)].
[8] V. I. Al'shits, E. V. Darinskaya, and E. A. Petrzhik, Mat. Sci. Eng. A **164**, 322 (1993).
[9] V. I. Al'shits, E. V. Darinskaya, O. L. Kazakova *et al.*, Izv. Ross. Akad. Nauk, Ser. Fiz. **57**, 2 (1993).
[10] V. I. Al'shits, E. V. Darinskaya, O. L. Kazakova *et al.*, J. Alloys and Compounds **211/212**, 548 (1994).
[11] V. I. Al'shits, E. V. Darinskaya, O. L. Kazakova *et al.*, JETP Lett. **63**, 668 (1996).
[12] Yu. I. Golovin and R. B. Morgunov, JETP Lett. **58**, 191 (1993).
[13] Yu. I. Golovin and R. B. Morgunov, Fiz. Tverd. Tela (St. Petersburg) **35**, 2581 (1993) [Phys. Solid State **35**, 1280 (1993)].
[14] Yu. I. Golovin and R. B. Morgunov, Fiz. Tverd. Tela (St. Petersburg) **37**, 1239, 1352, 2118 (1995) [Phys. Solid State **37**, 674, 734, 1152 (1995)].
[15] Yu. I. Golovin and R. B. Morgunov, JETP Lett. **61**, 596 (1995).
[16] Yu. I. Golovin, R. B. Morgunov, and A. V. Turunnik, Phys. Status Solidi B **189**, 1 (1995).
[17] M. I. Molotskiĭ, Fiz. Tverd. Tela (Leningrad) **33**, 3112 (1991) [Sov. Phys. Solid State **33**, 1760 (1991)].
[18] M. I. Molotskiĭ, Fiz. Tverd. Tela (St. Petersburg) **35**, 11 (1993) [Phys. Solid State **35**, 5 (1993)].
[19] M. I. Molotskiĭ, R. E. Kris, and V. Flerov, Phys. Rev. B **151**, 12531 (1995).
[20] Ya. B. Zel'dovich, A. L. Buchachenko, and E. L. Frankevich, Usp. Fiz. Nauk **155**, 3 (1988) [Sov. Phys. Usp. **31**, 385 (1988)].
[21] A.L. Buchachenko, R. Z. Sagdeev, and K. Z. Sadikov, *Magnetic Spin Effects in Chemical Reactions* [in Russian], Nauka, Novosibirsk (1978), p. 296.
[22] L. F. Mollenauer, S. Pan, and J. Winnacker, Phys. Rev. Lett. **26**, 1643 (1971).
[23] V. B. Pariĭskiĭ, A. I. Landau, and V. I. Startsev, Fiz. Tverd. Tela (Leningrad) **5**, 1377 (1963) [Sov. Phys. Solid State **5**, 1002 (1963)].
[24] S. Radhakrishna and B. V. R. Crowdari, Phys. Status Solidi A **14**, 11 (1972).
[25] J. H. Crawford and C. M. Nelson, Phys. Rev. Lett. **5**, 314 (1960).
[26] W. Haeys, J. Appl. Phys. **33**, 329 (1962).
[27] W. Haeys and J. Wilkens, Proc. Roy. Soc. A **281**, 340 (1964).
[28] M. L. Kats and V. Z. Semenov, Opt. Spektrosk. **4**, 637 (1958).
[29] I. A. Parfianovich, Opt. Spektrosk. **6**, 189 (1959).
[30] M. L. Kats, *Luminescence and Electron–Hole Processes in Photochemical Crystals of Alkali–Halide Compounds* [in Russian], Saratov University Press, Saratov (1960), p. 109.

Translated by M. E. Alferieff

Triangular antiferromagnets with a layered structure in a uniform field

R. S. Gekht and I. N. Bondarenko

L. V. Kirenskiĭ Institute of Physics, Siberian Branch of Russian Academy of Sciences, 660036 Krasnoyarsk, Russia

(Submitted 24 April 1996)
Zh. Éksp. Teor. Fiz. **111**, 627–643 (February 1997)

We study the magnetic states and phase transitions in layered triangular antiferromagnets and show that in compounds of the VBr_2 (or VCl_2) type the quantum effects alter the structure of the ground state and initiate a series of transitions as the magnetic field strength is increased. We establish that planar structures with different spin configurations are realized when the magnetic field strength is far from the saturation value, while a nonplanar structure of the umbrella type is realized in fields close to the saturation value. Finally, we build the phase diagram of the ground state and indicate a finite range of field strengths where a collinear phase is possible, too. © *1997 American Institute of Physics.* [S1063-7761(97)01702-2]

1. INTRODUCTION

Spin systems on triangular lattices are currently being widely studied.[1–7] It is well known that because of frustration effects, even systems with an exceptionally simple basic interaction exhibit a broad range of phases and phase transitions. In BX_2 compounds of halogen with $3d$-transition metals having a CdI_2 crystal structure (space group $P\bar{3}m1$), the magnetic ions lie in triangular layers perpendicular to the c axis, with the layers forming a hexagonal lattice along the c axis.[8] According to neutron-diffraction data,[9,10] in substances like VX_2 (X=Br,Cl) the interactions within and between the layers are antiferromagnetic. Below transition temperatures $T_N<40$ K the spins in a layer form a 120-degree structure, which remains unchanged down to extremely low temperatures.[11,12,6] The VX_2 systems can be described by Heisenberg spins: within the accuracy of resonance measurements the gyromagnetic ratio of vanadium ions is isotropic.[13]

A magnetic field applied to frustrated systems leads to many interesting effects (see, e.g., Ref. 14), which can often be explained in a classical manner. However, quantum fluctuations play an important role in systems with nontrivial continuous degeneracy.[5] These fluctuations not only lift the degeneracy but can, as a result of competition with other interactions, change the very nature of the structure.

The goal of the present work is to study the possible structures in compounds of the VBr_2 and VCl_2 type. In ordinary triangular antiferromagnets in an external magnetic field, quantum fluctuations do not alter the state with a nonplanar spin configuration. However, in compounds of the VX_2 type, where neighboring V^{2+} layers are separated by two X^- layers, the interplanar exchange J' is weaker than the intraplanar exchange J by a factor of 100 (see Refs. 9 and 10), with the result that the energy of zero-point vibrations may exceed the energy of the interaction between the layers. Hence the nonplanar state changes to a planar state, with the planar configuration changing as the field strength is increased (four planar phases and one collinear phase are possible in the field-induced phase transitions). The problem we are examining here can be described by the following Hamiltonian:

$$\mathscr{H}=2J\sum_{\langle i,j\rangle n}\mathbf{S}_{in}\cdot\mathbf{S}_{jn}+2J'\sum_{in}\mathbf{S}_{in}\cdot\mathbf{S}_{in+1}-\mu\mathbf{H}\cdot\sum_{in}\mathbf{S}_{in}, \tag{1}$$

where summation with respect to $\langle i,j\rangle$ is over all the nearest pairs in the nth layer; below we assume that the field is applied along the c axis (the z axis).

In purely two-dimension Heisenberg systems ($J'=0$), spin structures with minimum energy satisfy the condition

$$\mathbf{S}_1+\mathbf{S}_2+\mathbf{S}_3=\frac{\mu\mathbf{H}}{6J}, \tag{2}$$

where $\mathbf{S}_i$ is the spin of the ith sublattice. In a spherical system of coordinates ($S^{\pm}=S\sin\theta\exp(\pm i\varphi)$ and $S^z=S\cos\theta$), the solution for the inclination angles in (2) can be expressed as follows:

$$\begin{aligned}
&\cos\theta_3=3h-\cos\theta_2-\cos\theta_1,\\
&\tan\varphi_3=\frac{\sin\theta_1\sin\varphi_1+\sin\theta_2\sin\varphi_2}{\sin\theta_1\cos\varphi_1+\sin\theta_2\cos\varphi_2},\\
&\cos\theta_2=\frac{(3h-\cos\theta_1)/2+R\sin\theta_1\cos(\varphi_1-\varphi_2)}{1-u},
\end{aligned} \tag{3}$$

where

$$h=\frac{\mu H}{18JS},\quad R=\left[\Delta(1-u)-\frac{1}{4}\right]^{1/2},$$

$$\Delta=(9h^2-6h\cos\theta_1+1)^{-1},$$

$$u=\Delta\sin^2\theta_1\sin^2(\varphi_1-\varphi_2).$$

Obviously, a system with a planar or nonplanar spin configuration exhibits nontrivial degeneracy: for $h<1/3$ the angle θ_1 is arbitrary (and so are the angles φ_1 and φ_2), while the angles θ_2 and θ_3 vary in a nonequivalent manner. For $h>1/3$ the arbitrary values of θ_1 are limited to a finite interval: values of θ_1 near π are forbidden, with the forbidden region growing with h until all spins become aligned with the field at $h=1$.

Interplanar interaction and quantum fluctuations lift the continuous degeneracy of the structures. For instance, when

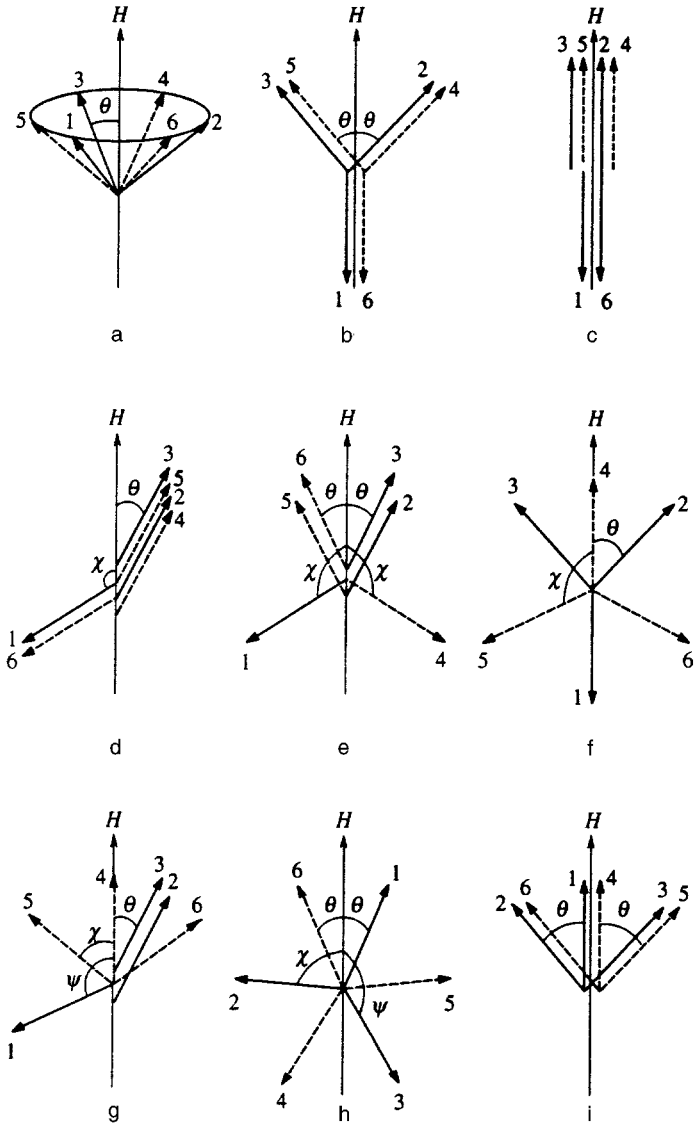

FIG. 1. Spin configurations of triangular antiferromagnets with a layered structure in an external magnetic field **H**: *a* is the nonplanar configuration of the umbrella type; *b*, *d*, *e*, *f*, *g*, *h*, and *i* are planar configurations; and *c* is the collinear phase. The arrows with solid and dashed lines correspond to the directions of spins in two different layer types.

J' is finite, of all the previously possible planar (say, with $\varphi_a = \pm\pi/2$ in (3)) and nonplanar structures those with the lowest energy have field-transverse spin components that form a 120-degree structure. At the same time it is known[15] that, in purely two-dimensional triangular antiferromagnets, of all the possible degenerate states, quantum fluctuations select those with planar spin configurations. Below we show that when J' is small the energy difference between different states is small, too, and can be balanced by quantum effects.

2. SPIN CONFIGURATIONS

In triangular magnetic substances with antiferromagnetic interaction between the layers, the ground state consists of six sublattices. The energy of six-sublattice structures with N spins on the sites can be written for large values of S as

$$\frac{E_0}{N} = J\sum_{\alpha>\beta} \mathbf{S}_\alpha\cdot\mathbf{S}_\beta + \frac{2}{3}\,J'\sum_\alpha \mathbf{S}_\alpha\cdot\mathbf{S}_{\alpha+3} - \frac{1}{6}\,\mu H\sum_\alpha S^z_\alpha. \tag{4}$$

The equations for the equilibrium state,

$$\frac{\partial E_0}{\partial\theta_\alpha} = 0, \quad \frac{\partial E_0}{\partial\varphi_\alpha} = 0, \tag{5}$$

have solutions with planar and nonplanar spin configurations. For the ground state we take nine possible structures: one with a nonplanar configuration, seven with planar configurations, and one collinear state (Fig. 1).

1. A nonplanar configuration of the umbrella type (configuration a in Fig. 1). The inclination angles of the sublattices and the structure's energy are

$$\theta_\alpha = \theta, \quad \varphi_\alpha = \begin{cases} 2(\alpha-1)\pi/3, & \text{if } \alpha = 1, 2, 3, \\ (2\alpha-5)\pi/3, & \text{if } \alpha = 4, 5, 6, \end{cases} \tag{6}$$

$$\frac{E_0}{N} = -(3J+2J')S^2 + (9J+4J')S^2 \times\cos^2\theta - \mu HS\cos\theta. \tag{7}$$

Substituting the equilibrium solution $\cos\theta = H/H_s$, where $H_s = (18J+8J')S/\mu$ is the saturation field, into (7), we arrive at the following expression for $E_0 = E_*$:

$$\frac{E_*}{N}=-(3J+2J')S^2-\frac{1}{2}\ \mu SH_s h^2,\quad h=\frac{H}{H_s}. \tag{8}$$

2. Planar configuration b. In calculating the energy of planar structures we always assume that $\varphi_\alpha=0$ and take θ_α from the interval $(-\pi,\pi)$. Then for b we have $\theta_1=\theta_6=\pi$ and $\theta_2=\theta_4=-\theta_3=-\theta_5=\theta$. The classical energy of this configuration is

$$\frac{E_0}{N}=2\left(J+\frac{J'}{3}\right)(\cos 2\theta-2\cos\theta)S^2 + \frac{1}{3}\mu HS(1-2\cos\theta). \tag{9}$$

The angles of inclination of the sublattices with respect to the field and the minimum energy are given to first order in $j=J'/J(\ll 1)$ by the following expressions:

$$\cos\theta=\frac{\mu H+2(3+j)JS}{4(3+j)JS}, \tag{10}$$

$$E_0=E_*+j(1-h^2)JS^2N. \tag{11}$$

A structure formed by cyclic permutation ($4\to6$, $5\to4$, $6\to5$) of the sublattices in the b configuration in Fig. 1 has the same energy. However, for other possible permutations of sublattices the structure with a configuration of the b type has a higher energy in the interval of angles from 0 to $\pi/3$. For instance, for structures with parallel sublattices 1 and 6, 2 and 5, and 3 and 4 (or 1 and 5, 2 and 4, and 3 and 6) we have

$$E_0=E_*+2(1+h)(1-2h)jJS^2N,$$

while for the structure where 1 and 4, 2 and 6, and 3 and 5 are parallel we have

$$E_0=E_*+2(1+h)^2jJS^2N.$$

The structure with the highest energy in this class of configurations is the one in which the directions of the spins in neighboring layers of the hexagonal lattice coincide: when 1 and 4, 2 and 5, and 3 and 6 are parallel, the difference E_0-E_* is greater than the difference in (11) by a factor of four.

3. Collinear structure c: $\theta_1=\theta_6=\pi$ and $\theta_2=\theta_3=\theta_4=\theta_5=0$. Its energy at large values of S is given by the following relationship:

$$E_0=E_*+\left[(1-3h)^2+\frac{4}{3}\,j(1-2h+3h^2)\right]JS^2N. \tag{12}$$

A similar expression exists for the structure formed by a permutation of the sublattices 6 and 5. The energy of the other structure (permutation of the sublattices 6 and 4) is greater than (12) by $8jJS^2N/3$.

4. Planar configuration d: $\theta_1=\theta_6=\chi$ and $\theta_2=\theta_3=\theta_4=\theta_5=\theta$. The classical energy of the given structure is given by the following relationship:

$$\frac{E_0}{N}=2\left(J+\frac{J'}{3}\right)S^2[1+2\cos(\theta+\chi)] - \frac{1}{3}\ \mu HS(\cos\chi+2\cos\theta). \tag{13}$$

In equilibrium we have $\partial E_0/\partial\theta=0$ and $\partial E_0/\partial\chi=0$, which yield

$$(3+j)\sin(\theta+\chi)-(9+4j)h\sin\theta=0,$$
$$2(3+j)\sin(\theta+\chi)-(9+4j)h\sin\chi=0. \tag{14}$$

The solution of these equations has the form

$$\cos\theta=\frac{3}{4}\ hk+\frac{1}{4hk},\quad \cos\chi=\frac{3}{2}\ hk-\frac{1}{2hk}, \tag{15}$$

where $k=(9+4j)/(9+3j)$. Plugging (15) into (13) and keeping only the linear approximation in j, we arrive at an expression for E_0 coinciding with (11). The given state is degenerate with respect to a permutation of the sublattices 6 and 5. But under a permutation of the sublattices 6 and 4 the difference E_0-E_* increases fourfold.

5. Planar configuration e: $\theta_1=-\theta_4=-\chi$ and $\theta_2=\theta_3=-\theta_5=-\theta_6=\theta$. Its energy is given by the following relationship:

$$\frac{E_0}{N}=2JS^2[1+2\cos(\theta+\chi)]+\frac{2}{3}\ J'(\cos 2\chi+2\cos 2\theta) - \frac{1}{3}\ \mu HS(\cos\chi+2\cos\theta). \tag{16}$$

The equilibrium values of θ and χ can be found from the equations

$$3\sin(\theta+\chi)-(9+4j)h\sin\theta+2j\sin 2\theta=0,$$
$$6\sin(\theta+\chi)-(9+4j)h\sin\theta+2j\sin 2\chi=0, \tag{17}$$

whose solution in the approximation linear in j has the following form:

$$\cos\theta=\frac{3}{4}\ h+\frac{1}{4h}+j\ \frac{(1-h^2)(3h^2-1)}{18h^3},$$
$$\cos\chi=\frac{3}{2}\ h-\frac{1}{2h}+j\ \frac{(1-h^2)(7-3h^2)}{18h^3}. \tag{18}$$

The minimum energy of this configuration is

$$E_0=E_*+\frac{(1-h^2)^2}{2h^2}\ jJS^2N. \tag{19}$$

The other two possible structures in the class of e configurations are degenerate, and their energy

$$E_0=E_*+\frac{(1-h^2)(13h^2-1)}{4h^2}\ jJS^2N$$

is higher either than the energy E_0 in (19) or than the energy of the planar configuration d.

The energy of the structures b, c, d, and e is higher than that of the nonplanar structure a for values of $H<H_s$. On the other hand, comparison of the energies of the planar structures shows that the b configuration has a lower energy if $h<1/3-2j/27$, the tapered d configuration has a lower energy if h lies in the interval $[1/3,1/\sqrt{3}]$, and the e configuration if $h>1/\sqrt{3}$. The collinear structure c for $j\neq0$ has a finite interval of field strengths $(1/3,(1-2j/9)/3)$ in which it is more preferable than the b, d, or e configuration.

6. Planar configuration f (a structure resembling a six-pointed star; Fig. 1f): $\theta_1=\pi$, $\theta_2=-\theta_3=\theta$, $\theta_4=0$, and $\theta_5=-\theta_6=\chi$. In this state the classical energy is

$$\frac{E_0}{N}=JS^2(\cos 2\theta+\cos 2\chi)-\left(2JS^2+\frac{\mu HS}{3}\right)\cos\theta + \left(2JS^2-\frac{\mu HS}{3}\right)\cos\chi-\frac{2}{3}J'S^2 \times[1-2\cos(\theta+\chi)]. \quad (20)$$

Minimizing the energy with respect to the angles θ and χ, we get

$$\cos\theta=\frac{3h+1}{2}-\frac{1}{3}jh, \quad \cos\chi=\frac{3h-1}{2}-\frac{1}{3}jh. \quad (21)$$

As a result the minimum energy of the f configuration for small values of j is given by the following expression:

$$E_0=E_*+j\{1-h^2-[(1-h^2)(1-9h^2)]^{1/2}\}JS^2N. \quad (22)$$

The difference between this energy and the energy of the umbrella structure a is positive for $H>0$, but E_0 of (22) is smaller than the energy (11) of the b configuration and, in contrast with it, coincides at $H=0$ with the energy E_* of the nonplanar structure. In weak fields ($h\ll 1$),

$$E_0\simeq E_*+j(4h^2+8h^4)JS^2N. \quad (23)$$

7. Planar configuration g: $\theta_1=\psi$, $\theta_2=\theta_3=\theta$, $\theta_4=0$, and $\theta_5=-\theta_6=\chi$. Its energy at large values of S is given by the following relationship:

$$\frac{E_0}{N}=2JS^2[\cos\chi+\cos^2\chi+\cos(\theta+\psi)] + \frac{2}{3}J'S^2(\cos\psi+2\cos\chi\cos\theta) - \frac{1}{6}\mu HS(1+\cos\psi+2\cos\theta+2\cos\chi). \quad (24)$$

At $j=0$ the equilibrium solutions for the angles coincide with the respective solutions in (19) and (21). The minimum energy of the g configuration is given by the following expression:

$$E_0=E_*+j\,\frac{(1-h^2)(5h-1)}{2h}\,JS^2N. \quad (25)$$

Note that this configuration is degenerate with respect to variations of the angle between two planes, one containing the spins of the sublattices 1, 2, and 3, and the other the spins of the sublattices 4, 5, and 6.

The other structures formed by permutations of the sublattices 4, 5, and 6 in Fig. 1g have equal energies

$$E_0=E_*+j\,\frac{1-h}{4h}\,[(1+h)(7h+1)+(3h+1) \times\sqrt{3(1+h)(3h-1)}]JS^2N;$$

in the given configuration class this energy is higher than E_0 in (25).

8. Planar configuration h: $\theta_1=-\theta_6=\theta$, $\theta_5=-\theta_2=\chi$, and $\theta_3=-\theta_4=\psi$. The energy of this structure is given by

$$\frac{E_0}{N}=2\left\{JS^2[\cos(\theta+\chi)+\cos(\psi-\theta)+\cos(\chi+\psi)] + \frac{1}{3}J'S^2[2\cos(\theta+\psi)+\cos 2\chi] - \frac{1}{6}\mu HS(\cos\theta+\cos\chi+\cos\psi)\right\}. \quad (26)$$

At $J'=0$ the structure is degenerate with respect to variations of the angle ψ, while the other two angles depend on ψ as follows:

$$\cos\theta=\frac{1}{12}\frac{\mu H}{JS}-\frac{1}{2}\cos\psi+R\sin\psi,$$

$$\sin\theta=-\frac{1}{2}\sin\psi+R\left(\frac{1}{6}\frac{\mu H}{JS}-\cos\psi\right),$$

$$\cos\chi=\frac{1}{12}\frac{\mu H}{JS}-\frac{1}{2}\cos\psi-R\sin\psi,$$

$$\sin\chi=\frac{1}{2}\sin\psi+R\left(\frac{1}{6}\frac{\mu H}{JS}-\cos\psi\right), \quad (27)$$

where

$$R=\left\{\left[\left(\frac{1}{6}\frac{\mu H}{JS}\right)^2-\frac{1}{3}\frac{\mu H}{JS}\cos\psi+1\right]^{-1}-\frac{1}{4}\right\}^{1/2}.$$

For $J'\neq 0$ the minimum energy of the h configuration can be found by varying the energy

$$E_0=E_*+\frac{4}{3}j[1-3h^2+\cos(\theta+\psi)+\cos^2\chi]JS^2N \quad (28)$$

with respect to ψ. Near $h=0$ the equilibrium value ψ_0 is $5\pi/6$, with the result that $\theta_0=\pi/6$ and $\chi_0=\pi/2$. Hence in weak fields

$$E_0\simeq E_*+j(8h^2-12\sqrt{3}h^3)JS^2N. \quad (29)$$

Comparison of (23) and (29) shows that for small values of h the classical energy of the f configuration is lower than its value in a state with the configuration of Fig. 1h (a P-state; see Ref. 16). But because of the minus in front of the term with h^3 in (29) the energy of the given configuration can be lower than that of the f configuration. Indeed, at $h=1/3$ the equilibrium value ψ_0 in (28) is $2\pi/3$, and Eqs. (27) yield $\theta_0=0$ and $\chi_0=\pi/3$. As a result, by comparing (22) and (28) we find that the energy of the h configuration is lower than that of the f configuration by $jJS^2N/3$.

Note that for $h>1/3$ the state in which the sublattices 1 and 6 in Fig. 1h are parallel is not an equilibrium one. Instead the state represented in Fig. 1i, with $\theta\leqslant\pi/2$, can serve as an equilibrium state.

9. Planar configuration i: $\theta_1=\theta_4=0$ and $\theta_3=\theta_5=-\theta_2=-\theta_6=\theta$. Its energy can be written as follows:

$$\frac{E_0}{N}=\frac{2}{3}\ J'S^2-\frac{1}{3}\ \mu HS+\left(4JS^2-\frac{2}{3}\ \mu HS\right)$$
$$\times\cos\ \theta+\left(2J+\frac{4}{3}\ J'\right)S^2\ \cos 2\theta. \tag{30}$$

The equilibrium value of the angle of inclination of the sublattices is

$$\cos\ \theta=\frac{\mu H-6JS}{4(3+2j)JS}, \tag{31}$$

so that for the minimum energy of the i configuration we have

$$E_0=E_*+2(1-h)^2jJS^2N. \tag{32}$$

Rastelli and Tassi[16] found that for $\theta<\pi/2$ the given state (the SF-state, according to their terminology) can be stable in the classical sense in the presence of a finite anisotropy of the easy-axis type.

Note that for $\theta>\pi/2$ the permutation of the sublattices 4 and 6 leads to a configuration that is the reciprocal of the b configuration, with H replaced by $-H$ and an energy coinciding with (11). The structures formed by other sublattice permutations in this class of configurations possess an energy higher than that of the i configuration or of the configuration that is the reciprocal of b.

Thus, for $j\neq 0$ the different structures have different energies and the nonplanar configuration a is the most advantageous one. Nevertheless, we expect that for $j\ll 1$ the quantum corrections will change the fine balance of the total energy in favor of planar structures (at least in fields whose strength is far from that initiating a transition to a homogeneous state).

3. MAGNETIC TRANSITIONS

Let us examine the effect of quantum fluctuations on the ground state of the system in an external field **H**. We transfer to a local system of coordinates (ξ,η,ζ), in which the quantization axis (the z axis) is selected in such a way that it coincides with the direction of the spin,

$$S_{in}^x=-S_{in}^\xi\ \sin\ \varphi_{in}-S_{in}^\eta\ \cos\ \theta_{in}\ \cos\ \varphi_{in}$$
$$+S_{in}^\zeta\ \sin\ \theta_{in}\ \cos\ \varphi_{in},$$
$$S_{in}^y=S_{in}^\xi\ \cos\ \varphi_{in}-S_{in}^\eta\ \cos\ \theta_{in}\ \sin\ \varphi_{in}$$
$$+S_{in}^\zeta\ \sin\ \theta_{in}\ \sin\ \varphi_{in},$$
$$S_{in}^z=S_{in}^\eta\ \sin\ \theta_{in}+S_{in}^\zeta\ \cos\ \theta_{in}, \tag{33}$$

and θ_{in} and φ_{in} coincide with the angles of inclination of the nine sublattices found earlier in the limit of large values of S. To describe the spin deviations from the equilibrium classical states we introduce six types of Bose operators $a_{k\alpha}$:

$$a_{in}=\sqrt{\frac{6}{N}}\sum_k\ a_{k\alpha}\ \exp(i\mathbf{k}\cdot\mathbf{r}_{in}),$$

where the wave vector $\mathbf{k}$ for each sublattice α lies in the first Brillouin zone. Below we limit our discussion to the cubic approximation in a_{in}:

$$S_{in}^\zeta=S-a_{in}^+a_{in},$$
$$S_{in}^\xi+iS_{in}^\eta=\sqrt{2S}\left(1-\frac{a_{in}^+a_{in}}{4S}\right)a_{in},$$
$$S_{in}^\xi-iS_{in}^\eta=\sqrt{2S}\ a_{in}^+\left(1-\frac{a_{in}^+a_{in}}{4S}\right), \tag{34}$$

so that the initial Hamiltonian can be written as

$$\mathscr{H}=E_0+\mathscr{H}^{(1)}+\mathscr{H}^{(2)}+\mathscr{H}^{(3)}. \tag{35}$$

The linear term in $\mathscr{H}$ is given by the following expression:

$$\mathscr{H}^{(1)}=-\frac{S}{2}\ \sqrt{\frac{SN}{3}}\sum_\alpha\ \left(\sum_\beta\ A_{\alpha\beta}(0)-i\ \frac{\mu H}{S}\ \sin\ \theta_\alpha\right)$$
$$\times a_{0\alpha}+\text{H.c.}, \tag{36}$$

where

$$A_{\alpha\beta}(\mathbf{k})=2J_{\alpha\beta}(\mathbf{k})\{\sin\ \theta_\beta\ \sin(\varphi_\alpha-\varphi_\beta)$$
$$+i[\sin\ \theta_\alpha\ \cos\ \theta_\beta-\cos\ \theta_\alpha\ \sin\ \theta_\beta$$
$$\times\cos(\varphi_\alpha-\varphi_\beta)]\}, \tag{37}$$

and $J_{\alpha\beta}(\mathbf{k})$ are the Fourier components of the exchange interaction between the spins belonging to different sublattices:

$$J_{\alpha\beta}(\mathbf{k})=\sum_{m-n}\ J_{m\alpha,n\beta}\ \exp(i\mathbf{k}\cdot\mathbf{r}_{m\alpha,n\beta}).$$

At $\mathbf{k}=0$ we have

$$\sum_\beta\ A_{\alpha\beta}(0)-i\ \frac{\mu H}{S}\ \sin\ \theta_\alpha$$
$$=\frac{6}{NS^2}\left(\frac{1}{\sin\ \theta_\alpha}\frac{\partial E_0}{\partial\varphi_\alpha}+i\ \frac{\partial E_0}{\partial\theta_\alpha}\right),$$

and, as expected, $\mathscr{H}^{(1)}$ vanishes in the case of equilibrium configurations.

In diagonalizing the quadratic term $\mathscr{H}^{(2)}$ we put $j=0$. We then compare the energy of zero-point vibrations of various configurations with the energy of structures with small values of j. The expression for $\mathscr{H}^{(2)}$ is

$$\mathscr{H}^{(2)}=-3JSN+3JS\sum_k\ \alpha_k^+M_k\alpha_k, \tag{38}$$

where $\alpha_k^+=(a_{k_1}^+,a_{k_2}^+,\ldots,a_{k_6}^+,a_{-k_1},a_{-k_2},\ldots,a_{-k_6})$, and

$$M_k=\begin{pmatrix} e(\mathbf{k}) & f(\mathbf{k}) \\ f^*(-\mathbf{k}) & e^*(-\mathbf{k})\end{pmatrix}.$$

The diagonal elements of the 6-by-6 matrices $e(\mathbf{k})$ and $f(\mathbf{k})$ are equal to unity and zero, respectively, and the nonzero off-diagonal elements can be written as

$$e_{\alpha\beta}(\mathbf{k})=e_{\beta\alpha}^*(\mathbf{k})=B_{\alpha\beta}^{(+)}(\mathbf{k}),$$
$$f_{\alpha\beta}(\mathbf{k})=f_{\beta\alpha}^*(\mathbf{k})=B_{\alpha\beta}^{(-)}(\mathbf{k}), \tag{39}$$

where

$$B^{\pm}_{\alpha\beta}=\frac{1}{2}\,\nu_k[(1\pm\cos\,\theta_\alpha\,\cos\,\theta_\beta)\cos(\varphi_\alpha-\varphi_\beta)$$
$$\pm\sin\,\theta_\alpha\,\sin\,\theta_\beta-i(\cos\,\theta_\alpha+\cos\,\theta_\beta)$$
$$\times\sin(\varphi_\alpha-\varphi_\beta)],$$

with

$$\nu_k=\frac{1}{3}\left[\exp(ik_x)+\exp\left(i\,\frac{-k_x+\sqrt{3}k_y}{2}\right)\right.$$
$$\left.+\exp\left(i\,\frac{-k_x-\sqrt{3}k_y}{2}\right)\right], \tag{40}$$

and the subscripts α and β are either 1,2,3 or 4,5,6. The remaining $e_{\alpha,\alpha\pm3}$ and $f_{\alpha,\alpha\pm3}$ matrix elements are zeros.

The spin-wave spectrum in the zero-point vibration energy

$$E^{(2)}=-3JSN+\frac{1}{2}\,S\sum_{k\alpha}\,\omega_\alpha(\mathbf{k}) \tag{41}$$

was found both analytically and numerically. For the nonplanar configuration a this spectrum is given by the following formula ($\varepsilon_\alpha=\omega_\alpha/6J$):

$$\varepsilon_\alpha(\mathbf{k})=\varepsilon_{\alpha+3}(\mathbf{k})=\{(1-\lambda_\alpha(\mathbf{k}))$$
$$\times[1+(2-3h^2)\lambda_\alpha(\mathbf{k})]\}^{1/2}-\sqrt{3}h\mu_\alpha(\mathbf{k}), \tag{42}$$

where

$$\lambda_\alpha(\mathbf{k})=\frac{1}{3}\left\{\cos\left[k_x+\frac{2\pi}{3}\,(\alpha-1)\right]\right.$$
$$\left.+2\cos\left[\frac{k_x}{2}-\frac{2\pi}{3}\,(\alpha-1)\right]\cos\,\frac{\sqrt{3}}{2}\,k_y\right\},$$
$$\mu_\alpha(\mathbf{k})=\frac{1}{3}\left\{\sin\left[k_x+\frac{2\pi}{3}\,(\alpha-1)\right]\right.$$
$$\left.-2\sin\left[\frac{k_x}{2}-\frac{2\pi}{3}\,(\alpha-1)\right]\cos\,\frac{\sqrt{3}}{2}\,k_y\right\}.$$

In a zero field, the frequency spectrum $\varepsilon(\mathbf{k})$, which in this case is the same for all structures, can be found by solving the following equation:

$$\varepsilon^6+3(|\nu_k|^2-1)\varepsilon^4+\frac{3}{4}\,P_k\varepsilon^2+Q_k=0,$$
$$P_k=9|\nu_k|^4+3(\nu_k^3+\nu_k^{*3})+27|\nu_k|^2+4,$$
$$Q_k=\frac{1}{3}\,(\nu_k^3+\nu_k^{*3})(\nu_k^3+\nu_k^{*3}+3|\nu_k|^2-7)$$
$$-\frac{9}{4}\,|\nu_k|^4+\frac{15}{4}\,|\nu_k|^2-1. \tag{43}$$

The positive values of the roots of the polynomial (43) are depicted in Fig. 2. We see that the three surfaces representing ε_α have common intersection points. Threefold degeneracy $\varepsilon^*_\alpha=1$ (as stated in Refs. 17 and 9, $J=16$ K in VBr_2, which corresponds to a frequency $\omega=2.2$ THz) appears at $\mathbf{k}=(2\pi/3,2\pi/3\sqrt{3})$ and at $\mathbf{k}=(0,4\pi/3\sqrt{3})$. The section plane

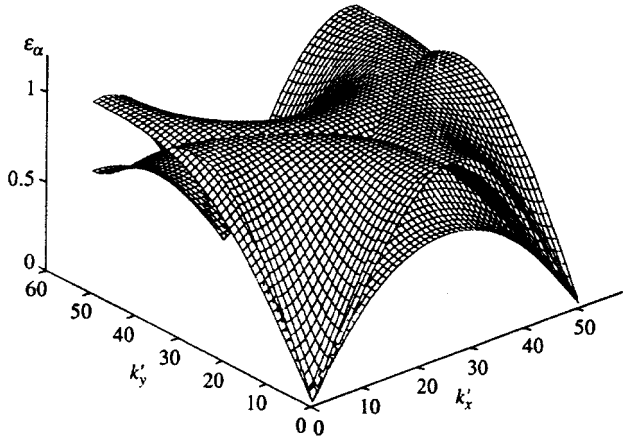

FIG. 2. The energy spectrum $\varepsilon_\alpha(\mathbf{k})$ of spin configurations in a zero magnetic field ($k_x=4\pi\tilde{k}_x/3\times50$ and $k_y=2\pi\tilde{k}_y/50\sqrt{3}$). Here $\varepsilon_\alpha=1$ at $\mathbf{k}=(2\pi/3,2\pi/\sqrt{3})$ and at $\mathbf{k}=(0,4\pi/3\sqrt{3})$.

$k_x=0$ containing the last point of threefold degeneracy also contains the line of intersection of two surfaces.

When there is a magnetic field, the lines of intersection, which are straight lines when $H=0$, become curved. However, the threefold degeneracy of the spectrum is present for the same $\mathbf{k}$'s and for the same value $\varepsilon^*_\alpha=1$. This is true not only for the umbrella configuration but also for all the planar configurations. In Fig. 3 we compare the spectrum $\varepsilon_\alpha=\varepsilon_{\alpha+3}$ ($\alpha=1,2,3$) of the configurations a and b at $H=0.3H_s$. Clearly, everywhere except at the symmetric points of the Brillouin zone the lower branch of the b configuration lies below the corresponding branch of the a configuration. Moreover, within a large range of $\mathbf{k}$'s the second branch of the b configuration also lies below the corresponding branch of the a configuration. Such a situation is observed when the spectra of the umbrella structure are compared with those of other planar structures. Hence one can

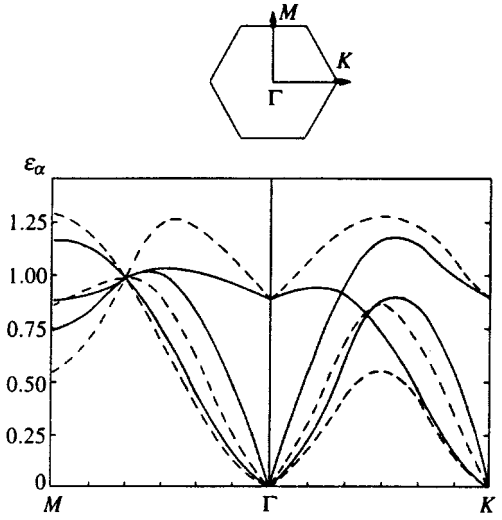

FIG. 3. The energy spectrum $\varepsilon_\alpha(\mathbf{k})$ of configurations a and b in an external field $H=0.3H_s$. The solid curves correspond to the nonplanar configuration a, and the dashed curves to the planar configuration b.

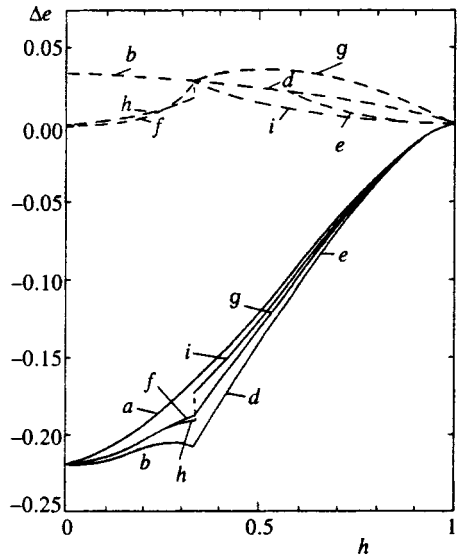

FIG. 4. The quantum corrections to the ground-state energy ($\Delta e=\Delta E/3JSN$) for eight spin configurations (solid curves) and the energy difference of classical structures with respect to the nonplanar configuration a at $jS=0.1$ (dashed curves).

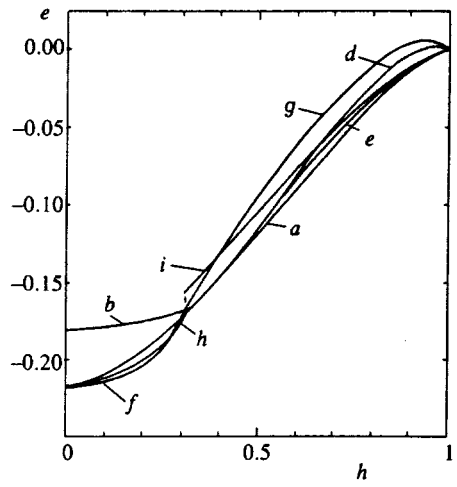

FIG. 5. The total normalized energy $e=E/3JSN$ of the ground state for eight spin configurations at $jS=0.1$. The e vs h dependence was measured with respect to $e_*=E_*/3JSN$ for the nonplanar structure a.

expect that the energy of zero-point vibrations of planar configurations is lower than that of the nonplanar configuration.

Below we calculate the $1/S$-correction to the ground-state energy for the nine configurations considered here. The results depicted in Fig. 4 show that the energy curve for the umbrella structure lies above all such curves for the other structures and that quantum corrections are most important for the b, d, and e configurations. These latter configurations, however, are never realized for $jS>0.082$, no matter how high the applied magnetic field is. Instead, because of the competition between quantum effects and interplanar interaction, in weak and intermediate magnetic fields the stable planar structures are f and h, while in fields close in strength to the saturation field the stable structure is the umbrella one. Note that the possibility of an h structure existing in Heisenberg systems was first pointed out by Rastelli and Tassi.[16] The diagram of the total energy for the various structures at $jS=0.1$ is depicted in Fig. 5. The additional states, b, d, and e, stabilize if $jS<0.082$. As jS decreases, the range where the phases f, h, and a can exist narrows, and in the limit of $jS=0$ such phases simply cannot exist. As Chubukov and Golosov[15] demonstrated, quantum fluctuations in purely two-dimensional triangular antiferromagnets separate structures of the b and d (e) type, and between the true structures the collinear phase is stable in a finite interval of magnetic field strengths.

In a nonzero field, quantum effects and interplanar interaction not only stabilize various classical structures but also modify them. Configurational variations are especially noticeable near the critical field of the transition to the collinear state ($h=1/3$), where the gain in energy due to quantum fluctuations and finite j's is the largest. Let us calculate the quantum corrections to the angles of inclination of equilibrium states. The cubic term in (35) is given by the following relationship:

$$\mathscr{H}^{(3)}=\frac{1}{4}\sqrt{\frac{3S}{N}}\sum_{k_1k_2k_3}\delta(\mathbf{k}_1+\mathbf{k}_2+\mathbf{k}_3)$$
$$\times\left[\sum_{\alpha}\left(\sum_{\beta}A_{\alpha\beta}(0)-i\,\frac{\mu H}{S}\sin\,\theta_\alpha\right)a^+_{k_3\alpha}a_{k_2\alpha}a_{k_1\alpha}\right.$$
$$\left.+4\sum_{\alpha\beta}A_{\alpha\beta}(\mathbf{k}_1)a^+_{-k_3\beta}a_{k_2\beta}a_{k_1\alpha}\right]+\text{H.c.}\qquad(44)$$

We replace two of the three operators in (44) by their expectation values in $\mathscr{H}^{(3)}$ substitute the angles $\theta_\alpha^{(0)}$ and $\varphi_\alpha^{(0)}$ for equilibrium classical configurations. The result is

$$\mathscr{H}^{(3)}=\sqrt{\frac{3S}{N}}\sum_{\alpha\beta}\sum_{k}[A_{\alpha\beta}(\mathbf{k})\langle a^+_{k\beta}a_{k\alpha}\rangle+A^*_{\alpha\beta}(-\mathbf{k})$$
$$\times\langle a^+_{k\beta}a^+_{-k\alpha}\rangle+A_{\beta\alpha}(0)\langle a^+_{k\alpha}a_{k\alpha}\rangle]a_{0\beta}+\text{H.c.}\quad(45)$$

Putting $\mathscr{H}^{(1)}+\mathscr{H}^{(3)}=0$, we arrive at equations for θ_α and φ_α; in the case of planar configurations these equations have the following form:

$$\sum_{\beta}J_{\alpha\beta}(0)\sin(\theta_\alpha-\theta_\beta)-\frac{\mu H}{2S}\sin\,\theta_\alpha$$
$$=\frac{1}{S}\sum_{\beta}I_{\alpha\beta}\sin\,(\theta_\alpha^{(0)}-\theta_\beta^{(0)}),\qquad(46)$$

where

$$I_{\alpha\beta}=\frac{6}{N}\sum_{k}[J_{\alpha\beta}(0)\langle a^+_{k\beta}a_{k\beta}\rangle+J^*_{\alpha\beta}(\mathbf{k})(\langle a^+_{k\alpha}a^+_{-k\beta}\rangle$$
$$-\langle a^+_{k\alpha}a_{k\beta}\rangle)].\qquad(47)$$

From (46) it follows that in the first order in $1/S$ the equations for the inclination angles in the classical setting are replaced by similar equations with renormalized values $\tilde{J}_{\alpha\beta}(0)$:

$$\tilde{J}_{\alpha\beta}(0)=J_{\alpha\beta}(0)-\frac{1}{S}\,I_{\alpha\beta}.\qquad(48)$$

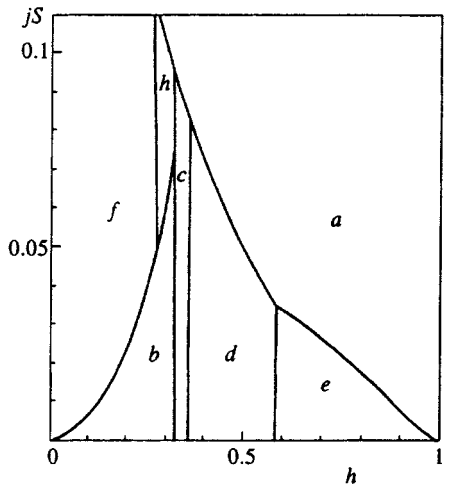

FIG. 6. The $jS-h$ phase diagram of the ground state (the $1/S$-approximation).

The results of calculations for the angle θ in a state with configuration b and for the angles θ and χ in a state with configuration d show that the collinear structure c emerges in the range of field strengths between

$$h_2=\frac{1}{3}-\frac{2}{27}\,j-\frac{0.018}{S} \quad \text{and} \quad h_3=\frac{1}{3}+\frac{0.043}{S}. \tag{49}$$

Clearly, the collinear phase is stabilized both by quantum fluctuations and by interplanar interaction, with the latter broadening the field interval of the given phase only into the region where $h<1/3$. The complete $jS-h$ phase diagram is depicted in Fig. 6. As expected, at $jS=0$ it becomes the phase diagram of a two-dimensional triangular antiferromagnet[15] (the d and e configurations are equivalent if $jS=0$).

Note that in contrast to systems with an anisotropy Δ of the easy-plane type,[5] in purely Heisenberg quasi-two-dimensional ($J'\ll J$) systems the umbrella configuration is not realized when the field is weak, because in such fields the energy difference between the configurations f and a is small and proportional to the second power of h, i.e., $E_0-E_*\sim jh^2JS^2N$, while in systems with easy-plane anisotropy the same difference between the planar and the nonplanar a configurations is finite even for $h=0(E_0-E_*\sim\Delta JS^2N)$. Hence in our case the quantum effects dominate in the weak-field range, and only when the field strength is close to that initiating a transition to the homogeneous state, where the effect of quantum fluctuations is minute but the effect of interplanar exchange coupling is great, does the umbrella structure stabilize.

In compounds of the VX_2 type the V^{2+} ions have an $S=3/2$ spin, and the exchange parameters for, say, VBr_2 are $J=16$ K and $J'=0.2$ K (see Ref. 9), with the result that $jS=0.019$. Thus, a change in structure can be expected at $h_1=0.18$, $h_2=0.31$, $h_3=0.36$, $h_4=0.58$, and $h_5=0.78$ (Fig. 6), which for VBr_2 (with the gyromagnetic ratio equal to two) corresponds to the fields $H_1=58$ T, $H_2=100$ T, $H_3=116$ T, $H_4=187$ T, and $H_5=251$ T. Fields of such magnitude can be achieved by using devices with pulsed fields.[18] At all critical points except h_3 the transition is not continuous. The jump in magnetization in such magnetic transitions is, respectively,

$$\Delta M_1=\frac{1}{3}\,jh_1M_0, \quad \Delta M_2=\frac{1}{9}\,jM_0,$$

$$\Delta M_4=\frac{1}{9}\left(1-\frac{1}{\sqrt{3}}\right)jM_0,$$

$$\Delta M_5=\frac{1}{54}\,\frac{(1-h_5^2)(3h_5^2+5)}{h_5^3}\,jM_0, \tag{50}$$

here where $M_0=\mu S$ is the saturation magnetization. Plugging j, h_1, and h_5 into (50), for VBr_2 we obtain $\Delta M_1/M_0=0.76\times10^{-3}$, $\Delta M_2/M_0=1.4\times10^{-3}$, $\Delta M_4/M_0=0.59\times10^{-3}$, and $\Delta M_5/M_0=1.3\times10^{-3}$.

Note that some compounds of the VX_2 family (such, for instance, as VI_2) exhibit considerable anisotropy of the easy-axis type. In this case the phase diagram may differ considerably from the one depicted in Fig. 6: the easy-axis anisotropy has an additional stabilizing effect on the planar and collinear phases but destabilizes phases with an umbrella-like structure. The latter may completely disappear at a certain critical value of anisotropy of order J'. The effect of anisotropy in such systems has been recently examined in Ref. 16.

We also studied the effect of thermal fluctuations on the stability of the structures. The contribution of entropy to the free energy

$$F=E_0-3JSN+\frac{S}{2}\sum_{k\alpha}\omega_\alpha(\mathbf{k})+T\sum_{k\alpha}\ln\left[1-\exp\left(-\frac{S\omega_\alpha(\mathbf{k})}{T}\right)\right]$$

TABLE I. The temperature dependence of the normalized field intervals Δh_a, Δh_b, Δh_c, Δh_d, Δh_f, and Δh_h of the respective configurations a, b, c, d, f, and h at $jS=0.1$ ($t=T/S\omega_*$).

t	Δh_f	Δh_h	Δh_b	Δh_c	Δh_d	Δh_a
0	0.263	0.032	–	–	–	0.695
0.05	0.267	0.048	–	0.015	–	0.648
0.10	0.269	0.049	–	0.039	–	0.563
0.15	0.270	0.050	–	0.040	0.025	0.473
0.20	0.271	0.037	0.013	0.039	0.055	0.374

was found numerically. The results indicate that as T grows the region occupied by the nonplanar structure a in the $jS-h$ phase diagrams shrinks because of the renormalization of the saturation field strength and because the structures b, c, and d become stabilized. The intervals Δh of stability of the structures f, h, b, c, d, and a are listed in Table I for different values of the normalized temperature $t=T/S\omega_*$ and $jS=0.1$. It is clear that the c, d, and b configurations occur when t is approximately equal to 0.05, 0.15, and 0.20, respectively, while the field interval of configuration a decreases with temperature. As for the h configuration, Δh first increases up to 0.05 and then, as the temperature grows still further, drops.

4. CONCLUSION

We have studied equilibrium states with different configurations of spins located in the triangular layers of a hexagonal lattice. We have found that in compounds of the VBr_2 and VCl_2 type the quantum effects compete with effects caused by interplanar antiferromagnetic interaction. For $H<H_1$ the planar configuration f with a structure resembling a six-pointed star is stabilized both by interplanar exchange and by quantum fluctuations; in the intermediate range $H_1<H<H_5$ the planar configurations b, d, and e are stabilized by quantum fluctuations, while nonplanar configurations of the umbrella type become stabilized in the $H>H_5$ range because of interplanar exchange. The magnetic transitions in the critical points, with the exception of $H=H_3$, are not continuous: the magnetization curve exhibits small jumps. We have found a finite region of field strengths where the collinear phase is stable. We have also discovered that in the spin configurations emerging in intermediate fields are additionally stabilized by thermal fluctuations.

In conclusion we note that the well-known compounds of the $ACrO_2$ type (A=H,Li,Na) also consist of triangular layers on which below T_N the Heisenberg spins form a 120-degree structure.[19,20,12] However, in contrast to compounds of the VX_2 type, here the triangular layers form a rhombohedral structure (the space group $R3m$). In view of this the system is frustrated not only in the plane but also in the third (spatial) direction, which leads to an additional degeneracy of classical structures.[21,22] We believe that in $ACrO_2$ compounds the f configuration, which is partially stabilized in VX_2 compounds by exchange coupling of the layers, is unlikely to occur no matter what value j assumes, while the planar configurations b, d, and e become even more stabilized because of quantum fluctuations.

The authors are grateful to E. Rastelli and A. Tassi for a copy of the paper cited in Ref. 16.

[1] D. H. Lee, J. D. Joannopoulos, J. W. Negele, and D. P. Landau, Phys. Rev. B **33**, 450 (1986).
[2] H. Kawamura, J. Phys. Soc. Jpn. **56**, 474 (1987).
[3] L. P. Regnault and J. Rossat-Mignod, in *Magnetic Properties of Layered Transition Metal Compounds*, edited by L. J. De Jongh, Kluwer Academic, Dordrecht (1990), p. 271.
[4] E. Rastelli, A. Tassi, A. Pimpinelli, and S. Sedazzari, Phys. Rev. B **45**, 7936 (1992).
[5] H. Shiba and T. Nikuni, in *Recent Advances in Magnetism of Transition Metal Compounds*, edited by A. Kotani and N. Suzuki, World Scientific, Singapore (1993), p. 372.
[6] J. Wosnitza, R. Deutschmann, H. V. Löhneysen, and R. K. Kremer, J. Phys.: Condens. Matter **6**, 8045 (1994).
[7] M. E. Zhitomirsky, O. A. Petrenko, and L. A. Prozorova, Phys. Rev. B **52**, 3511 (1995).
[8] K. S. Aleksandrov, I. O. Fedoseeva, and I. P. Spevakova, *Magnetic Phase Transitions in Crystals* [in Russian], Nauka, Novosibirsk (1983), p. 1.
[9] H. Kadowaki, K. Ubukoshi, and K. Hirakawa, J. Phys. Soc. Jpn. **54**, 363 (1985).
[10] H. Kadowaki, K. Ubukoshi, K. Hirakawa *et al.*, J. Phys. Soc. Jpn. **56**, 4027 (1987).
[11] K. Takeda, K. Ubukoshi, T. Haseda, and K. Hirakawa, J. Phys. Soc. Jpn. **53**, 1480 (1984).
[12] N. Kojima, K. Ito, I. Mogi *et al.*, J. Phys. Soc. Jpn. **62**, 4137 (1993).
[13] I. Yamada, K. Ubukoshi, and K. Hirakawa, J. Phys. Soc. Jpn. **53**, 381 (1984).
[14] R. S. Gekht, Usp. Fiz. Nauk **159**, 261 (1989) [Sov. Phys. Usp. **32**, 871 (1989)].
[15] A. V. Chubukov and D. I. Golosov, J. Phys.: Condens. Matter **3**, 69 (1991).
[16] E. Rastelli and A. Tassi, J. Phys.: Codens. Matter **8**, 1811 (1996).
[17] M. Niel, C. Cros, G. Le Flem *et al.*, Physica B + C **86–88**, 702 (1977).
[18] J. J. M. Franse, J. Magn. Magn. Mater. **90–91**, 20 (1990).
[19] J. L. Soubeyroux, D. Fruchart, J. C. Marmeggi *et al.*, Phys. Status Solidi **67**, 633 (1981).
[20] J. Ajiro, K. Kikuchi, S. Sugiyama *et al.*, J. Phys. Soc. Jpn. **57**, 2268 (1988).
[21] E. Rastelli and A. Tassi, J. Phys. C **19**, L423 (1986).
[22] S. S. Aplesnin and R. S. Gekht, Zh. Éksp. Teor. Fiz. **96**, 2163 (1989) [Sov. Phys. JETP **69**, 1224 (1989)].

Translated by Eugene Yankovsky

Polar Jahn–Teller centers and the anomalous isotope effect in copper–oxygen high-T_c superconductors

A. S. Moskvin and Yu. D. Panov

A. M. Gorky Ural State University, 620083 Ekaterinburg, Russia
(Submitted 5 May 1996)
Zh. Éksp. Teor. Fiz. **111**, 644–653 (February 1997)

We examine the isotope effect in copper–oxygen high-T_c superconductors using the model of polar Jahn–Teller centers, a variant of the local-boson model. The isotope-effect exponents for oxygen and copper depend on the structure of Jahn–Teller centers and its variation due to boson motion. A number of $YBa_2Cu_3O_{7-\delta}$-based compounds are used to illustrate the feasibility of quantitatively describing the experimentally observed values of α_{Cu} and α_O and their relationship to T_c. © *1997 American Institute of Physics.* [S1063-7761(97)01802-7]

1. INTRODUCTION

A model of polar Jahn–Teller centers that unifies in a natural manner the various model approaches based on the idea of local pairing and extremely strong electron–vibrational interaction and also partially reconciles the supporters of the ''charge,'' ''structural,'' and ''spin'' scenarios of high-T_c superconductivity has been proposed in Refs. 1 and 2. In this model copper oxides are interpreted as systems unstable under a disproportionation reaction accompanied by the formation of a system of hole (CuO_4^{5-}) and electron (CuO_4^{7-}) polar Jahn–Teller centers (*h*- and *e*-centers) differing by an *S*-boson, two electrons paired in a completely filled molecular shell. Actually the polar-center phase is a system of local *S*-bosons moving inside a lattice of Jahn–Teller hole centers, which insure both local pairing and effective screening of boson–boson repulsion.

The remarkable properties of polar Jahn–Teller centers follow from the quasidegeneracy in the ground state, i.e., the fact that the energies of the highly correlated states $^1A_{1g}$ (the Zhang–Rice singlet) of a configuration of the b_{1g}^2 type and $^{1,3}E_u$ of the $b_{1g}e_u$ Refs. 2 and 3 configuration are close, which leads to a multimode pseudo-Jahn–Teller effect with active displacement modes of the nuclei of CuO_4-clusters of the $Q_{b_{1g}}$, $Q_{b_{2g}}$, or Q_{e_u} type.

Thus, the formation of the structures of the ground and lower excited states of the Jahn–Teller lattice involves singlet and triplet spin states and even-nondegenerate and odd-degenerate orbital states of separate centers, and a number of active quadrupole ($Q_{b_{1g}}$ and $Q_{b_{2g}}$) and dipole (Q_{e_u}) local-displacement modes of the nuclei of CuO_4-clusters. The structure of the lower energy levels of a polar Jahn–Teller center of the CuO_4^{5-} or CuO_4^{7-} type is depicted schematically in Fig. 1. Note the quantity Δ_{AE}, the main parameter of the pseudo-Jahn–Teller effect. It determines the degree of $^1A_{1g}$–^1E_u hybridization, the parameters of the adiabatic potential of a Jahn–Teller center, and the singlet–triplet splitting parameter Δ_{st}, which plays an important role in the interaction of the charge and spin subsystems.[2]

The model of polar Jahn–Teller centers allows for a natural explanation of the entire spectrum of the extraordinary physical properties of copper oxides. Here, in spite of the complicated structure of Jahn–Teller centers, it is usually possible to build a simple and graphic physical picture of the various phenomena. We would like to illustrate this by using the example of the isotope effect, which historically has been one of the main factors in favor of the electron–vibrational mechanism of superconductivity.

Here we do not attempt to analyze the entire dramatic story of the discovery and study of the isotope effect in copper–oxygen high-T_c superconductors, but we do mention a number of important features.

1. The problem of obtaining reliable values of α, the isotope-effect exponent ($T_c \sim M^{-\alpha}$), in copper oxides is complicated by the irreproducibility of the results, the presence of various nonequivalent positions of the oxygen and copper atoms, the inaccuracies in determining T_c, and many other factors. The clearest illustration of these is provided by the work of Nickel *et al.*[4] and Zech *et al.*,[5] where the researchers obtained isotope shifts in T_c of opposite sign.

2. A remarkable feature of the isotope effect in copper oxides is the extremely broad range of the observed values of α (large positive $\alpha \sim 1.5$ (!) for oxygen and sizable negative values for copper).

3. A number of laws and empirical rules[6] have been discovered: (a) high values of T_c correspond to low values of α, small superconducting transition widths, and small baric coefficients $\partial T_c/\partial p$; (b) low values of T_c correspond to high values of α, large superconducting transition widths, and large baric coefficients $\partial T_c/\partial p$.

4. There is no theoretical model capable of explaining the principal features of the isotope effect, notwithstanding the large number of papers that explain individual experimental facts (see, e.g., Ref. 7).

In view of the attempts to theoretically explain the features of the isotope effect in copper–oxygen high-T_c superconductors we mention the model approaches of Kresin and Wolf[8] and Bar-Yam,[9] since some elements of these approaches are close to our concept of Jahn–Teller centers.

Today there exists a vast body of reliable experimental data on the different features of the isotope effect, primarily for $YBa_2Cu_3O_{7-\delta}$ systems with various substitutions (Pr, Pr:Ca, Zn, La, etc.).[6,11,14] Thus the situation is ripe for a theoretical model, which in turn must be a true component of a unique scenario of high-T_c superconductivity.

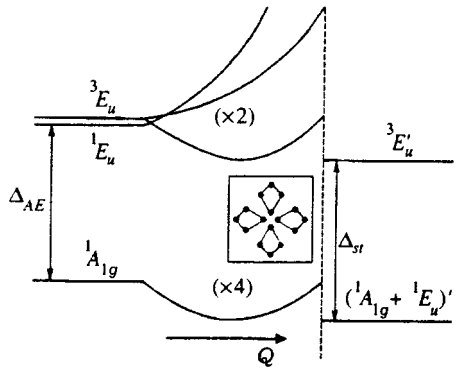

FIG. 1. The structure of the lower energy levels of a polar Jahn–Teller center. The four types of distortion of the square cluster CuO_4 corresponding to the four minima of the adiabatic potential are schematically depicted in the inset.

The complexity of this problem is due primarily to the possibility of extraordinary isotope-effect mechanisms manifesting themselves, mechanisms absent from standard BCS scenarios and BCS systems. In this connection we mention the percolation mechanism of formation of a three-dimensional superconducting state ''operating'' over large areas of the copper-oxide phase diagram.[2] The metal–insulator transition in such systems is realized through the formation of a phase-inhomogeneous state (phase separation), and the most important role here is played by areas of charge inhomogeneity (CI-centers) with centers of the Sr^{2+} or Ce^{4+} ion type, oxygen vacancies, ''extraneous'' oxygen ions in oxides of the type $La_{2-x}Sr_xCuO_4$, $Nd_{2-x}Ce_xCuO_4$, $YBa_2Cu_3O_{7-\delta}$, etc.[2]

It is the CI-centers that serve as nucleation centers for the polar-center phase. An increase in x, the concentration of CI-centers, is accompanied by an increase in the volume of the new phase, which under certain conditions ($x=x_{cr}$) leads to percolation and an increase in the transition temperature T_c with x. When a certain concentration x'_{cr} is reached, the new phase occupies the entire volume of the sample. Clearly, on the percolation section of the T_c vs x dependence ($x_{cr}<x<x'_{cr}$) the isotope effect can be related to the isotopic variation of the volume of the new phase.

Note that CI-centers form a narrow quasi-impurity band and determine the position of the Fermi level. This narrow band can be associated with low-frequency charge excitations of the acoustic-plasmon type,[7] excitations that ensure an effective screening of the electrostatic boson repulsion and a number of ''marginal'' properties of copper oxides.[7]

It is to the nature of the spatial distribution of the order parameter in CI-centers that the s- and/or d-scenario of superconductivity is related. The low-frequency charge and phase excitations in CI-centers manifest themselves in the spectra of inelastic neutron scattering and the spectra of angle-resolved photoemission.

An essentially ''oxide'' feature of the isotope effect in copper–oxygen high-T_c superconductors is the potentially strong effect of the $^{16}O\rightarrow{}^{18}O$ substitution ($\Delta M/M=12.5\%$!) on the variation of the lattice parameters, the Madelung potentials, crystalline fields, and other important physicochemical characteristics determining T_c.

2. THE JAHN–TELLER MECHANISM OF THE ISOTOPE EFFECT

The principal mechanism of the isotope effect in the homogeneous polar-center phase is linked to the dependence of the S-boson transfer integral on the parameters of the adiabatic potential of a Jahn–Teller center and the mass of vibration modes:

$$T_c\sim t=K_{eh}t^{(0)}, \tag{1}$$

where $t^{(0)}$ is the purely electron part of the transfer integral,

$$K_{eh}=\langle\chi_e|\chi_h\rangle^2 \tag{2}$$

is the vibronic reduction factor, and $\langle\chi_e|\chi_h\rangle$ is the overlap integral of vibrational states corresponding to a certain well of the adiabatic potential for the electron and hole polar centers.

What is important is that Eqs. (1) and (2) suggest the existence, at least in principle, of ''optimized'' systems in which the adiabatic potentials of the hole and electron Jahn–Teller centers coincide. In such systems $\langle\chi_e|\chi_h\rangle\equiv 1$, and the motion of S-bosons is not accompanied by a variation in the adiabatic potential of Jahn–Teller centers. Moreover, for an optimized system, the condition $K_{eh}=1$ corresponds to a maximum of the function $K_{eh}=K_{eh}(\Delta_e,\Delta_h,k_e,k_h,V_e,V_h,\dots)$ in the space of the different parameters of Jahn–Teller centers (here the k's are elastic constants and the V's vibronic constants):

$$\frac{\partial K_{eh}}{\partial\Delta_e}=\frac{\partial K_{eh}}{\partial\Delta_h}=\frac{\partial K_{eh}}{\partial k_e}=\cdots=0, \tag{3}$$

which leads to suppression of fluctuations in the vibronic reduction factor and, as a result, to suppression of fluctuations in the transfer integral and the transition temperature T_c in real systems.

In optimized systems, the charge, structural, and spin subsystems can be ''separated,'' with the effect of the Jahn–Teller lattice reduced to screening of the boson–boson repulsion. With such systems one should expect that

(a) T_c is at its maximum,

(b) the superconducting transition width is at its minimum,

(c) there is no isotope effect, and

(d) the values of the baric coefficient $\partial T_c/\partial p$ and similar ''susceptibilities'' are minimal.

Note that the absence of an isotope effect in optimized systems is a feature of the anomalously strong electron–vibrational interaction characteristic of the Jahn–Teller effect (rather than a weak electron–vibrational interaction).

For an optimized system, the parameters Δ_{AE} of ''initial'' $^1E_u-{}^1A_{1g}$-orbital splitting coincide, and so do the parameters Δ_{st} of singlet–triplet splitting (see Fig. 1) in the hole and electron centers. Hence the spin subsystem ceases to react to the transformation of charge correlations near T_c, which has an effect on the nature of magnetic inelastic neutron scattering.[10]

Of course, optimized systems are an exception, rather than the rule. Among the copper–oxygen high-T_c supercon-

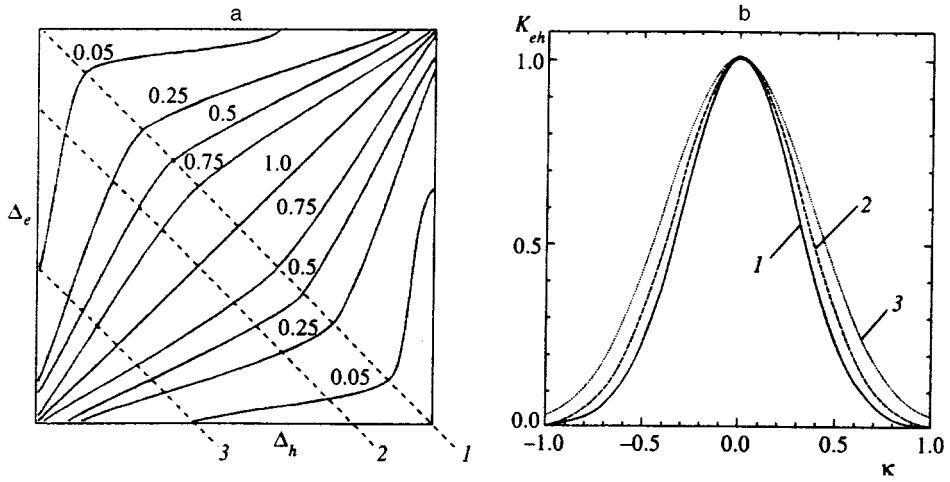

FIG. 2. a) Solutions of the equation $K_{eh}(\Delta_e,\Delta_h)=\text{const}$ for various values of κ. b) The dependence of the vibronic reduction factor K_{eh} on the dimensionless parameter κ (see text) in different cross sections (curves *1*, *2*, and *3*) of the (Δ_e,Δ_h) plane.

ductors the optimally doped $YBa_2Cu_3O_{7-\delta}$ compound with $0\leqslant\delta\leqslant 0.1$ Ref. 11 may serve as such a system.[1)]

In a more realistic situation, the motion of a local boson is accompanied by a variation in the adiabatic potential of a Jahn–Teller center, primarily because of the difference in the initial parameters Δ_{AE} for the hole and electron Jahn–Teller centers. This automatically leads to strong coupling of the charge, structural, and spin fluctuations[2)] and has a dramatic effect on all physical properties of copper oxides.

Even with the methods used in the theory of the Jahn–Teller effect,[12] analysis of the vibronic reduction factor constitutes an extremely complicated problem. Indeed, in the present situation of the pseudo-Jahn–Teller effect, the adiabatic potential has four minima. The normal vibration modes in the minima have a hybrid $(b_{1g}-e_u x)$- or $(b_{2g}-e_u y)$-nature. In other words, the cross section of the adiabatic potential near a minimum is the direct sum of two ellipses (polarization ellipses), in which the orientation and length of the semiaxes are complicated functions of the parameter Δ_{AE}, the vibronic constants, and atomic masses of oxygen and copper.

The wave function of the vibrational ground state is a scalar (an *s*-function) and has the usual form:

$$\chi(Q)=\pi^{-1/4}l^{-1/2}e^{-Q^2/2l^2}, \tag{4}$$

where l is the characteristic oscillator length, which is a complicated function of the parameters of the polarization ellipse. Calculating the overlap integral of the functions $\chi(Q)$ for the electron and hole Jahn–Teller centers, $\langle\chi_e|\chi_h\rangle$, generally constitutes a complicated problem because it proves impossible to separate the variables corresponding to the hybridizing modes, $Q_{b_{1g}}$ and $Q_{e_u x}$, and $Q_{b_{2g}}$ and $Q_{e_u y}$.

The functional dependence of the vibronic reduction factor has the form

$$K_{ch}=Ne^{-\gamma}, \tag{5}$$

with the pre-exponential factor N, which has a complicated structure, and the exponent γ, which depends on the oscillator masses and the distance between the corresponding minima of the adiabatic potential in *e*- and *h*-centers in approximately the same way as in the single-mode case:

$$\gamma\sim\sqrt{m}(\Delta Q). \tag{6}$$

Figure 2a depicts the solutions of the equation $K_{eh}(\Delta_e,\Delta_h)=\text{const}$, which can actually be interpreted as ''isotherms,'' i.e., solutions of the equation

$$K_{eh}=\frac{T_c(\Delta_e,\Delta_h)}{T_c(\Delta_e=\Delta_h)}=\frac{T_c}{T_c^{\max}}=\text{const}.$$

The pattern of ''isotherms'' clearly shows that T_c is not a single-valued function of Δ_e and Δ_h.

Figure 2b depicts the dependence of the vibronic reduction factor on the dimensionless parameter

$$\kappa=\frac{\Delta_e-\Delta_h}{\overline{\Delta}} \tag{7}$$

for different values of the parameter $\overline{\Delta}=\Delta_e+\Delta_h$, with Δ_e and Δ_h measured from the minimum value at which the adiabatic potential has four minima. All the other parameters of the Jahn–Teller problem for *e*- and *h*-centers were assumed equal, and were selected in such a way so as to ensure reasonable values of the oscillator energies ($\hbar\omega_0\sim 100\ \text{cm}^{-1}$), the Jahn–Teller stabilization energies ($E_{JT}\sim 1000\ \text{cm}^{-1}$), and the characteristic oscillator lengths ($l_0\sim 0.1$ Å).

As noted earlier, the factor K_{eh} is at its maximum ($\equiv 1$) at $\kappa=0$ and decreases as κ grows: it decreases slowly for κ small ($\partial K_{eh}/\partial\kappa\to 0$ as $\kappa\to 0$) and rapidly as $|\kappa|\to 1$. For compositions close to the optimized one ($\kappa=0$), the factor K_{eh} depends weakly on Δ_e and Δ_h, since for such compositions $\partial K_{eh}/\partial\Delta_e=\partial K_{eh}/\partial\Delta_h=0$.

The dependence of the vibronic reduction factor on the masses of oxygen and copper atoms makes the dominant contribution to the isotope effect for copper–oxygen high-T_c superconductors.

If within the framework of the theory of a lattice Bose gas[13] we put $T_c\sim t$, we get

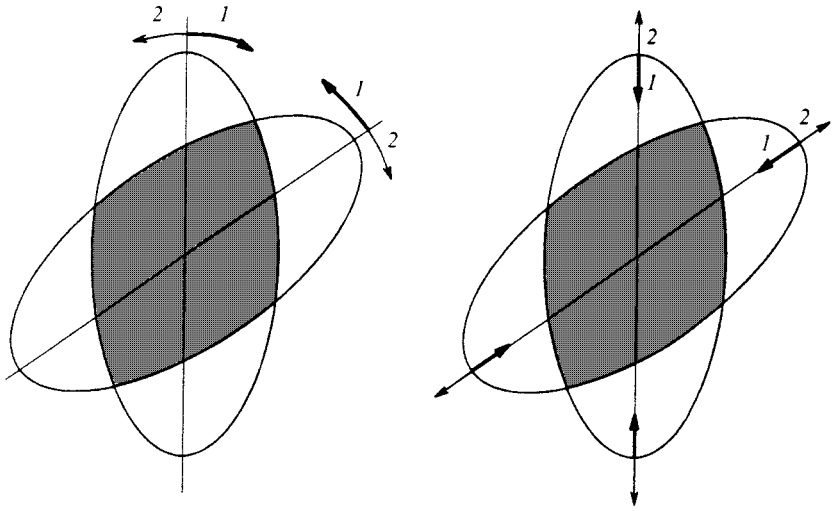

FIG. 3. Illustration of the dependence of the overlap integral of the vibrational functions of the electron and hole centers, $\langle \chi_e | \chi_h \rangle$, on the deformation and rotation of the polarization ellipses in the process of isotope substitution. Processes of type *1* (heavy arrows) lead to an increase in $\langle \chi_e | \chi_h \rangle$, and those of type *2* (light arrows) to a decrease in $\langle \chi_e | \chi_h \rangle$.

$$\alpha = -m\frac{\partial \ln T_c}{\partial m} = -m\frac{\partial \ln K_{eh}}{\partial m} = -m\frac{\partial \ln N}{\partial m} - m\frac{\partial \gamma}{\partial m}. \tag{8}$$

In the simple single-mode case, the pre-exponential factor N is independent of the mode mass m, and $\gamma \sim \sqrt{m}(\Delta Q)^2$, so that α is nonnegative and its value is determined primarily by the distance ΔQ between the minima of the adiabatic potential for the e- and h-centers.

In the multimode case the situation is much more complicated, with the isotope effect determined not only by ΔQ but also by the dependence on the atomic masses of the orientation and ratio of the semiaxes of the polarization ellipses. Variation of the atomic masses of oxygen and copper leads to deformation and rotation of the polarization ellipses of the vibrational modes in the e- and h-centers, which leads to a variation (increase or decrease) in the overlap integral $\langle \chi_e | \chi_h \rangle$ (see Fig. 3). As a result there emerges a nonzero contribution to α from the pre-exponential factor N, and the contribution may be either positive or negative (!).

In our model a negative isotope effect can be observed only in copper. To achieve this the positive γ-contribution to α_{Cu} must be suppressed, i.e., $\partial\gamma/\partial m_{\mathrm{Cu}} \ll 1$. This is the situation in the above (Δ_e, Δ_h)-model, in which the difference in the e- and h-center is assumed to exist only in the parameters Δ_e and Δ_h.

Figure 4 depicts the dependence on κ of α_{O} and α_{Cu} for different values of $\bar{\Delta}$. It also depicts the solutions of the equations $\alpha_{\mathrm{O}}(\Delta_e, \Delta_h) = \mathrm{const}$ and $\alpha_{\mathrm{Cu}}(\Delta_e, \Delta_h) = \mathrm{const}$. Note the intervals of possible variation of α_{Cu} and α_{O} and the fact that these solutions and ''isotherms'' do not coincide (see Fig. 2a), an indication, in particular, that the α vs T_c dependence is not single-valued.

Figure 5 depicts the dependences of the type $\alpha(K_{eh}) = \alpha(T_c/T_c^{\max})$ for α_{O} and α_{Cu}, corresponding to definite trajectories in the (Δ_e, Δ_h) plane that ensure either negative (curve *1* for α_{Cu}) or positive (curves *2* and *3*) for α_{Cu} values of the isotope effect for copper. A characteristic feature of compositions with $\alpha_{\mathrm{Cu}} < 0$ is a relatively large positive value of α_{O}, obtained as a result of adding a relative small negative contribution to α_{O} from a hybrid mode of a preferably copper e_u-type and a relatively large positive contribution to α_{O} from a vibrational mode of a preferably purely oxygen b_{1g}-type. Here α_{O} may reach values that are considerably higher than $\alpha_{\mathrm{BCS}} = 0.5$.

At the same time, for compositions with $\alpha_{\mathrm{Cu}} > 0$ the two contributions to α_{O} balance each other, so that the net value of α_{O} is small.

Figure 5 also shows some experimental values of α_{O} and α_{Cu} as functions of the reduced transition temperature $T_c/T_c^{\max}$ for the following compositions: $Y_{1-x}Pr_xBa_2Cu_3O_{7-\delta}$, $Y_{0.8-y}Pr_{0.2}Ca_yBa_2Cu_3O_{7-\delta}$, and $YBa_2Cu_{3-x}Zn_xO_{7-\delta}$ (see Ref. 6); $YBa_{2-x}La_xCu_3O_{7-\delta}$ (Ref. 14); and $YBa_2Cu_3O_{7-\delta}$ (Ref. 11). These compositions are inherently linked to the model optimized composition $YBa_2Cu_3O_{6.93}$ with $T_c^{\max} \approx 93$ K. It is natural, then, that in the general case for such systems the T_c vs x dependence corresponds to different ''trajectories'' in the (Δ_e, Δ_h) plane with different behavior of the function $\alpha(x)$.

Note the similarity in the dependences $\alpha_{\mathrm{O}}(T_c)$ in a 1-2-3 system with fixed δ and substitution in the Y- or Ba-sublattice, i.e., out of the active CuO_2-planes. This suggests that the nature of variation of the parameters Δ_e and Δ_h (with $\bar{\Delta}$ conserved) under such substitution is approximately the same (the respective (Δ_e, Δ_h)-trajectories are close).

A slightly different situation is observed in the 1-2-3 system when δ varies. In this case an increase in δ is accompanied by a sizable variation in $\bar{\Delta}$, which forces the system into a mode with a negative isotope effect for copper $(\alpha_{\mathrm{Cu}} < 0)$.

The absence, for all practical purposes, of an isotope effect in $YBa_2Cu_{3-x}Zn_xO_{7-\delta}$ over a wide range of values of T_c, with such an important characteristic of an optimized composition as the minimum superconducting transition width retained,[6] agrees with the ideas concerning the effect of Zn^{2+} on the disintegration of Jahn–Teller centers in CuO_2-planes combined with formation of large two-dimensional regions of a highly inhomogeneous normal phase, a process accompanied by a lowering of the transition

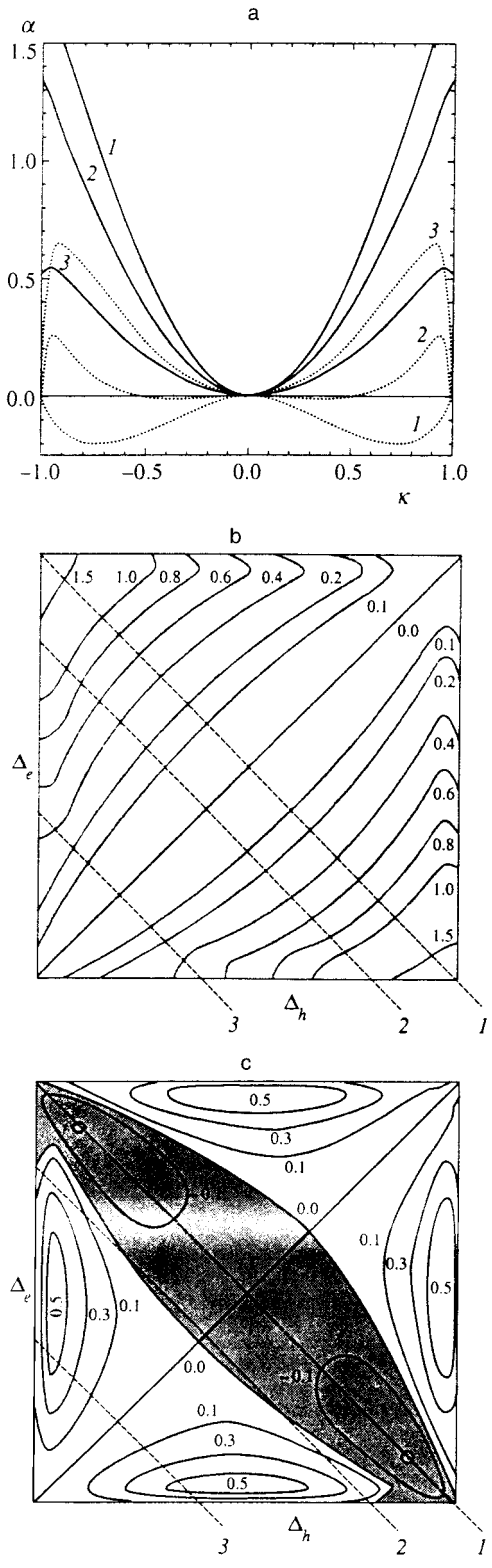

FIG. 4. a) The dependence on the parameter κ of the oxygen isotope-effect exponent α_O (solid curves) and the copper isotope-effect exponent α_{Cu}; the curves *1*, *2*, and *3* correspond to the cross sections of the (Δ_e, Δ_h) plane depicted by the dashed straight lines *1*, *2*, and *3* in Figs. 4b and 4c. b) Solutions of the equation $\alpha_O(\Delta_e, \Delta_h) = \text{const}$. c) Solutions of the equation $\alpha_{Cu}(\Delta_e, \Delta_h) = \text{const}$; the hatched region corresponds to negative values of α_{Cu}.

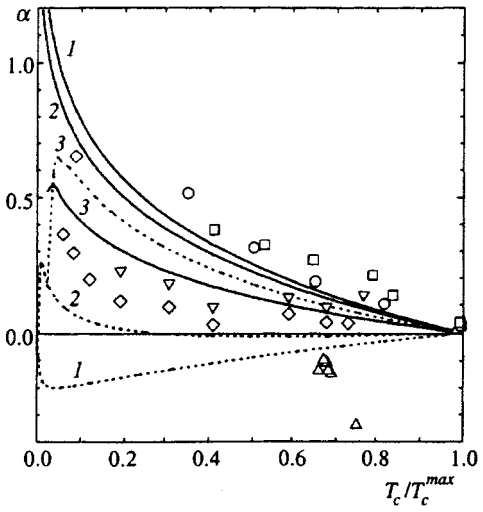

FIG. 5. The dependence on the reduced transition temperature $T_c/T_c^{\max}(\equiv K_{eh})$ of the theoretical and experimental results for the oxygen isotope-effect exponent α_O (solid curves) and the copper isotope-effect exponent α_{Cu} (dotted curves). The solid and dotted curves are theoretical curves corresponding to the cross sections *1*, *2*, and *3* of the (Δ_e, Δ_h) plane (see Figs. 2a, 4b, and 4c). The experimental values of the isotope-effect exponents are given for $YBa_2Cu_3O_{7-\delta}$-based systems: △—α_{Cu} for $YBa_2Cu_3O_{7-\delta}$ (Ref. 11); ◇—α_O for $YBa_2Cu_{3-x}Zn_xO_{7-\delta}$ (Ref. 6); ▽—α_O for $Y_{0.8-y}Pr_{0.2}Ca_yBa_2Cu_3O_{7-\delta}$ (Ref. 6); ○—α_O for $Y_{1-x}Pr_xBa_2Cu_3O_{7-\delta}$ (Ref. 6); and □—α_O for $YBa_{2-x}La_xCu_3O_{7-\delta}$ (Ref. 14).

temperature T_c of percolation nature. Here the $^{16}O \rightarrow {}^{18}O$ substitution has essentially no effect on the variation of the electron properties of the CuO_2-planes, which are in an optimized state except for regions of low T_c, where in view of the percolation nature of the transition the role of even small fluctuations sharply increases.

The data of Fig. 5 firmly suggest that a quantitative description of the rather intricate features of the isotope effect for oxygen and copper in copper–oxygen high-T_c superconductors is possible. At the same time this is only a small example illustrating the possibilities of the polar-center model in explaining and predicting physical phenomena and properties.

3. CONCLUSION

The model of polar Jahn–Teller centers provides not only a simple and graphic description of all, including the most exotic, qualitative features of the isotope effect in copper oxides but also explains the various quantitative laws.

On the whole, the experimental data on the isotope effect in copper oxides serve as a clearcut confirmation of the validity of the model of polar Jahn–Teller centers, not only in the general aspects but also in details. For instance, the discovery of an isotope effect for copper essentially unambiguously points to the active role of the unique hybrid Cu–O-mode Q_{e_u} of the local displacements of CuO_4-clusters, which in turn points to the active role of the electron E_u-state.

The results of our work illustrate the vast possibilities of the model of polar Jahn–Teller centers, not only in explaining certain physical properties of copper oxide but also in predicting their physical behavior. Here we are speaking pri-

marily of the existence of so-called optimized compositions with a unique set of physical properties (the highest possible values of T_c, the smallest superconducting transition widths, and maximum stability under various external influences, such as the presence of defects and mechanical stresses). In this connection we note the special role of pressure as a universal experimental tool that makes it possible to study the local characteristics of the vibronic reduction factor and to determine the prospects of achieving higher values of T_c in a specific ''unoptimized'' composition.

We would also like to note that in illustrating the results of the theory we selected a system based on $YBa_2Cu_3O_{7-\delta}$, for which there exists a vast body of experimental data. Unfortunately, studies of the isotope effect in another popular high-T_c system, $La_{2-x}M_xCuO_4$ ($M=Ba,Ca,Sr$) are less representative, although here too a number of interesting effects, meriting a separate investigation, have been discovered (large values of α_0 and the strong effect of $3d$-substitutions).[15]

This work was made possible by the partial financial support due to Grants Nos. a1394 and p459 from the ISSEP fund.

[1)]Note the decrease in the intensity of magnetic inelastic neutron scattering in this system.

[2)]Here we are dealing with singlet–triplet mixing and fluctuations of spin multiplicity.

[1] A. S. Moskvin JETP Lett. **58**, 345 (1993).
[2] A. S. Moskvin, *The Nature of the Extraordinary Physical Behavior of Copper Oxides* [in Russian] (Preprint), Ural State University, Ekaterinburg (1995).
[3] A. S. Moskvin, N. N. Loshkareva, Yu. P. Sukhorukov, M. A. Sidorov, and A. A. Samokhvalov, Zh. Éksp. Teor. Fiz. **105**, 967 (1994) [JETP **78**, 518 (1994)].
[4] J. H. Nickel, D. E. Morris, and J. W. Ager III, Phys. Rev. Lett. **70**, 81 (1993).
[5] D. Zech, H. Keller, K. A. Muller *et al.*, Physica C **235–240**, 1221 (1994); Nature **371**, 681 (1994).
[6] G. Soerensen and S. Gygax, Phys. Rev. B **51**, 11 848 (1995).
[7] É. A. Pashitskiĭ, Fiz. Nizk. Temp. **21**, 995 (1995) [Low Temp. Phys. **21**, 763 (1995)]; **21**, 1091 (1995) [**21**, 837 (1995)].
[8] V. Z. Kresin and S. A. Wolf, Phys. Rev. B **49**, 3652 (1994).
[9] Y. Bar-Yam, Phys. Rev. B **43**, 359 (1991).
[10] F. Onufrieva and J. Rossat-Mignod, Phys. Rev. B **52**, 7572 (1995).
[11] J. P. Franck and D. D. Lawrie, Physica C **235–240**, 1503 (1994).
[12] I. B. Bersuker and V. Z. Polinger, *Vibronic Interactions in Molecules and Crystals*, Springer-Verlag, Berlin (1989).
[13] R. Micnas, J. Ranninger, and S. Robaszkiewicz, Rev. Mod. Phys. **62**, 113 (1990).
[14] H. J. Bornemann and D. E. Morris, Phys. Rev. B **44**, 5322 (1991).
[15] N. A. Babushkina *et al.*, Physica C **235–240**, 845 (1994).

Translated by Eugene Yankovsky

The effect of magnetic ordering on the quantum temperature oscillations of current-carrier magnetization in strongly correlated systems

V. V. Val'kov* and D. M. Dzebisashvili

L. V. Kirenskiĭ Institute of Physics, Siberian Branch of the Russian Academy of Sciences, 660036 Krasnoyarsk, Russia and Krasnoyarsk State University, 660036 Krasnoyarsk, Russia
(Submitted 20 June 1996)
Zh. Éksp. Teor. Fiz. **111**, 654–668 (February 1997)

We show that the effect of magnetic ordering in magnetic semiconductors by the mechanism of $s-d(f)$ exchange interaction plays an important role in explaining the quantum temperature oscillations of band-electron magnetization that were discovered in the experiments of S. G. Ovchinnikov, V. K. Chernov, A. D. Balaev, N. B. Ivanova, B. P. Khrustalev, and V. A. Levshin (JETP Lett. **64**, 642 (1995)). We analyze how hybridization of band and localized electrons affects the amplitude of this effect. Finally, we establish that because of strong intratomic correlations the amplitude of the oscillation effects depends to a great extent on the sign of the exchange constant J. © *1997 American Institute of Physics.*
[S1063-7761(97)01902-1]

1. INTRODUCTION

Among the multitude of substances with strong electron correlations the so-called strongly correlated systems with low current-carrier concentration have lately drawn the interest of researchers. Representative of this class of materials are rare-earth compounds[1–4] with the general formula ReX, where Re stands for a rare-earth element and X for P, As, or Sb. The cerium compounds CeAs, CeSb, and CeP exhibit a number of nontrivial properties.[2–4] These compounds, which are semimetals, at low temperatures exhibit long-range magnetic order. The electronic structure of these cerium compounds is explained by the presence of a valence band whose top is at the Γ-point of the Brillouin zone and a conduction band near the X-point of the Brillouin zone. It has been experimentally established that the degree of electron–hole compensation in such compounds is high. Studies of the de Haas–van Alphen effect involving cerium compounds support the main features of the respective electronic structure. However, the fine details in the behavior of the de Haas–van Alphen oscillation frequencies have required new concepts for their explanation,[3,4] related primarily to the presence of magnetic ordering.

As is well known,[5,6] the effect of magnetic order on the electronic properties of materials manifests itself in magnetic semiconductors. In such compounds the hybridization interaction between collectivized and localized electrons can result in a dependence of kinetic characteristics on strong single-site correlation. Therefore, such magnetic semiconductors can be related to the systems with low current-carrier concentrations mentioned above. The ferromagnetic semiconductor $HgCr_2Se_4$ is an example of such a compound.

In a recent paper, Ovchinnikov *et al.*[7] reported the results of an experimental study of the quantum temperature oscillations of the current-carrier magnetization in $HgCr_2Se_4$. The existence of such oscillations was predicted earlier in Ref. 8. However, there exists a large discrepancy between the experimental data of Ref. 7 and the results of Ref. 8, which is due to the following fact. To reliably observe quantum temperature oscillations in experiments, the phases of the oscillating terms in the magnetization must change by more than 2π as the temperature changes from absolute zero to $T\sim\hbar\omega_c$ (at higher temperatures the oscillating terms are exponentially small). Achieving such a change in phase is difficult if the current-carrier concentration is low. Hence to interpret the results of Ref. 7 one needs an additional physical mechanism that would ensure that in the time it takes the temperature to vary the number of oscillations that the band-electron magnetization performs before such oscillations decay is sufficiently large.

As is well known,[5,6] the existence of a strong coupling of collectivized and localized electrons in magnetic semiconductors is corroborated in experiments by a shift of the optical absorption edge in the temperature range where magnetic ordering can take place. The physical reason for the shift of the bottom of the conduction band and/or the top of the valence band is the $s-d(f)$ exchange interaction between the spin angular momenta of the two groups of electrons.[9] It was this interaction that made it possible to interpret the experimental data on the extremely strong effect of a magnetic field on the optical properties of $HgCr_2Se_4$ recently discovered by Bol'nykh *et al.*[10]

Bearing all this in mind, we can easily assume that the $s-d(f)$ exchange interaction plays an important role in generating quantum temperature oscillations. The physics of the mechanism by which magnetic ordering affects quantum temperature oscillations is fairly simple. A rise in temperature lowers the magnetization of the localized subsystem. As a result and due to $s-d(f)$ exchange coupling the Landau levels begin to move. Some of the upper Landau levels become depleted, and the electrons involved go over to the localized state, thus increasing the number of bivalent chromium ions. What is important in this process is the proximity of the chemical potential values and the energy corresponding to the $Cr^{3+}\rightarrow Cr^{2+}$ transition. Such dynamics generates well-known oscillations of the density of the electronic states and manifests itself, in particular, in the oscillatory dependence of the collectivized-electron magnetization with in-

creasing temperature. With these ideas a simple criterion for the existence of quantum temperature oscillations can be derived. As the temperature grows from absolute zero to $T \sim \hbar\omega_c$ the magnetization decreases by a quantity of order $(\hbar\omega_c/4\pi sI)^{3/2}$. The effect is present if the level shift caused by $s-d(f)$ exchange is much larger than the distance between Landau levels:

$$\alpha \equiv \left| \frac{J}{4\pi sI} \right| \left(\frac{\hbar\omega_c}{4\pi sI} \right)^{1/2} \gg 1,$$

where J is the $s-d(f)$ exchange coupling constant, and I is the integral of the exchange interaction in the localized subsystem. If for the values of the various parameters we takes those that are characteristic of magnetic semiconductors, i.e., $J \sim 0.4$ eV, $4\pi sI \sim T_c \sim 10^2$ K, and $\hbar\omega_c \sim 10$ K, then $\alpha \approx 8$, and all the conditions needed for quantum temperature oscillations to set in are met.

Note, however, that the hybridization interaction tends to suppress the de Haas–van Alphen effect in general and quantum temperature oscillations in particular. Hence an estimate of the possibility of such an effect occurring based on the above criterion can be too optimistic in the presence of hybridization. In this connection it is important to take into account single-site correlations, which renormalize the hybridization coupling constant. For our further studies it is important to note that in certain conditions (see below) such renormalization may neutralize the negative effect of the mixing of collectivized and localized states and may make quantum temperature oscillations observable.

These ideas concerning magnetic semiconductors and submetallic cerium compounds are proof of the importance of studying the effect of magnetic ordering in strongly correlated system on both the de Haas–van Alphen effect and quantum temperature oscillations. In the present paper we study the case of ferromagnetic ordering in the subsystem of localized spins. This type of long-range magnetic order is realized in chalcogenide chrome spinels. Hence our results can be directly applied to $HgCr_2Se_4$ and can be used to interpret the quantum temperature oscillations discovered by Ovchinnikov *et al.*[7] Strongly correlated systems with antiferromagnetic order (the cerium compounds CeAs, CeSb, and CeP) will be studied separately. Here we only note that the qualitative aspect of the effect of long-range order in the localized subsystem on the initiation of quantum temperature oscillations is the same for both types of magnetic ordering.

The plan of this paper is as follows. In Sec. 2 we briefly describe a model of the electronic structure of $HgCr_2Se_4$ that allows for strong intratomic correlations. In Sec. 3 we derive the basic equations for the Green's functions and discuss the conditions for the applicability of the assumptions. The thermodynamic potential of the system in the presence of Landau quantization and hybridization interaction is calculated in Sec. 4. In Sec. 5 we analyze the effect of magnetic ordering on the temperature and field dependence of the band-electron magnetization. We show that the temperature-induced decrease in the magnetic order parameter via the mechanism of $s-d(f)$ exchange coupling can lead to intense motion of the Landau levels. This is the key issue in the quantitative description of quantum temperature oscillations. Finally, in Sec. 6 we discuss the results.

2. THE MODEL HAMILTONIAN

We examine the effect of magnetic ordering on quantum temperature oscillations in strongly correlated systems using the example of the model of the electronic structure of $HgCr_2Se_4$. The electronic structure of magnetic semiconductors in general and of chalcogenide chrome spinels in particular has been discussed in the monographs of Methfessel and Mattis[5] and Nagaev.[6] The concept of multielectron Hubbard operators,[11–13] which describes strong single-site correlations fairly well, was employed in the theory of chalcogenide chrome spinels in Refs. 14–16. Using these ideas, we can write the model Hamiltonian that reproduces the energy spectrum of $HgCr_2Se_4$ in the following form:

$$\begin{aligned}\mathscr{H} = & \sum_{\mathbf{k}\sigma} (\varepsilon_{\mathbf{k}\sigma} - \mu) c^+_{\mathbf{k}\sigma} c_{\mathbf{k}\sigma} + \sum_{f,m} (E_1 - g\mu_B H m \\ & - 3\mu) X_f^{mm} + \sum_{f,m'} (E_2 - g\mu_B H m' - 4\mu) X_f^{m'm'} \\ & - \frac{1}{2} \sum_{f,l} I_{fl} (\mathbf{S}_f \mathbf{S}_l) - \sum_f J (\mathbf{S}_f \boldsymbol{\sigma}_f) \\ & + \frac{1}{\sqrt{N}} \sum_{f\mathbf{k}\sigma} (v_{\mathbf{k}} \exp(-i\mathbf{k}\mathbf{R}_f) c^+_{\mathbf{k}\sigma} d_{f\sigma} + \text{H.c.}). \end{aligned} \tag{1}$$

The first term on the right-hand side describes the subsystem of collectivized electrons in a magnetic field H with an energy $\varepsilon_{\mathbf{k}\sigma} = \varepsilon_{\mathbf{k}} - 2\sigma\mu_B H$, where $\sigma = \pm 1/2$ and μ_B is the Bohr magneton. The second term takes into account the states of the trivalent chromium ions, which have an energy E_1 and a $3d^3$ outer-electron configuration. The presence of spin degrees of freedom is expressed by summation over the projections of spin angular momentum on the z axis, with the projection denoted by m. The $3d^3$ configuration (Cr^{3+}) corresponds to a spin quartet ($S = 3/2$), which splits in a magnetic field with a gyromagnetic ratio close to two because the orbital angular momentum in the crystal field is frozen. Summation with respect to m is over half-integral values from $m = -3/2$ to $m = 3/2$. The operators X_f^{nm} are the Hubbard operators known from the theory of strongly correlated systems.[11–13] Notwithstanding the relative complexity of the commutation relations for these operators, today we have effective methods for calculating systems in the atomic representation. Among these is the method of diagrams for the Hubbard operators.[17–19] The diagonal Hubbard operators X_f^{nn} are actually projection operators on a chosen subspace of atomic (ionic) states for site f. The off-diagonal operator X_f^{nm} describes the transition of the ion at site f from state $|f,m\rangle$ to state $|f,n\rangle$. In terms of Dirac's bra and ket vectors the Hubbard operators can be written as

$$X_f^{nm} \equiv |f,n\rangle\langle f,m|.$$

The third term on the right-hand side of Eq. (1) allows for the state of Cr^{2+} ions with an electron configuration $3d^4$ and an energy E_2. In the crystal field the states with spin angular

momentum $S=1$ correspond to this configuration. The triplet nature is reflected by the presence of summation over m' from $m'=-1$ to $m'=1$. The fourth term takes into account the exchange interaction between the spin angular momenta of the localized subsystems. The fifth term on the right-hand side of Eq. (1) describes the exchange coupling of localized and collectivized electrons within the framework of the $s-d(f)$ exchange interaction.[6,9] Finally, the last term describes processes of hybridization interaction, when the creation annihilation of an electron in the conduction band is accompanied by the transition of a chromium ion from state Cr^{2+} (Cr^{3+}) to state Cr^{3+} (Cr^{2+}). Here the electron operator $d_{f\sigma}$ is expressed as a linear combination of multielectron Hubbard operators:[14]

$$d_{f\uparrow}=-\frac{1}{\sqrt{3}}\,X_f^{1/2,1}-\sqrt{\frac{2}{3}}\,X_f^{-1/2,0}-X_f^{-3/2,-1},$$
$$d_{f\downarrow}=X_f^{3/2,1}+\sqrt{\frac{2}{3}}\,X_f^{1/2,0}+\frac{1}{\sqrt{3}}\,X_f^{-1/2,-1}, \tag{2}$$

where the half-integral values of the superscripts correspond to states of Cr^{3+} with half-integral values of the projection of the spin angular momentum, and the integral values number the states of Cr^{2+} with spin projections $m'=\pm 1, 0$.

3. THE GREEN'S FUNCTIONS AND THE ENERGY SPECTRUM

Examining de Haas–van Alphen effects and quantum temperature oscillations requires calculating the thermodynamic potential Ω of the system. A convenient approach here is to use the coupling-constant integration method.[20] Bearing this in mind, we define the Matsubara Green's functions needed for further investigations as follows:

$$G_{\mathbf{k}\sigma}(\tau-\tau')=-\langle T_\tau \tilde{c}_{\mathbf{k}\sigma}(\tau)\tilde{c}^{+}_{\mathbf{k}\sigma}(\tau')\rangle$$
$$=T\sum_{\omega_n}\exp(-i\omega_n(\tau-\tau'))G_{\mathbf{k}\sigma}(\omega_n),$$
$$F_{\mathbf{k}\sigma}(f;\tau-\tau')=-\langle T_\tau\,\tilde{d}_{f\sigma}(\tau)\tilde{c}^{+}_{\mathbf{k}\sigma}(\tau')\rangle \tag{3}$$
$$=T\sum_{\omega_n}\exp(-i\omega_n(\tau-\tau'))F_{\mathbf{k}\sigma}(f;\omega_n).$$

We start the derivation of a system of equations from which these Green's functions can be found by mentioning a fact that simplifies our problem. Nominally pure samples of $HgCr_2Se_4$ have n-type conductivity with a carrier concentration $\sim 10^{17}$–10^{18} cm^{-3}. At such low band-electron concentrations (the electron concentration n per site is $\sim 10^{-4}$–10^{-3}) the effect of the electrons on a state of the localized subsystem is negligible.[6] This means, for instance, that the temperature behavior of the magnetization of the subsystem of localized spins is determined to a high degree of accuracy by the properties of the localized subsystem proper. But at the same time, the spectral characteristics of the band electrons are controlled to a great extent by the degree of magnetic order through the mechanism of $s-d(f)$ exchange, and by single-site correlations through hybridization interaction. These main effects are described by terms of lower-order perturbation-theory, and only these terms will be taken into account. In diagram language[17–19] this approximation corresponds to allowing only for loopless diagrams, while in the equation-of-motion method it amounts to decoupling in the higher-order Green's functions.

On the basis of the above we can write the equations for the Green's functions in the adopted approximation as follows:

$$(i\omega_n-\tilde{\varepsilon}_{\mathbf{k}\sigma}+\mu)G_{\mathbf{k}\sigma}(\omega_n)=1+\frac{1}{\sqrt{N}}\sum_f v_{\mathbf{k}}e^{-i\mathbf{k}\cdot\mathbf{R}_f}F_{\mathbf{k}\sigma}(f;\omega_n),$$
$$(i\omega_n-\tilde{\varepsilon}_{d\sigma}+\mu)F_{\mathbf{k}\sigma}(f;\omega_n)=\frac{1}{\sqrt{N}}\,v^{*}_{\mathbf{k}}e^{i\mathbf{k}\cdot\mathbf{R}_f}K_\sigma G_{\mathbf{k}\sigma}(\omega_n), \tag{4}$$

where the renormalized energies are

$$\tilde{\varepsilon}_{\mathbf{k}\sigma}=\varepsilon_{\mathbf{k}\sigma}-\sigma JR,\quad \tilde{\varepsilon}_{d\sigma}=\varepsilon_d-\sigma\overline{H},\quad \sigma=\pm\frac{1}{2}. \tag{5}$$

Here R stands for the average value of the z-projection of the localized spin angular momentum,

$$R=\frac{1}{N}\sum_f\langle S_f^z\rangle, \tag{6}$$

and $\overline{H}$ for the effective field determining the splitting of the localized energy levels,

$$\overline{H}=g\mu_B H+I_0R+J\sigma_c, \tag{7}$$

with I_0 the Fourier transform of the exchange integral at $\mathbf{q}=0$, and σ_c the magnetization of the collectivized subsystem (in units of μ_B) per site, which can be ignored if the electron concentration values are those cited earlier.

The presence of single-site correlations is reflected by the factor

$$K_\sigma=\frac{1}{N}\sum_f\langle[d_{f\sigma},d^{+}_{f\sigma}]_{+}\rangle=\frac{1}{3}\left(\frac{3}{2}-2\sigma R+\frac{1}{2}\,n_d\right), \tag{8}$$

where

$$n_d=\frac{1}{N}\sum_f\langle X_f^{1,1}+X_f^{0,0}+X_f^{-1,-1}\rangle \tag{9}$$

determines the single-site concentration of Cr^{4+} ions.

Solving the system of equations (4), we find that

$$G_{\mathbf{k}\sigma}(\omega_n)=\frac{i\omega_n-\tilde{\varepsilon}_{d\sigma}+\mu}{(i\omega_n-E^{-}_{\mathbf{k}\sigma}+\mu)(i\omega_n-E^{+}_{\mathbf{k}\sigma}+\mu)},$$
$$\frac{1}{\sqrt{N}}\sum_f e^{-i\mathbf{k}\mathbf{R}_f}\,v_{\mathbf{k}}F_{\mathbf{k}\sigma}(f;\omega_n)$$
$$=\frac{K_\sigma|v_{\mathbf{k}}|^2}{(i\omega_n-E^{-}_{\mathbf{k}\sigma}+\mu)(i\omega_n-E^{+}_{\mathbf{k}\sigma}+\mu)}, \tag{10}$$

where the mixonic spectrum is determined by the ordinary expressions[13]

$$E^{\pm}_{\mathbf{k}\sigma}=\frac{1}{2}\,(\tilde{\varepsilon}_{\mathbf{k}\sigma}+\tilde{\varepsilon}_{d\sigma})\pm\sqrt{\left(\frac{\tilde{\varepsilon}_{\mathbf{k}\sigma}-\tilde{\varepsilon}_{d\sigma}}{2}\right)^2+K_\sigma|v_{\mathbf{k}}|^2}. \tag{11}$$

We see that because of single-site correlations the hybridization interaction parameter is renormalized. In view of the importance of this fact in the initiation of quantum temperature oscillations we shall dwell on the physical reason for the renormalization. At $T=0$ the Cr^{3+} ions are in a state with the projection m of the spin angular momentum equal to 3/2. Hence an electron with $\sigma=+1/2$ cannot go into a localized state (high-spin states have a higher energy and therefore are not included in the low-energy basis of ionic states). However, an electron with an oppositely directed projection of the spin angular momentum can always go into a localized state. This leads to a dependence of effective hybridization on the direction of the spin angular momenta of the electrons, and in the low-temperature range hybridization for electrons with $\sigma=+1/2$ proves to be suppressed.

Mathematically, a meaningful description of single-site correlations is provided by the algebra of Hubbard operators, and in the adopted approximation it formally manifests itself in multiplicative renormalization of the hybridization interaction, $|v_{\mathbf{k}}|^2 \to |\tilde{v}_{\mathbf{k}\sigma}|^2 = K_\sigma |v_{\mathbf{k}}|^2$. A similar renormalization is present in the slave-boson approach,[21] with K_σ acting as the number of slave bosons in the condensate. In our case, $K_\uparrow \to 0$ and $K_\downarrow \to 1$ as $T \to 0$, in accordance with the physical situation. Here in the expression for K_σ we ignored the band-carrier concentration due to the smallness of this quantity.

4. THE OSCILLATING PART OF THE THERMODYNAMIC POTENTIAL

As is known, in examining the de Haas–van Alphen effect we must calculate the trace of the statistical operator taken in the Landau representation.[22,23] When conduction-electron concentration is low, with only the states near the bottom of the conduction band contributing to the thermodynamic characteristics, the use of the effective-mass approximation[22] is justified. In this case the Landau spectrum can be written as

$$\varepsilon_{r\sigma}(p) = \left(r + \frac{1}{2}\right)\hbar\omega_c + \frac{p^2}{2m_\parallel} + 2\mu_B \sigma H, \quad \sigma = \pm 1/2, \tag{12}$$

where $\omega_c = eH/cm_\perp$ is the cyclotron frequency,[22] $m_\perp$ is the effective mass corresponding to transverse electron motion (in relation to the vector **H**), p is the electron momentum in the direction of the external magnetic field, and $m_\parallel$ is the effective mass corresponding to longitudinal electron motion.

When there is mixing of collectivized and localized electronic spectra, the resulting electron spectrum without Landau quantization is given by Eq. (11). Since we are interested only in states with small quasimomenta, we can ignore the dependence of the hybridization parameter $v_{\mathbf{k}}$ on $\mathbf{k}$. In this case, employing Onsager quantization,[22] we can easily see that the electron spectrum in a quantizing magnetic field is obtained from (11) by replacing $\varepsilon_{\mathbf{k}\sigma}$ with $\varepsilon_{n\sigma}(p)$. In the process the dependence of $E^\pm$ on the Landau representation indices becomes irrational. This makes a direct calculation of the trace of the statistical operator impossible.

To overcome this difficulty, Wassersman *et al.*[24] suggested using the Luttinger method[25] together with contour integration. Below, in deriving the oscillating part of the thermodynamic potential, we employ the ideas of Ref. 24.

We introduce a system Hamiltonian dependent on a parameter λ:

$$\mathscr{H}(\lambda) = \mathscr{H}_0 + \lambda \mathscr{H}_{\text{mix}}, \tag{13}$$

where $\mathscr{H}_{\text{mix}}$ is the operator describing hybridization interaction processes (the last term on the right-hand side of Eq. (1)). At $\lambda = 1$ the Hamiltonian (13) coincides with the Hamiltonian (1). The meaning of $\mathscr{H}_0$ immediately follows from this correspondence.

The thermodynamic potential corresponding to (13) also depends on the parameter λ:

$$\Omega(\lambda) = -T \ln \operatorname{Tr}(\exp(-\beta \mathscr{H})). \tag{14}$$

Introduction of a temperature scattering matrix[20]

$$S_\lambda(1/T) = T_\tau \exp\left\{-\lambda \int_0^{1/T} \mathscr{H}_{\text{mix}}(\tau)\, d\tau\right\} \tag{15}$$

makes it possible, as is known, to write the statistical operator in the form

$$\exp\{-\beta \mathscr{H}(\lambda)\} = \exp(-\beta \mathscr{H}_0) S_\lambda(1/T), \quad \beta = \frac{1}{T}. \tag{16}$$

These relationships yield the following exact equation:

$$\frac{\partial \Omega}{\partial \lambda} = \frac{2T}{\sqrt{N}} \sum_{\omega_n} \sum_{f\mathbf{k}\sigma} e^{i\omega_n \delta} e^{-i\mathbf{k}\mathbf{R}_f} v_{\mathbf{k}} F_{\mathbf{k}\sigma}(f;\omega_n), \quad \delta \to +0. \tag{17}$$

In the present approximation the unknown quantities in (17) are described by Eqs. (10). Hence

$$\frac{\partial \Omega}{\partial \lambda} = T \sum_{\omega_n \mathbf{k}\sigma} e^{i\omega_n \delta} \frac{2\lambda K_\sigma |v_{\mathbf{k}}|^2}{(i\omega_n - E^+_{\mathbf{k}\sigma} \mu)(i\omega_n - E^-_{\mathbf{k}\sigma} + \mu)} \tag{18}$$

with $\delta \to +0$. To remove the irrational dependence of the electron spectrum on the quantum numbers, we write the electron propagators in the following form:

$$\begin{aligned}
(i\omega_n - \tilde{\varepsilon}_{\mathbf{k}\sigma} + \mu)^{-1} &= -\int_b^{b+i\infty} \exp\{-s(\tilde{\varepsilon}_{\mathbf{k}\sigma} - \mu \\
&\quad - i\omega_n)\} ds, \quad \omega_n > 0, \\
(i\omega_n - \tilde{\varepsilon}_{\mathbf{k}\sigma} + \mu)^{-1} &= \int_{b-i\infty}^{b} \exp\{-s(\tilde{\varepsilon}_{\mathbf{k}\sigma} - \mu \\
&\quad - i\omega_n)\} ds, \quad \omega_n < 0,
\end{aligned} \tag{19}$$

with $b \to +0$. Using these relationships, we can write Eq. (18) in a form that makes it possible (later) to sum over the Landau representation indices:

$$\begin{aligned}
\frac{\partial \Omega}{\partial \lambda} &= T \sum_{\omega_n < 0} \sum_{\mathbf{k}\sigma} \int_{b-i\infty}^{b} \exp\{-s[\tilde{\varepsilon}_{\mathbf{k}\sigma} - \mu - i\omega_n \\
&\quad + \lambda^2 \psi_\sigma(\omega_n)]\} 2\lambda \psi_\sigma(\omega_n) ds \\
&\quad - T \sum_{\omega_n > 0} \sum_{\mathbf{k}\sigma} \int_b^{b+i\infty} \exp\{-s[\tilde{\varepsilon}_{\mathbf{k}\sigma} - \mu - i\omega_n \\
&\quad + \lambda^2 \psi_\sigma(\omega_n)]\} 2\lambda \psi_\sigma(\omega_n) ds,
\end{aligned} \tag{20}$$

where $\psi_\sigma(\omega_n)=K_\sigma|v|^2/(i\omega_n-\tilde{\varepsilon}_{d\sigma}+\mu)$. Here, in accordance with the earlier remark about the smallness of the volume of the region in the **k**-space we are interested in, we ignored the dependence of $v_{\mathbf{k}}$ on **k**, taking the value of the hybridization parameter at the point of extremum.

Integration of Eq. (20) leads to the following expression for Ω:

$$\Omega=\Omega_l-T\sum_{\omega_n<0}\sum_{\mathbf{k}\sigma}\int_{b-i\infty}^{b}\phi_{\mathbf{k}\sigma}(s,\omega_n)\,\frac{ds}{s}+T\sum_{\omega_n>0}\sum_{\mathbf{k}\sigma}\int_{b}^{b+i\infty}\phi_{\mathbf{k}\sigma}(s,\omega_n)\,\frac{ds}{s}, \tag{21}$$

where

$$\phi_{\mathbf{k}\sigma}(s,\omega_n)=\exp\{-s(\tilde{\varepsilon}_{\mathbf{k}\sigma}-\mu-i\omega_n+\psi_\sigma(\omega_n))\}. \tag{22}$$

The term Ω_l can easily be determined from the condition

$$\Omega=\Omega_0=-T\ \ln\ \mathrm{Tr}(\exp(-\beta\mathscr{H}_0))$$

when the hybridization parameter is zero. Since Ω_l is of no importance to our further discussion, we do not given the value of Ω_l here.

In a quantizing magnetic field summation over **k** is replaced by summation over the quantum numbers of the Landau representation:

$$\sum_{\mathbf{k}}\ \to\left(\frac{eHV}{4\pi^2\hbar c}\right)\int_{-\infty}^{+\infty}dk_z\sum_{r=0}^{\infty}\ .$$

Integrating with respect to k_z and summing over r, from (21) we obtain

$$\Omega=\Omega_l+\Omega_++\Omega_-, \tag{23}$$

where

$$\Omega_+=D\sum_\sigma\sum_{\omega_n>0}\int_b^{b+i\infty}\frac{ds}{s^{3/2}}\,\frac{\exp\{s(i\omega_n+\tilde{\mu}_\sigma-\psi_\sigma(\omega_n))\}}{2\sinh(s\hbar\omega_c/2)},$$

$$\Omega_-=D\sum_\sigma\sum_{\omega_n<0}\int_{b-i\infty}^{b}\frac{ds}{s^{3/2}}\,\frac{\exp\{s(i\omega_n+\tilde{\mu}_\sigma-\psi_\sigma(\omega_n))\}}{2\sinh(s\hbar\omega_c/2)}, \tag{24}$$

$$D=\frac{TVeH\sqrt{2\pi m_\parallel}}{(2\pi\hbar)^2c},\quad \tilde{\mu}_\sigma=\mu+2\sigma\mu_BH+\sigma JR.$$

Further calculations involve separating the oscillating part $\Omega_\sim$ from the rest of the thermodynamic potential Ω. Since $s=0$ is a branch point, we cut the complex s plane along the semiaxis of real negative values of s. This procedure closes the integration contours in the second and third quadrants for Ω_+ and Ω_-, respectively. The integrals along the upper and lower edges of the cut contribute to the monotonic component of the thermodynamic potential.[26] The oscillating part $\Omega_\sim$ is determined by the poles on the imaginary axis at $s\hbar\omega_c/2=\pm ik\pi$. After performing the necessary calculations we get

$$\Omega_\sim=\frac{TV(\hbar\omega_c)^{3/2}m_c\sqrt{m_\parallel}}{2\pi^2\hbar^3}\times\sum_\sigma\sum_{\omega_n>0}\sum_{k=1}^{\infty}\exp\left\{-\frac{2\pi k}{\hbar\omega_c}\ \omega_n\alpha_{n\sigma}\right\}\times\cos\left\{\frac{2\pi k}{\hbar\omega_c}\ \tilde{\mu}_{n\sigma}+\varphi_\sigma\right\}. \tag{25}$$

Here

$$\alpha_{n\sigma}=1+\Gamma_{n\sigma},\quad \Gamma_{n\sigma}=\frac{K_\sigma|v|^2}{\omega_n^2+(\tilde{\varepsilon}_{d\sigma}-\mu)^2},$$

$$\tilde{\mu}_{n\sigma}=\mu+\sigma JR+(\tilde{\varepsilon}_{d\sigma}-\mu)\Gamma_{n\sigma},$$

$$\varphi_\sigma=2\pi\sigma k\left(\frac{m_c}{m_0}\right)-\frac{\pi}{4}. \tag{26}$$

These formulas describe the essential effect of magnetic ordering on the de Haas–van Alphen effect and quantum temperature oscillations. The presence of a localized subsystem affects the oscillating part of the thermodynamic potential (and hence other physical characteristics) through two channels, so to say. First, through the mechanism of hybridization interaction the presence of localized states generally leads to a decrease in the oscillation amplitude (the effect of $\Gamma_{n\sigma}$ in $\alpha_{n\sigma}$). Here, as noted earlier, single-site correlations play an important role. Second, the s–$d(f)$ exchange interaction leads to an additive term in the expression for $\tilde{\mu}_{n\sigma}$. When the energy level $\tilde{\varepsilon}_{d\sigma}$ is close to the chemical potential, the latter becomes pinned. In view of this, $\tilde{\mu}_{n\sigma}$ acquires a strong temperature dependence, which ensures quantum temperature oscillations.

5. THE MAGNETIZATION OF COLLECTIVIZED ELECTRONS

Equation (25) readily leads to an expression for the oscillating part of the system's magnetization. Keeping the principal terms, we can write

$$M_\sim=-\sum_\sigma\sum_{k=1}^{\infty}\sum_{\omega_n>0}\frac{(-1)^kA_{k\sigma}(\omega_n)}{\sqrt{k}}\times\sin\left(\frac{2\pi k\mu_{n\sigma}}{\hbar\omega_c}+\phi_\sigma\right), \tag{27}$$

where the ''partial'' amplitudes are

$$A_{k\sigma}(\omega_n)=\left(\frac{TVe\tilde{\mu}_{n\sigma}}{\pi\hbar^2c}\right)\left(\frac{m_\parallel}{\hbar\omega_c}\right)^{1/2}\exp\left(-\frac{2\pi k\omega_n\alpha_{n\sigma}}{\hbar\omega_c}\right). \tag{28}$$

Mathematically, the presence of a hybridization interaction manifests itself in the appearance of an additional summation over the Matsubara frequencies. In the absence of hybridization ($v=0$), the summation over ω_n can be done explicitly. Since in this case $\Gamma_{n\sigma}=0$ and $\alpha_{n\sigma}=1$ hold, we find that

$$M_{\sim}=-\sum_{\sigma}\sum_{k=1}^{\infty}\frac{(-1)^k}{\sqrt{k}}\,B\left(\frac{\tilde{\mu}_{\sigma}}{\hbar\omega_c}\right)\sin\left(\frac{2\pi k\tilde{\mu}_{\sigma}}{\hbar\omega_c}+\phi_{\sigma}\right),$$
$$B=\left(\frac{TVe}{2\pi\hbar^2c}\right)(m_{\parallel}\hbar\omega_c)^{1/2}\sinh^{-1}\left(\frac{2\pi^2kT}{\hbar\omega_c}\right), \tag{29}$$

with $\tilde{\mu}_{\sigma}=\mu+\sigma JR$. These formulas make it possible to easily follow the effect of $s-d(f)$ exchange splitting of spin subbands on quantum temperature oscillations. Using the renormalized expression for the chemical potential, we find that the phases of the oscillating functions contain a term $\sim JR/\hbar\omega_c$. Since the parameter J in magnetic semiconductors may exceed $\hbar\omega_c$ by several orders of magnitude, even small variations in the magnetization of the localized subsystem may cause a noticeable change in the phases. Allowing for the fact that in the low-temperature range the Bloch law is valid in ferromagnetic semiconductors, we can write the expression for the average value of the projection of the spin angular momentum of the localized subsystem as follows:

$$R=S-\left(\frac{T}{4\pi sI}\right)^{3/2}Z_{3/2}(2\mu_BH/T), \tag{30}$$

where

$$Z_{\alpha}(x)=\sum_{n=1}^{\infty}\frac{\exp(-nx)}{n^{\alpha}}$$

is the generalized Riemann zeta function. In the case of a small effective mass of the current carriers ($m^*\sim 0.01m_0$ in $HgCr_2Se_4$) there is a temperature range $\mu_BH\ll T\leqslant\hbar\omega_c$ in which the following expansion holds:

$$Z_{3/2}(2\mu_BH/T)=\zeta(3/2)-2\sqrt{\frac{2\pi\mu_BH}{T}}+\frac{35\mu_BH}{12T},$$

with $\zeta(3/2)=2.612$. In this case

$$JR=JS-\zeta(3/2)t^{3/2}+2Jt\sqrt{h}-\frac{35}{48\pi}J\sqrt{th}, \tag{31}$$

where $t=T/4\pi IS$ and $h=\mu_BH/SI$. As the temperature rises, R decreases, which in accordance with what was said earlier leads to quantum temperature oscillations. The other feature is the presence of a term proportional to $\sqrt{h}$. Hence the total oscillation phase contains the term

$$2\pi k\sigma\left(\frac{m_c}{m_{\parallel}}\right)\left(\frac{T}{r\pi sI}\right)\left(\frac{J^2}{\mu_BHSI}\right)^{1/2}\sim\frac{1}{\sqrt{H}}. \tag{32}$$

If we take the values of the parameters characteristic of magnetic semiconductors, i.e., $J\sim 0.5$ eV, $T\sim 10$ K, $m_c/m_0\approx 0.01$, and $H\approx 50$ kOe, we find that the smallness of the first two factors on the left-hand side of Eq. (32) is balanced by the large value of the fourth factor. Hence the contribution of this term becomes essential and the oscillations of magnetization under variations of the external magnetic field cease to be strictly periodic in $1/H$. This can easily be verified if, taking into account the expansion (31), we write the oscillating factors in the form

$$\sin\left\{2\pi k\left(\frac{a}{H}+\frac{b}{\sqrt{H}}\right)\right\}, \tag{33}$$

where a and b are quantities independent of the magnetic field strength,

When the band-electron concentration is low, the exchange splitting of the spin subbands leads to a situation in which the electrons fill only states with one value of the projection of spin angular momentum. Here the sign of the exchange constant J, while affecting the polarization of the band electrons, has no effect on quantum temperature oscillations.

The situation is quite different when hybridization effects are taken into account. In this case the sign of J may be of great importance to the de Haas–van Alphen effect in general and quantum temperature oscillations in particular. To demonstrate this feature explicitly we ignore the dependence on ω_n of $\Gamma_{n\sigma}$, assuming that the main contribution is due to terms with small values of ω_n. Then after summation over ω_n we obtain a formula similar to (29) if the following replacements are performed:

$$B\to B_{\sigma}=\left(\frac{TVe}{2\pi\hbar^2c}\right)(m_{\parallel}\hbar\omega_c)^{1/2}\sinh^{-1}\left(\frac{2\pi^2kT}{\hbar\omega_c}\,\alpha_{0\sigma}\right),$$
$$\tilde{\mu}_{\sigma}\to\tilde{\mu}_{0\sigma}, \tag{34}$$

with $\alpha_{0\sigma}$ and $\tilde{\mu}_{0\sigma}$ defined in (26). We see that hybridization through the factor $\alpha_{0\sigma}$ may considerably lower the amplitude of oscillations of the band-electron magnetization. Here the presence of the factor K_{σ} leads to the strong dependence of the effect on the sign of the $s-d(f)$ exchange coupling constant, noted above. For instance, when J is positive, the band electrons are in states with spin ''up.'' Since $K_{\uparrow}\to 0$ as $T\to 0$, in this case $\alpha_{0\uparrow}\to 1$, and the amplitude of the effect at low temperature is renormalized only slightly. But if J is negative, the band electrons fill the subband with spin ''down.'' In this case, as noted earlier, the hybridization interaction channel is open and $\alpha_{0\downarrow}\gg 1$. This leads to a large decrease in the oscillation amplitude, so that reliable observation of the oscillation effect becomes impossible. The physics of the effect of single-site correlations on the efficiency of hybridization interaction was discussed earlier in this paper.

In a more general case the additional contribution to the total phase of the oscillating terms is determined not only by the magnetization of the localized subsystem but also by the term $(\tilde{\varepsilon}_{d\sigma}-\mu)\Gamma_{n\sigma}$. This fact considerably complicates the net effect of magnetic ordering when mixing is taken into account, and computer calculations are needed for quantitative results.

Figure 1 depicts the dependence of temperature quantum oscillations on the magnitude and sign of the $s-d(f)$ exchange coupling constant J. The following model parameters were used in the calculations: $v=0.05$ eV, $m^*=0.01m_0$, $n=3\times 10^{18}$ cm^{-3}, and $H=20$ kOe. We see that at $J=0$ there is only one oscillation $M_{\sim}$, in accordance with the nature of this behavior discussed earlier. When J is finite, the spin subbands experience additional motion, which manifests itself in a buildup in the number of oscillations. The curves *2*

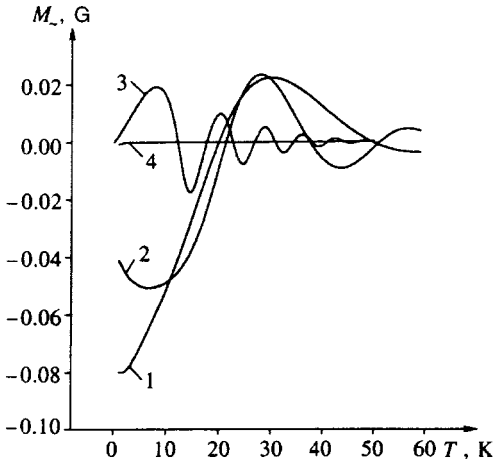

FIG. 1. Quantum temperature oscillations of magnetization for different values of the $s-d(f)$ exchange interaction parameter. $J=0$ (curve *1*), $J=0.1$ eV (curve *2*), $J=0.8$ eV (curve *3*), and $J=-0.8$ eV (curve *4*).

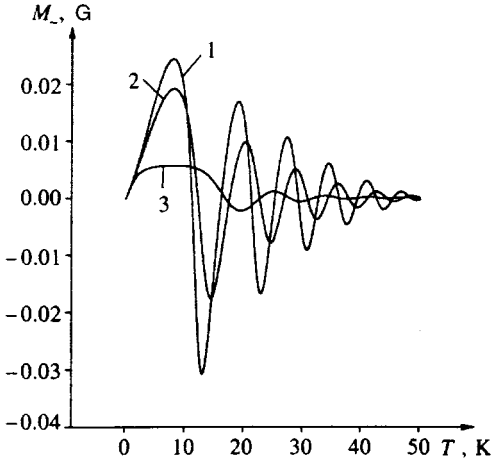

FIG. 2. Effect of the hybridization interaction on the quantum temperature oscillations of the band-electron magnetization. $v=0$ (curve *1*), $v=0.05$ eV (curve *2*), and $v=0.1$ eV (curve *3*).

and *3* were calculated for positive values of J. As noted earlier, in this case hybridization is effectively suppressed and the amplitude of the effect is sufficiently large for experimental observation of oscillations to be possible. But if J is negative, the collectivized states are strongly hybridized with localized states, and the amplitude of oscillations becomes too small for observation. This becomes especially evident if we compare curves *3* and *4*. The curve *4* was calculated for the same values of the parameters as curve *3* but with J of opposite sign. We see that because of interactions of the collectivized electron subsystem and the localized subsystem and strong intratomic correlations the amplitude of the oscillation effects is extremely sensitive to the sign of J. Satisfactory agreement with the experimental data on quantum temperature oscillations exists for $J=0.8$ eV. This value of J corresponds to the results of earlier studies of $HgCr_2Se_4$ (see Ref. 16). Moreover, the results of recent experiments[10] that established the presence of an extremely strong effect of an external magnetic field on the band gap of $HgCr_2Se_4$ can be correctly interpreted with the chosen value of J.

The high sensitivity of the effect to the magnitude v of the hybridization interaction is illustrated by Fig. 2, where we give the results of calculations of quantum temperature oscillations for three values of v at $J=0.8$ eV. The other parameters are the same as in Fig. 1. We see that hybridization strongly suppresses the oscillation amplitude and increases the distance between the nearest peaks. The latter effect is caused by the fact that $s-d(f)$ exchange interaction counteracts hybridization. When T rises, the $s-d(f)$ exchange interaction forces the bottom of the conduction band up, while hybridization forces it down. The competition of these two mechanisms ''flattens'' the $M_\sim$ vs T dependence (see the initial section of curve *3* in Fig. 2).

The effect of a magnetic field on quantum temperature oscillations is depicted in Fig. 3, where the temperature dependence of $M_\sim$ for two values of the magnetic field strength, $H=20$ and 60 kOe, is given. As expected, the amplitude and period of the oscillations increase with field strength. Such behavior of the magnetization irrevocably follows from Eqs. (25)–(27).

6. CONCLUSION

Several remarks are in order. The main conclusion that can be drawn is that magnetic ordering has a strong influence on quantum oscillation effects. The reason for this and the important role played by single-site correlations have been thoroughly discussed in this paper. Here we would only like to note that these effects may manifest themselves not only in magnetic semiconductors but also in many systems with strong correlations. In this respect mixed-valence compounds and heavy fermions (in addition to the cerium compounds CeAs, CeSb, and CeP) are especially interesting. Many of these exhibit antiferromagnetic order, and some mixed-valence compounds are ferromagnetically ordered. The large value of the band-electron concentration as compared to that discussed in the present work will require correcting the ap-

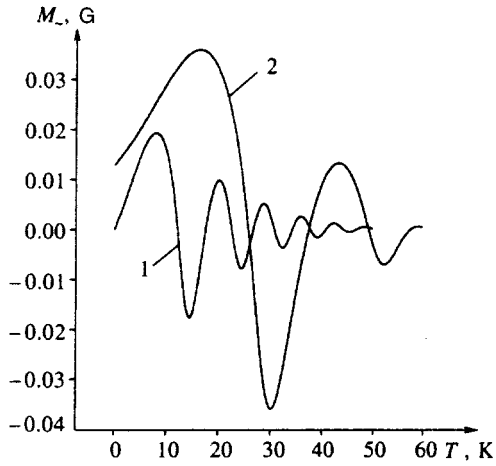

FIG. 3. Effect of a magnetic field on quantum temperature oscillations. $H=20$ kOe (curve *1*) and $H=60$ kOe (curve *2*).

proximations, but we believe that the main qualitative features of the effect of magnetic ordering on oscillation effects will be retained.

As is well known, the temperature dependence of the amplitude of the de Haas–van Alphen effect is used to determine the effective mass. Experimental studies of quantum temperature oscillations make it possible to extract much more information about the parameters of the electronic structure. In particular, the temperature profile of the band-electron magnetization provide estimates for J and the intensity of hybridization interaction. This means that experimental studies of quantum temperature oscillations may serve as an effective method for investigating the electronic structure of matter.

The authors would like to express their gratitude to S. G. Ovchinnikov and V. K. Chernov for the stimulating discussions concerning the results of the experiment in quantum temperature oscillations. The work was supported by grants from the Russian Fund of Fundamental Research (Grant No. 96-02-16075-a) and the Krasnoyarsk Science Fund (Grant No. 5F0158).

*e-mail: vvv@iph.krasnoyarsk.su

[1] B. R. Cooper, R. Siemann, D. Yang *et al.*, in *The Handbook on the Physics and Chemistry of the Actinides*, Vol. 2, edited by A. J. Freeman and G. H. Lander, North-Holland, Amsterdam (1985), p. 435.
[2] Q. R. Sheng and B. R. Cooper, J. Appl. Phys. **69**, 5472 (1991).
[3] T. Kasuya, J. Phys. Soc. Jpn. **64**, 1453 (1995).
[4] T. Kasuya, T. Suzuki, and Y. Haga, J. Phys. Soc. Jpn. **62**, 2549 (1993).
[5] S. Methfessel and D. C. Mattis, *Magnetic Semiconductors*, Springer, Berlin (1968).
[6] É. L. Nagaev, *Physics of Magnetic Semiconductors* Mir, Moscow (1983).
[7] S. G. Ovchinnikov, V. K. Chernov, A. D. Balaev, N. B. Ivanova, B. P. Khrustalev, and V. A. Levshin, JETP Lett. **64**, 642 (1995).
[8] V. V. Val'kov and S. G. Ovchinnikov, Fiz. Tverd. Tela (Leningrad) **23**, 3492, (1981) [Sov. Phys. Solid State **23**, 2032 (1981)].
[9] S. V. Vonsovskii, *Magnetism*, 2 vols., Wiley, New York (1974).
[10] I. K. Bol'nykh, A. V. Golovin, and G. N. Sever, Vestnik Moskov. Univ. **36**, 100 (1995).
[11] J. Hubbard, Proc. Roy. Soc. London, Ser. A **284**, 455 (1964).
[12] L. A. Maksimov and K. A. Kikoin, Fiz. Met. Metalloved. **28**, 43 (1969).
[13] L. A. Maksimov and K. A. Kikoin, Zh. Éksp. Teor. Fiz. **58**, 2184 (1970) [Sov. Phys. JETP **31**, 1179 (1970)].
[14] M. Sh. Erukhimov and S. G. Ovchinnikov, Fiz. Tverd. Tela **21**, 351 (1979).
[15] S. G. Ovchinnikov, Fiz. Tverd. Tela **21**, 2994 (1979) [Sov. Phys. Solid State **21**, 1724 (1979)].
[16] V. K. Chernov, V. A. Gavrichkov, N. B. Ivanova, G. S. Veisig, and Yu. V. Boyarshinov, Fiz. Tverd. Tela (Leningrad) **28**, 289 (1986) [Sov. Phys. Solid State **28**, 159 (1986)].
[17] R. O. Zaĭtsev, Zh. Éksp. Teor. Fiz. **70**, 1100 (1976) [Sov. Phys. JETP **43**, 574 (1976)].
[18] Yu. A. Izyumov and Yu. N. Skryabin, *Statistical Mechanics of Magnetically Ordered Systems* [in Russian], Nauka, Moscow (1987).
[19] Yu. A. Izyumov, M. I. Katsnel'son, and Yu. N. Skryabin, *The Magnetism of Collectivized Electrons* [in Russian], Nauka, Moscow (1994).
[20] A. A. Abrikosov, L. P. Gor'kov, and I. Ye. Dzyaloshinski, *Quantum Field Theoretical Methods in Statistical Physics*, Pergamon Press, New York (1965).
[21] P. Coleman, Phys. Rev. B **35**, 5072 (1987).
[22] I. M. Lifshits, M. Ya. Azbel, and M. I. Kaganov, *Electron Theory of Metals*, Plenum Press, New York (1973).
[23] D. Shoenberg, *Magnetic Oscillations in Metals*, Cambridge Univ. Press, Cambridge (1984).
[24] A. Wassersman, M. Springford, and A. C. Hewson, J. Phys.: Condens. Matter **1**, 2669 (1989).
[25] J. M. Luttinger, Phys. Rev. **121**, 1251 (1961).
[26] I. A. Kvasnikov, *Thermodynamics and Statistical Physics. The Theory of Equilibrium Systems* [in Russian], Moscow Univ. Press, Moscow (1991).

Translated by Eugene Yankovsky

Thermodynamic fluctuations in two-dimensional degenerate antiferromagnetic structures

V. M. Rozenbaum

Institute of Surface Chemistry, Ukrainian National Academy of Sciences, 252022 Kiev, Ukraine
(Submitted 27 June 1996)
Zh. Éksp. Teor. Fiz. **111**, 669–680 (February 1997)

A model of a two-dimensional antiferromagnet with an arbitrary anisotropic interaction that allows for degeneracy of the ground state is proposed. The lifting of degeneracy by thermodynamic fluctuations and the accompanying effects are studied by a method of self-consistent calculations of Gaussian angular fluctuations that is asymptotically exact at low temperatures. Fluctuations are shown to lead to collinear ordering of the orientations of magnetic sublattices, an effect that initiates long-range orientational order in systems with anisotropic interaction but retains only short-range order in systems with isotropic short-range interaction. The temperature patterns of the orientational correlators are given for the particular cases of dipole and isotropic short-range interaction models. The nature of the Ising-like behavior of the system is discussed for the case of a strong anisotropy of the correlators, which corresponds to quasi-one-dimensional behavior. © *1997 American Institute of Physics.* [S1063-7761(97)02002-7]

1. INTRODUCTION

Of the various systems with complicated periodic orientations of the magnetic or electric moments, those with a continuously degenerate ground state occupy a special place. Such degeneracy usually corresponds to certain rotations of the moments in antiferromagnetic sublattices and can be lifted by thermodynamic fluctuations, which occasionally leads to interesting physical effects. Among the structures that could be considered belonging to this class of systems are many spinels,[1,2] fcc antiferromagnets[3] (including, for instance, γ-Mn (Ref. 4) and $Cd_{1-x}Mn_xTe$ with large values of x (Ref. 5)), bcc antiferromagnets of the garnet type,[6] materials of the $Gd_3Ga_5O_{12}$ type with a complicated antiferromagnetic structure (which have lately been under intensive investigations),[7] and two-dimensional antiferromagnets with dipole–dipole interactions on square[8–10] and hexagonal[10–12] lattices.

The possibility of the moments in antiferromagnetic sublattices being ordered by thermodynamic fluctuations can be explained by the fact that in contrast to the ground-state energy H_0, the dispersion law $J_0(\mathbf{k})$ of spin-wave excitations (calculated for $T=0$) and the system's free energy

$$F(T\to 0)=H_0-\frac{T}{2}\sum_{\mathbf{k}}\ln\frac{2\pi T}{J_0(\mathbf{k})} \tag{1}$$

depend on the degeneracy parameter α. Minimization of (1) with respect to α suggests that a discrete symmetry with collinear orientations of the moments in the sublattices emerges.[3,10,13]

A special feature of two-dimensional degenerate systems is that they may have no long-range orientational order, defined by the following quantity:[14]

$$\rho_0=\lim_{|\mathbf{r}|\to\infty}\langle\cos(\varphi_{\mathbf{r}_1+\mathbf{r}}-\varphi_{\mathbf{r}_1})\rangle=\exp\left[-\frac{T}{N}\sum_{\mathbf{k}}\frac{1}{J_0(\mathbf{k})}\right] \tag{2}$$

(angular fluctuations $\varphi_{\mathbf{r}}$ are measured with respect to vectors of the ground-state magnetic moments). In this case we have $\rho_0=0$ because of the divergence of the integral of $J_0^{-1}(\mathbf{k})$ with respect to $\mathbf{k}$. But can such thermodynamic ordering exist, and if it can, will selection of collinear states result in long-range orientational order? Monte Carlo experiments, which by their very nature are limited to modeling finite systems, yield conflicting results, both supporting[15,16] and contradicting[17] the presence of a phase with a discrete symmetry in the systems being discussed.

In this paper an analysis of a new general model of a degenerate antiferromagnet on a square lattice is used to prove that in systems with isotropic short-range interaction a dispersion law $J(\mathbf{k})$ of spin excitations ($T\neq 0$) that has been renormalized by thermodynamic fluctuations ensures thermodynamic ordering of moments without long-range order ($\rho_0=0$). On the other hand, in systems with dipole–dipole interactions the renormalized function $J(\mathbf{k})$ and thermodynamic ordering lead to long-range orientational order ($\rho_0\neq 0$).

2. THE MODEL OF A TWO-DIMENSIONAL DEGENERATE ANTIFERROMAGNET ON A SQUARE LATTICE

Let us examine a system of magnetic or electric moments at the sites $\mathbf{r}$ of a planar Bravais lattice. The system Hamiltonian in the most general form is

$$H=\frac{1}{2}\sum_{\mathbf{r},\mathbf{r}'}V^{\alpha\beta}(\mathbf{r}-\mathbf{r}')e^{\alpha}_{\mathbf{r}}e^{\beta}_{\mathbf{r}'}=\frac{1}{2}\sum_{\mathbf{k}}\widetilde{V}^{\alpha\beta}(\mathbf{k})\widetilde{\mathbf{e}}^{\alpha}_{\mathbf{k}}\widetilde{\mathbf{e}}^{\beta}_{-\mathbf{k}}, \tag{3}$$

where the interactions $V^{\alpha\beta}(\mathbf{r})=V^{\alpha\beta}(-\mathbf{r})=V^{\beta\alpha}(\mathbf{r})$ can be anisotropic and long-range, the $\mathbf{e}_{\mathbf{r}}$ are the two-dimensional unit vectors specifying the orientations of the moments, $\alpha,\ \beta=x,\ y$, and summation over repeated Greek indices is assumed. The ground state of the system is determined by the smallest eigenvalue $\widetilde{V}_{\min}$ and the corresponding unit eigenvector (or eigenvectors) $\boldsymbol{\eta}_p$ of the tensor $V^{\alpha\beta}(\mathbf{k})$. To introduce a four-sublattice antiferromagnetic ground state with degenerate orientation of the magnetic moments in the sublattices, we will restrict our discussion to square lattices and

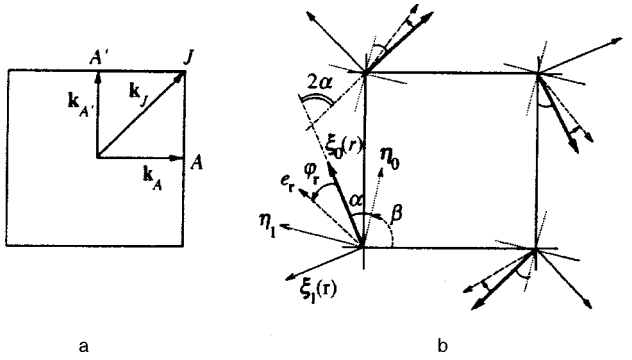

FIG. 1. (a) The first Brillouin zone of a square lattice, and (b) the four-sublattice structure of moments on a square lattice. The dotted lines correspond to the orthonormalized basis $\boldsymbol{\eta}_0, \boldsymbol{\eta}_1$, the solid heavy arrows specify the configuration of moments in the ground state $\boldsymbol{\xi}_0(\mathbf{r})$, and the solid light arrows specify the structure of the vectors $\boldsymbol{\xi}_1(\mathbf{r})$. The dashed arrows stand for the angular fluctuations of $\mathbf{e}_\mathbf{r}$ about the ground state.

require that the minimum value $\widetilde{V}_{\min}$ is attained at two symmetric points, $\mathbf{k}_A$ and $\mathbf{k}_{A'}$, of the first Brillouin zone (Fig. 1a). Then

$$\widetilde{V}^{\alpha\beta}(\mathbf{k}_A)\,\eta_0^\beta=\widetilde{V}_{\min}\eta_0^\alpha,\quad \widetilde{V}^{\alpha\beta}(\mathbf{k}_{A'})\,\eta_1^\beta=\widetilde{V}_{\min}\eta_1^\alpha, \tag{4}$$

with $\boldsymbol{\eta}_1\perp\boldsymbol{\eta}_0$, and the structure of the moments in the ground state, $\mathbf{e}_\mathbf{r}=\boldsymbol{\xi}_0(\mathbf{r})$, with an energy $H_0=N\widetilde{V}_{\min}/2$ is degenerate in the angular parameter α:

$$\boldsymbol{\xi}_0(\mathbf{r})=\boldsymbol{\eta}_0\,\exp(i\mathbf{k}_A\mathbf{r})\cos\,\alpha+\boldsymbol{\eta}_1\,\exp(i\mathbf{k}_{A'}\mathbf{r})\sin\,\alpha. \tag{5}$$

Since $\mathbf{r}=n_1\mathbf{a}_1+n_2\mathbf{a}_2$ (here $\mathbf{a}_1$ and $\mathbf{a}_2$ are the basis vectors of the lattice, and n_1 and n_2 are integers), $\mathbf{k}_A\mathbf{r}=\pi n_1$, and $\mathbf{k}_{A'}\mathbf{r}=\pi n_2$, the exponentials in (5) assume values ±1, and we obtain the four-sublattice structure depicted in Fig. 1b. For isotropic interactions $V^{\alpha\beta}(\mathbf{r})=V(\mathbf{r})\,\delta_{\alpha\beta}$ the orientations of the vectors $\boldsymbol{\eta}_0=(\cos\beta,\sin\beta)$ and $\boldsymbol{\eta}_1=(-\sin\beta,\cos\beta)$ with respect to the lattice axes are arbitrary. For anisotropic interactions the value of the parameter β is fixed (say, $\beta=\pi/2$ for dipole–dipole interactions). In both cases the angle 2α between the orientations of the dipole moments in sublattices shifted by the vector $\mathbf{a}_1$ or $\mathbf{a}_2$ remain arbitrary in the ground state.

In introducing the concept of angular fluctuations $\varphi_\mathbf{r}$ of vectors $\mathbf{e}_\mathbf{r}$ with respect to the orientational structure of the ground state it is convenient to employ an $\mathbf{r}$-dependent orthonormalized base of vectors $\boldsymbol{\xi}_0(\mathbf{r})$, $\boldsymbol{\xi}_1(\mathbf{r})$, where

$$\boldsymbol{\xi}_1(\mathbf{r})=\boldsymbol{\eta}_1\,\exp(i\mathbf{k}_A\mathbf{r})\cos\,\alpha-\boldsymbol{\eta}_0\,\exp(i\mathbf{k}_{A'}\mathbf{r})\sin\,\alpha, \tag{6}$$

and expand the vector $\mathbf{e}_\mathbf{r}$ in the basis vectors:

$$\mathbf{e}_\mathbf{r}=\boldsymbol{\xi}_0(\mathbf{r})\cos\,\varphi_\mathbf{r}+\boldsymbol{\xi}_1(\mathbf{r})\sin\,\varphi_\mathbf{r} \tag{7}$$

(such an expansion for an arbitrary Bravais lattice was suggested in Ref. 14). Plugging (7) into (3), we get

$$H=\frac{1}{2}\sum_{\mathbf{r},\mathbf{r}'}V^{\alpha\beta}(\mathbf{r}-\mathbf{r}')\sum_{\sigma=\pm1}[\zeta_\sigma^{\alpha\beta}(\mathbf{r},\mathbf{r}')\cos(\varphi_\mathbf{r}-\sigma\varphi_{\mathbf{r}'})+\sigma\widetilde{\zeta}_\sigma^{\alpha\beta}(\mathbf{r},\mathbf{r}')\sin(\varphi_\mathbf{r}+\sigma\varphi_{\mathbf{r}'})], \tag{8}$$

where

$$\zeta_\sigma^{\alpha\beta}(\mathbf{r},\mathbf{r}')=\frac{1}{2}[\xi_0^\alpha(\mathbf{r})\xi_0^\beta(\mathbf{r}')+\sigma\xi_1^\alpha(\mathbf{r})\xi_1^\beta(\mathbf{r}')],$$

$$\widetilde{\zeta}_\sigma^{\alpha\beta}(\mathbf{r},\mathbf{r}')=\frac{1}{2}[\xi_0^\alpha(\mathbf{r})\xi_1^\beta(\mathbf{r}')+\sigma\xi_1^\alpha(\mathbf{r})\xi_0^\beta(\mathbf{r}')]. \tag{9}$$

To calculate the low-temperature asymptotic behavior of the free energy in a meaningful manner, we must allow for the possibility that the correlators $\langle\varphi_\mathbf{r},\varphi_{\mathbf{r}'}\rangle$ may be divergent (as they are in the Berezinskiĭ–Kosterlitz–Thouless phase[18,19]) and the fact that an expansion of (8) up to terms quadratic in $\varphi_\mathbf{r}$ is not sufficient. There are various methods of specifying the principal contributions obtained in the summation of the series in $\varphi_\mathbf{r}$ (see Refs. 18–20). Here we will use a variational method (the most transparent one) that is asymptotically exact in the low-temperature limit. This method has been used to describe orientational ordering in two-dimensional systems with anisotropic and long-range interactions.[14]

We introduce the effective Hamiltonian of Gaussian angular fluctuations,

$$H_{\text{eff}}=\frac{1}{2}\sum_\mathbf{k}J(\mathbf{k})\widetilde{\varphi}_\mathbf{k}\widetilde{\varphi}_{-\mathbf{k}}, \tag{10}$$

with a function $J(\mathbf{k})$ minimizing the right-hand side of the Feynman inequality[21]

$$F\leqslant\frac{\mathrm{Tr}\,H\,\exp(-H_{\text{eff}}/T)}{\mathrm{Tr}\,\exp(-H_{\text{eff}}/T)}-T\,\frac{\partial}{\partial T}\left[T\,\ln\,\mathrm{Tr}\,\exp\left(-\frac{H_{\text{eff}}}{T}\right)\right]$$

$$=\frac{N}{4}\sum_\mathbf{r}\sum_{\sigma=\pm1}[W_0(\mathbf{r})+\sigma W_1(\mathbf{r})][\exp(i\mathbf{k}_A\mathbf{r})\cos^2\,\alpha+\sigma\,\exp(i\mathbf{k}_{A'}\mathbf{r})\sin^2\,\alpha]\rho(\mathbf{r}|\sigma)-\frac{T}{2}\sum_\mathbf{k}\,\ln\frac{2\pi eT}{J(\mathbf{k})}, \tag{11}$$

where Tr stands for integration over the complex-valued variables $\widetilde{\varphi}_\mathbf{k}=\widetilde{\varphi}^*_{-\mathbf{k}}$,

$$W_p(\mathbf{r})=\eta_p^\alpha V^{\alpha\beta}(\mathbf{r})\,\eta_p^\beta,\quad p=0,\ 1, \tag{12}$$

$$\rho(\mathbf{r}|\sigma)=\langle\cos(\varphi_{\mathbf{r}'+\mathbf{r}}-\sigma\varphi_{\mathbf{r}'})\rangle=\exp\left[-\frac{T}{N}\sum_\mathbf{k}\,\frac{1-\sigma\,\cos\,\mathbf{kr}}{J(\mathbf{k})}\right], \tag{13}$$

and we have used the identity

$$\langle\cos(\varphi_\mathbf{r}\pm\varphi_{\mathbf{r}'}+C)\rangle=\mathrm{Re}\,\exp\left[-\frac{1}{2}\langle(\varphi_\mathbf{r}\pm\varphi_{\mathbf{r}'})^2\rangle-iC\right]. \tag{14}$$

valid in averaging the Gaussian fluctuations of angles described by the Hamiltonian (10). Varying (11) with respect to $J(\mathbf{k})$ leads to the equation

$$J(\mathbf{k})=-\frac{1}{2}\sum_\mathbf{r}\sum_{\sigma=\pm1}[W_0(\mathbf{r})+\sigma W_1(\mathbf{r})]\times[\exp(i\mathbf{k}_A\mathbf{r})\cos^2\,\alpha+\sigma\,\exp(i\mathbf{k}_{A'}\mathbf{r})\sin^2\,\alpha]\times(1-\sigma\,\cos\,\mathbf{kr})\rho(\mathbf{r}|\sigma), \tag{15}$$

which defines the function $J(\mathbf{k})$.

3. GENERAL ANALYSIS OF THE EQUATIONS

First we note that at $T=0$ the correlators $\rho(\mathbf{r}|\sigma)$ are equal to unity and Eq. (15) immediately leads to the following expression:

$$J_0(\mathbf{k})=\widetilde{W}_1(\mathbf{k}+\mathbf{k}_A)\cos^2\alpha+\widetilde{W}_0(\mathbf{k}+\mathbf{k}_{A'})\sin^2\alpha-\widetilde{V}_{\min}, \tag{16}$$

which does indeed depend on α. In Secs. 4 and 5 we will see that this expression is reduced to well-known relationships for two short-range models.[13,17] In view of the definitions (4) and (12) we have $\widetilde{W}_0(\mathbf{k}_A)=\widetilde{W}_1(\mathbf{k}_{A'})=\widetilde{V}_{\min}$, so that allowing for the property

$$\widetilde{W}_p(\mathbf{k}+2\mathbf{k}_A)=\widetilde{W}_p(\mathbf{k}+2\mathbf{k}_{A'})=\widetilde{W}_p(\mathbf{k}),$$

yields

$$J_0(\mathbf{k}_J)=0, \quad \mathbf{k}_J=\mathbf{k}_A+\mathbf{k}_{A'}$$

(see Fig. 1a). Since for short-range and dipole–dipole interactions the quantities $\widetilde{V}^{\alpha\beta}(\mathbf{k})$ near the points $\mathbf{k}=\mathbf{k}_A$ and $\mathbf{k}_{A'}$ exhibit quadratic asymptotic behavior in the corresponding wave-vector shifts,[14,22] the function $J_0(\mathbf{k}+\mathbf{k}_J)$ is quadratic in $\mathbf{k}$ and the sums with respect to $\mathbf{k}$ in (13) diverge, provided that the quantities $1-\sigma\cos\mathbf{k}_J\mathbf{r}$ do not vanish. Such is the situation if we use the function $J_0\mathbf{k}$ (Eq. (16)) unrenormalized by thermodynamic fluctuations.

We can show that as $T\to 0$ (but $T\neq 0$), near the point $\mathbf{k}=\mathbf{k}_J$ a gap appears in the renormalized dispersion law $J(\mathbf{k})$. To this end we must employ the lattice–sublattice relationships of Refs. 22 and 23 and the fact that the tensors $\widetilde{V}^{\alpha\beta}(\mathbf{k})$ are isotropic at the symmetric points $\mathbf{k}=0$ and $\mathbf{k}_J$. As a result we get

$$J(\mathbf{k}+\mathbf{k}_J)\approx\frac{1}{2}\,[\widetilde{V}(0)-\widetilde{V}(\mathbf{k}_J)][\rho(\mathbf{a}_1|1)-\rho(\mathbf{a}_2|1)]\cos 2\alpha + J_0(\mathbf{k}+\mathbf{k}_J), \tag{17}$$

where we have left only the correlators that are not equal to unity and provide the main contribution to the formation of the gap.

Expanding the $\widetilde{W}_\sigma(\mathbf{k})$ at the points $\mathbf{k}_A$ and $\mathbf{k}_{A'}$,

$$\widetilde{W}_0(\mathbf{k}+\mathbf{k}_A)=\widetilde{V}_{\min}+C_x(\mathbf{k}\mathbf{a}_1)^2+C_y(\mathbf{k}\mathbf{a}_2)^2,$$

$$\widetilde{W}_1(\mathbf{k}+\mathbf{k}_{A'})=\widetilde{V}_{\min}+C_y(\mathbf{k}\mathbf{a}_1)^2+C_x(\mathbf{k}\mathbf{a}_2)^2, \tag{18}$$

we can write $J_0(\mathbf{k}+\mathbf{k}_J)$ in the form

$$J_0(\mathbf{k}+\mathbf{k}_J)=\frac{1}{2}\,(C_x+C_y)q^2(1-v\cos 2\theta_{\mathbf{k}}), \tag{19}$$

where

$$v=\frac{C_x-C_y}{C_x+C_y}\cos\alpha, \quad \mathbf{q}=\mathbf{k}a, \tag{20}$$

and $\theta_{\mathbf{k}}$ is the angle between the vector $\mathbf{k}$ and the x axis. The presence of a gap in the spectrum (17) prevents the correlators $\rho(\mathbf{a}_1|1)$ and $\rho(\mathbf{a}_2|1)$ from vanishing at finite temperatures. Indeed, substituting Eqs. (17) and (19) in (13) and performing asymptotic integration near the point $\mathbf{q}=0$, we obtain

$$\rho(\mathbf{a}_1|1)\approx\rho(\mathbf{a}_2|1)\approx\exp\left[-\frac{T|\ln\gamma(v)T|}{\pi(C_x+C_y)\sqrt{1-v^2}}\right],$$

$$|\rho(\mathbf{a}_1|1)-\rho(\mathbf{a}_2|1)|\propto T, \quad T\to 0, \tag{21}$$

where the coefficient $\gamma(v)$ is determined by integration over the first Brillouin zone for each specific model.

Since the size of the energy gap in Eq. (17) is proportional to temperature, for $T\to 0$ the gap can be ignored in calculations of physical quantities that have no singularities at the points where $J_0(\mathbf{k})=0$. This is the case with the entropy contribution to the free energy (1), which is linear in temperature. Allowing for the fact that under a rotation of the system of coordinates through 90° the quantities in Eq. (16) are transformed as

$$\widetilde{W}_{0,1}(\mathbf{k}+\mathbf{k}_A)\leftrightarrow\widetilde{W}_{1,0}(\mathbf{k}+\mathbf{k}_{A'}),$$

we can write the α-dependent contribution to the free energy:

$$\Delta F(\alpha)=\frac{T}{2}\sum_{\mathbf{k}}\ln J_0(\mathbf{k})=\frac{1}{4}\sum_{\mathbf{k}}\ln[A_+^2(\mathbf{k}) - A_-^2(\mathbf{k})\cos^2 2\alpha]\leqslant\frac{T}{4}\sum_{\mathbf{k}}\ln A_+^2(\mathbf{k}), \tag{22}$$

$$A_\pm(\mathbf{k})=\frac{1}{2}\,\{[\widetilde{W}_1(\mathbf{k}+\mathbf{k}_A)-\widetilde{V}_{\min}]\pm[\widetilde{W}_0(\mathbf{k}+\mathbf{k}_{A'})-\widetilde{V}_{\min}]\}.$$

This implies that collinear orientations of the moments in sublattices, i.e., $2\alpha=0$ and π, are preferable. Since the gap size in Eq. (17) is positive, the choice of $\alpha=0$ or $\pi/2$ with allowance for the sign of $\widetilde{V}(0)-\widetilde{V}(\mathbf{k}_J)$ (or C_x-C_y) fixes the sign of $\rho(\mathbf{a}_1|1)-\rho(\mathbf{a}_2|1)$.

If there is no single point except $\mathbf{k}=\mathbf{k}_J$ where $J_0(\mathbf{k})$ vanishes, the square of the long-range order parameter ρ_0, defined by Eq. (2) with a renormalized function $J(\mathbf{k})$, can be found by solving

$$\rho_0\approx\rho^{1/2}(\mathbf{a}_1|1), \tag{23}$$

and it proves to be nonzero. This is the situation for systems with dipole–dipole interaction,[24] which we will study in Sec. 4.

In the case of isotropic interactions, we have $W_0(\mathbf{r})=W_1(\mathbf{r})$, with the result that only terms with $\sigma=1$ remain in Eqs. (11) and (15), so that $J(0)=0$. For short-range interaction, the function $J(\mathbf{k})$ is characterized by a quadratic asymptotic behavior near $\mathbf{k}=0$, which results in the divergence of the integral of $J^{-1}(\mathbf{k})$ and an absence of long-range order ($\rho_0=0$ at $T\neq 0$). One of the possible examples of systems of this type is discussed in Sec. 5.

4. THE DIPOLE SHORT-RANGE MODEL

The nonzero components of the tensors describing the interaction of the dipole moments at neighboring sites of a square lattice are given by the following relationships:

$$V^{xx}(\mathbf{a}_1)=V^{yy}(\mathbf{a}_2)=W_1(\mathbf{a}_1)=W_0(\mathbf{a}_2)=-2V,$$

$$V^{yy}(\mathbf{a}_1)=V^{xx}(\mathbf{a}_2)=W_0(\mathbf{a}_1)=W_1(\mathbf{a}_2)=V, \tag{24}$$

$$\widetilde{V}^{xx}(\mathbf{q})=\widetilde{W}_1(\mathbf{q})=V(-4\cos q_x+2\cos q_y),$$

$$\widetilde{V}^{yy}(\mathbf{q})=\widetilde{W}_0(\mathbf{q})=V(2\cos q_x-4\cos q_y), \tag{25}$$

where $\mathbf{q}=\mathbf{k}a$, and $V=\mu^2/a^3$ is the characteristic dipole–dipole interaction energy, with μ the dipole moment and a the lattice constant. Within the chosen parametrization scheme, β in Fig. 1b is equal to $\pi/2$, and the degeneracy angles α specify the slope of the ground-state vectors with respect to the y axis of the square lattice. By introducing a compact notation for the nearest-neighbors correlators,

$$\rho_1=\rho(\mathbf{a}_1|1), \quad \rho_2=\rho(\mathbf{a}_2|1),$$

$$\rho_3=\rho(\mathbf{a}_1|-1), \quad \rho_4=\rho(\mathbf{a}_2|-1), \tag{26}$$

we can transform the function (15) to the following form:

$$J(\mathbf{k})=\frac{1}{2}\,|\widetilde{V}_{\min}|J(q_x,q_y),$$

$$J(q_x,q_y)=\rho_3(1+\cos q_x)+\rho_4(1+\cos q_y)$$
$$-v[\rho_1(1-\cos q_x)-\rho_2(1-\cos q_y)], \tag{27}$$

where

$$\frac{1}{2}\,|\widetilde{V}_{\min}|=C_x+C_y=3V, \quad v=\frac{1}{3}\cos 2\alpha. \tag{28}$$

The values $C_x=V$ and $C_y=2V$ agree with the definition of v in (20) and make it possible to estimate the low-temperature behavior of ρ_1 and ρ_2 by employing (21). At $T=0$, when all correlators are equal to unity, the function (27) coincides, to within notation and the choice of the parametrization scheme, with the expression in Ref. 17.

Calculating the integrals in (13) over the first Brillouin zone with the function (27), we arrive at the following system of equations for the correlators (26):

$$\rho_{1,2}=\frac{\rho_0^2}{\rho_{3,4}}, \quad \rho_0=\exp(-\tau L_0), \quad \tau=\frac{T}{3V}, \tag{29}$$

$$L_0=\frac{1}{(2\pi)^2}\int_{-\pi}^{\pi}\int\frac{dq_x dq_y}{J(q_x,q_y)}$$

$$=\frac{1}{\pi}\left[\frac{\rho_3\rho_4}{\rho_3^2\rho_4^2-v^2\rho_0^4}\right]^{1/2}K(m), \tag{30}$$

$$\rho_{3,4}=\exp(-\tau L_{3,4}),$$

$$L_{3,4}=\frac{1}{(2\pi)^2}\int_{-\pi}^{\pi}\int\frac{1+\cos q_{x,y}}{J(q_x,q_y)}\,dq_x dq_y$$

$$=\frac{\rho_{3,4}}{\rho_{3,4}^2\pm v\rho_0^2}\,[1-\Lambda_0(\varepsilon_{3,4},m)], \tag{31}$$

$$m=\frac{(\rho_3^2+v\rho_0^2)(\rho_4^2-v\rho_0^2)}{\rho_3^2\rho_4^2-v^2\rho_0^4},$$

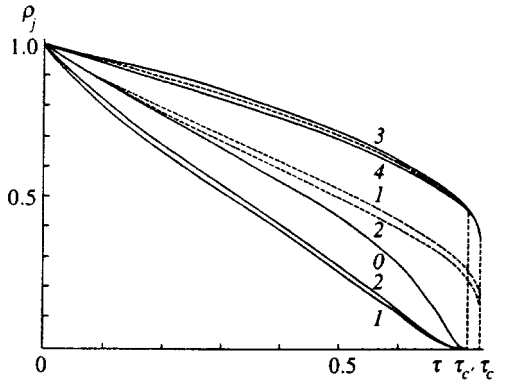

FIG. 2. The square of the long-range order parameter (curve *0*) and the nearest-neighbors correlators ρ_j (the curves $j=1,\ldots,4$) as function of temperature for the dipole (solid curves) and isotropic (dashed curves) short-range interaction models at $v=1/3$.

$$\varepsilon_{3,4}=\arcsin\left[\frac{\rho_3\rho_4\mp v\rho_0^2}{\rho_{3,4}(\rho_3+\rho_4)}\right]^{1/2}, \tag{32}$$

where $K(m)$ is the complete elliptic integral of the first kind, and $\Lambda_0(\varepsilon,m)$ is Heuman's lambda function.[25] The long-range order parameter $\rho_0^{1/2}$ links the nearest-neighbors correlators and assumes nonzero values in the low-temperature range for $\rho_3>\rho_4$. This inequality corresponds to structures with $\alpha=0$ for $v>0$, $\rho_1<\rho_2$, and the gap size satisfies $J(\pi,\pi)=2v(\rho_2-\rho_1)>0$. The parametrization scheme chosen in Ref. 24 corresponds to $\beta=0$ in the ground state, which results in $J(\pi,\pi)=2v(\rho_1-\rho_2)>0$ and $\rho_3<\rho_4$.

The system of Eqs. (29)–(32) allows for an analytic solution when the parameter v is small (or ρ_0 is small when $m\to 1$):

$$\rho_{3,4}=\rho\pm\delta, \quad \rho=\exp\left[-\frac{\tau}{2\rho}\right], \tag{33}$$

$$\rho_0=\exp\left\{\frac{\tau}{2(\pi\rho-2\tau)}\,\ln\frac{(\pi-2)v^2\tau}{4\rho^4[2\pi\rho-(\pi-2)\tau]}\right\},$$

$$\tau<\frac{\pi\rho}{2}, \tag{34}$$

$$\delta=\frac{(\pi-2)\rho_0^2 v\tau}{\rho[2\pi\rho-(\pi-2)\tau]}. \tag{35}$$

Equation (33) determines the variation of ρ from 1 to $e^{-1}\approx 0.3679$ as the temperature parameter τ grows from 0 to $\tau_c=2e^{-1}\approx 0.7358$. However, at the somewhat smaller value $\tau_{c'}=(\pi/2)\exp(-\pi/4)\approx 0.7162$ the denominator $\pi\rho-2\tau$ vanishes. At point $\tau=\tau_{c'}$ the logarithmic factor is negative for $v<v^*=2\exp(-\pi/2)[(6-\pi)/(\pi-2)]^{1/2}\approx 0.6579$, and the long-range order parameter $\rho_0^{1/2}$ also vanishes, which corresponds to spontaneous breaking of the discrete symmetry Z_4. In the narrow temperature interval $\tau_{c'}<\tau<\tau_c$ we have $\rho_0=\rho_1=\rho_2=0$, $\delta=0$, and the correlators $\rho_3=\rho_4=\rho$ change from $\exp(-\pi/4)\approx 0.4559$ to e^{-1}, with the result that only the phase with short-range order can be realized. The temperature patterns of $\rho_0,\rho_1,\ldots,\rho_4$ at $v=1/3$ are depicted in Fig. 2 by solid curves.

5. THE ISOTROPIC SHORT-RANGE MODEL

Let us examine a two-dimensional model of XY moments that allows for isotropic exchange interactions both between the nearest neighbors on the square lattice (V_1) and between the neighbors ''linked'' by the diagonals of the squares of the lattice (V_2) (see Refs. 3 and 13):

$$V^{\alpha\beta}(\mathbf{r})=V(r)\delta_{\alpha\beta}, \quad V(a)=V_1, \quad V(\sqrt{2}a)=V_2, \quad (36)$$

$$\widetilde{V}(\mathbf{q})=\widetilde{W}_0(\mathbf{q})=\widetilde{W}_1(\mathbf{q})=2V_1(\cos q_x+\cos q_y) + 4V_2 \cos q_x \cos q_y. \quad (37)$$

For $0<V_1<2V_2$ the system in the ground state is characterized by an energy $H_0=-2NV_2$ ($\widetilde{V}_{\min}=-4V_2$) and can be separated into two square ($\sqrt{2}\times\sqrt{2}$) sublattices, each of which is antiferromagnetically ordered and has arbitrary angles 2α between the orientations of the moments in the sublattices. Because of the isotropy of the interactions (36), the orientations of the moments are entirely independent of the orientations of the lattice axes, and in contrast to the dipole moment the angle β is also arbitrary. Such a model can be realized, for instance, in two adjacent square CuO_2 layers, with one centered above the other (as in some high-T_c superconductors), in which V_1 describes small interlayer exchange interactions.[13]

For the given model the function (15) assumes the form

$$J(\mathbf{k})=\frac{1}{2}|\widetilde{V}_{\min}|J(q_x,q_y),$$

$$J(q_x,q_y)=(\rho_3+\rho_4)(1-\cos q_x \cos q_y)+(\rho_3-\rho_4) \times \sin q_x \sin q_y+2v[\rho_1(1-\cos q_x) -\rho_2(1-\cos q_y)], \quad (38)$$

where

$$\rho_1=\rho(\mathbf{a}_1|1), \quad \rho_2=\rho(\mathbf{a}_2|1),$$

$$\rho_3=\rho(\mathbf{a}_1+\mathbf{a}_2|1), \quad \rho_4=\rho(\mathbf{a}_1-\mathbf{a}_2|1), \quad (39)$$

$$|V_{\min}|=C_x+C_y, \quad C_{x,y}=2V_2\pm V_1,$$

$$v=\frac{V_1}{2V_2}\cos 2\alpha. \quad (40)$$

At $T=0$ all correlators are equal to unity and (38) reduces to an expression obtained in Ref. 13. The correction (22) to the free energy becomes

$$\Delta F(\alpha)=\frac{NT}{2}\left\{-\ln 2+\frac{2}{\pi}\left[f\left(\frac{\pi}{2}+\delta\right)+f\left(\frac{\pi}{2}-\delta\right)\right]\right\} \xrightarrow[v\to 0]{} \frac{NT}{2}\left(\frac{4}{\pi}G-\ln 2-\frac{v^2}{\pi}\right), \quad (41)$$

where $f(\delta)$ is the Clausen integral, $\sin\delta=v$, and $G\approx 0.916$ is the Catalan constant.[25] The asymptotic behavior at small values of v described by (41) agrees with the results of a Monte Carlo calculation done by Fernandez *et al.*,[15] $\Delta F(\alpha)=\text{const}+0.04NT(2\alpha)^2$ (at $V_1=V_2$), and, to within the factor $\frac{1}{2}$ discarded in Ref. 13, coincides with the result obtained by the same researchers via numerical integration, $\Delta F(\alpha)\approx\text{const}-0.32NTv^2$ (the factor 0.32 is simply π^{-1}).

The integrals in (13) with the function $J(q_x,q_y)$ given by (38) can easily be calculated:

$$M_1(\rho_1,\rho_2,\rho_3,\rho_4)=\frac{1}{(2\pi)^2}\int_{-\pi}^{\pi}\int\frac{1-\cos q_x}{J(q_x,q_y)}\,dq_x dq_y =\frac{1}{\pi B^{1/2}}\ln\frac{(A+B)^{1/2}+(2B)^{1/2}}{(A-B)^{1/2}}, \quad (42)$$

$$A=2\rho_3\rho_4-2v^2\rho_1\rho_2+v(\rho_1-\rho_2)(\rho_3+\rho_4),$$

$$B=\rho_3\rho_4-v^2\rho_1^2,$$

$$M_2(\rho_1,\rho_2,\rho_3,\rho_4)=\frac{1}{(2\pi)^2}\int_{-\pi}^{\pi}\int\frac{1-\cos q_y}{J(q_x,q_y)}\,dq_x dq_y =M_1(-\rho_2,-\rho_1,\rho_4,\rho_3), \quad (43)$$

$$M_{3,4}(\rho_1,\rho_2,\rho_3,\rho_4) =\frac{1}{(2\pi)^2}\int_{-\pi}^{\pi}\int\frac{1-\cos(q_x\pm q_y)}{J(q_x,q_y)}\,dq_x dq_y =\frac{1}{\rho_{3,4}}\left\{\frac{1}{2}-v(\rho_1M_1-\rho_2M_2)+\text{sgn}(\rho_{3,4}-\rho_{4,3}) \times\left[1+\frac{1}{\pi}\arctan\frac{|\rho_3-\rho_4|}{(2A)^{1/2}}\right]\right\}, \quad (44)$$

and the correlators $\rho_1,\ldots,\rho_4$ are specified by the following system of equations:

$$\rho_j=\exp[-\tau M_j(\rho_1,\rho_2,\rho_3,\rho_4)], \quad j=1,\ldots,4, \quad (45)$$

where $\tau=T/2V_2$. Let us assume that $\rho_3>\rho_4$. Then Eq. (44) implies that $M_3>M_4$, and Eq. (45) that $\rho_3<\rho_4$. This contradiction shows that the only solutions of (45) are those with $\rho_3=\rho_4$.

The low-temperature behavior of the correlators ρ_1 and ρ_2 is determined by Eq. (21), while the temperature dependence of ρ_3 for $v\leqslant 0.5$ is described with a high degree of accuracy by the equation $\rho_3=\exp[-\tau/2\rho_3]$. At large distance $\mathbf{R}=2n_1\mathbf{a}_1+2n_2\mathbf{a}_2$, and for $\tau\ll 1$ the same correlators decrease like

$$\rho(\mathbf{a}_1+\mathbf{R}|1)\sim(\lambda_1 R/a\tau^2)^{-\tau/2\pi\sqrt{1-v^2}},$$

$$\rho(\mathbf{a}_1+\mathbf{a}_2+\mathbf{R}|1)\sim(\lambda_2 R/a)^{-\tau/\pi\sqrt{1-v^2}} \quad (46)$$

(λ_1 and λ_2 are constants independent of $\mathbf{R}$ and τ) and vanish as $R\to\infty$, which according to (2) corresponds to $\rho_0=0$.

The system of equations (45) with $v\to 0$ and $0<\tau<\tau_c\approx 2/e$ has the following asymptotic solution:

$$\rho_3=\rho_4=\exp[-\tau/2\rho_3],$$

$$\rho_1 = \exp\left[\frac{\tau}{2(\pi\rho_3 - \tau)}\ \ln\frac{v^2\tau}{4\pi\rho_3^3}\right], \quad \rho_1 - \rho_2 = \frac{\rho_1^2}{\pi\rho_3^2}\ v\tau. \tag{47}$$

The nature of the obtained temperature curves is illustrated by the dashed curves in Fig. 2.

6. DISCUSSION

Let us first discuss the range of applicability of the results obtained by the self-consistent method of calculating Gaussian angular fluctuations. In Ref. 14 it was shown that the method provides a correct description of low-temperature correlation functions when the statistics of rotations of the moments through large angle with respect to their orientations in the ground states can be ignored. This situation is inherent in degenerate systems (which are characterized by a well-defined value of the wave vector $\mathbf{k}$ at which $J(\mathbf{k})=0$) and in systems with a small perturbation lifting the degeneracy. A possible example of such perturbations can be seen in the potentials (examined in Ref. 14) $h_p \cos p\varphi_{\mathbf{r}}$, with $p=2,\ 3,\ \ldots$ and $h_p \to 0$, which in a two-dimensional system give rise to long-range order at low temperatures and to an intermediate phase with short-range order, starting from a certain value of p.

In this paper, anisotropic corrections proportional to the parameter v act as a similar perturbation. Indeed, Eq. (19) with $v=0$ implies that the asymptotic behavior of the dispersion law $J_0(\mathbf{k})$ near the point $\mathbf{k}=\mathbf{k}_J$ is isotropic. Moreover, at $v=0$ we have $\rho(\mathbf{a}_1|1)=\rho(\mathbf{a}_2|1)$, and the excitation spectrum (17) contains no gap, so that the functions $J(\mathbf{k})$ and $J_0(\mathbf{k})$ coincide. Thus, the small-perturbation condition, within which the above method can operate, is realized if $v \ll 1$. On the other hand, as $v \to 1$, the asymptotic behavior of $J_0(\mathbf{k}+\mathbf{k}_J)$ tends to $(C_x+C_y)a^2k_y^2$, which corresponds to a transition to a quasi-one-dimensional system with independent moment chains. The low values of interchain interactions as compared to those of intrachain interactions are the cause for Ising-like behavior of the systems and low transition temperatures.

For instance, for dipole–dipole interactions the coefficients C_x and C_y change from V and $2V$ for the short-range model to $0.1447V$ and $1.7873V$ when long-range interaction is taken into account,[14,22] which corresponds to v changing from 1/3 to 0.8502. The increase in the value of v leads to a more rapid decrease of the correlators (21) with increasing temperature. This agrees with the results of Monte Carlo modeling reported in Refs. 17 and 26, which indicate that the transition temperature drops from the value $T_c=(1.52\pm 0.01)V$ for the short-range model to the value $T_c \approx 0.75V$ when long-range dipole forces are taken into account. The first value proves to be close to the transition temperature $T_c=1.641V$ of a similar exactly solvable short-range Ising dipole model,[27] in which the dipoles can have four discrete orientations along the diagonals of the square lattice, corresponding to $\alpha=\pi/4$. The second value also correlates well with the result of the simple self-consistent interchain-field approximation ($T_c \approx 0.76$ V; see Ref. 28), which allows for Ising-like behavior of the dipole moments in the chains.

The analysis of the generalized model of planar degenerate antiferromagnetic structures performed in this paper explains the mechanism by which collinear orientations of the moments arise in the system due to the emergence in the spin-wave excitation spectrum of an energy gap whose size is a linear function of the temperature. The presence of such a gap is the cause of the specific temperature dependence of the nearest-neighbors correlators (21), which enter into the correlator

$$\langle \Psi_{\mathbf{R}} \rangle = \frac{1}{4}\langle (\mathbf{e}_{\mathbf{a}_1+\mathbf{a}_2+\mathbf{R}} - \mathbf{e}_{\mathbf{R}})(\mathbf{e}_{\mathbf{a}_1+\mathbf{R}} - \mathbf{e}_{\mathbf{a}_2+\mathbf{R}})\rangle$$

$$= \frac{1}{2}[\rho(\mathbf{a}_1|1)+\rho(\mathbf{a}_2|1)]\cos 2\alpha \tag{48}$$

determined from the Monte Carlo experiments of Refs. 15 and 17.

In the case of anisotropic interactions the system acquires long-range order characterized by the same temperature dependence of ρ_0 that exists in Eq. (21). Lately a similar temperature dependence of the long-range order parameter ($\rho_0 \sim \exp(-T|\ln T|)$) was proved to exist in a planar triangular antiferromagnet placed in a magnetic field.[29] For isotropic short-range interactions there can be no long-range order, but there is no obstacle for collinear orientations of magnetic moments over distances shorter than the correlation length of the Berezinskiĭ–Kosterlitz–Thouless phase.

The author would like to thank Profs. C. L. Henley and J. F. Fernandez for their critical remarks. This work was supported by the State Fund for Fundamental Research of the Ukrainian State Committee of Science and Technology (Project No. 2.4/308) and by a combined grant from the International Science Foundation and the Government of Ukraine (Grant No. K64 100).

[1] P. W. Anderson, Phys. Rev. **102**, 1008 (1956).
[2] J. Villain, Z. Phys. B **33**, 31 (1979).
[3] C. L. Henley, J. Appl. Phys. **61**, 3962 (1987).
[4] S. J. Kennedy and T. J. Hicks, J. Phys. F **17**, 1599 (1987).
[5] T. Giebultowicz, J. Magn. Magn. Mater. **54–57**, 1287 (1986).
[6] E. F. Shender, Zh. Éksp. Teor. Fiz. **83**, 326 (1982) [Sov. Phys. JETP **56**, 178 (1982)].
[7] P. Schiffer, A. P. Ramirez, D. A. Huse, and A. J. Valentino, Phys. Rev. Lett. **73**, 2500 (1994).
[8] P. I. Belobrov, R. S. Gekht, and V. A. Ignatchenko, Zh. Éksp. Teor. Fiz. **84**, 1097 (1983) [Sov. Phys. JETP **57**, 636 (1983)].
[9] V. M. Rozenbaum and V. M. Ogenko, Fiz. Tverd. Tela (Leningrad) **26**, 1448 (1984) [Sov. Phys. Solid State **26**, 877 (1984)].
[10] S. Prakash and C. L. Henley, Phys. Rev. B **42**, 6574 (1990).
[11] G. O. Zimmermann, A. K. Ibrahim, and F. Y. Wu, Phys. Rev. B **37**, 2059 (1988).
[12] V. M. Rozenbaum, Phys. Rev. B **51**, 1290 (1995).
[13] C. L. Henley, Phys. Rev. Lett. **62**, 2056 (1989).
[14] Yu. M. Malozovskiĭ and V. M. Rozenbaum, Zh. Éksp. Teor. Fiz. **98**, 265 (1990) [Sov. Phys. JETP **71**, 147 (1990)].
[15] J. F. Fernandez, M. Puma, and R. F. Angulo, Phys. Rev. B **44**, 10 057 (1991).
[16] J. N. Reimers and A. J. Berlinsky, Phys. Rev. B **48**, 9539 (1993).
[17] S. Romano, Physica Scripta **50**, 326 (1994).
[18] V. L. Berezinskiĭ, Zh. Éksp. Teor. Fiz. **59**, 907 (1970) [Sov. Phys. JETP **32**, 493 (1971)]; Zh. Éksp Teor. Fiz. **61**, 1144 (1971) [Sov. Phys. JETP **34**, 610 (1972)].
[19] J. M. Kosterlitz and D. J. Thouless, J. Phys. C **6**, 1181 (1973).

[20] V. L. Pokrovskiĭ and G. V. Uĭmin, Zh. Éksp. Teor. Fiz. **65**, 1691 (1973) [Sov. Phys. JETP **38**, 847 (1974)].
[21] R. P. Feynman, *Statistical Mechanics*, W. A. Benjamin, Reading, Mass. (1972).
[22] V. M. Rozenbaum, Phys. Rev. B **53**, 6240 (1996).
[23] V. M. Rozenbaum, Zh. Éksp. Teor. Fiz. **107**, 536 (1995) [JETP **80**, 289 (1995)].
[24] V. M. Rozenbaum, JETP Lett. **63**, 662 (1996).
[25] *Handbook of Mathematical Functions*, edited by M. Abramowitz and I. A. Stegun, National Bureau of Standards Applied Mathematics Series 55, Washington, D.C. (1964).
[26] S. Romano, Nuovo Cimento D **9**, 409 (1987).
[27] V. M. Rozenbaum and V. M. Ogenko, JETP Lett. **35**, 184 (1982).
[28] Yu. M. Malozovsky and V. M. Rozenbaum, Physica **175**, 127 (1991).
[29] R. Rustelli, A. Tassi, A. Pimpinelli, and S. Sedazzari, Phys. Rev. B **45**, 7936 (1992).

Translated by Eugene Yankovsky

Kinetic theory of semiconductor cascade laser based on quantum wells and wires

V. F. Elesin and A. V. Krasheninnikov

Moscow State Institute of Engineering Physics, 115409 Moscow, Russia
(Submitted 4 June 1996)
Zh. Éksp. Teor. Fiz. **111**, 681–695 (February 1997)

The paper presents a numerical solution of a system of nonlinear equations for the electron distribution functions in the upper and lower subbands between which lasing transitions occur and the number of nonequilibrium optical phonons in semiconducting cascade lasers based on quantum wells and wires. For the case of quantum wells, we propose an analytical solution of this system of equations, which is a generalization of the previously found solution [V. F. Elesin and Yu. V. Kopaev, Zh. Éksp. Teor. Fiz. **108**, 2186 (1995) [JETP **81**, 1192 (1995)]; V. F. Elesin and Yu. V. Kopaev, Sol. St. Commun. **96**, 897 (1995)] in a wider range of injection rates. The threshold injection rate can be significantly reduced owing to reabsorption and accumulation of nonequilibrium optical phonons, nonparabolicity of the subbands and different effective masses of electrons in different subbands. In the case of quantum wires, the threshold injection rate is considerably lower, and its decrease is even larger than in quantum wells. It is remarkable that, owing to the lower electron–electron relaxation rate in the one-dimensional case, the decrease in the threshold injection rate may be two or three orders of magnitude. The relation between the density of states and threshold current has also been studied. © *1997 American Institute of Physics.* [S1063-7761(97)02102-1]

1. INTRODUCTION

A new type of semiconductor laser (quantum cascade laser) proposed in the original publications by Kazarinov and Suris[1] has been implemented quite recently.[2,3] The interest in quantum cascade lasers based on electronic transitions between subbands in the conductance band is stimulated by the possibility of tuning them over a wavelength interval extending from the near to far infrared.

Since transitions between subbands due to emission of optical phonons are allowed, quantum cascade lasers are characterized by high threshold currents and highly nonequilibrium states of their electron systems. Specifically, the electron lifetime in the upper subband, equal to the time of optical phonon emission (τ_0), is short ($\tau_0 \approx 10^{-12}$–10^{-13} s) compared to the electron lifetime ($\tau_r \approx 10^{-10}$ s) in conventional semiconductor lasers based on transitions between the conduction and valence bands. As a result, it is difficult to create population inversion in the system and, since the electron system is far from equilibrium, a kinetic approach is indispensable in modeling the electron energy relaxation in such lasers.

In the first experiments with quantum cascade lasers,[2,3] the parameters of a semiconducting heterostructure were selected so that the electron transit time from the lower subband, τ_t, should be shorter than τ_0 in order to create the population inversion. This condition is inevitable if the laser is treated as a two-level system and band nonparabolicity is ignored.[2,4] With due account of the nonparabolicity, however, the situation is radically different.[5,6] In this case, radiative transitions occur in a fairly narrow energy range, so there is no need to satisfy the strict condition $\tau_0 \gg \tau_t$. As a result, full inversion of the subband populations is not necessary. This conclusion was confirmed by experiments shortly afterward.[7]

In addition to the nonparabolicity, another important effect is the considerable drop in the threshold current due to an increase in $\tau_t (\tau_0 \ll \tau_t)$, and accumulation and reabsorption of optical phonons.[5,6] In fact, these effects lead to a longer effective lifetime of electrons in the upper subband, hence a lower injection rate is needed to create conditions for the population inversion.

The calculations[5,6] for the case of quantum wells were based on an exact analytic solution of the system of kinetic equations for the electron distribution functions in the subbands and the number of phonons. The injection rate Q was assumed to be low in this case ($Q\tau_0 \ll 1$, linear approximation).

The aim of the present study was to find a solution of the system of kinetic equations for the electron distribution functions and threshold injection rates (hence the threshold currents) over a wide range of parameters of the kinetic model of the quantum cascade laser. We have studied both the two-dimensional model of a quantum-well laser and the one-dimensional model of a quantum-wire laser. The latter case is especially interesting in that it offers a way to substantially reduce the threshold current (our study has confirmed the feasibility of this effect). This reduction is due to singularities in the electron density of state in a one-dimensional system and a drastically lower electron–electron relaxation rate. Let us recall that, in the one-dimensional configuration of a single-band model, electron–electron scattering does not lead to energy relaxation[8] (this follows from energy and momentum conservation). An important point is that for $\tau_0 \ll \tau_t$ the threshold current is controlled by electron–electron relaxation.[5,6]

The paper is organized as follows. Section 2 describes the model and gives basic solutions. Section 3 presents an exact analytical solution of the system of kinetic equations for electrons and phonons in the quasilinear approximation,

 1063-7761/97/020375-08$10.00

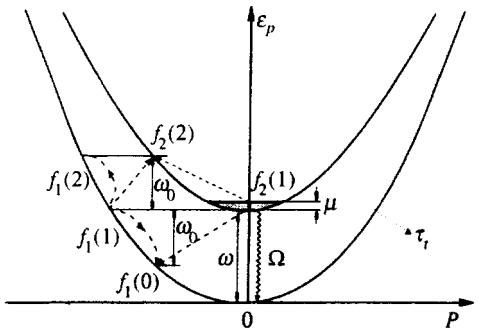

FIG. 1. Energy in the subbands versus quasimomentum. The dashed lines show transitions with emission of an optical phonon, the wavy line shows an optical transition.

which applies to a wide range of Q. Numerical solutions of the initial equation system in the case of quantum wells and their detailed analysis are given in Sec. 4. Section 5 presents a numerical solution of the system of nonlinear kinetic equations for the case of quantum wires.

2. BASIC EQUATIONS AND STATEMENT OF THE PROBLEM

As in the previous studies,[5,6] let us consider the following model (Fig. 1). Let there be two subbands with dispersions $\varepsilon_1(\mathbf{p})$ and $\varepsilon_2(\mathbf{p})$, such that transitions between them are accompanied by emission of phonons with the energy $\hbar\Omega$ (hereafter $\hbar=c=1$, where c is the speed of light in vacuum). Electrons are injected into the subband 2 at a rate Q and drain from the subband 1 with a probability τ_t^{-1}. The optimal conditions for operation of quantum cascade lasers are achieved by selecting the parameters of the quantum wells and barriers of the structure.[2–4]

In the present model, the main scatterers of electrons are optical phonons (the typical energy is $\omega_0\approx 0.034$ eV[7]). At $\mathbf{p}=0$ the difference between the subband energies $\omega=\varepsilon_2(0)-\varepsilon_1(0)$ is approximately several phonon energies ω_0. The parameter μ ($\mu\ll\omega_0$) is the spread of the injected electron energy.

Our main task is to determine the threshold injection rate Q_{th}. It can be derived by equating the gain $\alpha(\Omega)$ and the reciprocal of the photon lifetime τ in the cavity[5,6] controlled by the total losses:

$$\alpha(\Omega_0,J_{\text{th}})=\frac{1}{\tau},\quad \left.\frac{\partial\alpha(\Omega)}{\partial\Omega}\right|_{\Omega=\Omega_0}=0. \tag{1}$$

The latter condition is the equation for the lasing frequency. The expression for $\alpha(\Omega)$ describing electronic transitions between the subbands has the form[5,6]

$$\frac{\alpha(\Omega)}{\alpha_0}=\int_0^\infty \frac{d\varepsilon[f_2(\varepsilon)-f_1(\varepsilon)]\gamma}{(\xi_2(\varepsilon)-\xi_1(\varepsilon))^2+\gamma^2},\quad \alpha_0=\frac{e^2|V_{12}|^2}{\Omega\kappa}, \tag{2}$$

$$\xi_2(\varepsilon)=\varepsilon+\omega-\frac{\Omega}{2},\quad \xi_1(\varepsilon)=\varepsilon+\frac{\Omega}{2}, \tag{3}$$

where $f_2(\varepsilon)$ and $f_1(\varepsilon)$ are distribution functions of electrons in the subbands *2* and *1* (Fig. 1), γ is the damping factor of nondiagonal components of the density matrix (it is assumed to be constant with the energy), Ω is the electromagnetic field frequency, V_{12} is the matrix element of the electronic transition between the subbands, κ is the dielectric constant, and e is the electron charge.

If the band nonparabolicity is ignored, the difference $\xi_2-\xi_1=\omega-\Omega\equiv\delta$ is independent of the energy. In this case, the electronic transitions with emission (or absorption) of photons occur throughout the subband, and the system is equivalent to a conventional two-level system. The lasing condition in this approximation is[2,4]

$$\tau_t<\tau_0, \tag{4}$$

which is necessary to satisfy conditions (1) and (2).

The inclusion of the subbands nonparabolicity changes the situation radically.[5,6] First, the rigorous condition (4) is no longer necessary. Second, it becomes possible to significantly reduce Q_{th} because the subband nonparabolicity limits the lasing spectral range.

If we use the simplest approximation for the GaAs electronic spectrum,[9] the difference $\xi_2-\xi_1$ in the case of a deep quantum well can be expressed as[5,6]

$$\varepsilon_2-\varepsilon_1=\delta-\beta\varepsilon,\quad \beta=2\omega/\varepsilon_g, \tag{5}$$

where ε_g is the band gap width. Later similar results were obtained by Gelmont *et al.*[10] Faist *et al.*[7] studied a more complicated model taking into account features of real structures, and their results are approximately equal to those reported in Refs. 5 and 6 to within 25%.

By taking into account Eq. (5) and assuming that

$$f_2(\varepsilon)-f_1(\varepsilon)=\begin{cases}\Delta f, & 0<\varepsilon<\mu,\\ 0, & \mu<\varepsilon,\end{cases} \tag{6}$$

we derive from Eq. (1) at the resonant frequency

$$\Omega_0=\omega-\frac{\mu\beta}{2},$$

$$\frac{\alpha(\Omega_0)}{\alpha_0}=\frac{2\Delta f}{\beta}\arctan\frac{\mu\beta}{2\gamma}\approx\frac{\Delta f\pi}{\beta}$$

for $\mu\beta\gg 2\gamma$. The threshold population inversion is determined, correspondingly, by the expression

$$\Delta f_{\text{th}}=\frac{\beta}{\pi\tau\alpha_0}. \tag{7}$$

In order to determine Q_{th}, we need the relationship between $f_i(\varepsilon)$ and Q. It can be determined by solving the system of kinetic equations for $f_i(\varepsilon)$ and the number of optical phonons N.

The relevant kinetic equations were derived by Elesin and Kopaev.[5,6] They also reduced the system of equations to a system of coupled equations for the functions $f_1(n)$ and $f_2(n)$, where

$$f_1(n)\equiv f_1(\omega+(n-1)\omega_0)=f_1(\varepsilon),$$

$$f_2(n)\equiv f_2(\omega+n\omega_0)=f_2(\varepsilon),\quad n=0,1,2\ldots$$

The functions $f_1(n)$ and $f_2(n)$ describe the distribution of electrons with energies in a narrow interval $\mu\ll\omega_0$ around

the energies $\varepsilon=\omega\pm n\omega_0$. These equations have the form

$$f_1(0)[\xi+N(1+z)+f_1(1)+zf_2(1)] =(1+N)[f_1(1)+zf_2(1)], \quad (8)$$

$$f_1(0)[\xi+1+N(2+z)-f_1(0)+f_1(2)+zf_2(2)] =Nf_1(0)+(1+N)[f_1(2)+zf_2(2)], \quad (9)$$

$$f_2(1)[Q\tau_0+1+N(2+z)-f_1(0)+f_1(2)+zf_2(2)] =Nf_1(0)+(1+N)[f_1(2)+zf_2(2)]+Q\tau_0, \quad (10)$$

$$f_1(n)[\xi+(1+z)(1+2N)-f_1(n-1)-zf_2(n-1) +f_1(n+1)+zf_2(n+1)] =N[f_1(n-1)+zf_2(n-1)]+(1+N)[f_1(n+1) +zf_2(n+1)], \quad (11)$$

$$f_2(n)[(1+z)(1+2N)-f_1(n-1)-zf_2(n-1)+f_1(n +1)+zf_2(n+1)] =N[f_1(n-1)+zf_2(n-1)]+(1+N)[f_1(n+1) +zf_2(n+1)], \quad (12)$$

where $\xi=\tau_0/\tau_t$, $z=m_2/m_1$ is the ratio between the electron effective masses in the subbands *2* and *1*, respectively. In all our analytical calculations we take $z=1$ (the case $z\neq 1$ is considered in Sec. 4). Equations (11) and (12) are valid for $n\geqslant 2$. The system should be supplemented with an equation for the number N of optical phonons:[5]

$$N\frac{\tau_t}{\tau_{\rm esc}}=f_1(0)-\sum_{n=2}^{\infty}(n-1)f_1(n), \quad (13)$$

where $\tau_{\rm esc}$ is the time in which phonons escape from a region with given dimensions.[5]

Given that the functions $f_2(n)$ are nonzero in a narrow energy interval, the difference $f_2(\varepsilon)-f_1(\varepsilon)$ in Eq. (6) becomes equal to $f_2(1)$ at the generation threshold. Specifically, the electrons emitting optical phonons do not arrive at the bottom of the subband *1*, i.e., $f_1(\varepsilon)=0$ in the region where lasing occurs (Fig. 1), except the case of resonance, when $\omega=k\omega_0$.

3. EXACT ANALYTICAL SOLUTION IN THE QUASILINEAR APPROXIMATION FOR QUANTUM WELLS

An exact analytical solution of the Eqs. (8)–(13) in the approximation linear in f and $Q\tau_0$ was described in Refs. 5 and 6. It was assumed that the linear approximation ($f\ll 1$, $Q\tau_0\ll 1$) applied in a range extending to $Q\sim 1/\tau_0$, since the nonlinear terms in Eqs. (8)–(12), which were omitted in that approximation, were comparable to terms of order $1+3N$, where $N\sim 1$.

Numerical calculations and more accurate analysis, however, have revealed that some terms in the denominators of the expressions for f_i (their formulas are given below) cancel one another, and the linear approximation is valid when $Q\tau_0$ is limited to a quantity of order $\xi\ll 1$, rather than $1+3N\approx 4$.

At the same time, ''dangerous'' denominators that may lead to divergence are caused only by the term proportional to $Q\tau_0 f_2(1)$ on the left-hand side of Eq. (10). If this term is retained (we call this the quasilinear approximation), the linear system of equations derived from Eqs. (8)–(13) has an exact analytical solution in good agreement (see Sec. 4) with the numerical solution to Eqs. (8)–(13).

The solution of the system (8)–(13) in the quasi-linear approximation is as follows:

$$f_1(n)=A_1\,\exp(\alpha n), \quad f_2(n)=A_2\,\exp(\alpha n), \quad n\geqslant 2, \quad (14)$$

$$\widetilde{A}_1=A_1\,\exp(\alpha)=Q\tau_0\,\frac{(\xi+c)b}{(\xi+2b)\widetilde{\Delta}},$$

$$\widetilde{A}_2=A_2\,\exp(\alpha)=Q\tau_0\,\frac{(\xi+b)(\xi+c)}{(\xi+2b)\widetilde{\Delta}}, \quad (15)$$

$$\widetilde{\Delta}=(\xi+c)(c+Q\tau_0)-(1+N)(\xi+2c+Q\tau_0)-(1+N) \times(\xi+2c+Q\tau_0)[\exp(\alpha)+N/(\xi+2N)], \quad (16)$$

$$f_1(0)=Q\tau_0\,\frac{(1+N)(\xi+c)}{(\xi+2N)\widetilde{\Delta}}, \quad (17)$$

$$f_1(1)=Q\tau_0\,\frac{y}{\widetilde{\Delta}}, \quad y=(1+N)\exp(\alpha)+\frac{N(1+N)}{\xi+2N}, \quad (18)$$

$$f_2(1)=Q\tau_0\,\frac{\xi+c-y}{\widetilde{\Delta}}, \quad (19)$$

$$\exp(\alpha)=\frac{b(\xi+b)}{2(1+N)(\xi+2b)} -\sqrt{\left\{\frac{b(\xi+b)}{2(1+N)(\xi+2b)}\right\}^2-\frac{N}{1+N}}, \quad (20)$$

$$b=2(1+2N), \quad c=1+3N.$$

Equations (7) and (14)–(20) yield the threshold injection rate $Q_{\rm th}$ in a general form.

The solution (14)–(20) obtained in the quasilinear approximation differs from the linear solution[5,6] only in the denominator $\widetilde{\Delta}$, which contains $Q\tau_0$. We note that some errors slipped into the equations given in Ref. 5 (for example, Eq. (57) of Ref. 5 should contain $n\geqslant 2$), although these errors did not affect the final results and conclusions. The calculations performed in both linear and quasilinear approximations coincide in the limiting case $\xi\ll 1$, but some differences in numbers emerge for $\xi\gg 1$. Note that the solution (14)–(20) agrees well with numerical calculations (see Sec. 4).

It is interesting to investigate the limiting cases $\xi\ll 1$ and $\xi\gg 1$. In the first case, after expanding in $\xi\ll 1$ ($\xi\ll N$) and performing lengthy calculations, we derive from Eqs. (14)–(20)

$$f_1(0)\approx Q\tau_0\,\frac{1+N}{\xi(1+N)^2+Q\tau_0 N}, \quad (21)$$

$$f_2(1)\approx f_1(1)\approx Q\tau_0\ \frac{1+N}{\xi(1+N)^2+Q\tau_0 N}. \tag{22}$$

We see that $Q\tau_0$ in the denominators of Eqs. (21) and (22) should be compared not with $1+3N$, but with a parameter proportional to ξ. If

$$Q\tau_0<Q_c\tau_0=\xi(1+N)^2/N\sim 4\xi, \tag{23}$$

we obtain Eqs. (72) and (73) from Ref. 5. For $Q>Q_c$ [or $\xi<\xi_c=Q\tau_0 N/(1+N)^2$] the growth in $f_2(1)$ described by Eq. (22) saturates, i.e., $f_2(1)\to 1$.

In the quasilinear approximation, one can easily derive an equation for N:

$$\frac{N}{1+N}=Q\tau_{\rm esc}\ \frac{\xi(1-N^2)}{\xi(1+N)^2+Q\tau_0 N}. \tag{24}$$

For $Q<Q_c$ it transforms to Eq. (74) from Ref. 5. The value of N derived from this cubic equation is substituted into Eq. (22) to obtain $f_2(1)$ as a function of $Q\tau_0$ (see below Fig. 3a). The limit of N at $Q\tau_{\rm esc}\gg 1$ is of order unity (for details see Sec. 4).

Now let us determine the threshold injection rate using Eqs. (7) and (22):

$$Q_{\rm th}(\xi\ll 1)\approx\frac{(1+N)^2}{N\tau_t}\,\frac{q}{1-q}, \tag{25}$$

$$q=\beta/\pi\tau\alpha_0.$$

We can see that, owing to the effect of optical phonon reabsorption, $Q_{\rm th}$ is determined not by τ_0, but by the effective electron lifetime in the upper subband, $\tau_t N/(1+N)^2$.

Consider the opposite limit $\xi\gg 1$. By expanding in terms of the small parameter $1/\xi$ and assuming $\xi\gg N$, we obtain the following expressions:

$$f_1(0)\approx\frac{Q\tau_0(1+N)}{\xi(a+Q\tau_0)}, \tag{26}$$

$$f_2(1)\approx\frac{Q\tau_0}{a+Q\tau_0}, \tag{27}$$

where $a=N+\sqrt{1+3N+3N^2}$.

The equation for N in this case has the form

$$\frac{N}{Q\tau_{\rm esc}}=\frac{(1+N)(2+N-\sqrt{1+3N+3N^2})}{(\sqrt{1+3N+3N^2}-N)(\sqrt{1+3N+3N^2}+N+Q\tau_0)}. \tag{28}$$

In the case $Q\tau_{\rm esc}\gg 1$, we derive from Eq. (28) the limit of the phonon number N_0:

$$N_0=1.5.$$

Hence, $a=5$ at $N=N_0$, and the linear approximation is valid for $Q\tau_0\leqslant 5$.

At arbitrary $Q\tau_{\rm esc}$ the number of phonons as a function of $Q\tau_0$ can be determined by solving Eq. (28) numerically. These numerical calculations are shown in Fig. 2. The graph shows that $N_0=1.5$, in agreement with the analytical calculation. The dashed curve in Fig. 2 shows the function $N(Q\tau_0)$ calculated by numerically solving the system of nonlinear equations using the iterative technique (see Sec. 4).

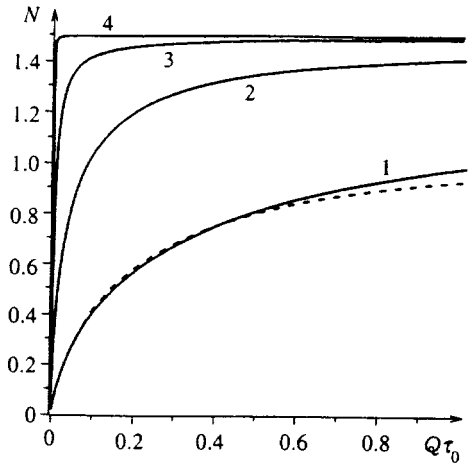

FIG. 2. The number of phonons N versus the injection rate $Q\tau_0$ obtained by solving Eq. (28) numerically. The curves were calculated at (*1*) $\tau_{\rm esc}/\tau_0=10$, (*2*) 10^2, (*3*) 10^3, and (*4*) 10^5. The dashed line corresponds to a numerical solution of nonlinear system of equations (8)–(13) at $\tau_t/\tau_0=0.1$ ($\xi=10$) and $\tau_{\rm esc}/\tau_0=10$.

The solid and dashed curves are very close, which proves that the quasilinear approximation can be used in calculating N.

Let us derive the threshold injection rate in the limit $\xi\gg 1$ from Eqs. (7) and (27):

$$Q_{\rm th}(\xi\gg 1)\approx\frac{5}{\tau_0}\,\frac{q}{1-q}. \tag{29}$$

By comparing Eqs. (25) and (29), we obtain the relation

$$\frac{Q_{\rm th}(\xi\ll 1)}{Q_{\rm th}(\xi\gg 1)}\approx\frac{(1+N)^2}{5N}\,\xi,$$

where $\xi\ll 1$ holds on the right-hand side. Assuming $N\approx 1$, we have an estimate

$$\frac{Q_{\rm th}(\xi\ll 1)}{Q_{\rm th}(\xi\gg 1)}\sim\xi, \tag{30}$$

which is almost identical to Eq. (76) in Ref. 5. It is clear that the threshold injection rate can be reduced proportionally to $\xi=\tau_0/\tau_t$ (for example, by increasing τ_t through the barrier thickness). We should stress that this result is valid for $Q\tau_{\rm esc}\gg 1$, but $Q_{\rm th}$ can be reduced for all $Q\tau_{\rm esc}\geqslant 1$.

4. NUMERICAL SOLUTIONS OF THE SYSTEM OF NONLINEAR KINETIC EQUATIONS FOR THE CASE OF QUANTUM WELLS

We have calculated numerical solutions of the nonlinear equation system (8)–(13) with the parameters $\tau_{\rm esc}$, τ_0, τ_t, and Q varied over wide ranges. This has been done using the iteration technique. On each step of the iteration process, the equation system (8)–(13) was considered as a system of linear algebraic equations, the functions $f_i(n)$ in the brackets on the left-hand side of Eqs. (8)–(13) being constants calculated in the previous iteration. All the times were measured in units of τ_0.

Since $f_2(1)$ determines, in fact, the threshold population inversion, it seems that the shape of this function is more

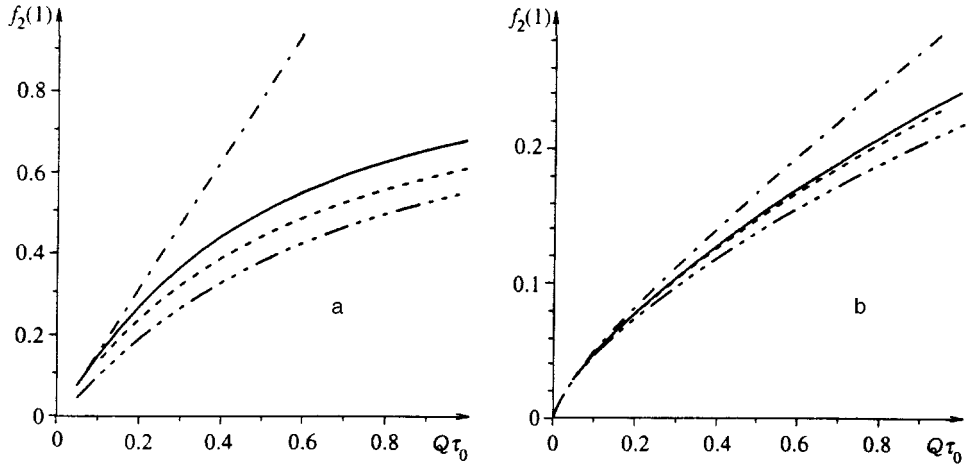

FIG. 3. The function $f_2(1)$ versus the injection rate $Q\tau_0$. The solid curve shows a numerical solution of the nonlinear equation system (8)–(13), the dashed curve a solution of Eqs. (8)–(13) in the quasilinear approximation, and the dash-dotted curve a solution of Eqs. (8)–(13) in the linear approximation. The dash-dotted line with three dots in a row is a calculation from Eq. (22) for the case $\xi=10$ and from Eq. (27) for the case $\xi=0.2$, $\tau_{esc}/\tau_0=10$. (a) $\tau_t/\tau_0=5$ ($\xi=0.2$); (b) $\tau_t/\tau_0=0.1$ ($\xi=10$).

helpful in understanding the system behavior and conveys more information. Figures 3–8 show typical curves of $f_2(1)$ and N as functions of τ_t/τ_0 and $Q\tau_0$.

Figure 3a demonstrates the coincidence among the curves of $f_2(1)$ versus $Q\tau_0$ calculated by Eq. (22) for the limiting case $\xi \ll 1$ (dash-dotted line with three dots in a row), of the numerical solution of Eqs. (8)–(13) in the quasilinear approximation (dashed curve), and of the numerical solution of the equation system (8)–(13) (solid curve). The graph indicates that the solution obtained in the quasilinear approximation is, in fact, identical to the numerical solution in the wide range of $Q\tau_0$, and the solution obtained in the linear approximation has a satisfactory accuracy up to $Q\tau_0 \sim \xi$.

Figure 3b shows similar curves at $\xi=10$. In the limit $\xi \gg 1$ the function $f_2(1)$ versus $Q\tau_0$ was calculated using Eq. (27). It is clear that in the limit $\xi \gg 1$ the analytical solution (27) is in good agreement with the numerical solutions of the nonlinear equation system and with solutions obtained in the linear and quasilinear approximations. Note that in all the limiting cases the quasilinear analytical solution (22), (27) is valid over a wide range of $Q\tau_0$.

Figure 4a shows $f_2(1)$ versus τ_t/τ_0 at $Q\tau_0=0.1$. The curve demonstrates the growth in $f_2(1)$ with τ_t/τ_0, in accordance with the analytical results (22) and (27) (see also Refs. 5 and 6). For example, in the case $Q\tau_0 \ll 1$, $Q\tau_{esc} \gg 1$ (Fig. 3b), we have $f_2(1) \sim 0.027$ at $\tau_t/\tau_0=0.1$ ($\xi=10$) and $f_2(1) \sim 0.25$ at $\tau_t/\tau_0=10$ ($\xi=0.1$). This is in agreement with the main conclusion that the threshold injection rate should decrease with τ_t. Note also that the increase in $f_2(1)$ is not so large at relatively large q/τ_0 [Eqs. (22) and (27)].

Up to this point, we have assumed that the electron masses in the subbands are equal. If we assume that they are different ($m_2 > m_1$), the solid curves with dots in Fig. 4, numerically calculated by solving Eqs. (8)–(13) at $m_2/m_1=1.5$, indicate that $f_2(1)$ becomes larger than for the calculation with equal electron masses (solid curve), all other conditions being equal.

5. NUMERICAL SOLUTIONS OF THE NONLINEAR KINETIC EQUATION SYSTEM FOR THE CASE OF QUANTUM WIRES

As was noted in Introduction, it is interesting to consider a kinetic model of a one-dimensional cascade laser in view of the slower electron–electron relaxation and singularities in the density of states in a one-dimensional system. The system of kinetic equations can be reduced in this case to a system of coupled equations in the form

$$f_1(0)\left[\xi+N\left(\frac{1}{\sqrt{w}}+\frac{x}{\sqrt{2\tilde{\mu}}}\right)+\frac{f_1(1)}{\sqrt{w}}+x\,\frac{f_2(1)}{\sqrt{2\tilde{\mu}}}\right] = (1+N)\left[\frac{f_1(1)}{\sqrt{w}}+\frac{f_2(1)}{\sqrt{2\tilde{\mu}}}\right], \tag{31}$$

$$f_1(1)\left[\xi+\frac{1+N}{\sqrt{w-1}}+N\left(x+\frac{1}{\sqrt{w+1}}\right)-\frac{f_1(0)}{\sqrt{w-1}}+\frac{f_1(2)}{\sqrt{w+1}}+xf_2(2)\right] = f_1(0)\frac{N}{\sqrt{w-1}}+(1+N)\left[\frac{f_1(2)}{\sqrt{w+1}}+xf_2(2)\right], \tag{32}$$

$$f_2(1)\left[Q\tau_0+\frac{1+N}{\sqrt{w-1}}+N\left(x+\frac{1}{\sqrt{w+1}}\right)-\frac{f_1(0)}{\sqrt{w-1}}+\frac{f_1(2)}{\sqrt{w+1}}+xf_2(2)\right] = f_1(0)\frac{N}{\sqrt{w-1}}+(1+N)\left[\frac{f_1(2)}{\sqrt{w+1}}+xf_2(2)\right]+Q\tau_0, \tag{33}$$

$$f_1(2)\left[\xi+\frac{1}{\sqrt{w}}+\frac{x}{\sqrt{2}}+N\left(\frac{1}{\sqrt{w+2}}+\frac{1}{\sqrt{w}}+\frac{x}{\sqrt{2\tilde{\mu}}}+\frac{x}{\sqrt{2}}\right)-\frac{f_1(1)}{\sqrt{w}}-x\,\frac{f_2(1)}{\sqrt{2\tilde{\mu}}}+\frac{f_1(3)}{\sqrt{w+2}}+x\,\frac{f_2(3)}{\sqrt{2}}\right]$$
$$=N\left[\frac{f_1(1)}{\sqrt{w}}+x\,\frac{f_2(1)}{\sqrt{2\tilde{\mu}}}\right]+(1+N)\times\left[\frac{f_1(3)}{\sqrt{w+2}}+x\,\frac{f_2(3)}{\sqrt{2}}\right], \tag{34}$$

$$f_2(2)\left[(1+N)\left(\frac{x}{\sqrt{2\tilde{\mu}}}+\frac{1}{\sqrt{w}}\right)+N\left(\frac{1}{\sqrt{w+2}}+\frac{x}{\sqrt{2}}\right)-\frac{f_1(1)}{\sqrt{w}}-x\,\frac{f_2(1)}{\sqrt{2\tilde{\mu}}}+\frac{f_1(3)}{\sqrt{w+2}}+x\,\frac{f_2(3)}{\sqrt{2}}\right]$$
$$=N\left[\frac{f_1(1)}{\sqrt{w}}+x\,\frac{f_2(1)}{\sqrt{2\tilde{\mu}}}\right]+(1+N)\left[\frac{f_1(3)}{\sqrt{w+2}}+x\,\frac{f_2(3)}{\sqrt{2}}\right], \tag{35}$$

$$f_1(n)\left[\xi+\frac{1}{\sqrt{w+n-2}}+\frac{x}{\sqrt{n}}+N\left(\frac{1}{\sqrt{w+n}}+\frac{1}{\sqrt{w+n-2}}+\frac{x}{\sqrt{n-2}}+\frac{x}{\sqrt{n}}\right)-\frac{f_1(n-1)}{\sqrt{w+n-2}}-x\,\frac{f_2(n-1)}{\sqrt{n-2}}+\frac{f_1(n+1)}{\sqrt{w+n}}+x\,\frac{f_2(n+1)}{\sqrt{n}}\right]$$
$$=N\left[\frac{f_1(n-1)}{\sqrt{w+n-2}}+x\,\frac{f_2(n-1)}{\sqrt{n-2}}\right]+(1+N)\times\left[\frac{f_1(n+1)}{\sqrt{w+n}}+x\,\frac{f_2(n+1)}{\sqrt{n}}\right], \tag{36}$$

$$f_2(n)\left[(1+N)\left(\frac{x}{\sqrt{n-2}}+\frac{1}{\sqrt{w+n-2}}\right)+N\left(\frac{1}{\sqrt{w+n}}+\frac{x}{\sqrt{n}}\right)-\frac{f_1(n-1)}{\sqrt{w+n-2}}-x\,\frac{f_2(n-1)}{\sqrt{n-2}}+\frac{f_1(n+1)}{\sqrt{w+n}}+x\,\frac{f_2(n+1)}{\sqrt{n}}\right]$$
$$=N\left[\frac{f_1(n-1)}{\sqrt{w+n-2}}+x\,\frac{f_2(n-1)}{\sqrt{n-2}}\right]+(1+N)\times\left[\frac{f_1(n+1)}{\sqrt{w+n}}+x\,\frac{f_2(n+1)}{\sqrt{n}}\right], \tag{37}$$

where $\xi=\tau_0/\tau_t$, $x=\sqrt{m_1/m_2}$, $w=\omega/\omega_0$, and $\tilde{\mu}=\mu/\omega_0$. In Eqs. (36) and (37) we have $n\geqslant 3$.

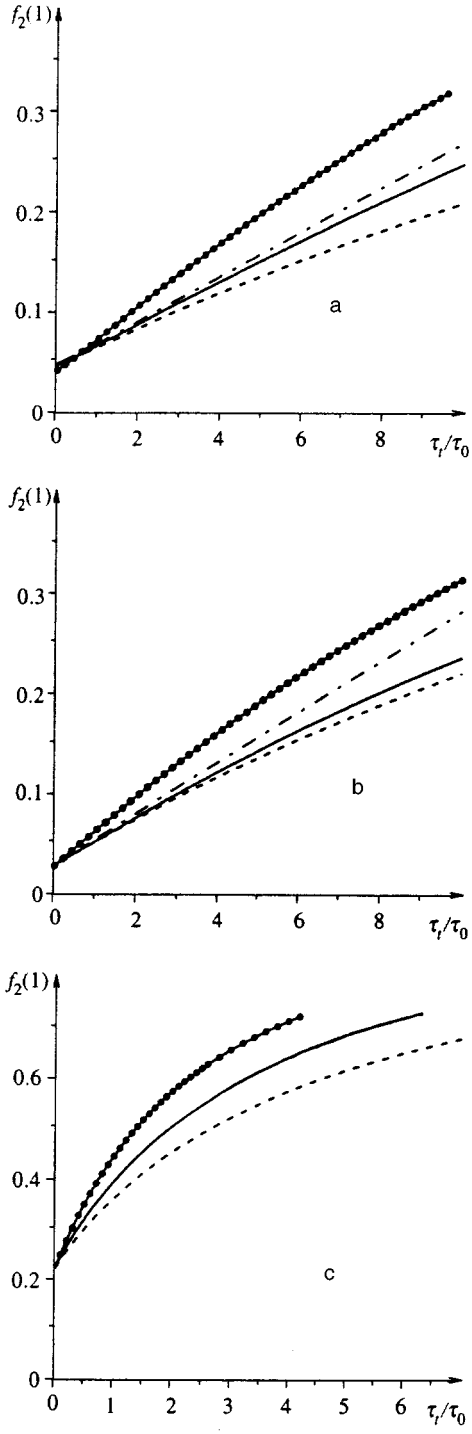

FIG. 4. The function $f_2(1)$ versus τ_t/τ_0. The solid curve shows a numerical solution of the system of nonlinear equations (8)–(13), the dashed line shows a solution in the quasi-linear approximation, the dash-doted line a solution in the linear approximation. The solid line with circles is a numerical solution of Eqs. (8)–(13) for a ratio between the effective masses in the subbands $m_2/m_1=1.5$. (a) $Q\tau_0=0.1$, $\tau_{esc}/\tau_0=10$; (b) $Q\tau_0=0.1$, $\tau_{esc}/\tau_0=100$; (c) $Q\tau_0=1$, $\tau_{esc}/\tau_0=10$.

This equation system should be supplemented with an equation for the phonon number[5] similar to Eq. (13). In the one-dimensional configuration, this equation may differ from the corresponding equations in the two-dimensional [Eq. (13)] and three-dimensional cases. In fact, one can easily

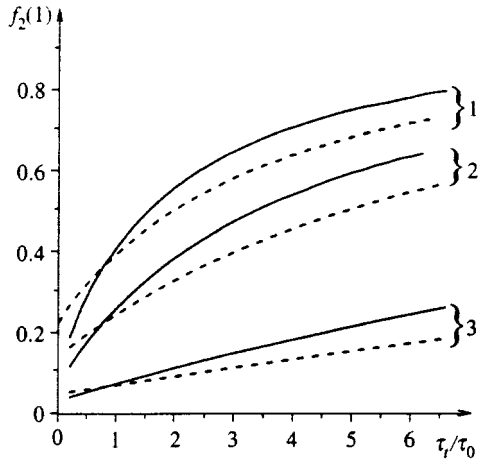

FIG. 5. Curves of $f_2(1)$ versus τ_t/τ_0 for quantum wires (solid lines) and quantum wells (dashed lines). The calculations were performed at (1) $Q\tau_0=1$, (2) 0.5, and (3) 0.1.

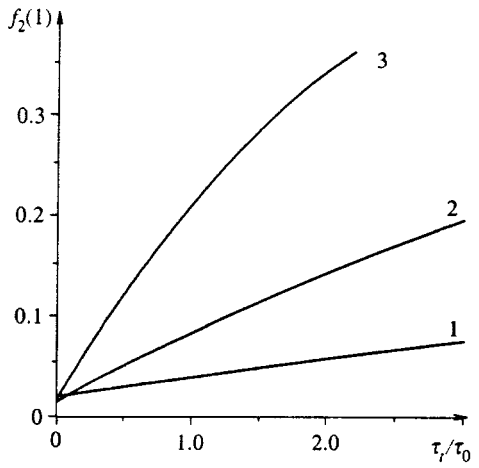

FIG. 7. The function $f_2(1)$ versus τ_t/τ_0 for quantum wires. (*1*) $\mu/\omega_0=0.2$, (*2*) 0.02, and (*3*) 0.002; $Q\tau_0=0.05$.

prove using the energy and momentum conservation that an optical phonon emitted by an electron can impart its energy only to the same electron. Therefore Eq. (13) should be, generally speaking, modified considerably. But in the real situation, when there are several types of optical phonons, these changes may be not so drastic.[11] Taking into account this factor and with a view to simplify the calculation, we use an equation similar to Eq. (13), but with allowance for the electron density of states in the one-dimensional case:

$$N\frac{\tau_t}{\tau_{\rm esc}}\frac{1}{\tilde{\mu}}=\frac{f_1(0)}{\sqrt{w-1}}-\sum_{n=2}^{\infty}\frac{(n-1)f_1(n)}{\sqrt{w+n-1}}. \tag{38}$$

Since the density of state in this case is a function of energy, the system of equations (31)–(38) is more complicated than in the case of quantum wells [Eqs. (8)–(13)], and we could not find an analytical solution. Both systems (31)–(38) and (8)–(13) have been solved by an iteration technique with the parameters $t_{\rm esc}$, τ_0, τ_t, Q, and μ varied over a wide ranges. In all these calculations the electron masses in the subbands were equal.

Figure 5 shows typical curves of $f_2(1)$ versus τ_t/τ_0 at various $Q\tau_0$ (see caption to Fig. 5). For comparison similar curves for the two-dimensional system are also shown. The solid curves show functions calculated numerically for the case of quantum wires, and dashed curves correspond to the case of quantum wells. One can see that in the one-dimensional system, as in the two-dimensional configuration, $f_2(1)$ increases with τ_t/τ_0, and at a higher rate. Thus we conclude that the threshold injection rate in quantum wires decreases with τ_t, and even faster than in quantum wells.

We have also thoroughly investigated $f_2(1)$ as a function of $Q\tau_0$. The curves are shown in Fig. 6. The gain in $f_2(1)$ is higher at small injection rates. It is interesting that for $\tau_t/\tau_0 \ll 1$ the gain in $f_2(1)$ for quantum wires is less than for quantum wells.

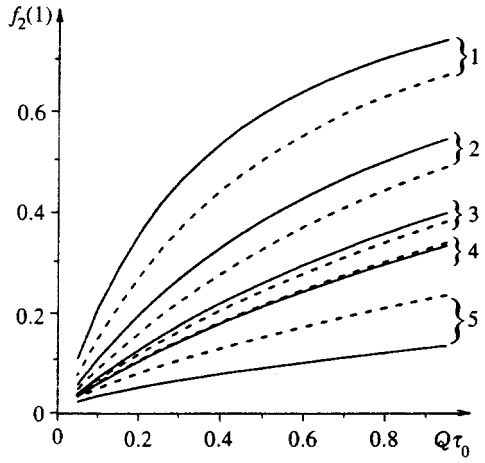

FIG. 6. Curves of $f_2(1)$ versus $Q\tau_0$ for the case of quantum wires (solid lines) and quantum wells (dashed lines). Calculations were preformed at (*1*) $\tau_t/\tau_0=5$, (*2*) 2, (*3*) 1, (*4*) 0.7, and (*5*) 0.1.

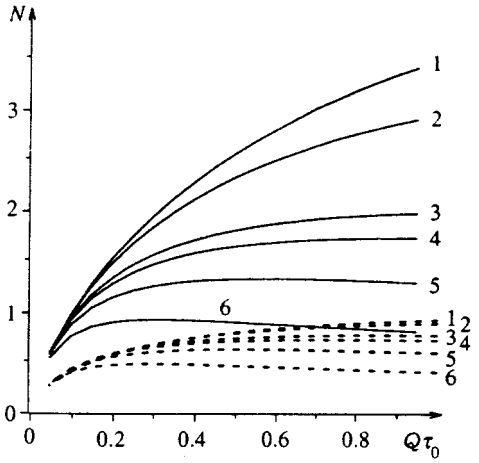

FIG. 8. The number of phonons N versus $Q\tau_0$ for the case of quantum wires (solid lines) and quantum wells (dashed lines). The curves were calculated at (*1*) $\tau_t/\tau_0=0.1$, (*2*) 0.2, (*3*) 0.7, (*4*) 1, (*5*) 2, and (*6*) 5.

The effect of the density of states is illustrated by Fig. 7, which shows $f_2(1)$ versus τ_t/τ_0 for various energy spreads μ of the injected electrons. If the electron energy distribution is narrower, the parameter $f_2(1)$ grows faster with τ_t/τ_0 owing to the singularity in the density of states described in Eqs. (31)–(35) by the terms proportional to $1/\sqrt{\tilde{\mu}}$.

The difference in $f_2(1)$ between two- and one dimensional systems is probably caused by the difference in the numbers of phonons in wires and wells for equal model parameters. This is illustrated by Fig. 8, which shows N as a function of $Q\tau_0$ at different τ_t (see caption to Fig. 8). Figure 8 demonstrates that in both quantum wells and quantum wires N rapidly saturates with the growth of the injection rate at $\tau_t<1$ ($N\sim 1$ even though $Q\tau_0 \ll 1$) because at large τ_t energy is accumulated not only by phonons, but also by the electrons of the lower subband.

6. CONCLUSION

Thus, numerical solutions of the system of nonlinear equations for the electron distribution functions $f_1(n)$ and $f_2(n)$ and the number of phonons N have confirmed the main conclusions of Refs. 5 and 6 about the possibility of reducing the threshold injection rate (threshold current) and about the kinetics of a quantum cascade quantum-well laser. We have determined $f_1(n)$, $f_2(n)$, and N with the model parameters and injection rate Q varied over wide intervals, and limits within which the linear approximation[5,6] applies. We have proved that the linear approximation is valid for $Q<Q_c$ [see Eq. (23)], where $Q\sim\xi$, i.e., in a relatively narrow range for $\xi\ll 1$ and over a wider range for $\xi\gg 1$.

On the other hand, the analytical solution in the quasilinear approximation described in the paper can be used over a wide interval of Q with good accuracy. Using this solution, one can obtain the threshold injection rate Q_{th} both in the general case and in specific limiting cases, and prove that, if phonons are accumulated ($Q\tau_{\text{esc}}\gg 1$), the threshold injection rate Q_{th} can be reduced notably and is controlled only by electron–electron and electron–phonon scattering. Note that estimates of τ_{esc} present some problems. The phonon decay rate $1/\tau_{\text{esc}}$ is determined by its departure from the active region (this time is evidently long, 10^{-8}–10^{-9} s[5,6]) and its decay into acoustic phonons. The latter process is faster. Its time is difficult to estimate, but it is probably considerably longer than τ_0.

The features of the electron kinetics in two-dimensional quantum cascade lasers are also typical of quantum-wire lasers. The exact numerical solutions of the respective kinetic equation system demonstrate that by increasing τ_t it is possible to reduce the threshold current even more than in a quantum-well laser.

Furthermore, τ_t in a quantum-wire laser can be increased to a higher value (10^{-10} s) owing to the lower intrasubband electron–electron relaxation rate,[8] so the threshold current may be two or three orders of magnitude lower.

The threshold current can be additionally reduced owing to singularities in the electron density of states and different effective masses in the subbands. To sum up, it is possible that quantum-wire lasers using transitions between subbands in the conductance band will have threshold currents comparable to those of conventional quantum-well lasers based on the transitions between the conductance and valence bands.

We are indebted to Yu. V. Kopaev for helpful discussions. The work was a part of the Physics of Solid-State Nanostructures Program sponsored by the Ministry of Science and Technology of Russia (grant No. 1-092/4), and was partially supported by the Russian Fund for Fundamental Research (Grant No. 96-02-17363a) and INTAS (Grant No. 93-1704-ext).

[1] A. F. Kazarinov, and R. A. Suris, Fiz. Tekh. Poluprovod. **5**, 797 (1971) [Sov. Phys. Semicond. **5**, 707 (1971)]; Fiz. Tekh. Poluprovod. **6**, 148 (1972) [Sov. Phys. Semicond. **6**, 120 (1972)]; Fiz. Tekh. Poluprovod. **7**, 488 (1973) [Sov. Phys. Semicond. **7**, 347 (1973)].
[2] J. Faist, F. Capasso, D. Sivco *et al.*, Science **264**, 553 (1994); Appl. Phys. Lett. **65**, 2901 (1994).
[3] J. Faist, F. Capasso, C. Sirtori *et al.*, Appl. Phys. Lett. **66**, 538 (1995); J. Faist, F. Capasso, C. Sirtori *et al.*, Appl. Phys. Lett. **67**, 3057 (1995).
[4] C. Sirtori, J. Faist, F. Capasso *et al.*, Appl. Phys. Lett. **68**, 1745 (1996).
[5] J. Faist, F. Capasso, C. Sirtori *et al.*, Phys. Rev. Lett. **76**, 411, (1996).
[6] A. S. Aleksandrov and V. F. Elesin, Zh. Eksp. Teor. Fiz. **58**, 1062 (1970) [Sov. Phys. JETP **31**, 571 (1970)].
[7] E. O. Kane, J. Phys. Chem. Sol. **1**, 249 (1957).
[8] B. Gelmont, V. Gorfinkel, and S. Luryi, Appl. Phys. Lett. **68**, 2171 (1996).
[9] R. Mickevicius, R. Gaska, V. Mitin *et al.*, Semicond. Sci. Technol. **9**, 886 (1994).

Translation was provided by the Russian Editorial office.

Microwave impedance of $Ba_{0.6}K_{0.4}BiO_3$ crystals: comparison with Nb

M. R. Trunin, A. A. Zhukov, and A. T. Sokolov

Institute of Solid-State Physics, Russian Academy of Sciences, 142432 Chernogolovka, Moscow Region, Russia
(Submitted 4 April 1996)
Zh. Éksp. Teor. Fiz. **111**, 696–704 (February 1997)

The surface impedance $Z_s = R_s + iX_s$ of samples of $Ba_{0.6}K_{0.4}BiO_3$ in the temperature range $4 < T < 50$ K is measured at 9.42 GHz. The BCS theory completely describes the electrodynamic properties of Nb in the dirty limit, and its application to $Ba_{0.6}K_{0.4}BiO_3$ allows determination of the London penetration depth $\lambda_L(0) = 3100 \pm 100$ Å. © *1997 American Institute of Physics.* [S1063-7761(97)02202-6]

The surface impedance of $Ba_{1-x}K_xBiO_3$ films forming a parallel-plate resonator was measured at 6.5 GHz in Ref. 1. Microwave measurements of the impedance $Z_s = R_s + iX_s$ of $Ba_{1-x}K_xBiO_3$ films have not been performed hitherto. An analysis of the temperature dependence of the surface resistance $R_s(T)$ and the surface reactance $X_s(T)$ of a superconductor determines the gap size, the London penetration depth, the presence of impurities in the sample, and, ultimately, the superconductive pairing mechanism. The recent investigations of $Z_s(T)$ for YBaCuO (Refs. 2–4) and BiSrCaCuO (Ref. 5) single crystals performed by a method that is convenient for measuring samples of small size (the ''hot-finger'' method) can serve as a example. These investigations allowed the two most probable pairing mechanisms (d or anisotropic s pairing) in these materials to be identified from the plethora of proposed models.

Unlike other high-temperature superconductors, the compound $Ba_{0.6}K_{0.4}BiO_3$ (BKBO), which does not contain copper and has a cubic perovskite structure, is apparently an ordinary isotropic type-II superconductor with a high superconducting transition temperature $T_c \approx 30$ K. In fact, many experimental findings can be explained within the Bardeen-Cooper–Schrieffer (BCS) model with a singlet type of carrier pairing.[6] Nevertheless, several anomalous properties, for example, the positive curvature of the temperature dependence of the second critical field, have been observed in the normal and superconductive states of BKBO.[7–9] In addition, the parameters of BKBO extracted from experiments, viz., the coupling constant,[10,11] the gap size,[12,13] the London penetration depth,[1,14] etc., differ considerably. The main reason for such disparate interpretations of the experiments is apparently the ''imperfect'' nature of the BKBO crystals investigated. In particular, according to dynamic susceptibility measurements, the width of their superconducting transition amounts to several degrees, and even in samples with a very small resistivity $\rho(T_c) < 100$ $\mu\Omega\cdot$cm the transition is inhomogeneous.[7]

In the present work the superconducting properties of BKBO crystals were studied in the 3-cm wavelength range. The effectiveness of the method used was tested in work with Nb samples. The measurements of the temperature dependence of the surface impedance exhibit inhomogeneous broadening of the superconducting transition and considerable residual losses in the BKBO crystals. Nevertheless, the experimental curves can be described within the BCS model, which takes into account both of these factors, over the entire temperature range.

The surface impedance of the Nb and BKBO samples was measured at $f_0 = 9.42$ GHz by a method that was first proposed in Ref. 15. A cylindrical resonator of length and diameter equal to 42 mm, which was cut on a lathe from pure niobium. Among the resonator was not subjected to any additional treatment. Among the important features of the design and operation of the resonator, the degree of coupling of waveguides with the resonator could be smoothly varied, a large frequency shift (>30 MHz) between the degenerate H_{011} and E_{111} modes could be achieved, and the working temperature of the resonator was constant at $T = 4.2$ K.

The experiments were carried out with Nb samples cut from the same original material as the resonator itself and with BKBO crystals, which were prepared by electrochemical crystallization.[16] Figure 1 presents typical plots of the temperature dependence of the real part of the dynamic susceptibility $\chi'(T)/\chi'(0)$ of BKBO single crystals of identical composition, whose synthesis conditions were varied in order to obtain a crystal having a narrow homogeneous transition to the superconducting state. Such a crystal has not yet been successfully grown: as is seen from Fig. 1, the set of plots of $\chi'(T)/\chi'(0)$ for different samples reveals the variation of their superconducting transitions from a very broad and smooth transition (sample *1*) to a ''two-stage'' transition (sample *3*), which begins at $T \approx 29$ K and changes slope at $T \approx 26$ K. Similar structures were previously observed for superconducting transitions in Ref. 7 when the magnetization of BKBO crystals grown by a similar method was measured. Below we present the results of measurements of the surface impedance of two samples having an approximately cubic shape: a 5.5 mm^3 sample of Nb and a 0.2 mm^3 sample of BKBO (sample *3*).

Each sample was fixed to the end surface of a sapphire rod and positioned at the center of the resonator, where the magnetic field H of the working mode H_{011} is uniform and axially directed. The entire resonator-sample assembly was placed in a high vacuum, which, together with the thermal insulation of the rod, provided for the possibility of externally regulating the temperature of the sample in the range from 4.2 to 50 K without heating the resonator itself. The Q factor of the resonator without the sample (but with a

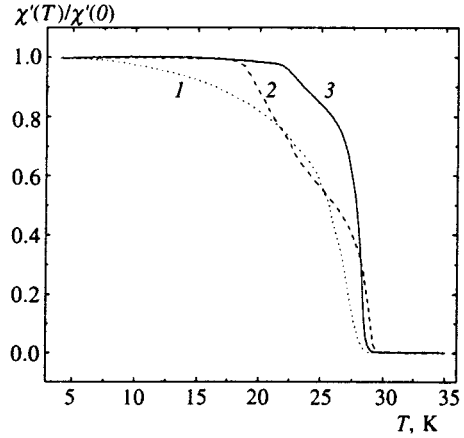

FIG. 1. Dynamic susceptibility of three BKBO crystals.

heated sapphire rod inside) did not vary in this temperature range, remaining equal to $Q_0(T)\approx 7.1\times 10^6$, and a small but reproducible shift $\Delta f_0(T)$ of the frequency f_0 of the resonator was observed. The accuracy of the measurements of the Q factor of the resonator was $\sim 1\%$; the error in setting and measuring the resonant frequency, as well as the instability of the frequency of the microwave synthesizer, did not exceed 10^{-9}.

Figure 2 presents the temperature dependence of the experimentally measured parameters, viz., the Q factor $Q(T)$ of the resonator with a Nb or BKBO sample, and the corresponding variations of the resonant frequency $\Delta f(T)-\Delta f_0(T)$. The surface resistance $R_s(T)$ of a sample and the variation of its reactance $\Delta X_s(T)$ are found from the relation

$$R_s(T)=\Gamma_s[Q^{-1}(T)-Q_0^{-1}(T)],$$

$$\Delta X_s(T)=-\frac{2\Gamma_s}{f_0}[\Delta f(T)-\Delta f_0(T)], \tag{1}$$

where

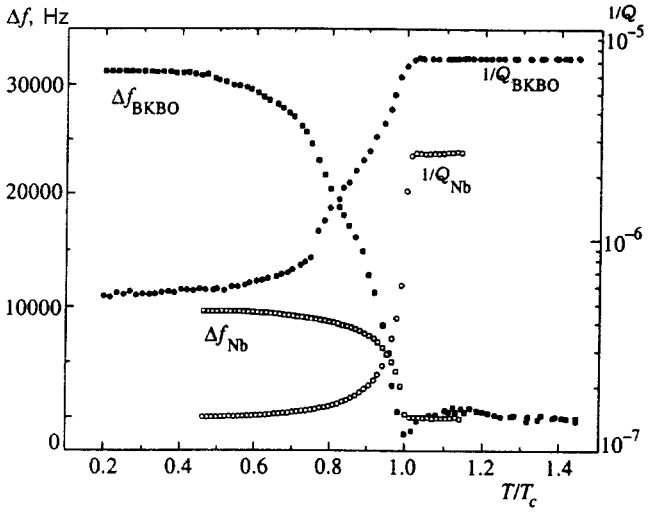

FIG. 2. Measured temperature dependences of $1/Q$ and Δf of a niobium sample (unfilled points) and a BKBO crystal (filled points).

$$\Gamma_s=\frac{\omega_0\mu_0\int_V dV\,H^2}{\int_s dS\,H_s^2} \tag{2}$$

is the geometric factor of the sample, whose unit of measure in the Système International is the ohm, $\omega_0=2\pi f_0$, $\mu_0=4\pi\cdot 10^{-7}$ H/m, the integration in the numerator of (2) is over the volume of the resonator, and the integration in the denominator is over the surface area of the sample. As is seen from (1) and (2), the determination of the absolute values of $R_s(T)$ and $X_s(T)=\Delta X_s(T)+X_0$ requires knowledge of two parameters: the additive constant X_0 and Γ_s. The former is found from the condition that the real R_n and imaginary X_n parts of the impedance in the normal state be equal $R_n=X_n$, since the criteria for the normal skin effect are satisfied for the Nb and BKBO samples that we investigated. The problem of calculating the latter parameter, i.e., Γ_s can be solved in the general case only by numerical methods. However, if the sample has an ellipsoidal shape and is positioned at the center of a resonator operating in the H_{011} mode, it is not difficult to obtain an analytical expression for Γ_s (Ref. 17). Therefore, our first step was to evaluate $\Gamma_{1,\mathrm{Nb}}$ and $\Gamma_{1,\mathrm{BKBO}}$ under the assumption that both samples are spheroids having volumes equal to the known volumes of the Nb and BKBO samples. The second step was based on the experimental method for determining Γ_{Nb}. Under the conditions of the normal skin effect, the surface resistance is $R_n=\sqrt{\omega\mu_0\rho/2}$. We measured the resistivity $\rho_{\mathrm{Nb}}(10\ \mathrm{K})\approx 3\mu\Omega\cdot$cm of a thin strip of Nb cut from the same material as the niobium sample itself. Next, equating R_n and $R_s(10\ \mathrm{K})$ from (1), we found the value $\Gamma_{\mathrm{Nb}}=1.38\times 10^4\Omega$, which is only 24% smaller than the value of $\Gamma_{1,\mathrm{Nb}}$ calculated by the first method. Taking into account the similarity between the shapes of the Nb and BKBO samples investigated, we set the geometric factor of the BKBO crystal equal to $\Gamma_{\mathrm{BKBO}}=0.76\cdot\Gamma_{1,\mathrm{BKBO}}=12.4\times 10^4\Omega$.

Figure 3 shows plots of $R_s(T)$ and $X_x(T)$ of a niobium sample, whose critical temperature is $T_c=9.2$ K. For $T>T_c$ (in the normal state) $R_n=X_n=\sqrt{\omega\mu_0 m/2ne^2\tau}\approx 33\ \mathrm{m}\Omega$. The value of the ratio of the effective mass m to the carrier density n in Nb is known:[18,19] $m/n\approx 1.5\times 10^{-59}$ kg$\cdot$m^3. We find the relaxation time of the carriers $\tau\approx 2\times 10^{-14}$ s and the mean free path $l=40$ Å, which is much smaller than the depth of the skin layer $\delta=\rho/R_n\approx 9000$ Å. In the superconducting state $X_s(T)$ practically reaches its minimum value $X_s(0)\approx 6\ \mathrm{m}\Omega$ for $T<5.5\mathrm{K}=0.6T_c$. the surface resistance $R_s(T)$ decreases by three orders of magnitude as the temperature varies from T_c to $0.5T_c$. Such behavior of $R_s(T)$ and $X_s(T)$ corresponds to the BCS model, and knowledge of the absolute values of $R_s(T)$ and $X_s(T)$ gives the superconducting parameters of Nb.

In the local case there is a simple relationship between the surface impedance of a superconductor and its complex conductivity $\sigma_s=\sigma_1-i\sigma_2$:

$$Z_s=R_s+iX_s=\left(\frac{i\omega\mu_0}{\sigma_1-i\sigma_2}\right)^{1/2}. \tag{3}$$

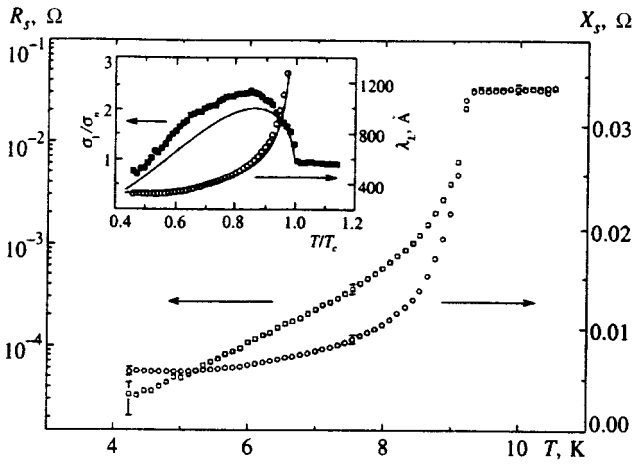

FIG. 3. Plots of $R_s(T)$ and $X_s(T)$ in Nb. The inset contains plots of the temperature dependence of the real part of the conductivity σ_1/σ_n (filled squares) and the London penetration depth λ_L (unfilled circles) found from the measured values of $R_s(T)$ and $X_s(T)$ using Eqs. (4) and (5) and the relation $\lambda_L(T)=0.4\lambda(T)$. The solid curves were calculated within the BCS model.[6,23]

After measuring R_s and X_s, from (3) we find the expressions for the real and imaginary components of the conductivity σ_s normalized to the value σ_n in the normal state:

$$\frac{\sigma_1}{\sigma_n}=\frac{4R_n^2R_sX_s}{(R_s^2+X_s^2)^2},\quad \frac{\sigma_2}{\sigma_n}=\frac{2R_n^2(X_s^2-R_s^2)}{(R_s^2+X_s^2)^2}. \tag{4}$$

The most striking feature of the BCS model,[6] which distinguishes it from all the other theories on the high-frequency response of superconductors, is the nonmonotonic dependence of $\sigma_1(T)$, which increases at $0.85<T/T_c<1$ and decreases at $T<0.85T_c$ (the so-called coherent peak). The amplitude of the peak decreases with increasing values of the frequency ω, the ratio l/ξ_0 (ξ_0 is the coherence length) and the electron-phonon coupling constant,[20] and the peak vanishes if this constant exceeds unity. We know of only one study,[21] in which the coherent peak in Nb was observed at 60 GHz. In the inset in Fig. 3 the solid line shows the temperature dependence of σ_1/σ_n calculated from the general formulas of the BCS theory[22] with known values of ω, τ, and m/n. The temperature dependence of the gap $\Delta(T)$ was taken from the same formulas: $2\Delta(0)=3.53kT_c$. There are no fitting parameters. The shaded squares in the inset represent the experimental dependence of $\sigma_1/\sigma_n(T/T_c)$ found from (4).

The imaginary part of the conductivity $\sigma_2(T)$ determines the depth $\lambda(T)$ to which a magnetic field penetrates into the superconductor:

$$\lambda=(\sqrt{\omega\mu_0\sigma_2})^{-1}. \tag{5}$$

At low temperatures ($T\ll T_c$) the dependence of $\lambda(T)$ coincides with $X_s(T)=\omega\mu_0\lambda(T)$, and from Fig. 3 we at once find $\lambda(0)=X_s(0)/\omega\mu_0\approx 800$ Å. In the dirty ($l<\sqrt{\xi_0 l}<\lambda$) low-frequency ($\hbar\omega\ll\Delta$) limit of the BCS theory, which is satisfied by the experiments under consideration, it is not difficult to obtain an exact analytical expression for σ_2

$$\frac{\sigma_2}{\sigma_n}=\frac{\pi\Delta(T)}{\hbar\omega}\tanh\left(\frac{\Delta}{kT}\right) \tag{6}$$

and an expression for σ_1 that is approximate near T_c, but quantitatively correct in the limit $T\ll T_c$:

$$\frac{\sigma_1}{\sigma_n}\approx\frac{\Delta(T)}{2kT}\cosh^{-2}\left(\frac{\Delta}{2kT}\right)\ln\left(\frac{\Delta}{\hbar\omega}\right). \tag{7}$$

The coherent peak appears because of the logarithmic factor in (7). In the dirty limit the London penetration depth $\lambda_L(0)$ is related to the measured depth $\lambda(0)$ by the expression $\lambda_L(0)=\lambda(0)\sqrt{l/\xi_0}$. After determining $\sigma_2(T)$ from (4) and $\lambda(T)$ from (5) and taking into account that $\sqrt{l/\xi_0}=\sqrt{\pi\Delta(0)\tau/\hbar}\approx 0.4$ holds for our Nb sample, we find the dependence of $\lambda_L(T)$ depicted by the circles in the inset in Fig. 3. The solid curve is a plot of $\lambda_L(T)$ calculated using Eqs. (6) and (5). The value found $\lambda_L(0)=320\pm 10$ Å coincides with the known literature data for Nb.[21,23,24]

Figure 4 presents plots of $R_s(T)$ and $X_s(T)$ of a BKBO crystal, which differ appreciably from the corresponding curves for Nb (Fig. 3). First, as the temperature varies from $T=T_c\approx 29$ K to $T=15$ K the surface resistance $R_s(T)$ decreases altogether by only a factor of 18, reaching an almost constant residual resistance $R_0\approx 49$ mΩ for $T<15$ K. Second, there is a broad inhomogeneous superconducting transition, which actually consists of two successive transitions: the first begins at $T\approx 29$ K, and the second begins at $T\approx 26$ K. They are also manifested in the measured temperature dependence of $1/Q$ and Δf in Fig. 2. In the normal state $R_s(40\text{ K})\approx 0.89$ Ω corresponds to $\rho(40\text{ K})\approx 2100\mu\Omega\cdot$cm, and for the ratio $m/n\approx 2.6\times 10^{-57}$ kg·m^3 in BKBO[13,25] we obtain $\tau\approx 0.5\times 10^{-14}$ s from the Drude formula.

Both features cited of the temperature dependence of the impedance of BKBO are related to the defect density in the surface layer of the crystal. We now show how to describe the experimental plots of $R_s(T)$ and $X_s(T)$ in Fig. 4 while remaining within the BCS model and taking into account the heterogeneity of the sample and the residual losses R_0 in it. For this purpose we utilize the ideas in Ref. 26, where the origin of the narrow incoherent peak in the microwave conductivity $\sigma_1(T)$ of YBaCuO single crystals was explained on the basis of the simple effective-medium approximation. Thus, we assume that different regions of our sample undergo the transition to the superconducting state at different critical temperatures lying in the range ΔT_c. If each of these regions is small compared with the London penetration depth, the distribution of the microwave currents over the sample is uniform, and the calculation of the effective impedance Z_{eff} of the sample reduces to two operations: first, the impedances Z_s of the regions of the sample (with different T_c) that are connected in a chain along a current line are summed, and then averaging over the volume of the sample is performed. As a result, we have

$$Z_{\text{eff}}(T)=\int_{\Delta T_c}Z_s(T,T_c)f(T_c)dT_c, \tag{8}$$

where the distribution function $f(T_c)$ is such that the fraction of the volume of the sample with critical temperatures in the range $T_c<T<T_c+dT_c$ equals $f(T_c)dT_c$. In the simplest

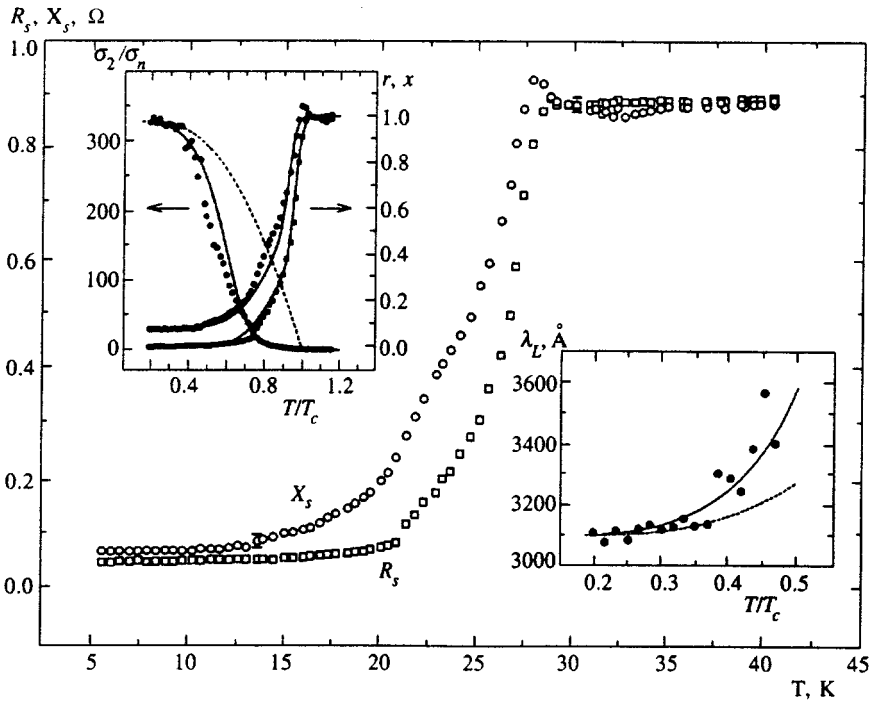

FIG. 4. Plots of $R_s(T)$ and $X_s(T)$ of a BKBO crystal. In the upper inset the points depict the temperature dependence of the relative values of the surface resistance (r) and the reactance (x) and the imaginary part of the conductivity σ_2, the solid lines are plots of the corresponding effective values found from Eq. (8), and the dashed line is a plot of the dependence (6). The lower inset presents plots of $\lambda_L(T)$ calculated in the dirty limit of the BCS theory (dashed line) and within a model which takes into account the presence of regions with different critical temperatures in the sample (solid line). The points depict the measured dependence of $\lambda_L(T)$.

case $f(T_c)$ is a Gaussian function. As for Fig. 4, the distribution function of the different regions of the sample with respect to T_c should reflect the two transitions observed: if we move from the low-temperature side, the broad transition with a maximum $f(T_{c2})$ at $T_{c2}\approx 26$ K rapidly transforms into a narrow transition with a maximum $f(T_{c1})$ at $T_{c1}\approx 28$ K.

The upper inset in Fig. 4 presents the temperature dependence of the relative quantities

$$r=\frac{R_s-R_0}{R_n-R_0}\approx\frac{R_s-R_0}{R_n},\quad x=\frac{X_s}{X_n-R_0}\approx\frac{X_s}{R_n}. \tag{9}$$

The numerator in the expression for r takes into account only the temperature-dependent part of the surface resistance, which is obtained from $R_s(T)$ by subtracting the residual resistance $R_0 \ll R_n$. We further note that, as follows from (1), r and x in (9) do not depend on the geometric factor (2) of the sample. The continuous lines correspond to the effective values of r and x from (8), in which the impedance $Z_s(T,T_c)$ was calculated using the general BCS formulas for the electromagnetic response of superconductors[22] with $2\Delta(0)=3.53kT_c$ and the values of τ and n/m indicated above for a BKBO crystal, and the expression

$$f(T_c)=\frac{2}{3}\sqrt{\frac{2}{\pi}}\left[\frac{1}{\Delta T_1}\exp\left\{-\frac{(T_{c1}-T)^2}{2(\Delta T_1)^2}\right\}+\frac{1}{\Delta T_2}\times\theta(T_{c2}-T)\exp\left\{-\frac{(T_{c2}-T)^2}{2(\Delta T_2)^2}\right\}\right]$$

with $T_{c1}=28$ K, $\Delta T_1=1$ K, $T_{c2}=26.5$ K, and $\Delta T_2=4.7$ K served as the distribution function $f(T_c)$. The points in this inset show the dependence of σ_2/σ_n on (T/T_c) found from measured values of r and x using Eq. (4), the solid line is a plot of the effective conductivity $\sigma_{2,\mathrm{eff}}/\sigma_n$, which is also found using (4), but from the effective values of r and x, and the dashed line is a plot of the dependence (6), which coincides with the preceding curve at $T<0.3T_c$. The minimum value of the imaginary part of the impedance $X_s(0)\approx X_s(5\ \mathrm{K})\approx 70\ \mathrm{m}\Omega$, and, therefore, $\lambda(0)=X_s(0)/\omega\mu_0\approx 9400$ Å. Taking into account the measurement error and the factor $\sqrt{l/\xi_0}\approx 0.33$, we find the London penetration depth of a magnetic field into a BKBO crystal at $T=0$: $\lambda_L(0)=3100\pm 100$ Å. The course of $\lambda_L(T)$, which is represented by the points in the lower inset in Fig. 4, follows the BCS law (dashed line) in the dirty limit with consideration of the deviation from it at $T>0.3T_c$ (solid line), which is obtained from the model of inhomogeneous broadening of the superconducting transition under consideration. The value found for $\lambda_L(0)$ is consistent with the recent measurements of $\lambda(0)$,[1,27] if the correction $\sqrt{1+\xi_0/l}$ due to scattering on impurities is taken into account in them: $\lambda_L(0)=\lambda(0)/\sqrt{1+\xi_0/l}$.

Thus, comparative measurements of the microwave surface impedance of Nb and BKBO have revealed distinct differences in the values of the residual surface resistance R_0 and the widths of the superconducting transitions of these samples. While the high-frequency response of Nb is faithfully described by the BCS model, the large value of the R_0 and the inhomogeneous broadening of the superconducting transition complicate the interpretation of the experimental data for BKBO. Nevertheless, the standard procedure of isolating the temperature-dependent part of the impedance $Z_s(T)$ and the use of a Gaussian distribution of the microscopic regions comprising the surface layer of the sample with respect to T_c enable us to describe the observed dependence of $Z_s(T)$ over the entire temperature range and to determine the value of the London penetration depth of a magnetic field into a BKBO crystal.

We thank V. F. Gantmakher and I. F. Shchegolev for supporting this research and following the work, A. A. Gol-

ubov and D. V. Shovkun for discussing the results, V L. Masalov and G. V. Merzlyakov for their technical assistance, and L. A. Klinkova and V. A. Chekalin for supplying the BKBO and Nb samples. This work was carried out under grants from the Russian Fund for Fundamental Research (No. 94-02-03236) and the State Superconductivity Program (No. 93-194).

[1] M. S. Pambianchi, S. M. Anlage, E. S. Hellman *et al.*, Appl. Phys. Lett. **64**, 244 (1994).
[2] D. A. Bonn, S. Kamal, K. Zhang *et al.*, Phys. Rev. B **50**, 4051 (1994).
[3] J. Mao, D. H. Wu, J. L. Peng *et al.*, Phys. Rev. B **51**, 3316 (1995).
[4] T. Jacobs, S. Sridhar, C. T. Rieck *et al.*, J. Phys. Chem. Solids **56**, 1945 (1995).
[5] T. Jacobs, S. Sridhar, Q. Li *et al.*, Phys. Rev. Lett. **75**, 4516 (1995).
[6] J. Bardeen, L. N. Cooper, and J. R. Schrieffer, Phys. Rev. **108**, 1175 (1957).
[7] M. Affronte, J. Marcus, C. Escribe-Filippini *et al.*, Phys. Rev. B **49**, 3502 (1994).
[8] N. V. Anshukova, A. I. Golovashchkin, L. I. Ivanova *et al.*, Zh. Éksp. Teor. Fiz. **108**, 2132 (1995) [JETP **81**, 1163 (1995)].
[9] V. F. Gantmakher, L. A. Klinkova, N. V. Barkovskii *et al.*, Phys. Rev. B **54**, 6133 (1996).
[10] W. Jin, M. H. Degani, R. K. Kalia *et al.*, Phys. Rev. B **45**, 5535 (1992).
[11] F. Marsiglio, J. P. Carbotte, A. Pushkov *et al.*, Phys. Rev. B **53**, 9433 (1996).
[12] M. Kosugi, J. Akimitsu, T. Ushida *et al.*, Physica C (Amsterdam) **229**, 389 (1994).
[13] A. V. Puchkov, T. Timusk, W. D. Mosley *et al.*, Phys. Rev. B **50**, 4144 (1994).
[14] F. J. Dunmore, H. D. Drew, E. J. Nicol *et al.*, Phys. Rev. B **50**, 643 (1994).
[15] S. Sridhar and W. L. Kennedy, Rev. Sci. Instrum. **54**, 531 (1988).
[16] L. A. Klinkova, N. V. Barkovskiĭ, S. A. Zver'kov *et al.*, Sverkhprovodimost': Fiz., Khim., Tekh. **7**, 1437 (1994).
[17] O. Klein, S. Donovan, M. Dressel *et al.*, Int. J. Infrared Millimeter Waves **14**, 2423 (1993).
[18] W. Schwarz and J. Halbritter, J. Appl. Phys. **48**, 4618 (1977).
[19] G. W. C. Kaye and T. H. Laby, *Table of Physical and Chemical Constants*, Longmans Green, London (1966).
[20] F. Marsiglio, Phys. Rev. B **44**, 5373 (1991).
[21] O. Klein, E. J. Nicol, K. Holczer *et al.*, Phys. Rev. B **50**, 6307 (1994).
[22] S. B. Nam, Phys. Rev. **156**, 470, 487 (1967).
[23] J. P. Turneaure, J. Halbritter, and H. A. Schwettman, J. Supercond. **4**, 341 (1991).
[24] S. M. Anlage, D.-H. Wu, J. Mao *et al.*, Phys. Rev. B **50**, 523 (1994).
[25] G. Kh. Panova, A. A. Shikov, B. I. Savel'ev *et al.*, Zh. Éksp. Teor. Fiz. **103**, 605 (1993) [JETP **76**, 302 (1993)].
[26] A. A. Golubov, M. R. Trunin, S. V. Shulga *et al.*, Physica C (Amsterdam) **213**, 139 (1993).
[27] C. Panagopoulos, J. R. Cooper, G. B. Peacock *et al.*, Phys. Rev. B **53**, R2999 (1996).

Translated by P. Shelnitz

Formation of spatial solitons and spatial shock waves in photorefractive crystals

V. A. Vysloukh, V. Kutuzov, V. M. Petnikova, and V. V. Shuvalov

International Laser Center, M. V. Lomonosov Moscow State University, 119899 Moscow, Russia
(Submitted 21 July 1996; resubmitted 17 September 1996)
Zh. Éksp. Teor. Fiz. **111**, 705–716 (February 1997)

An analytical model, which describes the drift and diffusion mechanisms for the formation of the nonlinear response (local and nonlocal nonlinearities) of photorefractive crystals on the microscopic level, is constructed. New types of stable self-consistent distributions of the light field intensity, i.e., spatial solitons, are found. The trajectories of their motion (self-bending) are calculated, and the possibility of observing a new nonlinear-optical effect in photorefractive crystals, viz., the formation of spatial shock waves, is demonstrated. The modulation instability appearing when plane waves propagate in photorefractive crystals is analyzed, and the characteristic spatial scales of the light field distribution formed as a result of self-interaction (fanning) are determined. The results of the analysis are confirmed by computer simulation data. [S1063-7761(97)02302-0]

1. INTRODUCTION

One of most interesting problems in contemporary nonlinear optics is the investigation of self-organization processes (phase transitions) in systems consisting of a nonlinear medium and a light field. While the stable self-consistent solutions of such problems (solitons) in media with a spatially localized (local) nonlinear response (the case of so-called Kerr nonlinearity[1]) have been studied quite thoroughly, our understanding of the physics of the formation of the analogous space–time structures in self-pumped systems on the basis of nonlocal nonlinearity of the photorefractive type is still on a fairly low level. Investigations of such systems are urgently needed, because photorefraction is one of the strongest mechanisms of nonlinearity, whose manifestations are observed at light intensities amounting to only several mW/cm^2 (Ref. 2).

Photorefractive crystals are characterized by delayed effects, which make it possible to regulate the time for the formation of the nonlinear response in the range from tens of seconds to a few milliseconds or less.[3] However, more importantly, owing to its nonlocal component, fundamentally new types of nonlinear optical signal conversion, such as two-beam energy coupling, the transfer of phase information, etc., can be realized.[4] A unique place among all these processes is occupied by wave-front reversal. This effect can also be observed in self-pumped devices, which are essentially four-photon and often mirrorless parametric light generators.[5] In such systems reversed waves can be generated even when the pump waves are incoherent.[6] In fact, this process is an example of such self-organization, i.e., a phase transition occurring in a nonlinear-medium–light-field system.[7]

The physics of the processes occurring in response to the spatially inhomogeneous illumination of a photorefractive crystal is presently well known.[8] The interference of external light fields and/or light fields generated in photorefractive crystals leads to the spatially inhomogeneous photogeneration of free carriers. This is followed by their spatial diffusion and drift in a static electric field. The subsequent capture of these fields by defects and impurities (''traps'') causes a spatially inhomogeneous distribution of the internal electric field to form. The influence of this field through the linear electro-optic effect leads to a spatially inhomogeneous distribution of the refractive index. The scattering of light on the resultant dynamic hologram closes a two-dimensional feedback loop, forming a complete self-consistent problem.

Although the system of material equations needed to describe photorefraction[8] and the possibility of creating various generation devices from photorefractive crystals[9] have been known for a fairly long time, only a stationary generation regime[5] and the transitional processes accompanying the nonlinear interaction of plane waves in photorefractive crystals[10] have been described on the microscopic level. The generation threshold of self-pumped devices and the characteristic time until they achieve a stationary regime have been evaluated. The main cause of this seemingly paradoxical situation is quite simple. The fact is that a very complicated nonlinear system of equations must be solved when the problem is formulated on the microscopic level. Unfortunately, its numerical integration requires the use of an excessively fine grid along the time and spatial coordinates.[11] Serious problems also arise in the interpretation of the complex structure of the nonstationary nonlinear wave fields obtained as a result of computer simulation. Under the analytical approach in Ref. 12, in which these problems are eliminated, the problem is always regularized, which sharply depletes the possible spatial spectrum of the interacting light fields. In the statistical description in Ref. 13 the problem is linearized through the use of numerous assumptions that greatly restrict its generality. The pump fields are assumed to be assigned, the role of the self-interaction and diffraction processes in higher orders is disregarded, etc. Actually, averaging of the system of nonlinear equations is carried out, which should not be done under the conditions of such strong nonlinearity. Thus, there is presently virtually no adequate description of the processes leading to the formation of stable solutions in self-pumped systems based on media with photorefractive nonlinearity. We also note that the problem of transforming dynamic images, i.e., wavefronts with regular dynamic spa-

tial modulation, can also lead to fundamentally new effects like stable space–time autowave solutions.[14]

Soliton effects play a very important role in the formation of nonlinear wave fields in photorefractive crystals. The pioneering work in Ref. 15 was devoted to a theoretical analysis of these effects. The experimental realization of a soliton regime for the propagation of light beams in photorefractive crystals was first demonstrated in Refs. 16 and 17. The further progress in this area has been largely associated with the analysis of new types of soliton solutions, such as ''dark,''[18] ''gray,''[19] ''vector,''[20] ''vortex,''[21] and other solitons.

The purpose of the present work was to investigate the formation and propagation of the known stationary wave packets of the soliton type, as well as a new self-consistent spatial distribution of a light field, viz., spatial shock waves, in systems with local and nonlocal components of the nonlinear response. We succeeded in constructing a physically explicit and fairly general model based on a microscopic description of the processes occurring in a nonlinear-medium–light-field system. In the process we were able to dispense with numerous traditional approximations that would have restricted the generality of the solutions obtained and to correctly describe the fairly complex and unusual spatial structure of self-consistent light beams propagating in such a nonlinear medium.

2. INITIAL MODEL

The model of the nonlinear response of photorefractive crystals that we used is based on the classical system of material equations for the internal electric field $E_{sc}(x,t)$ (Ref. 8) written for the two-dimensional case without consideration of the photovoltaic effect:

$$\frac{\partial n}{\partial t}=\frac{\partial N_d^+}{\partial t}-\frac{1}{e}\frac{\partial j}{\partial x},$$

$$\frac{\partial N_d^+}{\partial t}=s(I+I_0)(N_d-N_d^+)-\gamma_R n N_d^+, \tag{1}$$

$$j=e\mu n(E_0+E_{sc})-\mu\Theta\frac{\partial n}{\partial x},$$

$$\frac{\partial E_{sc}}{\partial x}=\frac{4\pi e}{\varepsilon}(n+N_a-N_d^+).$$

Here n, N_d, N_d^+ and N_a are the number densities of the free carriers, donors, ionized donors, and acceptors, respectively; s is the cross section of the photoionization process; $I(x,t)$ is the radiated intensity; I_0 is a parameter which describes the dark conductivity of photorefractive crystals and specifies the rate of the dark ionization of the donors as sI_0; γ_R is the pair recombination constant; e and μ are the charge and mobility of the free carriers with consideration of their signs, which are negative for electrons and positive for holes; ε is the static dielectric constant of the photorefractive crystal; and Θ is its temperature in energy units. It is assumed that an external static electric field E_0 is applied to the photorefractive crystal in the transverse direction (along the x axis); therefore, both the drift and diffusion components of the current density j in that direction are taken into account. It is assumed that the optical radiation propagates along the z axis.

The system of material equations (1) is solved together with the standard reduced wave equation for the complex amplitude of a light field $A(x,z,t)$:

$$i\frac{\partial A}{\partial z}=\frac{1}{2k}\frac{\partial^2 A}{\partial x^2}+k\frac{\delta\eta}{\eta}A, \tag{2}$$

which is written in the paraxial approximation without consideration of the absorption. Here k is the wave number; $\delta\eta=(1/2)r_{\text{eff}}\eta^3E_{sc}(x,z,t)$ is the nonlinear addition to the refractive index η; and r_{eff} is the effective electro-optical coefficient. The variation of the refractive index caused by the static field E_0, which is uniform with respect to x, was omitted in (2). Equations (1) and (2) form a self-consistent problem, in which the mutual influence of the redistribution of the light intensity and the redistribution of the electric field in the bulk of the photorefractive crystal is taken into account. Such a model faithfully describes experiments with so-called slit beams,[22] which are widely used in practice in investigations of soliton effects in photorefractive crystals because of the strong anisotropy of the nonlinear response of the latter.

3. SOLUTION OF THE SYSTEM OF MATERIAL EQUATIONS

The system of material equations (1) is solved in the stationary approximation $\partial/\partial t\to 0$, $j=j(x)$. As a result, j and N_d^+ are eliminated from it, and

$$En-E_0n_0=\frac{\Theta}{e}\frac{\partial n}{\partial x}, \tag{3}$$

$$n=s(I_0+I)(N_d-N_a)\left(1+a\chi\frac{\partial E}{\partial x}\right)\Big/\gamma_R N_a\left(1-a\frac{\partial E}{\partial x}\right). \tag{4}$$

Here n_0 is the dark density of free carriers. In (4) we have introduced the notation

$$a=\frac{\varepsilon}{4\pi eN_a},\quad E=E_0+E_{sc},\quad \chi=\frac{N_a}{N_d-N_a}, \tag{5}$$

and it is assumed that $N_a\gg n$. For photorefractive crystals with a large dark conductivity, i.e., when the inequality $I_0\gg I$ holds, the system of equations (3) and (4) is linearized with respect to I, E_{sc}, and n. Now, under the assumption that $a\partial E/\partial x\ll 1$ it can be reduced to a single linear equation that is second-order with respect to E_{sc}

$$\frac{\partial^2 E_{sc}}{\partial x^2}-\frac{eE_0}{\Theta}\frac{\partial E_{sc}}{\partial x}-\frac{e}{\Theta a(\chi+1)}E_{sc}=\frac{1}{a(\chi+1)I_0}\left(\frac{eE_0}{\Theta}I-\frac{\partial I}{\partial x}\right). \tag{6}$$

Its solution can be represented in the form

$$E_{sc}=-\frac{1}{a(\chi+1)I_0(\lambda_1-\lambda_2)}\left[\lambda_1\int_{-\infty}^{x}I(\xi)\times\exp[\lambda_2(x-\xi)]d\xi+\lambda_2\int_{x}^{\infty}I(\xi)\exp[\lambda_1(x-\xi)]d\xi\right], \tag{7}$$

$$\lambda_{1,2}=\frac{eE_0}{2\Theta}\pm\sqrt{\left(\frac{eE_0}{2\Theta}\right)^2+\frac{e}{a\Theta(\chi+1)}},$$

which also specifies the nonlinear addition to the refractive index on the right-hand side of Eq. (2).

When (7) is integrated, $I(\xi)$ can be expanded into a series in the vicinity of the point x. This enables us to write the solution of (7) in the form of an expansion in derivatives of the radiated intensity

$$E_{sc}=\frac{1}{aI_0(\chi+1)(\lambda_1-\lambda_2)}\sum_{m=0}^{\infty}\left(\frac{\lambda_1}{\lambda_2^{m+1}}-\frac{\lambda_2}{\lambda_1^{m+1}}\right)\frac{\partial^m I(x)}{\partial x^m}. \tag{8}$$

The relation between the spatial distributions of the internal field and the radiated intensity is even more transparent in the spectral representation. It is easily seen that in shaping the spatial spectrum of the distribution of the internal field $E_{sc}(\kappa)$ the photorefractive crystal actually plays the role of a field of the spatial frequencies κ with the transmission coefficient

$$T(\kappa)=-\frac{E_0}{I_0}\frac{1+i\kappa\Theta/eE_0}{1-i\kappa aE_0(\chi+1)+\kappa^2a\Theta(\chi+1)/e} \tag{9}$$

with respect to the spatial spectrum of the distribution of the light intensity $I(\kappa)$. The expressions for $T(\kappa)$ in the cases of pure drift of the free carriers and their pure spatial diffusion can easily be obtained from (9) after the limiting transitions $\Theta\to 0$ and $E_0\to 0$:

$$T_{dr}(\kappa)=-\frac{E_0}{I_0}\frac{1}{1-i\kappa aE_0(\chi+1)}, \tag{10}$$

$$T_{df}(\kappa)=-i\kappa\frac{\Theta}{eI_0}\frac{1}{1+\kappa^2a\Theta(\chi+1)/e}. \tag{11}$$

We note that (10) and (11) can be simplified significantly, if the terms proportional to κ and κ^2 in their denominators are neglected or $T_{dr}(\kappa)$ and $T_{df}(\kappa)$ are expanded in power series in κ with retention of only the linear terms. The latter can nearly always be done, since under the conditions of any real experiment in external fields up to 10 kV/cm at $\Theta\sim 300$ K all the subsequent terms become significant only for spatial scales of variation of the light field smaller than the wavelength. This actually means that in the expansion (8) we can retain only the first two terms, which are proportional to $I(x)$ and $\partial I/\partial x$ and which we shall henceforth call the local and nonlocal components of the nonlinear response.

4. SPATIAL SOLITONS AND "SHOCK WAVES"

Let us discuss some very important solutions of the self-consistent problem formulated by Eqs. (2) and (8). We attempt to find solutions which fit the case of the separation of variables

$$A(x,z)=Y(x)\exp(-i\nu z), \tag{12}$$

where the real function $Y(x)$ assigns the distribution of the field along the transverse coordinate x, and the positive constant ν specifies the nonlinear phase trajectory of the solution along z. Thus, the problem is to attempt to find intensity distributions that are stationary with respect to z and t. It is easy to see that the substitution of (12) into (2) leads to an equation for the spatial profile of the amplitude having the form

$$\frac{d^2Y}{dx^2}-4\frac{\alpha kE_0}{I_0}\left[\frac{\Theta}{eE_0}+a(\chi+1)E_0\right]\times Y^2\frac{dY}{dx}+2k\left(\frac{\alpha E_0}{I_0}Y^3-\nu Y\right)=0, \tag{13}$$

where $\alpha=kr_{\rm eff}\eta^2/2$ and the first two terms of the expansion (8) have been retained (see above). In the case of focusing Kerr nonlinearity ($\delta\eta>0$), it is convenient to introduce the dimensionless coordinates $\xi=x/x_0$ and $\zeta=z/L_d$ and the normalized amplitude of the light field $\rho(\xi)=Y(\xi)\sqrt{R/I_0}$ into (13). Here x_0 is determined by the characteristic transverse scale of the problem, for example, by the width of the incoming beam; $L_d=kx_0^2$ is the diffraction length corresponding to x_0; $R=L_d/L_r>0$; and $L_r=1/\alpha E_0$ is the nonlinear refraction length. Now (13) becomes

$$\frac{d^2\rho}{d\xi^2}+2\gamma\rho^2\frac{d\rho}{d\xi}+2(\rho^3-\beta\rho)=0, \tag{14}$$

where the parameter

$$\gamma=-2\frac{\alpha kE_0}{R}\left[\frac{\Theta}{eE_0}+a(\chi+1)E_0\right]x_0$$

characterizes the magnitude of the nonlocal component of the nonlinear response, and $\beta=L_d\nu$. Below we shall say more regarding the case of $\gamma>0$, which can occur when the orientation of the photorefractive crystal and the direction of E_0 are chosen appropriately.

4.1. Modulation instability

It is easy to see that, as in a medium with pure Kerr nonlinearity, a plane wave with an amplitude $\rho(\xi)=\rho_0$ is a trivial solution of (14) when $\beta=\rho_0^2$. Let us consider the stability of this solution toward small ($\delta\rho_0\ll 1$) harmonic disturbances of the distribution $\delta\rho(\xi)=\delta\rho_0\cos(\Omega\xi)$ at the dimensionless spatial frequency $\Omega=\kappa x_0$. Using the linearization technique developed by Bespalov and Talanov[23] and the results obtained in Ref. 24, we can easily show that the amplitude of such a disturbance increases exponentially as ζ increases with the growth rate

$$g=\mathrm{Im}\left(\frac{1}{2}\sqrt{\Omega^2(\Omega^2-4\rho_0^2)+i\gamma\Omega\rho_0^2}\right). \tag{15}$$

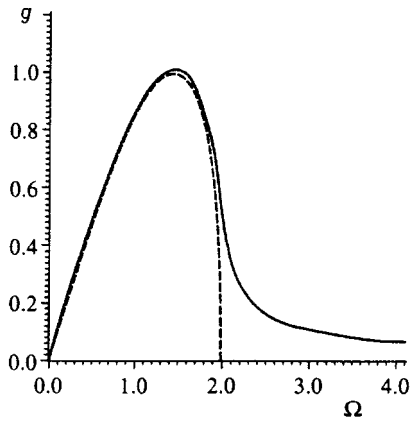

FIG. 1. Dependence of the growth rate of a small disturbance on the dimensionless spatial seed modulation frequency Ω: local (Kerr) nonlinearity — dashed line; photorefractive crystals with local and nonlocal responses ($\rho_0=1$, $\gamma=1$) — solid line.

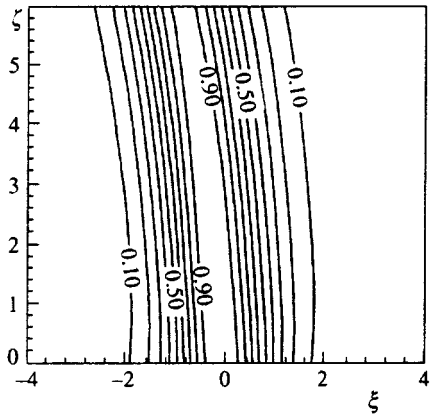

FIG. 2. Self-bending of the trajectories of motion of spatial solitons: contours of the distribution of the normalized intensity in the (ξ,ζ) plane with spacing 0.1.

We note that the familiar result for a medium with a Kerr nonlinearity follows in the limit $\gamma\to 0$. As we know,[23] in the latter case the exponential increase in the amplitude of the disturbances occurs only in the restricted band of spatial frequencies $0<\Omega<\Omega_b=2\rho_0$, and the maximum value of g is achieved at $\Omega=\Omega_m=\sqrt{2}\rho_0$. The appearance of a term proportional to $d\rho/d\xi$ in Eq. (14) expands the modulation instability band to infinity, but even for $\gamma\approx 1$, its half-width is close to the half-width of the instability band for the case of Kerr nonlinearity, and the frequency where the maximum gain is achieved is close to Ω_m (Fig. 1).

Thus, in a medium with nonlocal nonlinearity the plane waves are unstable, although they fall into the class of solutions with separated variables. In the case of exceedingly small seed modulation with a sufficiently broad spectrum such a plane wave breaks up as it propagates into comparatively thin filaments with a mean dimensionless spatial period $\Lambda=2\pi/\Omega_m$ and a mean thickness equal to the reciprocal width of the instability band. The first experimental observation of modulation instability in a photorefractive crystal was reported in Ref. 24.

4.2. Spatial solitons

In the preceding case of Kerr nonlinearity ($\gamma=0$), Eq. (14) has a well-known single-soliton solution of the form $\rho(\xi)=\mathrm{sech}(\xi)$, which is written out here for $\beta=1/2$. Although it is known that this solution is stable,[22] in real experiments the necessary one-dimensionality of the diffraction and self-interaction processes is achieved only by using slit beams, which have a uniform field distribution in the direction orthogonal to the ξ axis. The possibility of the development of modulation instability along the length of the crystal with resultant filamentation of the beam in that direction must then be considered. We note that the stability of two-dimensional solitons is achieved because the nonlinearity is saturable.

Let us examine the question of the influence of the nonlocal component of the nonlinear response on the propagation of solitons of such form in a photorefractive crystal. We note at once that this question is directly related to the self-bending of laser beams.[25–28] Therefore, we turn to Eq. (2), introducing the normalized complex amplitude $q(\xi,\zeta)=A(\xi,\zeta)\sqrt{R/I_0}$ into it in analogy to (14):

$$i\frac{\partial q}{\partial\zeta}=\frac{1}{2}\frac{\partial^2 q}{\partial\xi^2}+\frac{\gamma q}{2}\frac{\partial|q|^2}{\partial\xi}+|q|^2 q. \tag{16}$$

Now, assuming $\gamma<1$, we seek the solution of Eq. (16) in the self-similar form

$$q_s(\xi,\zeta)=K\,\mathrm{sech}[K(\xi-V\zeta)]\exp[i\Phi(\xi,\zeta)], \tag{17}$$

$$\Phi(\xi,\zeta)=-V\xi+\frac{1}{2}(V^2-K^2)\zeta.$$

Here the form factor $K(\zeta)$ describes the dependence of the amplitude and width of the soliton on the longitudinal coordinate ζ, and $V(\zeta)$ specifies the angle between the current direction of propagation of the soliton and the ζ axis. Utilizing the tools of perturbation theory,[1] we can show that the soliton amplitude remains unchanged to first order in γ and that $V(\zeta)$ satisfies the ordinary differential equation

$$\frac{dV}{d\zeta}=-\frac{8}{15}\gamma K^2 \tag{18}$$

with the initial condition $V(0)=0$. It follows from (18) that in a photorefractive crystal the soliton vertex (17) with the coordinate ξ_s moves along the parabolic trajectory $\xi_s=-4\gamma K^2\zeta^2/15$. This analytical result is in excellent agreement with the data from direct numerical integration of the quasioptical equation with the initial condition $q(\xi,0)=\mathrm{sech}(\xi)$, which are presented in Fig. 2 in the form of contours of constant intensity in the (ξ,ζ) plane. For example, for $\gamma=0.1$ and $\zeta=6$, the error in the analytical determination of the current coordinate of the soliton vertex is less than 5%. An increase in the nonlocal component of the response results only in a slight decrease in the soliton amplitude in the outgoing plane. Thus, the appearance of a term responsible for a nonlocal nonlinear response in Eq. (16) removes the single-soliton solutions from the class of solutions with separated variables.

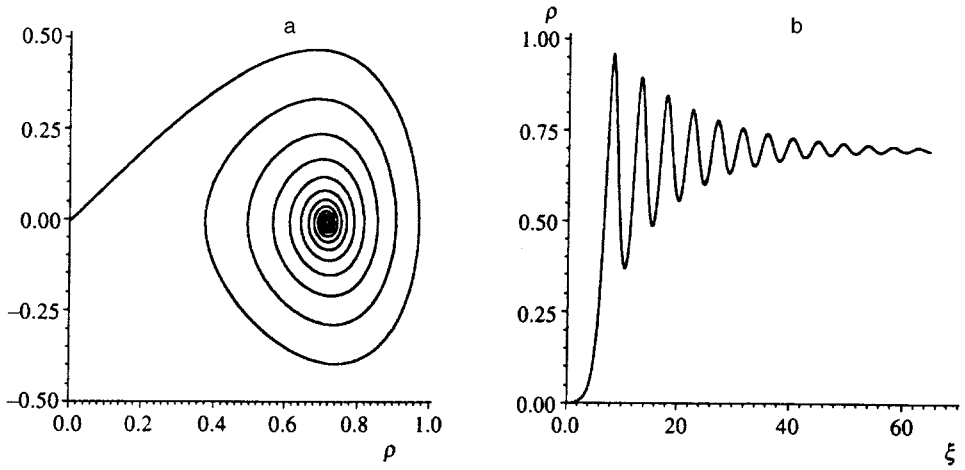

FIG. 3. Profile of a spatial shock wave for $\beta=0.5$ and $\gamma=0.15$: in the phase plane (a) and in the coordinate space (b).

4.3. Spatial shock waves

Let us now examine the fairly unusual stationary, spatially unrestricted solutions that appear in a medium with a nonzero nonlocal component of the nonlinear response. The special features of the solutions of this type, which we have termed spatial shock waves, are conveniently analyzed on the phase portrait of Eq. (14), i.e., in the $(\rho,\partial\rho/\partial\xi)$ plane. Here we can take advantage of the direct mathematical analogy between the character of $\rho(\xi)$, which is assigned by (14), and the nonlinear oscillations of an oscillator in the potential

$$U(\rho)=\frac{1}{2}\rho^4-\beta\rho^2 \tag{19}$$

with nonlinear damping described by the term $2\gamma\rho^2 d\rho/d\xi$. The potential energy of such an oscillator has three local extrema, which correspond to three critical points of the phase portrait. The two minima of $U(\rho)$ lying on the ρ axis with the coordinates $\rho_{1,2}=\pm\sqrt{\beta}$ are points of stable equilibrium, i.e., focal points, and the single maximum $(\rho=d\rho/d\xi=0)$ is a point of unstable equilibrium, i.e., a nodal point. Linearization of (14) in the vicinity of the nodal point gives the equation

$$d^2\rho/d\xi^2-2\beta\rho=0, \tag{20}$$

which has the exponentially increasing solution $\rho(\xi)\propto\exp(\sqrt{2\beta}\xi)$ in addition to the trivial solution $\rho=0$. In the vicinity of either of the focal points the same procedure gives the equation of damped oscillations

$$\frac{d^2u}{d\xi^2}+2\gamma\beta\frac{du}{d\xi}+4\beta u=0 \tag{21}$$

for the small displacements $u(\xi)=\rho(\xi)-\rho_{1,2}$ from the equilibrium position. The solutions of Eq. (21) correspond to periodic ($\gamma<2/\sqrt{\beta}$, frequency $\omega=\sqrt{4\beta-(\gamma\beta)^2}$) or aperiodic ($\gamma\ll 2/\sqrt{\beta}$) passage to the corresponding focal point when $\xi\to\infty$.

Although the exact solution of Eq. (14) cannot be written in elementary functions, the character of $\rho(\xi)$ is described quite well by the approximate solutions presented above. This was confirmed by the numerical integration of (14). The initial conditions employed were assigned at the point $\xi_0\ll 0$ on the basis of the asymptotic dependence $\rho(\xi_0)=\exp(\sqrt{2\beta}\xi_0)$, $d\rho/d\xi=\sqrt{2\beta}\exp(\sqrt{2\beta}\xi_0)$, which corresponds to the vicinity of a nodal point in the phase plane. The corresponding phase trajectory, which is shown in Fig. 3a, has the form of a spiral, which converges to the stable focal point ρ_1. A profile of the amplitude $\rho(\xi)$ of a spatial shock wave is shown in Fig. 3b. The characteristic features of solutions of this type, viz., the abrupt spatial shock wave front, which rises exponentially from zero, reaches a plateau with amplitude oscillations that are damped with respect to ξ, and then achieves the stationary value ρ_1, are clearly seen. The frequency of these oscillations and the damping coefficient agree well with the values predicted by Eq. (21). At large values of γ the approach to ρ_1 becomes aperiodic.

An analytical investigation of the stability of the solutions obtained as they propagate along ζ [the evolutionary equation (16)] raises some definite difficulties in view of the lack of an explicit expression for the spatial distribution of the field. The asymptotic transition of the shock wave to a plane wave as $\xi\to\infty$ provides some basis to assume that the modulation instability can develop in that region. Nevertheless, the computer simulation results convince us that waves of this new type can be produced experimentally in photorefractive crystals. Figure 4a illustrates the stable propagation of an undisturbed (to within ''computer noise'') spatial shock wave over a distance $\zeta=2$, which corresponds to a length of a photorefractive crystal of about 1 cm on the real scale. Figure 4b shows its structural stability when the outgoing field amplitude profile is significantly (20% in terms of intensity) disturbed by Gaussian noise. Thus, spatial shock waves in photorefractive crystals represent a new type of soliton-type solutions that belong to the class of solutions with separated variables.

4.4. Evolution of a stepped intensity distribution

To illustrate the importance of the particular solutions obtained above to the structure of the nonlinear wave fields formed in the general case, we present data from the direct computer simulation of the evolution of a laser beam with the stepped incoming amplitude profile $q(\xi,0)$

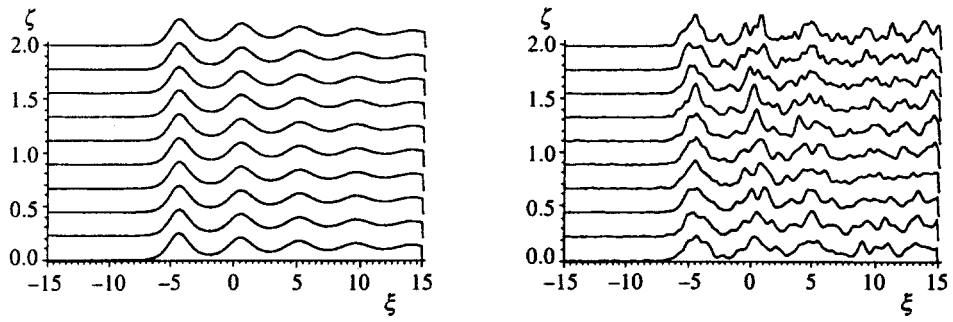

FIG. 4. Profile of a spatial shock wave for $\beta=0.5$ and $\gamma=0.15$ in successive cross sections of photorefractive crystals along ζ: in the absence of disturbances (a) and at a noise level of 20% intensity (b).

$=[1+\tanh(\xi)]/2$ in a photorefractive crystal with local and nonlocal nonlinearity. Figure 5 shows spatial profiles of the intensity $|q(\xi)^2|$ in successive cross sections of a crystal for the values $\gamma=0$, 1. As the radiation propagates, a diffraction spike forms on the front of the initial intensity distribution and then transforms into a soliton due to the local component of the nonlinearity. Simultaneously, it is gradually deflected from the ζ axis by the nonlocal component of the response. As the beam propagates further, the next solitons split off from the front of the intensity distribution. At all times the remainder of the beam has a structure similar to a spatial shock wave. Thus, although we were dealing with a very complicated nonlinear superposition of fields in the computer experiment, understanding the structure of the elementary self-consistent solutions obtained above significantly facilitates its analysis.

5. CONCLUSIONS

Summarizing the work, let us briefly recount its main results and formulate several conclusions. Thus, starting out from a very general microscopic model of the formation of the nonlinear response of photorefractive crystals, we have obtained a fairly simple and physically explicit expansion for it in both coordinate (8) and spectral (9) representations. Taking into account the nonlocal component of the nonlinear response, we have succeeded in refining the physical picture of the development of modulation instability (fanning) in photorefractive crystals.[24] An analytical numerical analysis of the role of this component of the response in the dynamics of the propagation of spatial solitons has shown that in first-order perturbation theory it leads to self-bending of the trajectories of motion of the solitons[25] and that in second-order perturbation theory it leads to a decrease in their amplitude and an increase in their width.

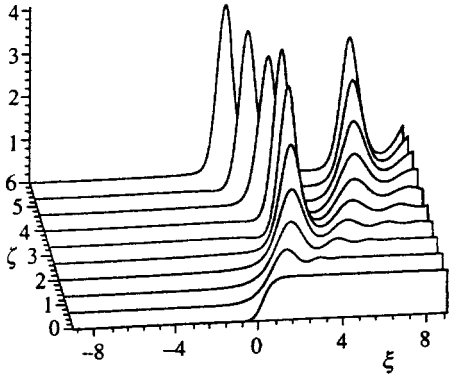

FIG. 5. Formation of spatial solitons and spatial shock waves from a stepped intensity distribution: intensity profiles in successive cross sections of the crystal along ζ for $\gamma=0.1$.

We have succeeded in obtaining solutions in the form of spatial shock waves in photorefractive crystals for the first time. The numerical experiments conducted here have shown that such elementary solutions are not only physically feasible, but are also clearly traceable in the structure of the nonlinear wave fields formed in photorefractive crystals from incoming radiation with an arbitrary transverse intensity distribution.

Concluding this paper, we should mention the possible areas for further research. We associate the most important prospects both with an analysis of the self-organization processes that take place under the conditions of defocusing nonlinearity and lead to the formation of so-called dark solitons[18] and with stochastic generalizations of the regular problems considered above.[28]

This work was performed with financial support from the Russian Fund for Fundamental Research (Grant No. 96-2-16238) and the US Army Research Laboratory (Contract No. DAAL01-95-R-2008).

[1] S. A. Akhmanov, V. A. Vysloukh, and A. S. Chirkin, *Optics of Femtosecond Laser Pulses*, American Institute of Physics, New York (1992).
[2] *Photorefractive Materials and Applications (Topics in Applied Physics, Vol. 61)*, P. Gunter and J.-P. Huignard (eds.), Springer, Heidelberg (1988).
[3] *Photorefractive Materials and Applications (Topics in Applied Physics, Vol. 62)*, P. Gunter and J.-P. Huignard (eds.), Springer, Heidelberg (1988).
[4] M. P. Petrov, S. I. Stepanov, and A. V. Khomenko, *Photorefractive Crystals in Coherent Optical Systems*, Springer-Verlag, Berlin–New York (1991).
[5] S. G. Odulov, M. S. Soskin, and A. I. Khizhnyak, *Optical Oscillators with Four-Wave Mixing*, Harwood Academic, Chur, 1991.
[6] M. Cronin-Colomb, B. Fisher, J. O. White, and A. Yariv, IEEE J. Quantum Electron. **QE-20**, 12 (1984).
[7] D. Engin, S. Orlov, M. Segev *et al.*, Phys. Rev. Lett. **74**, 1743 (1995).
[8] N. Kukhtarev, V. Markov, S. Odulov *et al.*, Ferroelectrics **22**, 949 (1979).
[9] J. Feinberg, Opt. Lett. **7**, 486 (1982).
[10] A. A. Zozulya, Kvantovaya Elektron. **19**, 733 (1992) [Sov. J. Quantum Electron. **22**, 677 (1992)]
[11] V. A. Vysloukh, V. Kutuzov, and V. V. Shuvalov, Kvantovaya Elektron. **23**, 157 (1996).
[12] A. V. Mamaev and A. A. Zozulya, Opt. Commun. **79**, 373 (1990).
[13] N. I. Bel'dyugina and V. V. Shkunov, Kvantovaya Elektron. **21**, 234 (1994).
[14] M. A. Vorontzov, ICONO'95 Tech. Digest (St. Petersburg, Russia) **1**, 345 (1995).
[15] M. Segev, B. Crosignani, and A. Yariv, Phys. Rev. Lett. **68**, 923 (1992).

[16] M. D. Iturbe Castillo, P. A. Marquez Aguilar, J. J. Sanchez Mondragon, *et al.*, Appl. Phys. Lett. **64**, 408 (1994).
[17] G. Duree, J. Shultz, G. Salamo *et al.*, Phys. Rev. Lett. **71**, 533 (1994).
[18] G. C. Valley, M. Segev, B. Crosignani *et al.*, Phys. Rev. A **50**, R4457 (1994).
[19] D. N. Christodoulides and M. I. Carvalho, J. Opt. Soc. Am. B **12**, 1628 (1995).
[20] M. Segev, G. C. Valley, S. R. Singh *et al.*, Opt. Lett. **20**, 1764 (1995).
[21] G. Duree, M. Morin, G. Salamo *et al.*, Phys. Rev. Lett. **74**, 1978 (1995).
[22] G. Duree, G. Salamo, M. Segev *et al.*, Opt. Lett. **19**, 1195 (1994).
[23] V. I. Bespalov and V. I. Talanov, JETP Lett. **3**, 307 (1966).
[24] D. Iturbe Castillo, M. Torres Cisneros, J. J. Sanchez Mondragon *et al.*, Opt. Lett. **20**, 1 (1995).
[25] J. Feinberg, J. Opt. Soc. Am. **72**, 46 (1982).
[26] D. N. Christodoulides and M. I. Carvalho, Opt. Lett. **19**, 1714 (1994).
[27] A. A. Zozulya, M. Saffman, and D. Z. Anderson, Phys. Rev. Lett. **73**, 818 (1994).
[28] O. V. Lyubomudrov and V. V. Shkunov, Kvantovaya Elektron. **21**, 561 (1994).

Translated by P. Shelnitz

Why have no manifestations of the excitonic mechanism been detected in Ginzburg sandwiches?

Yu. A. Krotov

P. N. Lebedev Institute of Physics, Russian Academy of Sciences, 117924 Moscow, Russia

I. M. Suslov

P. L. Kapitsa Institute of Physical Problems, Russian Academy of Sciences, 117334 Moscow, Russia
(Submitted 28 June 1996)
Zh. Éksp. Teor. Fiz. **111**, 717–729 (February 1997)

Using spatially inhomogeneous Éliashberg equations in the local-interaction limit, an exact solution of the problem of the superconducting transition temperature in a Ginzburg sandwich (a superconducting film coated with a dielectric layer containing Bose-type excitations, i.e., excitons) in the first order in a/L (where a is the interatomic distance and L is the film thickness) has been obtained. The result has been found to be independent of the exciton frequency. The excitonic mechanism appears only in second order in a/L since both components of the Cooper pair should enter a layer of thickness $\sim a$ in order to interact through the exchange of excitons. Numerical estimates indicate that manifestations of the excitonic mechanism are practically undetectable in systems with $L \gg a$. Calculations for the model with a narrow-gap and a wide-gap dielectric have been performed and compared to experimental data. © *1997 American Institute of Physics.* [S1063-7761(97)02402-5]

1. INTRODUCTION

In 1964 in his famous paper,[1] Ginzburg set forth a new method for creating high-temperature superconductors. If a thin metal film is coated with a layer of a dielectric (Fig. 1) containing high-frequency boson excitations, i.e., excitons, whose frequency ω_{ex} is considerably higher than the phonon frequency ω_{ph} in the metal, the combination of the finite electron density of states on the interface and the high excitation frequency should lead, according to the BCS formula, to a high local value of the superconducting transition temperature T_c. The theory of Ginzburg sandwiches has been developed by many authors (see Ch. 8 in Ref. 2 and references therein), but the available estimates of T_c are unsatisfactory because all these theories ignore the problems related to the spatial inhomogeneity of sandwiches. All of them were based on the use of the BCS or MacMillan-type formulas and rough estimates of their parameters. Below we shall demonstrate that such an approach leads to qualitatively erroneous results.

Following the terminology of Ref. 2, we define sandwiches as structures manufactured using the appropriate technology, such that their metal film thickness L is essentially larger than the interatomic distance a.[1)] Structures with $L \sim a$ should be treated as quasi-two-dimensional, and this topic is beyond the scope of this paper. Besides, we assume that the superconductivity in the film is three-dimensional since the predicted surface superconductivity of Tamm states[1,5] has not been detected with certainty in any material.

It is clear from general principles that the difference between T_c in a sandwich and T_{c0} in the bulk material of the film should be proportional to a/L:

$$\frac{\delta T_c}{T_{c0}} \equiv \frac{T_c - T_{c0}}{T_{c0}} = C\,\frac{a}{L}. \tag{1}$$

All the existing theories[2] are based on the assumption that, in the formal limit $\omega_{ex} \to \infty$, the factor C should diverge, and its large value should compensate for the smallness of the ratio a/L or, at least, make the exciton-mediated interaction dominant over all other effects, which yield $C \sim 1$. In this paper, however, we demonstrate that

$$C(\omega_{ex}) = \text{const} \quad \text{for} \quad \omega_{ex} \gtrsim \omega_{ph}. \tag{2}$$

This result, however strange it may seem at first sight, is natural. In order to interact through the exchange of excitons, both components of a Cooper pair must reach a layer with thickness of the order of a, and the probability of this event is $\sim (a/L)^2$, hence the excitonic mechanism should not appear to first order in a/L. If the term quadratic in a/L is considered, after the dimensionless interaction constant λ_0 in the bulk metal is factored out, we have

$$\frac{\delta T_c}{T_{c0}} = \frac{A}{\lambda_0}\frac{a}{L} + \frac{B(\omega_{ex})}{\lambda_0}\left(\frac{a}{L}\right)^2 + \ldots, \tag{3}$$

and the coefficients in this formula can be estimated as[2)]

$$B(\omega_{ex}) = B_0 + B_1\lambda_0 \ln\frac{\omega_{ex}}{\omega_{ph}}, \quad A,\ B_0,\ B_1 \sim 1, \tag{4}$$

i.e., the coefficient of $(a/L)^2$ in fact diverges as $\omega_{ex} \to \infty$. The factors λ_0^{-1} arise in Eq. (3) because the variation of the BCS formula $T_c \sim \overline{\omega}\exp(-1/\lambda)$ with respect to $\overline{\omega}$ and λ yields $\delta T_c/T_{c0}$ proportional to $\delta\overline{\omega}/\overline{\omega}$ and $\delta\lambda/\lambda_0^2$, respectively, i.e., the relative change in λ is multiplied by the factor λ_0^{-1}, as compared to the relative change in $\overline{\omega}$. According to Eqs. (3) and (4), the ratio of the contribution of the excitonic mechanism to the total change in T_c is

$$\frac{(\delta T_c)_{ex}}{(\delta T_c)_{tot}} \sim \frac{a}{L}\,\lambda_0 \ln\frac{\omega_{ex}}{\omega_{ph}}. \tag{5}$$

 1063-7761/97/020395-07$10.00

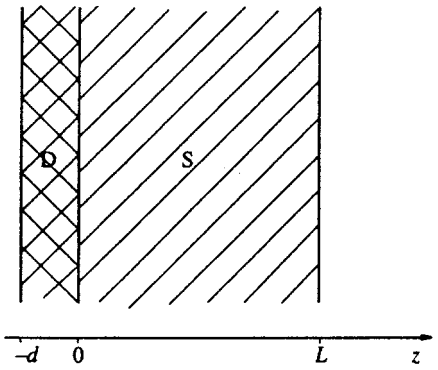

FIG. 1. A Ginzburg sandwich is a thin superconducting film S with a deposited dielectric layer D with high-frequency bosons excitations, whose exchange should increase T_c considerably.

The limitations due to the Tolmachev logarithm[2] lead to the inequality $\omega_{ex}/\omega_{ph} \lesssim 10^2$, and for typical values $\lambda_0 = 0.2-0.3$[3)] we have $\lambda_0 \ln(\omega_{ex}/\omega_{ph}) \sim 1$, hence the excitonic contribution is always small at $L \gg a$. This means that any attempts to detect the excitonic effects in the ''small correction regime'' are doomed to failure: when a metal film is coated with a dielectric, the change in T_c may be controlled by all effects, except the exchange of excitons. This is, apparently, the main reason why this effect has not been detected in experiments.

A formula for T_c, naturally, cannot be derived for an arbitrary spatially inhomogeneous system, but this is possible for the case of a local spatial inhomogeneity, when its dimension d is smaller than the coherence length ξ_0 or the total system dimension L (if $L \lesssim \xi_0$). These formulas were derived earlier[6,7] and used to study the localization of the order parameter localization, quantum oscillations of T_c, the contribution of an interface between two materials to T_c as a function of material parameters, etc.[6–9] All these studies used the Gor'kov equation,[10,11] which does not allow for the spatial dependence of the cut-off frequency $\overline{\omega}$. In the weak-coupling regime, this dependence expressed by $\overline{\omega(\mathbf{r})}$ usually leads only to small corrections determined by the parameter

$$\lambda_0 \ln \frac{\overline{\omega}_{max}}{\overline{\omega}_{min}} \ll 1. \tag{6}$$

In the case of a large disparity in the frequencies, $\overline{\omega}_{max} \gg \overline{\omega}_{min}$, the condition (6) may be violated even for $\lambda_0 \ll 1$, and this is the case in a Ginzburg sandwich.

In the present study, formulas for T_c similar to those in Refs. 6 and 7 are derived from the spatially inhomogeneous Éliashberg equations.[10] Since Ginzburg's concept does not depend on the nature of the high-frequency bosons, we have used the Éliashberg equations for the case of electron–phonon interaction. Their structure is, in fact, identical for any bosons with frequencies small in comparison to the Fermi energy ϵ_F. This statement especially applies to the limit of local interaction (Sec. 3), in which no specific information about phonons is essential.

2. SPATIALLY INHOMOGENEOUS ELIASHBERG EQUATIONS

Consider the Hamiltonian of electron–phonon interaction in the form

$$H_{int} = -\int d\mathbf{r} \hat{\psi}_\sigma^+(\mathbf{r}) \mathbf{u}_n \mathbf{g}_n(\mathbf{r}) \hat{\psi}_\sigma(\mathbf{r}), \tag{7}$$

where $\hat{\psi}_\sigma^+$ and $\hat{\psi}_\sigma$ are electron operators, $\mathbf{u}_n$ is the displacement vector of the nth ion, and $\mathbf{g}_n(\mathbf{r})$ is the deformation potential which in the rigid-ion approximation takes the form[12]

$$\mathbf{g}_n(\mathbf{r}) = \nabla U_n(\mathbf{r} - \mathbf{R}_n), \tag{8}$$

where $U_n(\mathbf{r})$ is the potential of the nth ion and $\mathbf{R}_n$ is its equilibrium position. Following the standard procedure,[10] we obtain the spatially inhomogeneous Éliashberg equations $[x = (\mathbf{r}, \tau)]$

$$\begin{aligned}
&\left(-\frac{\partial}{\partial \tau} - \hat{H}_0 + \mu \right) G(x,x') = \delta(x-x') - \int dx_1 G(x,x_1) \\
&\qquad \times D(x,x_1) G(x,x') + \int dx_1 \\
&\qquad \times F(x,x_1) D(x,x_1) F^+(x_1,x'), \\
&\left(-\frac{\partial}{\partial \tau} - \hat{H}_0 + \mu \right) F(x,x') = -\int dx_1 G(x,x_1) D(x,x_1) \\
&\qquad \times F(x_1,x') - \int dx_1 F(x,x_1) \\
&\qquad \times D(x,x_1) G(x',x_1),
\end{aligned} \tag{9}$$

where G and F are the normal and anomalous Green's function and μ is the chemical potential. Unlike Eq. (35.2) in Ref. 10, all the functions in Eq. (9) depend on the two coordinates, not just on their difference, the operator $\hat{p}^2/2m$ is replaced by a one-particle Hamiltonian $\hat{H}_0$ of general form, and the coupling constant g is included in the definition of the phonon Green's function:

$$D(x,x') = \sum_{\alpha,\alpha'} \sum_{n,n'} g_n^\alpha(\mathbf{r}) g_{n'}^{\alpha'}(\mathbf{r}') D_{nn'}^{\alpha\alpha'}(\tau - \tau'), \tag{10}$$

where $D_{nn'}^{\alpha\alpha'}$ is the Green's function in the site representation, which can be expressed in terms of eigenvectors $B_\alpha^{(s)}(n)$ and eigenvalues ω_s^2 of the dynamic operator matrix:[13]

$$D_{nn'}^{\alpha\alpha'}(\Omega) = -\frac{\hbar}{\sqrt{M_n M_{n'}}} \sum_s \frac{B_\alpha^{(s)}(n) B_{\alpha'}^{(s)}(n')}{\Omega^2 + \omega_s^2}, \tag{11}$$

M_n is the mass of the nth ion, and Ω is the Matsubara frequency.

In order to determine T_c, we must linearize Eq. (9) in F. If we rewrite these equations in the symbolic form

$$\begin{aligned}
&\left(-\frac{\partial}{\partial \tau} - \hat{H}_0 + \mu + GD \right) G = 1, \\
&\left(-\frac{\partial}{\partial \tau} - \hat{H}_0 + \mu + GD \right) F = -FDG,
\end{aligned} \tag{12}$$

we note that G is the Green's function for the operator in parentheses and can rewrite the second equation in (12) as $F=-GFDG$. In the explicit form, after transformation to the Matsubara representation and complex conjugation, we have

$$F^{+}_{\omega}(\mathbf{r},\mathbf{r}')=-T\sum_{\Omega}\int d\mathbf{r}_1\int d\mathbf{r}_2 G_{-\omega}(\mathbf{r}_1,\mathbf{r}) \times D_{\Omega}(\mathbf{r}_1,\mathbf{r}_2)F^{+}_{\omega-\Omega}(\mathbf{r}_1,\mathbf{r}_2)G_{\omega}(\mathbf{r}_2,\mathbf{r}'). \quad (13)$$

Let us introduce the order parameter

$$\Delta_{\omega}(\mathbf{r},\mathbf{r}')=-T\sum_{\Omega} F^{+}_{\omega-\Omega}(\mathbf{r},\mathbf{r}')D_{\Omega}(\mathbf{r},\mathbf{r}'), \quad (14)$$

and rewrite Eq. (13) in the form

$$\Delta_{\omega}(\mathbf{r},\mathbf{r}')=-T\sum_{\omega'}\int d\mathbf{r}_1 d\mathbf{r}_2 D_{\omega-\omega'}(\mathbf{r},\mathbf{r}') \times G_{-\omega'}(\mathbf{r}_1,\mathbf{r})G_{\omega'}(\mathbf{r}_2,\mathbf{r}')\Delta_{\omega'}(\mathbf{r}_1,\mathbf{r}_2). \quad (15)$$

In Eqs. (13)–(15) Ω is the boson frequency, and ω and ω' are fermion frequencies. Note that Eq. (15) contains only renormalized Green's functions.

3. THE LOCAL-INTERACTION LIMIT

Equation (15) has a form similar to that of the Gor'kov equation[10,11] and reduces to the latter if two approximations typical of the BCS theory are used:

$$D_{\omega-\omega'}(\mathbf{r},\mathbf{r}')\to -V_{\omega-\omega'}(\mathbf{r})\,\delta(\mathbf{r}-\mathbf{r}'), \quad (16)$$

$$V_{\omega-\omega'}(\mathbf{r})\to V(\mathbf{r})\,\theta(\overline{\omega}-|\omega|)\,\theta(\overline{\omega}-|\omega'|) \quad (17)$$

[as a result, $\Delta_{\omega}(\mathbf{r},\mathbf{r}')\to\Delta(\mathbf{r})\,\delta(\mathbf{r}-\mathbf{r}')\,\theta(\overline{\omega}-|\omega|)$]. Equation (17) means that the spatial dependence of the cut-off frequency is ignored, and it will not be used further. This does not cause any complications because all the relevant equations can be solved by removing the logarithmic singularity (Ref. 2, p. 90).

The approximation expressed by Eq. (16) corresponds to the physically transparent local-interaction limit and has several advantages: (a) it yields simple and easily understandable results; (b) it does not demand a specification of the Fermi surface shape; (c) it does not demand detailed information about the electron–phonon interaction since, in fact, an interaction constant $V_{\omega}(\mathbf{r})$ which is an arbitrary function of the frequency and coordinates is introduced into Eq. (16), and so the generalization to other types of interaction is possible; (d) the structure of the expression for T_c is identical to that derived from the Gor'kov equation, and earlier results[6–9] can be automatically generalized to the case of the cut-off frequency depending on coordinates. The absence of the effect of the excitonic mechanism to lowest order in a/L can also be proved with due account of the nonlocality, but the expressions in this case would be too lengthy.

We should stress that the local interaction limit is a physical approximation and cannot be introduced by a mathematically rigorous procedure. In fact, if the function $D_{\omega}(\mathbf{r},\mathbf{r}')$ is assumed to be short-range and expressed as

$$D_{\omega}(\mathbf{r},\mathbf{r}')\approx\delta(\mathbf{r}-\mathbf{r}')\int d\mathbf{r}' D_{\omega}(\mathbf{r},\mathbf{r}'), \quad (18)$$

the integral on the right-hand side is zero because the integral of $\mathbf{g}_n(\mathbf{r})$ vanishes since the deformation potential is generated by redistribution of charges and can be described as a superposition of fields generated by dipoles. In the rigid-ion approximation it follows directly from Eq. (8). The local approximation is resonable from the physical viewpoint because the expression for T_c is, in effect, determined by the integral in Eq. (18) over the region $|\mathbf{r}'|\lesssim k_F^{-1}$, where k_F is the Fermi momentum. This can be proved by taking the result for the spatially homogeneous case in Ref. 2, Ch. 4.

If we assume the approximation described by Eq. (16), we have $\Delta_{\omega}(\mathbf{r},\mathbf{r}')=\Delta_{\omega}(\mathbf{r})\,\delta(\mathbf{r}-\mathbf{r}')$, and Eq. (15) takes the form

$$\Delta_{\omega}(\mathbf{r})=T\sum_{\omega'} V_{\omega-\omega'}(\mathbf{r})\int d\mathbf{r}' K_{\omega'}(\mathbf{r},\mathbf{r}')\Delta_{\omega'}(\mathbf{r}'), \quad (19)$$

where

$$K_{\omega}(\mathbf{r},\mathbf{r}')=G_{-\omega}(\mathbf{r}',\mathbf{r})G_{\omega}(\mathbf{r}',\mathbf{r}). \quad (20)$$

If the system is invariant under time reversal, the kernel $K_{\omega}(\mathbf{r},\mathbf{r}')$ is symmetric with respect to the exchange of $\mathbf{r}$ and $\mathbf{r}'$ and is positive. If for $G_{\omega}(\mathbf{r},\mathbf{r}')$ one-particle Green's functions are used, the following sum rule applies to the kernel:[11]

$$\int d\mathbf{r}' K_{\omega}(\mathbf{r},\mathbf{r}')=\frac{\pi}{|\omega|}\,N(\mathbf{r}), \quad (21)$$

where $N(\mathbf{r})$ is the local density of states at the Fermi level,

$$N(\mathbf{r})=\sum_{n}|\psi_n(\mathbf{r})|^2\,\delta(\epsilon_F-\epsilon_n), \quad (22)$$

determined by the one-particle eigenfunctions $\psi_n(\mathbf{r})$ and eigenvalues ϵ_n. With due account of interaction effects, Eq. (21) can be considered as a definition of the local density of states $N(\mathbf{r})$. In the spatially homogeneous case this parameter (independent of $\mathbf{r}$) enters in the BCS formula.

4. THE EXPRESSION FOR T_c IN THE CASE OF LOCAL SPATIAL INHOMOGENEITY

Suppose that the system varies as a function of z, and the inhomogeneity is localized in the region $|z|\lesssim d$. Since $\Delta_{\omega}(\mathbf{r})$ is independent of the longitudinal coordinate $\mathbf{r}_{\parallel}$, Eq. (19) takes the form

$$\mathbf{\Delta}(z)=\int dz'\,\hat{Q}(z,z')\mathbf{\Delta}(z'), \quad (23)$$

where $\mathbf{\Delta}=(\Delta_{\omega_1},\Delta_{\omega_2},\ldots)$. If the system transverse dimension satisfies $L\ll\xi_0$, the solution can be sought in the form[6,7]

$$\mathbf{\Delta}(z)=\boldsymbol{\psi}+\mathbf{\Delta}_0(z), \quad (24)$$

where the function $\boldsymbol{\psi}$ is independent of z and $\mathbf{\Delta}_0(z)$ is localized in the region $|z|\lesssim d$. Substituting Eq. (24) into (23), we obtain

$$\boldsymbol{\psi}=\int dz'\,\hat{Q}(\infty,z')\boldsymbol{\psi}+\int dz'\,\hat{Q}(\infty,z')\mathbf{\Delta}_0(z'), \quad (25)$$

$$\mathbf{\Delta}_0(z)=\int dz'[\hat{Q}(z,z')-\hat{Q}(\infty,z')]\boldsymbol{\psi}+\int dz'[\hat{Q}(z,z')-\hat{Q}(\infty,z')]\mathbf{\Delta}_0(z'). \quad (26)$$

In deriving these equations we have taken into account that for $|z|\gtrsim d$ the kernel $\hat{Q}(z,z')$ is independent of z and equals $\hat{Q}(\infty,z')$. The sum rule (21) implies the estimate $\hat{Q}\sim 1/L$, and the second terms on the right-hand side of Eqs. (25) and (26) are small $\sim d/L$. In order to calculate T_c with to $\sim d/L$ inclusive, we can omit the second term on the right-hand side of Eq. (26) and substitute the resulting $\mathbf{\Delta}_0(z)$ into Eq. (25). Given that $K_\omega(\infty,z')\approx L^{-1}\int dz K_\omega(z,z')$, we obtain with due account of Eq. (21) an equation for $\boldsymbol{\psi}$ in the explicit form

$$\psi_\omega=\pi T\sum_{\omega'}\frac{L(\omega,\omega')}{|\omega'|}\,\psi_{\omega'}, \quad (27)$$

$$L(\omega,\omega')=V_{\omega-\omega'}(\infty)N(\infty)+\frac{1}{L}\int dz\,\pi T\sum_{\omega''}\frac{1}{|\omega''|}\,V_{\omega-\omega'}(\infty)N(z)\times[V_{\omega''-\omega'}(z)N(z)-V_{\omega''-\omega'}(\infty)N(\infty)]. \quad (28)$$

Equation (27) can be solved by removing the logarithmic singularity.[4)] By taking advantage of the fact that the summation over Fermi frequencies yields

$$\pi T\sum_{|\omega|<\overline{\omega}}\frac{1}{|\omega|}=\ln\frac{1.14\overline{\omega}}{T}, \quad (29)$$

we transform Eq. (27) to

$$\psi_\omega=L(\omega,\omega_0)\psi_{\omega_0}\ln\frac{1.14\overline{\omega}}{T}+f(\omega), \quad (30)$$

where $\omega_0=\pi T$, and the function

$$f(\omega)=\pi T\sum_{|\omega'|>\overline{\omega}}\frac{L(\omega,\omega')\psi_{\omega'}}{|\omega'|}+\pi T\sum_{|\omega'|<\overline{\omega}}\frac{L(\omega,\omega')\psi_{\omega'}-L(\omega,\omega_0)\psi_{\omega_0}}{|\omega'|} \quad (31)$$

is introduced. After setting $\omega=\omega_0$ and $L(\omega_0,\omega_0)\approx L(0,0)$ in Eq. (30), we have the expression for T_c:

$$T_c=1.14\overline{\omega}e^{-1/L(0,0)}, \quad (32)$$

where $\overline{\omega}$ is defined by the condition $f(\omega_0)=0$. After replacing summation by integration in Eq. (31) and substituting ψ_ω in the lowest-order approximation [i.e., neglecting $f(\omega)$ in Eq. (30)], we obtain for $\overline{\omega}$

$$\ln\overline{\omega}=-\frac{1}{L(0,0)^2}\int_0^\infty \ln\omega[L(0,\omega)L(\omega,0)]'_\omega d\omega. \quad (33)$$

Substitution of Eq. (28) into (32) and (33) and expansion in terms of d/L yield the variation in T_c relative to T_{c0} in the spatially homogeneous system

$$\frac{\delta T_c}{T_{c0}}=\frac{1}{\lambda_0^3 L}\int dz W_0 N(z)[W(z)N(z)-W_0N_0]; \quad (34)$$

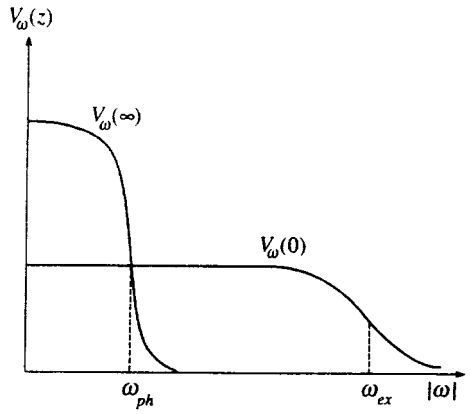

FIG. 2. Typical behavior of the parameter $V_\omega(z)$ as a functions of ω deep inside the metal film ($z=\infty$) and on the metal–dielectric interface ($z=0$).

here $\lambda_0=V_0(\infty)N(\infty)$, $W_0=W(\infty)=V_0(\infty)$, and the function

$$W(z)=V_0(z)-2N(\infty)\int_0^\infty d\omega\,\ln\frac{\omega}{\overline{\omega}}[V_\omega(\infty)V_\omega(z)]'_\omega, \quad (35)$$

is introduced, where $\overline{\omega}$ is calculated in the zeroth approximation,

$$\ln\overline{\omega}=-\frac{1}{V_0(\infty)^2}\int_0^\infty d\omega\,\ln\omega[V_\omega(\infty)^2]'_\omega, \quad (36)$$

corresponding to a spatially homogeneous system [so that $T_{c0}=1.14\overline{\omega}\exp(-1/\lambda_0)$]. If $V_\omega(z)$ is a step function of the frequency,

$$V_\omega(z)=V(z)\,\theta(\overline{\omega(z)}-|\omega|), \quad (37)$$

it follows from Eq. (36) that $\overline{\omega}=\overline{\omega(\infty)}$, and Eq. (35) yields

$$W(z)=V(z)\left[1+\lambda_0\ln\frac{\min\{\overline{\omega(\infty)},\overline{\omega(z)}\}}{\overline{\omega(\infty)}}\right]. \quad (38)$$

For $\overline{\omega(z)}=\text{const}$ we have $W(z)=V(z)$, and Eq. (34) becomes identical to the result obtained in Ref. 7. It becomes clear that the spatial dependence of the cut-off frequency does not change the structure of Eq. (34), but only replaces $V(z)$ with a more complicated function $W(z)$.

For a Ginzburg sandwich, the main contribution to the integral in Eq. (34) comes from the region $|z|\lesssim a$ near the interface, and the relative variation of T_c is $\sim a/L$. It is essential that the function $V_\omega(z)$, which contains information about the exciton frequency ω_{ex} at $|z|\lesssim a$ (Fig. 2), is multiplied in Eq. (35) by the function $V_\omega(\infty)$, which decreases fast at $|\omega|\gtrsim\omega_{\text{ph}}$. As a result, ω_{ex} is not included in Eqs. (34) and (35), which determine T_c. In the approximation described by Eq. (37), this directly follows from Eq. (38). This approximate result holds for all orders in λ_0 [Eqs. (34) and (35) were derived via iterations in this parameter]. Specifically, consider the eigenvalue equation

$$\nu\psi_\omega=\pi T\sum_{\omega'}\frac{V_{\omega-\omega'}(\infty)N(\infty)}{|\omega'|}\,\psi_{\omega'}, \quad (39)$$

which is identical to Eq. (27) for a spatially homogeneous system at $\nu=1$. If $\nu(T)$ is the maximal eigenvalue of Eq. (39), T_{c0} is determined by the condition $\nu(T_{c0})=1$. Let ψ_ω and $\underline{\psi}_\omega$ be the solution to Eq. (39) and its adjoint solution at $\nu=1$. Then the perturbation calculation in the parameter $\sim d/L$ in Eq. (28) yields

$$\delta T_c=-\frac{1}{\nu'(T_{c0})\lambda_0^2 L}\int dz W_0 N(z)[W(z)N(z)-W_0N_0] \tag{40}$$

with the function $W(z)$ defined by the equation

$$W(z)=\frac{\lambda_0}{\pi T\Sigma_\omega|\omega|^{-1}(\overline{\psi_\omega})^2}\,\pi T \times\sum_{\omega'}\frac{\overline{\psi_{\omega'}}}{|\omega'|}\,\pi T\sum_{\omega''}\frac{\overline{\psi_{\omega''}}}{|\omega''|}\,V_{\omega''-\omega'}(z), \tag{41}$$

using $\underline{\psi}_\omega=|\omega|^{-1}\overline{\psi_\omega}$. It follows from the analysis of Eq. (39) that ψ_ω decreases rapidly as a function of ω beyond $\omega_{\rm ph}$, therefore the summation over the frequency in Eq. (41) is limited to the region $|\omega'|\lesssim\omega_{\rm ph}$, $|\omega''|\lesssim\omega_{\rm ph}$, and the frequency $\omega_{\rm ex}$ in the function $V_{\omega''-\omega'}(z)$ does not affect the final result.

5. ESTIMATE OF THE GINZBURG EFFECT

By iterating Eqs. (25) and (26) up to second order in d/L,

$$\boldsymbol{\psi}=\int dz'\hat{Q}(\infty,z')\boldsymbol{\psi}+\int dz'\int dz''\hat{Q}(\infty,z')[\hat{Q}(z',z'')-\hat{Q}(\infty,z'')]\boldsymbol{\psi}+\int dz'\int dz''\int dz'''\hat{Q}(\infty,z')\times[\hat{Q}(z',z'')-\hat{Q}(\infty,z'')][\hat{Q}(z'',z''')-\hat{Q}(\infty,z''')]\boldsymbol{\psi}, \tag{42}$$

we obtain Eq. (27) with a function $L(\omega,\omega')$ differing from that defined by Eq. (28) by an additional term $\sim(d/L)^2$, which leads to a second-order correction to T_c:

$$\left(\frac{\delta T_c}{T_{c0}}\right)_2=\frac{1}{\lambda_0}\frac{1}{V_0(\infty)}\frac{1}{L}\int dz'dz''N(z')\pi T \times\sum_{\omega'}\frac{V_{\omega'}(\infty)}{|\omega'|}\,T\sum_{\omega''}[V_{\omega'-\omega''}(z')K_{\omega''}(z',z'') -V_{\omega'-\omega''}(\infty)K_{\omega''}(\infty,z'')]\pi T\sum_{\omega'''}\frac{V_{\omega'''}(\infty)}{|\omega'''|} \times[V_{\omega''-\omega'''}(z'')N(z'')-V_{\omega''-\omega'''}(\infty)N(\infty)]. \tag{43}$$

The summation over ω' and ω''' is limited to the region $|\omega'|,|\omega'''|\lesssim\overline{\omega}\sim\omega_{\rm ph}$. By performing the summation with logarithmic accuracy and separating the contribution of the high-frequency region, we obtain the change in T_c due to the exciton-mediated interaction:

$$\left(\frac{\delta T_c}{T_{c0}}\right)_{\rm ex}=\frac{1}{\lambda_0^3 L}\,V_0(\infty)\int dz'dz''N(z')N(z'')T \times\sum_{|\omega|>\overline{\omega}}V_\omega(z')K_\omega(z',z'')V_\omega(z''). \tag{44}$$

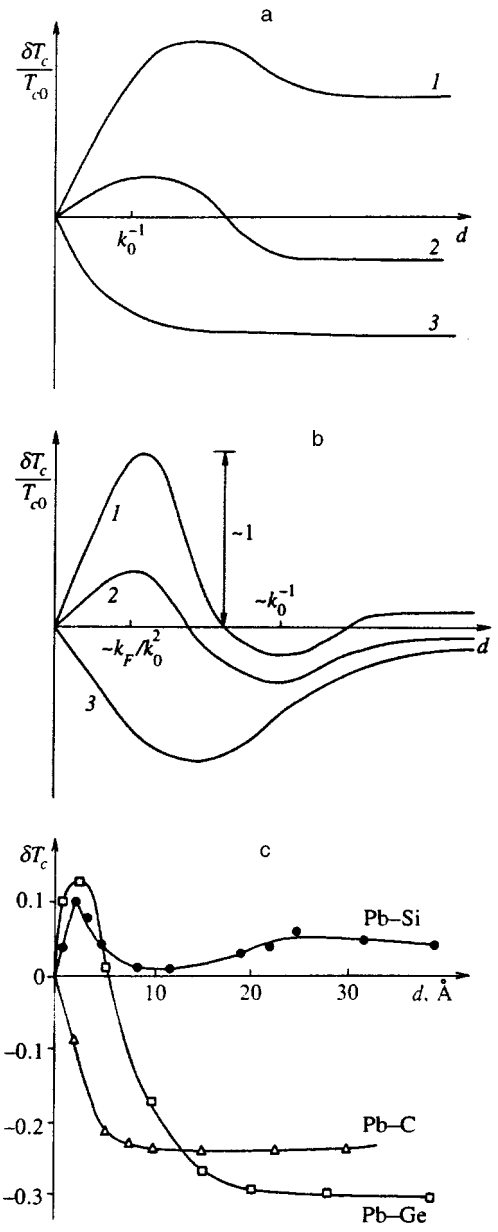

FIG. 3. (a) Calculated T_c in a metal–dielectric sandwich as a function of the dielectric thickness for a narrow-gap dielectric ($U-\epsilon_F\ll\epsilon_F$); curves *1*, *2*, and *3* correspond to $W_1/W_0>7/2$, $3/2<W_1/W_0<7/2$, and $W_1/W_0<3/2$; (b) similar curves for a wide-gap dielectric ($U\gg\epsilon_F$) in the cases (curve *1*) $W_1/W_0>3k_0^2/k_F^2$, (*2*) $3k_0^2/k_F^2>W_1/W_0>3k_0^2/k_F^2$, and (*3*) $W_1/W_0<k_0^2/2k_F^2$; (c) experimental curves of T_c as a function of the dielectric thickness d in Pb–Si, Pb–Ge, and Pb–C sandwiches.[14]

If the local density of states $N(z)$ in the sandwich (Fig. 1) varies near the interface faster than $V_\omega(z)$, then, using the sum rule, we can assume that

$$K_\omega(z,z')\simeq\frac{\pi N_0}{|\omega|L}\,\theta(z)\theta(z'),\quad N(z)=N_0\theta(z); \tag{45}$$

hence

$$\left(\frac{\delta T_c}{T_{c0}}\right)_{\rm ex} \simeq \frac{1}{\lambda_0^2}\frac{N_0^2}{L^2}\int_0^L dz'\int_0^L dz''\pi T\sum_{|\omega|>\overline{\omega}}\frac{V_\omega(z')V_\omega(z'')}{|\omega|}. \tag{46}$$

Since the integrand is a logarithmic function of the cut-off frequency, Eq. (46) is valid in a fairly large region. In the simplest case, when

$$V_\omega(z)=\begin{cases} V_0\theta(\omega_{\rm ph}-|\omega|), & z>a,\\ V_1\theta(\omega_{\rm ex}-|\omega|), & z<a,\end{cases} \tag{47}$$

we have

$$\left(\frac{\delta T_c}{T_{c0}}\right)_{\rm ex} \simeq \left(\frac{a}{L}\right)^2\frac{V_1^2}{V_0^2}\ln\frac{\omega_{\rm ex}}{\omega_{\rm ph}}. \tag{48}$$

Since it is unlikely that the coupling constant V_1 for high-frequency excitations is larger than for low-frequency excitations (V_0), the contribution of the excitonic mechanism given by Eq. (48) is always smaller than the main contribution $\sim a/\lambda_0 L$ determined by Eq. (34).

6. MODEL CALCULATIONS TO FIRST ORDER IN *a*/*L* AND COMPARISON WITH EXPERIMENTAL DATA

Let us perform calculations with Eq. (34) using the simplest model: the function $W(z)$ is piecewise continuous and takes the values W_0 and W_1 in the metal and dielectric, respectively, and the electronic spectra of these materials are determined by the equations

$$\epsilon_M(k)=\frac{k^2}{2m},\quad \epsilon_D(k)=\frac{k^2}{2m}+U, \tag{49}$$

where $U>\epsilon_F$ and ϵ_F is the Fermi energy in the metal. For a thin layer of dielectric with thickness d inside a metal plate with thickness L, the expression for $N(z)$ has the form

$$N(z)=\frac{m}{(2\pi)^2}\int_{q_0}^{k_0}dq\,\frac{q}{k}\,H(k,iq,z)|_{k=\sqrt{k_0^2-q^2}}, \tag{50}$$

where

$$q_0=\sqrt{k_0^2-k_F^2},\quad k_0=\sqrt{2mU},$$

and the function $H(k,iq,z)$ is defined by Eq. (22) in Ref. 9. Consider two limiting cases corresponding to a narrow-gap semiconductor and a wide-gap dielectric.

(a) $0<U-\epsilon_F\ll U$.

The result for $U\to\epsilon_F$ and $q_0\to 0$ coincides with the $q_F\to 0$ limit in Eq. (24) of Ref. 9:

$$\frac{\delta T_c}{T_{c0}}=\frac{1}{\lambda_0 k_F L}\left[\frac{W_1}{W_0}\,P_1(k_0d)+P_2(k_0d)\right], \tag{51}$$

where the functions $P_1(x)$ and $P_2(x)$ are those plotted in Fig. 2 of Ref. 9. This result for finite but small q_0 differs from Eq. (51) only in that for $d\gtrsim q_0^{-1}\gg k_0^{-1}$ the algebraic approach to a constant value as $d\to\infty$ described by $P_1(x)$ and $P_2(x)$ is replaced by an exponential behavior. Depending on the ratio W_1/W_0, curves of one of the three types shown in Fig. 3a are realized.

(b) $U\gg\epsilon_F$.

In this case $q_0\approx k_0$, and the limits of integration in Eq. (50) are close. By assuming $q\simeq k_0$ and expanding in terms of k_F/k_0, we obtain for $W_1/W_0\sim k_0^2/k_F^2$

$$\frac{\delta T_c}{T_{c0}}=\frac{1}{\lambda_0 k_F L}\begin{cases}\left(\dfrac{W_1}{W_0}-\dfrac{k_0^2}{2k_F^2}\right)k_Fd, & k_0d\ll k_F/k_0,\\ -\dfrac{2\pi}{3}\dfrac{k_F^2}{k_0^2}\dfrac{1}{(k_0d)^2} & \\ +\dfrac{16}{9}\dfrac{k_F^5}{k_0^5}\dfrac{W_1}{W_0}\dfrac{1}{(k_0d)^3}, & k_F/k_0\ll k_0d\ll 1,\\ \dfrac{1}{3}\dfrac{k_F^3}{k_0^3}\left(\dfrac{W_1}{W_0}\dfrac{2k_F^2}{3k_0^2}-1\right) & \\ -\dfrac{8\pi}{3}\dfrac{k_F^2}{k_0^2}\,e^{-2k_0d}, & k_0d\gg 1.\end{cases} \tag{52}$$

Similarly to the previous case, depending on the ratio W_1/W_0, the function $T_c(d)$ has one of three typical shapes shown in Fig. 3b. It is remarkable that all three types of curves were recorded by Orlov *et al.*[14] in Pb–Si, Pb–Ge, and Pb–C sandwiches (Fig. 3c). Since the experiments obviously satisfy $U\sim\epsilon_F$, the experimental curves present an intermediate case between the curves of Figs. 3a and 3b.

Note that for $\overline{\omega(z)}=\text{const}$, when $W(z)=V(z)$, holds the condition $V_1>V_0$, which is intuitively obvious, is insufficient for increasing T_c. A stronger condition is necessary:

$$\frac{V_1}{V_0}>C,\quad C=\begin{cases}3/2, & U-\epsilon_F\ll\epsilon_F,\\ U/2\epsilon_F, & U\gg\epsilon_F\end{cases}, \tag{53}$$

which is very limiting in the case of a wide-gap dielectric. The point is that for $V(z)=\text{const}$ a spread δ of the step in the function $N(z)$ defined by Eq. (45) has a negative effect proportional to δ [see Eq. (34)]. It can be compensated for by the positive effect $\sim\delta(V_1-V_0)/V_0$ due to the increase in the constant V in the dielectric, and in this case condition (53) with $C>1$ holds.

7. CONCLUSIONS

The issue of the efficiency of the exciton-mediated pairing in layered structures has many aspects, most of which have not been discussed in the paper, namely, whether there are appropriate excitons in the dielectric, whether they penetrate into the metal film to a sufficient depth, whether the excitonic exchange leads to attraction between two electrons, how strong this attraction sufficiently is, etc. The main conclusion of our study is that, even under the most favorable conditions, when the answers to all the above questions are positive (as a result of which, T_c should be high at $L\sim a$), the effect of exciton-mediated pairing would not be detectable at $L\gg a$. Therefore the failure of all the attempts to detect it in sandwiches does not mean that its search in quasi-two-dimensional systems should be abandoned.

[1)]Modern technologies can produce fairly uniform films with a thickness of several angstroms,[3] but superconductivity in them is suppressed owing to their highly disordered structure that leads to localization effects.[4]

[2)]Note that this result is not contained in the MacMillan formula, which is, apparently, the main reason why it has not been discovered previously. It can be derived qualitatively from the Éliashberg equations for the homogenous medium if the Eliashberg function is presented in the form $\lambda_{ph}\omega_{ph}\delta(\omega-\omega_{ph})+\lambda_{ex}\omega_{ex}\delta(\omega-\omega_{ex})$ and it is assumed that $\lambda_{ex}\sim a/L$.

[3)]Notice that λ is defined in terms of the BCS theory; the values $\lambda\sim 1$ are obtained using MacMillan-type formulas, in which $1/\lambda_{BCS}$ is replaced by a combination of the form $(1+\lambda)/(\lambda-\mu^*)$, where μ^* is the Coulomb pseudopotential.[2]

[4)]Application of this technique directly to the Matsubara representation is notably easier than with a preliminary analytic continuation (Ref. 2, Ch. 4) and yields identical results.

[1] V. L. Ginzburg, Zh. Éksp. Teor. Fiz. **47**, 2318 (1964) [Sov. Phys. JETP **20**, 1549 (1965)]; Phys. Lett. **13**, 101 (1964).

[2] *High-Temperature Superconductivity*, ed. by V. L. Ginzburg and D. A. Kirzhnits, Consultants Bureau, New York, 1982.

[3] S. M. Durkin, J. E. Cunningham, M. E. Mochel, and C. P. Flynn, J. Phys. F **11**, L223 (1981).

[4] B. N. Belevtsev, Usp. Fiz. Nauk **160**, 65 (1990) [Sov. Phys. Uspekhi **33**, 36 (1990)].

[5] V. L. Ginzburg and D. A. Kirzhnits, Zh. Éksp. Teor. Fiz. **46**, 397 (1964)[Sov. Phys. JETP **19**, 219 (1964)].

[6] I. M. Suslov, Zh. Éksp. Teor. Fiz. **95**, 949 (1989) [Sov. Phys. JETP **68**, 546 (1989)].

[7] I. M. Suslov, Sverkhprovodimist': Fizika, Khimiya, Tekhnologiya **4**, 2093 (1991).

[8] Yu. A. Krotov and I. M. Suslov, Zh. Éksp. Teor. Fiz. **102**, 670 (1992); **103**, 1394 (1993); Physica C **213**, 421 (1993); **245**, 252 (1995).

[9] Yu. A. Krotov and I. M. Suslov, Zh. Éksp. Teor. Fiz. **107**, 512 (1995). [Sov. Phys. JETP **80**, 275 (1995)].

[10] A. A. Abrikosov, L. P. Gor'kov, and I. E. Dzyaloshinskii, *Methods of Quantum Field Theory in Statistical Physics*, Prentice-Hall, Englewood Cliffs, NJ, 1963.

[11] P. G. De Gennes, Rev. Mod. Phys. **36**, 225 (1964).

[12] J. Ziman, *Electrons and Phonons*, Oxford University Press (1960).

[13] A. A. Maradudin, E. W. Montroll, G. H. Weiss, and I. P. Ipatova, *Theory of Lattice Dynamics in the Harmonic Approximation*, Academic Press, New York–London (1971).

[14] A. F. Orlov, A. K. Milai, and V. P. Dmitriev, Fiz. Tverd. Tela **18**, 1470 (1976) [Sov. Phys. Solid State **18**, 854 (1976)].

Translation was provided by the Russian Editorial office.

Spin dynamics of the muon in muonium in normal metals

A. N. Belemuk, Yu. M. Belousov, and V. P. Smilga

Moscow Physicotechnical Institute, 141700 Dolgoprudnyi, Moscow Region, Russia
(Submitted 25 July 1996)
Zh. Éksp. Teor. Fiz. **111**, 730–736 (February 1997)

The question of the charge state of the proton (the positive muon) in metals is of fundamental importance for the theory of metal hydrides. The theory developed here permits determination of the charge state of μ^+ in normal metals. The experimental possibilities of the observation of Mu atoms in metals at various strengths of the external magnetic field and various temperatures are analyzed. © *1997 American Institute of Physics.*
[S1063-7761(97)02502-X]

1. The charge state of the positive muon in metals or, equivalently, the state of the proton is a question of vital interest primarily in connection with the attention that has been attracted by metal hydrides. However, this problem has not yet been solved theoretically or experimentally. Moreover, even if it is assumed that the proton does not form a chemical compound with lattice atoms and is localized in some interstitial site, it is not clear whether it forms a bound state with a conduction electron of the metal, i.e., whether there is a ''local level'' for an electron. It would be strange if such a bound state were absent from all metals and especially from semimetals.

Thus, the entire problem is of general significance to solid-state physics.

It is presently tacitly assumed in the analysis of the results of μSR experiments that the muonium atom Mu (the bound charge state μ^+e^-) is absent in metals. In fact, the precession of muon spin polarization with a frequency close to the precession frequency of muon spin polarization in a vacuum heretofore has generally been observed (see, for example, Refs. 1 and 2). The only exceptions are the experiments in Sb, in which an anomalously large frequency shift was observed in the temperature range [3] $2<T<300$ K. However, since this shift is proportional to the field up to $B=9$ kG, it is naturally identified with the Knight shift.[1)]

2. As is generally known,[1,2] the precession of muon spin polarization with muonium frequencies may not be observed even in the presence of Mu atoms.

In fact, because of the high exchange frequencies with conduction electrons at $T>1$–5 K, the hyperfine interaction in the Mu atom is ''broken,'' and the ''bare'' muon μ^+ is effectively observed, i.e., it can be stated that ''spin muonium'' is absent even if ''Coulomb muonium'' is present.

Equations describing the behavior of muon spin polarization when muonium atoms form in a metal were derived in Ref. 5. Recommendations for the experimental identification of Mu atoms were also given in that paper. However, several experimentally important ramifications were not presented in Ref. 5, partially because the authors restricted the analysis to only the experimental possibilities for the instrumentation available at that time. During the past 20 years the possibilities for μSR experiments have expanded significantly, primarily in regard to the temporal resolution of polarization precession. Investigations at very low temperatures ($T<0.1$ K) have become commonplace.

Even if Mu atoms form in a metal, the hyperfine splitting frequency ω_0 of the Mu atoms in a metal should differ significantly from the vacuum value, $\omega_0^{\rm vac}=2.8\times10^{10}$ s^{-1}, because of the shielding by the conduction electrons. We introduce the dimensionless parameter $\alpha=\omega_0/\omega_0^{\rm vac}$. When $\alpha\sim10^{-3}$, the ''diameter'' of a Mu atom in a metal is of the order of 5 Å, which significantly exceeds the lattice constants for all metals. Evaluations give the typical value $\alpha\leqslant10^{-2}$–10^{-1} ($\omega\leqslant3\times10^8$–$3\times10^9$ s^{-1}, $\hbar\omega_0\leqslant0.2\times10^{-2}$– 0.02 K).

Since at the initial moment in time an ensemble of muonium atoms is an incoherent mixture of $|+\rangle|+\rangle$ and $|-\rangle|+\rangle$ states, the polarization of the muon spin in a zero external field, disregarding the interaction with the medium, is clearly

$$P(t)=[1+\cos(\omega_0 t)]P(0)/2. \tag{1}$$

Oscillations occur because the initial $|-\rangle|+\rangle$ state is not an eigenstate of the spin Hamiltonian.

3. When there is an interaction with the medium, the behavior of $P(t)$ can change drastically. Let us determine the real conditions under which the observation of ''spin muonium'' is possible. Before proceeding to an analysis of the possibilities of the experimental observation of Mu atoms in a metal, we write the relaxation equation for the spin density matrix of muonium. In a metal the electron spin relaxation of muonium is governed mainly by exchange scattering on electrons of the medium; therefore, the approximation of short correlation times is applicable for the relaxation equations. In this case the basic relaxation equations have the form[2,6]

$$\frac{\partial\rho_{mn}}{\partial t}+\frac{i}{\hbar}[H_0+\Gamma,\rho]_{mn}$$
$$=\sum_{k,l}\left\{\left[\Gamma_{mkln}(\omega_{ln})+\Gamma_{lnmk}(\omega_{mk})\exp\left(-\frac{\hbar\omega_{mk}}{T}\right)\right]\rho_{kl}\right.$$
$$\left.-\Gamma_{mkkl}(\omega_{kl})\exp\left(-\frac{\hbar\omega_{kl}}{T}\right)\rho_{ln}-\Gamma_{knlk}(\omega_{lk})\rho_{ml}\right\}, \tag{2}$$

where $\hat{H}_0$ is the Hamiltonian of muonium, $\omega_{kl}=(E_k-E_l)/\hbar$, E_k is the spectrum of $\hat{H}_0$, and the coefficients are determined by the operator for the interaction of muonium with the heat reservoir $\hat{V}$:

$$\Gamma_{mkln}(\omega_{ln})=\frac{\pi}{\hbar}\sum_{\alpha,\alpha'} V_{m\alpha k\alpha'}V_{l\alpha' n\alpha}\rho_{\alpha'\alpha}\delta(\omega_{ln}+\omega_{\alpha'\alpha}), \tag{3}$$

$$\Gamma_{mk}=\wp\sum_{\alpha,\alpha' l} V_{m\alpha l\alpha'}V_{l\alpha' k\alpha}\rho_{\alpha\alpha}(\omega_{ln}+\omega_{\alpha'\alpha})^{-1}. \tag{4}$$

Here $\omega_{\alpha\alpha'}=(\varepsilon_\alpha-\varepsilon_{\alpha'})/\hbar$ [ε_α is the spectrum of the heat reservoir (the conduction electrons of the metal)], the symbol $\wp$ indicates that the sum (4) should be understood in the sense of a principal value, and $\rho_{\alpha'\alpha}=\delta_{\alpha'\alpha}\exp[(F-\varepsilon_\alpha)/T]$ is the density matrix of the heat reservoir.

We write the operator of the spin-exchange interaction of a muonium atom (a paramagnetic impurity) with the conduction electrons of the metal, as usual, in the form[7,8]

$$\hat{V}=\frac{J}{n}\sum_{\mathbf{k}\sigma\mathbf{k}'\sigma'} \mathbf{s}_e\mathbf{s}_{\mathbf{k}\sigma,\mathbf{k}'\sigma'}a^+_{\mathbf{k}\sigma}a_{\mathbf{k}'\sigma'}, \tag{5}$$

where J is the exchange coupling constant, n_0 is the density of the conduction electrons, and $\mathbf{s}_e$ and $\mathbf{s}_{\mathbf{k}\sigma,\mathbf{k}'\sigma'}$ are, respectively, the spin operators of the muonium electrons and the medium. It is clear that since $V_{m\alpha n\alpha}\neq 0$, we assign the part of the interaction that is diagonal with respect to the heat reservoir to the Hamiltonian $\hat{H}_0$, and we should substitute $\hat{V}=\hat{V}-\hat{V}_d$, where $(\hat{V}_d)_{mn}=\Sigma_\alpha V_{m\alpha n\alpha}\rho_{\alpha\alpha}$, into Eqs. (3) and (4).

After some fairly cumbersome mathematical manipulations, we obtain the expression for the relaxation coefficients (3)

$$\Gamma_{mkln}(\omega_{ln})=\frac{\pi}{2}\left(\frac{3J}{\varepsilon_F}\right)^2\omega_{ln}\coth\frac{\hbar\omega_{ln}}{2T}\mathbf{s}_{mk}\mathbf{s}_{ln}, \tag{6}$$

and the expression for the matrix, which determines the energy shift, retaining only the main terms:

$$\Gamma_{mn}\approx\frac{3}{4}\left(\frac{3J}{4\varepsilon_F}\right)^2\varepsilon_F\delta_{mn}. \tag{7}$$

The part of the interaction that is diagonal with respect to the heat reservoir is determined by the polarization of the electrons of the metal. In fields that are not very strong we have

$$V_d=-2\mu_0\left(\frac{J}{\varepsilon_F}\right)\mathbf{s}\cdot\mathbf{B}, \tag{8}$$

where μ_0 is the Bohr magneton. We see that the energy shift (7) is inconsequential in our case, since it does not influence the hyperfine structure of muonium, and that the correction (8) effectively reduces to renormalization of the magnetic moment of the muonium electron. The sign of the correction is opposite to the sign of the exchange integral.

Under the condition $T\gg|\hbar\omega_{ln}|$, which holds even for vacuum muonium at $T>1$ K in the fields $B<10^4$ G, the relaxation coefficients have a very simple form:

$$\Gamma_{mkln}\approx\nu\mathbf{s}_{mk}\mathbf{s}_{ln}, \tag{9}$$

where

$$\nu=\frac{\pi}{\hbar}\left(\frac{3J}{\varepsilon_F}\right)^2 T.$$

In this case the relaxation equation reduces to the simple Wangsness–Bloch equation, whose Hamiltonian should take into account the effective renormalization of the magnetic moment of the muonium electron:

$$\dot{\hat{\rho}}+\frac{i}{\hbar}[\hat{H}_{\text{eff}},\hat{\rho}]=\frac{\nu}{2}(\hat{\boldsymbol{\sigma}}_e\hat{\rho}\hat{\boldsymbol{\sigma}}_e-3\hat{\rho}). \tag{10}$$

In the low-temperature range $T\leqslant 0.1$ K the relaxation equation is very complicated;[5] however, it can be solved over the entire temperature range in a zero external magnetic field. Let us first consider the case of small effective exchange frequencies ($|\Gamma_{mkln}|\ll\omega_0$), in which oscillations of the polarization with the hyperfine splitting frequency should be observed. If the terms of order ν/ω_0 are disregarded, we can write the polarization in the form

$$P(t)\approx\frac{1}{2}\left[\exp\left(-\frac{t}{\tau_1}\right)+\exp\left(-\frac{t}{\tau_2}\right)\cos(\omega_0 t)\right]P(0), \tag{11}$$

where

$$\tau_1^{-1}=\frac{\nu}{2}\left(1+\frac{\hbar\omega_0}{2T}\coth\frac{\hbar\omega_0}{2T}\right), \tag{12}$$

$$\tau_2^{-1}=\tau_1^{-1}+\nu\frac{\hbar\omega_0}{4T}\coth\frac{\hbar\omega_0}{2T}. \tag{13}$$

As can be seen, when $T\to 0$ ($T<\hbar\omega_0$), the depolarization rates of the nonoscillating and oscillating components tend to constant values:

$$\tau_1^{-1}=\frac{\pi\omega_0}{2}\left(\frac{3J}{\varepsilon_F}\right)^2,\quad \tau_2^{-1}=2\tau_1^{-1}. \tag{14}$$

Accordingly, for $\omega_0=10^8$ s^{-1} and $J/\varepsilon_F=0.1$ we obtain the appreciable value $\tau_1^{-1}\approx 3\times 10^7$ s^{-1}, and for $J/\varepsilon_F=0.01$ we have $\tau_1^{-1}\approx 3\times 10^5$ s^{-1}.

If $\hbar\omega_0/T\ll 1$, we obtain $\tau_1^{-1}=\nu$ and $\tau_2^{-1}=3\nu/2$.

We note that the muonium electron spin relaxes in the stochastic nuclear fields, $b\sim 1$–5 G (muon spin relaxation can be neglected in stochastic nuclear fields) at a rate of order $|\gamma_e|b\sim 10^7$–5×10^7 s^{-1}. Since the spin-spin coupling in a Mu atom is not ''broken,'' this damping will be transferred to the muon. Therefore, the experiment should be carried out in metals with zero nuclear spins (for example, in Mg[24,26], Ti[46,48,50], etc.). Most metals have stable isotopes with zero spin (see, for example, Ref. 9). Experiments in a zero magnetic field probably are the simplest way to detect muonium.

4. Let us now consider the high-temperature range $T\gg\hbar\omega,\hbar\omega_0$, in which the relaxation equation reduces to the Wangsness-Bloch equation. The solution of Eq. (10) for the transverse polarization $P_\perp=P_x+iP_y$ gives

$$P_\perp(t)=\sum_{k=1}^{4} A_k\exp\left(\frac{\lambda_k\omega_0 t}{2}\right). \tag{15}$$

Here the λ_k are the roots of the characteristic equation[2,5,10,11]

$$(\lambda+a)(\lambda+a+\gamma)(\lambda+b)^2+(2\lambda+a+b)\times(2\lambda+a+b+\gamma)=0, \tag{16}$$

where $a=2i\zeta x$, $b=\gamma-2ix$, $\zeta=1/207$, $\gamma=4\nu/\omega_0$, and $x=\omega/\omega_0$.[2)]

We solve Eq. (16) for $x,\gamma\ll 1$ (i.e., $\nu\ll\omega_0$, $\omega\ll\omega_0$). For $\nu\sim 10^8 T\ \mathrm{s}^{-1}$ and $\alpha\sim 10^{-2}$ this condition requires $T\sim 0.01$–0.1 K and $B\sim$ 5 G. In the solution we disregarded ζx in comparison to γ and x.

Let $\gamma\ll x$. Then

$$P_\perp(t)=\exp(-\nu t)\exp\left(\frac{i\omega t}{2}\right)\left\{\exp\left(-\frac{\nu t}{2}\right)\cos(\omega_0 t)+\frac{1}{2}\left[\exp\left(-i\frac{\omega^2}{4\omega_0}t\right)+\exp(-\nu t)\times\exp\left(i\frac{\omega^2}{4\omega_0}t\right)\right]\right\}\frac{P_\perp(0)}{2}. \tag{17}$$

We note that the last two terms, which correspond to the triplet-triplet transitions ω_{12} and ω_{23}, respectively, decay at different rates. When $\gamma\to 0$, Eq. (17) gives the muon spin polarization in ''vacuum'' muonium.

Let $\gamma\sim x$. Then $\lambda_{1,2}=-3\gamma/4+i(x\pm 2)$, $\lambda_3=-\gamma/2+ix(1-x^2/2)$, and $\lambda_4=-\gamma+ix(1+x^2/2)$. The polarization now has the form

$$P_\perp(t)=\exp(-\nu t)\exp\left(\frac{i\omega t}{2}\right)\left[\exp\left(-\frac{\nu t}{2}\right)\cos(\omega_0 t)+\left(1-i\frac{\omega}{4\nu}\right)\exp\left(-i\frac{\omega^3}{4\omega_0^2}t\right)+i\frac{\omega}{4\nu}\times\exp(-\nu t)\exp\left(i\frac{\omega^3}{4\omega_0^2}t\right)\right]\frac{P_\perp(0)}{2}. \tag{18}$$

We note the fundamental difference between the last two terms in Eq. (18) and the corresponding terms in Eq. (17). First, at frequencies corresponding to triplet-triplet transitions, an addition that is cubic with respect to the field is observed instead of the quadratic addition, and, second, the form of the amplitudes corresponding to these transitions is altered.

In the case of $x\ll\gamma$, we have

$$P_\perp(t)=\exp(-\nu t)\left[\exp\left(-\frac{\nu t}{2}\right)\cos(\omega_0 t)+\exp\left(-\frac{i\omega t}{2}\right)\right]\frac{P_\perp(0)}{2}. \tag{19}$$

Oscillations of the polarization with a frequency of order ω_0 will be observed for $\nu\ll\omega_0$ and for longitudinal polarization. When $\nu\sim 10^8 T\ \mathrm{s}^{-1}$, the necessary conditions are $T\sim 0.01$–0.1 K and $B\sim 50$ G. We have[2,5]

$$P_\parallel(t)=\frac{1}{1+x^2}\left[(1+2x^2)\exp\left(-\frac{t}{\tau_1}\right)+\exp(-2\nu t)\cos(\omega_{24}t)\right]\frac{P_\parallel(0)}{2}, \tag{20}$$

where $\omega_{24}=\omega_0\sqrt{1+x^2}$ and $\tau_1^{-1}=\nu/(1+x^2)$.

5. It would be interesting to investigate the mean longitudinal polarization

$$\langle P\rangle=\frac{1}{\tau_\mu}\int_0^\infty\exp\left(-\frac{t}{\tau_\mu}\right)P_\parallel(t)dt. \tag{21}$$

Here $\tau_\mu=2.2\times 10^{-6}$ s is the mean lifetime of the muon. We obtain

$$\langle P\rangle=\frac{1}{1+\tau_\mu\nu}\frac{P(0)}{2}. \tag{22}$$

The temperature dependence of $\langle P(T)\rangle$ (at $T\sim 0.01$–0.1 K) permits refinement of the value of the exchange integral.

As was pointed out in Ref. 12, the search for Mu atoms in superconductors, in which the density of electrons with unpaired spins decays with the temperature according to the exponential law $\exp(-\Delta/T)$, is very promising. It can be expected that the frequency ν of muonium electron spin flips will behave similarly if the local distortion caused by a single paramagnetic impurity (muonium atom) is smaller than the correlation length ξ in a superconductor (see, for example, Ref. 13). It was also noted there that μSR can be used, in principle, to measure the energy gap width Δ. Muonium was first observed in the compound Rb_3Co_{60} in Ref. 14. Muonium has since been observed in various fullerenes.[15]

6. The situation in which $\nu\gg\omega_0$ is most widely encountered. It has been investigated in detail, for example, in Refs. 1, 2, and 5. We note that in the limit where the Wangsness–Bloch equation is valid (for example, $B=10^2$–10^3 G, $T\geqslant 1$ K), the longitudinal polarization decays exponentially with the characteristic rate[1,2,5]

$$\tau_1^{-1}=\nu\omega_0/(4\nu^2+\omega^2+\omega_0^2), \tag{23}$$

which has the maximum $\tau_{\max}^{-1}=1/(4\sqrt{\omega^2+\omega_0^2})$ at the temperature

$$T^*=\frac{\hbar}{2\pi}\left(\frac{\varepsilon_F}{3J}\right)^2\sqrt{\omega^2+\omega_0^2}.$$

For example, when $B=100$ G, we have $T^*\sim 1$ K and $\tau_{\max}^{-1}\sim 10^7\ \mathrm{s}^{-1}$, and when $B=10^3$ G, we have $T^*\sim 10$ K and $\tau_{\max}^{-1}\sim 10^6\ \mathrm{s}^{-1}$. The characteristic temperature dependence of the depolarization rate of the longitudinal polarization was presented in Refs. 1 and 2. For the ''bare'' muon the relaxation rate of the longitudinal polarization is of order $\gamma_\mu b\sim 10^5$–$5\times 10^5\ \mathrm{s}^{-1}$ and thus differs significantly from the rate in the case of ''Coulomb muonium.''

A different effect associated with the formation of muonium in metals is observed in strong magnetic fields ($\hbar\omega\gg T$). In the fields $B\sim 10^3$–10^4 G this limit is achieved at $T\leqslant 0.01$ K. The precession frequency of the transverse polarization (see Ref. 5)

$$\Omega_{\perp} = \zeta\omega + \omega_0/2 \tag{24}$$

differs from the precession frequency of the ''bare'' muon by the shift $\omega_0/2 \sim 10^8$ s^{-1} when $\alpha \sim 10^{-2}$. Since the best results regarding the resolution of the precession frequency $\Delta\omega \sim 10^{10}$ s^{-1} were achieved in the experiments in Ref. 16, the indicated possibility of measuring the frequency shift $\omega_0/2$ can be easily achieved.

In conclusion, let us examine the conditions under which second-order perturbation theory can be significant at low temperatures ($T < 1$ K) when the scattering of a conduction electron of the metal on a muonium atom (the Kondo effect) is considered. Using the Born approximation, we should correct the formula for the effective frequency of muonium electron spin flips. According to the qualitative theory in Refs. 7 and 17, ν should be replaced by

$$\tilde{\nu} = \nu(1+\Delta)^2, \quad \text{where} \quad \Delta \sim \frac{J}{\varepsilon_F} \ln \frac{\varepsilon_F}{\max(\hbar\omega, \hbar\omega_0, T)}. \tag{25}$$

An analysis reveals that at $\nu \leqslant 10^8 T$ s^{-1}, at which Mu atoms can be observed through two-frequency precession [Eqs. (17) and (18)], the correction Δ is insignificant. If $\nu > 10^8 T$ s^{-1}, the observation of Mu atoms through the shift of the precession frequency of the transverse polarization in a strong magnetic field is most reliable.

Thus, the recommendations presented by us make it possible to experimentally observe muonium atoms in metals in the temperature range $T \sim 0.01$–0.1 K and at $T \geqslant 1$ K.

We express our gratitude to Prof. D. Kondo for some useful discussions.

[1)] Some very recent experiments performed to study the temperature dependence of the muon spin depolarization rate in Sb single crystals showed that Mu atoms nevertheless form.[4]

[2)] We note that in Refs. 5, 10, and 11 the roots of the characteristic equation were calculated with a smaller accuracy.

[1] Yu. M. Belousov, V. N. Gorelkin, A. L. Mikaélyan, V. Yu. Miloserdin, and V. P. Smilga, Usp. Fiz. Nauk **129**, 3 (1979).
[2] *The Muon Method in Science (Proceedings of the Lebedev Physics Institute, Academy of Sciences of the USSR, Vol. 219)*, V. P. Smilga and Yu. M. Belousov (eds.), Nova Science, Commack, N.Y. (1994).
[3] O. Hartmann, E. Karlsson, L. O. Norlin *et al.*, Hyperfine Interact. **4**, 828 (1978).
[4] T. M. S. Johnson, K. H. Chow, S. Dunsiger *et al.*, in *Proceedings of the μSR-96 Conference, Nikko, Japan* (1996).
[5] Yu. M. Belousov, V. N. Gorelkin, and V. P. Smilga, Zh. Éksp. Teor. Fiz. **72**, 2189 (1977) [Sov. Phys. JETP **45**, 1150 (1977)].
[6] K. Blum, *Density Matrix Theory and Its Applications*, Plenum Press, New York (1981) [Russ. transl., Mir, Moscow (1984)].
[7] A. A. Abrikosov, *Fundamentals of the Theory of Metals*, Elsevier, New York (1988).
[8] C. Kittel, *Quantum Theory of Solids*, Wiley, New York (1963) [Russ. transl., Nauka, Moscow (1972)].
[9] S. V. Vonsovsky, *Magnetism of Elementary Particles*, Mir, Moscow (1975).
[10] I. G. Ivanter and V. P. Smilga, Zh. Éksp. Teor. Fiz. **54**, 559 (1968) [Sov. Phys. JETP **27**, 301 (1968)].
[11] I. G. Ivanter and V. P. Smilga, Zh. Éksp. Teor. Fiz. **55**, 1521 (1968) [Sov. Phys. JETP **28**, 796 (1969)].
[12] V. N. Gorelkin and V. P. Smilga, Zh. Éksp. Teor. Fiz. **69**, 949 (1975) [Sov. Phys. JETP **42**, 482 (1975)].
[13] A. A. Abrikosov, L. P. Gor'kov, and I. E. Dzyaloshinskiĭ, *Methods of Quantum Field Theory in Statistical Physics*, Prentice-Hall, Englewood Cliffs, N.J. (1963).
[14] W. A. MacFarline, R. F. Kiefl, K. H. Chow *et al.*, Hyperfine Interact. **86**, 467 (1994).
[15] W. A. MacFarline, R. F. Kiefl, J. E. Fischer *et al.*, in *Proceedings of the μSR-96 Conference, Nikko, Japan* (1996).
[16] R. F. Kiefl, E. Holzschuh, H. Keller *et al.*, Hyperfine Interact. **53**, 90 (1984).
[17] W. A. Harrison, *Solid State Theory*, McGraw-Hill, New York (1970) [Russ. transl., Mir, Moscow (1972)].

Translated by P. Shelnitz

Magnetically stabilized electron–hole liquid in indium antimonide

I. V. Kavetskaya, N. V. Zamkovets, N. N. Sibeldin, and V. A. Tsvetkov

P. N. Lebedev Institute of Physics, Russian Academy of Sciences, 117924 Moscow, Russia
(Submitted 12 August 1996)
Zh. Éksp. Teor. Fiz. **111**, 737–758 (February 1997)

Luminescence spectra of sufficiently pure *n*-type indium antimonide crystals ($N_D-N_A=(1-2)\cdot 10^{14}$ cm^{-3}) in a magnetic field of up to 56 kOe, at temperatures of 1.8–2 K, and high optical pumping densities (more than 100 W/cm^2) have been studied. More evidence of the existence of electron–hole liquid stabilized by magnetic field has been obtained, and its basic thermodynamic parameters as functions of magnetic field have been measured. When the magnetic field increases from 23 to 55.2 kOe, the liquid density increases from $3.2\cdot 10^{15}$ to $6.7\cdot 10^{15}$ cm^{-3}, the binding energy per electron–hole pair rises from 3.0 to 5.2 meV, and the binding energy with respect to the ground exciton level (work function of an exciton in the liquid) rises from 0.43 to 1.2 meV. © *1997 American Institute of Physics.* [S1063-7761(97)02602-4]

1. INTRODUCTION

The formation of an electron–hole liquid in a semiconductor is possible if it is stable against decay into free excitons, i.e., when the binding energy per electron–hole pair in the ground state is higher in absolute value than the exciton binding energy.[1)]

Theoretical calculations indicate that in a model semiconductor with simple isotropic and nondegenerate bands at sufficiently low temperatures, the ground state of a system of nonequilibrium carriers with a moderate density of electron–hole pairs ($n \ll a_{\rm ex}^{-3}$, where $a_{\rm ex}$ is the exciton Bohr radius) is a gas of noninteracting excitons.[1,2] In real semiconductors the liquid phase is energetically favored, owing to various stabilizing factors. For example, in polar semiconductors, such as GaAs, CdS, etc., the liquid state is stable because of interaction between charge carriers and longitudinal optical phonons.[3–6] In germanium and silicon, traditional materials for studies of electron–hole liquid, in which it has been studied comprehensively, the liquid is stable owing to the high orbital degeneracy of electron states due to the multivalley structure of the conductance band in these materials.[7–13] Like the multivalley spectrum, any complication in a semiconductor electron spectrum favors stabilization[2)] of the electron–hole liquid if it leads to a higher density of states near the top of the valence band or the bottom of the conduction band.[12,14–18]

The electron–hole liquid in semiconductors and semimetals with a strong anisotropy of the electron spectrum was studied theoretically in Refs. 21–23. In addition to semiconductors and semimetals with multiple valleys, quasi-one-dimensional (systems of parallel conducting wires) and quasi-two-dimensional (parallel conducting planes) systems with separations between neighboring wires or planes smaller than $a_{\rm ex}$ have been studied, as well as bulk semiconductors under very strong magnetic fields. It was found that under certain conditions, a ''highly compressed'' electron–hole liquid with a density much higher than the reciprocal exciton volume in the respective anisotropic system, and with a binding energy per electron–hole pair much higher than the exciton binding energy, should be formed. The main contribution to the binding energy, is due to spatial correlations between particles populating different equivalent minima of the bands in the multivalley semiconductors with sufficiently large numbers of valleys, or in neighboring conducting wires or planes in quasi-one-dimensional and quasi-two-dimensional structures, respectively, or on neighboring Landau cylinders under strong magnetic fields. The correlation energy in such systems (the exchange energy in the considered density range is much lower) can be expressed in terms of the asymptotically accurate formula

$$E_{\rm corr}=-An^{1/4}, \tag{1}$$

where A is a factor that depends on the nature of the system and features of its band spectrum.[21,22] This formula for $E_{\rm corr}$ allows one to derive simple analytic expressions for the density and energy of the ground state of a highly compressed electron–hole liquid in such anisotropic systems.

This paper describes an experimental study of electron–hole liquid stabilization due to a strong magnetic field. It is noteworthy that this case is formally equivalent to the quasi-one-dimensional case—as the resulting expressions are essentially identical after substitution of the magnetic field strength H multiplied by a factor proportional to the density of the parallel wires.[22] Therefore the main features of a system of nonequilibrium charge carriers in quasi-one-dimensional structures should be roughly consistent with the behavior of that system in a strong magnetic field.

In a strong magnetic field such that $a_H \ll a_{\rm ex}$, where $a_H=\sqrt{\hbar c/eH}$ is the magnetic length, the exciton effective volume is of the order of $a_{\rm ex}a_H^2$ (such excitons are usually termed diamagnetic[24–26]), and the condition of strong compression of electron–hole plasma is expressed by the first of the following two inequalities:[21]

$$(a_{\rm ex}a_H^2)^{-1} \ll n \ll a_H^{-3}. \tag{2}$$

Under strong compression, the electron–hole system is a degenerate Fermi liquid, and its energy as a function of density has a minimum at $n=n_0$. In the ultraquantum limit, when the second of the inequalities (2) is satisfied, the equi-

librium density of a highly compressed electron–hole liquid is $n_0 \propto H^{8/7}$, and the energy per electron–hole pair in the ground state is $|E(n=n_0)| \equiv |E_0| \propto H^{2/7}$ (Refs. 21, 27, 28).[3)] Since the ionization energy of diamagnetic excitons increases with field strength more slowly than E_0, ($|E_{ex}| \propto \ln^2 H$; see Ref. 29) the stability of the liquid state, characterized by the exciton work function in the liquid state, $\varphi = E_{ex} - E_0$, should increase with magnetic field strength in a strong field. Moreover, in a strong magnetic field the liquid phase may become stable ($\varphi > 0$) even if it is unstable at zero magnetic field. An electron–hole liquid stabilized by a magnetic field $H \gtrsim 20$ kOe was found by us[30] in indium antimonide.[4)]

Indium antimonide is the most suitable material for studies of the effect of a magnetic field on weakly bound electronic states. The electron effective mass in this semiconductor is extremely small, so that in a field of only several kilo-oersted the magnetic length is smaller than the excitonic radius and the electron cyclotron energy is larger than the excitonic Rydberg. Moreover, the existing growth technology allows one to fabricate highly regular single crystals with few residual impurities.

In this paper, we present a detailed study of luminescence spectra of fairly pure single crystals of indium antimonide in magnetic fields of up to 56 kOe, at temperatures of 1.8–2 K, and high (more than 100 W/cm^2) intensities of optical pumping, and of the effect of electric fields on these spectra. We have obtained additional evidence for the existence of an electron–hole liquid stabilized by magnetic field and measured its basic thermodynamic parameters. The renormalized band gap and Fermi energies of particles in the liquid have been derived from the shapes of luminescence spectra of the liquid phase. As the magnetic field rises from 23 to 55.2 kOe, the liquid density linearly grows from $3.2 \cdot 10^{15}$ to $6.7 \cdot 10^{15}$ cm^{-3}, and the binding energy per electron–hole pair in the ground state increases from 3.0 to 5.2 meV. At the same time, the exciton work function in the liquid also increases from 0.43 to 1.2 meV. This feature qualitatively distinguishes it from the electron–hole liquid in germanium, which is stable at zero magnetic field and has a constant exciton work function in magnetic fields up to 190 kOe.[35]

Note that the numerical values of the exciton work function and density of electron–hole liquid given in this paper are slightly different from those in our earlier publication,[36] since the data of this paper were derived from measurements with due account of the Landau level broadening and the complex structure of the valence band.

2. EXPERIMENTAL TECHNIQUES

The basic experiments were performed using n-InSb samples with a differential impurity concentration $N_D - N_A = (1–2) \cdot 10^{14}$ cm^{-3} and degree of compensation $k \simeq 50\%$. Mechanically polished samples were processed in CP-4A polishing etchant. Typical dimensions of the samples were $5 \times 5 \times (0.1–0.25)$ mm^3. The larger faces of the samples were perpendicular to the $\langle 211 \rangle$ crystal axis. A studied sample was freely suspended at the center of a superconducting solenoid so that the magnetic field was perpendicular to its larger faces, and during experiments the sample was immersed in superfluid helium. The measurements were made at $T = 1.8–2$ K.

The source of quasi-continuous optical pumping was a cw Nd^{3+}YAG laser generating a wavelength $\lambda = 1.06$ μm with a maximum power of about 1 W. The pumping radiation was chopped at a frequency of 1 kHz by a mechanical chopper and focused on the wider sample face. The pumping intensity was varied using neutral-density optical filters.

The recombinataion radiation was collected either from the face exposed to the laser light (back-scattering configuration) or from the opposite face (transmission configuration). This radiation was dispersed by an MDR-2 monochromator with a 100 lines/mm diffraction grating and detected by a Ge:Au photoresistor cooled to a temperature of about 100 K. In magnetic fields of several kilo-oersted or higher the recorded luminescence spectra were identical in both configurations; therefore this paper only presents data derived from measurements in the transmission configuration.

In order to compare the spectral positions of the recorded luminescence lines with the energies of diamagnetic excitons, we recorded reflection spectra in magnetic field. In these measurement the broad-band source of light was a globar, and the reflected light was analyzed by the same monochromator as the recombination radiation.

In order to measure the luminescence distribution over the sample volume,[11,13,15,20] an additional horizontal slit was placed in front of the (vertical) monochromator entrance slit so that their planes coincided. The wider sample face through which the recombination radiation was transmitted was imaged one-to-one in this plane by a condenser. The exciting laser beam was focused on the opposite face into a spot about 0.2 mm in diameter at the center of the rectangular image of the opening formed by the crossed slits. The luminescence spatial distribution was measured by varying the width of the horizontal slit. The width of the monochromator entrance slit was maintained constant (it was 300 μm) so that the spectral resolution would not change.

As will be described below, the luminescence line of electron–hole liquid emerging in a magnetic field under sufficiently high pumping power is superimposed on luminescence lines due to shallow donors and magnetically stabilized exciton–impurity complexes (bound excitons).[30,37,38] These three lines overlap and form a relatively wide spectral range (which is structureless at the highest pumping power), so they cannot be resolved using conventional techniques. In order to separate the liquid luminescence line, we used two methods: the differential technique with low modulation amplitude of the pumping radiation,[39] and application to the sample of an electric field whose strength was sufficient to cause impact ionization of shallow donors and bound excitons.[40] The low-amplitude modulation was performed by a mechanical chopper with a perforated disk made from photographic film whose emulsion was removed. This disk modulated the laser beam with an amplitude of about 20%. The applied electric field was perpendicular to the magnetic field. It was applied using indium contacts attached to the opposite narrow faces of the samples. In both cases we detected luminescence from a 0.3×0.3 mm^2 area within the

laser spot, whose diameter in these experiments was about 0.4 mm.

Low-temperature measurements performed at high pumping powers may be misleading owing to sample overheating by the laser beam. In order to test the thermal conditions, we lowered the duty cycle of the pumping pulses from 1/2 to 1/10. This change did not notably affect the shapes of recorded luminescence spectra. Since the intensity of the luminescence light due to bound excitons stabilized by magnetic field is very sensitive to temperature,[37,38] we concluded that sample overheating was insignificant throughout the range of pumping powers used in our experiments. It is known that, even if a bubble of gaseous helium is produced on the sample surface at the laser focus, sample overheating will not be very high[41–43] (this issue was discussed in detail in Ref. 20). The sample temperature increases considerably at pumping powers much higher than the bubble formation threshold, when the whole sample is surrounded by a gas jacket.[41] Under conditions of our experiments with low modulation amplitude, overheating affected our results significantly only at pumping power densities higher than $\simeq 600$ W/cm^2.

3. EXPERIMENTAL RESULTS

Without magnetic field, the main luminescence line of the studied samples at low pumping powers is entirely in the spectral range below the band gap.[38,44] Its maximum is at $h\nu_{\max} \simeq 235.3$ meV (the band gap at $T=2$ K is $E_g = 236.8$ meV[45]), and its FWHM is about 1.5 meV. This line is due to the transitions of electrons from the levels of shallow donors to the valence band, and its position and shape are controlled by large-scale fluctuations in the concentration of charged impurities, which cause bending of the semiconductor energy bands (see Refs. 38, 44).[5)] In a magnetic field, the main (donor) line shifts to shorter wavelengths with increasing magnetic field strength, becomes more narrow, and its intensity drops.[37,38] In magnetic fields of 5–7 kOe, a narrow luminescence line due to bound excitons stabilized by the magnetic field (BE_{II} line in the notation of Ref. 38) emerges in the low-energy wing of the initial line; it dominates the spectrum at high magnetic fields.[30,37,38] Luminescence spectra of one sample recorded at a relatively low pumping power at $H=46$ kOe are given in Fig. 1 (curve *3*) and in the insert of Fig. 5a.

Changes in the shape of luminescence spectra due to higher pumping power in strong ($H \gtrsim 20$ kOe) and weak magnetic fields are qualitatively different. Luminescence spectra in the field $H=46$ kOe recorded at different pumping powers are shown in Fig. 1. The intensity of the donor luminescence line grows faster with the pumping power density than that of bound excitons (at low pumping powers the latter grows linearly[38]). At high powers these two lines merge into a single relatively broad band. Figure 1 also shows that the luminescence spectrum broadens on the long-wave side and develops a ''tail'' extending to the region of lower energies. At the same time, the shape of the short-wave wing of the resulting spectrum is essentially the same as that of the donor line.

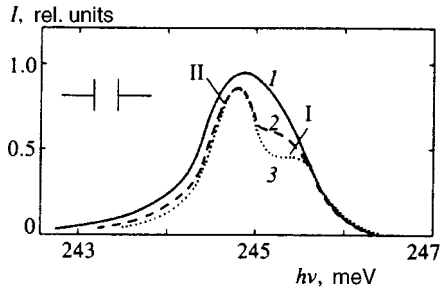

FIG. 1. Luminescence spectra in a magnetic field $H=46$ kOe. The pumping power density (*1*) $P \simeq 210$ W/cm^2, (*2*) 140W/cm^2, and (*3*) 100 W/cm^2. The spectra are normalized to equalize the intensities at $h\nu = 245.7$ meV (I is a donor line; II is a bound exciton line).

The behavior of the luminescence spectrum in a relatively weak magnetic field ($H<20$ kOe) is markedly different. At higher pumping powers the structure of the luminescence spectrum is also blurred. In this case, however, not the long-wave, but the short-wave edge of the structureless band broadens (Fig. 2), i.e., the shape of the high-energy edge of the luminescence spectrum demonstrates behavior similar to that of the zero-field case.[44,51] At the same time, in the studied range of pumping powers, no features were detected at the low-energy edge of the recorded luminescence band that could be attributed to an induced emission line[44,50,51] under the intense pumping, contrary to the case of zero magnetic field.[6)]

In order to avoid misunderstanding, we stress from the start that the change in the low-energy edge of the luminescence spectrum in high magnetic field is in no way related to the amplification of recombination radiation. Above all, this is suggested by the character of changes due to a higher pumping power, the position, and the shape of the long-wave radiation band emerging at high excitation intensity (see below). This statement, however, is confirmed by the aggregate of experimental facts, which have led us to the conclusions presented below.

In what follows, we will limit our discussion to results obtained in strong magnetic fields. Figure 3 shows luminescence intensities as functions of the pumping power, measured at high excitation in a magnetic field $H=46$ kOe for the three energies of detected photons corresponding to different sections of the spectra shown in Fig. 1. One of these energies corresponds to the maximum of the donor line at low pumping powers ($h\nu = 245.4$ meV), the second to the

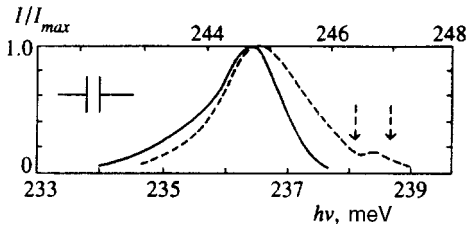

FIG. 2. Luminescence spectra in magnetic fields $H=46$ kOe (solid line, upper scale) and $H=9.2$ kOe (dashed line, lower scale) under high-intensity excitation. The pumping power density $P \simeq 500$ W/cm^2. The arrows mark absorption lines of atmospheric water vapor.

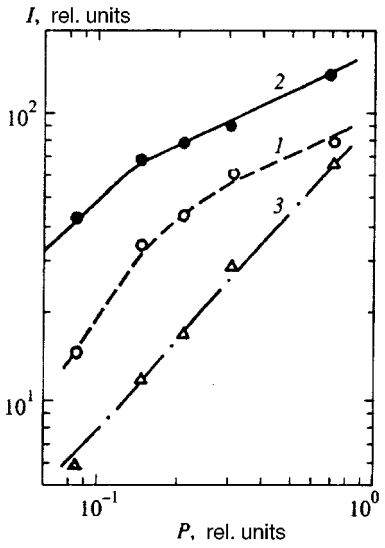

FIG. 3. Luminescence intensity as a function of pumping power at high excitation levels for three spectral positions: (*1*) $h\nu=245.4$ meV, (*2*) 244.8 meV, and (*3*) 244.2 meV (see Fig. 1). $H=46$ kOe. The maximum pumping power density is about 480 W/cm^2. Luminescence was collected from a 0.3×0.5 mm^2 area centered at the laser focus.

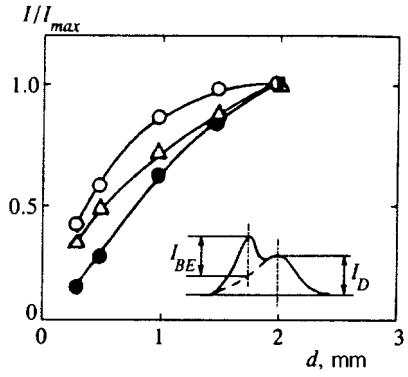

FIG. 4. Intensities of bound exciton I_{BE} (full circles) and donor I_{D} (open circles) lines and their ratio $I_{\mathrm{BE}}/I_{\mathrm{D}}$ (triangles) as a function of the horizontal slit width d. The pumping power density is about 140 W/cm^2, $H=46$ kOe. The insert schematically shows the luminescence spectrum.

maximum of the bound exciton line ($h\nu=244.8$ meV), and the third one to an arbitrarily selected point of the long-wave edge of the luminescence spectrum ($h\nu=244.2$ meV). The curves in Fig. 3 demonstrate that at the highest pumping power the intensities of the donor (curve *1*) and bound exciton (curve *2*) lines change relatively slowly, whereas the intensity of the low-energy edge (curve *3*) is essentially linear with the pumping power. The emergence of the low-energy tail demonstrating a dependence on the pumping power different from those of the initial two components is attributed to a new band on the low-energy edge, which can be isolated from the total spectrum by recording the luminescence intensity derivative with respect to the pumping power.[30]

Before proceeding to the results obtained using this technique, let us discuss measurements of the spatial distribution of the luminescence intensity due to donors (I_D) and bound excitons (I_{BE}). These intensities as functions of the size of the observed region of the sample (width of the horizontal slit; see Sec. 2) are plotted in Fig. 4. These curves demonstrate that the luminescent region is much larger than the laser spot diameter, which is $\simeq0.2$ mm, and since the donor line intensity is a steeper function of the pumping power (Fig. 3), the intensity ratio I_{BE}/I_D increases with horizontal slit width (Fig. 4). The data plotted in Figs. 3 and 4 indicate that at high pumping density, when the intensities I_{BE} and I_D saturate, the main contribution to the increase in these intensities with pumping power comes from the periphery of the laser spot. For this reason, luminescence from within the laser spot was detected in measurements of the long-wave band emerging at high pumping powers using the differential technique in order to reduce the contributions of the donor and bound exciton lines to the differential spectrum.

Luminescence spectra recorded at high pumping power and 100% (curve *1*) and 20% (curve *2*) modulation of the pumping intensity are given in Fig. 5a. The latter was multiplied by a constant so that it could be compared to that recorded at 100% modulation amplitude. Spectrum *3* in Fig. 5a is the difference between spectra *1* and *2*. It occupies the same spectral range as the luminescence spectra at low pumping powers (insert of Fig. 5a). In accordance with the above reasoning, however, the lines of donors and bound excitons are not resolved in the difference spectrum *3*, whereas at lower pumping powers these lines are clearly resolved in the difference spectrum (curve *2* in Fig. 5b). The arrow in Fig. 5a marks the energy of the transition to the lowest-lying state of free diamagnetic excitons, as derived from the position of the long-wave component of the excitonic reflection spectrum in magnetic field.[37,38]

Jumping ahead, we note that experiments with electric field have demonstrated that at the highest pumping powers, the radiation from donors and bound excitons contributes little to the differential spectrum *2* in Fig. 5a, whereas at intermediate pumping power densities (140–250 W/cm^2) it appreciably distorts the short-wave wing of the differential spectrum.[30]

We now discuss experiments with electric field. By applying an electric field sufficient to collisionally ionize impact ionization of shallow donors and bound excitons, one can quench luminescence lines due to these species and thus separate the long-wave line which emerges at higher pumping powers.[30] Figure 6 shows dark current–voltage characteristics of one sample at various magnetic fields. Owing to the increase in ionization energy of shallow donors with magnetic field,[52] the sample resistance at fields below breakdown (at low voltage U across the sample), the breakdown voltage, and the steepness of the breakdown region of the current–voltage characteristics also increase.

The effect of a dc electric field on the photoluminescence spectrum at an intermediate pumping power such that the donor and bound exciton lines are clearly seen in the spectrum is illustrated by Fig. 7. At higher voltage across the sample, the intensities of these lines are lower. At $U\simeq15$ V the spectrum contains only a broad band whose shape is similar to that of the differential spectrum *2* in Fig. 5a obtained at 20% modulation amplitude of the pumping intensity, and which has approximately the same spectral position.

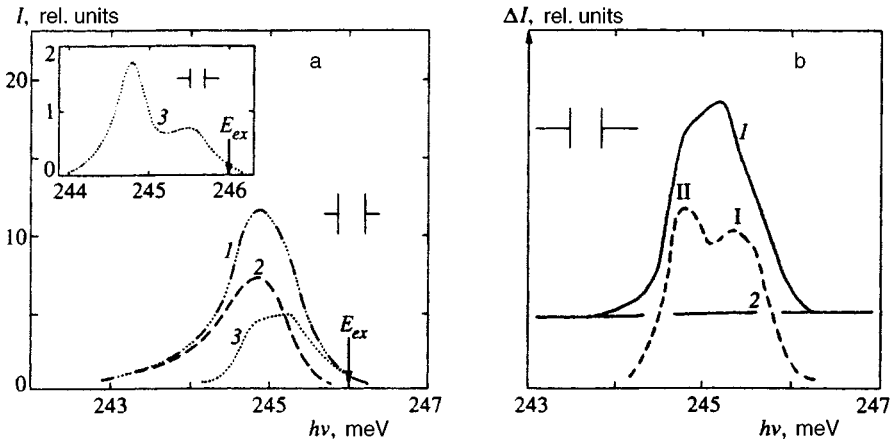

FIG. 5. Luminescence spectra recorded under intense pumping in a magnetic field $H=46$ kOe: (a) $P\simeq 500$ W/cm^2. The modulation amplitudes are (*1*) 100% and (*2*) about 20%. Curve *3* shows the difference between spectra *1* and *2*. The arrow shows the energy of the optical transition to the diamagnetic exciton ground state. Luminescence was collected from an area of 0.3×0.3 mm^2. The insert shows the spectrum at low excitation ($P\simeq 50$ W/cm^2). (b) Difference luminescence spectra at (*1*) $P\simeq 500$ W/cm^2 and (*2*) 140 W/cm^2 (I is a donor line, II is a bound exciton line).

Figure 7 also shows that the electric field has little effect on the shape of the low-energy wing of the luminescence spectrum. At the same time, the intensity of the long-wave band increases with electric field strength. This increase is clearly demonstrated by the differential spectra recorded by applying a square-wave voltage with a frequency of 1 kHz and a 50% duty cycle under cw optical excitation of the sample. The donor and bound exciton lines are clearly resolved in the luminescence spectrum differential with respect to the electric field (Fig. 8). The signal at these lines has a positive phase, corresponding to an intensity decrease caused by the electric field. The negative signal at the long-wave edge is due to an increase in the long-wave luminescence intensity. Its absolute value grows with the pumping power.

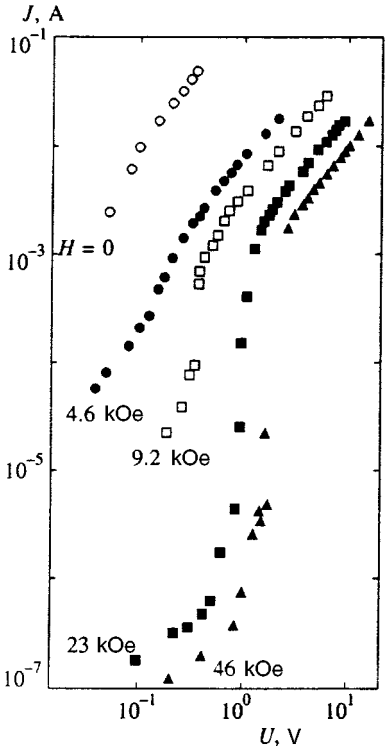

FIG. 6. Current–voltage characteristics of a sample in the dark at different magnetic fields strengths and $T=2$ K.

It is noteworthy that donor and bound exciton lines are quenched by the electric field at a notably higher voltage across the sample than that of donor collisional ionization in the dark (compare Figs. 6 and 7). This probably occurs for two reasons. First, the electric field in the excited region is likely to be lower than the mean field in the sample. This is supported by observed data plotted in Fig. 9. As the laser spot dimension gets larger, the curve of the bound exciton line intensity versus electric field becomes steeper, and complete quenching occurs at a lower voltage. Second, the electric field at which donors are almost fully ionized is known to be several times the breakdown field.[53,54] These two factors probably prevented us from observing quenching in an electric field separately for close-lying donor and bound exciton lines.

Thus the results discussed above have demonstrated that in magnetic fields $H>20$ kOe, at high pumping powers, an additional spectral band emerges at the long-wave edge of the indium antimonide luminescence spectrum, which can be separated from the resultant spectrum by either recording the spectrum differential with respect to the pumping power or applying a dc electric field. Unlike the other two components of the spectrum, this band grows in intensity with the voltage across the sample. This means that the band is associated

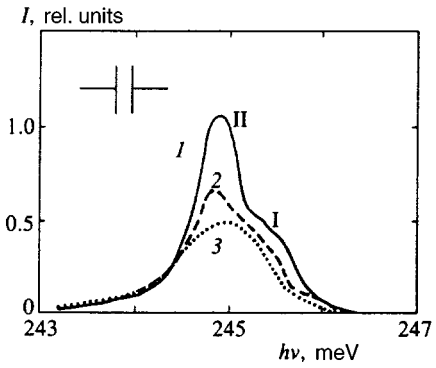

FIG. 7. Luminescence spectra in a magnetic field $H=46$ kOe at various dc voltages across the sample: (*1*) $U=0$; (*2*) 10 V; (*3*) 15 V. The pumping power density is $\simeq 140$ W/cm^2; $T=2$ K. The modulation amplitude of the pumping power is 100%. The spectra are normalized to equalize the intensities at $h\nu=244.4$ meV (I is a donor line; II is a bound exciton line).

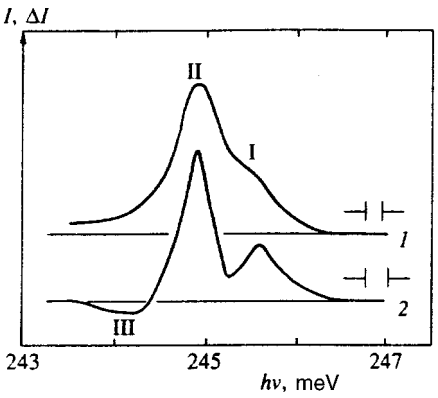

FIG. 8. Luminescence spectra recorded at 100% modulation amplitude of the pumping power (curve *1*: electric field is absent, $U=0$) and under square-wave voltage (curve *2*: $U=10$ V, cw excitation). $H=46$ kOe, the pumping power density about 140 W/cm^2 (I is a donor line, II is a bound exciton line and III is an electron–hole liquid line).

with the recombination of electrons and holes populating states which are not depleted in the electric field, although it is close in energy to the donor and bound exciton lines—but these features are destroyed by collisional ionization.

Therefore, the electron states in question are inherently substantially different from atomic or molecular states, i.e., those containing small numbers of interacting particles (donors and acceptors, free and bound excitons, etc.). The behavior of the long-wave emission band in an electric field indicates that it is due to the recombination of particles in an electron–hole plasma whose energy is reduced owing to interparticle interactions. Its increase in intensity in an electric field and at the same time the constancy of its low-energy edge shape may indicate that the volume occupied by the plasma in the semiconductor increases. The high-energy edge of the long-wave band loses an appreciable amount of energy relative to the transition to the free exciton ground state (see Figs. 5a and 7; $h\nu_{\rm ex}=246$ meV at $H=46$ kOe), i.e., the energy of plasma particles is lower than that of electron–hole pairs bound in excitons.

Thus, we conclude that we are dealing with a plasma of interacting particles stable against decay into free excitons,

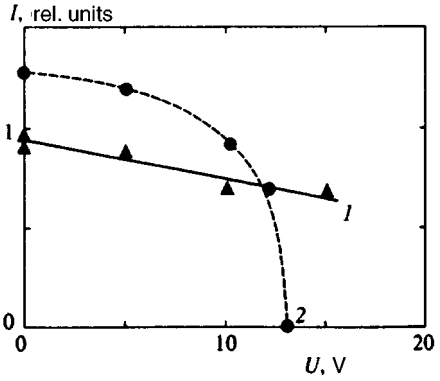

FIG. 9. Intensity of bound exciton line versus voltage across the sample at different diameters of the exciting laser spot. $H=46$ kOe. The pumping power is $\simeq 40$ mW. The laser spot diameter is (*1*) $\simeq 0.2$ mm and (*2*) $\simeq 0.4$ mm. The ordinate scales for curves *1* and *2* are different.

i.e., it is an electron–hole liquid.[30] Since the heating of free carriers by an electric field should broaden the high-energy wing of the plasma luminescence line, its constant shape, independent of the technique used to separate it from the other spectral lines (the applied electric field or 20% modulation of the pumping power), provides additional evidence favoring the electron–hole liquid interpretation.

To conclude this section, we note that a long-wave line emerging at high magnetic fields under intense optical pumping was detected more or less clearly in essentially all sufficiently pure *n*-type InSb samples, with various concentrations of the majority and compensating impurities, that we studied. A list of the samples was given in Refs. 36 and 38. The highest intensity of luminescence due to the electron–hole liquid was, however, detected in the samples studied in the work reported here. These samples were selected for studies of the electron–hole liquid with a view to deriving its basic thermodynamic parameters for this reason, and because their luminescence spectra contain only one line of bound excitons stabilized by magnetic field (in some samples up to three bound exciton lines were detected in a magnetic field).[36,38]

4. ANALYSIS OF EXPERIMENTAL DATA

One convincing argument for interpreting the corresponding luminescence band as a spectral line in the electron–hole liquid is the good fit of a theoretical curve to the recorded spectrum shape. Furthermore, the analysis of the spectral line shape yields the most reliable values of the characteristics energies of particles in the electron–hole liquid and its density.[8,9,11,14,15,17]

The shape of the recombination radiation spectrum of the electron–hole liquid in indium antimonide in magnetic field can be analyzed using the conventional formula for direct allowed optical transitions:

$$I(h\nu)\propto \nu^2 g(h\nu) f_e f_h, \tag{3}$$

where f_e and f_h are the Fermi distribution functions for electrons and holes with Fermi energies E_{Fe} and E_{Fh}, respectively, and the density of states is[55]

$$g(h\nu)=\frac{\sqrt{2m_r}}{(2\pi\hbar)^2}\frac{eH}{c} \times \sqrt{\frac{(h\nu-E_{gL})/\Gamma+\sqrt{[(h\nu-E_{gL})/\Gamma]^2+1}}{2\Gamma\{[(h\nu-E_{gL})/\Gamma]^2+1\}}}. \tag{4}$$

Here m_r is the reduced effective mass of electrons and holes in the bands between which recombination transitions occur, E_{gL} is the renormalized band gap in the electron–hole liquid, and Γ is the damping parameter, which eliminates singularities in the density of states at Landau levels.

For simplicity, we assumed that throughout the studied range of $h\nu$, the electron and hole energies in the expressions for f_e and f_h were related to the emitted photon energy by $E_e=(m_r/m_e)(h\nu-E_{gL})$ and $E_h=(m_r/m_1)(h\nu-E_{gL})$, respectively, which apply to the case of direct transitions between parabolic electron and hole bands (m_e is the electron effective mass and m_1 is the hole effective mass in the

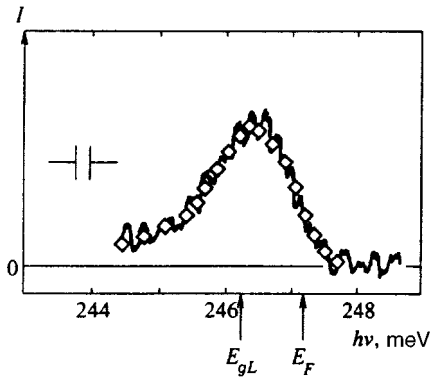

FIG. 10. Measured and calculated (squares) by Eqs. (3) and (4) luminescence spectra of electron–hole liquid. $H=55.2$ kOe, $P\simeq 500$ W/cm^2. The values of E_{gL} and E_F obtained by fitting the calculations are marked by arrows.

upper magnetic subband of the valence band). We assumed in addition that the damping parameter Γ was independent of both E_e and E_h.

Further analysis was performed in two stages. First, the calculated spectrum was fitted to the experimental data in the two-band approximation, i.e., the holes were assumed to occupy only the upper magnetic subband of the valence band[36] (below we will find that a great many holes are contained in the next magnetic subband). As concerns the distribution of electrons, over the present magnetic field range, all the electrons in the liquid are in the lowest spin subband of the zeroth Landau electron subband. In this case, the electron and hole Fermi energies are related to each other in the same way as E_e and E_h, i.e., $E_{Fe}=(m_r/m_e)E_F$ and $E_{Fh}=(m_r/m_1)E_F$, where $E_F=E_{Fe}+E_{Fh}$.

The differential luminescence spectrum of the electron–hole liquid (with respect to the pumping power) at $H=55.2$ kOe, and its fit calculated by Eqs. (3) and (4) in the two-band approximation, are given in Fig. 10. This fit obtained at $m_e=0.014m_0$ and $m_1=0.075m_0$ (this value of m_1 yields the best agreement between the experimental and calculated spectra, m_0 is the free electron mass) yielded the damping parameter $\Gamma=0.55$ meV, the renormalized band gap $E_{gL}=246.26$ meV, and the sum of the electron and hole Fermi energies $E_F=0.95$ meV.

Then the luminescence spectra of the electron–hole liquid were analyzed under the assumption that two magnetic subbands of the valence band were populated (it followed from our analysis that higher hole subbands were not occupied), and the main point was determination of new values of electron and hole Fermi energies. The hole Fermi energy was calculated by numerically solving the equation

$$\int_{-\infty}^{E_{Fe}} g_e(E)dE=\int_{-\infty}^{E_{Fh}} g_{h1}(E)dE+\int_{-\infty}^{E_{Fh}-\Delta E_{12}} g_{h2}(E)dE, \tag{5}$$

which is valid, strictly speaking, at $T=0$, and represents the electrical neutrality of the electron–hole liquid: $n_e=n_1+n_2$, where n_1 and n_2 are the concentrations of holes populating the two magnetic subbands considered. The electron concentration is determined by the left-hand side of Eq. (5) with the density of states

$$g_e(E)=\frac{\sqrt{2m_e}}{(2\pi\hbar)^2}\frac{eH}{c}\sqrt{\frac{E/\Gamma_e+\sqrt{(E/\Gamma_e)^2+1}}{2\Gamma_e[(E/\Gamma_e)^2+1]}}, \tag{6}$$

where Γ_e is the electron damping parameter. Similar expressions describe the hole density of states g_{h1} and g_{h2} in the respective magnetic subbands (with m_e and Γ_e replaced by m_1 and Γ_1 or m_2 and Γ_2). We assumed that the damping parameters of electrons and holes were related to each other by $\Gamma_e=(m_r/m_e)\Gamma$, $\Gamma_1=(m_r/m_1)\Gamma=(m_e/m_1)\Gamma_e$, and $\Gamma_2=(m_e/m_2)\Gamma_e$, following from the proportionality between the damping parameters and Fermi energies in parabolic bands.[17]

When the hole Fermi energy E_{Fh} was derived from Eq. (5), the value of the Fermi energy E_{Fe} substituted into its left-hand side was found from the spectrum shape fit in the two-band approximation, the hole effective mass in the second subband was equated to $m_2=0.045m_0$, and the gap between the two upper subbands of the valence band was determined by the formula $\Delta E_{12}=\mu H$, where $\mu=7.5\cdot 10^{-3}$ meV/kOe. The resulting E_{Fh} was substituted into the Fermi distribution function f_h and then the spectrum defined by Eqs. (3) and (4) was again fitted to the experimental spectrum, and, as a result, the corrected electron Fermi energy was determined. Note that the shape of the luminescence spectrum was still described by Eqs. (3) and (4), because electron transitions to the second hole subband are forbidden, and the population of the second subband affects the luminescence spectrum through the change in the Fermi energies, which are no longer related by the above simple formulas, which hold in the two-band model.

This procedure of deriving electron–hole liquid parameters from luminescence spectra yields values of Γ, E_{gL}, and E_{Fe} that are essentially identical to those obtained using the two-band model (E_{Fe} changes by several percent). Therefore the inclusion of the second magnetic hole subband has little effect on the accuracy of the liquid density determined from the derived value E_{Fe}. At the same time, in a relatively weak magnetic field, where the hole population of the second subband is relatively high and affects the position of the hole Fermi level, it should be taken into account in deriving the liquid binding energy from experimental data. This is illustrated by the data plotted in Fig. 13, which will be discussed below.

Luminescence spectra recorded at different magnetic field strengths were analyzed similarly (the magnetic field strength at which calculations were performed correspond to the experimental points in Figs. 11–14). The damping parameter Γ is independent of the magnetic field to within the experimental uncertainty, and its average value is $\Gamma_{av}\simeq 0.58$ meV.

The liquid density $n_0\equiv n_e=n_1+n_2$, determined at $T=0$ by the integral on the left-hand side of Eq. (5), was obtained by integrating numerically the density of states given by Eq. (6) up to E_{Fe} derived from the luminescence spectra. Neglect of the thermal spread of the electron distri-

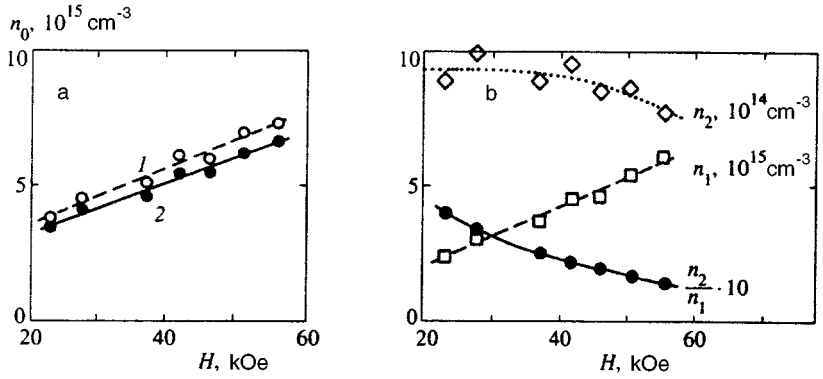

FIG. 11. (a) Density of the electron–hole liquid (curve *1* shows data from Ref. 36, curve *2* of the present work) and (b) populations of the two upper magnetic subbands of the valence band (n_1 and n_2) and their ratio as functions of magnetic field.

bution gives rise to a density uncertainty of about 4%. The electron–hole liquid density as a function of magnetic field strength is plotted in Fig. 11a (filled circles), and Fig. 11b shows how populations of the first and second hole subbands vary with magnetic field [as determined by the first and second integrals, respectively, on the right-hand side of Eq. (5)]. Figure 11a also shows, for comparison, results of our previous investigation[36] (open circles), in which the liquid density was calculated using a formula for the density of states that does not include broadening of the Landau levels (this is the limit of Eq. (6) as $\Gamma_e \to 0$). The graphs in Fig. 11a indicate that the magnetically stabilized electron–hole liquid in indium antimonide is highly compressed by an external magnetic field, in accordance with theory[21,22,27,28,31,32] and experimental results for germanium.[35]

The work function of an exciton in the liquid was determined using the formula

$$\varphi = h\nu_{\rm ex} - (E_{gL} + E_{Fe} + E_{Fh}),$$

where $h\nu_{\rm ex}$ is the energy of the transition to the ground state of a free diamagnetic exciton. In calculating φ, we used $h\nu_{\rm ex}$ derived from measured reflection spectra in magnetic field (Fig. 12; see also Ref. 38). The work function at different magnetic field strengths is plotted in Fig. 13 (filled circles). Here we also show the results of work function measurements from Ref. 36 obtained in the two-band approximation (open circles). The data plotted in Figs. 12 and 13 demonstrate that unlike germanium,[35] the stability of the electron–hole liquid against decay to free excitons in indium antimonide increases dramatically with magnetic field.

In order to derive the energy E_0 per electron–hole pair in the liquid ground state from the experimental data, which is the main calculated parameter in the theory of electron–hole liquid, we need the binding energy of diamagnetic excitons, since $E_0 = E_{\rm ex} - \varphi$. In calculating E_0 we used $E_{\rm ex}$ derived from spectra of oscillating absorption in magnetic field[56] using the theory developed by Gelmont *et al.*[57] (the

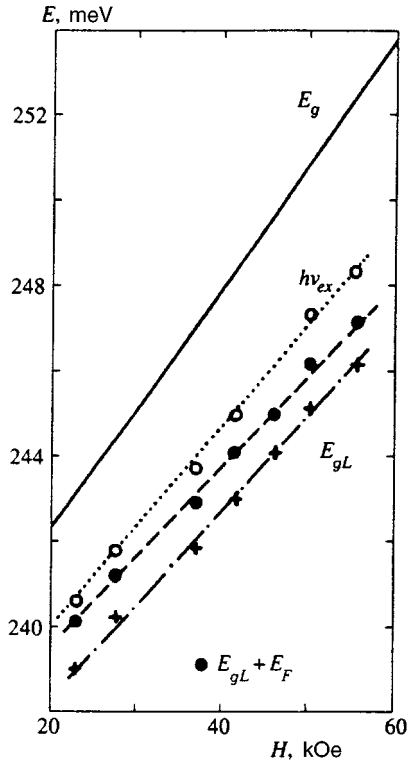

FIG. 12. Renormalized band gap E_{gL}, energy of transitions to the level of chemical potential in the electron–hole liquid $E_{gL}+E_F$ ($E_F = E_{Fe}+E_{Fh}$), energy of the transition to the diamagnetic exciton ground state $h\nu_{\rm ex}$ (the dotted line shows calculations), and band gap E_g (theory) as functions of magnetic field.

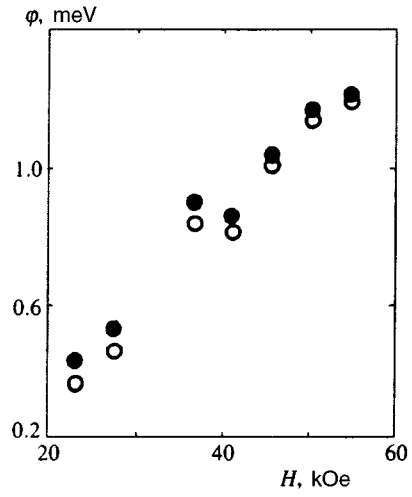

FIG. 13. Exciton work function in the electron–hole liquid versus magnetic field: ○) Ref. 36, ●) this work.

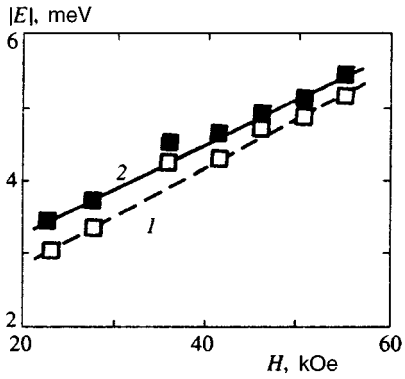

FIG. 14. Absolute values of (*1*) the energy per electron–hole pair in the liquid ground state $|E_0|$ and (*2*) sum of exchange and correlation energies $|E_{xc}|$ as functions of magnetic field.

two theoretical straight lines in Fig. 12 are the result of these calculations; $E_{\rm ex}=h\nu_{\rm ex}-E_g$).[7)] The energy per pair of particles in the liquid ground state versus magnetic field is shown in Fig. 14.

To conclude this section, we note an important circumstance that was not mentioned in our discussion of the theoretical analysis of luminescence spectra. In fitting the spectra calculated using Eqs. (3) and (4) to the experimental data, we had to substitute into the Fermi functions f_e and f_h in Eq. (3) a temperature about 10% lower than that of the liquid helium heat bath; in other words, the electron–hole liquid temperature turned out to be lower than that of the crystal. This we did in analyzing all the luminescence spectra recorded at different magnetic field strengths.

This effect might be due to purely technical inconsistencies, namely, the short-wave edge of the luminescence spectrum differential with respect to the pumping power (the temperature affects mostly the short-wave edge of the spectrum) might be slightly deformed by bound exciton and shallow donor lines overlapping with the liquid line (Figs. 1, 5, and 7). But that would more likely broaden the short-wave edge of the differential spectrum. This edge of the spectrum may also be deformed because of the amplification of recombination radiation, which quite often occurs in direct band gap semiconductors.[17] We have, however, no experimental facts that would support this interpretation. Thus the question remains open and requires further investigation.

5. DISCUSSION

The experimental data described above have yielded basic thermodynamic parameters and characteristics energies of the electron–hole liquid in indium antimonide stabilized by magnetic field as functions of the magnetic field strength (Figs. 11–14). Let us compare our results to predictions of the theory of electron–hole liquid highly compressed by strong magnetic field based on the asymptotic formula (1) for the correlation energy.[21,22,27,28] We should stress before starting this discussion that the theory does not apply to our case because at real liquid densities (Fig. 11a) the condition of strong compression (i.e., the first of inequalities (2)) is not satisfied, hence Eq. (1) cannot be used in calculating the energy of the observed electron–hole liquid.[8)] Furthermore, although the second of inequalities (2) is formally valid, the ultraquantum limit for holes is not achieved, as follows from the data in Fig. 11b. Nevertheless, it makes sense to compare our data to the theoretical predictions.

The theory yields the equilibrium density of the electron–hole liquid,

$$n_0(H)\simeq 0.03\left(\frac{m_h}{m_e}\right)^{1/7}\left(\frac{a_{\rm ex}}{a_H}\right)^{16/7}a_{\rm ex}^{-3}\propto H^{8/7}, \tag{7}$$

and the energy per pair of particles in the liquid ground state,

$$E_0(H)\simeq 0.84E_{\rm ex}\left(\frac{m_h}{m_e}\right)^{2/7}\left(\frac{a_{\rm ex}}{a_H}\right)^{4/7}\propto H^{2/7}. \tag{8}$$

The graphs in Figs. 11a and 14 demonstrate that the liquid density grows with the magnetic field slower than predicted by Eq. (7), and the energy per electron–hole pair grows more rapidly than in Eq. (8). The latter circumstance probably results from the rapid growth with magnetic field in the sum of the exchange and correlation energies E_{xc} (Fig. 14), which was calculated by the formula $E_{xc}=E_{gL}-E_g+(2/3)E_F$. Note that the theory of strongly compressed electron–hole liquid whose electrons and holes have very different effective masses for the case when the ultraquantum limit is achieved only for the lighter carriers yields a steeper function $E_0(H)$ ($E_0\propto H^{2/5}$) than that in Eq. (8). But in this case the density n_0 also grows more rapidly with the magnetic field ($n_0\propto H^{6/5}$).[12,18]

The density and energy per electron–hole pair in the liquid ground state estimated using Eqs. (7) and (8) at $m_e=0.014m_0$, $m_h=m_1=0.075m_0$, $a_{\rm ex}=800$ Å, and $|E_{\rm ex}|=0.5$ meV are $n_0\simeq 2.6\cdot 10^{15}$ cm^{-3} and $|E_0|\simeq 1.7$ meV at $H=23$ kOe and $n_0\simeq 7\cdot 10^{15}$ cm^{-3}, $|E_0|\simeq 2.1$ meV at $H=55.2$ kOe. The estimates of n_0 are in excellent agreement with the experimental data given in Fig. 11a (this agreement is probably accidental), whereas the estimates of $|E_0|$ are lower than the experimental values (Fig. 14). However, in light of the above reasoning concerning the applicability of this theory to our results, we should not have expected quantitative agreement between the theory and experiment.

The theory of electron–hole liquid in strong magnetic fields predicts emergence of a dielectric gap in its energy spectrum because of the quasi-one-dimensional nature of the carrier motion,[21,27,28,58] and the formation of a dielectric liquid is more probable at ''intermediate'' magnetic field strengths.[28] It seems probable that the ''overcooling'' of the electron–hole liquid with respect to the crystal lattice discussed at the end of the previous section may indicate the emergence of a dielectric gap in the spectrum.

In conclusion, let us compare the density of the electron–hole liquid in InSb stabilized by magnetic field to that of liquids in other semiconductors. As usual, we will characterize it by the dimensionless parameter $r_s=[(4/3)\pi a_{\rm ex}a_H^2n_0]^{-1/3}$. As the magnetic field varies between 23 and 55 kOe, r_s increases from $\simeq 1.5$ to $\simeq 1.6$. These values of r_s are greater than that in the electron–hole liquid in germanium ($r_s=0.5$) and silicon ($r_s=0.86$), but

lower than in direct band gap semiconductors ($r_s \simeq 2$), and it approximately equals that in strongly deformed germanium and silicon.[14–17]

6. CONCLUSIONS

As a result of our studies, we have demonstrated that formation of electron–hole liquid stabilized by applied magnetic field in semiconductors is possible. In indium antimonide it is stable in a magnetic field stronger than $\simeq 20$ kOe. Unlike germanium, not only the binding energy per electron–hole pair in the liquid ground state increases with the magnetic field in its stability region, but the exciton work function in the liquid (i.e., the liquid stability) also increases and reaches $\simeq 1.2$ meV at $H \simeq 55$ kOe. This statement relates to unstrained germanium. It is possible that magnetically stabilized electron–hole liquid also exists in highly deformed germanium.[59]

In our opinion, similar experiments in stronger magnetic fields would be interesting. Under these conditions one could measure the basic thermodynamic parameters of the electron–hole liquid as functions of the magnetic field intensity when the ultraquantum limit has been reached not only for electrons, but also for holes. One could also investigate the feasability of forming a dielectric liquid, metal–dielectric transition in the liquid phase, and other interesting phenomena.[12,18,21,27,28,58]

It is noteworthy that investigations of an electron–hole liquid and other electronic systems in strong magnetic fields are not only interesting in themselves, but can be also applied to systems with a quasi-one-dimensional spectrum without magnetic field. Experimental investigation of the conditions under which the electron–hole liquid can emerge in quasi-one-dimensional systems and other low-dimensional structures have been started quite recently (e.g., see Ref. 60), and such research may be interesting with a view toward studying interparticle interactions in such systems.

We are deeply grateful to L. V. Keldysh, Yu. V. Kopaev, and Al. L. Efros for their attention and fruitful discussions of this work, and to M. L. Skorikov for help in data processing and discussions.

This work was supported by the International Science Foundation and Russian Government (Project No. JGY100), by the Russian Fund for Fundamental Research (Projects Nos. 93-02-2356 and 96-02-18237), and the Scientific Council on Physics of Solid-State Nanostructures (Project No. 1-010).

[1)]Strictly speaking, the liquid binding energy per pair should be compared to the energy per exciton in an excitonic molecule (biexciton). For brevity, we do not consider this fact, all the more so since in most cases the possibility of biexciton formation can be disregarded because of their low binding energy.

[2)]The literature dedicated to the stability of the electron–hole liquid, the nature of its ground state, and phase transitions in a system of nonequilibrium charge carriers is voluminous. These and some other topics considered in this paper are discussed in the reviews[11–20] and references therein.

[3)]These relationships between n_0 and E_0 on the one hand, and H on the other, were derived using the asymptotic expression (1) for $E_{\rm corr}$.

[4)]In addition to the references mentioned above, the electron–hole liquid in a strong magnetic field was studied theoretically by Chui[31] and Bütner.[32] The concept of the magnetic stabilization of electron–hole liquid was also used by Kalugina and Skok[33,34] in their interpretation of some features in the behavior of induced radiation lines from indium antimonide. These features, however, were detected at magnetic fields considerably lower than those needed for the liquid stabilization, so an alternative interpretation is required.

[5)]Other views on the nature of this luminescence line are presented in Refs. 46–50. References to earlier publications and detailed discussion of this issue can be found in Refs. 38, 44, and 51.

[6)]The line emerging at zero field was also studied in Refs. 46 and 47. It was called the B-line and interpreted in a different way.

[7)]We express our gratitude to Al. L. Efros, who made available for us the results of these calculations and also the calculations of the indium antimonide valence band energy spectrum in magnetic field, from which we could derive the values of m_1, m_2, and μ.

[8)]The condition of strong compression would be satisfied in indium antimonide at $H > 5 \cdot 10^5$ kOe.

[1] W. F. Brinkman, T. M. Rice, P. W. Anderson, and S. T. Chui, Phys. Rev. Lett. **28**, 961 (1972).
[2] P. Vashishta, P. Bhattacharyya, and K. S. Singwi, Phys. Rev. Lett. **30**, 1248 (1973); Phys. Rev. B **10**, 5108 (1974).
[3] L. V. Keldysh and A. P. Silin, Zh. Éksp. Teor. Fiz. **69**, 1053 (1975) [Sov. Phys. JETP **42**, 535 (1975)].
[4] G. Beni and T. M. Rice, Phys. Rev. Lett. **37**, 874 (1976).
[5] M. Rössler and R. Zimmermann, Phys. St. Sol. (b) **83**, 85 (1977).
[6] G. Beni and T. M. Rice, Phys. Rev. B **18**, 768 (1978).
[7] V. S. Bagaev, T. I. Galkina, O. V. Gogolin, and L. V. Keldysh, JETP Lett. **10**, 195 (1969).
[8] Ya. E. Pokrovskii and K. I. Svistunova, Fiz. Tekh. Poluprovod. **4**, 491 (1970).
[9] A. S. Kaminskii, Ya. E. Pokrovskii, and N. V. Alkeev, Zh. Éksp. Teor. Fiz. **59**, 1937 (1970) [Sov. Phys. JETP **32**, 1048 (1970)].
[10] V. S. Bagaev, T. I. Galkina, and O. V. Gogolin, in *Excitons in Semiconductors* [in Russian], B. M. Vul (ed.), Nauka, Moscow (1971), p. 19.
[11] Ya. E. Pokrovskii, Phys. St. Sol. (a) **11**, 385 (1972).
[12] L. V. Keldysh, in *Modern Problems in Condensed Matter Sciences*, ed. by V. M. Agranovich and A. A. Maradudin (eds.), North-Holland, Amsterdam (1983), vol. 6: *Electron-Hole Droplets in Semiconductors*, C. D. Jeffries and L. V. Keldysh (eds.), Introduction, p. XI.
[13] V. S. Bagaev, T. I. Galkina, and N. N. Sibeldin, in Ref. 12, Ch. 4, p. 267.
[14] T. M. Rice, in *Solid State Physics*, H. Ehrenreich, F. Seitz, and D. Turnbull (eds.), Academic Press, New York (1977), Vol. 32, p. 1.
[15] J. C. Hensel, T. G. Phillips, and G. A. Thomas, in Ref. 14, p. 88.
[16] P. Vashishta, R. K. Kalia, and K. S. Singwi, in Ref. 12, Ch. 1, p. 1.
[17] V. D. Kulakovskii and V. B. Timofeev, in Ref. 12, Ch. 2, p. 95.
[18] L. V. Keldysh, Contemp. Phys. **27**, 395 (1986).
[19] S. G. Tikhodeev, Usp. Fiz. Nauk **145**, 3 (1985) [Sov. Phys. Usp. **28**, 1 (1985)].
[20] L. V. Keldysh and N. N. Sibeldin, in *Modern Problems in Condensed Matter Sciences*, V. M. Agranovich and A. A. Maradudin (eds.), North-Holland, Amsterdam (1986), Vol. 16: *Nonequilibrium Phonons in Nonmetallic Crystals*, W. Eisenmenger and A. A. Kaplyanskii (eds.), Ch. 9, p. 455.
[21] L. V. Keldysh and T. A. Onishchenko, JETP Lett. **24**, 59 (1976).
[22] E. A. Andryushin, V. S. Babichenko, L. V. Keldysh *et al.*, JETP Lett. **24**, 185 (1976).
[23] E. A. Andryushin, L. V. Keldysh, and A. P. Silin, Zh. Éksp. Teor. Fiz. **73**, 1163 (1977) [Sov. Phys. JETP **46**, 616 (1977)].
[24] R. J. Elliott and R. Loudon, J. Phys. Chem. Sol. **15**, 196 (1960).
[25] B. P. Zakharchenya and R. P. Seisyan, Usp. Fiz. Nauk **97**, 193 (1969) [Sov. Phys. Usp. **12**, 70 (1969)].
[26] R. P. Seisyan, *Spectroscopy of Diamagnetic Excitons* [in Russian], Nauka, Moscow (1984).
[27] T. A. Onishchenko, Trudy FIAN **123**, 7 (1980).
[28] A. P. Silin, in Ref. 12, Ch. 8, p. 619.
[29] L. P. Gor'kov and I. E. Dzyaloshinskii, Zh. Éksp. Teor. Fiz. **53**, 717 (1967) [Sov. Phys. JETP **26**, 449 (1967)].
[30] I. V. Kavetskaya, Ya. Ya. Kost', N. N. Sibel'din, and V. A. Tsvetkov, JETP Lett. **36**, 311 (1982).
[31] S. T. Chui, Phys. Rev. B **9**, 3438 (1974).
[32] H. Bütner, in *Proc. 12th Int. Conf. Phys. Semicond.*, Teubner, Stuttgart (1974), p. 81.
[33] N. A. Kalugina and É. M. Skok, JETP Lett. **38**, 297 (1983).
[34] N. A. Kalugina and É. M. Skok, Fiz. Tverd. Tela **27**, 528 (1985).

[35] H. L. Störmer and R. W. Martin, Phys. Rev. B **20**, 4213 (1979).
[36] I. V. Kavetskaya, N. N. Sibeldin, and V. A. Tsvetkov, Sol. St. Comm. **97**, 157 (1996).
[37] I. V. Kavetskaya and N. N. Sibel'din, JETP Lett. **38**, 76 (1983).
[38] I. V. Kavetskaya, N. N. Sibel'din, and V. A. Tsvetkov, Zh. Éksp. Teor. Fiz. **105**, 1714 (1994) [JETP **78**, 926 (1994)].
[39] V. D. Kulakovskii, I. V. Kukushkin, and V. B. Timofeev, Zh. Éksp. Teor. Fiz. **81**, 684 (1981) [Sov. Phys. JETP **54**, 366 (1981)].
[40] V. B. Stopachinskii, Zh. Éksp. Teor. Fiz. **72**, 592 (1977) [Sov. Phys. JETP **45**, 310 (1977)].
[41] T. M. Bragina, Yu. S. Lelikov, and Yu. G. Shreter, JETP Lett. **29**, 115 (1979).
[42] M. Greenstein and J. P. Wolfe, J. de Phys. **42**, Suppl. 12, C6-276 (1981).
[43] N. V. Zamkovets, N. N. Sibel'din, and V. A. Tsvetkov, Zh. Éksp. Teor. Fiz. **105**, 1066 (1994) [JETP **78**, 572 (1994)].
[44] I. V. Kavetskaya, N. B. Kakhramanov, N. N. Sibel'din, and V. A. Tsvetkov, Zh. Éksp. Teor. Fiz. **100**, 2053 (1991) [Sov. Phys. JETP **73**, 1139 (1991)].
[45] L. M. Kanskaya, S. I. Kokhanovskii, and R. P. Seisyan, Fiz. Tekh. Poluprovod. **13**, 2424 (1979).
[46] V. I. Ivanov-Omskii, S. I. Kokhanovskii, R. P. Seisyan *et al.*, Fiz. Tekh. Poluprovod. **17**, 532 (1983) [Sov. Phys. Semicond. **17**, 334 (1983)].
[47] R. P. Seisyan and Sh. U. Yuldashev, Fiz. Tverd. Tela **30**, 12 (1988) [Sov. Phys. Solid State **30**, 6 (1988)].
[48] M. S. Bresler, O. B. Gusev, and A. O. Stepanov, Fiz. Tekh. Poluprovod. **17**, 1195 (1983) [Sov. Phys. Semicond. **17**, 755 (1983)].
[49] M. A. Alekseev, M. S. Bresler, O. B. Gusev *et al.*, Fiz. Tekh. Poluprovod. **19**, 722 (1985) [Sov. Phys. Semicond. **19**, 443 (1985)].
[50] M. S. Bresler, O. B. Gusev, and A. O. Stepanov, Fiz. Tverd. Tela (Leningrad) **28**, 1387 (1986) [Sov. Phys. Solid State **28**, 781 (1986)].
[51] I. V. Kavetskaya, N. N. Sibel'din, and V. A. Tsvetkov, Fiz. Tverd. Tela (Leningrad) **34**, 857 (1992) [Sov. Phys. Solid State **34**, 458 (1992)].
[52] Y. Yafet, R. W. Keyes, and E. N. Adams, J. Phys. Chem. Sol. **1**, 137 (1956).
[53] É. I. Zavaritskaya, Trudy FIAN **37**, 41 (1966).
[54] K. Seeger, *Semiconductor Physics*, Springer-Verlag, Wien, New York (1973).
[55] B. Lax and S. Zwerdling, in *Progress in Semiconductors*, A. F. Gibson and R. E. Burgess (eds.), Temple Press, London (1960), Vol. 5, p. 221.
[56] S. I. Kokhanovskii, PhD Thesis [in Russian], A. F. Ioffe Institute of Physics and Technology, Leningrad (1982).
[57] B. L. Gel'mont, R. P. Seisyan, Al. L. Éfros, and A. V. Varfolomeev, Fiz. Tekh. Poluprovod. **11**, 238 (1977).
[58] V. S. Babichenko and T. A. Onishchenko, JETP Lett. **26**, 68 (1977).
[59] V. B. Timofeev and A. V. Chernenko, JETP Lett. **61**, 617 (1995).
[60] H. Kalt, R. Nötzel, and K. Ploog, Sol. St. Comm. **83**, 285 (1992).

Translation was provided by the Russian Editorial office.

Effect of the features of the low-energy spectrum of vibrational states in disordered systems on the probability of the Mössbauer effect and the Debye–Waller temperature factor

L. L. Buishvili,*) L. Zh. Zakharov, I. N. Kakhniashvili, and G. L. Topchishvili

Institute of Physics, Georgian Academy of Sciences, 380077 Tbilisi, Republic of Georgia
(Submitted 27 August 1996)
Zh. Éksp. Teor. Fiz. **111**, 759–762 (February 1997)

We study the effect of the additional density of vibrational states inherent in disordered systems on the Mössbauer effect and the Debye–Waller temperature factor at temperatures of about 10 K. We show that the effect of the additional density of vibrational states shows up as an increase in the exponent in the temperature dependence of the mean-square displacement and should manifest itself in measurements of the temperature factor and the probability of a recoilless process. © *1997 American Institute of Physics.* [S1063-7761(97)02702-9]

Lately there has been an upsurge of interest in the physical properties of such disordered systems as glassy semiconductors and insulators, and metallic glasses. Studies have revealed that below 1 K neither the Debye theory nor its modifications can describe the many properties of disordered systems. To overcome this difficulty Anderson and Phillips introduced the model of two-level tunneling systems.[1] A two-level system is an atom that can be in two almost equivalent states, and tunneling is the mechanism by which a transition from one state to the other is achieved. The main characteristic feature of these excitations is that the density of states in them is only weakly dependent on energy and reaches a value of order $10^{46}\mathrm{J}^{-1}\cdot\mathrm{m}^{-3}$.

The Mössbauer effect for nuclei in samples containing two-level systems was studied in Ref. 2, where it was found that below 10 K the contribution of two-level system dominates.

Another temperature range (in addition to $T<1$ K) that is of interest here is 10 K$<T<$30 K. At such temperatures, experiments involving incoherent neutron scattering and Raman scattering of light make it possible to establish the properties that are characteristic of the spectrum of low-energy vibrational states in disordered systems and are the same both for glassy semiconductors and insulators and for metallic glasses.[3]

These experiments revealed the presence of an additional density of vibrational states in the 3–15 K interval. The nature of this additional density of states has yet to be clarified. However, it has been established that the vibrational excitations responsible for the excess density of vibrational states in glasses are localized in regions containing from several dozen to several hundred atoms. Moreover, the analysis of the spectra shows that these excitations obey Bose statistics, in view of which the excess density of vibrational states is called the bosonic peak.[3]

The bosonic peak has the form

$$\Delta f(\omega)=\Delta f_m(\omega)\exp\left[-\frac{\ln(\omega/\omega_m)}{2\sigma^2}\right],$$

where σ is a parameter equal to 0.48 that characterizes the width of the bosonic peak, $\Delta f_m(\omega)$ is the maximum value of the additional density of vibrational states, and ω_m is the frequency corresponding to this maximum. According to the experimental data, $\Delta f_m(\omega)$ exceeds the density of vibrational states in the Debye model by a factor of two to ten.[3]

The aim of the present work is to study the effect of the bosonic peak in calculations of the probability of a recoilless process. The probability of the Mössbauer effect is given by[4]

$$f=\exp(-k^2\langle u^2\rangle),$$

where k is the wave vector of a gamma ray, and $\langle u^2\rangle$ is the mean-square displacement from the equilibrium position.

As is known,[4]

$$\langle u^2\rangle=\int_0^{\omega_D}f(\omega)u(\omega)d\omega$$

$$=\int_0^{\omega_D}f(\omega)\frac{\hbar}{m_aN}\left[\frac{1}{\exp(\hbar\omega/k_BT)+1}+\frac{1}{2}\right]\frac{d\omega}{\omega},$$

where N is the number of particles in the system, m_a is the mass of the atom, $f(\omega)$ is the density of vibrational states, ω_D is the Debye frequency corresponding to the Debye temperature Θ, and k_B is the Boltzmann constant.

With allowance for the bosonic peak,

$$f(\omega)=a\left\{f_D(\omega)+10f_D(\omega_D)\exp\left[\frac{-\ln^2(\omega_m/\omega)}{2\sigma^2}\right]\right\},$$

where a is the normalization constant, which to high accuracy can be assumed equal to $9N/\omega_D^3$, and $f_D(\omega)$ is the Debye density of states, equal to $a\omega^2$.

Taking all this into account, we can now write

$$\langle u^2\rangle=\langle u^2\rangle_D+\langle u^2\rangle_{\mathrm{bos}},$$

where $\langle u^2\rangle_D$ the mean-square displacement in the Debye model, and $\langle u^2\rangle_{\mathrm{bos}}$ is the displacement that results from the presence of an additional density of vibrational states. As is known, in the $T\ll\Theta$ approximation the expression for $\langle u^2\rangle_D$ has the form

$$\langle u^2\rangle_D=\frac{9\hbar^2}{m_ak_B\Theta}\left[\frac{1}{4}+\left(\frac{T}{\Theta}\right)^2\frac{\pi^2}{6}\right].$$

 1063-7761/97/020417-02$10.00

For $\langle u^2\rangle_{\rm bos}$ we can write

$$\langle u^2\rangle_{\rm bos}=\frac{10\times 9\hbar^2}{m_a k_B\Theta}\,\frac{\hbar\omega_m}{k_B\Theta}\int_0^{\omega_D}\left[\frac{1}{\exp(\hbar\omega/kT)+1}+\frac{1}{2}\right]\times\exp\left[\frac{-\ln^2(\omega_m/\omega)}{2\sigma^2}\right]\frac{d\omega}{\omega}. \quad (1)$$

To describe the contribution of the additional density of vibrational states to the total probability of the Mössbauer effect we examined Ir^{193}, Au^{197}, and Eu^{153} nuclei, which were impurities in solids with a Debye temperature $\Theta \sim 1000$ K. The values of the gamma ray energy and the recoil energy were taken from Ref. 4 and are, respectively, 73 and 1.5×10^{-5} keV, 77.3 and 1.6×10^{-5} keV, and 97.4 and 3.3×10^{-5} keV. Bearing in mind what was said earlier about the probability of a recoilless process calculated by the Debye method, we have

$$f_D(\mathrm{Ir}^{193})\propto\exp(-0.26-0.17\times10^{-5}T^2),$$

$$f_D(\mathrm{Au}^{197})\propto\exp(-0.28-0.18\times10^{-5}T^2),$$

$$f_D(\mathrm{Eu}^{153})\propto\exp(-0.57-0.38\times10^{-5}T^2).$$

To estimate the contribution of the additional density of vibrational states to the total probability of recoilless process, we integrated Eq. (1) numerically and found that

$$f_{\rm bos}(\mathrm{Ir}^{193})\propto\exp(-7.9\times10^{-2}-0.50\times10^{-5}T^{2.5}),$$

$$f_{\rm bos}(\mathrm{Au}^{197})\propto\exp(-8.0\times10^{-2}-0.51\times10^{-5}T^{2.5}),$$

$$f_{\rm bos}(\mathrm{Eu}^{153})\propto\exp(-6.2\times10^{-2}-0.40\times10^{-5}T^{2.5}).$$

In addition to entering into the probability of the Mössbauer effect, $\langle u^2\rangle$ enters into the formula for the Debye–Waller temperature factor, which according to Ref. 5 has the form

$$I=e^{-2B},$$

where

$$B=8\pi^2\langle u^2\rangle\frac{\sin\alpha}{\lambda^2},$$

with λ the wavelength of the x rays, and α is the diffraction angle.

As an example we study the variation of the temperature dependence of $\langle u^2\rangle$ in the presence of an additional density of vibrational states for Al^{27}. After plugging the values of the parameters of Al^{27} into Eq. (1) and numerically integrating this equation, over the $0<T<\hbar\omega_m/k_B$ temperature range we have

$$\langle u^2\rangle_{\rm bos}\approx 7\times10^{-7}T^{2.5}+1.1\times10^{-2},$$

and

$$\langle u^2\rangle_D\approx 7\times10^{-7}T^{1.9}+0.9\times10^{-2}.$$

Our studies suggest that in calculating the probability of the Mössbauer effect and the Debye–Waller factor near 10 K, one must allow for special features of the low-energy spectrum of vibrational states; in particular, for the additional density of vibrational states and the effect of two-level systems (the latter has been examined in Ref. 2). The effect of the additional density of vibrational states shows up as an increase in the exponent in the temperature dependence of $\langle u^2\rangle$ from 2 to 2.5–2.7 and should manifest itself in measurements of the temperature factor and the probability of the Mössbauer effect.

This work was made possible by a grant from the International Science Foundation (Grant No. MX K000).

*)Deceased.

[1] B. P. Smolyakov and E. P. Khaĭmovich, Usp. Fiz. Nauk **136**, 317 (1982).
[2] L. L. Buishvili, L. Zh. Zakharov, G. L. Topchishvili, A. I. Tugushi, and D. A. Éristavi, Zh. Éksp. Teor. Fiz. **106**, 1436 (1994) [JETP **79**, 775 (1994)].
[3] V. K. Malinovskiĭ, V. N. Novikov, and A. P. Sokolov, Usp. Fiz. Nauk **163**, No. 5, 119 (1993) [Phys. Usp. **36**, 440 (1993)].
[4] V. S. Shpinel', *Resonance of X Rays in Crystals* [in Russian], Nauka, Moscow (1969).
[5] A. Guinier, *X-Ray Crystallographic Technology*, Hilger & Watts, London (1952).

Translated by Eugene Yankovsky

Erratum: The induced phase transition of a nonlinear oscillator interacting with a coherent electromagnetic field [JETP 83, 653–660 (1996)]

P. I. Bardetskiĭ

Moldova Technical University, 277068 Kishinev, Republic of Moldova

N. A. Enaki

Institute of Applied Physics, Moldavian Academy of Sciences, 277028 Kishinev, Republic of Moldova

D. Michalache

Institute of Atomic Physics, Bucharest, Republic of Romania

The spelling of the last name of the third author should read as follows: ''D. MIHALACHE''.

The affiliation of the third author should read as follows: ''Institute of Atomic Physics, Bucharest, Romania''.

 1063-7761/97/020419-01$10.00